

XV INTERNATIONAL SCIENTIFIC CONGRESS

WINTER SESSION

14 - 17.03.2018, BOROVELTS BULGARIA



MACHINES. TECHNOLOGIES. MATERIALS 2018

PROCEEDINGS

VOLUME I

ISSN 2535-0021 (PRINT)

ISSN 2535-003X (ONLINE)

SCIENTIFIC-TECHNICAL UNION OF MECHANICAL ENGINEERING - INDUSTRY 4.0
BULGARIA

INTERNATIONAL SCIENTIFIC CONFERENCE
MACHINES. TECHNOLOGIES. MATERIALS

14-17.03.2018, BOROVELTS, BULGARIA

PROCEEDINGS

YEAR II, ISSUE 1 (8), SOFIA, BULGARIA 2018

VOLUME I

ISSN 2535-0021 (PRINT)
ISSN 2535-003X (ONLINE)

PUBLISHER:

**SCIENTIFIC TECHNICAL UNION OF MECHANICAL
ENGINEERING
INDUSTRY-4.0**

108, Rakovski Str., 1000 Sofia, Bulgaria
tel. (+359 2) 987 72 90,
tel./fax (+359 2) 986 22 40,
office@mtmcongress.com
www.mtmcongress.com

INTERNATIONAL EDITORIAL BOARD

Chairman: Prof. DHC Georgi Popov

Members:

Acad. Ivan Vedyakov	RU
Acad. Yuriy Kuznetsov	UA
Prof. Aleksander Mihaylov	UA
Prof. Anatoliy Kostin	RU
Prof. Adel Mahmud	IQ
Prof. Ahmet Ertas	TR
Prof. Andrzej Golabczak	PL
Prof. Boncho Bonev	BG
Prof. Gennady Bagluk	UA
Prof. Detlef Redlich	DE
Prof. Dipten Misra	IN
Prof. Dmitry Kaputkin	RU
Prof. Eugene Eremin	RU
Prof. Ernest Nazarian	AM
Prof. Juan Alberto Montano	MX
Prof. Esam Husein	KW
Prof. Ivo Malakov	BG
Prof. Krasimir Marchev	USA
Prof. Leon Kukielka	PL
Prof. Lyudmila Ryabicheva	UA
Prof. Milan Vukcevic	ME

Vice Chair: Prof. Dr. Eng. Tsanka Dikova

Prof. Mladen Velez	BG
Prof. Mohamed El Mansori	FR
Prof. Movlazade Vagif Zahid	AZ
Prof. Nikolay Dyulgerov	BG
Prof. Oana Dodun	RO
Prof. Olga Krivtsova	KZ
Prof. Peter Kostal	SK
Prof. Raul Turmanidze	GE
Prof. Renato Goulart	BR
Prof. Roumen Petrov	BE
Prof. Sasho Guergov	BG
Prof. Seiji Katayama	JP
Prof. Sergej Dobatkin	RU
Prof. Sergej Nikulin	RU
Prof. Stefan Dimov	UK
Prof. Svetan Ratchev	UK
Prof. Svetlana Gubenko	UA
Prof. Tale Geramitchioski	MK
Prof. Vadim Kovtun	BY
Prof. Viktor Vaganov	RU
Prof. William Singhose	USA
Prof. Yasar Pancar	TR

CONTENTS

SECTION MACHINES

ROTATIONAL MOTION OF TOWER CRANE - DYNAMIC ANALYSIS AND REGULATION USING SCHEMATIC MODELING Prof.dr. Doçi Ilir, Prof.ass. Lajqi Shpetim	5
EFFECT OF BORONIZING PARAMETERS AND MATRIX STRUCTURES ON THE WEAR PROPERTY OF DUCTILE IRON Ass. Prof. Dr. Toktaş A., Ass. Prof. Dr. Toktaş G., MSc. Mech. Eng. Gülsün K.	10
ERGONOMIC ASPECTS WHEN DESIGNING LUMINAIRES BASED ON LED LAMPS Ass Prof.Vinogradov V.V., Ass Prof.Mokretsova L.O.	14
MODEL FOR DETERMINING THE STATIC LOAD ON MOVABLE SPATIAL CONSOLE LATTICE GIRDER BOUNDED WITH CLAMPS Prof. Dr. Sc. Hristovska E., mech. eng., Assis. Prof. Dr. Sc. Sevde Stavreva, Prof. Dr. Sc. Vangelica Jovanovska, Assoc. Prof. Dr. Sc. Ivo Kuzmanov, Assoc. Prof. Dr. Sc. Zlatko Sovreski	20
CHANGE IN OPERATING PARAMETERS OF TURBOCHARGED DIRECT INJECTION DIESEL ENGINE DURING THE INJECTED FUEL MASS FLOW VARIATION PhD. Mrzljak Vedran, PhD Student Eng. Poljak Igor, Student Žarković Božica	23
ENERGY EFFICIENCY AND ENERGY POWER LOSSES OF THE TURBOGENERATORSTEAM TURBINE FROM LNG CARRIER PROPULSION SYSTEM PhD. Mrzljak Vedran, PhD. Senčić Tomislav, Prof. Prpić-Oršić Jasna	27
THE IMPACT OF THE CONSTRUCTIVE PARAMETERS OF THE BUMPER OVER THE CONSEQUENCES DERIVING FROM THE PROCESS OF COLLISION M. Sc. Gjakovski I., M. Sc. Shareska-Gjakovska V., Ph.D. Brkovski D., M.Sc. Milev S.	31
EMBEDDED RESEARCHES ON ADAPTIVE PARAMETRIC MODELING OF HYDRAULIC GEAR PUMPS Lecturer PhD. Eng. Ghionea Gabriel Ionuț, Prof. PhD Eng. Opran Constantin Gheorghe, Lecturer PhD Eng. TARBĂ Cristian Ioan, PhD. Eng. Ćuković Saša	35
THE TIMELESS DESIGN OR THE WELL DONE OLD гл. ас. д-р Кремена Маркова	39
NUMERICAL SIMULATION ON THE VIBRATION OF A VEHICLE DRIVETRAIN WITH DUAL MASS FLYWHEEL Assist. Prof. Eng. Pavlov N. PhD	42
KINEMATIC AND POWER ANALYSIS OF MULTI-STAGE PLANETARY GEARBOXES THROUGH THE TORQUE METHOD Assoc. Prof. Dr. Karaivanov D., Velyanova M., Bakov V.	46
<u>SECTION TECHNOLOGIES</u>	
ON THE APPLICATION OF FUNCTIONAL APPROACH TO CREATING AND PROVIDING OPERATIONAL CHARACTERISTICS OF ULTRALIGHT THERMAL PROTECTION OF REUSABLE LAUNCH SPACECRAFT Prof. Dr. Eng. Salenko O., Prof. Ph. D. Eng. Shchetynin V., Lashko E., Ph. D. Eng. Potapov O., Ph. D. Eng. Gusarova I.	53
BUSINESS CLIMATE AND PRECONDITIONS FOR REVIVING THE BULGARIAN INDUSTRY Mina Angelova, Valentina Nikolova-Alexieva	61
USING THE PLANNING PROCESS TO CONSTRUCTION MANAGEMENT OF THE IRRIGATION INFRASTRUCTURE Assos. Prof. Eng. Banishka N. PhD., Eng. Vasileva M. PhD St.	64
RESEARCH OF INTELLIGENT TRANSPORT SYSTEMS MANAGEMENT OF CONVOY OF UNMANNED VEHICLES WITH THE LEAD PILOT VEHICLE FOR WORK IN THE NORTH OF THE RUSSIAN FEDERATION IN THE ARCTIC AND ANTARCTIC Dr.Sci.Tech, Saykin A., Ph.D., Endachev D., Ph.D., associate professor, Karpukhin K., Ph.D Kolbasov A.	67
DEPENDENCE OF THE ACTIVE POWER OF THE SERIAL RESONANT BRIDGE CONVERTER FROM THE PHASE DIFFERENCE AND THE DUTY CYCLE Assist. prof. Dr. Eng. Stefanov G., Prof. Dr. Eng. Karadzinov Lj., Assos. prof. Dr. Eng. Sarac V., Prof. Dr. Eng. Atanasova-Pacemska T., Assist. M.Sc. Kukuseva Paneva M., Prof. Dr. Eng. Dambov R.	71
PRECISE 3D CARTOGRAPHIC DESIGN USING BING-MAPS RESOURCES, 3D BLENDER AND THE SPECIALIZED BLENDERGIS-ADDON APPLICATION Tihomir Dovramadjiev PhD	75
THE DEVELOPMENT OF CALIBRATION FOR THE ROLLING BALLS OF DIAMETER 40 MM IN CONDITIONS OF JSC "SSGPO" D.t.s., professor Naizabekov A., c.t.s., associate professor Lezhnev S., Stepanov E., PhD Panin E.	77

MICROBIAL CLEANING OF MINE WATERS FOLLOWED BY ELECTRICITY GENERATION Irena Spasova, Marina Nicolova, Plamen Georgiev, Stoyan Groudev, Veneta Groudeva	80
EXTRACTION OF PRECIOUS METALS FROM A PYRITIC CONCENTRATE PRETREATED BY MICROBIAL OXIDATION Irena Spasova, Marina Nicolova, Plamen Georgiev, Stoyan Groudev	82
INFLUENCE OF GRID LAYOUT AND WHITE SPACE ON THE COMPOSITION OF WEB TYPOGRAPHY гл. ас. д-р Илиев И.	84
ADVANCED HYDROGEN STORAGE TECHNOLOGIES Gjorgji Dosev, Nikola Sokolov, Assoc. Prof. Aleksandar Kostikj, PhD	87
THE INVESTIGATION OF THE NANORELIEFS OF OPTICAL ELEMENTS OF MEASURING INSTRUMENTS, WHICH MODIFIED BY ELECTRON-BEAM MICROPROCESSING Skoryna E., Medyanyk V., PhD. Bondarenko M., PhD Bondarenko I., PhD Bilokin S., Prof. dr. eng. Antoniuk V.	90
THEORETICAL AND NUMERICAL ASPECTS REGARDING THE THERMOELASTIC BEHAVIOUR OF RUBBERLIKE POLYMERS M.Sc. Szüle V.	94
OPTIONS OF REAL TIME MONITORING METALWORKING FLUIDS Ing. Jurina F., Prof. Dr. Ing. Peterka J.	98
CONTEMPORARY METHODS FOR OBTAINING NON-FERROUS AND RARE METALS FROM PRIMARY AND TECHNOGENIC RAW MATERIALS Assoc. Prof. PhD Vania Vassileva, Eng. Georgi Savov, Prof. DSc. PhD Katia Vutova, Assoc. Prof. PhD Valeriya Kovacheva-Ninova, Eng. Evgeni Petrov	102
MODELLING CONCEPTS FOR EFFICIENT PORT LOGISTICS MANAGEMENT Senior Assistant Prof. PhD Varbanova A.	107
EVALUATING THE IMPACT OF SECURITY MEASURES ON CONTAINER SUPPLY CHAINS Senior Assistant Prof. PhD Varbanova A.	110
ADMINISTRATIVE PROCESS MODELING: BASIC STRUCTURES AND MODELING M.Sc. Trashlieva V., M.Sc. Radeva T. PhD	114
<u>SECTION MATERIALS</u>	
NEW STEELS FOR METAL CONSTRUCTIONS IN THE DESIGN STANDARDS AND REGULATIONS Vedyakov I.I. the Doctor of Technical Sciences, Professor, Odessky P.D. the Doctor of Technical Sciences, Professor, Gurov S.V. engineer, Konina S.M. engineer	118
ION PLAZMA NITRIDING OF MECHANICAL PARTS Ass. Jashari N. MSc, Prof. Dr Cvetkovski. S. PhD., Nacevski G. PhD.....	124
SOFTWARE DEVELOPMENT FOR NUMERICAL SIMULATION OF FORMATTING THE PERIODIC NANOSTRUCTURES AFTER LASER IRRADIATION B.Sc. Phys. Zaimis U., Prof. Dr. Sc. Comp. Jansone A.	127
STUDY OF STRUCTURE FORMATION AND HARDENING IN CARBON STEELS DURING HPT AT TEMPERATURES BELOW RECRYSTALLIZATION Dr.Sci. Raab G., Dr.Sci. Aleshin G., Kodirov I., Raab A.	132
THE LABORATORY TESTING OF STEEL 20MnCr5 Opačak I., mag.ing.mech., Marić A., dipl.ing., Hon.D.Sc. Dašić P., Prof. dr. sc. Marušić V.	136
EFFECTS OF MECHANOCHEMICAL TREATMENT OF ThO₂ WITH UO₃ AND CeO₂ Assoc. Prof. P. Kovacheva PhD, Prof. D. Todorovsky DSc, M. Sc. N. Mirchev	140
APPLICATION OF NONLINEAR CONTROLLED COOLING REGIMES FOR STRUCTURE FORMATION MANAGEMENT IN EUTECTOID STEEL Ph.D. Kaverinsky V., Prof., Dr.Sc. Trotsan A., eng. Sukhenko Z. , Prof., Dr.Sc. Bagliuk G.	144
A INVERSE PROBLEM IN ULTRASONIC TESTING AND MECHANICAL PROPERTIES OF POLYCRYSTALLINE MATERIALS Assoc. Prof, PhD. Alexander Popov, MSc Eng. Georgy Dobrev	146
MICROSTRUCTURAL EVOLUTION AND MECHANICAL PROPERTIES OF ALUMINUM IN THE PROCESS "PRESSING-DRAWING" Prof. dr. Nayzabekov A., Ass.prof. Lezhnev S., Ph.D. Volokitina I., Volokitin A.	148

ROBUST BI-CRITERIA APPROACH TO OPTIMIZE THE COMPOSITION AND PROPERTIES OF MAGNESIUM ALLOY Yordan Kalev, Hai Hao, Nikolay Tontchev	151
THE IMPACT OF ELECTRIC FIELD DISTRIBUTION DURING Ti – Al – C SYSTEM BLEND PREPARATION ON PHYSICAL-MECHANICAL PROPERTIES OF CONSOLIDATED MATERIALS Prof., Dr. of Science Sizonenko O., PhD Zaichenko A., Lypian Ye., PhD Prystash M., Torpakov A., PhD Trehub V.	156
SOLIDIFICATION ON SURFACE Ass. Prof. Eng. St. Bushev PhD, Ass. Prof. Eng. I. Georgiev PhD	160
МЕТОДИ И СРЕДСТВА ЗА ОПТИМИЗАЦИЯ НА ТЕХНОЛОГИЧНИ РЕЖИМИ ПРИ ЛЕЕНЕ ВЪЗ ОСНОВА НА ЧИСЛЕНА СИМУЛАЦИЯ Asst. Prof. Emil Yankov. PhD.	164
ТЕОРЕТИЧЕН АНАЛИЗ НА ПРОЦЕСА ХИДРАВЛИЧНО ИЗДУВАНЕ Asst. Prof. Emil Yankov. PhD.	165

ROTATIONAL MOTION OF TOWER CRANE - DYNAMIC ANALYSIS AND REGULATION USING SCHEMATIC MODELING

Prof.dr. Doçi Ilir, Prof.ass. Lajqi Shpetim*

Faculty of Mechanical Engineering –University of Prishtina, Kosovo (ilir.doci@uni-pr.edu)

*Corresponding author (shpetim.lajqi@uni-pr.edu)

Abstract: This paper deals with dynamic analysis of particular type Construction Cranes known as tower crane during rotational motion of its jib. Methodology of analysis consists of Schematic Design of model, which implements schemes with block diagrams to analyze cranes and their parts during particular work cycle. This procedure consists of crane model development of interconnected elements that represents crane parts, 3-D visualization and simulation of motion. Analysis will be carried out through simulations, and solution of Euler differential equations of second order gained from schematic model. Dynamic parameters investigated are: acceleration, angular velocity, forces and torques in main parts of crane, and influence of load swinging. Diagrams will be presented for main parts of crane as the solution results of the analyzed system. Results gained will be used to get conclusions about dynamic behavior of crane, present graphs of main parameters and search for regulation of optimal jib rotation. Analysis will be done using modeling and simulations with computer application MapleSim. Also, results gained from simulations will be compared with those from experimental measurements.

Keywords: TOWER CRANE, CRANE'S JIB, SCHEMATIC DESIGN, DYNAMIC ANALYSIS, ROTATIONAL MOTION, SYSTEMS REGULATION, MODELING, SIMULATIONS

1. Introduction

Tower crane taken for analysis is tower crane, the type of construction cranes with horizontal jib attached to the mast. Model of tower Crane is designed with software MapleSim 6.1 [3]. It is created based on data from manufacturer Wolff (Fig.1), [1]. Technical data for the model of crane are: Length of Jib: $L_j = 44 \text{ m}$, Mass of Jib: $m_j = 5230 \text{ kg} = 51.3 \text{ kN}$; Mass of counterweight jib: $m_{lj} = 2000 \text{ kg} = 19.62 \text{ kN}$; Counterweight mass: $m_{co} = 8000 \text{ kg} = 78.48 \text{ kN}$; Height of Mast: $L_{ms} = 28.7 \text{ m}$, Height of upper mast: $L_{ums} = 4 \text{ m}$, Mass of mast: $m_a = 27310 \text{ kg} = 268 \text{ kN}$; Max carrying load: $Q_{max} = 62 \text{ kN}$; Jib angular velocity: $\omega = 3.5 \text{ deg/s}$. (Fig.2)



Fig. 1. Crane type Wolff 6531.6, at the place of work [1]

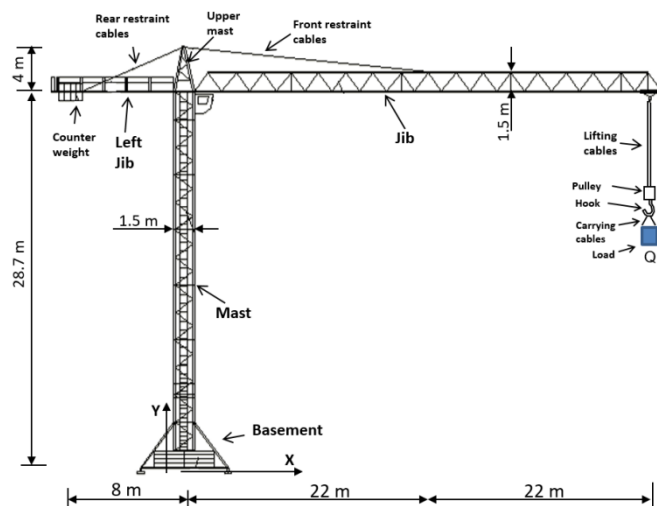


Fig.2. Tower crane main parts and dimensions [1]

Study is based in the theory of crane dynamics, multibody dynamics and systems design. It is a contribution to the topics of cranes: dynamic analysis, Modeling & Simulation of construction cranes, control and optimization of rotational motion, Sustainable design and control, Safety of heavy lifting devices.

2. Schematic design of Tower crane

In Fig. 3 is presented schematic design and block diagram of tower crane created with software MapleSim 6.1, which enables topological representation and interconnects related components [3]. Schematic diagram is created in order to apply analysis, generate differential equations and apply simulations. Elements of diagram are chosen to best represent parts of crane and its motion through simulations.

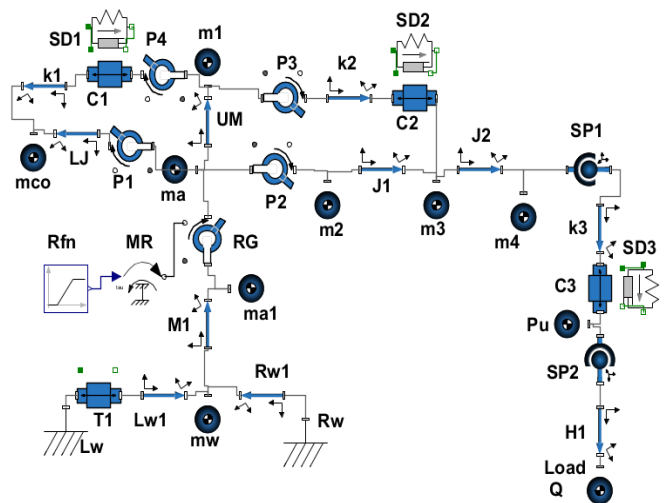


Fig. 3. Block Diagram of tower crane with jib rotational motion

Block diagram starts from left, with basement and mast of crane, and continues to the right where hoisting and Load Q is connected. All crane parts are designed with these elements (Fig.3):

- **Rigid body frames (bars):** Basement frames, left and right – $Lw1$ & $Rw1$; Mast- $M1$; Upper Mast- UM ; Counterweight Jib- LJ ; Jib first part- $J1$; Jib second part- $J2$;

- **Fixed Frames** – Left basement restraint - Lw ; Right basement restraint – Rw .

- **Concentrated masses:** Basement mass – mw ; Mass of mast – ma , $ma1$; Mass of upper mast- $m1$, Counterweight mass - mco ; Masses of Jib- $m2$, $m3$, $m4$; Mass of Pulley system – Pu ; Load - Q ;

- **Revolute joints**: Rotation Gear - RG; Rotation links - P1, P2, P3, P4; **Spherical links**: Link between jib and telpher - SP1; Hook link with pulley system - SP2.

On the Rotation Gear - RG is attached rotation motor MR, the element that gives the power - torque necessary to rotate the crane with angular velocity $\omega = 3.5 \text{ deg/s}$. For best simulation scenario is implemented ramp function connected to rotation motor - Rfn.

- **Restrain cables** - are created with spring and dumping elements SD1 & SD2, translation link - C1 & C2, cable length - k1 & k2. Left side restraint cables elements - k1, C1, SD1; Right side restraint cables elements - k2, C2, SD2; Spring constant for restraint cables is $k = 500 \text{ kN/m}$ and Damping constant is $d = 7 \text{ kNm/s}$ [11].

- **Lifting cables** - are created with Spring and dumping element SD3, translation link - C3, cable length - k3; For the element SD1, pring constant for lifting cables is $k = 400 \text{ kN/m}$ and Damping constant is $d = 7 \text{ kNm/s}$ [11].

- **Carrying cables** - created with cable length element - H1.

Elements SP1, SD3, C3, k3, Pu, H1 and Q represents hoisting mechanism, and are modelled as double pendulum system. [2],[12]

In Fig. 3 is presented discrete-continuous model of crane used for model view and simulation. This model is 3-D visualization created by software recurring from Block diagram in Fig. 3. On this model, simulations will be performed in time frame of $0 < t < 20 \text{ s}$. During this simulation time, crane will rotate 50° .

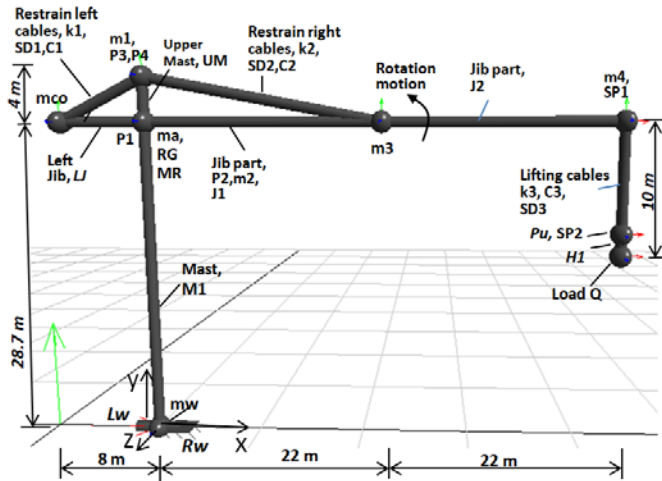


Fig. 4. Discrete-continuous model of tower crane in the form of 3-D visualization

3. Differential equations of tower crane for the case of rotational motion

To formulate dynamics of this system, standard Euler-Lagrange methods are applied, by considering the crane as a multi-body system composed by links and joints. For a controlled system with several degrees of freedom (DOF), the Euler-Lagrange equations are given as [7], [4], [8]:

$$\frac{d}{dt} \left(\frac{\partial E_k}{\partial \dot{q}_i} \right) + \frac{\partial E_p}{\partial q_i} = Q_i \quad (i=1, 2, \dots, n) \quad (3.1)$$

Where: q_i - are generalized coordinates for system with n degrees of freedom, E_k is Kinetic Energy, E_p is Potential energy, Q is the n -vector of external forces acting at joints. Kinetic energy for mechanical systems is in the form:

$$E_k(q, \dot{q}) = \frac{1}{2} \dot{q}^T \cdot M(q) \cdot \dot{q} \quad (3.2)$$

$E_p(q)$ - is potential energy that is a function of systems position.

$M(q)$ - is a symmetric and positive matrix of inertias [6].

Modern software's calculate physical modeled systems through mathematical models, numeric methods and Finite Elements Method. These calculations are based on Euler-Lagrange Equation (3.1), and forces acting on crane applied for regulation [5]. The modeling result is an n -degree-of-freedom crane model whose position is described by generalized coordinates $\mathbf{q} = [q_1 \dots q_n]^T$, and which is enforced, in addition to the applied forces, by m actuator forces/moments $\mathbf{u} = [u_1 \dots u_m]^T$, where $m < n$, [7]. The crane dynamic equations can be written in the following second order differential equation:

$$M(q) \cdot \ddot{\mathbf{q}} + C(q, \dot{\mathbf{q}}) \cdot \dot{\mathbf{q}} + \frac{\partial E_p}{\partial \mathbf{q}} = \mathbf{Q}(q, \dot{\mathbf{q}}) - \mathbf{B}^T \cdot \mathbf{u} \quad (3.3)$$

where \mathbf{M} is the $n \times n$ generalized mass matrix, $C(q, \dot{\mathbf{q}})$ is $n \times n$ matrix of Coriolis Forces, $\frac{\partial E_p}{\partial \mathbf{q}}$ is the vector of gravity, \mathbf{Q} is n -vector of generalized applied forces, and \mathbf{B}^T is the $n \times m$ matrix of influence of control inputs \mathbf{u} on the generalized actuating force vector $\mathbf{f}_u = -\mathbf{B}^T \mathbf{u}$, [7].

After completion and testing of model, Software Maplesim has powerful module for symbolic generation of differential equations. There are 18 DOF from crane model (Fig. 3), which gives 18 differential equations. Variables in differential equations are:

$C1_F(t)$ - force in translational joint C1; $C1_F2(t)$ - force 2 in translational joint C1 (towards y); $C2_F(t)$ - force in translational joint C2; $C2_F2(t)$ - force 2 in translational joint C2 (towards y); $C3_F(t)$ - force in C3 translational joint; $C3_s(t)$ - motion in C3 translational joint; $Pu_y(t)$, $Pu_z(t)$, $Pu_x(t)$ - variables of pulley mass Pu; $Q_y(t)$, $Q_z(t)$, $Q_x(t)$ - variables of load Q; $RG_M(t)$ - variable of moment-torque in the RG rotation Gear; $P1_t(t)$ - Rotational variable of P1 revolute joint; $P2_t(t)$ - Rotational variable of P2 revolute joint; $RG_z(t)$ - Rotation of revolute joint (rotation gear) RG; $SD2_s_rel(t)$ - Relative length of right restraint cables SD2; $SD1_s_rel(t)$ - Relative length of left restraint cables SD2.

3.1. Differential equations

There are 18 Differential equations that represents rotation motion of crane. They are long; we will present them in short form:

$$-4 \cdot \sin(P1(\theta(t))) = 0 \quad \dots(3.1.1)$$

$$4 \cdot \sin(P1(\theta(t))) = 0 \quad \dots(3.1.2)$$

$$-4 + 4 \cdot \cos(P2(\theta(t))) - SD2_s_rel(t) = 0 \quad \dots(3.1.3)$$

$$4 - SD1_s_rel(t) - 4 \cdot \cos(P1(\theta(t))) = 0 \quad \dots(3.1.4)$$

$$-C3_F(t) - 400000 \cdot C3_s(t) - 7000 \cdot \left(\frac{d}{dt} C3_s(t) \right) = 0 \quad \dots(3.1.5)$$

$$576000 \cdot \sin(P1(\theta(t))) \cdot \left(\frac{d}{dt} RG_t(t) \right)^2 \cdot \cos(P1(\theta(t))) - 4 \cdot \sin(P1(\theta(t))) \cdot C1_F(t) + 4 \cdot \cos(P1(\theta(t))) \cdot C1_F2(t) + \frac{5760000001}{10000} \cdot \frac{d}{dt} \left(\frac{d}{dt} P1(\theta(t)) \right) - 706320 \cdot \cos(P1(\theta(t))) = 0 \quad \dots(3.1.6)$$

$$-292180 \cdot \cos(RG_t(t)) \cdot \cos(P2_t(t)) \cdot \sin(Pu_z(t)) \cdot \sin(Pu_y(t)) \cdot \cos(Pu_z(t)) \cdot \left(\frac{d}{dt} Pu_z(t) \right)^2 \cdot C3_s(t) + 1112320 \cdot \cos(RG_t(t)) \cdot \cos(P2_t(t)) \cdot \dots \cdot \cos(Q_z(t)) \cdot \left(\frac{d}{dt} Q_z(t) \right) - 291280 \cdot \sin(RG_t(t)) \cdot \cos(P2_t(t)) \cdot \sin(Pu_z(t)) \cdot \cos(Pu_y(t)) \cdot \left(\frac{d}{dt} C3_s(t) \right) + \frac{3}{5000} \cdot \frac{d}{dt} \left(\frac{d}{dt} RG_t(t) \right) - RG_M(t) = 0 \quad \dots(3.1.7)$$

$$-66200 \cdot \cos(Pu_z(t))^2 \cdot \left(\frac{d}{dt} Pu_z(t) \right)^2 \cdot \cos(Pu_t(t))^2 + 6620 \cdot \left(\frac{d}{dt} Pu_z(t) \right)^2 \cdot C3_s(t) \cdot \cos(Pu_t(t))^2 + 6620 \cdot \cos(Pu_z(t))^2 \cdot C3_s(t) \cdot \left(\frac{d}{dt} Pu_y(t) \right)^2 \cdot \dots - 12640 \cdot \sin(Q_y(t)) \cdot \sin(Q_z(t)) \cdot \sin(Q_x(t)) \cdot \left(\frac{d}{dt} Q_z(t) \right)^2 \cdot \sin(Pu_z(t)) \cdot \sin(Pu_y(t)) \cdot \sin(Pu_z(t)) = 0 \quad \dots(3.1.8)$$

$$12640 \cdot \sin(\text{Pu}_\xi(t)) \cdot \sin(\text{Pu}_\eta(t)) \cdot \left(\frac{d}{dt}\text{Pu}_\xi(t)\right)^2 \cdot \text{C3}_s(t) \cdot \cos(\text{Pu}_\eta(t)) \cdot \sin(\text{Q}_\xi(t)) \cdot \sin(\text{Q}_\eta(t)) + \dots + 126400 \cdot \cos(\text{Q}_\xi(t)) \cdot \sin(\text{Q}_\xi(t)) \cdot \cos(\text{Q}_\eta(t)) \cdot \sin(\text{Pu}_\xi(t)) \cdot \cos(\text{Pu}_\eta(t)) \cdot \cos(\text{Pu}_\zeta(t)) \cdot \frac{d}{dt}\left(\frac{d}{dt}\text{Pu}_\theta(t)\right) + \frac{252800001}{10000} \cdot \frac{d}{dt}\left(\frac{d}{dt}\text{Q}_\eta(t)\right) = 0 \quad \dots(3.1.9)$$

$$-2912800 \cdot \sin(\text{RG}_\zeta(t)) \cdot \sin(\text{P2}_\theta(t)) \cdot \cos(\text{Pu}_\zeta(t)) \cdot \cos(\text{Pu}_\xi(t)) \cdot \frac{d}{dt}\left(\frac{d}{dt}\text{Pu}_\zeta(t)\right) + \dots + 582560 \cdot \sin(\text{RG}_\theta(t)) \cdot \sin(\text{P2}_\theta(t)) \cdot \sin(\text{Pu}_\xi(t)) \cdot \sin(\text{Pu}_\eta(t)) \cdot \sin(\text{Pu}_\zeta(t)) \cdot \frac{d}{dt}\left(\frac{d}{dt}\text{Pu}_\zeta(t)\right) \cdot \left(\frac{d}{dt}\text{C3}_s(t)\right) = 0 \quad \dots(3.1.10)$$

$$132400 \cdot \text{C3}_s(t) \cdot \frac{d}{dt}\left(\frac{d}{dt}\text{Pu}_\eta(t)\right) + 6620 \cdot \text{C3}_s(t)^2 \cdot \frac{d}{dt}\left(\frac{d}{dt}\text{Pu}_\eta(t)\right) - 662000 \cdot \cos(\text{Pu}_\xi(t))^2 \cdot \frac{d}{dt}\left(\frac{d}{dt}\text{Pu}_\eta(t)\right) + 126400 \cdot \sin(\text{Pu}_\zeta(t)) \cdot \sin(\text{Pu}_\xi(t)) \cdot \cos(\text{Pu}_\eta(t)) \cdot \sin(\text{Q}_\eta(t)) \cdot \cos(\text{Q}_\xi(t)) \cdot \sin(\text{Q}_\zeta(t)) \cdot \frac{d}{dt}\left(\frac{d}{dt}\text{Q}_\xi(t)\right) = 0 \quad \dots(3.1.11)$$

$$\frac{d}{dt}\text{SD1}_s_rel(t) = \frac{-1}{7000} \cdot \text{C1}_F(t) - \frac{500}{7} \cdot \text{SD1}_s_rel(t) \quad \dots(3.1.17)$$

$$\frac{d}{dt}\text{SD2}_s_rel(t) = \frac{-1}{7000} \cdot \text{C2}_F(t) - \frac{500}{7} \cdot \text{SD2}_s_rel(t) \quad \dots(3.1.18)$$

4. Experimental measurements

Measurements in the tower crane are done in the place of work, where crane is mounted, in one local company in Prishtina, Kosovo (Fig.1 and Fig.5). They will be used for validation of results. Main measured parameter was force in carrying cables – F_h (F_y). It was measured with dynamometer type *Dini Argeo* attached to the Hook [10], during the rotation of crane (Fig.5). There were 5 measurements achieved, and results are shown in Table.1:

Time (s)	Force in carrying cables - F_y (N)
1	61800
5	62600
8	63100
11	62350
17	62150

Table 1. Results of F_h (F_y) with dynamometer in carrying cables

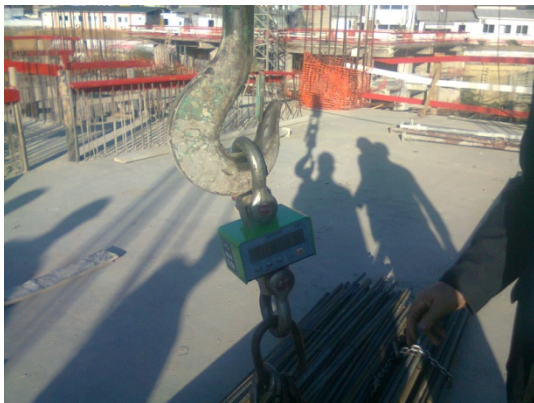


Fig.5. Measurements with Dynamometer during rotation of crane

5. Graphical results for main parts of crane

Based on the model created, differential equations gained, and simulations, results are achieved for main dynamic parameters [2], [9]: Velocity (v) (m/s), Acceleration (a) (m/s^2), Angular velocity (w) (rad/s), Angular acceleration (α) (rad/s^2), Force (F) (N), Force Moment-Torque (T) (Nm). Results are achieved after simulations are applied on designed system, Fig.3 & Fig.4. Simulations are planned to reflect real rotation of crane in order to achieve reliable results and comparable with experimental measurements. Time of simulation is $t = 20$ s.

Rotation motion is achieved with moment-torque generated from rotation motor MR, as a power element in the system (fig.3). It enables simulation of jib rotation. Simulation has three phases (Fig.6) [4],[9]:

First phase – Initial rotation. Value of power torque is $M_t = 70000$ Nm. Time of rotation is $0 \leq t < 14$ s. *Second phase* – Stopping phase of Jib rotation that usually lasts few seconds, while there is no sudden stop of motion in reality. This phase starts after first phase, and lasts 3 seconds, at simulation time $14 \leq t < 17$ s. *Third phase* – there is no torque from motor MR, value is $M_t = 0$. Jib rotation will slow down until it stops. It lasts between time $17 \leq t < 20$ s, which is the end of simulation. It is implemented in order to monitor end of rotation.

Simulation of crane rotation is achieved with adjustment of torque given from rotation motor RM, using ramp function Rfn (Fig.3, Fig.6). Regulation of rotation motion with regulation of torque is achieved through numerous tests in order to achieve planned simulation and angular velocity $\omega = 3.5$ deg/s, and to get best results with less oscillations [2], [9], [4]. The value of torque gained from simulations that accurately represents rotation of jib is $M_t = 70000$ Nm = 70 kNm. This is the main process of regulation and control of crane rotation in this paper [5]. Other important parameters for regulation are:

- Hoisting mechanism - Spring and dumping element SD3 and translation link C3, in order to minimize effect of vibrations which appears in lifting cables and jib during rotation [7]. Spring constant for SD3 is determined with value $k = 400$ kN/m and damping constant is $d = 7$ kNm/s [11].
- Restrain cables - elements SD1, C1, SD2, C2. Spring constant for SD1 and SD2 is determined with value $k = 500$ kN/m and damping constant is $d = 7$ kNm/s [4]. Restrain cables have higher stiffness than lifting cables.

Next will be presented graphical results for main parts of crane, where horizontal axis is time ($t = 0 \dots 20$ s) and vertical axes are corresponding values of dynamic and kinematic parameters. Only most significant graphs will be shown.

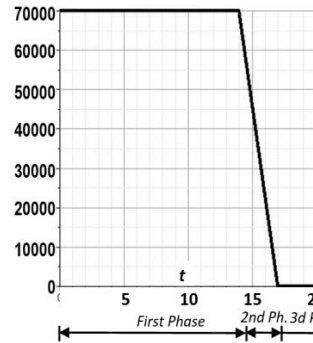


Fig.6. Ramp function Rfn of torque M_t , (Nm)

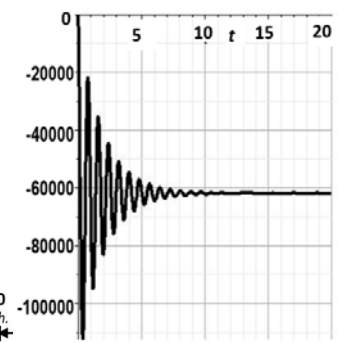


Fig.7. Force F_h (F_y) in carrying cables (ro1), (N)

5.1. Results for carrying cables $H1$ and Load Q

Carrying cables – $H1$ (fig.3) and load Q are connected together as part of hoisting mechanism, and are being carried by crane's jib. Load Q makes swinging and oscillations during rotation motion. This behavior influences directly and indirectly other parts of tower crane. Results of main parameters are shown in Fig.7 to Fig.11. It is important to identify dynamic behavior of carried load in order to understand dynamic occurrences that affect other parts of crane.

In Fig.7 is graph of vertical force F_y in carrying cables $H1$. Force $F(y)$ is Componential Force towards y axis, in negative direction. It has average value of $F(y) \approx |-61000|$ N, which is close to measurements in Tab.1. This validates results achieved with modelling and simulations. Values of other components $F(x)$ or $F(z)$ are small and will not be shown in graphs. In Fig.8 are shown acceleration $a(y)$ and angular acceleration $\alpha(x)$ for carrying cables $H1$. Graph of acceleration $a(y)$ in cables is more intense at the start of rotation. Graph of angular acceleration $\alpha(x)$ has heavy dynamic curve at entire process of rotation.

In Fig.9 are given graphs of load Q changing position in distance x and y , during rotation.

In Fig.10 are given velocity components $v(y)$ and $v(z)$, which concludes that load Q has irregular motion and oscillations. $v(y)$ is very intense at the start of motion, due to swinging of load toward y axes, but after time $t \approx 10$ s it has low oscillations. $v(z)$ is velocity on z axes, that increases until $t = 14$ s, and after that it stops, due to decrease and stop of motor torque M_t (Fig6). $v(z)$ has less oscillations than $v(x)$.

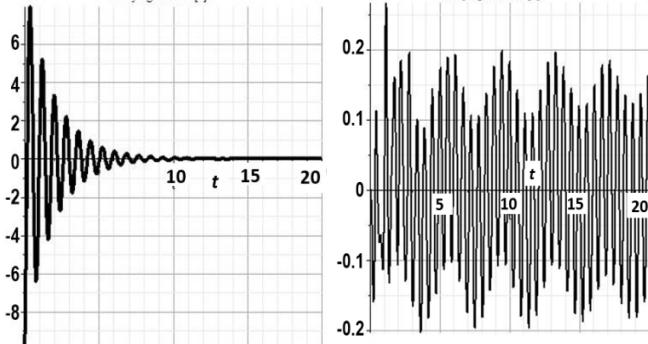


Fig.8. Carrying Cables H1 – acceleration $a(y)$ (m/s^2) and angular acceleration $a(x)$ (rad/s^2)

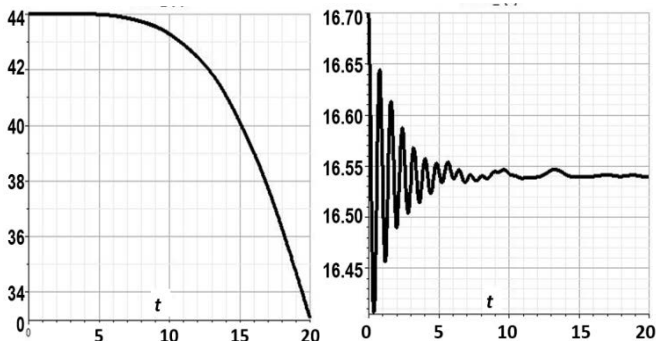


Fig.9. Position of Load Q – in x and y axes (m)

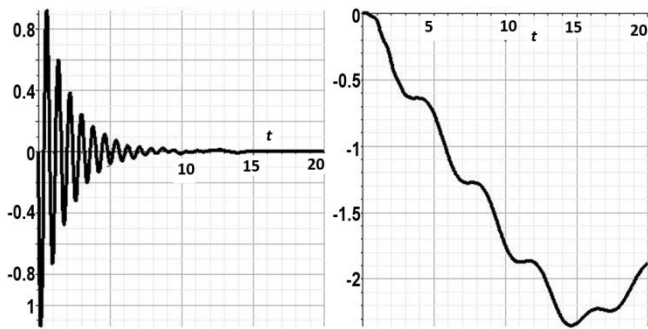


Fig.10. Load Q – Velocity $v(y)$ and $v(z)$, (m/s)

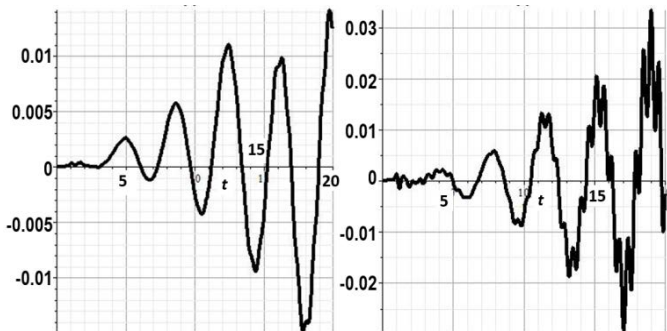


Fig.11. Load Q – angular velocity $w(x)$ and angular accel. $a(x)$

In Fig.11 are given graphs of angular velocity $w(x)$ and angular acceleration $a(x)$ of load Q . Curve of these parameters is dynamic, in a form of sinusoids, with medium periods of oscillations and high amplitudes, which are intense after $t > 5$ s.

5.2. Results for Crane's Jib

Jib of tower crane is considered most important part for rotation motion (Fig.1 & Fig.2). It is a horizontal metallic structure with the grid of beams. Dynamics and oscillations from the load Q and hoisting mechanism are passed on the Jib. Results of main parameters – kinematic and dynamic for the Jib first part-J1 are shown in Fig. 12 to Fig.15. Important conclusion is that oscillations occurring on Load Q and lifting cables are passed on the Jib of crane with similar form of curve, periods, and frequencies.

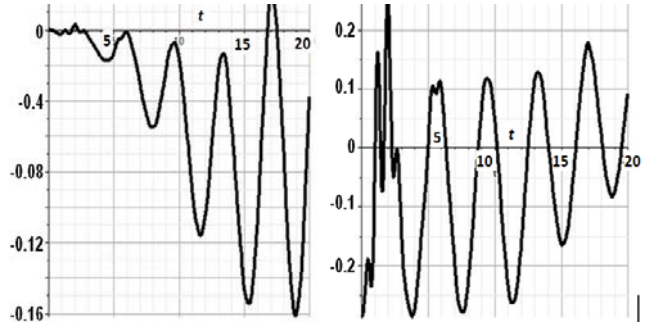


Fig. 12. Acceleration $a(x)$ and $a(z)$ in the Jib, (m/s^2)

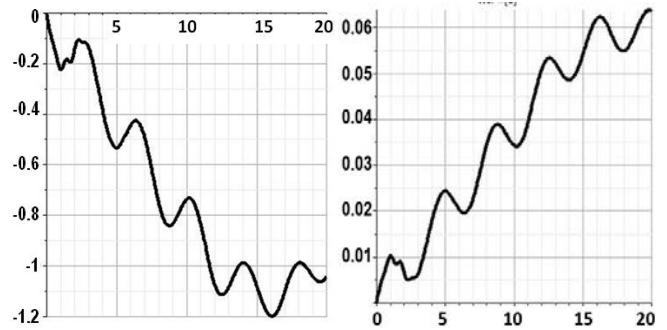


Fig. 13. Velocity $v(z)$ (m/s), and Angular velocity $w(y)$ (rad/s) in the Jib

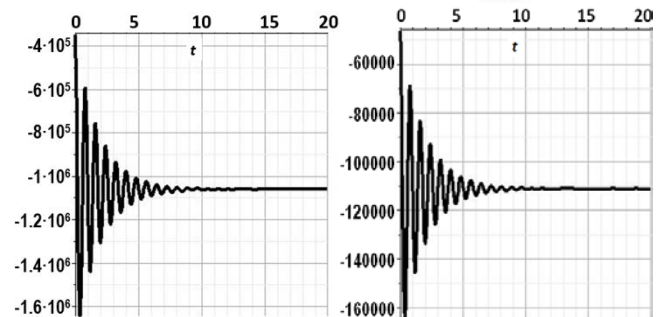


Fig. 14. Force components $F(x)$ and $F(y)$ in the Jib, (N)

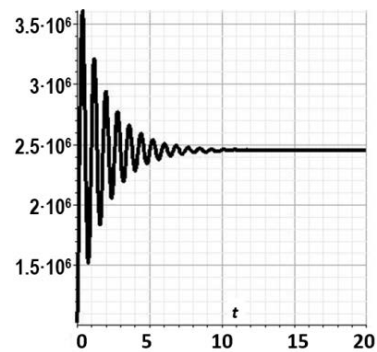


Fig. 15. Torque $T(z)$ in the Jib (Nm)

Based on graphs and parameters taken for analysis, we can conclude that parameters are dynamic in nature, almost on entire process of Jib motion, with high oscillations and amplitudes at the start of rotation process.

5.3. Results for Restraint cables

Restraint cables ($k1$ and $k2$) have stabilizing effect for crane's Jib and counterweight Jib. In fig.16 are given graphs of acceleration $a(x)$ and angular acceleration $\alpha(y)$. Conclusion is that these cables are under heavy dynamic process with high amplitudes.

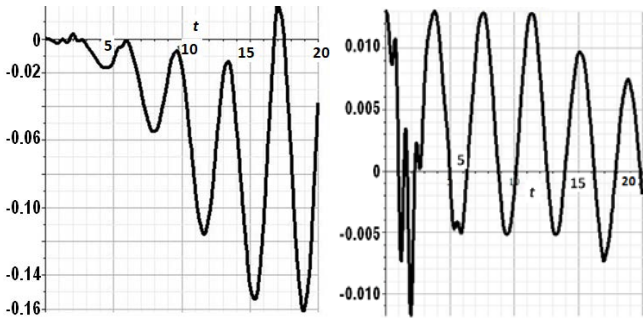


Fig. 16. Acceleration $a(x)$ (m/s^2), and angular acceleration $\alpha(y)$ in Right restraint Cables, ($1/s^2$)

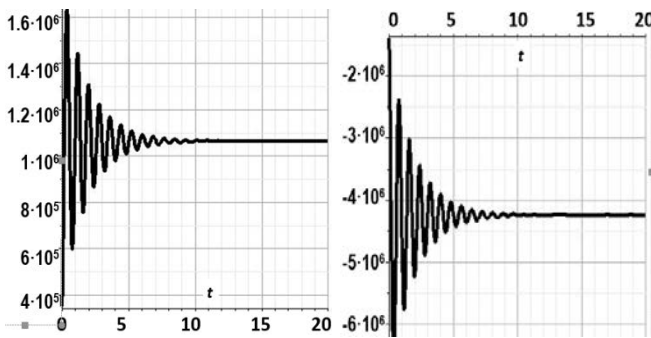


Fig. 17. Force $F(x)$ (N), and torque $T(z)$ (Nm), in Right restraint Cables

In fig. 17 are shown graphs of active force component $F(x)$ and Torque $T(z)$ that act on right restraint cables. At the beginning they undergo heavy oscillations, which after $t > 10$ s decrease.

5.4. Results for Crane's Basement

Basement of crane is part where crane is mounted on the ground. In Fig. 2 is shown with two Fixed Frames named Lw and Rw , bars $Lw1$ and $Rw1$ and mass mw . Force component $R(y)$ in Fig. 18 is reaction force. Graph has dynamic form of curve, with oscillations at the start of rotation. Max value of force $F(y)$ is: $F_{y,max} = |-570000|$ N, at the start of rotation process. After time $t > 5.5$ s, values are lower and less dynamic, with low oscillations. Values of $R(x)$ and $R(z)$ are small and not shown.



Fig.18. Force component $R(y)$

Fig.19. Torque $T(x)$ (Nm)

In Fig.18 to Fig.21 are given graphs of components for moment-torque in the Basement. Oscillations from the Jib and Restraint cables are passed at the Basement, which most important support for keeping the stability of crane. In Fig. 20, value of torque is similar in form as initial torque given by the motor MR (Fig.6). Negative values of torques, and for other parameters in this work, are based on orientation towards referent coordinate system, originating in the Basement's center point (Fig.2, Fig.4).

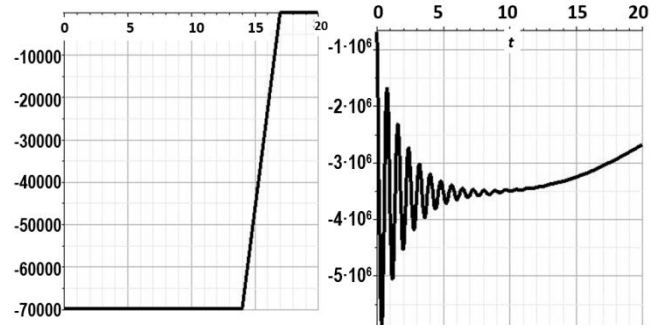


Fig.20. Basement - Torque $T(y)$

Fig.21. Basement - Torque $T(z)$

6. Conclusions

The main problem in tower cranes during rotation are oscillations as dynamic occurrences. It is important to identify and regulate them. Essential to the design of high performance motion control is the development of accurate mathematical models – in order to describe the crane dynamics [12]. To do this we created crane model with schematic design and 3-D visualization. Important part of analysis is creating accurate model and implementing proper simulations plan that reflects real crane's rotation motion, so that results are reliable. Results are gained for main dynamic parameters and compared with experimental measurements. From results it can be concluded that oscillations in all parts of crane are heavy and mostly with irregular occurrence. They occur in different planes. Oscillations have high intensity are mostly at the start of process. Minimizing oscillations was achieved through planning of rotation torque, parameters of hoisting mechanism, parameters of restraint cables and numerous simulations, in order to find optimal rotation [4], [8]. This is done with the aim to optimize the value of rotation torque in the motor which is important parameter for regulation and optimization. This work is also important for safety at work with cranes. It can be used also for further optimization analysis for other work processes like load lifting and telpher travel of tower crane.

7. References

- [1] Construction crane manual, type Wolf 6531.6, Germany.
- [2] Doçi I., Hamidi B., *Studying rotational motion of Luffing Jib Cranes with maximum load using simulations*, International Journal for science, technics and innovations for the industry-MTM 2015; 1(12): 20-24.
- [3] *MapleSim User Guide*, Maplesoft, a division of Waterloo Maple Inc., 2014.
- [4] Dresig, H., *Shwingungen mechanischer Antriebssysteme, Modellbildung, berechnung, analyse, synthese*, Springer Verlag, Berlin, 2001.
- [5] S. Joe Qin, Badgwell Th.A., *An overview of industrial model predictive control technology*, Control Engineering Practice, A Journal of IFAC, ISSN: 0967-0661, 2003.
- [6] La Hera, P. M., *Dynamics modeling of an electro-hydraulically-actuated system*, Umea University, 2011.
- [7] Garcíaorden, J. Carlos, Goicolea, José M., Cuadrado Javier, *Multibody Dynamics, Computational methods and applications*, p.91, Springer, 2007.
- [8] Vaughan J., *Dynamics and control of mobile cranes*, Georgia Institute of Technology, 2008.
- [9] Doçi Ilir, Lajqi Naser, *Development of schematic design model of gantry crane for dynamic analysis and regulation of travel motion*, MTM Journal, Issue 6/2017, p.268.
- [10] <http://www.diniargeo.com/men/scales/weight-indicators.aspx>
- [11] http://www.engineeringtoolbox.com/wire-rope-strength-d_1518.html
- [12] F. Ju a, Y.S. Choo a, F.S. Cui, *Dynamic response of tower crane induced by the pendulum motion of the payload*, International Journal of Solids and Structures 43 (2006) 376–389.

EFFECT OF BORONIZING PARAMETERS AND MATRIX STRUCTURES ON THE WEAR PROPERTY OF DUCTILE IRON

Ass. Prof. Dr. Toktaş A.¹, Ass. Prof. Dr. Toktaş G.², MSc. Mech. Eng. Gülsün K.³
^{1,2}Department of Mechanical Engineering, Balıkesir University - Balıkesir, TURKEY
³Balıkesir Electromechanical Industrial Plants Corporation, 10100, Balıkesir, TURKEY

E-mail: atoktas@balikesir.edu.tr, gzeytin@balikesir.edu.tr, kenan.gulsun@besttransformer.com

Abstract: In this study, the effects of matrix structure (pearlitic, tempered martensitic, lower ausferritic, and upper ausferritic), boronizing temperature (800, 825, and 850°C) and time (3, 4.5 and 6 hours) on the wear behaviour of Cu-Ni-Mo alloyed ductile iron were investigated. Wear tests were performed on ball-on-disc type wear tester under the load of 6.8 N, at sliding speed of 6.5 mm/s, at room temperature and dry sliding conditions. The mass losses were measured after wear tests and the friction coefficients were obtained during wear tests. The hardnesses and thicknesses of boride layers, microstructures and worn surface examinations (SEM) of the matrix structures and borided layers were performed. The surface hardnesses of borided samples were obtained three or four times more than that of the matrix structures. The best wear performance was observed for the sample borided at 850°C for 6 h. The mass loss of this boronizing condition is 0,2 mg and this value is nine times less compared with that of the as-cast pearlitic structure.
KEYWORDS: DUCTILE IRON, MATRIX STRUCTURE, BORONIZING, MASS LOSS

1. Introduction

Bronizing, which is conventionally carried out by holding the materials at 700-1100°C in a boron-rich environment for diffusion of boron atoms into the material in order to form a boride layer, is very attractive thermochemical surface treating technique for ferrous alloys[1]. Boronizing medium can be in the form of a solid powder, paste, liquid, or gas. Pack boronizing is the most widely used boriding process because of its relative ease of handling, safety, and the possibility of changing the composition of the powder mix, the need for limited equipment, and the resultant economic savings[2,3].

The boronizing treatment mostly forms two boride phases; FeB (more externally) and Fe₂B. The significant features of these borides are their high melting points (1540°C for FeB and 1390°C for Fe₂B), metallic resistivity, high hardness, and excellent wear, friction, and corrosion resistance[4]. The coefficient of expansion of Fe₂B ($2,9 \times 10^{-8} \text{ K}^{-1}$) is less than that of iron ($5,7 \times 10^{-8} \text{ K}^{-1}$) and hence this phase remains in compression after cooling, while that of FeB ($8,7 \times 10^{-8} \text{ K}^{-1}$) is greater than iron or Fe₂B and therefore remains in tension[2]. This disparity in residual stress can result in the formation of cracks in the region of the FeB-Fe₂B interface, especially when a component is subjected to thermal and/or mechanical shock[5].

Generally, the formation of a monophase (Fe₂B) with saw-tooth morphology is more desirable than a double-phase layer with FeB and Fe₂B for industrial applications[6]. The degree of teething depends on the quantity of alloying elements, carbon concentration, temperature and time[7]. Industrial boriding can be carried out on most ferrous materials such as structural steels, cast steels, Armco iron, grey iron and ductile iron[8]. The most significant parameters that determine the characteristics of boride layer are processing temperature and time. Alloying elements mainly retard the boride layer thickness (or growth) caused by restricted diffusion of boron into the substrate because of the formation of a diffusion barrier[9].

Ductile iron is a member of cast iron family which draws great interest due to its unique mechanical properties. Most of this superiority is achieved by heat treating and surface hardening processes. Ductile iron can gain variety of matrix structures via heat treating, an example of which is ausferrite. Almost all surface hardening processes, applicable for steels, can be successively

performed on ductile irons. The aim of the present study is to investigate the effect of boronizing parameters (temperature and time) and matrix structure on the wear properties of Cu, Ni, and Mo alloyed ductile iron.

2. Experimental Procedures

The chemical composition of the ductile iron is given in Table 1. The nodule diameter and nodule count range between 29–37 μm and 100–155 mm^{-2} , respectively. The nodularity is above 90%.

Table 1. Chemical composition of the ductile iron (wt.%)

C:	3.730	Mg:	0.044
Si:	2.550	Cu:	1.030
Mn:	0.300	Ni:	1.250
P:	0.045	Mo:	0.180
S:	0.023	Cr:	0.032

The heat treatments, given in Table 2, were carried out in order to obtain various matrix structures, namely tempered martensitic (TM), low ausferritic (LA), and upper ausferritic (UA). Test materials were machined and ground to a cylindrical shape with dimensions of 15 mm diameter and 20 mm length. Pack boronizing technique was performed in a solid commercial Ekabor 2 (B₄C - SiC - KBF₄) powder with grain size range of 75-106 μm . All samples were packed in the powders mix and sealed in a stainless steel container. Boronizing was performed in an electrical resistance furnace under atmospheric pressure at various temperatures (800, 825, and 850°C) for 3, 4.5, and 6 h, respectively. The steel box was followed by cooling in air to room temperature.

Table 2. Matrix structures and heat treatment parameters

Matrix	Austenitizing temperature/time, T _γ / t _γ	Tempering and/or cooling conditions
TM	900 °C / 1 h	Oil quenching, tempering at 400 °C for 1 h, air cooling
LA	900 °C / 1 h	Austempering at 300 °C for 1 h, air cooling
UA	900 °C / 1 h	Austempering at 365 °C for 1 h, air cooling

The hardness of borided surfaces and matrix structures were measured on the cross-sections using Metkon Mh-3 Vickers indenter with a load of 1 kg.

An Eclipse MA100 optical microscope was used to examine the microstructures and depth of boride layers of polished and etched (with 5% nital solution) specimens, and a Zeiss Evo40 scanning electron microscope for the worn surface of specimens.

The ball-on-disc abrasive wear tests were performed on metallographically polished samples at room temperature with the humidity of 45±5%. A constant load of 6,8 N, a sliding velocity of 6,5 mm/s, and a sliding distance of 140 m were used. For the counter body, 5 mm diameter tungsten carbide ball with 68 HRC hardness was selected. The samples were cleaned by ethyl alcohol and dried before and after the wear tests. Then, the mass losses were measured by a balance with sensitivity of 10⁻⁴ g. The friction force was monitored continuously by means of a force transducer. The friction coefficients were recorded during the tests. The wear tests were repeated three times for each boriding parameters and matrix structures.

3. Results and Discussion

The microstructures of as-cast (pearlitic), TM, LA, and UA matrix structures of the ductile iron are illustrated in Fig.1. The as-cast microstructure consisted of bull's eye structure; ferrite surrounding graphite nodules in a pearlitic matrix (Fig 1a). While LA structure shows fine acicular ferrite (dark needles) in Fig 1c, UA structure shows coarse feathery ferrite (Fig 1d) in the ausferritic structure.

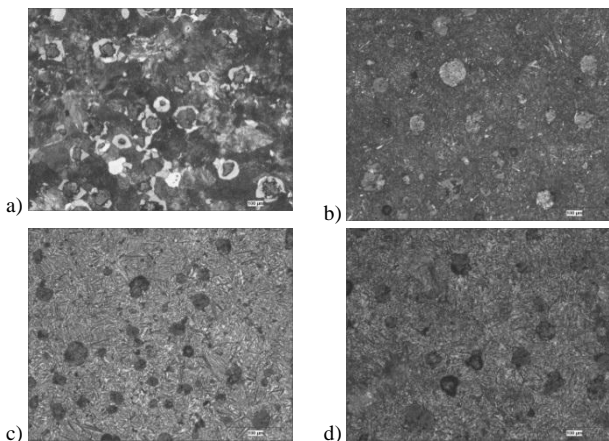


Figure 1. Microstructures of the matrix structures of a) as-cast, b) TM, c) LA, and d) UA (200X)

The hardness values of matrix structures are given in Table 3. The TM structure has the highest hardness due to the brittleness effect of martensite. The UA structure has higher hardness than the LA one. This result may be due to the second stage reaction. This reaction occurs at high austempering temperatures, and/or long durations. High carbon austenite decomposes into carbides and ferrite by the second reaction. These carbides rise the hardness and lower the strength and toughness of ductile iron. [10]

Table 3. Hardnesses and mass losses of the matrix structures

Matrix	Hardness [HV ₁]	Mass loss [mg]
As-cast(pearlitic)	413	1,8
TM	614	1,2
LA	464	1,4
UA	494	1,3

The surface hardnesses of borided samples are given in Figure 2. The values varied between 1280-1685 HV₁. The hardness of the boride layer was found to be three or four times higher than that of the as-cast structure. This result is well agree with the previous study[11]. The hardnesses increased with both the boronizing temperature and time. This increase is more clear at 850°C. The durations at 800 and 825°C made no significant variations in surface hardness values.

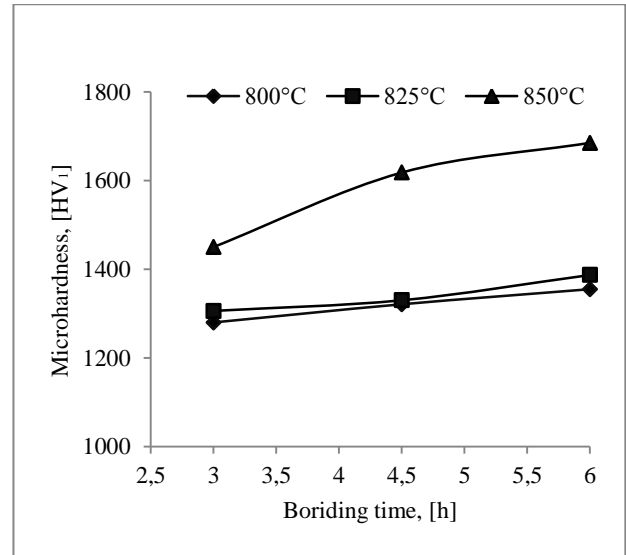


Figure 2. Microhardnesses of the borided surfaces

The microstructures of the borided layers are given in Figure 3 for 6h boriding time at 800, 825, and 850°C temperatures, respectively. The layer thickness is increased with the boronizing temperature. The boride layer has a tooth-shaped structure. It is observed that nonuniform light lines present at interface between the matrix and the borided layer. These lines are thought to be silicon-rich zones. Silicon has no solubility in iron boride. Therefore, during the boronizing process, silicon atoms diffuse inwards and produce silicon-rich zone[11].

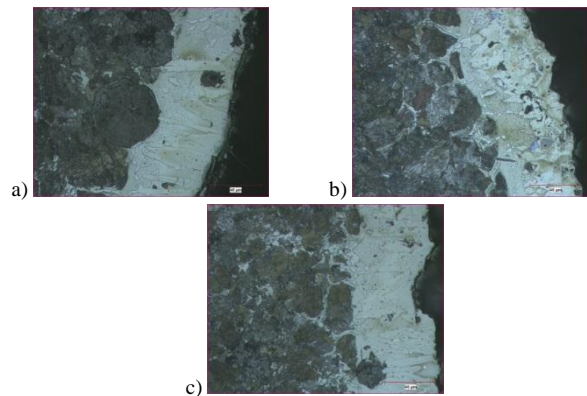


Figure 3. Microstructures of the boride layers boronized for 6 h at a) 800°C, b) 825°C, and c) 850°C (500X)

The effect of boronizing parameters on the boride layer thickness is given in Figure 4. As the boronizing temperature and time increased, the boride layer also increased as consistent with the previous studies[12,13]. The thickness and hardness of the boride layer depends on the substrate material being processed, boron potential of the boronizing compound, boronizing temperature-time, boronizing mediums and their compositions[3]. The increase rates

of boride layer by the boriding time have close values of approximately 64, 59, and 60% at 800, 825, and 850°C, respectively.

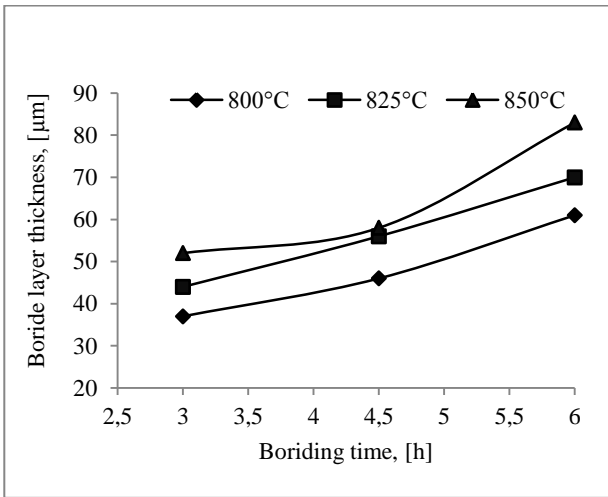


Figure 4. Thicknesses of the boride layers

The mass losses of matrix structures are given in Table 3. The values are varied inversely proportion with their hardness values. Namely, the highest hardness structure showed the least mass loss such as in TM structure. This result confirms that hard surfaces are more resistant to wear.

The mass losses by the boronizing temperature and time are given in Fig 5. At 825 and 850°C boronizing treatments, mass losses are decreased by the process duration. An opposite and unexpected result is observed at 800°C. For all durations at 800°C, due to having low microhardness values (Fig 2.), the mass losses are unexpectedly lower than that of 825°C. It can be concluded that 800°C boronizing temperature is not enough for the studied alloyed ductile iron. As the alloying elements retard the diffusion rate of boron into the substrate, the higher boronizing temperatures are required for the expected performance. The durations at 850°C is more effective in mass loss as in boride layer. Boronizing at 850°C for 6h showed the least mass loss among all parameters as 0,2 mg. C. Li et al. [14] reported that higher temperature and longer process duration result in more excellent wear resistance. The pearlitic as-cast structure showed nine times more mass loss comparing to that of specimen boronized at 850°C for 6h (Table 4 and Fig. 5).

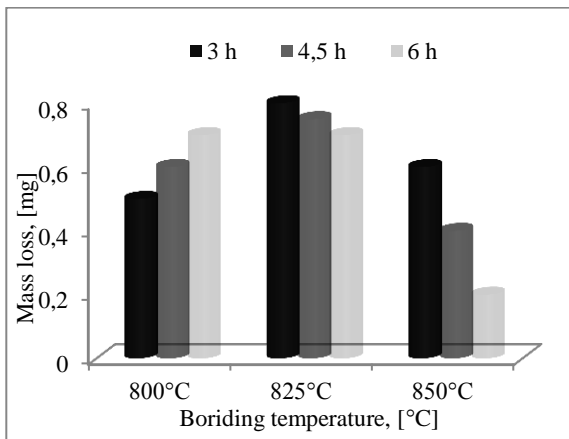


Figure 5. Mass losses by the boronizing temperature and time

The friction coefficients of the pearlitic, TM, LA, and UA structures are given in Fig 6. At the beginning of wear tests, the friction of coefficients increased to high values and then lowered and caught the steady state for all structures. The as-cast pearlitic structure has the lowest friction coefficient with more steady distribution.

Having many boriding variables, it was not possible to illustrate the friction coefficient distributions of borided surfaces in a graph. Wider distributions in friction coefficients of borided surfaces were observed compared with that of the matrix structures. The values are ranged between 0.15-0.65 at 800 and 825°C boriding temperatures for all durations. However, a narrow range of values between 0.15-0.3 was observed at 850°C. Moreover, the distributions of friction coefficients were more steady at 850°C.

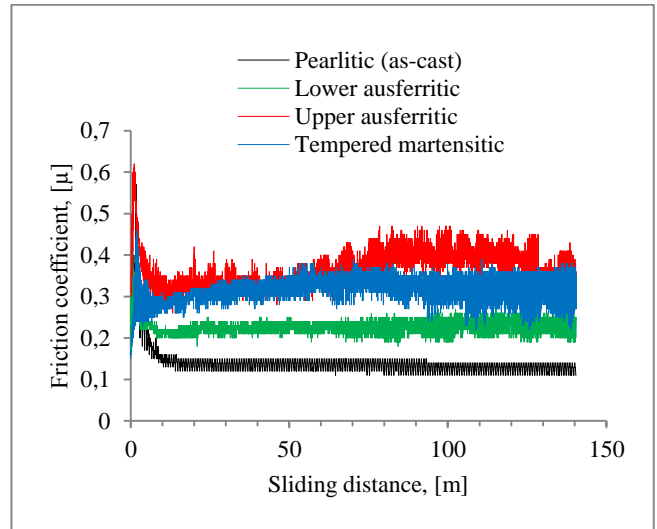


Figure 6. The friction coefficients of the matrix structures

Figure 7 illustrates the SEM graphs of worn surfaces of the matrix structures (TM and LA) and surfaces borided for 6 h at 800°C and 850°C temperatures. The micro scratches in the matrix and the micro cracks, formed at graphite-matrix interface, are dominant in the TM structure (Fig 7a). An adhesive wear mechanism is more effective with significant plastic deformation in the LA structure (Fig 7b). The worn surface of sample borided at 800°C for 6 h showed remarkable amount of cracks (Fig 7c)

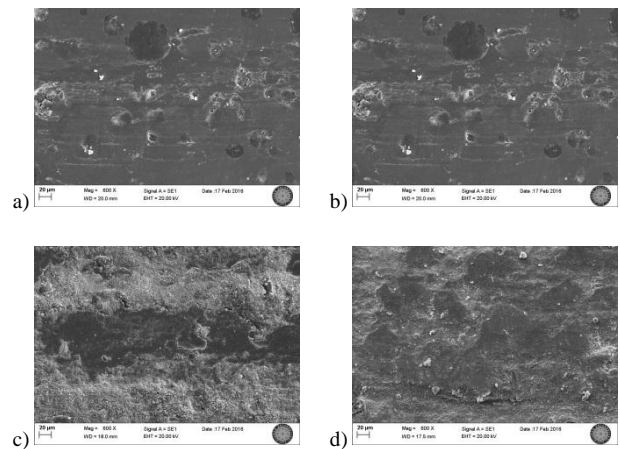


Figure 7. SEM graphs of the worn surfaces of structures a) TM and b) LA and surfaces borided for 6 h at c) 800°C and 850°C (600X)

4. Conclusion

The following conclusions can be drawn from the present study:

- The hardness values of the borided surfaces increased three and/or four times higher than that of the as-cast structure.
- The surface hardnesses increased with both the boronizing temperature and time. This increase is more clear 850°C temperature.
- The boride layer thickness increased with both the boronizing temperature and time. This increase rates by the boriding time have approximately close values as 64, 59, and 60% at 800, 825, and 850°C, respectively.
- 800°C boronizing temperature is found to be low to generate expected boride layer on the studied alloyed ductile iron. Many micro cracks were detached on the worn surface of 800°C/6 h borided sample.
- Boronizing at 850°C for 6 h showed the least mass loss among all parameters as 0,2 mg. The pearlitic structure showed nine times more mass loss according to that of this boriding parameter.
- The friction coefficients were more steady for the matrix structures than the borided ones. The as-cast pearlitic structure has the most steady and lowest friction coefficient value.

4. Literature

- [1] M. Baydogan, S. I. Akray, Successive boronizing and austempering for GGG-40 grade ductile iron, *Journal of Iron and Steel Research , International*, 16, 2009, 50-54.
- [2] L. C. Casteletti, A. N. Lombardi, G.E. Totten, Boriding, *Encyclopedia of Tribology*, Q. J. Wang, Y. Chung (Eds), 2013, 249-254.
- [3] M. Kul, K.O. Oskay, A. Temizkan, B. Karaca, L.C. Kumruoğlu, B. Topçu, Effect of boronizing compositions on boride layer of boronized GGG-60 ductile cast iron, *Vacuum*, 126, 2016, 80-83.
- [4] U. Sen, S. Sen, F. Yilmaz, An evaluation of some properties of borides deposited on boronized ductile iron, *Journal of Materials Processing Technology*, 148, 2004, 1-7.
- [5] P.A. Dearnley, T. Bell, Engineering the surface with boron based materials, *Surface Engineering*, 1, 1985, 203-217.
- [6] Ö. Özdemir, M. Usta, C. Bindal, A.H. Üçışık, Hard iron boride (Fe₂B) on 99.97 wt% pure iron, *Vacuum*, 80, 2006, 1391-1395.
- [7] B. S. Ünlü, E. Atik, Investigation of tribological properties of boronized Fe-based SAE 102 and TS-DDK 40 journal bearing at high loads, *materials Design*, 31, 2010, 2690-2696.
- [8] U. Sen, S. Sen, S. Köksal, F. Yılmaz, Fracture toughness of borides formed on boronized ductile iron, *Materials and Design*, 26, 2005, 175-179.
- [9] Boriding, J.R. Davis, editor, *Surface Hardening of Steels*, ASM International, 2002, 213-216.
- [10] J. Olofsson, D. Larsson and I.L. Svensson, Effect of austempering on plastic behavior of some austempered ductile iron alloys, *Metallurgical and Materials Transactions A*, 42(13), 2011, 3999-4007.
- [11] Y. Yalçın, A. M. Yazıcı, The effect of boro-tempering heat treatment on the properties of ductile cast iron, *Metallic Materials*, 45, 2007, 51-57.
- [12] S. Şahin, C. Meriç, Investigation of the effect of boronizing on cast irons, *Materials Research Bulletin*, 37, 2002, 971-979.
- [13] U. Sen, S. Sen, S. Köksal, F. Yılmaz, Fracture toughness of borides formed on boronized ductile iron, *Materials and Design*, 26, 2005, 175-179.
- [14] C. Li, B. Shen, G. Li, C. Yang, Effect of boronizing temperature and time on microstructure and abrasion wear resistance Cr12Mn2V2 high chromium cast iron, *Surface and Coating Technology*, 202, 2008, 5882-5886.

ERGONOMIC ASPECTS WHEN DESIGNING LUMINAIRES BASED ON LED LAMPS.

Ass Prof.Vinogradov V.V., Ass Prof.Mokretsova L.O.
 MISIS NATIONAL UNIVERSITY OF SCIENCE and TECHNOLOGY, Moscow, Russia
 vladimir@vinogradov.us

Annotation: Some initial information is given for the competent design of household LED lighting fixtures

KEYWORDS: LED LAMP, VISUAL PERCEPTION, COLOR TEMPERATURE, MELANOPSIN

Introduction

Fixtures based on LEDs lamps are of interest now, as the direction of actively developing lighting systems and devices.

When designing LED luminaires, tasks are set for matching ergonomic studies to reduce the contrast of the light pattern, eliminate the light drop and uniformity of the illuminated space.

It should be noted the current trend in designing fixtures-reducing size, weight, saving materials.

Fundamentals

The starting points for creating a good living environment lighting: parameters are formed as a result of studying the visually perceptible space, taking into account human physiology.

Lighting by LED emitters performs the following tasks:

- operational (allows you to read, recognize visual information of all kinds, navigate in space)
- psychological (creates favorable incentives, comfort, entertainment and mood)
- provides and creates prerequisites for greater safety of work and leisure
- hygienic (stimulates the maintenance of cleanliness)

The main factors of visual perception:

-maximum improvement of perception of visual information for performance of work.

-provision of an appropriate level of performance of tasks:

-maximum work safety assurance

-provision of necessary level of visual comfort.

Level of required illumination is determined by the following parameters:

- the smallest object size of view, in mm (from 0.15 to 5)

-the scope of visual work: (from the 1st to the 9th)

-contrast of the object of view with the background (small, medium, large)

-characteristics of the background (dark, medium, light)

Dependence of the visual system on the surrounding space

Perception in the work area allows you to determine the characteristics of the reliability of human performance.

The quality of lighting of any premises should be evaluated complex, according to the requirements and various lighting factors.

Artificial lighting is divided into:

general,

local,

combined and special (with specific technical characteristics: scattered, directional, reflected)

The color of light, or the spectral composition of the light flux, affects the appearance of the illuminated object. Because of the brilliance in direct lighting, the reading efficiency, after 3 hours is reduced by 80%, with a system of reflected light and no glare, the reduction is -10%.

Calculation of the required number of luminaires of general lighting in the premises is made by the formula (the height of the suspension of luminaries -1000mm above the illuminated surface)

$$n = \frac{1 \times b \times Em \times k}{\Phi}$$

where "n" is the number of fixtures, pcs.; "k"-coefficient for the color and tone of walls, floor and ceiling (1,5-2,5); "l" - length of the room, m; "b" - width of the room, m; "Em" - illumination given, lx; "Φ"-light stream of light sources of one lamp, lm. The level of illumination depends on the height of the suspension and decreases in proportion to the square of its change:

The number of lamps must be increased in proportion to the square of the height change.

For local illumination of the workplace in combination with general lighting should be at least -20% of the workplace illumination.

Optimal lighting is designed according to

Project parameters	Distance value Contrast The property of the illuminated surface Dynamics and time Color Specifications Physiological - enables a person to see, work, create
Performance characteristics	Age of the person Restriction of sight Visual adaptation Perception of colors Depth of field
Lighting characteristics	Levels of illumination Distribution of brightness Spectral composition-color rendition (the accuracy of the perception of the color of the object depending on the color of light) The absence of zones of glare (glare) Flicker (light pulsation) The distribution of the shadow and the direction of light (light flux)
Specificity of the consumer situation	Influence of the human pose Visual field limitation Technical requirements for railroad cars - safety during operation Recycling Ecological compatibility Accuracy of visual work: -negated -very high -medium

*With age, sensitivity decreases: the need for a person in the illumination of 30 years of age is 2 times, for a 40-year-old at 3, and for a 50-year-old is 6 times greater than for a ten-year-old.

Advantages when using LED lights:

- there is no flicker of light.
- small size and weight.
- high light output with low power consumption.
- fast turning lights on and off - instant.
- increased stability to vibrations and impacts to other external influences.
- white light of high quality, color rendering index in the range of 80-95.

- optimal radiation pattern depending on the purpose of illumination with the possibility of creating scattered light or directional light.
- absence in the radiation spectrum of the infrared component and low heat generation, lack of heating of surrounding objects and surfaces.
- warranty guarantee with any humidity and ambient temperature from -50 to +50 ° C.
- simplified the supply and management of electricity.
- miniature sizes of radiating elements allow to widely embed LEDs in bearing structures and elements of lighting systems.
- the maintenance and operation of the luminaire is simplified.
- automatic control of the luminous flux and the process of switching on the luminaire is possible.
- color temperature control can be provided by electronic sensors and logic systems). Comfort is provided in use, high consumer qualities are formed.
- LED lights have a very high efficiency, reaching 75% or more, which allows you to significantly (in 4-5 times) reduce power, load on the network. The costs associated with the cost of consumed electricity are reduced.

Such technological and design solutions are appropriate.

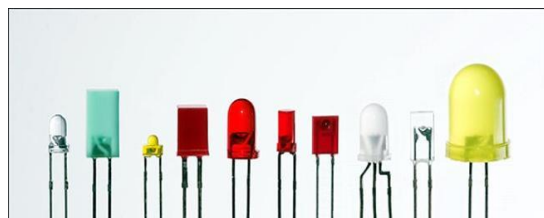


Fig.1, LEDs produced in a very wide range of colors - up to IR and UV ranges.

They can be either monochrome or multicolored (when several crystals of x colors are concentrated in one body), for example, RGB.

One of the drawbacks of these LEDs is the low scattering angle of the light flux: usually not more than 60°.



Fig.2, SMD LED

In addition to LEDs, SMD LEDs are also available. This includes super bright white and color LEDs with a power of about 0.1 W in a surface mount case. The dimensions of the housings are usually standard for any SMD type elements: 0603, 0805, 1210, etc., where the marking denotes length and width in hundredths of an inch or in millimeters. In this case, there are both varieties with a convex lens, and without it. Clearly classifying all the variety of LEDs is difficult, because rarely those or other LEDs are produced for some specific purposes. Nevertheless, the main directions of their application - indication and lighting - remain the same for the time being, and the classification given here is suitable for creating a general idea of the types of LEDs.

Specificity and design features of fixtures:

As a rule, the design of the luminaire consists of a support base, a fixing element, a rod, a bracket, a reflector. Also, the lamp is equipped with a diffuser of light or diffuser.

Achievement of uniformly illuminated space is achieved. The problems of reducing the contrast of the light pattern are solved, and the difference in the illumination is eliminated.

The luminaire provides the possibility of using in a complex spatial situation-placement and illumination in hard-to-reach places.

When designing, it is envisaged that the luminaire can be easily mounted and adjusted for operation.

The envelope of the radiating element is of small size (its size is a multiple of the design of the lamp). Weight devices are relatively small, there is a significant savings in materials (while reducing the cost of the lamp).



Fig.3, Waterproof version of LED for bathroom

No deposits are formed, maintenance and care (removal of dust, insects, other contaminants) are facilitated.

The electrical safety is easily ensured. The risk of injuries and life threatening effects is reduced (the work of the light system is ensured by a low current and voltage strength-usually designed for safe voltages of 12 ÷ 24V).

The mechanical durability of the LEDs is large. Their service life is up to 50000 hours. Therefore, a long service life allows you to increase the period between repair and maintenance.



Fig.4, Demonstration of formation on the example of LEAD

Influence of modern lamps on health and human vision:

The negative effects of blue LEDs on humans are noted. The blue spectrum, when viewed, causes overstrainment of the visual area of the brain in a matter of minutes.

There are risks of disability in sight at working age. When working with color information, there is also a danger to health. It has been shown to have a negative effect on the retina of the eye; for example, blue light abruptly suppresses the production of melatonin in humans, there is a risk of blindness. With LED light, a large proportion of blue falls on the retina of the eye, than in sunlight with the same illumination of the retina. In sunlight, the ratio of the various components of its spectrum is adequate and does not lead to unnecessary intensity of the human eye.

With a large dose of blue in the spectrum of lighting, the so-called Melanopsin forms a signal to reduce the diameter of the pupil. This reduces the energy illumination of the retina, protecting it from exposure to a large dose of blue light. Melanopsin has 2 peaks of maximum photosensitivity - at 460 nm and 480 nm. The dose of blue light that gets on the retina depends on the pupil ø, which decreases depending on the amplitude at 480nm, the LED has a dip of 480nm. With LED lighting, this ratio is not respected, since there is a dip in the spectrum of such a light source. With a large

dose of blue in the spectrum, melanopsin does not form a signal to reduce the diameter of the pupil. Thus, most of the blue light of the LED hits the retina of the eye.

Comparison of TRI-R technology with filters in a conventional LED:

The newest LEDs of Sun Like emit purple, and the light is not blue, which then passes through a layer of phosphorus with three light filters - for blue. Interlayer technology is called TRI-R. The principle of technology - purple crystals 420 nm, which are painted with red, blue and green phosphors. In the white light spectrum of LEDs (TRI-R technology), the dip at 480 nm is eliminated and there is no excess dose of blue. The spectrum is close to solar.

Advantages of LED lamps using TRI-R technology:

- lighting is optimal in magnitude, close to the calculated
- the spectrum is close to solar
- the lack of pulsation in time and noise from the ballast (ballast)
- uniform distribution of lighting of the working area in accordance with the design
- high manufacturability and structural variability

Prospects for the development and expansion of the use of LEDs:

Designers create conceptual models (Fig.11), prototypes of future systems. The appearance of the lamp is developed in both traditional and retro style(Fig.6), classical or the latest avant-garde trends. Formed not stylized eclectic forms, but the most rational solutions from the structural and aesthetic side.



Fig.6



Fig.7, Design models of non-traditional forms are created, with new consumer functions.

The possibility of dynamic editing is provided. Providing rotation, shearing and moving in space.

A separate class of luminaires with autonomous power supply (energy sources with solar panels and batteries)

When manufacturing, progressive production processes -3D printers and other modern technologies can be used. They allow the integration of light-emitting diodes into various materials (such as

polycarbonate, polyethylene, epoxy compositions and others) electrical elements.

LED systems are now actively developing in landscape (Fig.8) architecture. In the design of the lighting system in this case, it is easy to take into account various weather factors, difficult weather conditions. The ventilation of the lighting system is simplified.

Low accumulation of moisture in the luminaire (there is a slight formation of condensation).



Fig.8, Fashionable and conceptual form of a landscape lamp

The experience of architectural application proves the perspective of light sources on light-emitting diodes. They allow you to get a light spot of any shape with minimal loss. There are solutions that allow using a single LED illuminator to highlight light columns, bridges and similar architectural elements.(Fig.9)



Fig.9, Formation of a light image in the interior

Based on LEDs, you can create light sources with a small beam angle of $5 \div 10^\circ$.

Technologies on light-emitting diodes allow to pass from static illumination of architectural elements of buildings to dynamic and colorful color representations, to reveal features of architectural objects (Fig.10).To ensure comfortable lighting in various areas and appearance.

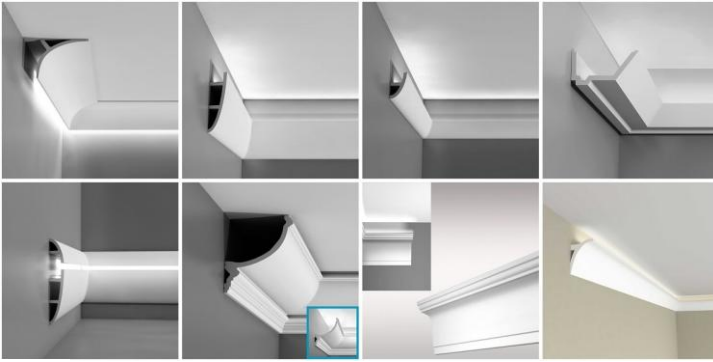


Fig.10

The use of light-emitting diodes for illumination of pools and in premises with high humidity has widely spread.

The main models of luminaires based on LEDs

Fixtures are developed practically for all household needs: floor, table, suspended, wall, portable, for exterior, landscape use, souvenir and others.

Performed in designs for lighting paintings, equipment, highlighting exhibits.

Dynamic lighting using LEDs influences the visual estimation of interiors, the perception of dimensions, details, and its color solution. LED lighting fixtures help to harmonize physiological processes in a person, provide vital modes rhythmically, "around the clock".



Fig.11, Forms of LED lighting fixtures in retro or parametrizm style

There are models for building graphical interfaces, other information carriers and systems (visual communications and other information tools).

The so-called "Art objects" based on LED systems stand out as a separate consumer niche of household lamps.



Fig.12 Forms of LED lamps are simple and geometric

They are designed to perform decorative equipment, functions of symbolic indexing of space or creation of the necessary imaginative atmosphere and toys.

Used LEDs of different designs, creating almost all the colors of the rainbow.

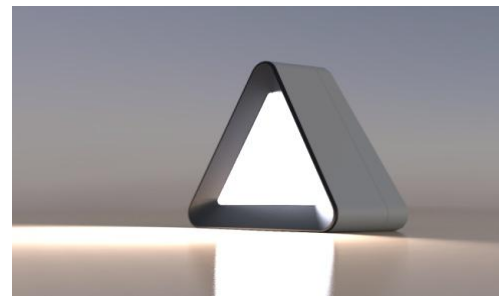


Fig.13, A typical example of the shaping of a lamp based on LED



List of sources used:

-F.E. Schubert, "LEDs", FIZMATLIT, 2008 year.
 -A.Polischuk, A.Turkin. "Prospects of using lamps with light-emitting diodes for energy-saving lighting", Energy saving, №2, 2008.

<http://finelighting.ru/svetilniki/lampy/svetodiodnye/svetovoj-potok-kratkaya-xarakteristika-osobnosti.html>
<http://ledno.ru/svetodiody/vidy-led.html>

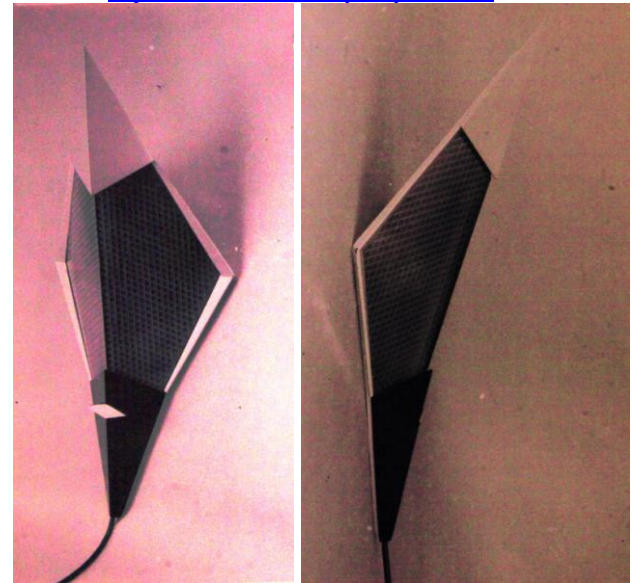


Fig14, Wide possibilities of shaping

As an illustration of the appearance of the luminaire on the LEDs, the "Danko" system is presented, (overall size - 750mm x 280mm, Material of construction - plastic).



Conclusion

Based on the results outlined above.

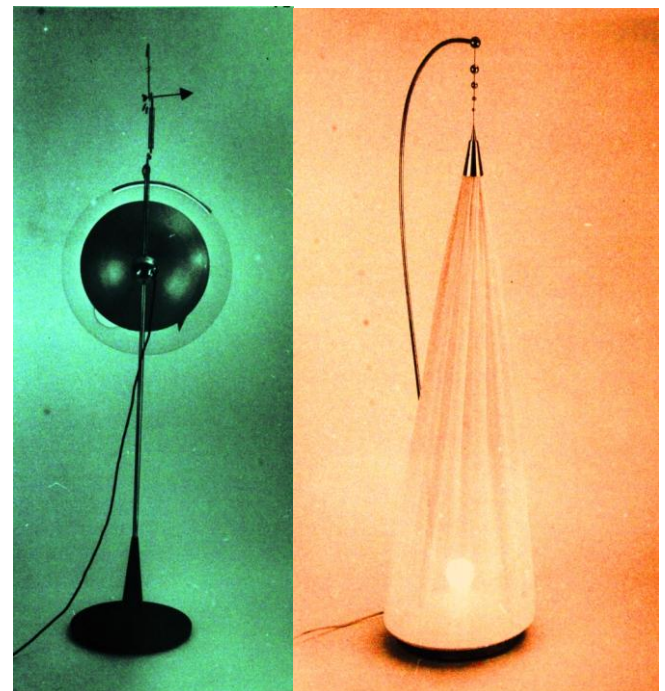
It is necessary to take into account socio-cultural factors, styles of basic aesthetic trends. It is possible to carry out synthesis of modern art and the latest technologies; there are the most extensive opportunities for creating a form. Such technological and design solutions are suitable for providing comfort when using LED, and their high consumer qualities are formed. I believe powerful LEDs will soon replace outdated light sources.

There is a tendency: designers develop "disposable" models of fixtures using LEDs.

The cost of replacing the LED element and repair is comparable to the production of the entire product and may exceed the cost of the lamp itself. This contributes to the marketing appeal. It is easier and cheaper to design LEDs.

Thus, they reflect the latest trends. Optimization contributes to improving consumer properties and quality of household products based on LEDs.

Now the technologies of LED lamps are actively developing, so final standards and standards have not been developed yet.

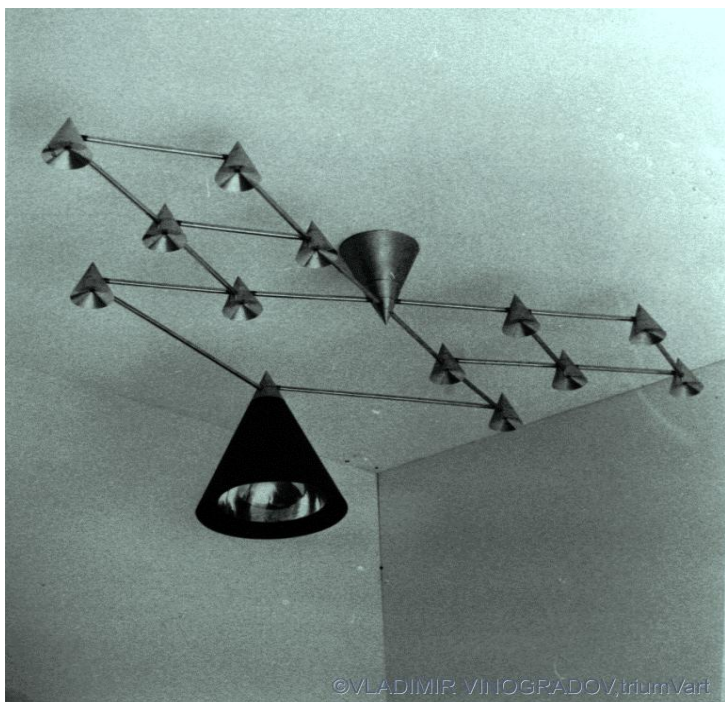


The "Eol" system is presented, Lamp for comfort in the living room (overall size -1800mm xØ600mm, Material of execution - steel chromeplated).

The "Shaherezada" system is presented, Floor lamp for creating a cozy atmosphere in the home (overall size -1600mm x Ø350mm, material of the lampshade-Silk, base -Cu).



The "Malevich" system is presented, for changing the position of the luminaire suspension in a dwelling (overall size -* Ø270mm x1000mm, Material of execution - steel chromeplated).



As an illustration of the appearance of the luminaire on the LEDs, the "Galaxy" system is presented, (overall size -2000mm x1000mm, Material of execution - steel chromeplated).

A feature of this model is the function of changing the location of the LED modules (conical shape). The lighting system has a shaped star structure and is easily transformed. The central reflector can be lowered down for local illumination-an additional function for providing effective and comfortable illumination of space.

Design this model (only 5 models)

© Vladimir Vinogradov

MODEL FOR DETERMINING THE STATIC LOAD ON MOVABLE SPATIAL CONSOLE LATTICE GIRDER BOUNDED WITH CLAMPS

Prof. Dr. Sc. Hristovska E., mech. eng.¹, Assis. Prof. Dr. Sc. Sevdje Stavreva¹, Prof. Dr. Sc. Vangelica Jovanovska²,
 Assoc. Prof. Dr. Sc. Ivo Kuzmanov¹, Assoc. Prof. Dr. Sc. Zlatko Sovreski¹

¹Faculty of Technical Sciences – Bitola, University St. Kliment Ohridski, Republic of Macedonia

²Faculty of Biotechnical Sciences – Bitola, University St. Kliment Ohridski, Republic of Macedonia

elizabetha.hristovska@uklo.edu.mk

Abstract: This paper presents a model for determining the static load on movable spatial console lattice girder and the clamps which bounded the same one. The paper presents guidelines for theoretical determination of the static load using an appropriate software package and conducted modeling for this purpose. Also, the paper displays the methodology for experimental determining the static load by setting a model for the experimental measurement on the specific measuring points of the clamps and the characteristic positions of the carrying console. The research is carried out on a concrete real object and the results are shown numerically and graphically, which enables carrying out an analysis of the load and deducing concreting conclusions about the research object.

Keywords: CARRYING CONSOLE, CLAMPS, STATIC LOAD, THEORETICAL DETERMINATION, EXPERIMENTAL MEASUREMENT

1. Introduction

The carrying construction of the working wheel on a rotating excavator is a spatial steel console bounded with clamps, which can be moved in a horizontal and vertical plane. In the horizontal plane, moving this console is enabled by turning the lower construction of the excavator. In the vertical plane, the moving is from nethermost position where digging is below the ground level to the uppermost position at the maximum digging height above the ground level.

The spatial carrying console is with a lattice design, which at its first end is jointly connected, and at the free end carries the working (rotating) wheel of the excavator. The console is bounded with two clamps, usually with a rectangular cross-section, which with the opposite ends are carried on to the upper construction of the counterweight of the excavator (ballast construction).

The static load of the clamps of this spatial console lattice girder is by its own weight from the construction that they hold, and theoretically these are the load sizes for the standby condition of the excavator. In particular, the static loads of the clamps are tensile forces as a reaction from the weights of the elements on the working wheel and its carrying construction.

The static load of the clamps can be determined by theoretical and experimental way. The theoretical determination is based on a static calculation of the forces in the clamps using the static balance conditions for the three characteristic positions of the carrying console - uppermost, horizontal and nethermost position. The experimental determination is based on an experimental measurement of the forces in the clamps, at measuring spots (points) in the most loaded cross-section of the clamps, for the characteristic positions of the carrying console.

2. Theoretical determination of the static load

For theoretical determination of the static loads onto the clamps, it is necessary to set up the model of the carrying console and its clamps. The mathematical (numerical) model needs to implement a computer static calculation, and the same one should be close to the real model.

For a concrete rotating excavator, the excavator SRs-630/I product of the German company TAKRAF, which works in the coalmine "Suvodol" Bitola, sets the real and mathematical model of the carrying console and its clamps (Figure 1 and Figure 2).

Knowing the technical characteristics of the construction and application of a matrix analysis of the construction with a software package for this purpose, the static loads for the characteristic positions of the load carrying construction are determined, or loads on the excavator's standby without taking into account the working conditions.

The theoretical (analytical) determination of the static loads on the clamps of the rotating excavators finds justification in the development phase of the excavators (even when there is no real object) because it is a faster and cheaper way but with less accuracy than the experimental determination.

Calculated sizes of forces in the clamps which come from static load, using the SAP 2000 software package, are listed in Table 1.

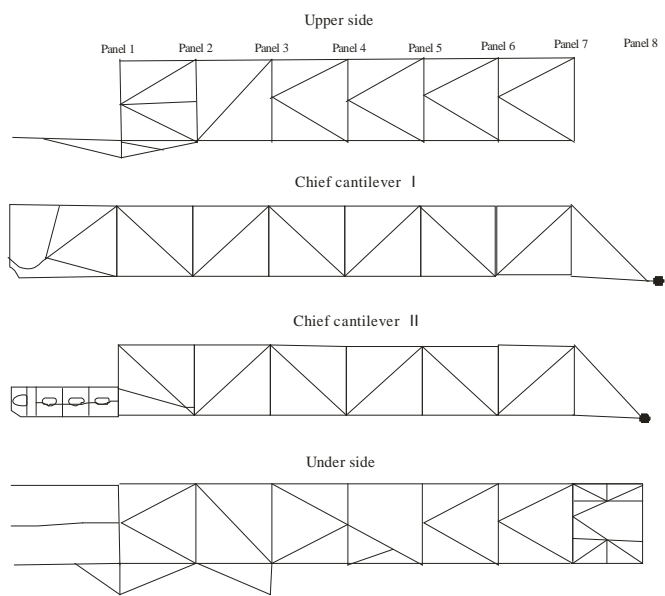


Fig. 1 Real model of the carrying console

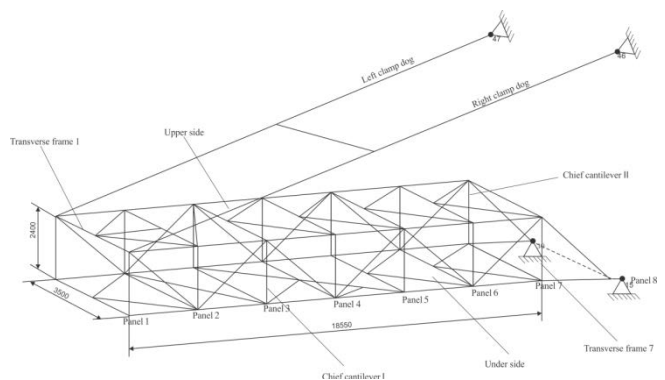


Fig. 2 Mathematical model of the carrying console and its clamps

Table 1. Theoretical sizes of forces from static load

Position of carrying structure	Tension force in [kN]	
	Right clamp	Left clamp
Uppermost	773.13	748.01
Horizontal	850.32	823.39
Nethermost	819.47	792.92

3. Experimental determination of the static load

The experimental determination of the static loads on the clamps of the carrying consoles could be done by measuring the strains to which they are exposed when the excavator is on standby, for characteristic positions of the console. The strains in excavator standby position are reaction to the own weight of the structural elements.

Stresses measurement of clamps is carried out in an indirect way, or by measuring the dilatations at certain measuring spots of the clamps with the most used method for this purpose - the tensiometric method. The dilatations of the measuring points are measured with the set measuring strain gages, and the connection of the dilatations with stresses and stresses with loads should be established using certain settings of the materials strength.

The measurement of the static loads of the two clamps on the carrying console of the rotating excavator working wheel requires a longer and more difficult preparation, given the working conditions of the excavator which is carried out according to a conceptual methodology for this purpose.

For the measurements of the excavator SRs-630 onto the both clamps there are placed five measuring gages for measuring axial stresses, with different layout on each clamp. The measuring gages on the two clamps are placed in the intersection, which according to the estimation is considered to be the most overloaded, and is located at the transition from the constant cross-section of the clamps toward the tilt, where the clamps with the little axles are joined to the carrying console of the excavator's wheel. The arrangement of the measuring gages for the right clamp is shown in Figure 3, and for the left clamp in Figure 4.

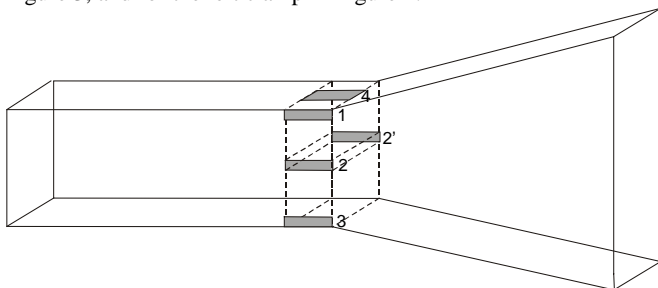


Fig. 3 Measuring gages on the right clamp, with an inside view

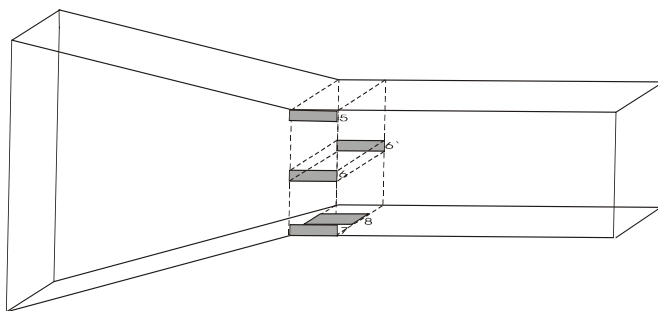


Fig. 4 Measuring gages on the left clamp, with an inside view

The measured sizes of loads from the static load, at each of the measuring points (spots) of the both clamps are shown in Table 2 for the three characteristic positions of the carrying console on the excavator's working wheel.

Table 2. Experimental sizes of forces from static load

Position of carrying structure	Magnitude of force from static load in [kN]							
	Right clamp				Left clamp			
	Measuring point				Measuring point			
	1	2	3	4	5	6	7	8
Uppermost	1270.08	812.45	555.31	1248.91	1141.9	788.26	604.65	782.01
Horizontal	826.56	853.07	1031.28	770.16	904.93	822.53	940.56	955.79
Nethermost	685.44	832.76	1150.28	666.09	1292.76	856.80	537.47	695.12

In order to obtain a clearer picture of the measurement magnitudes obtained by the experimental measurement, all the final results of the performed measurements are processed and systematized and the diagrammatic shown in Figure 5.

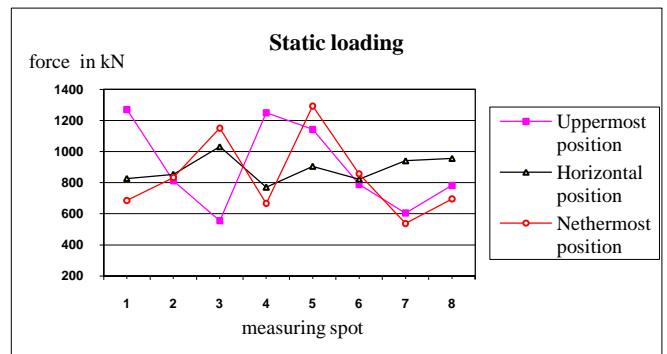


Fig. 5 Static load on the clamps for the characteristic positions of the carrying console

4. Measurement characteristics

The static load of the clamps was measured by the following way: the carrying structure of the working wheel was leaning in a lower position at rest, on supports with hydraulic pumps, in which position the clamps were loosened, or unloaded. This condition is the conditional zero of the load on the clamps. The carrying console is raised by about 2 m and the static load on both clamps is measured for a horizontal position. The carrying console was then lifted up to its uppermost position, for which position the static load of the clamps was measured. The static load on the clamps was also measured for the nethermost position of the carrying console on the working wheel.

During the measurement, the static load change in the clamps was followed from the influence of:

- removal of the hydraulic support of the carrying console;
- turning the console left and right ;
- turning the working wheel without load;
- the work of the conveyor tape on the carrying console without load;
- the transport of the excavator.

From all previously mentioned the following conclusion is ascertained:

The extraction of hydraulic supports does not cause a change in the static load on the right clamp, while in the left this change is small by increasing on the measuring spot 6 and decreasing on the measuring spot 7.

When turning the carrying console to the right, change in the load on the right and left clamp is recorded. On the right clamps - the measuring spot 1 and 4 have a lower force, which is 62% and 59% respectively of the load size in this position of the console before the turning starts; at the measuring spot 3, an increase of 69% of the load before turning; no change in load was recorded at measuring spot 2. On the left clamp - at the measuring spot 5 there is a 38% reduction in the load; on measuring spots 7 and 8 there is an increase of 100%; while no change has been recorded at measuring spot 6.

When turning the carrying construction to the left it is recorded for the two clamps the same load change at measuring spots as when turning to the right, but with some smaller forces.

The rotating of the working wheel without load does not cause a change in the load condition of the clamps.

The work of the conveyor tape without load does not cause a change in the load on the clamps.

The transport of the excavator also does not cause a significant change in the load. Negligible oscillatory load changes are recorded at measuring spot 3 on the right clamp and measuring spot 6 on the left clamp.

5. Conclusion

The theoretical determination results of the static loads on the clamps of carrying console should be treated as orientation values because they do not take into account the specific working environment impacts and the actual technical condition of the excavator, as well as the change in the size of the forces at different positions at the cross-section of the clamps.

The experimental determination results of the static loads on the clamps of carrying consoles are relevant for further analysis. The analysis of the results of the experimental measurement showed that the relevant sizes for the loads of the clamps are the measured forces at the neutral axis of the cross-section of the clamp (measuring spot 2 at the right and the measuring spot 6 on the left clamp).

The static loads of the clamps are the largest for the horizontal position of the carrying console, with the note that the load on the right clamp is greater.

The display on the same diagram of the measured forces for the two clamps per measuring spots and positions of the carrying console allows us to perceive the difference in the load sizes of the two clamps for the same position of the carrying console, for all measuring spots, as well as the difference in the load per measuring spots for the characteristic positions of the console.

6. References

- [1] Hristovska, E., Characteristic of the working load on the rotating excavator, 8th International Conference "Machinery, technology, materials", Sofia, Bulgaria, 2010.
- [2] Hristovska, E. etc., Measurement and testing of loads and stress deformed state of the carrying construction of the excavator SRs-630/1 in the coalmine Suvodol-Bitola, Application project, Faculty of Mechanical Engineering-Skopje, Macedonia
- [3] Hristovska, E. etc., Analysis of the stability of the excavator SRs-630 with the reconstruction of the working wheel, Application project, FAKOM engineering-Skopje in cooperation with Faculty of Technical sciences-Bitola and Faculty of Mechanical Engineering-Skopje, Macedonia
- [4] Operating instructions for the excavator SRs-630 and other technical documentation for this excavator, REK-Bitola
- [5] Technical documentation from the excavator SRs-630 manufacturer, TAKRAF-Germany

CHANGE IN OPERATING PARAMETERS OF TURBOCHARGED DIRECT INJECTION DIESEL ENGINE DURING THE INJECTED FUEL MASS FLOW VARIATION

PhD. Mrzljak Vedran¹, PhD Student Eng. Poljak Igor², Student Žarković Božica¹

¹Faculty of Engineering, University of Rijeka, Vukovarska 58, 51000 Rijeka, Croatia,

²Department of maritime sciences, University of Zadar, Mihovila Pavlinovica 1, 23000 Zadar, Croatia

E-mail: vedran.mrzljak@riteh.hr, ipoljak2@unizd.hr, bozica.zarkovic@gmail.com

Abstract: A change in essential operating parameters of a high speed direct injection turbocharged diesel engine MAN D0826 LOH15 during the injected fuel mass flow variation was presented. Based on two measurement sets, performed with standard diesel fuel, several operating parameters were calculated: engine torque, effective power, excess air ratio, specific effective fuel consumption and heat released per engine process. All of the calculated parameters are presented for a wide engine operating range. Along with calculated, several important parameters were measured, in addition to those presented in measurement sets. Additional measured parameters were lubrication oil temperature and exhaust gas temperature before and after the turbocharger turbine. Those calculated and measured parameters allow deep insight not just into the engine process, but also in the process of turbocharging, which is very important in the analyzed diesel engine operation.

Keywords: DIESEL ENGINE, TURBOCHARGER, FUEL MASS FLOW VARIATION, EXPERIMENTAL ANALYSIS

1. Introduction

From the invention of an internal combustion engine, experimental measurements are the basis for their operating parameters analysis, [1] and [2]. Along with internal combustion engine measurements, numerical simulations have been developed to make easier, faster and cheaper investigations of engine operating parameters.

Today, several types of diesel engine numerical models were developed: 0D (zero dimensional) models [3], multizone models [4], quasi dimensional models [5] and [6], while the last and most detailed ones are CFD (Computational Fluid Dynamic) models [7]. In order to determine the accuracy and precision of each model, they must necessarily be validated in several different measuring points of the tested engine. Therefore, experimental engine measurements are inevitable, even nowadays.

To reduce diesel engine emissions and improve engine operating parameters, researchers are intensively involved in implementing combustion of different alternative fuels in existing diesel engines. Two researches of alternative fuel usage in diesel engines are [8] and [9]. A complete review of green fuels as alternative fuels for diesel engines is presented in [10] while review of performance, combustion and emission characteristics of bio-diesel fuelled diesel engines presented authors in [11].

In this paper was presented change in the operating parameters of a high speed direct injection turbocharged diesel engine during the injected fuel mass flow variation. Operating parameters analysis was based on two measurements set at different engine rotational speeds. Measurements were obtained with a standard diesel fuel D2. Analyzed parameters can be divided in two groups: calculated ones and measured ones. Calculated operating parameters were engine torque, effective power, excess air ratio, specific effective fuel consumption and heat released per engine process. Measured operating parameters were a temperature of lubrication oil and exhaust gas temperatures before and after the turbocharger turbine. The presented operating parameters allow insight into a wide operating range of the analyzed engine.

2. Investigated diesel engine specifications

The investigated diesel engine was a high speed direct injection turbocharged diesel engine MAN D0826 LOH15, designed for a truck or small ship drive. The main engine specifications and characteristics are presented in Table 1. The piston geometry is characterized by an eccentric hole in piston head which is used for the fuel injection. In order to maximize the suction and exhaust valve flow rate, the fuel injector is positioned eccentrically and hence the hole in the piston head is positioned in the same way.

Table 1. Engine specifications

Number of cylinders	6
The total operating volume	6870 cm ³
Peak effective power	160 kW
Cylinder bore	108 mm
Cylinder stroke	125 mm
Compression ratio	18
Crank radius	62.5 mm
Length of the connecting rod	187.2 mm
Nozzle diameter	0.23 mm
Number of nozzle holes	7

3. Diesel engine measurement results and measuring equipment

Engine measurement was performed in the Laboratory for Internal Combustion Engines and Electromobility, Faculty of Mechanical Engineering, University of Ljubljana, Slovenia.

Measured engine was connected to an eddy current brake Zöllner B-350AC, Fig. 1. Measurements control was secured with a control system KS ADAC/Tornado. Cylinder pressure was measured with pressure sensor AVL GH12D, placed in an extra hole in the cylinder head. The cylinder pressure signal was led to a 4-channel amplifier AVL MicroIFEM.

The piston top dead center was determined by a capacitive sensor COM Type 2653, and the crankshaft angle was measured by crank angle encoder Kistler CAM UNIT Type 2613B with an accuracy of 0.1° crank angle.

Lubrication oil temperature was measured with Greisinger GTF 401-Pt100 Immersion probe while the flue gas temperature at the turbocharger turbine inlet and outlet was measured with two Greisinger GTF 900 Immersion probes.

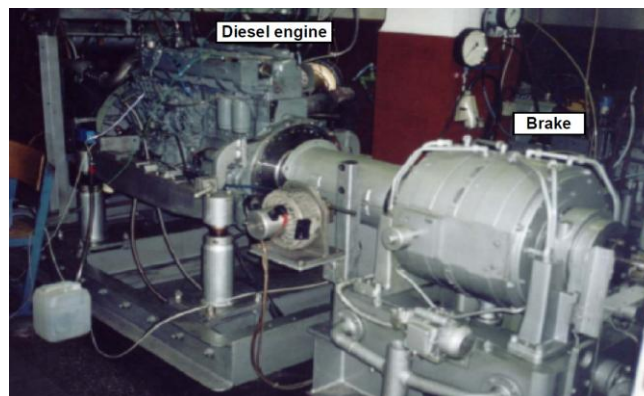


Fig. 1. Diesel engine MAN D0826 LOH15 connected to eddy current brake during the measurements

Several measurement sets were carried out and for analysis in this paper are selected two measurement sets presented in Table 2 and Table 3. Each measurement set has almost constant engine rotational speed (1500 rpm and 2400 rpm), but in each measurement set fuel and air mass flow constantly increases from operating point 1 to 4. Air mass flow must have the same trend as fuel mass flow in order to obtain complete combustion.

Table 2. Obtained measurement results - Set 1

Measurement No.	Fuel mass flow (kg/h)	Air mass flow (kg/s)	Rotational speed (rpm)	Brake reaction force (N)	BMEP* (bar)
1	9.198	0.10076	1498	292.2	5.10
2	13.447	0.11192	1502	449.7	7.86
3	18.040	0.12672	1502	594.6	10.39
4	22.453	0.14146	1501	735.0	12.84

* BMEP = Brake Medium Effective Pressure

From the measurement Set 2, Table 3, is visible that at the higher engine rotational speed (2400 rpm) injected fuel mass flow increases in comparison with measurement Set 1 (Table 2), along with simultaneous increase in air mass flow.

Table 3. Obtained measurement results - Set 2

Measurement No.	Fuel mass flow (kg/h)	Air mass flow (kg/s)	Rotational speed (rpm)	Brake reaction force (N)	BMEP* (bar)
1	14.774	0.19158	2401	234.4	4.09
2	21.815	0.22495	2402	391.1	6.83
3	28.842	0.26069	2399	525.4	9.18
4	35.364	0.29387	2399	638.4	11.15

* BMEP = Brake Medium Effective Pressure

4. Equations for calculating engine operating parameters

In each operating point engine torque was calculated according to the equation:

$$M = F \cdot R \quad (1)$$

where M (Nm) is torque, F (N) is brake reaction force and R (m) is the brake prong length on which the reaction force is measured. For eddy current brake Zöllner B-350AC, brake prong length amounts $R = 0.955$ m.

Engine effective power was calculated by using an equation:

$$P_{ef} = \frac{M \cdot 2 \cdot \pi \cdot n}{60 \cdot 1000} \quad (2)$$

where P_{ef} (kW) is effective power and n (rpm) is engine rotational speed.

Excess air ratio was calculated according to the equation:

$$\lambda = \frac{\dot{m}_a \cdot 3600}{\dot{m}_f \cdot L_{st}} \quad (3)$$

where λ (-) is excess air ratio, \dot{m}_a (kg/s) is an air mass flow, \dot{m}_f (kg/h) is the fuel mass flow and L_{st} (-) is a stoichiometric air mass, which is dependable on used fuel properties. During measurements is used standard diesel fuel D2, which lower heating value (H_d) amounts $H_d = 42700$ kJ/kg and stoichiometric air mass amounts $L_{st} = 14.7$.

Specific effective fuel consumption was calculated by using an equation:

$$b_{ef} = \frac{\dot{m}_f \cdot 1000}{P_{ef}} \quad (4)$$

where b_{ef} (g/kWh) is specific effective fuel consumption.

The heat released per process is obtained with an equation:

$$Q_{pp} = \frac{\dot{m}_f \cdot H_d}{n \cdot 60} \quad (5)$$

where Q_{pp} (kJ/proc.) is heat released per process.

5. Change in calculated and measured engine operating parameters with discussion

During the lower engine rotational speed (Set 1), an increase in engine torque is much sharper than for the higher engine rotational speed (Set 2), Fig. 2. For the engine rotational speed of 1500 rpm, maximum obtained torque was 701.93 Nm, while at a rotational speed of 2400 rpm maximum torque was 609.67 Nm. The change of engine torque, in each observed measurement set is almost linear (engine torque linearly increases with the increase in fuel mass flow). For the same fuel mass flow, significantly higher engine torque is obtained at lower engine rotational speed.

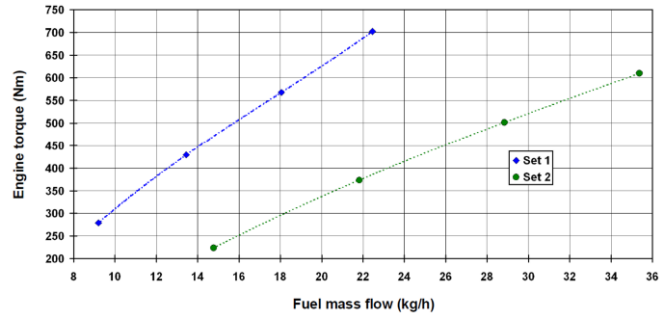


Fig. 2. Change in engine torque for each measurement set

For each engine rotational speed, effective power has the same trend - it increases during the increase in engine fuel mass flow. The maximum effective power in measurement Set 1 is 110.3 kW, while in measurement Set 2 maximum effective power amounts 153.2 kW, Fig. 3. For the same fuel mass flow, the higher effective power is obtained at lower engine rotational speed. From that fact can be concluded that for the tested engine during the same fuel mass flow, higher torque at 1500 rpm has a greater impact on engine effective power increase than the increase in rotational speed from 1500 rpm to 2400 rpm.

Gasoline engines operate strictly with air excess ratio equal to 1 (because of the three-way catalyst) while diesel engines operate with excess air ratio bigger than 1. For the analyzed engine, excess air ratio in each measurement set decreases during the increase in fuel mass flow, according to equation (3). In measurement Set 1 (1500 rpm) excess air ratio decreases from 2.68 at the lowest fuel mass flow to the 1.54 at the highest fuel mass flow, Fig. 4. In measurement Set 2 (2400 rpm) excess air ratio has significantly higher values than in measurement Set 1. In Set 2 excess air ratio

decreases from 3.18 at the lowest fuel mass flow to the 2.04 at the highest fuel mass flow. At the higher engine rotational speed, for the same fuel mass flow, the engine consumes much bigger air mass flow.

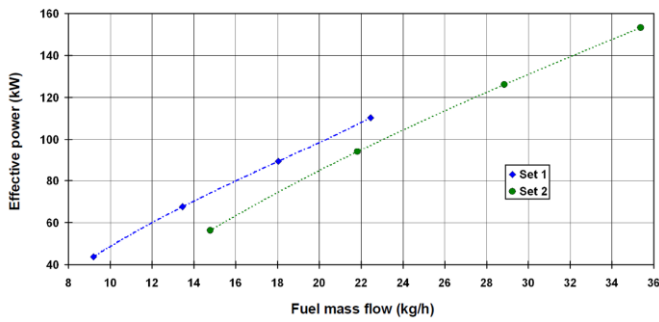


Fig. 3. Change in engine effective power for each measurement set

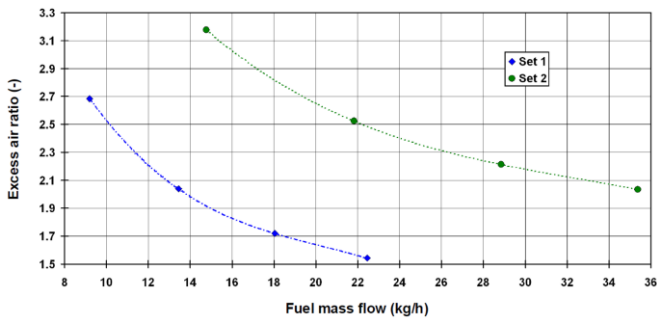


Fig. 4. Engine excess air ratio change for each measurement set

Specific effective fuel consumption, for engine measurement Set 1 and Set 2 is presented in Fig. 5. For both engine measurement sets, specific effective fuel consumption, calculated by using equation (4), firstly decreases after which follows the slight increase during the increase in fuel mass flow.

In measurement Set 1 (1500 rpm) specific effective fuel consumption amounts 210.12 g/kWh at the lowest fuel mass flow and 203.57 g/kWh at the highest fuel mass flow. The lowest value of specific effective fuel consumption in measurement Set 1 amounts 199.04 g/kWh for fuel mass flow of 13.447 kg/h.

In measurement Set 2 (2400 rpm) specific effective fuel consumption amounts 262.57 g/kWh at the lowest fuel mass flow and 230.85 g/kWh at the highest fuel mass flow. The lowest value of specific effective fuel consumption in measurement Set 2 amounts 228.82 g/kWh for fuel mass flow of 28.842 kg/h.

From Fig. 5 can be seen that at the higher engine rotational speed, specific effective fuel consumption has much higher values in comparison with the lower rotational speed.

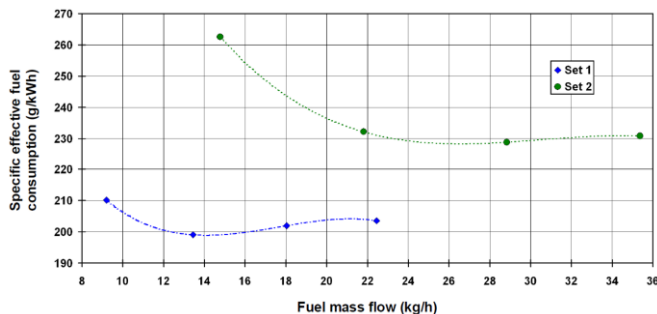


Fig. 5. Specific effective fuel consumption change for each engine measurement set

The heat released per engine process for both analyzed engine measurement sets is presented in Fig. 6. For the same fuel mass flow, heat released per engine process is much higher in Set 1 (1500 rpm) in comparison with Set 2 (2400 rpm).

In measurement Set 1 heat released per engine process amounts 4.37 kJ/proc. at the lowest fuel mass flow and 10.65 kJ/proc. at the highest fuel mass flow while in measurement Set 2 heat released per engine process amounts 4.38 kJ/proc. at the lowest fuel mass flow and 10.49 kJ/proc. at the highest fuel mass flow.

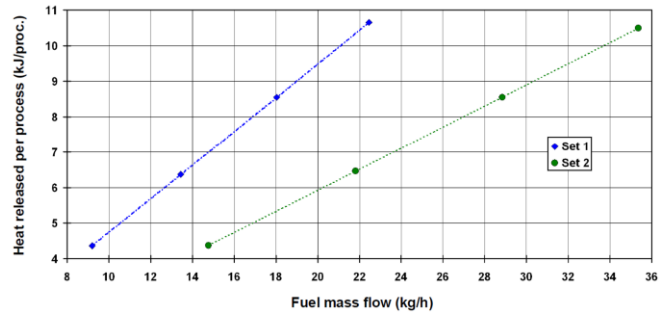


Fig. 6. The heat released per engine process change for each measurement set

A temperature change of engine lubrication oil is presented in Fig. 7 for each observed measurement set. Engine lubrication oil temperature change has the same trend in each measurement set, temperature increases during the increase in fuel mass flow. However, the curves which described oil temperature changes are not of the same type in each measurement set.

In measurement Set 1 engine lubrication oil temperature increases from 96.33 °C at the lowest fuel mass flow until 105.42 °C at the highest fuel mass flow. In measurement Set 2 engine lubrication oil temperature increases from 103.14 °C at the lowest fuel mass flow until 111.45 °C at the highest fuel mass flow.

Lubrication oil temperature is not an essential engine operating parameter, but it is important to measure it in order to maintain lubrication oil temperature within the range recommended by the producer.

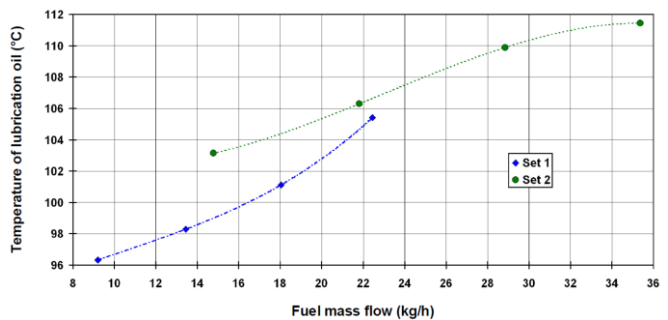


Fig. 7. Engine lubrication oil temperature change for each measurement set

Exhaust gas temperature has the highest value before the engine turbocharger turbine. It is important to measure exhaust gas temperature before and after turbine in order to calculate turbine power which is transferred directly to air blower. On that way can also be calculated air pressure after blower and compared with measurement results.

At each measurement set, exhaust gas temperature before the turbine increases during the increase in fuel mass flow, Fig. 8. In measurement Set 1 exhaust gas temperature before the turbine increases from 344.39 °C to 623.54 °C while in measurement Set 2 exhaust gas temperature before the turbine increases from 387.44 °C to 632.93 °C from the lowest to the highest fuel mass flow in each measurement set.

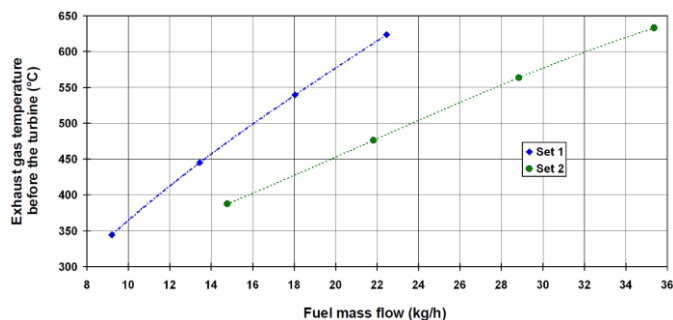


Fig. 8. The change of exhaust gas temperature before the turbine for each measurement set

Exhaust gas temperature after the turbine has the same trend as exhaust gas temperature before the turbine, Fig. 9, it increases during the increase in fuel mass flow for each measurement set. The same trend of temperatures before and after the turbine provides information about the satisfactory operation regime of turbocharger turbine, without its detail analysis.

In measurement Set 1 exhaust gas temperature after the turbine increases from 307.67 °C to 543.6 °C while in measurement Set 2 exhaust gas temperature after the turbine increases from 317.52 °C to 486.79 °C from the lowest to the highest fuel mass flow in each measurement set.

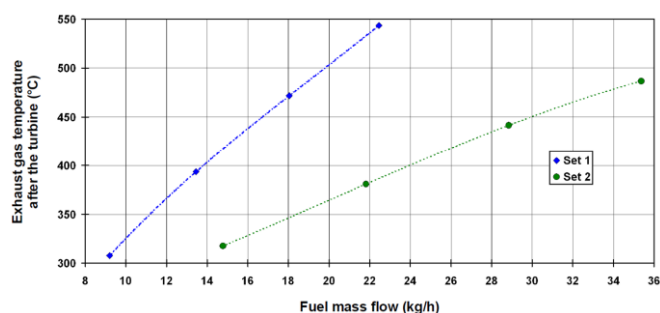


Fig. 9. The change of exhaust gas temperature after the turbine for each measurement set

6. Conclusions

In this paper is presented a change in operating parameters for a high speed direct injection turbocharged diesel engine MAN D0826 LOH15 during the injected fuel mass flow variation.

Based on a two measurement sets at different engine rotational speed (1500 rpm and 2400 rpm) is presented change of different engine operating parameters. Calculated engine operating parameters, based on measurement results, were engine torque, effective power, excess air ratio, specific effective fuel consumption and heat released per engine process.

Measured temperature of lubrication oil increases during the increase in engine fuel mass flow and it is important to maintain the oil temperature within the range recommended by the producer. Measured exhaust gas temperature change before and after the turbocharger turbine are the important elements in the analysis of turbocharging process and its efficiency.

Engine analysis was performed with standard diesel fuel. In future research will be interesting to compare the same operating parameters when engine uses alternative fuels or its blends with standard diesel fuel. This thought will be the guiding idea in future investigation of this engine.

7. Acknowledgment

The authors express their thankful regards to the whole team at the Laboratory for Internal Combustion Engines and Electromobility (LICEM), at the Faculty of Mechanical Engineering, University of Ljubljana, Slovenia. This work was supported by the University of Rijeka (contract no. 13.09.1.1.05).

8. References

- [1] Rakopoulos, C. D., Giakoumis, E. G.: *Diesel Engine Transient Operation - Principles of Operation and Simulation Analysis*, Springer-Verlag London, 2009. (doi:10.1007/978-1-84882-375-4)
- [2] Park, S., Kim, Y., Woo, S., Lee, K.: *Optimization and calibration strategy using design of experiment for a diesel engine*, Applied Thermal Engineering, 123, p. 917–928, 2017. (doi:10.1016/j.applthermaleng.2017.05.171)
- [3] Medica, V.: *Simulation of turbocharged diesel engine driving electrical generator under dynamic working conditions*, Doctoral Thesis, Rijeka, University of Rijeka, 1988.
- [4] Škifić, N.: *Influence analysis of engine equipment parameters on diesel engine characteristics*, Doctoral Thesis, Rijeka, University of Rijeka, 2003.
- [5] Mrzljak, V., Medica, V., Bukovac, O.: *Volume agglomeration process in quasi-dimensional direct injection diesel engine numerical model*, Energy, 115, p. 658–667, 2016. (doi:10.1016/j.energy.2016.09.055)
- [6] Mrzljak, V., Medica, V., Bukovac, O.: *Simulation of a Two-Stroke Slow Speed Diesel Engine Using a Quasi-Dimensional Model*, Transactions of Famena, 2, p. 35–44, 2016. (doi:10.21278/TOF.40203)
- [7] Jafari, M., Parhizkar, M.J., Amani, E., Naderan, H.: *Inclusion of entropy generation minimization in multi-objective CFD optimization of diesel engines*, Energy, 114, p. 526–541, 2016. (doi:10.1016/j.energy.2016.08.026)
- [8] Jamrozik, A.: *The effect of the alcohol content in the fuel mixture on the performance and emissions of a direct injection diesel engine fueled with diesel-methanol and diesel-ethanol blends*, Energy Conversion and Management, 148, p. 461–476, 2017. (doi:10.1016/j.enconman.2017.06.030)
- [9] Hoseini, S.S., Najafi, G., Ghobadian, B., Rahimi, A., Yusaf, T., Mamat, R., Sidik, N.A.C., Azmi, W.H.: *Effects of biodiesel fuel obtained from Salvia Macrosiphon oil (ultrasonic-assisted) on performance and emissions of diesel engine*, Energy, 131, p. 289–296, 2017. (doi:10.1016/j.energy.2017.04.150)
- [10] Othman, M.F., Adam, A., Najafi, G., Mamat, R.: *Green fuel as alternative fuel for diesel engine: A review*, Renewable and Sustainable Energy Reviews, 80, p. 694–709, 2017. (doi:10.1016/j.rser.2017.05.140)
- [11] Tamilselvan, P., Nallusamy, N., Rajkumar, S.: *A comprehensive review on performance, combustion and emission characteristics of biodiesel fuelled diesel engines*, Renewable and Sustainable Energy Reviews, 79, p. 1134–1159, 2017. (doi:10.1016/j.rser.2017.05.176)

ENERGY EFFICIENCY AND ENERGY POWER LOSSES OF THE TURBO-GENERATOR STEAM TURBINE FROM LNG CARRIER PROPULSION SYSTEM

PhD. Mrzljak Vedran, PhD. Senčić Tomislav, Prof. Prpić-Oršić Jasna
Faculty of Engineering, University of Rijeka, Vukovarska 58, 51000 Rijeka
E-mail: vedran.mrzljak@riteh.hr, tsencic@riteh.hr, jasna.prpic-orsic@riteh.hr

Abstract: Turbo-generator (TG) steam turbine energy efficiency and energy power losses in a wide range of turbine loads were presented in this analysis. For TG steam turbine was investigated influence of steam specific entropy increment from the real (polytropic) steam expansion on energy power losses and energy efficiency. TG turbine energy power losses, during the all observed loads, were in the range from 646.1 kW to 685.5 kW. The most influenced parameter which defines change in TG turbine energy power losses is steam mass flow change, while for small steam mass flow changes, influence of steam specific entropy increment on steam turbine energy power losses is the most influential. Steam specific entropy incremental change can be used to estimate the change of TG steam turbine energy efficiency. Increase in steam specific entropy increment resulted with a decrease in TG turbine energy efficiency and vice versa. Analyzed steam turbine energy efficiency ranges from 53.84 % to 60.12 %, what is an expected range for low power steam turbines.

Keywords: TURBO-GENERATOR, STEAM TURBINE, ENERGY EFFICIENCY, ENERGY POWER LOSSES

1. Introduction

Marine steam turbine propulsion plants nowadays can be found in a number of LNG carriers [1]. Such steam propulsion plant consists of many constituent components [2] and one of them is turbo-generator (TG) which steam turbine is analyzed in this paper from the aspect of energy.

The analyzed LNG carrier has at disposal two identical turbo-generators which are designed to cover all ship requirements for electrical power. Each TG turbine has identical operating parameters (inlet and outlet temperatures, pressures and mass flows) and for the analysis is selected one of them. Steam turbine for each electric generator comprises of nine Rateau stages. Steam turbines with Rateau stages and their complete analysis can be found in [3]. Many details of the classic and special designs of marine steam turbines and their auxiliary systems are presented in [4] and [5].

The goal of the TG steam turbine analysis was to determine the specific entropy increment increase during steam expansion from the real exploitation for different steam turbine loads. Increase in steam specific entropy increment, usually indicate an increase in system energy power losses (in this analysis system is a TG steam turbine). It was examined the influence of steam specific entropy increment change on TG turbine energy power losses and energy efficiency change, at each observed operating point.

Main characteristics of the LNG carrier in which steam propulsion system is mounted analyzed turbo-generator are presented in Table 1.

Table 1. Main specifications of the LNG carrier

Dead weight tonnage	84,812 DWT
Overall length	288 m
Max breadth	44 m
Design draft	9.3 m
Propulsion turbine	Mitsubishi MS40-2 (max. power 29420 kW)
Turbo-generators	2 x Shinko RGA 92-2 (max. power 3850 kW each)

2. Equations for steam turbine energy analysis

2.1. General equations for the energy analysis

Energy analysis is defined by the first law of thermodynamics, which is related to the conservation of energy [6]. Mass and energy balance equations for a standard volume in steady state disregarding potential and kinetic energy can be expressed according to [7] and [8] as:

$$\sum \dot{m}_{IN} = \sum \dot{m}_{OUT} \quad (1)$$

$$\dot{Q} - P = \sum \dot{m}_{OUT} \cdot h_{OUT} - \sum \dot{m}_{IN} \cdot h_{IN} \quad (2)$$

Energy power of a flow for any fluid stream can be calculated according to the equation [9]:

$$\dot{E}_{en} = \dot{m} \cdot h \quad (3)$$

Energy efficiency may take different forms depending on the type of the system. Usually, energy efficiency can be written as [10]:

$$\eta_{en} = \frac{\text{Energy output}}{\text{Energy input}} \quad (4)$$

2.2. Turbo-generator turbine energy efficiency and energy power losses

Steam turbine for each turbo-generator drive is condensing type and consists of nine Rateau stages [11]. Schematic view of steam turbine directly connected to an electric generator (the whole set of steam turbine and electric generator is called turbo-generator) is presented in Fig. 1. In Fig. 1 is also presented steam mass flow along with specific enthalpy and specific entropy at the steam turbine inlet and outlet.

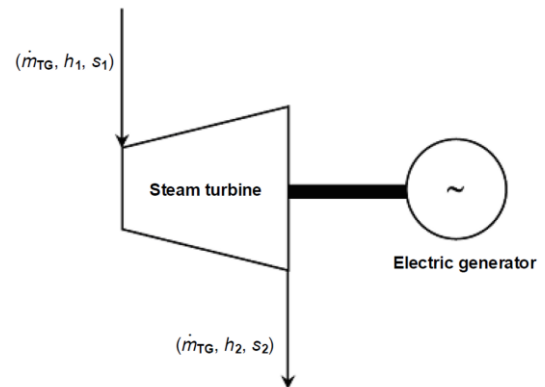


Fig. 1. Specific enthalpy, specific entropy and steam mass flow through the turbo-generator turbine

Steam mass flow in relation to the real developed turbine power for TG turbine, regarding the producer specifications, is presented in Fig. 2.

Real TG turbine power calculation at different loads was necessary for the TG turbine correct energy analysis. The turbine real developed power curve was approximated by the third degree polynomial using data from Fig. 2:

$$P_{TG,RE} = -4.354 \cdot 10^{-10} \cdot \dot{m}_{TG}^3 + 6.7683 \cdot 10^{-6} \cdot \dot{m}_{TG}^2 + 0.251318 \cdot \dot{m}_{TG} - 256.863 \quad (5)$$

where $P_{TG,RE}$ was obtained in (kW) when \dot{m}_{TG} in (kg/h) was placed in the equation (5). Steam mass flow through the TG turbine (\dot{m}_{TG}) was measured component, while the developed real TG turbine power was calculated according to equation (5).

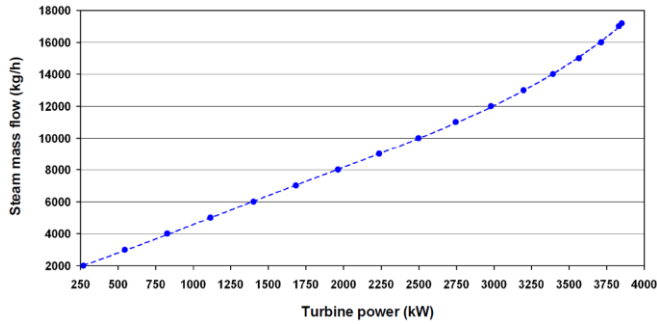


Fig. 2. Real TG turbine power in relation to the steam mass flow [11]

During measurements, no steam leakage on the analyzed TG turbine was observed, so the mass balance for the TG steam turbine inlet and outlet is valid as:

$$\dot{m}_{TG,1} = \dot{m}_{TG,2} = \dot{m}_{TG} \quad (6)$$

According to Fig. 1 and Fig. 3, h_1 is steam specific enthalpy at the turbine inlet, and h_2 is steam specific enthalpy at the turbine outlet after real (polytropic) expansion. Steam specific enthalpy at the turbine inlet was calculated from the measured pressure and temperature. Steam specific entropy at the turbine inlet s_1 was also calculated from measured steam pressure and temperature at the turbine inlet. Steam real specific enthalpy at the turbine outlet was calculated from the turbine power $P_{TG,RE}$ in (kW) and measured steam mass flow \dot{m}_{TG} in (kg/s) according to [12] by using an equation:

$$h_2 = h_1 - \frac{P_{TG,RE}}{\dot{m}_{TG}} \quad (7)$$

The steam real specific entropy at the turbine outlet s_2 was calculated from steam real specific enthalpy at the turbine outlet h_2 , calculated by using equation (7), and measured pressure at the turbine outlet.

Steam specific enthalpy after isentropic expansion h_{2S} was calculated from the measured steam pressure at the turbine outlet p_2 and from known specific entropy at the turbine inlet s_1 . Ideal isentropic expansion assumes no change in steam specific entropy ($s_1 = s_{2S}$), Fig. 3.

Steam specific enthalpy at the turbine inlet, steam specific enthalpy at the end of isentropic expansion and both steam specific entropies (at the turbine inlet and outlet) were calculated by using NIST REFPROP 8.0 software [13].

To proper described TG turbine energy power losses, in any steam turbine operating range, it must be known the real turbine developed power and isentropic power, which can be developed in the ideal situation (when the change in steam specific entropy does not occur). Isentropic steam turbine power, according to Fig. 3, should be calculated as:

$$P_{TG,IS} = \dot{m}_{TG} \cdot (h_1 - h_{2S}) \quad (8)$$

Isentropic steam turbine power will always be higher than the real developed power, because of higher specific enthalpy difference (increment) during the isentropic expansion in comparison to the real polytropic expansion.

Steam turbine (TG turbine) energy power losses can be calculated as:

$$\dot{E}_{TG,en,PL} = P_{TG,IS} - P_{TG,RE} = \dot{m}_{TG} \cdot (h_2 - h_{2S}) \quad (9)$$

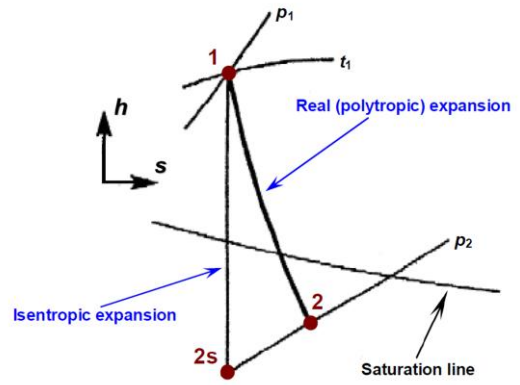


Fig. 3. Turbo-generator steam turbine real (polytropic) and ideal (isentropic) expansion

Energy efficiency of TG steam turbine can be calculated according to [14] and [15] by using the following equation:

$$\eta_{TG,en} = \frac{(h_1 - h_2)}{(h_1 - h_{2S})} = \frac{P_{TG,RE}}{P_{TG,IS}} \quad (10)$$

3. Measurement results and measuring equipment of the analyzed TG steam turbine

Measurement results of required operating parameters for TG turbine are presented in relation to the propulsion propeller speed, Table 2. Propulsion propeller speed is directly proportional to steam system load, higher propulsion propeller speeds denote higher steam system loads and vice versa.

Table 2. Measurement results for TG turbine

Propulsion propeller speed (rpm)	Steam pressure at the TG turbine inlet (MPa)	Steam temperature at the TG turbine inlet (°C)	Steam pressure at the TG turbine outlet (MPa)	Steam mass flow through TG turbine (kg/h)
25.00	6.21	491.0	0.00541	4648.83
41.78	6.22	491.0	0.00489	4556.16
56.65	5.97	490.5	0.00425	4000.58
65.10	6.07	491.0	0.00392	3838.78
70.37	6.07	502.5	0.00397	3778.91
76.56	6.01	504.5	0.00420	4070.84
80.44	5.89	501.5	0.00554	4689.03
83.00	5.90	493.5	0.00561	4487.93

All the measurement results were obtained from the existing measuring equipment mounted on the TG turbine inlet and outlet. List of all used measuring equipment was presented in the Table 3.

Table 3. Used measuring equipment for the TG turbine analysis

Steam temperature (TG inlet)	Greisinger GTF 601-Pt100, Immersion probe [16]
Steam pressure (TG inlet)	Yamatake JTG980A, Pressure Transmitter [17]
Steam pressure (TG outlet)	Yamatake JTD910A, Pressure Transmitter [18]
Steam mass flow (TG inlet)	Yamatake JTD960A, Pressure Transmitter [18]
Propulsion propeller speed	Kyma Shaft Power Meter, (KPM-PFS) [19]

4. TG steam turbine energy analysis results with the discussion

Steam specific entropy difference (increment) between the inlet and outlet of the TG steam turbine is presented in Fig. 4 for all the observed steam system loads. As the steam specific entropy at a TG turbine inlet is almost constant during the all propulsion propeller speeds, specific entropy increment is the most influenced by steam specific entropy at the TG turbine outlet.

From the lowest to the highest observed propulsion propeller speeds, TG turbine steam specific entropy increment (difference) firstly increases from 1.69 kJ/kg·K at 25.00 rpm up to 2.02 kJ/kg·K at propulsion propeller speed of 70.37 rpm, after which decreases to the lowest value of 1.69 kJ/kg·K at 83.00 rpm.

Increase in steam specific entropy increment, usually indicates an increase in system energy power losses, for a large number of different systems [14]. It will be interesting to analyze does the same conclusion is valid for the TG steam turbine.

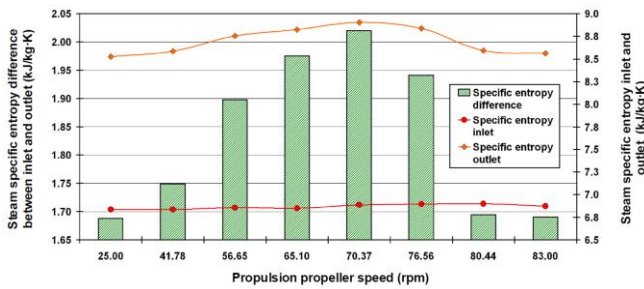


Fig. 4. Steam specific entropy change at the TG turbine inlet and outlet along with specific entropy difference (increment) between inlet and outlet

TG steam turbine isentropic and real power is presented in Fig. 5. The change in both TG turbine power for all observed propulsion propeller speeds must have the same trend. Isentropic TG turbine power can theoretically be developed by using the real operating parameters, but without any losses (without change in steam specific entropy). TG real power is the power developed according to real measured operating parameters in the LNG carrier propulsion system during navigation.

In the whole range of observed steam system loads, isentropic TG turbine power varies from 1423 kW up to 1711 kW, while in the same load range real TG turbine power varies from 766 kW up to 1025.5 kW. The real TG turbine power depends on the current need for electricity and it changes depending on the inclusion or exclusion of the individual electrical consumers.

The difference in isentropic and real TG turbine power represents energy power losses of the real TG steam turbine process in comparison with ideal one.

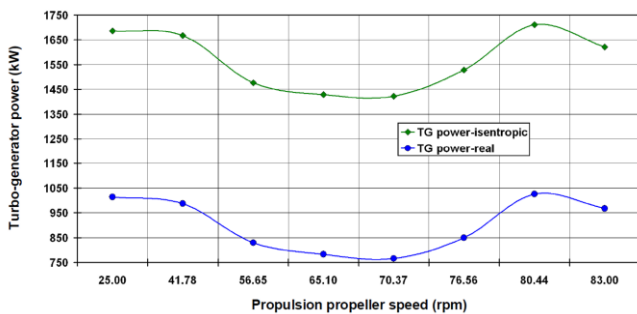


Fig. 5. Change in TG turbine power (real and isentropic) for all observed propulsion propeller speeds

Increase in steam specific entropy increment reduces available steam specific enthalpy difference which will be used in steam turbine. As a result, increase in steam specific entropy increment will cause a decrease in real developed steam turbine power.

From Fig. 4 and Fig. 6 can be seen that the change in TG turbine specific entropy increment does not have the most significant influence on TG steam turbine energy power losses. For example, between propulsion propeller speed of 41.78 rpm and 56.65 rpm, steam specific entropy increment increases, Fig. 4, while for the same propulsion propeller speeds TG turbine energy power loss decreases, Fig. 6. The same occurrence is visible between propulsion propeller speeds of 76.56 rpm and 80.44 rpm when steam specific entropy increment decreases while for the same propulsion propeller speeds TG turbine energy power loss increases.

The most significant influence on TG steam turbine energy power losses has steam mass flow through the turbine. In general, increase in steam mass flow will increase TG turbine energy power losses, while a decrease in steam mass flow will decrease TG turbine energy power losses. TG steam turbine energy power losses, between some observed operating points, during a small change in steam mass flow are also influenced by steam specific entropy increment.

Between propulsion propeller speed of 41.78 rpm and 56.65 rpm, TG turbine energy power losses decrease, Fig. 6, because of a noticeable decrease in steam mass flow from 4556.16 kg/h to 4000.58 kg/h, Table 2. Increase in steam specific entropy increment between these two propulsion propeller speeds does not have significant influence on energy power losses change, Fig. 4.

Also, between propulsion propeller speeds of 76.56 rpm and 80.44 rpm TG turbine energy power losses increases, Fig. 6, because of noticeable increase in steam mass flow from 4070.84 kg/h to 4689.03 kg/h, Table 2, regardless of steam specific entropy increment noticeable decrease, Fig. 4.

On the other side, for a small change in steam mass flow, steam specific entropy increment can have an important influence on TG turbine energy power losses change. When compared propulsion propeller speeds of 65.10 rpm and 70.37 rpm, steam mass flow decreases from 3838.78 kg/h to 3778.91 kg/h, Table 2, but this steam mass flow decrease does not cause a decrease in TG turbine energy power losses, Fig. 6. Between these two propulsion propeller speeds, increase in TG turbine energy power losses occurs because of a notable increase in steam specific entropy increment, Fig. 4.

Final conclusion which can be derived is that the most influenced parameter on TG turbine energy power losses is steam mass flow. For a small change in steam mass flow, steam specific entropy increment takes a leading role in affecting the change of TG turbine energy power losses.

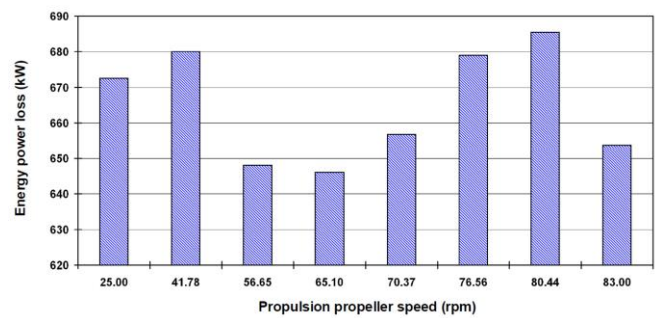


Fig. 6. TG turbine energy power loss change in all observed propulsion propeller speeds

Steam specific entropy increment can be used as an essential parameter for evaluation of TG steam turbine energy efficiency change. During the increase in steam specific entropy increment, TG turbine energy efficiency decreases and during the decrease in steam specific entropy increment, TG turbine energy efficiency increases. This conclusion is valid for every two observed propulsion propeller speeds, during the whole investigated TG turbine load range, Fig. 4 and Fig. 7.

The highest TG turbine energy efficiency of 60.12 % was obtained for the lowest steam specific entropy increment of 1.69

kJ/kg·K at the propulsion propeller speed of 25.00 rpm (the lowest observed TG turbine load), Fig. 7. The lowest TG turbine energy efficiency of 53.84 % was obtained for the highest steam specific entropy increment of 2.02 kJ/kg·K at the propulsion propeller speed of 70.37 rpm.

The analyzed TG steam turbine is a low power steam turbine. Its energy efficiency, for the observed loads, ranges from 53.84 % to 60.12 %, what is an expected range of energy efficiency for low power steam turbine in general [9].

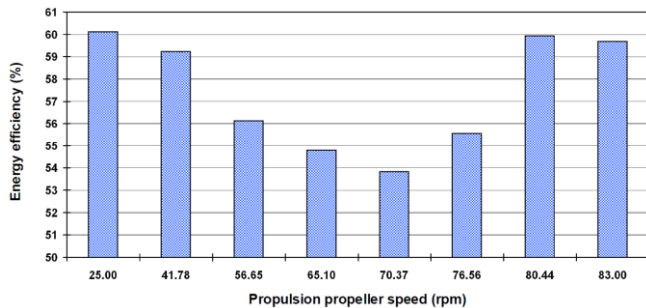


Fig. 7. TG turbine energy efficiency change in all observed propulsion propeller speeds

5. Conclusions

This paper presents an analysis of energy efficiency and energy power losses for low power steam turbine, in a wide range of turbine loads. For the analyzed TG steam turbine was investigated influence of steam specific entropy increment from the real (polytropic) expansion process on energy power losses and energy efficiency.

TG steam turbine energy power losses were calculated as a difference between steam turbine real developed power (polytropic steam expansion) and power which can be developed in an ideal situation without any specific entropy increment (isentropic steam expansion). It was found that TG turbine energy power losses, during the all observed loads, were in the range from 646.1 kW to 685.5 kW. Steam specific entropy increment does not have a major influence on TG turbine energy power losses change in general, but for small steam mass flow change, influence of steam specific entropy increment on steam turbine energy power losses is dominant. The most influenced parameter which defines change in TG turbine energy power losses is steam mass flow - increase in steam mass flow caused an increase in TG turbine energy power losses and vice versa.

Steam specific entropy increment change can be used to estimate the change of TG steam turbine energy efficiency. Increase in steam specific entropy increment resulted with a decrease in TG turbine energy efficiency and decrease in steam specific entropy increment resulted with an increase in TG turbine energy efficiency.

NOMENCLATURE

Abbreviations:

LNG Liquefied Natural Gas
TG Turbo generator

Greek symbols:

η efficiency, -

Latin Symbols:

\dot{E} stream flow power, kJ/s
 h specific enthalpy, kJ/kg
 \dot{m} mass flow, kg/s or kg/h
 p pressure, MPa
 P power, kJ/s
 \dot{Q} heat transfer, kJ/s
 s specific entropy, kJ/kg·K

Subscripts:

en energy
IN inlet
IS isentropic (ideal)
OUT outlet
PL power loss
RE real

6. Acknowledgment

The authors would like to extend their appreciations to the main ship-owner office for conceding measuring equipment and for all help during the exploitation measurements. This work was supported by the University of Rijeka (contract no. 13.09.1.1.05) and Croatian Science Foundation-project 8722.

7. References

- [1] Schinas, O., Butler, M.: *Feasibility and commercial considerations of LNG-fueled ships*, Ocean Engineering 122, p. 84–96, 2016. (doi:10.1016/j.oceaneng.2016.04.031)
- [2] Fernández, I. A., Gómez, M. R., Gómez, J. R., Insua, A. A. B.: *Review of propulsion systems on LNG carriers*, Renewable and Sustainable Energy Reviews 67, p. 1395–1411, 2017. (doi:10.1016/j.rser.2016.09.095)
- [3] Bloch, H. P., Singh, M. P.: *Steam turbines-Design, Applications and Re-rating*, 2nd edition, The McGraw-Hill Companies, Inc., 2009.
- [4] Baldi, F., Ahlgren, F., Melino, F., Gabriellii, C., Andersson, K.: *Optimal load allocation of complex ship power plants*, Energy Conversion and Management 124, p. 344–356, 2016. (doi:10.1016/j.enconman.2016.07.009)
- [5] Haglund, F.: *Variable geometry gas turbines for improving the part-load performance of marine combined cycles - Combined cycle performance*, Applied Thermal Engineering 31, p. 467–476, 2011. (doi:10.1016/j.applthermaleng.2010.09.029)
- [6] Kaushik, S. C., Siva Reddy, V., Tyagi, S. K.: *Energy and exergy analyses of thermal power plants: A review*, Renewable and Sustainable Energy Reviews 15, p. 1857–1872, 2011. (doi:10.1016/j.rser.2010.12.007)
- [7] Hafidhi, F., Khir, T., Ben Yahyia, A., Ben Brahim, A.: *Energetic and exergetic analysis of a steam turbine power plant in an existing phosphoric acid factory*, Energy Conversion and Management 106, p. 1230–1241, 2015. (doi:10.1016/j.enconman.2015.10.044)
- [8] Tan, H., Zhao, Q., Sun, N., Li, Y.: *Enhancement of energy performance in a boil-off gas re-liquefaction system of LNG carriers using ejectors*, Energy Conversion and Management 126, p. 875–888, 2016. (doi:10.1016/j.enconman.2016.08.031)
- [9] Mrzljak, V., Poljak, I., Mrakovčić, T.: *Energy and exergy analysis of the turbo-generators and steam turbine for the main feed water pump drive on LNG carrier*, Energy Conversion and Management 140, p. 307–323, 2017. (doi:10.1016/j.enconman.2017.03.007)
- [10] Mrzljak, V., Poljak, I., Medica-Viola, V.: *Dual fuel consumption and efficiency of marine steam generators for the propulsion of LNG carrier*, Applied Thermal Engineering 119, p. 331–346, 2017. (doi:10.1016/j.applthermaleng.2017.03.078)
- [11] *Final drawing for generator turbine*, Shinko Ind. Ltd., Hiroshima, Japan, 2006., internal ship documentation
- [12] Ahmadi, G., Toghraie, D., Azimian, A., Akbari, O. A.: *Evaluation of synchronous execution of full repowering and solar assisting in a 200 MW steam power plant, a case study*, Applied Thermal Engineering 112, p. 111–123, 2017. (doi:10.1016/j.applthermaleng.2016.10.083)
- [13] Lemmon, E.W., Huber, M.L., McLinden, M.O.: *NIST reference fluid thermodynamic and transport properties-REFPROP*, version 8.0, User's guide, Colorado, 2007.
- [14] Kanoğlu, M., Çengel, Y.A., Dincer, I.: *Efficiency Evaluation of Energy Systems*, Springer Briefs in Energy, Springer, 2012. (doi:10.1007/978-1-4614-2242-6)
- [15] Ganjehkaviri, A., Mohd Jaafar, M. N., Hosseini, S. E.: *Optimization and the effect of steam turbine outlet quality on the output power of a combined cycle power plant*, Energy Conversion and Management 89, p. 231–243, 2015. (doi:10.1016/j.enconman.2014.09.042)
- [16] <https://www.greisinger.de>, (accessed 15.11.17.)
- [17] <http://www.industriascontrolpro.com>, (accessed 15.11.17.)
- [18] <http://www.krtproduct.com>, (accessed 12.11.17.)
- [19] <https://www.kyma.no>, (accessed: 13.11.17.)

THE IMPACT OF THE CONSTRUCTIVE PARAMETERS OF THE BUMPER OVER THE CONSEQUENCES DERIVING FROM THE PROCESS OF COLLISION

M. Sc. Gjakovski I.¹⁾; M. Sc. Shareska-Gjakovska V.²⁾; Ph.D. Brkovski D.³⁾ M.Sc. Milev S.⁴⁾
UNIQA Macedonia AD¹⁾, Standardization Institute of the Republic of Macedonia²⁾, RZ Inter-transped AD Skopje³⁾ Macedonia, Faculty of Mechanical Engineering - Goce Delcev University in Stip⁴⁾, Macedonia
E-mail: ivan_gjakovski@yahoo.com, shareska.violeta@yahoo.com, dean_brkovski@intertransped.com.mk, sasko.milev@ugd.edu.mk;

Abstract: *With the analysis and synthesis of the process of crashing, the impact of every factor is estimated in the generation and the development of the accident, and conclusions are drawn regarding the impact of particular elements from the vehicle over the consequences from the accident.*

The bumper system is a component of the vehicle intended to reduce the effects of the bumps on the front and the rear of the vehicle, its components and the shell. The cost of the damage and the protection regarding the bumper are the main criteria used to evaluate the efficiency of the impact of the bumper system, especially at low impact velocity.

This paper is representing the results of a deducted analysis and an investigation of the influence of the bumper system alongside its constructive parameters to the extent of the damage in low impact velocity. The investigation is primarily relating to statistical analysis of average damage, overall weighted average damage and variations in the amount of damage.

KEYWORDS: bumper system, accident damage, overall weighted average damage.

1. Introduction

The automotive industry has been known to be very competitive as far as its design and material usage are concerned. The automotive industry always faces greater market pressure to develop high quality products more quickly at lower costs, reduce weight in order to improve fuel efficiency and costs. One of the many purposes of the traffic jam safety measures is a construction of a safe vehicle which regarding its functions is supposed to represent the least influencing factor in the generation of causes that lead to creating detrimental consequences over all participants in the traffic jam and its environment, and, at the same time, in case an accident has occurred, to reduce or to completely baffle all possible consequences. The vehicle, regarding its constructive-technical and exploitative assets, the maintenance during the exploitation and the method of commandeering in traffic is one of the most important factors regarding safety. Starting from this particular definition regarding a vehicles safety in traffic, a broad space for investigation of all parameters is unclogged, which through the stage of projecting will lead to increase in the total value of safety regarding vehicles.

Systematizing the characteristics of the safety of the vehicle according to its specifics, they can be divided into three categories:

- Characteristics of active safety, which include all parameters that have an impact on the possibility of occurrence of an accident;
- Characteristics of passive safety, which include the parameters that have a preventive impact over the consequences of the accident; when the vehicle is partaking in an accident, the construction of the vehicle and the construction of its parts and units and their setting, to enable minimal or no injuries to the passengers in the vehicles and the incoming pedestrians, and also minimize the material damage of the vehicles, participants in the accident, the road and the environment.
- Characteristics of a catalytic safety, which include the parameters which indirectly contribute to the occurrence of the accident or increment the consequences of that accident.

The characteristics of the passive safety refer to all of the parts, units and elements which affect the consequences of the prompted accident in any way. The process of crashing is complex and dependent on various factors and their correlation. The subject of investigation in this paper is confirmation of the contribution of the bumper, with its constructive parameters to the consequences of the crash where the participants are moving with low speed. Through analysis of series of experimental crashes carried out in controlled

conditions, certain conclusions will be drawn concerning the estimate of the safety capabilities of the vehicle regarding its bumpers.

There are two significant aspects of the impact of the vehicle on the aftereffects of the accident regarding the bumper:

- The impact over the size of the injuries on a pedestrian regarding the incursion of the vehicle with the pedestrians.
- The impact over the size of the damage of the vehicles participants in the accident.

The main target of this paper is expansion and deepening the knowledge about the impact of the bumper with its constructive characteristics on the damage of the vehicle low impact velocity.

2. The role of the bumper in the safety capacities of the vehicle

The automobile bumper is a structural component of a vehicle that contributes to the improvement of the total asperity of the vehicle and its protection at front or rear impact. The bumper, firstly and mostly is intended to protect the body, the headlights or the stoplights, the indicators, the hood, the coolers and the other safety-bounded components of the vehicles in a low impact velocity.

But of course, the most important factor that affects the outcome of the accident is the impact velocity. The size of the damage of the vehicles is proportional to the impact velocity of the vehicles that partake in the accident. At higher impact velocities their impact over the damage of the vehicles is primary and dominant and the impact of the vehicle with its constructive characteristics and in that context also the bumper, is secondary. At low impact velocities of the vehicles the impact of the construction of the vehicles over the aftereffects of the accident is significant.

In 2002 IIHS conducted a research in traffic accidents in five big cities, recorded in their native departments for estimation of damage of the insurance companies. One of the conclusions of this study was that 14% of the accidents in the urban areas were impact with low impact velocities.

The bumper system is generally composed of four main elements: bumper cover, absorber, bumper carrier and holders, which are used for attachment with the body (the shell) of the vehicle.



Figure 1: *The main components that constitute the bumper system and their relation [2]*

The leading restricting constructive factor for the bumper system regarding the construction of the entire vehicle is its volume. The bumper cover for the most part has a design function while its function regarding the vehicle's safety is minor. Because of that, and in order to achieve low production costs, this element at today's modern vehicles is only fabricated out of plastic: polystyrene, polycarbonate or acrylonitrile butadiene styrene. The carrier is the most significant element of the bumper system which protects the vehicle against frontal impacts and rear impacts. The carrier is manufactured out of steel sheet, aluminum, fiberglass, composite material or plastic. Commonly, an element which absorbs the energy from the crash is set between the carrier and the cover. Unlike the carriers, the absorbers are made out of low density materials. The bumper system is attached to the shell of the vehicles via holders through a rigid frame or via elastic framework as the newer constructive solutions suggest, using special mechanisms so-called shock absorbers, which have additional meaning, to absorb a part of the kinetic energy of the crash.

The geometry, stability and the capability to absorb energy from the crash are the key qualities of a good bumper system. Its width and length and the vehicle's height position, its capability to prevail the integrity, form and position before and after a low impact collision. The bumper also has to be constructed in a way to be manageably mending, easy and by low costs, after a collision at low speed of the vehicles.

There are various concepts used while projecting the bumpers, even for same class vehicles or models from the same manufacturer. The bumper system is a compromise of its design, its capability to absorb a part of the energy of the crash and its manufacturing costs. Some manufacturers pay special attention to the style and the visual effect on the account of the safety possibilities of the bumper which results in high damage costs in collision at low speed of the vehicles.

By analyzing the behavior of the bumpers, in the implementation of a controlled series of collisions, a relevant conclusion can be drawn that today's modern bumpers are not improved with safety features in relation to bumpers in older vehicles.

3. Regulatory normative regarding the vehicle bumpers

The need for reaching a certain level of standardized quality of the bumpers sets the necessity for establishing a certain regulative in this area.

ECE Regulation No 42, adopted by the United Nations Economic Commission for Europe, requires the vehicle's safety system to continue to operate normally after the front or rear of the vehicle is under the influence of a pendulum set at 455 mm above

the ground, loaded or unloaded at speed from 4 km per hour, along the entire length, i.e. 2.5 km per hour when operating in the corner on the bumper.

49 CFR part 581, American standard, prescribes requirements regarding the vehicles performance in a collision, front or rear, at low speed. The requirements apply to both the front and rear bumper of the vehicle, with a demand to prevent damage to the body and other equipment when hitting a barrier at a speed of 2 miles per hour along the entire length of the bumper i.e. 1miles per hour in a hit of the corner on the bumper.

Canadian regulation is very similar to the American. Also, this area is subject of regulation from the norms, the rulebooks of many scientific organizations, but not the NCAP programs for assessing the safety capabilities of the vehicle.

4. Realization of an engineering experiment. Discussion.

In this paper, by using statistical methods, the dependence of the height of the damage to the vehicle on the characteristics of the bumper system is analyzed and assessed, in the event of a low-speed collision, that is, the subject of statistical analysis are the results obtained from a series of experimental collisions in controlled conditions, realized by IIHS [3], according to the Bumper Test Protocol (Version VIII, September 2010) [4]. In this case, four types of impacts of the vehicle in a stationary obstacle are analyzed, which is simulating a bumper of another vehicle at rest: impact with front bumper, corner impact with front bumper, impact



with rear bumper and corner impact with rear bumper.

Figure 2: *Impact with front bumper; corner impact with front bumper; impact with rear bumper; corner impact with rear bumper*

The analyzed vehicles are classified into the following four groups: mini urban vehicles, small urban vehicles, medium-sized vehicles and limousines.

The subject of calculation and analysis is the average level of damage segmented by vehicle groups and impact type, overall weighted average damage (OWAD), level of variation and source of variations. In order for the measured sample to be considered relevant for further processing and withdrawing valid conclusions, it is necessary to be made a revision in the case of existence of rough errors and their elimination and to check out the fulfillment of the conditions of normality and homogeneity of the measured sample. For the four groups of vehicles, or their database, using the Grabs test, a conclusion can be drawn as the absence of a rough error. The high values of the p - indicator, significantly larger than the adopted level of risk of 5%, confirm the basic hypothesis that the data in the analyzed bases of the four groups of vehicles, follow the regularity of normal distribution.

TABLE 1: Average costs of damage from the performance of experimental crashes for the four groups of vehicles.

From the display it is obvious that the average costs for the calculated damage of the vehicles for the front impact are significantly higher in relation to rear impact whether it is a full or corner impact. Considering the configuration of the vehicle, the greater compactness in the rear as well as the existence of essential parts in the front of the vehicle, this conclusion is completely understandable. To see the level of variation, we will analyze the characteristic sizes of the normal distribution of the so-called overall weighted average damage (OWAD). OWAD is calculated when the amount of damage from the front and rear full impact is multiplied by two, and then collected with the amounts of damage to the corner front and rear impact. The amount thus obtained is divided by six and the value of the OWAD is obtained.

TABLE 2: Values of the characteristic sizes in the analysis of the OWAD values for the four groups of vehicles.

Group of vehicles	No. of vehicles in the group	Average OWAD (\$)	Standard Deviation (\$)	Coefficient of variation (%)
Mini urban vehicles	7	1.776	609	34 %
Small urban vehicles	21	1.718	558	32 %
Medium-sized vehicles	24	1.834	624	34 %
Limousines	11	2.463	884	36 %

Since it is about analysis of the results of destructive tests, the ANOVA method is used to determine the contribution of both factors: the type of vehicle and the impact side (front or rear) on the total variations in the group. In doing so, we must start with the hypothesis for the homogeneity of the examined series of samples, that is, all the samples in the examined series are sufficiently identical for us to be able to consider that we operate with the same types.

From Table 3, it can be seen that the influence of the vehicle on the OWAD of the vehicle type with its structural features and in this context on the bumpers, is significantly greater in relation to the impact side – front or rear. This influence is stronger in full, compared to corner impacts, i.e. at vehicles with larger mass and dimensions compared to vehicles with smaller dimensions and mass.

TABLE 3: Determining the contribution of the type of the analyzed vehicle and the impact side on OWAD

Group of vehicles	FRONT OR REAR FULL IMPACT		FRONT OR REAR CORNER IMPACT	
	% Influence of vehicle type	% Influence of impact side	% Influence of vehicle type	% Influence of impact side
Mini urban vehicles	70%	30%	54%	46%
Small urban vehicles	70%	30%	54%	46%
Medium-sized vehicles	100%	0%	80%	20%
Limousines	95%	5%	73%	27%

Group of vehicles	FULL IMPACT		CORNER IMPACT	
	Front (\$)	Rear (\$)	Front (\$)	Rear (\$)
Mini urban vehicles	2.119	1.388	2.161	706
Small urban vehicles	2.553	1.308	1.505	888
Medium-sized vehicles	2.244	1.455	1.938	1.193
Limousines	3.421	1.657	2.614	1.055

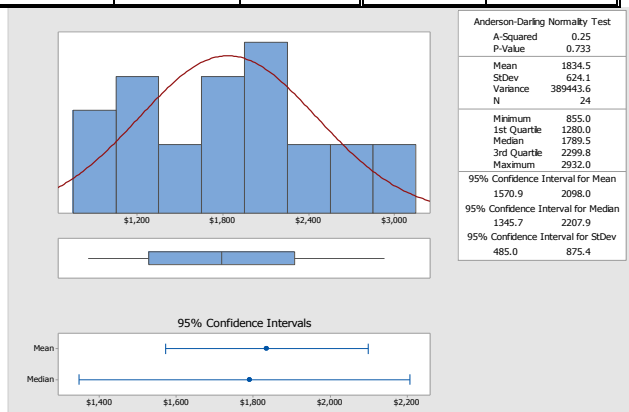


Figure 3: Diagram of probable distribution of OWAD for the group of medium-sized vehicles.

Although the number of motor vehicles that were the subject of this analysis differed significantly in each of the four groups, the obtained results show a high degree of coincidence. The height of the OWAD (table 2) ranges from \$ 1,718 in the group of small urban vehicles up to \$ 2,463 for the limousine group.

What is particularly noticeable are the huge coefficients of variation in the height of the OWAD, ranging from 32% to 36%. What is the reason for such variations in the level of damage in the groups?

5. Conclusion

Thanks to the results of the experimental impacts published by the IIHS, potential buyers are able to obtain adequate information about the amount of damage to vehicles at impacts conducted under controlled conditions. It is a motive for vehicle manufacturers to work on improving the performance of bumpers at vehicles, in

order to reduce the consequences of a traffic accident at low speeds of the vehicles.

Today's modern vehicles do not have bumpers with better impact resistance compared to older models. In support of this conclusion is the fact that the OWAD for all four groups of analyzed vehicles are higher than \$ 1,500, the boundary for poor and unacceptable quality of the bumper, according to the criteria established by IIHS. At the same time, the high level of variations in the OWAD in the realized experiment also speaks of the great possibilities for making improvements of the bumper system regarding the safety measures, starting from the design process and construction, selection of material, up to its testing.

Finally, the experiment and its results, as well as the requirements of customers for bumpers with an increased level of impact resistance, impose the question of the expediency of a more rigorous legal standardization of the quality of the bumper system.

6. Literature

- [1] Danev Dragi – Construction of motor vehicles, University St. Cyril and Methodius, Skopje, Faculty of mechanical engineering, Skopje, 2000
- [2] J.T.Wang – An extendable and retractable bumper, General Motor Corporation United States, Paper No. 05-0144 ,
- [3]<http://www.iihs.org/iihs/ratings/bumpers?classType=Midsize%20moderately%20priced%20cars>
- [4] Insurance Institute for Highway Safety – Bumper Test and Rating Protocol, Version VIII, September 2010,

EMBEDDED RESEARCHES ON ADAPTIVE PARAMETRIC MODELING OF HYDRAULIC GEAR PUMPS

Lecturer PhD. Eng. Ghionea Gabriel Ionuț¹, Prof. PhD Eng. Opran Constantin Gheorghe¹,

Lecturer PhD Eng. TARBĂ Cristian Ioan¹, PhD. Eng. Čuković Saša²

Faculty of Engineering and Management of Technological Systems, University POLITEHNICA of Bucharest, Romania ¹

Swiss Federal Institute for Technology – ETH, Institute for Biomechanics, Zurich, Switzerland ²

ionut76@hotmail.com, constantin.opran@ltpc.pub.ro, ticris@gmail.com, sasa.cukovic@hest.ethz.ch

Abstract: *This paper presents some of the research results on a fundamental and applicative procedures regarding the integrated intelligent conception of a Romanian series of hydraulic gear pumps. Following the analysis of the pump series in the manufacturing process, the requirement for a modernized parametric design of this product has been identified. Thus, we observed the beneficiaries' requirement for certain flows that are currently not provided by the current range of pumps. The parametric design of the pump leads to an easy and adaptive modification of the supplied flows, resulting in an innovative methodology which is very useful for the design and process engineers. The methodology is based on a computer-aided 3D modeling, specific pressure, drive torque, flow rate, etc. Each of these parameters leads to the intelligent modification of the certain geometric and functional features of the pump series designed to be adaptable to the dynamic demands of a modern economy.*

Keywords: GEAR PUMP, CAD MODEL, PARAMETERIZATION, PRESSURE, GEOMETRIC VOLUME

1. Introduction

Hydraulic gear pumps, due to their constructional simplicity, reduced number of components, high performance and reliability, low manufacturing cost and operational safety, are widely used to drive hydraulic fluids (for increasingly various industrial applications, from automotive to medical) in complex installations of different types and sizes.

Generally, these pumps contain two meshed gear wheels (spur or helical gears). The driving gear (driven by a motor or by an induced magnetic field) rotates in a certain direction and trains the driven gear in the opposite direction. Thus, by engaging the gears, the liquid between the teeth and closed by the pump elements (body, cover, bearing blocks) is transferred from the suction zone (inlet) to the discharge zone (outlet). The pumped liquid is trained around the two gears and not through the gears, thereby creating a pressure inside the pump [1, 2]. The liquid is transferred without flow pulse. Some pumps allow the fluid to be transferred in both directions, being called bidirectional pumps, which is one of the main advantages the user is looking for when selecting a pump.

Another important advantage of this type of pumps is given by the self-priming capability because at the moment of engagement/meshing the air is discharged from the gaps between the teeth, pressure is created and the liquid is aspirated due to the formation of an instant vacuum, sufficient for priming [3].

The precise way the pump components are manufactured, especially the meshing gears and the suction and discharge chambers, allows the hydraulic pumps to reach high pressure values with a very good efficiency (75-85%). For this purpose, strict tolerance conditions [4] have to be observed/fulfilled, the wheels have corrected teeth profile and often asymmetrical flanks [5, 6].

The current research on hydraulic gear pumps is associated with the creation of functional models that allow operation at high and constant pressures, with high efficiency and low weight (certain pump components are made of composite polymeric materials or light metal alloys). Also, a current requirement is a low noise and vibration level [3, 7], but also the ability to quickly create customized pumps when the manufacturer's standard range does not meet a particular market demand.

In order to improve modern pumps, to simulate and implement them, a comprehensive computer-optimized design study, many calculations, numerical simulations and tests are required [8, 9, 10].

The latest researches in the field, carried out within an important Romanian pump company [11], highlighted concerns about reducing the size and weight of the pumps components, developing micro-pumps, and replacing their current materials (alloys of steel and aluminum) with polymeric composite materials, one of the stated goals being the costs reduction for production and maintenance [12].

2. Main steps in the conception and parametric design of hydraulic gear pumps

In this paper we did a research on conception and computer aided design for improved and new models of hydraulic gear pumps, their static and dynamic analysis, functional tests etc.

The studied pumps have an important applicability in the automotive field, operate at high speeds and have good volumetric efficiency. The constructive and functional parameters of the pumps are carefully considered. It is observed how modifications of certain component dimensions influence the flow range, their weight and of the pump assembly, the driving torque and the efficiency.

During the conception stage, we performed calculations, created several 3D pump models using the CATIA v5 product and, thus, many constructive variants were analyzed.

We considered the variations in the pressures of the hydraulic fluid, the speed and friction between the pump components, the type, shape and dimensions of the meshing gears. All these parameters developed the CAD models and, together with mathematical models, were useful and necessary tools in the stages of the dynamic evaluation of pumps behavior to reduce noise, vibration, friction, etc.

Thus, for each pump model, we considered the following steps: analysis of the functional role of the pump and its structure, identification of dimensions, tolerances and assembly conditions, technological possibilities of manufacturing certain components, 3D parametric design of the pump assembly [13, 14], establishing the connections between the dimensions of its components, FEM simulations of the gears behavior in conditions imposed by hydrostatic pressure [9, 10, 15].

In the 3D modeling steps, we performed a study of the fluid flow transmitted by the pump, a comparison between the data resulted from the numerical calculations and those obtained from the experiments. Thus, we observed a mathematically correct correlation on how the fluid flow increases with the rising of an important characteristic of the pump: the geometric volume.

The results of this analysis showed that the parametric 3D model of the pump based on the variation of this geometric volume can be particularly important for the design and development of the pump series, also allowing the determination of the minimum and maximum pressures (and their variation) in the gaps of the meshing teeth. This reduces the noise and vibrations during operation, but especially the mistakes/errors that can lead to failures in pump's priming, early wear or even tearing of the teeth after many hours of service.

We constantly paid attention to the importance of simulating the functioning of the parametric model pumps to determine their predictable behavior after manufacturing and installing in the hydraulic installations.

In the research, for the parametric 3D modeling, we also took into consideration the technologies of manufacturing the pump components, the control and assembly methodologies and the analysis of the running behavior.

3. Parametric conception of a series of pumps

By the parametric design, we generated the drawing and optimized the teeth profiles (Fig. 1), using involute equations, 3D creation of the spur gears and then of the pump assembly, using numerous relations and equations [16, 17] and a methodology presented in [10, 18, 19]. With this parametric approach applied on the gear profile, it is possible to change all these parameters easily, which leads to several pump variants and, consequently, to the change of the fluid flow transmitted by it.

The main data involved in the design and modeling of the pump are: geometric and operating parameters (Q_p – flow rate, V_g – geometric volume/displacement, pressure p_p , speed n_0 , efficiency η , other conditions and constraints).

We considered some variants such as pumps with one, two or more rotors, number of teeth, module, gear width, pressure angle, etc. Generally, the pump is driven by a constant-speed electric motor, but we focused our attention towards the design and implementation of the magnetic actuator [20]. For this, however, certain pump components should be made of polymeric composite materials to reduce the pumps weight and the driving torque required to rotate the meshing gears [21].

Figure 1 presents the parametric profile of the pump teeth.

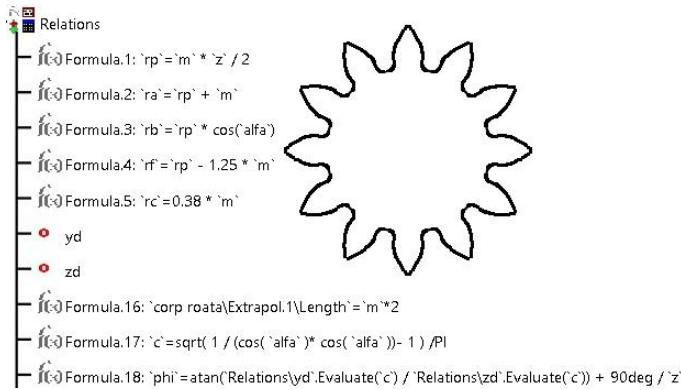


Fig. 1. Parametric creation of the gears profile

The parametric design of the gear pump assembly should be characterized by: constructive simplicity, compactness, operational safety and low noise [10].

The gaps between the gearing's teeth form conveyor cups for the hydraulic fluid. The cups volume is determined by the

geometrical elements of the involute tooth gears [17] supported by the bearings blocks.

Both gears have the same number of teeth. As the gears rotate, they separate on the intake side of the pump, creating a vacuum and suction which is filled by the fluid. The driving gear z_1 rotates at a constant speed n_0 in one direction and the driven gear z_2 rotates in the opposite direction (Fig. 2).

The fluid is aspirated through the Inlet aperture at the atmospheric pressure p_0 and is carried by the gears to the discharge (Outlet) aperture of the pump, where the meshing of the gears displaces the fluid (flow Q_p , l/min and pressure p_p , bar). The mechanical clearances are small, in the order of $10 \mu\text{m}$. The tight clearances [4], along with the speed of rotation, effectively prevent the fluid from leaking backwards.

The Q_p and p_p values represent the basic characteristics of the pump [16], being particularly important for the user in selecting the pump and dimensioning the hydraulic system.

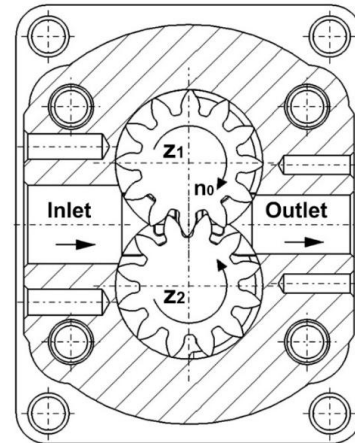


Fig. 2. Section through the gear pump

The 3D CAD model of the pump in Figure 3 was created based on the specific parameters: number of teeth $z_1 = z_2 = 12$, center distance $A = 31.4 \text{ mm}$, module $m = 2.54 \text{ mm}$ (normal specific displacements $x_n = 0.2 \text{ mm}$ pinion z_1 , $x_n = 0.199 \text{ mm}$ gear z_2 and frontal specific displacement $x_f = 0.2 \text{ mm}$), gear width $b = 18.3 \text{ mm}$, pitch circle diameter $d_d = 30.48 \text{ mm}$, outside circle diameter $d_a = 37.413 \text{ mm}$, rolling circle diameter $d_r = 31.4 \text{ mm}$, base circle diameter $d_b = 28.642 \text{ mm}$, pressure angle $\alpha = 20^\circ$, teeth height $h = 6.205 \text{ mm}$, normal gear pitch p_n , normal arc of dividing the tooth/gap s_n/e_n , frontal contact ratio $\epsilon = 1.494$, constant chord $s_c = 3.85 \text{ mm}$.

The parameter values are based on the numerical methods [10, 17] and standards in the field [4, 11]. Analysis of these data shows that the involute teeth gear is corrected [22, 23].

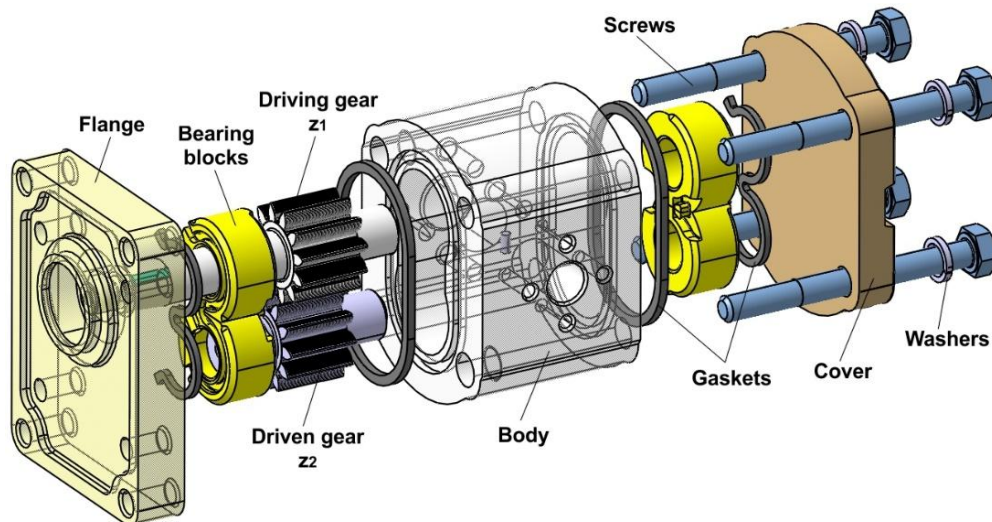


Fig. 3. The 3D model of the gear pump

Figure 4 contains a 3D detail of the gear, marked as a gap (cup) of/between two successive teeth, its volume is denoted as $V_{gt} = b \cdot A_p$, mm^3 , where b , mm, is the gear width and A_p , mm^2 , is the area of the cup profile.

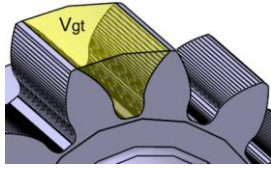


Fig. 4. The cup volume between two successive teeth

The geometric volume V_g of the pump is calculated by the formula (1), [16]:

$$V_g = 2 \cdot z \cdot V_{gt} \cdot 10^{-3}, [\text{cm}^3/\text{rot}] \quad (1)$$

The pump flow Q_p results from the formula (2), [16, 17]:

$$Q_p = \frac{V_g \cdot n_0}{10^3} \cdot \eta_v, [\text{l}/\text{min}] \quad (2)$$

where: n_0 is the driving speed (rot/min), z the number of teeth for each gear and η_v the volumetric efficiency (%).

High speeds, over 1500-2000 rot/min, lead to appearance of the cavitation process, which reduces the pump flow, efficiency and gas occurrence in the hydraulic fluid.

With the 3D CAD model of the pump created in CATIA v5 and knowing the influence of parameters on the pump's flow, we developed a program in Visual Basic Application (VBA) that directly modifies certain values based on a selection (Fig. 5) of the pump's geometric volume. For a certain value of the pump's geometric volume and the speed n_0 at which the pump operates (between the min and max limits imposed by the manufacturer), the pump will provide a certain flow, according to the formula (2).

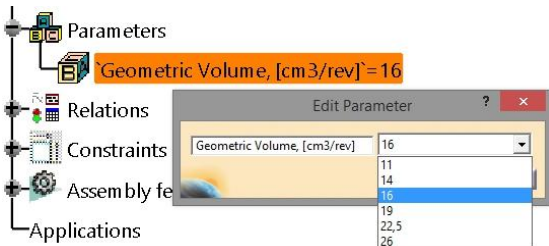


Fig. 5. User selection of the geometric volume

Figure 6 is a short sequence from the parametric modification of the pump assembly by the VBA code. The geometric volume selection paragraphs are observed, as shown in Figure 5, calculating and imposing certain values for dimensional parameters of many pump's components. We previously determined the values based on a numerical measurements and calculations [10, 18].

```

Inputs :
parameter: Real
if 'Geometric Volume, [cm3/rev]' == 11
(Corp\PartBody\Pad.1\FirstLimit\Length = 28.17mm
'roata conducatoare\PartBody\Pad.1\FirstLimit\Length' = 9.09mm
'roata condusa\PartBody\Pad.1\FirstLimit\Length' = 9.09mm
'Surub M10\Length' = 90mm
'Surub M10\threading' = 30mm
Corp\PartBody\Hole.2\Diameter = 20mm
Corp\PartBody\Hole.2\Sketch.11\Offset.164\Offset = 26.8mm)
else if 'Geometric Volume, [cm3/rev]' == 14
(Corp\PartBody\Pad.1\FirstLimit\Length = 30.67mm
'roata conducatoare\PartBody\Pad.1\FirstLimit\Length' = 11.59mm
'roata condusa\PartBody\Pad.1\FirstLimit\Length' = 11.59mm
'Surub M10\Length' = 90mm
'Surub M10\threading' = 30mm
Corp\PartBody\Hole.2\Diameter = 20mm
Corp\PartBody\Hole.2\Sketch.11\Offset.164\Offset = 31.3mm)
else if 'Geometric Volume, [cm3/rev]' == 16
(Corp\PartBody\Pad.1\FirstLimit\Length = 32.37mm
'roata conducatoare\PartBody\Pad.1\FirstLimit\Length' = 13.29mm
'roata condusa\PartBody\Pad.1\FirstLimit\Length' = 13.29mm
'Surub M10\Length' = 100mm
'Surub M10\threading' = 30mm
Corp\PartBody\Hole.2\Diameter = 20mm
Corp\PartBody\Hole.2\Sketch.11\Offset.164\Offset = 34.7mm)

```

Fig. 6. Visual Basic code sequence

The dimensional modifications shown in Figures 7 and 8 applied to the pump assembly represent two extreme variants of the pump series [10, 17], according to the selection in Figure 5.

Each constructive design passed through the complex FEM simulation process to determine the forces and pressures generated in the real operating conditions [9, 19]. When the situation imposed it, certain components changed their dimensional parameters (behavioristic 3D modelling).

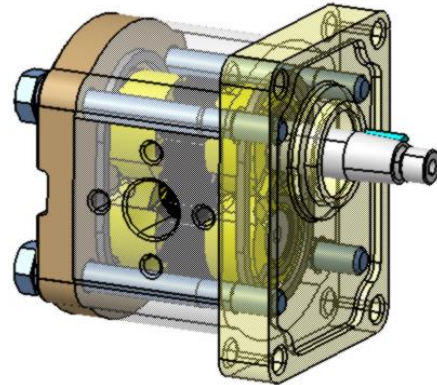


Fig. 7. Pump assembly for $V_g=11 \text{ cm}^3/\text{rev}$

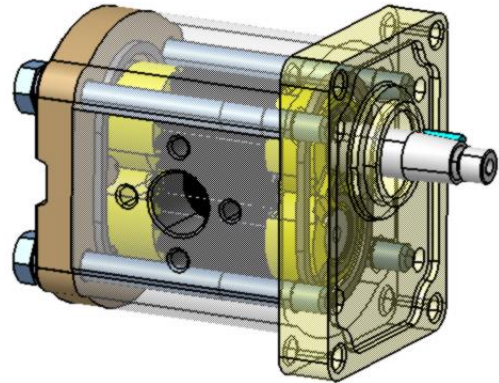


Fig. 8. Pump assembly for $V_g=26 \text{ cm}^3/\text{rev}$

For the magnetic drive pump [24, 25] variant, we will replace the flange and re-design the pump body and the driving gear (pinion) from Figure 3 to fulfill the main condition of complete sealing of the hydraulic fluid from the external environment (this is one of the main imposed conditions for this type of pumps).

The gearing calculations and FEM simulations for the forces and pressures will be resumed in multiple iterations to reach the optimal solution. Calculations and tests will also be performed to design and optimize the choice of magnetic elements (stator and rotor) and their integration solution in the new pump assembly.

The goal is, of course, to convert the current pumps (Figure 9, as a test variant or another constructive variant) into a magnetically driven and highly leak-proof pump [26]. Some components will be made of composite polymeric materials [27].



Fig. 9. Actual pump in a test configuration [11]

4. Conclusions

This paper presents preliminary results of the research conducted within the research project GEX, Ctr. No. 57/2017, *Composite Magnetic Pumps* and new concepts of pumps applicable in industrial environment. The proposed methodology of parametric design of a gear pump series [28] is conditioned by knowing the influence of the dimensional parameters of the pump on forces, moments and pressures in real operation in the certain hydraulic installations. This allows an optimal 3D design and product validation, important steps in the testing and launch process in serial production, with further development potential.

The parametric design procedures lead to the optimal conception of the constructive variants of the magnetic drive pump with the elaboration of a methodology for the selection and calculation deviation values and tolerances in the case of the gear parametric design.

The pump body will also be conceived and developed based on a precision criterion, but also on the fact that the ingot stock used as the body of the magnetic drive variant must remain in certain dimensions not to incur additional costs. Both for the series of pumps developed by parametric design, especially for the magnetic drive variant [26], we will consider the optimal solution of the technological and manufacturing parameters.

Acknowledgement: This work is funded by the University Politehnica of Bucharest, through the “Excellence Research Grants” Program, UPB – GEX 2017, Ctr. No. 57/2017.

5. References

1. Radzevich, S., P., *Dudley’s Handbook of Practical Gear Design and Manufacture*. CRC Press, Taylor&Francis Group, LLC, ISBN 978-1-4398-6602-3, Boca Raton, USA, 2012.
2. Opran, C., Pricop, M., Teodoru, C., *Researches on design and manufacturing of innovative double gears pumps*; Proceedings of the 25th DAAAM International Symposium on Intelligent Manufacturing and Automation, *Procedia Engineering*, pp.475 – 481, Elsevier, ISSN 1877-7058, Vienna, Austria, 2015.
3. Åkerblom, M., *Gear geometry for reduced and robust transmission error and gearbox noise*, Report, Maskinkonstruktion, School of Industrial Engineering and Management, Machine Design, Trita-MMK, ISSN 1400-1179, Stockholm, Sweden, 2008.
4. ***, DIN 3962/3963/3964, *Tolerances for cylindrical gear teeth package*. AGMA 201.02, *Tooth proportions for coarse pitch involute spur gear*, ISO 53: 1998, ISO 1326, *Cylindrical gears for general and heavy engineering - Standard basic rack tooth profile*, Bucher Hydraulics.
5. Alipiev, O., *Geometric design of involute spur gear drives with symmetric and asymmetric teeth using the realized potential method*, mechanism and machine, 2011.
6. Chira, F., Banica, M., Lobontiu, M., *Optimising involutes asymmetrical teeth gears software*; Chapter 38 in *DAAAM International Scientific Book*, pp. 363-376, Published by DAAAM International, ISBN 978-3-901509-69-8, ISSN 1726-9687, Vienna, Austria, 2009.
7. Faggioni, M., Samani, F., Bertacchi, G., Pellicano, F., *Dynamic optimization of spur gears*. *Mechanism and Machine Theory* 46, Elsevier, pp. 544–557, ISSN 0094-114X, 2011.
8. Corney J. R., *Modeling a variable speed drive for positive displacement pump*, *IEEE/ASME International Conference on Advanced Intelligent Mechatronics*, 2014.
9. Kollek, W., & Radziwanowska, U., *The modernization of gear micropump casing with the use of finite element method*. *International Journal of Research in Engineering & Technology*, ISSN(E) 2321-8843, vol. 2, issue 7, pp 69-76, 2014.
10. Opran, C., Ghionea, I., Pricop, M., *Embedded modelling and simulation software system for adaptive engineering of hydraulic gear pumps*, Proceedings of the 26th DAAAM International Symposium, Published by DAAAM International,

ISBN 978-3-902734-07-5, ISSN 1726-9679, pp. 0311-0319, DOI:10.2507/26th.daaam.proceedings.042, Vienna, Austria, 2016.

11. ***, Hesper, Rexroth, www.hesper.ro, Company catalogs.
12. Ghionea, I., *Stude of computer aided design and simulation importance in the conception and development phases of a product*. Proceedings of the IMC 2013 International Multidisciplinary Conference, North University of Baia Mare România – University College of Nyiregyhaza Hungary. pp.55-58. Bessenyei Publishing House, ISBN 978-615-5097-66-9, 2013.
13. Hu, S.J., Ko, J., Weyand, L., ElMaraghy, H.A. et al., *Assembly system design and operations for product variety*. *CIRP Annals – Manufacturing Technology* 60, pp. 715-733, 2011.
14. Rekiek, B., Dolgui, A., Delchambre, A., Bratcu, A., *State of art of optimization methods for assembly line design*. *Annual Reviews in Control* 26, pp. 163-174, 2002.
15. Casoli, P., Vacca, A., Franzoni, G., *A numerical model for the simulation of external gear pumps*, Proceedings of the 6th JFPS International Symposium on Fluid Power, TSUKUBA, ISBN 4-931070-06-X, pp. 705-710, 2005.
16. Oprean, A., *Machine-tools hydraulics*, Third edition. Didactic and Pedagogical Publishing House, Bucharest Romania, 1983.
17. Ghionea, I., *Researches on optimization by simulation of the industrial products design*. Phd. Thesis, University Politehnica of Bucharest, Romania, 2010.
18. Pupăză, C., Kaloudis, A., Athanasiadis, G., *Model for gear contact simulation*, The 17th International DAAAM Symposium on Intelligent Manufacturing & Automation: Focus on Mechatronics & Robotics, ISSN 1726-9679, ISBN 3-901-509-57-7, Vienna, Austria, 2006.
19. Linke, H., Hantschack, F., Trempler, U., Baumann, F., *New results on the calculation of the load capacity of internal gears*. *International Conference on Gears*. VDI-Society for Product and Process Design. VDI-Berichte 2108, ISBN 978-3-18-092108-2, Technical University of Munich, Germany, 2010.
20. Ashouri M., Shafii M. B., Moosavi A., *Theoretical and experimental studies of a magnetically actuated valveless micropump*, *Journal of Micromechanics and Microengineering*, 27(1), 2017.
21. Goldsteins L., Buceniaks I., Buligins L., *A simplified model of the centrifugal electromagnetic induction pump (CEMIP) with rotating permanent magnets*, *Magneto-hydrodynamics*, 50, 2014.
22. Lianfu, H., Changfeng, F., Wang, J., Tang, W., *Outlier detection and correction for the deviations of tooth profiles of gears*, *measurement science review*, vol. 13, no. 2, *Journal of the Institute of Measurement Science*, Slovak Academy of Sciences, Walter de Gruyter GmbH, Berlin, ISSN 1335 – 8871, Germany, 2013.
23. Shanmugasundaram, S., Maasanamuthu, S. R., Muthusamy, N., *Profile modification for increasing the tooth strength in spur gear using CAD*, *Engineering Design SCIRP* vol. 2, *Scientific Research*, ISSN 1947-3931, 2010.
24. Li, F.W., *Theoretical study and application of magnetic gears*. *For. Mach. Woodwork. Equip* 38, 2010.
25. Masaru, O., Masato E., *Study on the development of the surface magnet type magnetic gear*, *International Conference on Electrical Machines (ICEM)*, IEEE Publishing, ISBN 978-1-4799-4389-0, 2017.
26. Steven, E. O., *Advantages of a magnetically driven gear pump*, *Micropump*, USA, 2016.
27. ***, *Iwaki magnetic gear pumps*, Instruction manual.
28. Ghionea I., Ionescu, N., Ghionea, A., Ćuković S., Tonoiu, S., Catană, M., Jamshed, I., *Computer aided parametric design of hydraulic gear pumps*, *Acta Technica Napocensis*, vol. 60, issue I, Series: Applied Mathematics, Mechanics and Engineering, Technical University of Cluj-Napoca, ISSN: 1221-5872, WOS: 000416959000017, pp. 113-124, Cluj-Napoca, Romania, 2017.

ВЕЧНИЯТ ДИЗАЙН ИЛИ ДОБРЕ НАПРАВЕНОТО СТАРО

THE TIMELESS DESIGN OR THE WELL DONE OLD

гл. ас. д-р Кремена Маркова
Технически университет – Варна, България

kremenacankova@abv.bg

Abstract: The report focuses on the concept of "timeless design" and explores the parameters of this concept. Formulate principles that characterize it. Explore examples from different historical periods of the development of product design as a process, making comparisons and analogies. He draws conclusions about the dynamics of human-product-environment relationship.

Keywords: PRODUCT CHARACTERISTICS, TIMELESS DESIGN, PRODUCT DESIGN

1. Увод

Определението за „вечен“ засяга основно три положения: относно нещо, което не престава да съществува, няма край, безкрайно; относно нещо, което не прекъсва, безсрочно; и относно нещо, **което се повтаря, което остава постоянно.**

В настоящия доклад фокусът е върху продуктивния дизайн и поради това първите две положения не могат да бъдат актуални. Така се оформя хипотезата, че „вечен дизайн“ е онзи, който остава непроменен за период от много години, който повтаря своите структурни, функционални и естетически характеристики и продължава да бъде обект на желание у потребителя.

Разбира се, определението "за много години" също трябва да се конкретизира. Рационално е за отправна точка на проучване да се вземе началото на 20 век, защото продуктивният дизайн е обвързан с производството на стоки за масово потребление. Революционаризирането на вида на потребителските стоки след създаването на Веркбунда (1907), развитието на "Модерното движение" в Европа, рекламиращо полезните качества на машините и на продуктите, произведени чрез машини и развиването на един нов дизайнерски подход в Америка, подчинен на пазара - това са отправните точки за анализ откъм критерия "време". Най общо - около 100 години.

2. Резултати и дискусия

Анализирайки визуалните и функционални характеристики на изделия (разгледани по-долу), създадени основно около първата половина на упоменатия времеви период, се обособиха редица принципи, оформящи изискването за "вечен дизайн". Тези принципи засягат както характеристиките на формата, така и функционални, ергономични и технологични характеристики на продуктите, като основен критерий за оценка е човешкият фактор.

Разгледаните и анализирани примери са подбрани според адекватното им присъствие на днешния пазар като съвременно произвеждани продукти.

Принципи:

1. Форми с прост визуален модел. Симетрия.

Простотата на формата е може би най-ключовата и адекватна характеристика на продуктите на "вечния" дизайн. Обусловено от възможностите на човешките зрителни възприятия, формата с прост визуален модел се запомня лесно и трайно. Простата форма е лесно сравнима с базовите геометрични модели и затова е подходяща за интергриране в среда от различен тип,

стил, вид. Простите форми обикновено са тектонични (особено ако са съобразени със структурата на природния порядък), имат малък брой структурни елементи и установяват трайни връзки с потребителите, защото с тях се борави лесно. Простата форма без украсни орнаменти е наподвластна на мода и модни тенденции и затова има дълъг живот.

От друга страна наличието на симетрия осигурява визуален порядък и визуален баланс. Дори и най-сложната форма ако бъде повторена огледално спрямо ос на симетрия, то има осигурена визуална "завършеност" на наблюдаваното благодарение на заложената еднаквост. Базовите геометрични форми, които са наш отправен мисловен ориентир също са симетрични.



Фиг. 1 *Cyclone dining table* - Isamu Noguchi; *Stool 60* - Alvar Aalto; *Acrilica table lamp* - Joe Colombo;

Примери: **Cyclone dining table** на Isamu Noguchi е с прост визуален модел. Геометричният модул (дублирането на окръжностите) е контрастиран от седемте модула, оформящи "крака" на масата, върху които е приложена ротационна симетрия. Продуктът е създаден 1957 година (61 години) и се предлага на съвременния пазар от фирмата Knoll.

Подобен формообразуващ принцип е използван и при табулетката, която Alvar Aalto създава през 1932 година за общинската библиотека във Viipuri. **Stool 60** има възможно най-опростена визуална и геометрична структура и е съставен единствено от четири структурни елемента. Произвеждан от 1935 година от фабрика Artek днес използваме дизайнерски продукт на 85 години.

Формата на **Acrilica table lamp** на Joe Colombo (създадена през 1962 година) не използва геометричен модел, но има опростена и симетрична структура. Два функционални елемента са обединени формално в един, като този начин е постигната максимална визуална и фактологична простота. Произвежда се от Oluse.

2. Продукти, които позволяват промяна в технологията за тяхното производство, без да бъдат засегнати (променени) основните структурни, функционални и естетически характеристики.

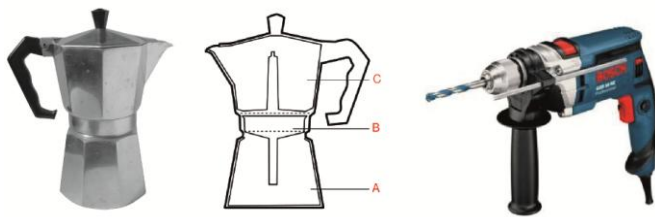


Фиг. 2. *Mulded Armchair* и *Mulded Side chair* - Ray and Charles Eames

Добър пример за илюстриране на този принцип са двете серии ляти (mulded) столове на Ray and Charles Eames - **Armchair** и **Side chair**. Създадени през 1950 година и внедрени от Herman Miller столовете запазват неизменна своята седалка (един излят елемент-черупка), като благодарение на технологичната еволюция тя може да бъде изработена от формован шперплат, фибростъкло или пластмаса. Дизайнерският проект предвижда модулет-седалка да бъде съчетаван с различна база според функционални и естетически съображения. Ергономично проектираните седалки са запазили своите формални характеристики вече 68 години.

3. Продукти, които имат функция, която продължава да бъде необходима, не е изместена от нови потребителски нужди.

Продуктите, илюстриращи този принцип в по-голямата си част са средства или инструменти. Техният дизайн е обвързан с техническите им характеристики и обикновено е дискретен, като оставя поле за изява на потребителя.



Фиг. 3 *Moka Express* - Alfonso Bialetti; *Строителен перфоратор* - Robert Bosch GmbH

Кафе машината **Moka Express** на Alfonso Bialetti се произвежда от 1933 година (от 85 години). И въпреки, че през годините са произвеждани множество вариативни решения, то структурата и принципът на функциониране на машината остават непроменени - долната камера (A) съдържа вода, която при нагряване преминава през контейнера със смляно кафе (B) и напитката се събира в горната камера (C).

Подобен е и примерът със строителния перфоратор, който Robert Bosch GmbH патентова през 1932 година като иновационен продукт и чиято основна структура и принцип на функциониране са същите и днес.

4. Комбинация от материали, доказали се в исторически план като:

- издръжливост;
- полезност;
- символ на лукса;
- естетически символ (класика)



Фиг. 4 *666 Superleggera* - Gio Ponti; *Wassily chair* - Marsel Breuer

Столът **666 Superleggera** на Gio Ponti е вдъхновен от традиционните италиански занаятчийски столове, в които седалката е постигната посредством оплетка на растителни влакна върху дървена рамка. Тази комбинация на материали е възприета от Cassina като устойчива, когато през 50-те години на 20 век започват производството на стола. Днес столът се предлага със седалка от индийска тръстика, както и с кожени и текстилни тапицерии.

Столът **Wassily** на Marsel Breuer е създаден 1925 година, когато мебелите с тръбна конструкция са иновационни продукти. Комбинацията от метал и кожа е все така устойчива и след 93 години, което е доказателство за формирането на една "издръжлива" естетика.



Фиг. 5 *606 Universal Shelving System* - Dieter Rams; *Playwood elephant* - Ray and Charles Eames; *Womb Chair* - Eero Saarinen;

Покриването на критерия "полезност" е ясно изразен в системата **606 Universal Shelving System** на Dieter Rams. Леката алуминиева конструкция, произвеждана от Vitsoe от 1960 година е определена като "вечна" в сайта на компанията. Едновременно с опростената визия на цялото, елементите на системата могат лесно да бъдат манипулирани от потребителите като им позволяват създаването на лични интериорни решения.

Playwood elephant на Ray and Charles Eames обединява функциите на играчка и на столче. Създадено през 1945 година и произвеждано днес от Vitra, слончето от формован шперплат доказва полезността на своя дизайн вече 73 години.

Креслото Утроба (**Womb Chair**) на Eero Saarinen е създадено в параметрите на иновативните за 40-те години на 20 век столове с монолитни седалки-черупки. Но облечено в текстил и снабдено с меки възглавници, то доказва своите удобство и полезност благодарение на ергономичното си проектиране. Произвежда се от 70 години непроменено от Knoll.



Фиг.6 *Barcelona chair* - Mies van der Rohe; *Eames Lounge chair*; *Artichoke pendant lamp* - Poul Henningsen; *LC3 Grand Confort* - Le Corbusier; *Arco lamp* - Achille Castiglioni;

Някои дизайнерски решения се асоциират като символи на лукса. Основните фактори за това са иновативността в конструкцията, която нова за времето си технология успява да предложи и комбинацията от използваните материали. Така се

създават такива формални качества на продуктите, каквито не е било възможно да бъдат постигнати в по-ранен времеви период. В резултат продуктите са технологичен и търговски хит на своето време, натоварени са смислово с претенция, стават лусозни стоки.

Такъв пример е столът **Barcelona** на Mies van der Rohe, създаден 1929 година за немския павилион на Световното изложение в Барселона. Идеята, че столът може да послужи за отпих на испанската кралица по време на посещението ѝ допълнително му помага за изграждане на бляскав статут и така той става предмет на лукса, неизменна част от престижни обществени и домашни интериори.

Съчетанието между бляскавата студенина на метала и черната телешка кожа все още се възприема и като образец за добър вкус.

Истински луксозна мебел е и **Eames Lounge chair**, създаден през 1956 година като модерен съвременен продукт от палисандър, кожа и алуминий. Технологичният процес по слепване на 7 слоя палисандрова дървесина в „черупки“ е все още нов за времето си и позволява реализирането на уникална форма. Ергономичните характеристики на стола също му създават висока репутация.

През 50-те години на 20 век Poul Henningsen създава серия висящи лампи, чиито структурни характеристики са такива, че не позволяват заслепяване със светлина на ползвателите. Заради високите си потребителски качества тези лампи станали толкова модни, че самото им присъствие в интериора сякаш карало и хората да изглеждат по-значими. Тук е представена **Artichoke pendant lamp**, създадена през 1958 година и произвеждаща се по настоящем от Louis Poulsen.

Дизайнерски продукти, превърнали се в естетически символи, иконични обекти, „класика“ са продукти, представящи за времето на създаването си не само иновация в технологията, материала и формата, но и позиционирани в центъра на нов културен феномен или пропагандиращи нова идея. По този начин **LC3 Grand Confort** на Le Corbusier от 1929 пропагандира идеята за пуризма. А **Arco lamp** на Achille Castiglioni със своите 210 см височина оспорва идеята за интериорно осветително тяло – възприема се повече като архитектурен, а не като интериорен елемент.

3. Заключение

Динамиката в отношението човек-изделие-среда се определя главно от човешкия фактор, защото човекът е този, който моделира средата и изделията спрямо своите лимити в психо-физиологичен аспект. Продуктовият дизайн е съществена част от това отношение. Еволюцията на продуктивния дизайн създаде феномен, наречен "вечен дизайн", който остава непроменен за период от много години, който повтаря своите структурни, функционални и естетически характеристики и продължава да бъде обект на желание у потребителя.

4. Източници

1. <https://www.knoll.com> (19.02.2018)
2. <https://www.artek.fi> (19.02.2018)
3. <http://www.oluce.com> (19.02.2018)
4. <https://www.hermanmiller.com> (19.02.2018)
5. <https://en.wikipedia.org> (19.02.2018)
6. <https://www.bosch.com> (19.02.2018)
7. <https://www.cassina.com> (19.02.2018)
8. <https://www.vitsoe.com> (19.02.2018)
9. <https://www.vitra.com> (19.02.2018)
10. <https://www.louispoulsen.com> (19.02.2018)

NUMERICAL SIMULATION ON THE VIBRATION OF A VEHICLE DRIVETRAIN WITH DUAL MASS FLYWHEEL

Assist. Prof. Eng. Pavlov N. PhD
Faculty of Transport, Technical University of Sofia, Bulgaria

npavlov@tu-sofia.bg

Abstract: This paper describes the results of numerical simulations of a vehicle drivetrain model with dual mass flywheel. The differential equations of the model are given. The vehicle inertia, the tire torsional stiffness and the transmission gear ratios are taking into account. Numerical simulations with given mass, elastic and damping parameters are carried out. Natural frequencies of the system are determinate. Vibrational characteristics of the system are shown and analysed.

Keywords: DUAL MASS FLYWHEEL, TRANSMISSION, DRIVELINE, DYNAMICS, VIBRATION

1. Introduction

The Dual Mass Flywheel (DMF) is widely used in modern diesel or gasoline direct injection engines. Downsizing and downspeeding of engines, lowering friction in gearboxes and lightweighting of transmissions and drivelines cause increased vibration and noise. The periodic combustion cycles of a four-stroke engine create torque and speed fluctuations which cause torsional vibration to be passed down the drivetrain (Fig. 1). The resulting noise and vibration, such as gear rattle, body boom and load change vibration, results in a decrease in comfort [1].

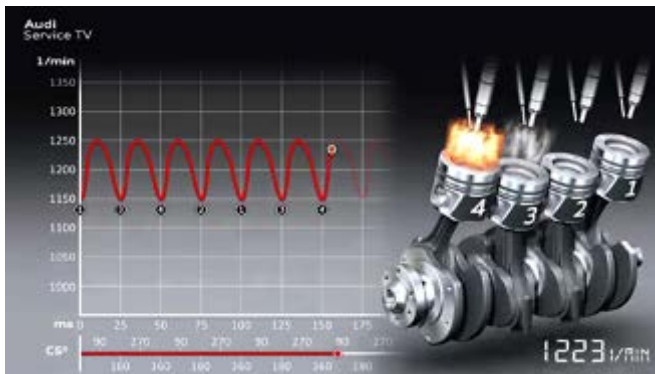


Fig. 1 Angular speed fluctuation of four-cylinder four-stroke engine [2]

The dual mass flywheel consist two masses free to rotate independently on a ball bearing. Two long coil springs lower the value of the natural frequency of the system (Fig. 2). Damping device is also present [3]. The secondary mass helps to increase the mass moment of inertia on the gearbox side. The total inertia of the DMF is the same as that of the rigid flywheel.



Fig. 2 Dual mass flywheel (DMF)[4]

As the DMF has an integral spring-damper system a rigid clutch driven disc without a torsion damper is normally used [1]. Owing to

the additional mass on the transmission input shaft, the vibration torque range, which is normally between 1200 min⁻¹ and 2400 min⁻¹ with original stiffer torsion dampers in the driven disc, is moved to a lower resonance speed range. This ensures excellent damping of engine vibration even at idle speeds [1]. Driving with less angular speed can reduce fuel consumption and CO₂ emissions [4, 5].

There are many books and research articles on DMF problems [4, 5, 6, 7, 8 and 9]. Their authors examine two or three degree of freedom engine-transmission model. But the system is more complicated because the vehicle mass should be reduced to the engine crankshaft and this is shown in [10, 11] but without mathematical description. The tire torsional stiffness has to be given an account too. Thus, the model whose scheme is given in source [12] most accurately reflects the essence of the real system. Unfortunately, the author does not present the mathematical description of this model, as well as numerical studies with specific values of the parameters. In textbook [13] a modal analysis of a vehicle drivetrain with and without dual mass flywheel is performed. In work [14] a dynamic model of friction self-excited vibration of a vehicle drivetrain with conventional damper in the driven clutch disc is created and numerical simulations are performed. In [15] dynamic model of a vehicle drivetrain with spring and friction damper in driven clutch disk is presented and test results for amplitude-frequency characteristics are shown. In work [16] a linear mechanical model of hybrid electric vehicle drivetrain is considered, a modal analysis is performed and the effect of the control of the drivetrain on the eigenvalues of the vibrational system is studied. In this regard, the purpose of this publication is to draw out the differential equations of dynamic drivetrain model with dual mass flywheel with taking into account of the vehicle inertia, the tire torsional stiffness and the transmission gear ratios and to carry out numerical simulations with given mass, elastic and damping parameters.

2. Dynamic Model

A front wheel drive vehicle with dual mass flywheel drivetrain and its kinematic scheme are shown in Fig. 3 and 4 respectively. The system mainly consists of engine, dual mass flywheel (DMF), gearbox, final drive, drive shafts, drive wheels, driven wheels and car body. The symbols used in kinematic scheme are:

- J_c – mass moment of inertia of the crankshaft;
- J_{f1} – mass moment of inertia of the primary mass of the flywheel;
- J_{f2} – mass moment of inertia of the secondary mass of the flywheel and clutch pressure disc;
- J_{g1} – mass moment of inertia of the clutch driven (friction) disc and primary shaft with drive gears of the gearbox;
- J_{g2} – mass moment of inertia of the secondary shaft with driven gears of the gearbox;
- J_0 – mass moment of inertia of the final gear and the differential;
- J_d – mass moment of inertia of the drive shafts;
- J_w – mass moment of inertia of the wheels;
- m – vehicle mass;

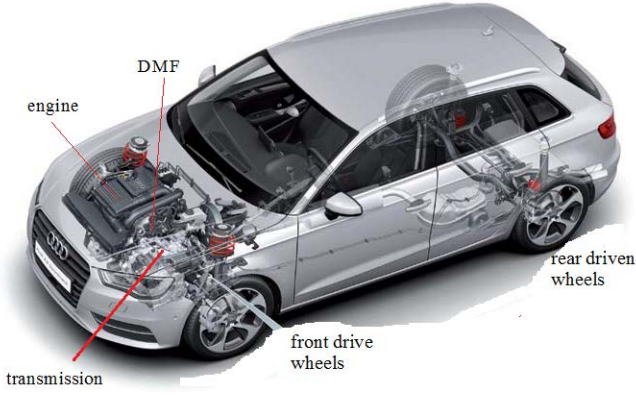


Fig. 3 Front wheel drive vehicle with DMF [17]

J_{g2} – mass moment of inertia of the secondary shaft of the gearbox;

J_0 – mass moment of inertia of the final gear and the differential;

J_d – mass moment of inertia of the drive shafts;

J_w – mass moment of inertia of the wheels;

m – vehicle mass;

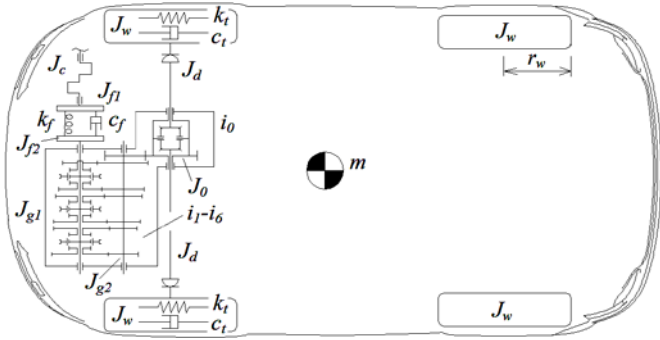


Fig. 4 Vehicle drivetrain kinematic scheme

i_{1-6} – gear ratios of the six speed gearbox;

i_0 – gear ratio of the final drive;

r_w – rolling radius of the wheels;

k_f, c_f – spring stiffness and damping of the dual mass flywheel;

k_t, c_t – tire torsional stiffness and damping of the drive wheels.

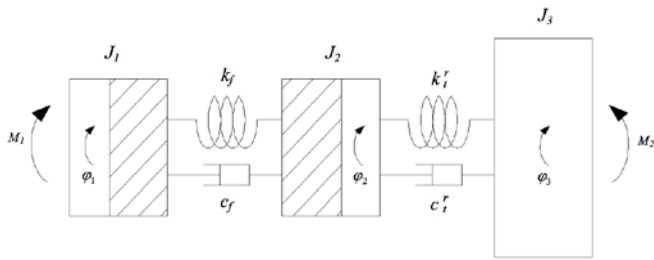


Fig. 5 Equivalent 3 DOF vehicle drivetrain dynamic model

The equivalent dynamic model shown in Fig. 5 has three degrees of freedom (3 DOF) and the vector of generalized coordinates is:

$$q = [\varphi_1 \quad \varphi_2 \quad \varphi_3]^T$$

The mass moments of inertia of the dynamic model are:

$$J_1 = J_c + J_{f1}$$

$$J_2 = J_{f2} + J_{g1} + J_{g2}^r + J_0^r + 2J_d^r + 2J_w^r$$

$$J_3 = 2J_w^r + J_v^r$$

J_1 – mass moment of inertia of the crankshaft and primary mass of the flywheel;

J_2 – mass moment of inertia of the secondary mass of the flywheel, clutch, gears and shafts of the gearbox and final drive, drive shafts and drive wheels;

J_3 – mass moment of inertia of the driven wheels and mass of the car body reduced to the engine crankshaft;

The mass moments of inertia reduced (referred) to the crankshaft are [18, 19]:

$$J_{g2}^r = \frac{J_{g2}}{i_{1-6}^2}$$

$$J_0^r = \frac{J_0}{i_{1-6}^2 i_0^2}$$

$$J_d^r = \frac{J_d}{i_{1-6}^2 i_0^2}$$

$$J_w^r = \frac{J_w}{i_{1-6}^2 i_0^2}$$

$$J_v^r = m \left(\frac{r_w}{i_{1-6} i_0} \right)^2$$

where superscript r means *reduced* or *referred* to the crankshaft;

J_v^r – reduced mass moment of inertia of translating mass of the vehicle to the crankshaft.

For the generalized coordinates can be written:

$$\varphi_1 = \varphi_c = \varphi_{f1}$$

$$\varphi_2 = \varphi_{f2} = \varphi_{g1} = \varphi_{g2} i_{1-6} = \varphi_0 i_{1-6} i_0 = \varphi_w i_{1-6} i_0$$

$$\varphi_3 = \varphi_w i_{1-6} i_0 = \frac{S i_{1-6} i_0}{r_w}$$

where S is the driving distance, m .

$$k_t^r = \frac{k_t}{i_{1-6}^2 i_0^2}; \quad c_t^r = \frac{c_t}{i_{1-6}^2 i_0^2}$$

where k_t^r, c_t^r – tire torsional stiffness and damping reduced to the engine crankshaft.

The differential equations of the model are:

$$J_1 \ddot{\varphi}_1 + k_f (\varphi_1 - \varphi_2) + c_f (\dot{\varphi}_1 - \dot{\varphi}_2) = M_1$$

$$J_2 \ddot{\varphi}_2 - k_f (\varphi_1 - \varphi_2) + k_t^r (\varphi_2 - \varphi_3) - c_f (\dot{\varphi}_1 - \dot{\varphi}_2) + c_t^r (\dot{\varphi}_2 - \dot{\varphi}_3) = 0$$

$$J_3 \ddot{\varphi}_3 - k_t^r (\varphi_2 - \varphi_3) - c_t^r (\dot{\varphi}_2 - \dot{\varphi}_3) = -M_2$$

The excited moment from the engine is:

$$M_1 = M_o + M \sin \omega t$$

And

$$M_2 = \frac{M_R}{i_{1-6} i_0}$$

where M_R is resistive moment acted on the vehicle. It includes rolling resistance, road inclines and aerodynamic drag.

3. Numerical Simulation

The numerical simulations are performed in program field of MATLAB. The parameters of the model are taken from different literature sources [13, 14, 19 and 20]. The actual values of the parameters are given in Table 1. Some of the parameters are reduced (referred) according to the formulas given above to the engine crankshaft for the accurate conduction of the simulations.

Table 1: Parameters of the dynamic model

Parameter	Value	Dimension
J_c	0,045	kg.m ²
J_{f1}	0,115	kg.m ²
J_{f2}	0,115	kg.m ²
J_{g1}	0,004	kg.m ²
J_{g2}	0,004	kg.m ²
J_0	0,003	kg.m ²
J_d	0,015	kg.m ²
J_w	0,850	kg.m ²
m	1765	kg
i_{1-6}	3,615; 1,947; 1,281; 0,973; 0,778; 0,646	-
i_0	4,056	-
r_w	0,316	m
k_f	600	Nm/rad
c_f	100	Nms/rad
k_t	35000	Nm/rad
c_t	50	Nms/rad

Natural frequencies of the system when 1st gear is engaged:

$$\omega_1 = 0 \text{ - rotation of the system}$$

$$\omega_2 = 15,3 \text{ Hz}$$

$$\omega_3 = 4,2 \text{ Hz}$$

Natural frequencies of the system when 6th gear is engaged:

$$\omega_1 = 0 \text{ - rotation of the system}$$

$$\omega_2 = 19,9 \text{ Hz}$$

$$\omega_3 = 9,12 \text{ Hz}$$

In overcritical operating conditions ($\omega_{ex} > \omega_{nat}$), it must be ensured that the minimum excitation frequency will in all operating points will remain to a sufficient degree above the natural frequency and the excitation frequency from the engine is [21]:

$$\omega_{ex} = \frac{z}{2} \cdot \frac{n}{60}$$

where z is the number of cylinders;

n – engine speed, min⁻¹.

For 4-cylinder engine on idle speed - 900 min⁻¹:

$$\omega_{ex} = \frac{4}{2} \cdot \frac{900}{60} = 30 \text{ Hz}$$

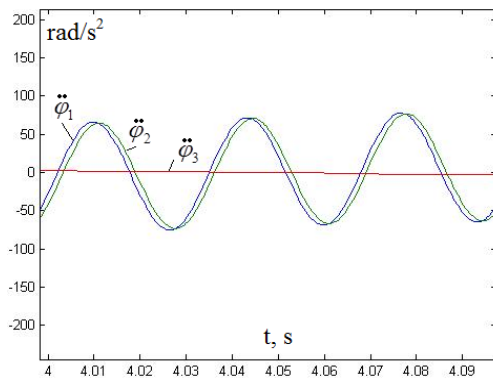


Fig. 7 Angular acceleration of the first (blue), second (green) and third (red) mass of the model on idle speed - 900 min⁻¹ on 1st gear

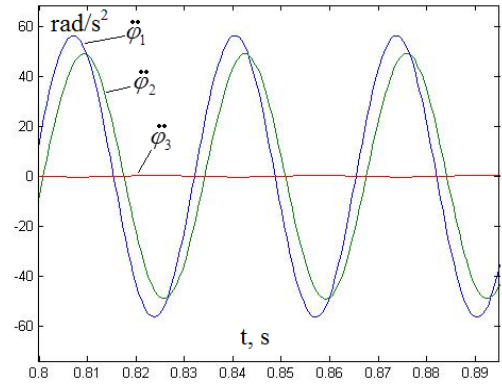


Fig. 8 Angular acceleration of the first (blue), second (green) and third (red) mass of the model on idle speed - 900 min⁻¹ on 6th gear

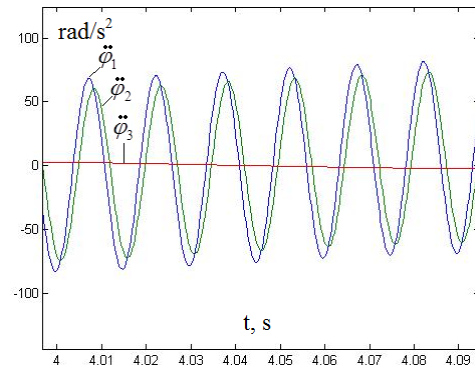


Fig. 9 Angular acceleration of the first (blue), second (green) and third (red) mass of the model, 2000 min⁻¹ on 1st gear

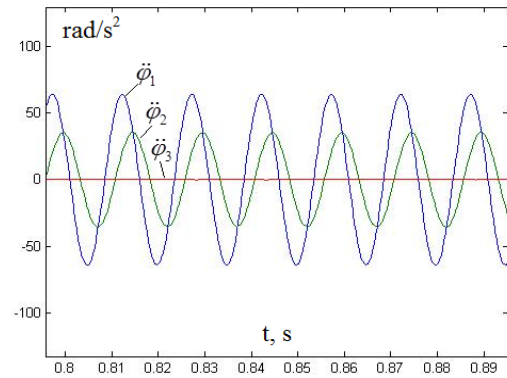


Fig. 10 Angular acceleration of the first (blue), second (green) and third (red) mass of the model, 2000 min⁻¹ on 6th gear

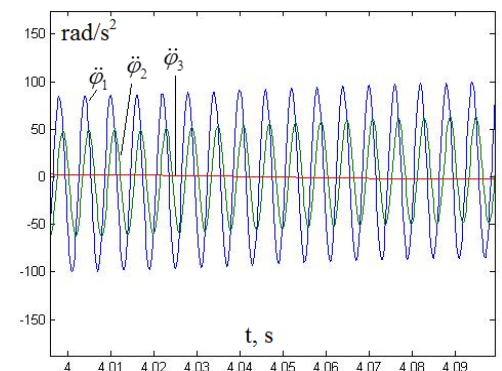


Fig. 11 Angular acceleration of the first (blue), second (green) and third (red) mass of the model, 5000 min⁻¹ on 1st gear

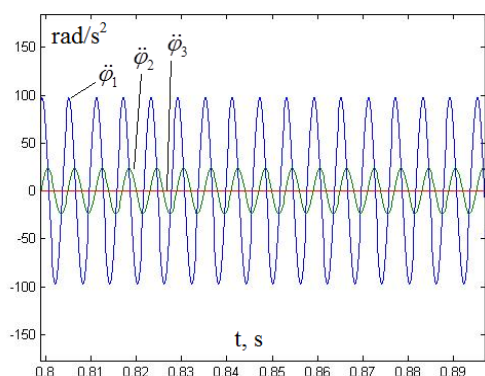


Fig. 12 Angular acceleration of the first (blue), second (green) and third (red line) mass of the model, 5000 min^{-1} on 6th gear

Analysis of the results for excited vibration shown in Fig. 7 to Fig. 12 indicates that the system effectively lowers the acceleration of the vehicle body (third mass of the model) and allows driving the vehicle on low engine angular speed. The acceleration of the second mass is less when the higher gear is engaged. Acceleration decrease when increase the angular speed of the engine.

4. Conclusion

The considered model enable to study the vibration in vehicle drivetrain and fluctuation in linear movement of the vehicles with dual mass flywheel. The shown consideration for reduction of all parameters to the engine crankshaft allows to be studied the vibration on various gears in vehicle gearbox. The numerical experiments with given parameters show good damping of acceleration of the third mass (vehicle) in all speed range of the engine and for all gears of the gearbox. The acceleration of the second mass (transmission) decreased with increase the angular speed and with engagement of the higher gear in the gearbox.

References:

- [1]. LuK. Dual Mass Flywheel: Technology / Failure Diagnosis Special Tool / User Instructions, 2013.
- [2]. <https://www.youtube.com/watch?v=nvgEiArV45c>
- [3]. Genta, G., L. Morello. The Automotive Chassis. Vol. 1: Components Design. Springer, 2009.
- [4]. Walter, A. Das Zwei Massen Schwungrad als Virtueller Sensor. MTZ 06, 2007.
- [5]. Micknass, W. Kupplung, Getriebe, Antriebswellen. Vogel, 2004.
- [6]. Suryanarayana, A. Engine Dynamics and Torsion Vibration Reduction. Chalmers, 2015.
- [7]. Johansson, D. Simulation Models of Dual Mass Flywheels. Chalmers, 2017.
- [8]. Bourgois, G. Dual Mass Flywheel for Torsional Vibrations Damping. Chalmers, 2016.
- [9]. Walter, A. et al. Estimation of the Instantaneous Engine Torque for Vehicles with Dual Mass Flywheel (DMF). IFAC Proceedings, Vol. 40, issue 10, 2007.
- [10]. Albers, A. Advanced Development of Dual Mass Flywheel (DMFW) Design - Noise Control for Today's Automobiles.
- [11]. Wallentowitz, H. Longitudinal Dynamics of Vehicles. Aachen, 2004.
- [12]. Schulz, M. Maschinendynamik in Bildern und Beispielen. De Gruyter, 2017.
- [13]. Dresig, H., F. Holzweißig. Dynamics of Machinery. Theory and Applications. Springer, 2010
- [14]. Sinpov, P. Frictional self-excited vibration occurring in machine aggregates. PhD Thesis, 2010.
- [15]. Barsky, I. Clutches for Transport and Traction Machines. Mashinostroenie, 1989.
- [16]. Schulz, M. Low-frequency Torsional Vibrations of a Power Split Hybrid Electric Vehicle Drive Train. Journal of Vibration and Control, 11, 2005.
- [17]. SSP. Audi 1.2l and 1.4l TFSI Series EA211 Engines. 2013.
- [18]. Rusev, R. Automotive engineering 2. Ruse, 2006.
- [19]. Citovich, I., V. Algin. Vehicle Dynamics. Nauka i tehnika, 1981.
- [20]. http://www.automobile-catalog.com/car/2013/1764725/audi_a3_sportback_1_4_tfsi.html
- [21]. Technical Information - Highly Flexible Couplings. Voith Turbo.

KINEMATIC AND POWER ANALYSIS OF MULTI-STAGE PLANETARY GEARBOXES THROUGH THE TORQUE METHOD

Assoc. Prof. Dr. Karaivanov D., Velyanova, M., Bakov, V.
 University of Chemical Technology and Metallurgy, Sofia, Bulgaria
 E-mail: dipekabg@yahoo.com, m.velyanova95@abv.bg, vencobakov@gmail.com

Abstract: The basics of applying the torque method for kinematic and power analysis of planetary gear trains are presented. With the help of the method, the speed ratios and efficiency of a real planetary gearbox are determined when operating on different gears (speeds).

KEYWORDS: CHNGE-GEAR TRAIN, EFFICIENCY, PLANETARY GEAR TRAIN, RELATIVE POWER, SPEED RATIO, TORQUE

1. Introduction

Due to its undeniable qualities, planetary gear trains (PGT) have a wide spread [8, 12, 14, 20, 21, 25]. The input and output shaft coaxiality makes them suitable for wind turbines [10, 11]. But they are particularly suited to automatic gearboxes because, unlike non-planetary gear trains, all gear wheels are engaged in all cases of operating (speeds) and no switching (entry and exit of meshing) [16, 20, 26, 27]. Steering is done with brakes. On the other hand, the kinematic and efficiency analysis of planetary gear trains, especially of the more complex ones (such as gearboxes), creates considerable difficulties for the designers. Classical methods of kinematic analysis, Willis's analytic [28] and Kutzbach's graphic [19], are quite labor-intensive in complex, compound gears. An easy-to-use, eye-catching and definitely engineering method for kinematic and power analysis is the torque method.

The purpose of this paper is to demonstrate the capabilities of the torque method in the kinematic and efficiency analysis of complex composite planetary gears, in particular gearboxes.

2. Essence of the torque method

The method is proposed by K. Arnaudov in [1], and further developed in many publications [2, 3, 4, 5, 6, 7, 13, 14, 15, 17]. It is presented in detail in [8] in Bulgarian and in [9] in English. Its essence is as follows:

1.) The well-known symbol of Wolf [29] (Figure 1) is used, in which, due to its circular shape the elementary planetary gear is depicted with a circle, and the three outgoing shafts – with lines. With purpose of achieving maximum visibility, Wolf's symbol is used not in its original form but modified, as the three outgoing shafts of the gear, as appropriate are designated with different lines as follows:

- The two shafts with unidirectional ideal external torques T_1 and T_3 (the sun gear 1 and the ring gear 3) are designated with single lines, but of different thickness, depending on the magnitude of the respective torque. Since $T_1 < T_3$, the sun gear 1 is denoted by a thin single line and the ring gear shaft 3 is a thick single line;
- The torque T_H of the carrier H is indicated by a double line as the largest. It is the opposite of the other two and equal in absolute value to their sum

$$T_H = -(T_1 + T_3) \quad (1)$$

In this case, the three **ideal external torques** (determined without taking the losses into account) of the gear are arranged in the following way

$$T_1 < T_3 < |T_H| \quad (2)$$

2.) A **torque ratio** t of one-direction torques is defined

$$t = \frac{T_3}{T_1} = \frac{z_3}{z_1} = -i_0 > 1 \quad (3)$$

where z_1 and z_3 are teeth number of sun gear 1 and ring gear 3 and i_0 is basic speed ratio of PGT (with fixed carrier).

It should be noted that **not** all types of PGTs is in effect dependent $t = -i_0$ and that's not some general relation (it's not the same at positive-ratio PGTs!) [8].

The defined **torque ratio** t is very convenient to work with (and not only at \overline{AI} -PGT). It can express the ideal external torque as follows

$$T_3 = +t \cdot T_1 \quad \text{and} \quad T_H = -(T_1 + T_3) = -(1+t)T_1 \quad (4)$$

If we accepted $T_1 = +1$, so-called specific torques are obtained

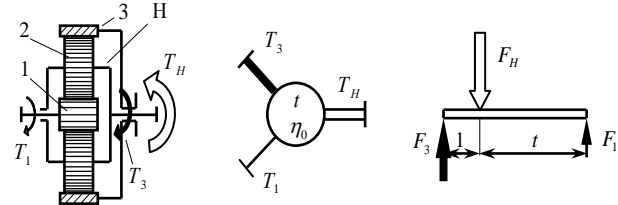
$$T_3 = +t \quad \text{and} \quad T_H = -(1+t) \quad (5)$$

and it's very easy to work with them.

Using these dependencies, it is easy to determine the sum of the three external torques:

$$\sum T_i = T_1 + T_3 + T_H = 1 + t - (1+t) = 0 \quad (6)$$

This dependence provides a good opportunity to verify the correctness of the calculations, an option that is lacking in the methods of Willis and Kutzbach.



Prerequisites: $\eta_0 = \eta_{13(H)} \approx \eta_{3(H)} = 1$

$$t = \frac{T_3}{T_1} = \frac{F_3}{F_1} > +1$$

Torques:

$$T_1 < T_3 < |T_H|$$

$$T_1 : T_3 : T_H = +1 : +t : -(1+t)$$

$$\sum T_i = T_1 + T_3 + T_H = 0$$

Powers:

$$F_1 < F_3 < |F_H|$$

$$F_1 : F_3 : F_H = +1 : +t : -(1+t)$$

$$\sum F_i = F_1 + F_3 + F_H = 0$$

Figure 1. \overline{AI} - planetary gear train – kinematic scheme, external torques, modified Wolf symbol and lever analogy

3.) It is also very important to bear in mind that the three ideal external torques T_1 , T_3 and T_H are in constant ratio

$$T_1 : T_3 : T_H = T_1 : +t \cdot T_1 : -(1+t)T_1 = +1 : +t : -(1+t) \quad (7)$$

however

- how many degrees of freedom F the gear train operates, with $F = 1$ or with $F = 2$;
 - which gear train element is stationary at $F = 1$ degree of freedom;
 - what is the power transmission direction, i.e. whether the gear train is operating as a reducer or a multiplier with $F = 1$, or as summation or dividing gear train at $F = 2$, i.e. as a differential;
 - whether the gear train is operating alone or as part of a composite multi-stage gear train.
- 4.) From the exposed dependencies for the three ideal external torques of the shafts of the PGT it is not difficult to establish that there is an analogy of the gear with a lever loaded with three forces, i.e. there is a leverage analogy. In Fig. 1 is given a comparison of PGT with a straight lever, showing the full analogy. This lever analogy with its visibility is very useful for easier understanding and insight into the work of PGT.
- 5.) Ideal external torques – input T_A , output T_B and reaction T_C

(of the stationary element) – are used to determine speed ratio i when PGT operates with $F = 1$ degree of freedom (not with $F = 2!$). It proceeds from the law of conservation of energy, assuming that the gearbox operates without loss, i.e. that the basic efficiency $\eta_0 = 1$. By denoting the input power with P_A and the output with P_B , the energy conservation condition is expressed in the following way:

$$\sum P_i = P_A + P_B = T_A \cdot \omega_A + T_B \cdot \omega_B = 0 \quad (8)$$

From here for the **speed ratio** is obtained [20]

$$i = \frac{\omega_A}{\omega_B} = -\frac{T_B}{T_A} \quad (9)$$

6.) **Real external torques** T_1', T_3', T_H', T_A' and T_B' , considering the losses in the gear train, are determined by the direction of the relative power P_{rel} , specifically:

- if P_{rel} is transmitted from the sun gear 1, through the planets 2, to the ring gear 3;
- or vice versa;
- from the ring gear 3 to the sun gear 1.

These real external torques allow the determination of efficiency of the gear train. This is done by initially determining the so-called **torque transmit ratio** from the real external torques of the input A and the output B of the gear train

$$i_T = \frac{T_B'}{T_A'} \quad (10)$$

This ratio is used to define efficiency η [20]

$$\eta = -\frac{i_T}{i} \quad (11)$$

As opposed to the torque transmit ratio i_T , the speed ratio i is also called kinematic speed ratio and in some cases for the sake of clarity is indicated with index k , i.e. i_k .

Formula (11) is derived from the expression

$$\sum P' = P_A \cdot \eta + P_B = \eta \cdot T_A' \cdot \omega_A + T_B' \cdot \omega_B = 0, \quad (12)$$

where the formula is obtained (11)

$$\eta = -\frac{P_B'}{P_A'} = -\frac{T_B' \cdot \omega_B}{T_A' \cdot \omega_A} = -\frac{T_B'/T_A'}{\omega_A/\omega_B} = -\frac{i_T}{i} \quad (13)$$

3. Kinematic and power planetary gearbox analysis

A real automatic planetary gearbox [20] consisting of a three-stage planetary gear and a hydrotransformer (Figure 2) is considered.

3.1. Kinematic scheme

As is shown in Figure 2 kinematic scheme shows that the gearbox performs five gear ratios (forward) and one backward (R). Table 1 shows which brakes/clutches are switched on in the different speed ratios (gears).

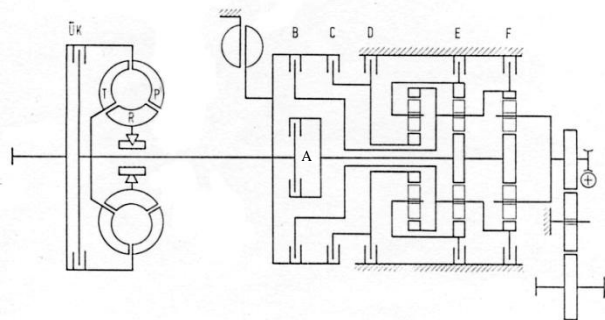


Figure 2. Kinematic scheme of a three-stage planetary gearbox [18]

Table 1. Combinations of the brakes/clutches switched on in the various speed ratios (gears) of the gearbox from Figure 2

Gear	Ük	A	B	C	D	E	F
1	○	●					●
2	○	●				●	
3	●	●			●		
4	●	●	●				
5	●		●		●		
R	○			●			●

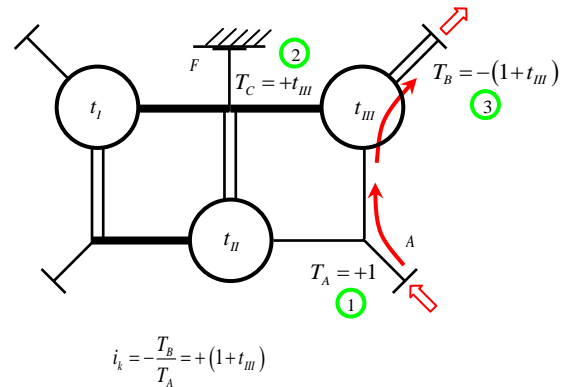
3.2. Determination of the speed ratios

In the figures below, the component gear trains are depicted with the Wolf's modified symbol and the switched on brakes/clutches are indicated.

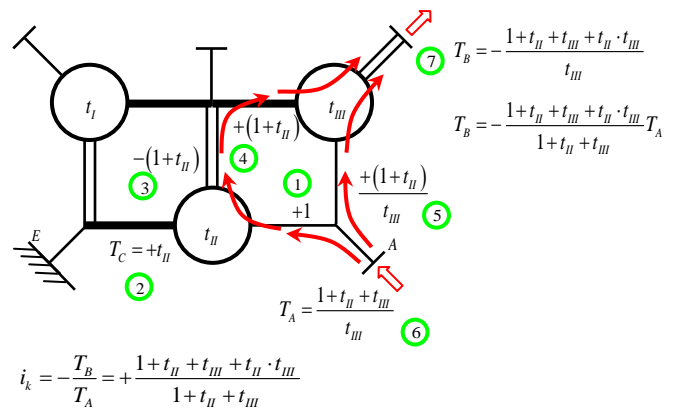
Torque ratios t_I, t_{II} and t_{III} of the three stages of the gear train are known.

The ideal torques (without counting the losses) of the loaded shafts are determined, as with the numbers in the green circles is shown the sequence of their determination. It is most convenient to start by setting a +1 value to the torque of any of the sun gears [6, 8, 9, 13, 17] (not obligatory). Then the rates of the torques, in this component gear train, are determined by (5). The transition to the next component gear train is through the compound internal shaft, at both ends of which operate the same size and different by direction torques. The red arrows show the direction of power flow of the gear train. It should be noted that a different input torque is created with the help of the hydrotransformer, which is not relevant in the kinematic analysis of PGT.

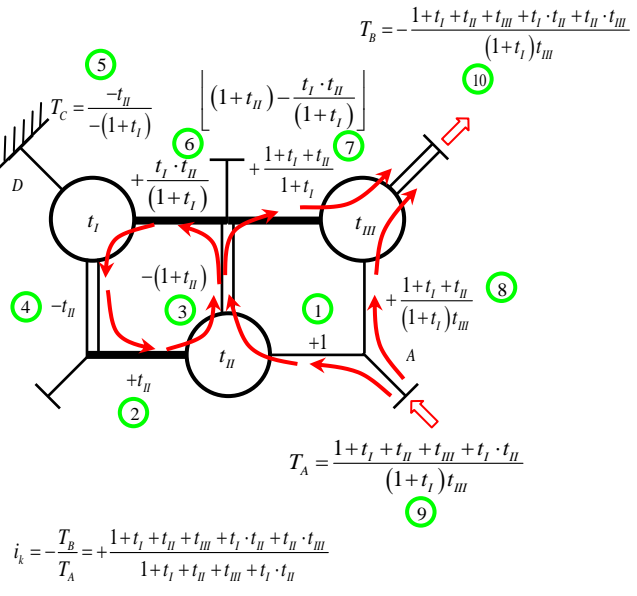
First gear:



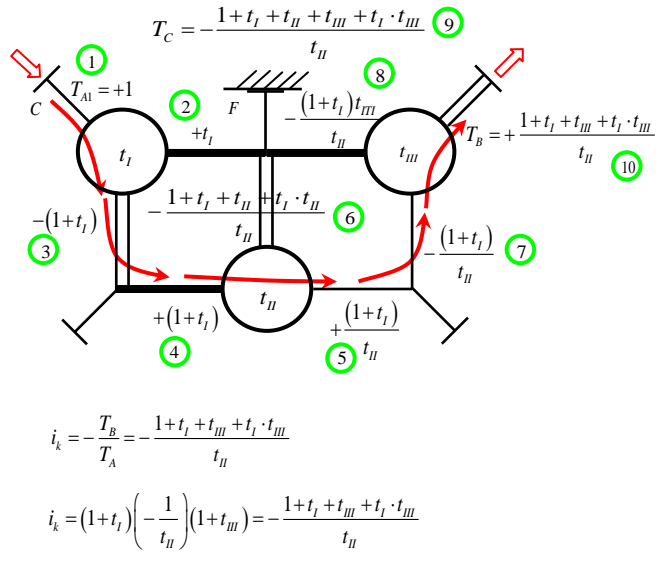
Second gear:



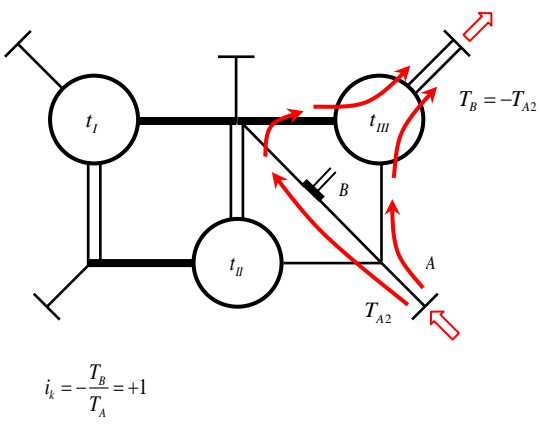
Third gear:



Reverse (rare) gear:



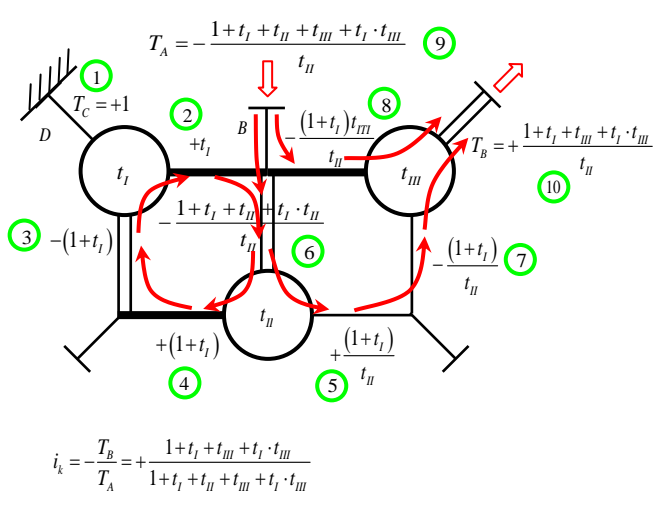
Forth gear:



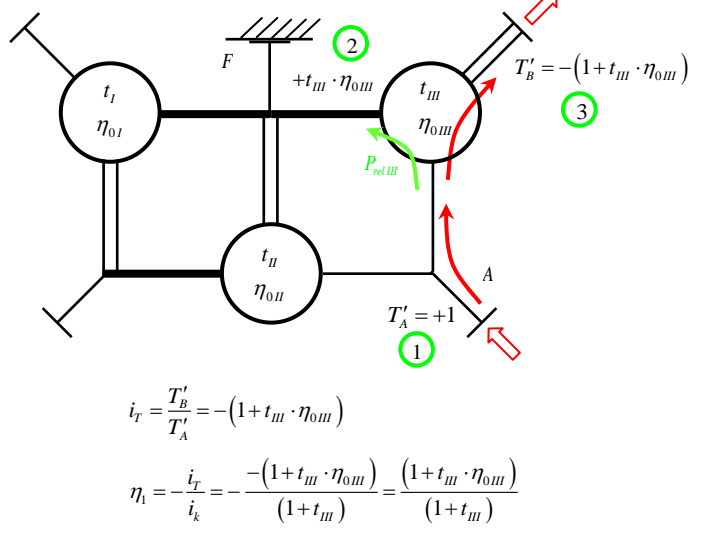
3.2. Determination of the efficiency
 The efficiency for the different cases of work is defined in p. 6 of section 2. For this purpose, in addition to the torque ratios t_I , t_{II} and t_{III} , the basic efficiencies η_{0I} , η_{0II} and η_{0III} (in the case of the operating gear with fixed carrier) must be known about the three stages of the gear. The real torques (taking the losses into account) of the loaded shafts are determined, considering the direction of the relative power P_{rel} in the corresponding gear [6, 8, 9, 13, 17] shown in the figures with a green intermittent arrow.

In some cases this direction is obvious (first gear, reverse gear), in others it has to be determined, for example by the method of samples [22]. Then by (10) the power ratio is determined, and by (11) – the efficiency of the entire gearbox for the relevant case.

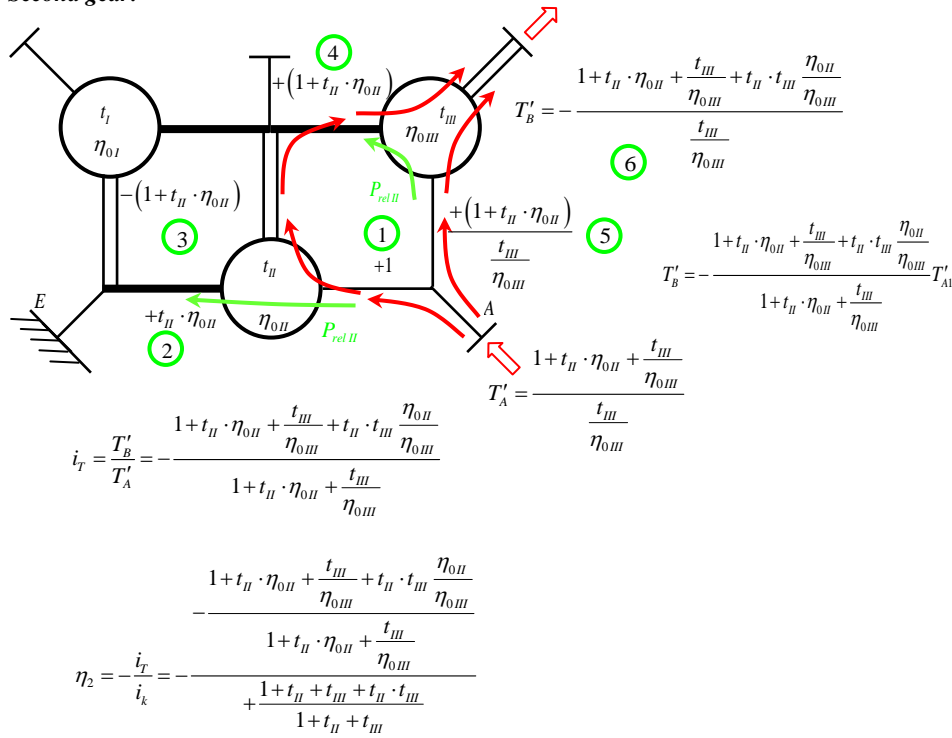
Fifth gear:



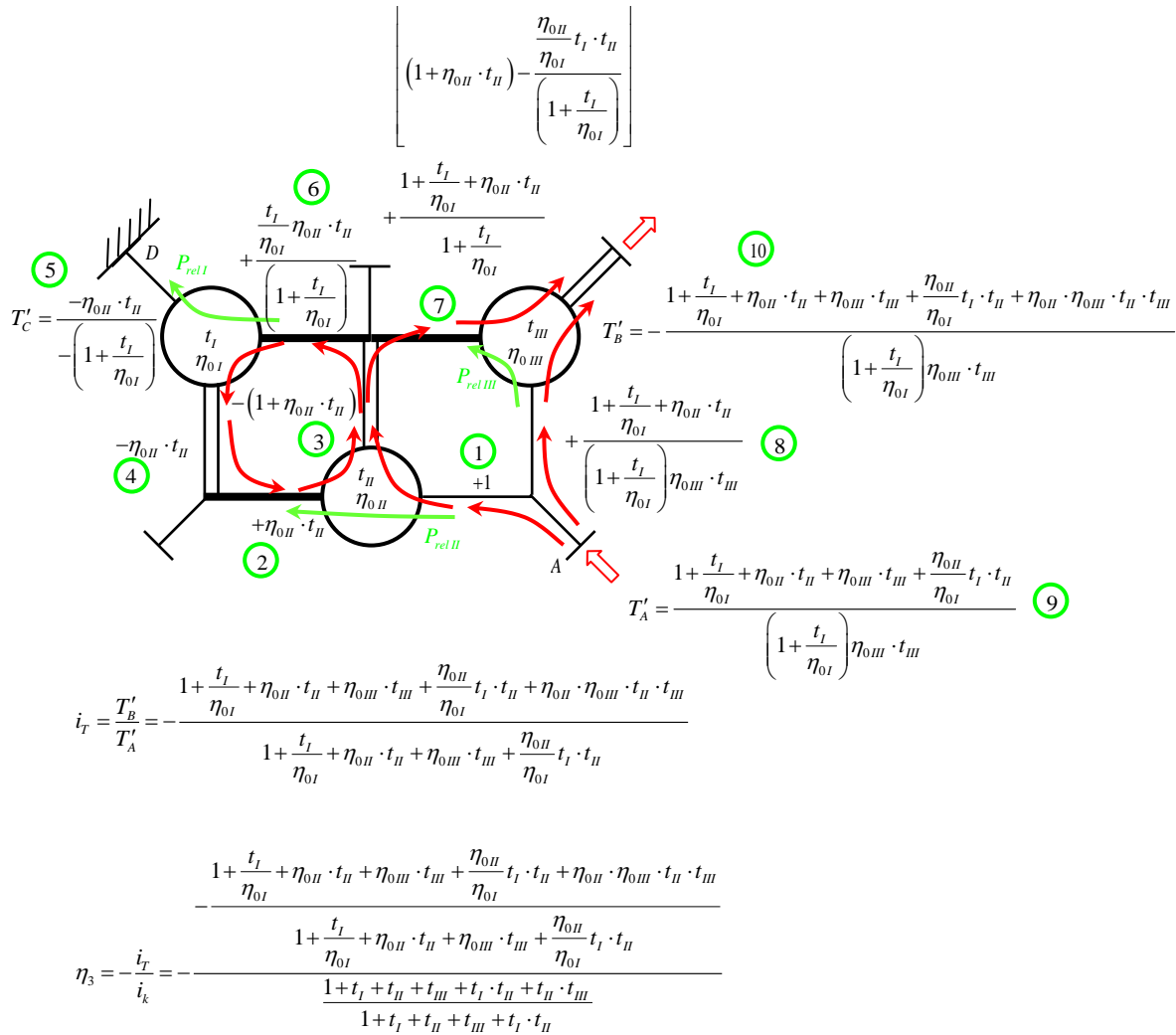
First gear:



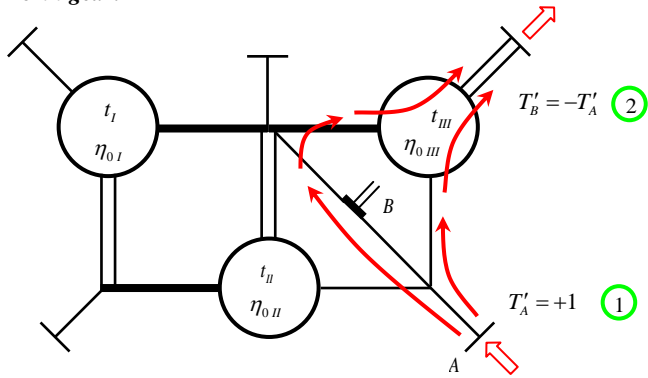
Second gear:



Third gear:



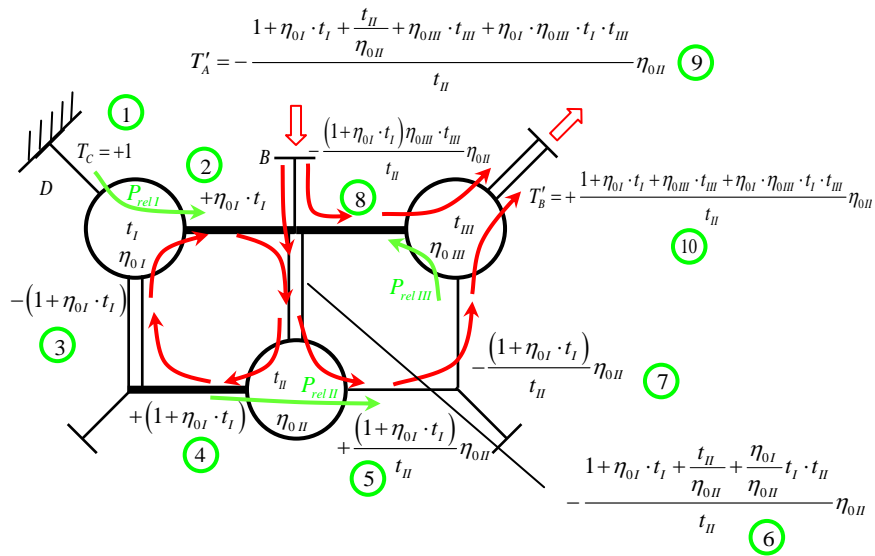
Forth gear:



$$i_T = \frac{T'_B}{T'_A} = -1$$

$$\eta_A = -\frac{i_T}{i_k} = 1$$

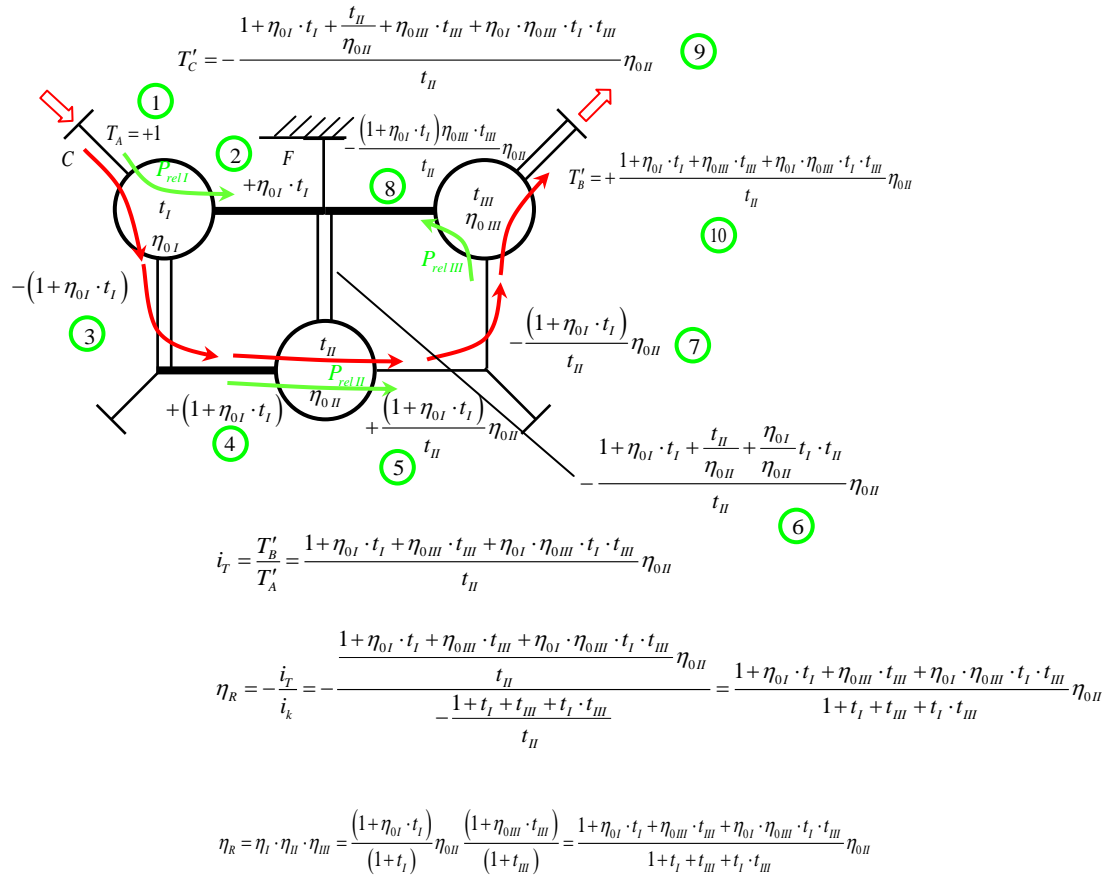
Fifth gear:



$$i_T = \frac{T'_B}{T'_A} = -\frac{1 + \eta_{0I} \cdot t_I + \eta_{0III} \cdot t_{III} + \eta_{0I} \cdot \eta_{0III} \cdot t_I \cdot t_{III}}{1 + \eta_{0I} \cdot t_I + \frac{t_{II}}{\eta_{0II}} + \eta_{0III} \cdot t_{III} + \eta_{0I} \cdot \eta_{0III} \cdot t_I \cdot t_{III}}$$

$$\eta_5 = -\frac{i_T}{i_k} = -\frac{\frac{1 + \eta_{0I} \cdot t_I + \eta_{0III} \cdot t_{III} + \eta_{0I} \cdot \eta_{0III} \cdot t_I \cdot t_{III}}{1 + \eta_{0I} \cdot t_I + \frac{t_{II}}{\eta_{0II}} + \eta_{0III} \cdot t_{III} + \eta_{0I} \cdot \eta_{0III} \cdot t_I \cdot t_{III}}}{\frac{1 + t_I + t_{III} + t_I \cdot t_{III}}{1 + t_I + t_{II} + t_{III} + t_I \cdot t_{III}}}$$

Reverse (rare) gear:



4. Analysis of the obtained results

When driving the car forward (from first to fifth gear) the speed ratio of the gearbox is positive (the input and output shaft are rotating in the same direction).

At first gear the power passes only through the third component PGT, which works with a fixed ring gear as a reducer.

At second gear, the second and third component PGTs operate with internal power division, and the gearbox works as reducer.

At third gear, the power passes through all of the three component gear train, as in the closed loop between the first and the second there is an internal circulation of power, and between the second and third there is an internal division of power.

In this case, the triple shaft is an internal compound shaft and the torques of the coupling shafts are in equilibrium (their sum is zero). The gearbox works as a reducer.

At the fourth gear, the third component gear train works as a block (gear wheels are not moving with each other) and the speed ratio is +1 (direct gear). At fifth gear, the gearbox works as a multiplier. The triple compound shaft is input. Here as in the third gear, the power passes through all of the three component gear train, as in the closed loop between the first and the second there is an internal circulation of power, and between the second and third there is an internal division of power.

The triple shaft is fixed at the reverse gear and the three component gear trains operate with one degree of freedom, as sequentially (in series) connected simple planetary gear trains. This way, there are no closed power loops. The gearbox speed ratio is negative and can be achieved both by the torque method and by multiplying the speed ratios of the three component gear trains.

5. Example

As an example, gearbox speed ratios and efficiency are defined with the following output parameter values:

$$t_I = t_{II} = t_{III} = 3;$$

$$\eta_{0I} = \eta_{0II} = \eta_{0III} = 0,98$$

The received results are:

Gear	First (1)	Second (2)	Third (3)	Fourth (4)	Fifth (5)	Rare (R)
i_k	+4	+2,2857	+1,47	+1	+0,84	-5,333
η	0,98	0,999	0,949	1	0,992	0,950

6. Conclusion

The possibilities of the torque method in the kinematic and efficiency analysis of complex compound planetary gear trains, in particular gearboxes, have been demonstrated.

Dependencies have been derived to determine the speed ratios and efficiency of a particular gearbox when operating on different gears. The derived dependencies are convenient for use in the optimization analysis [13, 23, 24, 26, 27] of the gearbox under consideration.

7. References

1. Arnaudov, K. An engineering analysis of coupled (two-carrier) planetary gear trains. In: Proceedings of the National youth school of the heavy machine-building, Varna, 1984,

- [microfiche]. (in Bulgarian)
2. Arnaudov, K., D. Karaivanov. Engineering analysis of the coupled two-carrier planetary gearing through the lever analogy. In: Proceedings of the Int. Conf. on Mechanical Transmissions, Chongqing [China]: China Machine Press, 5 – 9 Apr., 2001, pp. 44- 49.
 3. Arnaudov, K., D. Karaivanov. Systematik, Eigenschaften und Möglichkeiten von zusammengesetzten Mehrsteg-Planetengetrieben. *Antriebstechnik*. 2005, Nr. 5, S. 58-65.
 4. Arnaudov, K., D. Karaivanov. Higher compound planetary gear trains. *VDI-Berichte 1904-1*, 2005, pp. 327-344. ISSN 0083-5560
 5. Arnaudov, K., D. Karaivanov. The complex compound multi-carrier planetary gear trains – a simple study. *VDI-Berichte 2108 – 2*, 2010, pp. 673-684. ISSN 0083-5560
 6. Arnaudov, K., D. Karaivanov. Alternative method for analysis of complex compound planetary gear trains: Essence and possibilities. *Mechanisms and Machine Science*, 13 (2013), Power Transmissions, Proceedings of the 4th International Conference, Sinaia, Romania, June 20-23, 2012, Editor Georg Dobre, Springer Dordrecht Heidelberg New York London, pp. 3-20. ISSN 2211-0984.
 7. Arnaudov, K., D. Karaivanov. The torque method used for studying coupled two-carrier planetary gear trains. *Transactions of FAMENA*. 2013, 37 (1), No. 1, pp. 49-61. ISSN 1333-1124.
 8. Arnaudov, K., D. Karaivanov. Planetary gear trains. Sofia: Bulgarian Academy of Sciences Publ. “Prof. Marin Drinov”, 2017, 368 p., ISBN 978-954-322-885-0. (in Bulgarian)
 9. Arnaudov, K., D. Karaivanov. Torque method for analysis of compound planetary gear trains. Beau Bassin [Mauritius]: LAP Lambert Academic Publishing, 2017, 92 p., ISBN 978-620-2-01693-3.
 10. Giger, U., K. Arnaudov. Redesign of a gearbox for 5 MW wind turbines. In: Proceedings of the 11-th ASME International Power Transmissions and Gearing Conference (PTG), August 28-31, 2011, Washington DC [USA].
 11. Giger, U., K. Arnaudov. New drive train design for ultra large 15 MW wind turbine. *VDI-Berichte 2199*, 2013, pp. 101-112. ISSN 0083-5560
 12. Henriot, G. Gear and planetary gear trains. Publisher: Brevini [Italy], 1993.
 13. Karaivanov, D. Theoretical and experimental studies of the influence of the structure of coupled two-carrier planetary gear trains on its basic parameters. Dissertation. Sofia: Univ. of Chemical Technology and Metallurgy, 2000. (in Bulgarian)
 14. Karaivanov, D. Structural analysis of the coupled planetary gears with considering the efficiency of the coupling gears. In: Proceedings of the 2th Int. Conf. on Manufacturing Engineering (ICMEN), Kallithea of Chalkidiki [Greece], October 5 – 7, 2005, pp. 381-387. ISBN 960-243-615-8.
 15. Karaivanov, D. Structural Analysis of Compound Planetary Gear Trains. *Balkan Journal of Mechanical Transmissions*, 2011, 1 (1), pp. 33-45. ISSN 2069-5497.
 16. Karaivanov, D., S. Troha. Examining the possibilities for using coupled two-carrier planetary gears in two-speed mechanical transmissions. *Machinebuilding and electrical engineering*, 2006, No. 5 – 6, pp. 124-127. ISSN 0025-455X.
 17. Karaivanov, D. and others. Analysis of complex planetary change-gears through the torque method. *Machines, Technologies, Materials*, X (2016), No. 6, pp. 38-42. ISSN 1313-0226.
 18. Kudryavtsev, V. N., Y. N. Kiryashev. Planetary trains. Handbook. Leningrad: Mashinostroenie, 1977.
 19. Kutzbach, K. Mehrgliedrige Radgetriebe und ihre Gesetze. *Maschinenbau*. 1927, Nr. 22, S. 1080.
 20. Looman, J. Zahnradgetriebe – Grundlagen, Konstruktion, Anwendung in Fahrzeugen. 3. Auflage, Berlin: Springer-Verlag, 1996.
 21. Müller, H. W. Epicyclic drive trains. Detroit: Wayne State University Press, 1992.
 22. Seeliger, K. Das einfache Planetengetriebe. *Antriebstechnik*. 1964, S. 216-221.
 23. Stefanović-Marinović, J., Petković, M., Stanimirović I., Milovančević, M. A model of planetary gear multicriteria optimization, *Transactions of FAMENA*. 2011, 35(4), pp. 21-34. ISSN 1333-1124.
 24. Stefanović-Marinović, J., Troha, S., Milovančević, M. An Application of Multicriteria Optimization to The two-Carrier Two-Speed Planetary Gear Trains, *FACTA UNIVERSITATIS Series: Mechanical Engineering*, 2017, vol. 15, no. 1, pp. 85-95. ISSN 0354-2025.
 25. Tkachenko, V. Planetary Mechanisms. Optimal Design, Kharkiv: HAI Publ., 2003. (in Russian)
 26. Troha, S. Analysis of a planetary change gear train’s variants. Dissertation: Engineering Faculty, University of Rijeka (Croatia), 2011. (in Croatian)
 27. Troha, S., R. Zigulic, D. Karaivanov. Kinematic operating modes of two-speed two-carrier planetary gear trains with four external shafts. *Transactions of FAMENA*, 2014, 38 (1), pp. 63-76. ISSN 1333-1124.
 28. Willis, R. Principles of Mechanism. London: John W. Parker, 1841.
 29. Wolf, A. Die Grundgesetze der Umlaufgetriebe. Braunschweig: Friedr. Vieweg und Sohn, 1958.

ON THE APPLICATION OF FUNCTIONAL APPROACH TO CREATING AND PROVIDING OPERATIONAL CHARACTERISTICS OF ULTRALIGHT THERMAL PROTECTION OF REUSABLE LAUNCH SPACECRAFT

Prof. Dr. Eng. Salenko O.¹, Prof. Ph. D. Eng. Shchetynin V.², Lashko E.³,
Ph. D. Eng. Potapov O.⁴, Ph. D. Eng. Gusarova I.⁵

Kremenchuk Mykhailo Ostrohradskyyi National University^{1,2,3}, Yuzhnoye Design Office^{4,5} – Kremenchuk, Dnipro, Ukraine
Salenko2006@ukr.net

Abstract:

The main task of the research is to establish the regularities of the formation of a non-detachable compound of thin-walled elements from the Ni-20Cr-6Al-1Ti-1Y2O3 alloy and to determine the functional condition of the influence of soldering modes on the physical-mechanical characteristics of the compound. It has been shown the modeling of temperature fields in ANSYS 18.1. It has been established that the process of vacuum soldering should take place at a temperature of 1350°C for 15-20 min; the strength of the resulting compound is 390-420 MPa when the sample is stretched. The obtained information can be used as a theoretical basis for the development of the manufacturing process of the elements of the spaceship heat-shielding system.

KEYWORDS: WELDING; SOLDERING; HEAT TRANSFER; VACUUM; HEAT-RESISTANT MULTICOMPONENT ALLOYS

1. INTRODUCTION

Thermal protective structures of reusable aircraft with an outer metal panel are developed by specialists of all leading space countries of the world. This thermal protection consists of individual tiles, fixed on the hull of the spacecraft, and consisting, as a rule, of the upper and lower casings, between which is the honeycomb aggregate. So, NASA Langley Research Center (USA) was developed thermal protection with high resistance to high-speed collisions with space trash in orbit (fig.1). The outer support panel was a three-layer honeycomb panel, which is made of Inconel 617 alloy and designed for operation in the temperature range 600-

980 °C [1]. On the European demonstrator IXV for flight testing, the thermal protection was installed with the honeycomb panel «TIMETAL 1000» by «Astrium» company, designed for use at temperatures up to 850 °C and made of orthorhombic TiAl (Ti₂AlNb) or TiAl reinforced with TiB. (fig.2) [2].

The outer metal panel is fixed to the hull of the spacecraft with the help of racks, plates or other elements that ensure reliable retention of the tiles during the flight. Between themselves, the tiles are installed end-to-end or with some overlap.

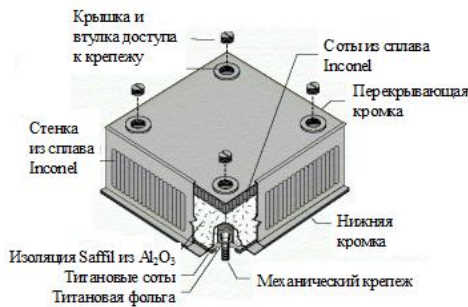


Figure 1 – Thermal protective structures with high resistance to high-speed collisions

In this case, the main drawback of such structures is the possibility of penetration of hot gases into the gaps between individual tiles, which leads to an unacceptable increase in temperatures at the junction points with a violation of the thermal protection performance and the spacecraft as a whole.

Ukrainian experts are also developing thermal protective structures with a metal three-layer outer panel and internal thermal insulation for the windward part of the orbital spacecraft [3]. To

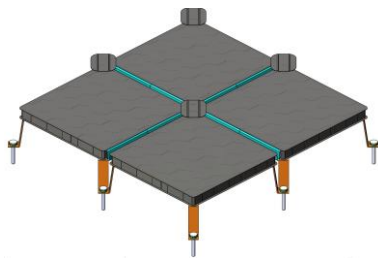


Figure 3 – Panel in assembly

In this case, the U-shaped element itself must be hermetically and reliably connected to tiles, the outer walls of which are thin, thermal resistant plates. Despite the fact that today there are

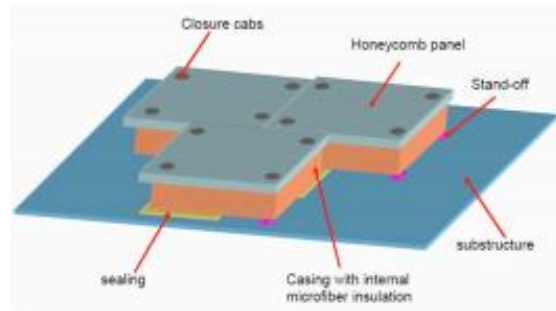


Figure 2 – Thermal protection with panel «TIMETAL 1000» by «Astrium» company

ensure complete sealing action of joints and free movement of the edges of the tile with thermal deformations between them, it is proposed to use flexible connecting U-shaped elements acting as expansion joints for the temperature expansion of tiles (fig. 3). This structure completely excludes the penetration of hot gases and atmospheric moisture under the panel of tiles and does not prevent their expansion when heated. The principle of operation of the U-shaped element is shown in fig. 4.

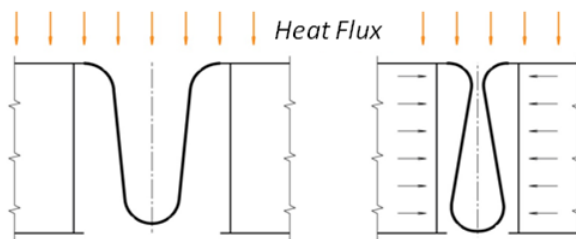


Figure 4 – Scheme of operation of the connecting element

significant developments in the field of welding (in particular, diffusion welding) and soldering elements from thermal resistant alloys [4], it is difficult to apply them for developing technologies

for joining non-rigid thin elements into a single structure. The reason is that the materials used are obtained by powder metallurgy, followed by plastic deformation (rolling) to obtain the required sheet thickness. This changes the porosity of the workpiece, and thermal loads lead to structural-phase changes, the formation of intermetallide inclusions and oxides on the surface and in the surface layer, the removal of which is associated, as a rule, with a number of difficulties.

Various heat-resistant alloys are used for manufacturing honeycomb thermal protection. The most perspective of them is the powdered dispersed nano-reinforced material Ni-20Cr-6Al-1Ti-1Y2O3, which has significant perspective in use due to its thermal resistance properties.

Heat-resistant multicomponent alloys, in particular Ni-20Cr-6Al-1Ti-1Y2O3, are used in special engineering, since they successfully withstand the effects of high temperatures (up to 1100-1200 °C), while retaining satisfactory strength, bending linear hardness, other important mechanical characteristics.

Studies aimed at developing ways and methods for obtaining non-detachable compounds (eg, diffusion welding, soldering in vacuum, contact welding on a previously applied substrate), show that the most qualitative for today is diffusion welding in vacuum. The latter involves the creation of not only the high temperatures necessary to activate the diffusion process between the interconnected surfaces, but also significant pressures at the point of contact (up to 50-75 MPa), which, as a rule, are provided, due to the temperature expansion of connected elements those which are enslaved in a special equipment. Typically, such elements are firm

and solid specimens, that withstand specified pressures without significant deformations, which lead to errors in the shape of the finished product.

The preparation of specimens, which are spatial non-rigid elements that contact several planes of a small area, did not succeed in this way, which requires the search for methods and techniques for carrying out similar operations with simultaneous optimization of the stiffness parameter of the seam and the absence of significant thermal deformations. An example of products that require the assembly of individual elements in a single design, is a three-layer cellular panel, used, for example, as the re-usable thermal protection of a space vehicle.

The multicomponent Ni-20Cr-6Al-1Ti-1Y2O3 alloy is sufficiently investigated by scientists and technical specialists [1-3], with some papers indicating that the alloy is satisfactorily exposed to diffusion welding and welding-soldering [1].

At the same time, it is noted that the traditional technologies of formation of an indivisible connection of thin plates by loading the junction zone with the nickel-based solder on the basis of nickel with stresses of 35-70 MPa with a subsequent shut-off at a temperature of 1250-1350°C for 15-20 minutes in a vacuum are ineffective. The reason lies in the fact that places for soldering of heat-protective elements are difficult to access; elements and systems of the cellular panels are not rigid, and it is practically impossible to provide such a level of prior compression of surfaces.

Suppose you want to connect two flat elements on the surface, which is a thin strip (fig. 5).

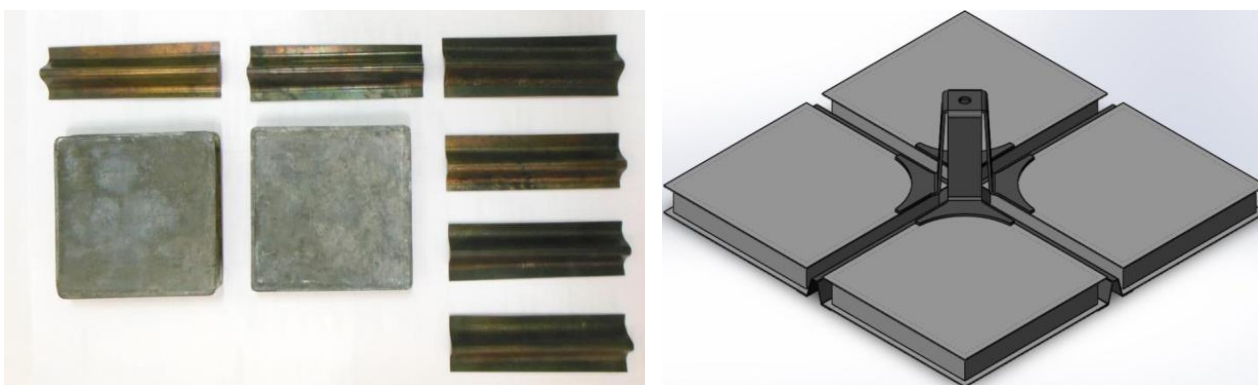


Figure 5 – The unit that is exposed to soldering in a vacuum and its calculation scheme

To ensure reliable welding of plates, two conditions must be fulfilled:

- the pressure between the welded plates should be at least p_{min} ;
- the temperature of the connection place should be $T_n=1330-1350^\circ\text{C}$ and be uniform throughout the length of the seam.

Variation of temperature can lead to incomplete soldering or to the appearance of burning and reflow zones.

Since the connection is performed in a vacuum, the heating of the welding zone is mainly due to heat radiation and, to a lesser extent, due to the contact of one of the welded elements with a heated base.

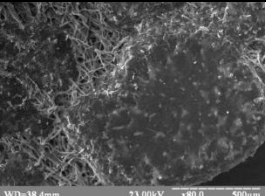
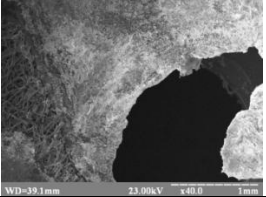
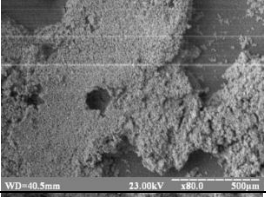
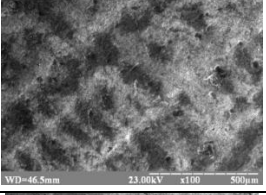
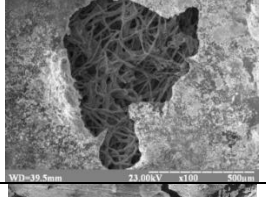
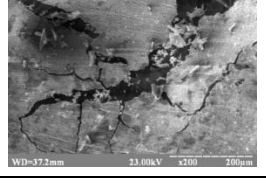
Microelectronic and photo-optical studies of the state of elements exposed to soldering in a vacuum are systematized and summarized in table 1. The composition of the material of the plates exposed to soldering, the tendency to form intermetallide inclusions and various defects of the structure during heating, as well as high activity of the components to carbon, necessitated the complete abandonment of graphite-containing substrates and expanded stacks,

since in this case, the processes of adhesion were actively manifested and there was no qualitative seam; the microelectronic investigation showed the presence of a graphitized layer, which reduces mechanical properties, mainly in the zone around the seam. Lowering the temperature to prevent curvatures deprived the ability to receive a molten solder in the contact zone of connecting elements (as a result of which the seam simply crumbled), and the temperature rise of more than 1750 K resulted in the combustion of samples on the stocks.

We also observed a characteristic of the alloy, manifested in involuntary start the exothermic reaction in some points of the surface, as a result of which it could be formed burnout of the material.

Use nickel powder without additives as solder led to the fact that the melt layer acquired a fibrous structure and did not provide a seam density. At the same time, the small amount of W in the solder precedes the occurrence of pores in the steam and the area around the seam.

Table 1 – Condition of elements and defects that occur when soldering

Research result	Soldering modes	Macro and micro photos	
Adhesion of the specimen before the substrate	$T=1300^{\circ}\text{C}$, $\tau=20$ min, $p=10^{-1}$ Pa		
Burnout of the part of material, fistula formation	$T=1380^{\circ}\text{C}$, $\tau=15$ min, $p=10^{-1}$ Pa		
Incomplete soldering with a fault under the action of a bending moment	$T=1250^{\circ}\text{C}$, $\tau=20$ min, $p=10^{-1}$ Pa		
Deformation of the finer part of the connection	$T=1380^{\circ}\text{C}$, $\tau=15$ min, $p=10^{-1}$ Pa		
The appearance of the fistula and the porosity of the seam	$T=1400^{\circ}\text{C}$, $\tau=15$ min, $p=10^{-1}$ Pa		
Cracking and fracture of a thinner plate	$T=1380^{\circ}\text{C}$, $\tau=20$ min, $p=10^{-1}$ Pa		

At this stage, a number of unsatisfactory results were received which can be divided into the following groups:

- 1) Adhesion of the specimen before the substrate;
- 2) Combustion of the specimen when there is cobalt in the chamber;
- 3) Incomplete soldering with a fault under the action of a bending moment as a result of temperature deflection in the furnace from a cycle given by controller during asymmetrical loading of the chamber;
- 4) Burnout of the part of the specimen, fistula formation;
- 5) Deformation of the finer part of the connection due to the temperature act and asymmetry of the applied load;
- 6) Cracking and fracture of a thinner plate;
- 7) The appearance of fistulas (both in machining and during sintering) and the porosity of the seam.

To improve the quality of solder connections and ensure the strength optimization was conducted full-scale experiments.

The regulated parameters were chosen: the maximum temperature of the process T , $^{\circ}\text{C}$, and excerpt time at the maximum temperature (τ , min), stress in the contact area σ_k , created by the compression of elements between themselves by force P . An additional factor was chosen h – the thickness of the workpiece. Getting regression models that connect the output parameters to

each other - the strength of the connection σ and temperature deformation, which manifest them in the error of form ρ_i – and the entrance – carried out according to the classical technique. Total number of experiments $N=2^k+2k+k_0=25$, where $k=4$ – number of factors; $2^k=16$ – full factorial experiment (plan core); $2k=8$ – star points (magnitude star shoulder $\alpha=2$); $k_0=1$ – experiments in the center of the plan.

Levels of variation of factors are shown in table 2. The samples were examined by means of electron microscopy and subjected to mechanical tests. In order to detect the effect of many repetition of soldering cycles on mechanical properties of Ni-20Cr-6Al-1Ti-1Y₂O₃ alloy elements, six times the duplication of heating (according to the thermal soldering cycle) was performed. Such studies are due to the fact that the complete assembly of the honeycomb system in one cycle is complicated.

For soldering using solder: P1 - BIP36 (composition 0,2% C, 8...10% Cr, 2,5-6,0% Al, 1,4...2,0% Mo, 2...5% Nb, 2...6% W, 2,5...3,0% B, other – Ni); P2 - finely divided powder Ni; P3 – composition Ni, 5% W, 1,0-1,5% B, other - Ni. Soldering was performed by stepped temperature increase on 450-500 $^{\circ}\text{C}$ with short endurance (near 10-15 min) at each level of temperature.

Table 2 – Intervals of variation of factors

Name of factors	Levels of variation		Interval of variation
	-1	+1	
T – soldering temperature, °C	1200	1450	175
τ – duration of the process at maximum temperature, min	15	90	37,5
σ_k – pressing pressure, MPa	0,1	1	0,45
h – workpiece thickness, mm	0,1	1,5	0,7

As a result of optimization of the soldering process, it was possible to obtain a satisfactory qualitative connection of two plates with different thicknesses overlapped with an overlap of 7,2 mm. The area of the adhesive contact during measurements is 68 mm², cracks and leakiness at the contact point are completely absent. The thickness of the soldered joint is 0,05-0,15 mm and is due to the initial spatial deviations of the blanks at the point of contact.

To check the accuracy of predictive calculations for a rational mode of soldering, soldering 4 plates of different thicknesses into a single structure was performed in accordance with fig. 3.

Microelectronic studies of the soldering place and mechanical tests have shown the following. On a plate of the largest (0,8 mm) thickness, when a load greater than 25 N was applied, one joint was destroyed. There was also a spreading of solder on the contact surfaces, which not only worsened the appearance of the joint but also changed the mechanical properties of the plate. This is especially dangerous both from the point of view of a slight increase in the mass of the system and from the point of view of the changes in modulus of elasticity and the relative elongation of the base material.

An electron microscopic analysis of the samples shown that in the process of vacuum soldering of the blanks between the united surfaces a nickel adhesive layer is formed, which for solder P2 has a clearly pronounced porous structure, and for solders P1 and P3 – uniform dense (fig. 6). The absence of pores can be explained by the presence B, which somewhat reduces the melting point Ni, and W, which is as a reinforcing layer. Attempt to enter WC instead of W according to results [13], did not give the desired result: even minor content or contact with carbon-containing materials resulted in active carbon erosion of thin plates.

The presence in P1 Al in the solder leads to the formation of intermetallide combinations, which adversely affects the complex of physical and mechanical properties. Spherical aluminides of nickel were also observed in the study of the surface of the adjoining zone, which is conditioned by a slow (about 3-4 hours) cooling of the workpiece together with a vacuum furnace. Such intermetallide inclusion provoked the appearance of grid of microcracks in adjoining zone, which greatly reduced the fracture resistance of connected elements. So, when attempting to perform bending of the plate, the relative elongation of the material on separate layers within 2-3% caused the destruction of the workpiece, and in the crack there was a layered structure due to previous operations of multi-stage rolled sheet and emerging microcracks.

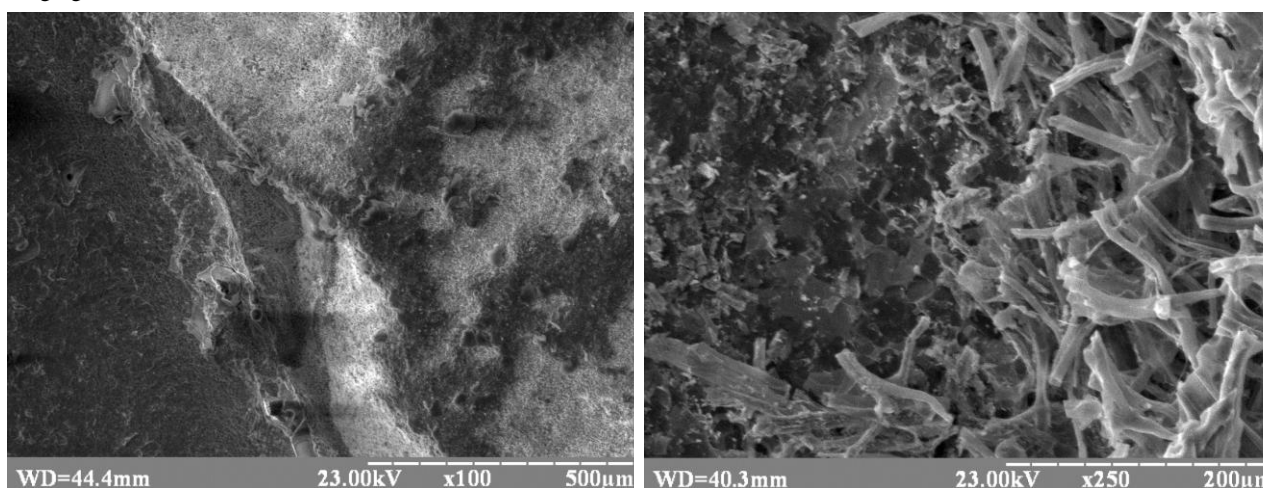


Figure 6 – Comparison of the heat affected zone, formed with the use of tungsten-containing (a) solder P3 and solder without tungsten P2 (b)

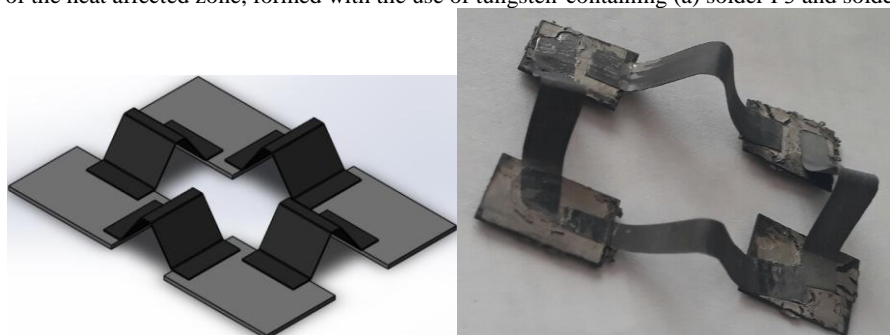


Figure 7 - Soldered structure from 4 plates of different thicknesses: 0,15 mm, 0,4 mm and 0,8 mm. The dimensions of the plates are 6×6 mm, the width of the connecting u-like tapes is 2,0 mm, the thickness of the tapes is 0,15 mm, the theoretical contact area is 7,0 mm²

Such a conclusion is made for the following reasons. The layer of solder that spreads on the surface has a porous structure, and in the case of alternating cyclic loads, it can cause cohesive damage

of the material at the places of contact with the surface by the growth of microcracks oriented at angles to the contact surface.

We also proved the conclusion about the need for a correct geometric docking of the elements before welding, since the existing spatial deviations are not satisfactorily reflected in the strength of the joint.

Testing the strength of the resulting connection by force loading of the plates on the bursting machine showed that the destruction of the specimen occurred when the load reached 520 N, corresponding to the voltage at the intersection of the gap of 320 ± 10 MPa, and the destruction itself was not on the welded seam, but in the zone of spreading solder on a plate, in a place in front of a soldered seam. The difference in the claimed strength limit of 991 MPa can be explained by the following reasons:

1) thin specimens exhibit somewhat different properties compared to the specimens in the form of rods, thick plates, etc.;

2) after welding by volumetric heating in the material, certain processes of intermetallide formation probably take place, which can reduce the ultimate strength, yield stress, elasticity and elongation of the material. To clarify these circumstances, more research is needed;

3) in the place of destruction, there are defects that can be stress concentrators, which reduces the resistance to fracture of the material.

In order to improve the soldering of products and increase the strength of the joining, it is advisable to use a function-oriented approach.

Functional approach to development and creation of new machines, objects and complex technical systems was studied by many researchers, in particular, E.I. Galibardov [6]. He states that any material object is characterized by a certain totality (matrix) of functions among which it is possible to single out useful, harmful

$$F_p = F_{pz}, F_v = 0, F_n \rightarrow \min, \quad (1)$$

where F_{pz} – product useful functions having the following matrix of consumer properties:

$$P = \sum_{i=1}^l F_{pi} + \sum_{j=1}^m F_{nj} + \sum_{k=1}^p F_{vk}. \quad (2)$$

Hence, an equation of restrictions (1) and optimization (2) makes it possible to choose the most rational material carriers of functions on the basis of morphological analysis, then to pass to material carriers in the technological process creating these functions.

As there is a functional interrelation between separate functions, i.e.

$$F_v = pF_p, F_n = qF_p. \quad (3)$$

taking into account the fact that a function is created by a separate TP step in the form of transformation element W_p , (2) can be presented in the following form:

$$P = \sum_{i=1}^l W_p F_{pi} + \sum_{j=1}^m W_n q F_{pj} + \sum_{k=1}^p W_v p F_{pk}. \quad (4)$$

Taking into consideration the fact that TP cannot be aimed at creation of harmful functions and properties in the product, minimization of the unnecessary functions is expressed by dependence:

$$P = \sum_{i=1}^l W_p F_{pi} + \sum_{j=1}^m \overline{W}_p q F_{pj} + \sum_{k=1}^p \overline{W}_p p F_{pk}, \quad (5)$$

or, after transformation, in the following way:

$$P = \sum_{i=1}^l F_{pi} (W_p + \overline{W}_p q + \overline{W}_p p). \quad (6)$$

Approaching of the totality of the product properties to the ideal implies transformation of summands $\overline{W}_n q$ and $\overline{W}_v p$ into zero, which is possible under the condition of absence of functional relation between useful and harmful properties of the product or under the conditions that the process of obtaining useful properties due to a particular TP step is at the same time the inverse one as to the occurring harmful functions. Availability and interrelation of TP separate elements enable presentation of (6) in the following way:

$$P = \sum_{i=1}^l F_{pi} (W_p + \overline{W}_p q + \overline{W}_p p + \overline{W}_p (p + q)). \quad (7)$$

For totality of alternative variants of TP the obtained equality is supplemented by quantitative signs of every function the integral sum of which is equal to 1, then

$$I = \sum_{i=1}^l F_{pi} (b_{ki} W_{pi} - b_{vi} \overline{W}_{pi} p - b_{ri} \overline{W}_{pi} (p + q)). \quad (8)$$

under the condition that $\overline{b}_{ni} \overline{W}_{pi} q = 0$. Here b_{ki} , b_{vi} – corresponding weight coefficients of each of the useful, harmful functions;

b_{ri} – weight coefficients of interaction of independent steps revealing reserves in improvement of output properties of the final product.

Describing the object by setting its initial condition C_n , as a totality of parameters characterizing the form and dimensions of the workpiece, its physical and mechanical properties and final condition C_k via particular forms (dimensions, relative position of the surfaces, physical and mechanical properties, etc.), the technological transformation function φ_0 is presented as:

and neutral functions. Unlike a material approach, a functional approach is based on the fact that the product is made to perform a number of functions provided by corresponding material carriers (the cheapest ones or the ones with the least costly manufacturing steps).

This approach can also be applied to working technologies: the manufacturing process expressed through material carriers is to be minimized according to criteria taken into consideration – working time, cost price, quality. Systemized data of this approach are presented in a number of papers, e.g. [7]-[9].

The idea of modularity of technological processes (TP) and their functional orientation can develop in the following direction.

As all types of functions (useful, neutral and harmful) are available in a final product, manufacturing steps are to be oriented in such a way that harmful functions be weakened and useful ones, in their turn, be obtained in the minimum number of steps. Under these conditions a technological process can be considered prospective if weakening or complete elimination of harmful functions takes place along with creation of useful functions during the steps.

Analysis of typical products of mechanical engineering from the point of view of functional approach reveals that practically always creation of a particular useful consumer function F_p will go together with manifestation of neutral F_n and harmful F_v functions. Then a product having only useful (under certain conditions) functions is ideal from the point of view of operation:

$$\varphi_0: \begin{Bmatrix} C_{n1} \\ C_{n2} \\ \vdots \\ C_{nR} \end{Bmatrix} \rightarrow \begin{Bmatrix} C_{k1} \\ C_{k2} \\ \vdots \\ C_{kT} \end{Bmatrix} \quad (9)$$

where C_{nR} – R -th elementary property of the workpiece; C_{kT} – t -th elementary property of the product; R, T – total number of parameters of the workpiece and the product, respectively. The function $\varphi_0 = \sum W_i E_j$, E_j – the product separate elements creating its properties.

As the product separate functions expressed via obtaining parameters of geometric accuracy, condition, structure, etc. can be generated in different ways, it is expedient to create morphological tables that may provide the basis for search of more rational variants of combination of technological actions.

The product properties are generated as a result of a number of manufacturing steps during which a complete or partial change of the initial properties takes place. Technological transformation of a workpiece into a product is achieved by purposeful total technological impacts $W_{ij}(t_k)$ of material $S_o(t_k)$, energy $E_o(t_k)$ and information $I_o(t_k)$ types which enables presentation of a scheme of output properties generation according to Fig.3 and writing down:

$$W_{ij}(t_k) = S_o(t_k) \cup E_o(t_k) \cup I_o(t_k).$$

Then, on the grounds of the condition that tool technological impacts on the product are to be performed at the levels from nano-areas to the product on the whole, and the product is a 3D object, to realize the totality of variants of technological impacts the morphological matrix will correspond to the following form:

$$A_3^{\Pi} = \left\| \begin{array}{cccccccccccc} \Pi_{11}^s & \Pi_{12}^s \dots & \Pi_{21}^s & \Pi_{22}^s \dots & H_{11}^s & H_{12}^s \dots & H_{21}^s & H_{22}^s \dots & E_{11}^s & E_{12}^s \dots & E_{21}^s & E_{22}^s \dots \\ \Pi_{11}^t & \Pi_{12}^t \dots & \Pi_{21}^t & \Pi_{22}^t \dots & H_{11}^t & H_{12}^t \dots & H_{21}^t & H_{22}^t \dots & E_{11}^t & E_{12}^t \dots & E_{21}^t & E_{22}^t \dots \\ \Pi_{11}^v & \Pi_{12}^v \dots & \Pi_{21}^v & \Pi_{22}^v & H_{11}^v & H_{12}^v \dots & H_{21}^v & H_{22}^v \dots & E_{11}^v & E_{12}^v \dots & E_{21}^v & E_{22}^v \dots \end{array} \right\|$$

where $\Pi_{11}^s, \Pi_{12}^s, \dots; \Pi_{21}^s, \Pi_{22}^s, \dots; \Pi_{11}^t, \Pi_{12}^t, \dots; \Pi_{21}^t, \Pi_{22}^t, \dots; \dots; \Pi_{11}^v, \Pi_{12}^v, \dots; \Pi_{21}^v, \Pi_{22}^v, \dots; \dots$ – variants of discontinuous technological actions along the corresponding axes s, t and v of the coordinate system of s, t, v ; $H_{11}^s, H_{12}^s, \dots; H_{21}^s, H_{22}^s, \dots; H_{11}^t, H_{12}^t, \dots; H_{21}^t, H_{22}^t, \dots; \dots; H_{11}^v, H_{12}^v, \dots; H_{21}^v, H_{22}^v, \dots$ – different variants of continuous technological actions along the axes s, t and v of the coordinate system of s, t, v ; $E_{11}^s, E_{12}^s, \dots; E_{21}^s, E_{22}^s, \dots; \dots$ – different variants of one-time technological actions.

Presence of variants of discontinuous technological actions makes it possible to consider processing of one element of the product in the form of a successive totality of different actions. In this case if the element geometric characteristics (e.g. flatness, accuracy of linear dimensions) are its output index, this process can be realized by different types of actions that more completely correspond to the properties of the workpiece elements.

For the problems of ensuring the quality of soldering, we need to provide such a redistribution of temperatures, in which the optimum must to be a warmed end-to-end zone of soldering, and minimal - the planes of the honeycomb.

It is known that the amount of energy emitted by a surface element dF , oriented at a spatial angle $d\Omega$ and φ - the angle between the direction of radiation and the normal to the surface, will be determined as

$$dQ_\varphi = E_n d\Omega dF \cos \varphi, \quad (10)$$

where $E_n = 4,9 \frac{\varepsilon}{\pi} \left(\frac{T}{100} \right)^4$; ε – the degree of blackness of the radiating body; then

$$dQ_\varphi = 4,9 \frac{\varepsilon}{\pi} \left(\frac{T}{100} \right)^4 d\Omega dF \cos \varphi.$$

Since the heated body has a sufficient length, the temperature regime at each particular point can be determined by the third-generation boundary conditions

$$\lambda \frac{\partial T(M, t)}{\partial n} \bar{l}_n = \sigma (T_2^4 - T_1^4(M, T)),$$

where σ – constant Stefan-Boltzmann: $\sigma = 5,67 \times 10^{-8} \text{ W}/(\text{m}^2 \text{K}^4)$; \bar{l}_n – vector normal to the surface of the body; λ – coefficient of thermal conductivity of the absorbing body.

Simultaneously with the transfer of heat by radiation, the specimen will receive heat and from the base on which it is located, which is determined by the boundary conditions of the 4th genus:

$$\lambda \frac{\partial T(M, t)}{\partial n} \bar{l}_n = \lambda_2 \frac{\partial T_2(M, t)}{\partial n} \bar{l}_n, \quad (11)$$

where λ_1, λ_2 – the coefficient of thermal conductivity of the absorbing and radiating body, respectively.

The simplified amount of transferred heat Q_2 from the N heating lamellae of the vacuum chamber, taking into account the partial reflection from the body, which is heated, predetermined ε , can be defined as:

$$Q_{\Sigma} = Q_k + NQ_z - Q_o = \frac{\lambda}{H} ts(T_1 - T_2) + N\gamma s \sigma T_1^4 - F\omega \cos \beta \varepsilon \sigma T_1^4 \quad (12)$$

where φ – coefficient of «not blackness», ω – the corporal angle in which radiation occurs, β – the angle between the direction of radiation and the normal to the surface.

For a cylindrical coordinate system, the temperature change T on the surface of the plate, which receives heat by radiation from heaters:

$$\frac{\partial T_1}{\partial n} = \alpha \nabla^2 T_1 + \frac{q}{c\rho}, \quad \nabla^2 T_1 = \frac{\partial^2 T}{\partial r^2} + \frac{1}{r} \frac{\partial T}{\partial r} + \frac{1}{r^2} \frac{\partial^2 T}{\partial \varphi^2} + \frac{\partial T^2}{\partial z^2}.$$

Here r , φ and z – radial, angular and axial coordinates respectively.

An increase in the temperature of a specimen causes its thermal expansion, which for a plate is defined as follows: $\Delta l = \alpha T l_0$ then the emerging stresses with a solid latching of plate will be: $\sigma_t = \alpha E T$.

Since the heating of the plate occurs with several lamellae, located around the base at a certain distance, and the plate itself is on the heat insulating surfaces, it is quite difficult to obtain a picture of the temperature deformations in general. To solve this problem, and taking into account the configuration of the body, which is heated, perform modeling of temperature fields in ANSYS 18.1. Let's take into account the real design features of the used vacuum equipment: the diameter of the platform for installation 320 mm; plate dimensions 75×75 mm; plate thickness

$h_1=0,4$ mm; $h_2=0,14$ mm. The soldered elements are located on ceramic plates in the thickness of 7,5 mm; the thermal conductivity of which is much less than the thermal conductivity of the base and the soldered elements.

The transition from the plate to the assembled cellular structure requires taking into account the temperature change in height and on the surface of the heated body. In order to prevent the overheating of the cellular structure during the soldering, thermal ballasts in the form of heat sinks made of solid alloy are installed on the table. Their diameter is $d_b=35$ mm, $h_b=50$ mm.

Figure 8 shows the results of calculations of the thermal field at the time of heating end and the picture of thermal radiation of elements that are on the table.

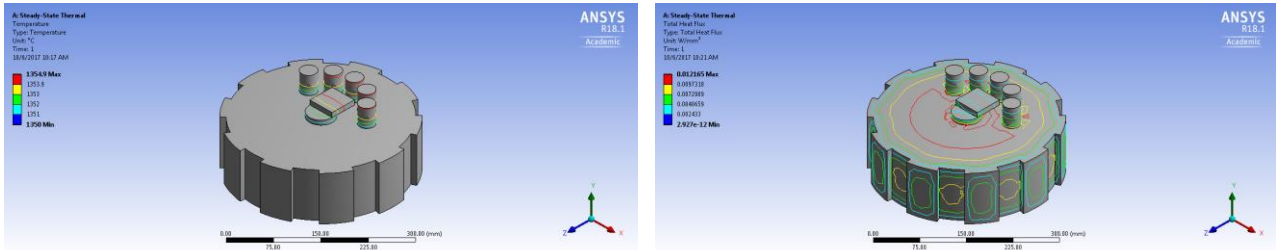


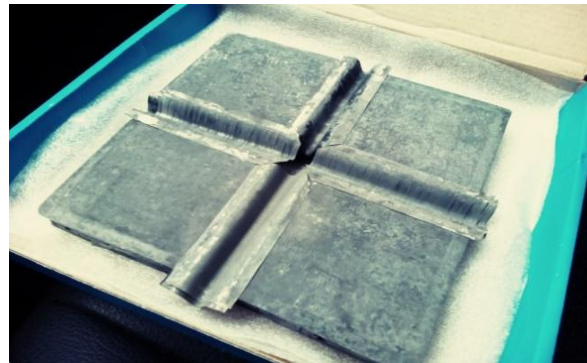
Figure 8 – Temperature fields and radiation of heated bodies in the chamber of vacuum furnace

It is shown that on the plate the temperatures are distributed unevenly, which will result the hogging of the plate or the structure as a whole. It is possible to reduce deformation of elements by using clamping plates, the mass m_p of which should be sufficient to prevent hogging, and at the same time, not cause significant deformations of the construction for which $\sigma_{\sigma}^{1500 K}=45$ MPa.

Thus, solving the problem of ensuring the quality of solder joining of elements in a single design requires the definition of rational solder conditions, the placement of ballasts for changing the conditions of absorption of radiant heat, as well as the scheme of loading the seams with clamping elements.



a



b

Figure 9 – Scheme of placement of elements during soldering the design on the palette of the vacuum furnace (a) and layout after soldering in the vacuum furnace (b)

In order to detect the effect of several soldering cycles on the mechanical properties of Ni-20Cr-6Al-1Ti-1Y2O3 alloy elements, we performed a duplication of heating with a thermal soldering cycle. It was established that after a 3-fold heating, thin plates of the experimental specimens began to be rapidly destroyed with the formation of end defects in the form of burns and fistulas.

Thus, since the soldering temperature of the elements with high-temperature solders is 1350-1375°C, it can be concluded that it is desirable to assemble the construction with the minimum number of operations (possibly one).

Consequently, as a result of our work, we were able to gradually test the technologies of obtaining the welded-soldered joints elements into a single system and prove the perspective of using Ni-20Cr-6Al-1Ti-1Y2O3 material for use in ultra-light thermal protection of reusable spacecraft with appropriate technological upgrading of the design, refining it to process ability and adapting to the conditions of assembly into a single system.

CONCLUSION

As a result of the work, samples of permanent joints were obtained: a single plate, a model of a multiplanar system with u-shaped bridges; sample mock-up.

It has been established that a dense non-porous seam is obtained with the use of solders ВПр36 (WPr36) and own solder with a content of W 8-9%, and the process of vacuum soldering should take place at a temperature of 1350°C for 15-20 minutes. The strength of the obtained compound is 390-420 MPa when the specimen is stretched by a tensile machine (with the appearance of tangential stresses). Surfaces for connection must be cleaned chemically and mechanically up to Ra 1,25-2,5 μ m, non-flatness and deformation of the surfaces are not allowed (permissible deviation is 0,03 mm/100 mm of reference length).

The soldering of the heat-protective system is desirable to be carried out in a single setup in a vacuum chamber, while the control of the process should be carried out at the temperature in the soldering spot.

Promising is the approach of using heat shields and heat conductors, which at the same time serve as means for compressing the soldering zone to a value of 0,6-0,8 MPa.

4. REFERENCE

- [1] Metallic Thermal Protection System Requirements, Environments, and Integrated Concepts / John T. Dorsey, Carl C. Poteet, Kathryn E. Wurster et al. Journal of Spacecraft and Rockets. 41 (2) (2004) 162-172.
- [2] Improving Metallic Thermal Protection System Hypervelocity Impact Resistance Through Numerical Simulations / Carl C. Poteet, Max L. Blosser. Journal of Spacecraft and Rockets. 41 (2) (2004) 221-231.
- [3] Metallic Thermal-Protection-System Panel Flutter Study / Roger R. Chen, Max L. Blosser. Journal of Spacecraft and Rockets. 41 (2) (2004) 207-212.
- [4] Poteet C.C., Blosser M.L., Improving Metallic Thermal-Protection-System Hypervelocity Impact Resistance Through Numerical Simulation, journal of spacecraft and rockets Vol. 41, No. 2, March-April 2004.
- [5] European Directions for Hypersonic Thermal Protection Systems and Hot Structures/ David E. Glass NASA Langley Research Center, Hampton// 31st Annual Conference on Composites Materials and Structures Daytona Beach, FL, January 22, 2007.
- [6] Заявка на патент України № И 2013 13658 от 25.11.13г., Потапов А.М.,

Шевцов Е.И., Тихий В.Г., Гусарова И.А., Скороход В.В., Фролов Г.А.,

Солнцев В.П., «Багатошарова теплозахисна система багаторазового космічного апарату».

[7] Проблемы создания теплозащиты возвращаемых аэрокосмических

аппаратов / Гусарова И.А., Потапов А.М., Манько Т.А. – «Технологические системы», - г. Киев, - 2017.

[8] Багрянский К. В. Теория сварочных процессов / К. В. Багрянский, З. А.

Добротина, К. К. Хренов. – К.: Вища школа, 1976. – 524 с.

[9] Коперсак В.М. Теорія зварювальних процесів-2. Фізико-хімічні та

металургійні процеси при зварюванні : текст лекцій / В.М. Коперсак. – К.:

Вид-во НТУУ «КПІ», 2011 – 252 с.

BUSINESS CLIMATE AND PRECONDITIONS FOR REVIVING THE BULGARIAN INDUSTRY

Mina Angelova, Valentina Nikolova-Alexieva
University of Plovdiv Paisii Hilendarski, mina.marinova@abv.bg,
University of food technologies, Plovdiv, valentina_nikolova@abv.bg

Abstract: *The inadequate economic policy in 90's brings to destruction of basic sectors of the Bulgarian industry. Bulgaria is one of European's countries mostly engaged with deindustrialization process. Nowadays we have to pay more attention to high technological sectors in industry which are based upon theoretical and practical knowledge that by its side is based of enormous investments in science. The condition of Bulgarian industry needs to focus urgently towards inculcating innovations and investments for increasing the enterprise competitiveness. The introducing innovations needs special attention nowadays because the rapidly speed of changes. The world had gone through the industrial time to the age of knowledge. In the fast developing global environment the strategic advantage can be brought by leaders of changes and the only way for that is by introducing innovations. An important role for the long term competitiveness of the Bulgarian economy has the increasing level of innovative enterprises which produce and inculcate new products and processes and the participation of the country in the global high technological manufacture. The reviving of the Bulgarian industry is connected with building new high-tech enterprises and a good example for that is Trakia economic zone (Plovdiv region, Bulgaria).*

Keywords: innovations, technology, crisis, economics, management, industry

1. Introduction

The crisis is a widely held view and its indications affect different aspects of the financial, social, spirit life of the nation. First of all when we talk about crisis it's important to accent not only to the consequences of its manifestation but also to the opportunities for overcoming. The careful analysis of the crisis nature in Bulgaria and the mass of its acts force to introducing the next limitations according the theme:

-as a small country with poor developed and strongly open economy, Bulgaria cannot be isolated by the world financial – economic crisis;

-the human resources – a factor for industrial growth and overcoming the crisis.

The Republic of Bulgaria is a small country in Southeastern Europe, located in the east part of the Balkan peninsular. Its uniqueness is hidden in the balanced combination of incredible nature, Black sea strip of wonderful beaches, beautiful mountains for summer and winter tourism, rivers and so on. But besides all these natural resources Bulgaria is a country with poorly developed economy and is far behind the economics of other countries in the European Union.

To receive a total explicit idea of the level of Bulgarian's economic development in accordance with the global standards and the vulnerable level toward outside economic treats it can be used the level of competitive power. According the macro-economic competitive power stranded on the World economic forum for 2008-2009 Bulgaria takes 76th place by 134 countries in this research and a last place in the EU. But Bulgaria takes better position and shows *a positive economic growth* according the data from the last World economic forum 2016-2017. According data of the same forum the index of internet web readiness Bulgaria is on 68th place from 134 countries. This means that in front our countries are all the participants and candidates in the EU, the countries of OPEC /organization of the petroleum exported countries/ but also around 30-35 poorly developed countries from Africa, South Asia, Latin America. In comparison in the World economic forum in 2016-2017 Bulgaria takes 57th place and proves *a better economic environment* in the country.

The aggregated index for competitive power is calculated based upon 85 analytical macro and micro economics indexes. According some of the micro ratio especially on the company's level Bulgaria is classified between 100th and 120th place of all 134 countries (incl. quality of business functioning, quality of company's management, technological level of manufacture, an assimilation speed for new

technologies, employee qualification and fluctuation etc.). This is a very serious reason for anxiety.

Bulgaria still poorly utilizes the advantages of the global process for raising the national competitive power, realizing an economic structural reorganization and modernization of the technical manufacture. This situation is determined by the action of different factors some of which are: decreasing the general economic potential of the country, the technical level of effectiveness of the national manufacture in times of reforms, the specification of the national economic development till 1989 and so on.

Especially in this moment of reorganization and reforms the world and Bulgaria meet the real global economic crisis that puts new records in all its acts. The current economic crisis is very important because it leded the country till the edge of the economic shock, providing its citizens with new stress and unclear conditions. Nowadays subject is the decrease of the national domestic product, mass bankruptcies and unemployment, lowering the life level of the nation.

The global financial crisis worsens the conditions that were reached for labor market development in the first decade of 21 century. The country was hit hard by the crisis; it broke the relative balance of the stock markets, it leded to commerce contraction and to investment restrictions. The decrease of investments, commerce and real economy reflected to the labor markets and a considerable shrinkage in labor search and unemployment enhancement. The economic and political leaders tried to fight with the challenges using packages of programs and restrictions. Their research is necessary to clear the adequacy, effectiveness and timeliness of the actions in the short and long run.

The negative crisis influences over the employment in a world scale and in Europe in private reflect over the employment decrease and raising the unemployment as well as in intensifying the structure misbalances standing out the instability of separate groups on the labor market – youths, middle-aged people, and lowly qualified workers.

In Europe the crisis measures a loss of more than 1.9 mln working places just for the end of first three months in 2011 that reflects to decrease of the employment with 1.3% yearly based. This is the biggest decrease in employment after 1995. The flowing down in GDP with 4.8% for the end of the second three-months in 2011 because of the manufacture and service compression leads to decrease of the number of employee as the number of man - hours.

In Europe the crisis from 2008 in its extent and depth has a different display. For some of Eastern European countries it's more considerable and brings back their economic and social

development with years, deletes their efforts and achievements from the transition period and the years of participation in EU. In countries like Bulgaria the crisis started later. The population of the country still remembers the big economic crisis of the 90s, *the high unemployment level, the mass poorness and insecurity, the various strata of society*. The most significant unemployment decrease is in Baltic countries, Spain and Ireland. The unemployment reduction corresponds with the strong compression of the economic activity. The most evident is the reduction in the countries with biggest decrease in the economic activity and the number of employed (Lithuania, Estonia, Latvia, Ireland and Spain). Totally for the EU-27 the unemployment reached 9.5% in January 2012 as it has a lot varieties in different countries: from two-digits for Latvia (22,9 %), Spain (18,8 %) and other 5 countries (Ireland, Slovakia, Hungary, Portugal and France) to the lowest levels in Holland (4,2%), Austria (5,2%) and round 10 countries with unemployment level between 6-9%, incl. Bulgaria (8,1%).

The Bulgarian crisis influenced summary at the next fields:

- Lowering the economic growth rate and limited market search;
- In the real sector – manufacture compression with strongest attitude in building, metallurgy, machine-building, chemical and textile industries;
- In the financial sector – instability and collapse in the stock exchange;
- In the bank sector – restrictions in crediting through compression of the mortgage and consumer credits, slowing down the temps of crediting the private sector, raising the interests.

• Decrease in investment exportation;

• Increase in unemployment;

• Raising the food prices, etc.

Prognosis

- As a whole in Europe the decrease in economic growth in 2014 is 1.9% in prognosis by the International Monetary Fund drop till 1.5% on average.
- In 2016 is expected bigger decrease in economic growth that will contribute to the Central and Eastern Europe. It's expected raising the inflation in short-term but slacken the pace in long-term because of the reduction in supply and demand.
- In Bulgaria the reduction of growth rates will be weaker but is expected decrease of revenues by taxes (VAT, corporation tax and others) that will reflect over budget expenses and budget surplus.
- It will decrease the money float by Bulgarian emigrants to Bulgaria.
- The treats for Bulgaria are connected with the existence of additional factors like corruption, weaknesses in the judgment system, bad infrastructure.
- The Bulgarian economic dependence of outside resources exposes it to risk, instability and more expensive outside resources.
- By one side is expected rise in service price but without better the quality.
- Enhancement of the deficit of budget balance that now is fulfilled by outside credits, euro funds etc.

Positive points of view by the crisis

- As a whole the stability of the financial system is based upon the currency board. This is a condition for stability of the bank system. The crisis forced banks to balance the crediting that is useful for the bank system. The crisis stimulated these

institutions to renovate the service packages and restructure their portfolio. This forces the bank competitiveness that is a positive for the whole system.

- The increased inflation by other side leads to convergence in price level with that in the EU.
- In the real sector positive effects are the lack of non-elastic companies and compressions of additional costs in stimulating the more effective labor.
- A positive tendency is the reduction in petrol prices and gas crisis that stimulates developing the opportunities of alternative energy sources.
- It's found new opportunities for stimulating the agriculture because of the price raising.

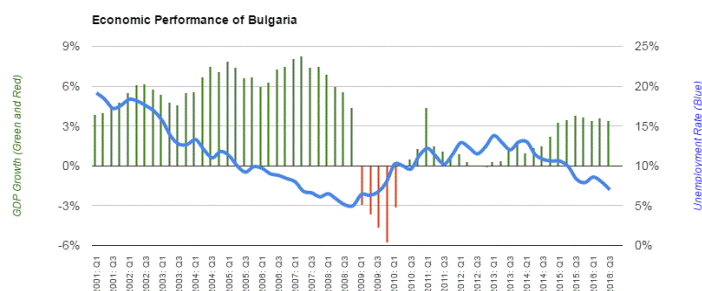


Fig. 1 Positive indicators for the Bulgarian economy: high GDP growth and falling unemployment

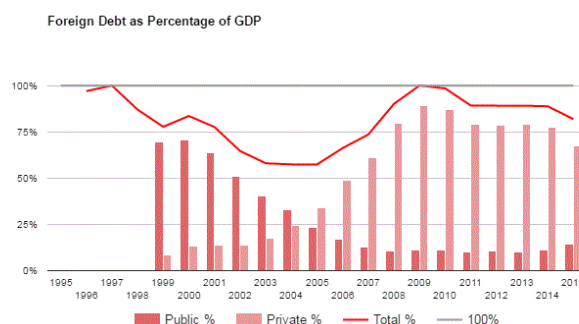


Fig. 2 Negative indicators for the Bulgarian economy: levels of foreign debt are at the same levels as during the last financial crisis, of 1996

2. Undertaken anti - crisis measures in macro and micro level till the end of 2017

- Decrease to minimum the cash bank ratio and increase of the credit resource;
- Changes in BNB in the regulations for capital adequacy and for the evaluation of client's solvent;
- Bank promotions for deposits, fund extraction that are not in the bank system – around 200 mln.lv.;
- A coordination between the system for prudential supervision of credit institutions and the one in EU;
- Force the activity of BNB for credit development for SMEs and enhancement of the sum for credit guarantee;
- When gathering euro funds to be provided bigger advance for financial compensations;
- Budget financing of projects in education, health care, ecology;
- Strengthen the financial supervision and control;
- Decrease in ministry expenses till 70% of the stipulated ones;

- Redistribution of the social dues as the country takes 12% of all the payments;
- Funds for unemployed, young families who would like to buy a house and raising the children additional payments;
- Creating conditions for temporary employment, temporary release and saving the working places;
- Creating stimulus for employers who hire released workers.

3. Propositions

- Preparing a plan of the EU for reinforcing the credit inflow in the region, broaden the range of anti-crisis measures of Central and Eastern Europe;
- Elaboration of new credit products, enhancement of the market transparency;
- Decrease of the insurance charge;
- Increase in the export crediting;
- Marking priority fields in the expenses in every ministry;
- Reducing the period for VAT refund;
- Increase the expenses for advertisement in tourism
- Increase in public investments, opening new working places;
- Improvement of the organization for structure funds absorption, fighting with the misappropriations;
- Accent over applying the legislation and especially the normative acts.

4. Conclusion

The review of the crisis effects over the labor markets and applied policies for reducing the negative effects give opportunity for the next generalizations:

1. In accordance with the crisis duration the labor market reacts with actions following short term and long term scenario. The short term scenario includes measurements for stable employment (flexible working time and labor organization, different training opportunities and social defense) and including unemployed people (programs for temporary employment, public-investment projects and training of unemployed). However these actions lose their meaning in long term crisis periods. In accordance with this the long term actions must begin in time.

2. The programs with long term impact are forced toward improving the competitiveness (through integrated education, technical help and support for the small and medium-sized enterprises); improving the services in the system for qualification and teaching; making better the forming, training and employment of the human capital and flexibility of the system for unemployed defense. The applying of such programs and policies leads to new quality of the human resources and their organization that will enable the faster after crisis economic reconstruction and abilities for reaching better development in long term periods.

3. On the background of the European practice, the Bulgarian labor market remains stable but this is as a consequence of the later crisis development in the country. The short term measures for minimizing the crisis effects over the labor market include a wide range of measurements and programs that are improved their effectiveness in the European practice. A matter of fact is their contribution to the retaining a moderate level of unemployment in Bulgaria in accordance with the EU.

4. Trakia Economic Zone (TEZ) is one of the biggest economic projects in Bulgaria, a public-private partnership that includes six major industrial zones in the region of Plovdiv.

Together the zones in TEZ have attracted over 1.2 billion euro of fixed-capital investments.

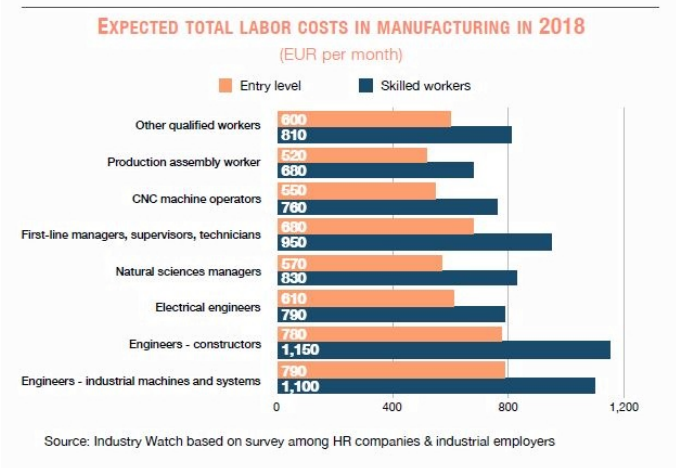


Fig. 3 Expected total labor costs in manufacturing in 2018

5. The elaboration of development programs is an obligation and responsibility not only to the government but also of the social partners, the civil community and the science potential of the country.

REFERENCES

1. *Economic review*, BNB, 1/2015-09-03
2. *A review Employment and unemployment*, NSI, 2015
3. *EU summit to tackle unemployment*, http://news.xinhuanet.com/english/2009-06/17/content_11557002.htm
4. *Communication from the Commission to the European Parliament, the Council, the European economic and social committee and the committee of regions, A shared commitment for employment*, Brussels, 3.6.2009, COM (2009) 257
5. *Employment Summit*, 7 May 2009, Main messages, EU <http://ec.europa.eu/social/main.jsp>
6. *Quarterly EU LM Review*, Summer 2009
7. *Sharp increase in unemployment in the EU*, Eurostat, Statistics in focus, 53/2009
8. *Economic downturn in the EU: the impact on employment in the business economy*, Eurostat, Statistics in focus, 60/2009
9. *Bulgaria Economic Outlook*, <http://www.focus-economics.com/countries/bulgaria>
10. *Bulgaria. Economic Forecasts 2016-2020 Outlook*, <http://www.tradingeconomics.com/bulgaria/forecast>
11. Project: "Bulgarian development policy: a transparency in the creation of normative and program frame"
12. ANGELOV, I. (2010), *Svetovnata ikonomicheska kriza i Bulgaria*, izd."Prof. Marin Drinov", S.
13. MARINOVA, Cv, *Problems and perspectives in front Bulgaria in the context of crisis of the economic and monetary union*, NBU, http://eprints.nbu.bg/1834/1/BG_EMU.pdf

USING THE PLANNING PROCESS TO CONSTRUCTION MANAGEMENT OF THE IRRIGATION INFRASTRUCTURE

Assos. Prof. Eng. Banishka N. PhD., Eng. Vasileva M. PhD St.
 Faculty of Structural Engineering – University of Architecture, Civil Engineering and Geodesy, Bulgaria
 nbanishka@abv.bg

Abstract: The poor technical condition of the existing irrigation infrastructure in our country and “Common Strategy for Management and Development of Hydro melioration and Protection against Harmful Effects of Water”, which was prepared by a World Bank, give us reason to expect the financing of projects for the rehabilitation and modernization of irrigation systems. Analyzed good practice in this area shows that project management is essential to the qualitative and effective achievement of the main goal.

In the report, special attention has been paid to the process of planning certain priority projects for the rehabilitation and reconstruction of irrigation infrastructure at the construction stage and an analysis has been carried out for the different areas of management (time, costs, quality, human resources, communications, supplies and risks).

Keywords: CONSTRUCTION MANAGEMENT, IRRIGATION INFRASTRUCTURE, PLANNING PROCESS

1. Introduction

Lack of investment in irrigation infrastructure for more than two decades has contributed to a significant deterioration of its condition, which has reached a critical level to now. Thefts in the linear and basic facilities, strong depreciation of the intake and distribution network, water losses in irrigation systems amounting to 70-80% are one of the reasons for the development of a "Common Strategy for Management and Development of Hydro-melioration and Protection against Harmful Effects of Water ". It identifies as an important priority the rehabilitation and modernization of irrigation and drainage infrastructure in our country and the necessary capital expenditures for this are more than one billion euro [1].

For this reason, it was urgent to draw up a proposal from the team of World Bank staff and consultants for a framework, programming and prioritization of funding from the European Agricultural Fund for Agricultural Rural Development and the Rural Development Program (RDP). The main aim of this project is to contribute to improving the competitiveness of agriculture, together with promoting effective water consumption and increasing the environmental sustainability of irrigated areas [2].

Based on this project, the most favorable impacts are expected to be achieved within RDP Area 5A Increasing agricultural water efficiency, namely: Measure M4 Investments in tangible assets, Sub-measure 4.3 aimed at supporting investments in irrigation and drainage infrastructures [3]. For the purpose of programming and defining priority irrigation systems, it is recommended to use a multi-criteria assessment to allow the ranking of a list of rehabilitation and modernization projects for irrigation systems.

Beneficiaries of the Sub-measure 4.3 will be Regional Public Hydro- melioration Enterprises (it is expected that the Irrigation Systems Company will be restructured into such), Irrigation Associations (According to the Irrigation Associations law) and Municipalities, which there are at least one Irrigation Association on their territory and apply for financial support with the associations.

Good practices analyzed related to the construction of irrigation infrastructure show that project management in this area is essential to the qualitative and effective achievement of the ultimate goal. The project management process groups include planning processes, implementation processes, monitoring and control processes and completion processes. Interaction between the management processes is shown in Fig. 1.

The purpose of this report is to analyse the group of planning processes at the construction stage of certain rehabilitation and reconstruction projects for irrigation infrastructure for the

different areas of management (time, cost, quality, human resources, communications, supply and risk) [4].

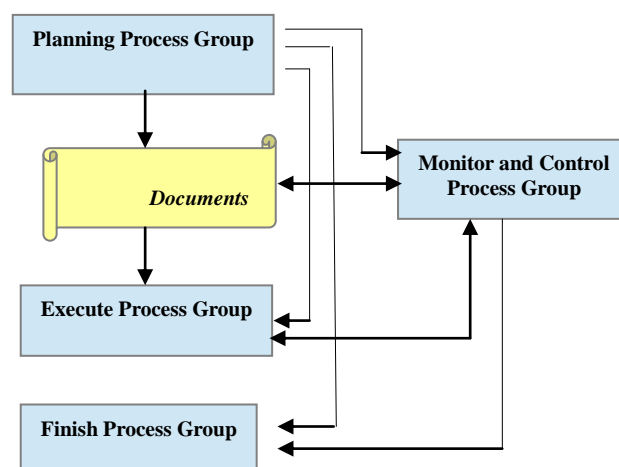


Fig. 1 Interaction between the management processes

2. Results and discussion

The planning process group at the irrigation infrastructure construction stage aims at establishing the overall scope of the activity, defining and refining the objectives and developing an action plan in each management area (Fig.2).

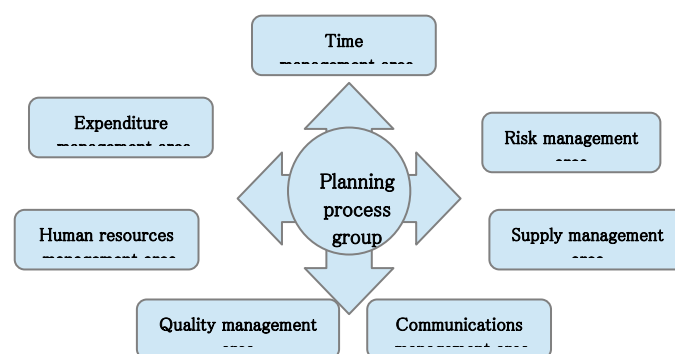


Fig. 2 The planning process group and each management area of the construction of irrigation systems

2.1 Planning in the time management area

The planning processes in the time management area for the irrigation infrastructure construction stage are mainly limited to:

- Definition and decomposition of the activities for the implementation of the construction stages of the site, including preparation of the construction site, main construction and finishing works
- Choosing the resources needed to implement the activities, including human resources, construction mechanization, materials
- Determination of the sequence of execution of individual works and elaboration of working calendar (linear or network model) with critical path analysis and certain time reserves for the respective types of works
- Assessment of the duration of the execution of the construction works and the optimization of the working schedule if necessary

Effective time planning will ensure consistency of costs and time for building the site; availability and coordination of resources used; possibility to predict contingencies; clarity for the execution of the site within the agreed deadline.

2.2 Planning in the expenditure management area

The planning processes in the expenditure management area are:

- Planning the financial means according to the budget envisaged for the implementation of the site during the design phase and the working calendar schedule
- The analysis and evaluation of the financial charts are the term of construction – an integrated and differential flowchart of cash funds.

The cost estimate is designed to be controlled over time, provide funding during site construction, resource allocation

Based on the preliminary planning of the funds for the individual decomposed activities for the construction stage of the site, the baseline framework of costs over time is established and approved.

2.3 Planning in the supply management area

Planning processes in the supply management area include:

- Preparation of a supply management plan – the plan provides a description of how the procurement processes will be managed – from supplier selection to the completion of the contractual relationship with them. Selected suppliers will need to equip irrigation systems with water meters, water level controllers, gates, management and control systems, pumps and the other.
- An outline of delivery work – the information contained in this process may include technical specifications of deliveries; quantity; requirements for: quality level; delivery and installation time; warranty terms; technical support during the operation of the site, etc.
- Delivery documents – these documents include a statement of the supply work, including and binding clauses of contracts with suppliers; technical capabilities of the selected suppliers, production capacity, etc.

The supply planning processes are closely related to the working calendar schedule. For this reason, the decisions made in the delivery of the supply management plan should be integrated with the schedule preparation processes.

2.4 Planning in the quality management area at the stage of construction of the irrigation infrastructure

Quality planning in the construction of the irrigation infrastructure is limited to ensuring the quality of the site construction works and the quality of the management process. For this purpose, it is necessary to have clear technical specifications for the implementation of the site, use of Bulgarian and European standards regarding building materials, experience of the construction company in building similar sites, use of skilled labor and modern construction machinery.

2.5 Planning in the human resources management area

The planning process in the human resources management area at the irrigation infrastructure construction stage involves the development of a human resources plan on the basis of which the posts, responsibilities and relationships between human resources are planned; their working hours, wages, needs, technical safety of work, etc.

2.6 Planning in the communications management area

The planning process in the area of communications involves the planning of communication channels and the process of exchange of information between participants in the construction process. The Communication Management Plan provides stakeholders' requirements for the type and manner of dissemination of the information; the deadlines and frequency of transmission of the requested information; restrictions on communication usually imposed by regulatory or company policies, etc.; a schedule for project team meetings, etc., which would improve communications.

2.7 Planning in the risk management area

The planning processes in the area of risk management are:

- Identifying possible sources of risk
- Analysis and assessment of possible consequences when the risk occurs
- Analyzing and assessing the possibilities for mitigating the effects of the risk development of a risk control and management plan

The planning processes in each area build up the project management plan and its documentation. During the implementation period, additional planning may be required due to the accumulation of additional information or the clarification of certain features. Significant changes that occurred during the implementation of the site triggered the need to review some of the planning processes and to gradually detail the project management plan. The update resulting from the approved changes during the construction of the sites may significantly affect parts of the project management plan. Updating these documents provides greater precision in terms of calendar planning; the spending of the funds for the implementation of the site; preventing risks or minimizing their impact, etc.

3. Conclusion

In line with the state of the irrigation systems and facilities, the priorities and measures formulated in the current programming period 2014-2020 under the Rural Development Programme as well as those developed by the World Bank and endorsed by the Council of Ministers in August 2016, a "Common Strategy for Management and Development of Hydro-melioration and Protection against Harmful Effects of Water" give us reason to expect the preparation, implementation and management of investment hydro-melioration projects concerning construction, reconstruction and modernization of irrigation systems and facilities. The restore of irrigation

infrastructure will not only increase the competitiveness of farms but shall also ensure effective, rational and environmentally sound management of available water resources.

For this reason, the beneficiaries of the selected priority projects for the reconstruction and modernization of irrigation systems and facilities need to focus on effective planning of the building construction stage in all areas of management, namely: time, cost, quality, human resources, communications, supplies and risk. All this will lead not only to the qualitative and timely implementation of the projects but also to the efficient spending of the financial resources under the Operational Programme.

4. References

- [1] Ministry of agriculture and food, Common Strategy for Management and Development of Hydro-melioration and Protection against Harmful Effects of Water, 2016.

- [2] Ministry of agriculture and food, Proposals for Programming and Prioritization Framework for funding through the European Agriculture Fund for Rural Development and the National Rural Development Program, 2015
- [3] Ministry of agriculture and food, Rural Development Program 2014-2020
- [4] Project Management Institute, A Guide to the Project Management Body of Knowledge (PMBOK GUIDE) - Fourth edition, 2009.

Thankfully

The study, presented in this report, is funded by the Research, Consultancy and Design Centre at the University of Architecture, Civil Engineering and Geodesy under Contract No. Д 102 / 17

RESEARCH OF INTELLIGENT TRANSPORT SYSTEMS MANAGEMENT OF CONVOY OF UNMANNED VEHICLES WITH THE LEAD PILOT VEHICLE FOR WORK IN THE NORTH OF THE RUSSIAN FEDERATION IN THE ARCTIC AND ANTARCTIC

Dr.Sci.Tech, Saykin A.¹, Ph.D., Endachev D.², Ph.D., associate professor, Karpukhin K.³, Ph.D Kolbasov A.^{4,5}
Head of department ¹, Head of department², Head of department ³, Head of research division ⁴ – NAMI Russian State Scientific Research Centre, Moscow, 125438, Russia
⁵Aleksey.kolbasov@nami.ru

Abstract: In the Russian Federation the problem of creating a transport system to control movement of the column of unmanned vehicles to enhance the efficiency and safety of passenger transportation in remote regions of the North, the Arctic and Antarctica is solved for the first time. The study was first developed mathematical models and algorithms for control and interaction of intelligent transport systems of traffic control columns, control system movement of the lead pilot vehicle of a column of unmanned vehicles, the motion control system driven unmanned vehicle convoys of unmanned vehicles.

KEYWORDS: INTELLIGENT TRANSPORTATION SYSTEM, UNMANNED VEHICLE, MOTION CONTROL SYSTEM, VISION, NAVIGATION, COMMUNICATIONS, ACTUATORS, RADAR, CAMERA, ALGORITHMS, AND SOFTWARE.

1. Introduction

During the development of electric vehicles and unmanned vehicles [1] in the Russian Federation, a number of works on the study of intelligent transport systems are carried out. One of the objects of the research is the intelligent traffic control system for unmanned vehicles with a leading pilot vehicle, improving the efficiency and safety of cargo and passenger traffic in remote regions of the North, the Arctic and Antarctica.

Leading international firms such as Daimler-benz, Volvo, IVECO, MAN, Scania etc. are actively working on the creation of autopilots for commercial vehicles in the convoy with a pilot car driven by drivers.

However, repetition of the foreign technical solutions providing satisfactory functioning of control systems of unmanned trucks as a part of columns in road climatic conditions of the Western Europe appears impossible for road climatic conditions of the Arctic zone of the Russian Federation.

It is generally accepted that the use of unmanned cargo vehicles in the convoy is the most effective, in which the following results are expected:

- improvement of road safety, as it minimizes the negative impact of the human factor, which according to statistics is the cause of almost 80 % of road accidents;
- achieving fuel savings of up to 20 % ;
- increase in transportation productivity by 1.3-1.4 times;
- providing comfortable working conditions for drivers in driven trucks;
- minimization of harmful effects on the environment;
- reducing the need to maintain a large staff of professional drivers with high wages;
- the possibility of integration of unmanned transport systems into the technological process of enterprises, primarily large transport and logistics centers, ports, etc., ensuring their continuous round-the-clock operation.

The problem of increasing the productivity of road transport is a priority. The prospects of logistics are based on the development of transport and infrastructure technologies. At present, domestic and foreign transport enterprises implementing a modern logistics technology, transportation and freight handling: the telecommunication system forwarding, terminal system for the carriage of goods, transportation of "door to door", etc.

According to well – known estimates, the cost of transportation of goods ranges from 20 to 70% of the total cost of logistics, while the price of goods transport component has a different share depending on the type of products: 2...3% – for electronics, 5...6% – for food, 7...12% – for machinery and equipment, 40...60% -for raw materials, 80...85% for mineral products. According to experts' calculations, the introduction of information systems can increase the average speed of vehicles by 10 ... 30 km/h.

From the standpoint of the organization of freight transport in General, a promising step is to unite the idea of unmanned transport and cargo convoy. As a result, there are two types of transport systems and infrastructure for them:

- "road train" with a virtual trailer;
- convoy (with virtual connections);
- intelligent logistics center.

2. Prerequisites and means to solve the problem.

Road and climatic conditions of the Arctic zone of the Russian Federation are characterized by the following features:

- abnormally low temperatures (up to -60 ° C), impeding the start of engines and limiting the normal operation of the technical means of autopilots;
- heavy traffic conditions on off-road terrain allowing operation of vehicle only in winter conditions;
- undirected terrain that makes it difficult to visually determine the location of the pilot vehicle on the route;
- snow drifts, which does not allow to recognize a road marking and impeding the functioning of the devices technical vision;
- constancy of reduced visibility in conditions of polar night;
- unpredictable influence of geomagnetic situation and state of the earth troposphere and ionosphere in polar latitudes on the conditions of uninterrupted reception of satellite navigation signals.

The technical solutions of control systems developed in this applied scientific research and experimental development should take into account the above peculiarities of the road and climatic conditions of the Arctic zone of the Russian Federation.

In the course of the work, the following goals were set:

- creation of an intelligent traffic management system column unmanned vehicles with a leading pilot vehicle, improving the efficiency and safety of cargo and passenger traffic in remote regions of the North of the country, the Arctic and Antarctica;
- obtaining significant scientific results, allowing to move to the creation of new types of cargo vehicles in unmanned design, providing a significant increase in freight traffic;
- market launch of new intellectual goods vehicles with a qualitatively new higher technical characteristics;
- ensuring better connectivity of the territory of the Russian Federation through the creation of intelligent transport and telecommunication systems, as well as holding leading positions in the creation of international transport and logistics systems, development and use in the North of the country and the Arctic and Antarctic.

For example, in the North of Russia, the Arctic and the Antarctic, the use of modern cruise control systems is impossible without improvement. Sensors serial systems do not work properly at low temperatures, which can lead to emergency situations.

In snowfall, a large amount of snow sticks to the front bumper of the car and partially closes the front radar view [2]. this, in turn, leads to inaccurate detection of the road situation and increases the risk of collision [3].

The climate of the North of Russia is characterized by strong winds that have a strong impact on the vehicle. This impact may result in unstable acceleration/deceleration of vehicles by the active

cruise control system, which in turn can cause severe discomfort to the driver.

The software part of the existing cruise control systems takes into account the current value of the vehicle speed, the value of the speed of approach with the driving car and the relative distance. Based on these data, the algorithms calculate a target deceleration for the asphalt pavement of the roadway. The presence of snow and ice on the roads increases the braking distance, which in turn reduces the efficiency of the active cruise control system and can lead to a traffic accident [4]. In order to ensure an adequate level of safety, a number of calibrations are needed that will increase the distance between vehicles in pursuit mode. Also changes logic of operation: the system is the cruise control needs to begin braking at a larger distance to the leading vehicle, but with a lower maximum deceleration. This configuration will minimize the impact.

By analyzing the characteristics of the chassis design of an unmanned cargo vehicle, it is possible to draw the following conclusions.

The chassis of the unmanned cargo vehicle intended for operation as a part of a column in the conditions of the Far North, the Arctic and Antarctica shall possess high passability for what should be equipped with the drive of at least 4 wheels.

The chassis of an unmanned cargo vehicle can be equipped with a power plant of any type used in automotive technology, but it is preferable to use the electric drive of the driving wheels without speed transmissions. This conclusion is formulated on the basis of the analysis of world experience, according to which almost all modern unmanned vehicles (both freight and passenger) are equipped with electric drive.

Modern models of unmanned cargo vehicles are based on the technologies of leading manufacturers of cars and automotive components for electronic driver assistance systems (ADAS).

In the conditions of operation of a column of unmanned vehicles with a pilot driving vehicle in the conditions of the Far North, the Arctic and Antarctica there are additional restrictions associated with natural features characteristic of these areas.

One of them should include:

- lack of navigational guidance on a virtually homogeneous desert area;
- polar night periods of up to six months, making it difficult to visually detect obstacles on the lane;
- the lack of paved roads and with recognizable markings;
- increased frequency of failures in satellite navigation due to changes in geomagnetic conditions and other external factors (interference);
- abnormally low temperatures (up to minus 60 ° C and below) and winds with speeds up to 25 m / s and above;
- snow drifts that make it difficult for visual recognition of the lane itself;
- low grip of the tyres when driving on ice, snow and dirt ruts filled with water;
- the increased fuel consumption of vehicle caused by low speeds of the movement on the lowered transfers and practically the round-the-clock mode of operation of internal combustion engine in the conditions of abnormally low temperatures.

In view of the above, the navigation system, including satellite, inertial and wheeled navigation system, is required to provide high-precision positioning solutions in the conditions of loss of radio visibility of satellites, the drift of coordinates of the inertial system and wheel errors. Accuracy can be raised through the use of a weather forecast system, which will give an understanding of the roadway condition and traffic conditions [5].

3. Results and discussion

Mathematical models and control algorithms are the conceptual core of intelligent control systems, largely determines the technical characteristics and basic consumer properties of the final product. One of the obvious and main requirements for mathematical models and algorithms used is their adequacy in the entire operating range of parameter changes, along with the possibility of their use for indirect measurements and for the formation of control actions.

3.1 Description of mathematical models of longitudinal movement of the center of mass of the driven unmanned vehicles

For the development of control algorithms and interaction of intelligent transport control system column below is a description of the mathematical models of longitudinal motion of the center of mass of the guided unmanned . To determine the control actions on the engine, transmission and brake system adequate mathematical model of longitudinal motion of the center of mass of the vehicle.

As a vector of control actions is considered.

- (1) $U = (U_1, U_2, U_3)^T$, when
 U_1 – gearbox transmission number $1 \leq U_1 \leq U_{1max}$; $U_1 = 0$ – corresponds to the neutral state of gearbox;
- (2) $U_2 = 2 \sin^2(\frac{\varphi_{ap}}{2})$ – the control action of the accelerator corresponding to the rotation angle of the throttle φ_{ap} engine;
- (3) $U_3 = P_T P_{Tmax}^{-1}$ – control action on a braking system equal to the ratio of pressure P_T κ its maximum allowable value P_{Tmax} .

The longitudinal motion of the center of mass of the car is described by a system of differential equations, in which the first equation of the system is a special case of the second Newton's law, and the second equation is the definition of speed as a derivative of the path [6]:

$$(4) \begin{cases} \dot{V}_m = a_m = a_{dT}(U) - k_x m_0^{-1} V_m^2 - k_{Tp} g - \alpha_T g \\ \dot{L}_m = V_m \end{cases}$$

when

- $a_m = \dot{V}_m$ – longitudinal acceleration of the centre of mass;
- (5) $a_{dT} = a_d(U_1, U_2) - a_T(U_3)$ – traction and acceleration created by the engine to the transmission to the drive wheels (a_d) and brake deceleration (a_T), generated by the braking system;
- (6) $k_x = 0,5 C_x S_x \rho$ – drag coefficient, aerodynamic drag;
- C_x – specific coefficient of aerodynamic drag;
- S_x – cross-sectional area (midsection) of the object;
- m_0 – vehicle weight;
- k_{Tp} – the coefficient of rolling friction of the tires;
- α_T – pitch angle equal to the angle of slope of the road surface to the horizon;
- g – acceleration of gravity.

Drag coefficient, aerodynamic drag k_x and rolling friction of tires k_{Tp} unknown in advance and determined experimentally.

3.2. Development of the algorithm of brake control

The problem of development of the brake control algorithm is solved for the adaptive cruise control system, advanced emergency braking system and auxiliary braking system.

The principal differences of the considered algorithm of automatic braking of the developed systems of power-driven vehicles from those used in existing foreign systems of active safety are:

- installed on modern vehicles, automatic emergency braking (AEB) systems are used in braking ABS function, therefore, they have all the disadvantages of anti-lock systems, namely the cyclic principle of action, which does not allow for effective braking on slippery and uneven surfaces. The algorithm does not depend on ABS and works on the principle of limiting the braking deceleration, taking into account the slippery surface;
- preventing collisions with passing objects in the rear hemisphere is not part of the functions of the currently used systems. However, the danger of such collisions and the severity of their consequences is no less significant than in the front hemisphere.

To describe the algorithm of automatic braking should describe the conditions of collisions of objects when moving in the same lane.

Consider the differential equations of distances L_1 and L_2 between the driven car and the obstacles in the front and rear traffic lights on the same lane:

$$(7) \begin{cases} \frac{dL_1}{dt} = V_{np1}(t) - V_m(t); \\ \frac{dL_2}{dt} = V_m(t) - V_{np2}(t), \text{ when} \end{cases}$$

$V_m(t)$ – speed of driven car,
 $V_{np1}(t)$ and $V_{np2}(t)$ – speed front and rear obstacles.

Figure 1 shows the relative position of the front and rear obstacles on the lane..

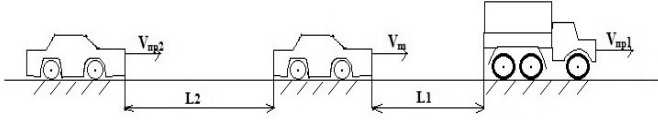


Figure 1-Relative positioning of the front and rear passing obstacles on the lane

The solution of differential equations (8), presented on the time interval $(t \div t_s)$ to the complete stop of objects:

$$(8) \begin{cases} L_1(t_s) = L_1(t) + \int_t^{t_s} [V_{np1}(\tau) - V_m(\tau)] d\tau; \\ L_2(t_s) = L_2(t) + \int_t^{t_s} [V_m(\tau) - V_{np2}(\tau)] d\tau. \end{cases}$$

A natural condition for preventing collisions is the implementation of inequalities $L_1(t_s) > 0$ and $L_2(t_s) > 0$, which are converted to the following:

$$(9) \begin{cases} L_1(t) > \int_t^{t_s} [V_m(\tau) - V_{np1}(\tau)] d\tau; \\ L_2(t) > \int_t^{t_s} [V_{np2}(\tau) - V_m(\tau)] d\tau \end{cases}$$

The right-hand sides of the inequalities (9) represent the lower bounds of safe distances ΔL_{rp1} и ΔL_{rp2} to front and rear hurdles.

Given the time lag of actuation of the brake systems of the vehicle τ_m and rear obstacles τ_{np2} the lower bounds of the safe range ΔL_{rp11} and ΔL_{rp21} at intervals, delays are:

$$(10) \begin{cases} \Delta L_{rp11} = 0,5\hat{a}_{np1}\tau_m^2 + (V_m - V_{np1})\tau_m; \\ \Delta L_{rp21} = 0,5\hat{a}_{Tm}\tau_{np2}^2 + (V_{np2} - V_m)\tau_{np2}, \text{ when} \end{cases}$$

\hat{a}_{np1} – projected estimation of the deceleration of the front obstacle;

\hat{a}_{Tm} – forecast estimate of deceleration of the driven vehicle.

The second pair of lower boundaries of safe distances ΔL_{rp1} and ΔL_{rp2} determined at the time interval until the complete stop:

$$(11) \begin{cases} \Delta L_{rp12} = V_m\tau_m + 0,5V_m^2\hat{a}_{Tm}^{-1} - 0,5V_{np1}^2\hat{a}_{np1}^{-1}; \\ \Delta L_{rp22} = V_{np2}\tau_{np2} + 0,5V_{np2}^2\hat{a}_{np2}^{-1} - 0,5V_m^2\hat{a}_{Tm}^{-1}. \end{cases}$$

The resulting bounds of the safe range ΔL_{rp1} and ΔL_{rp2} defined as the maximum of a pair $(\Delta L_{rp11}, \Delta L_{rp12})$ and a pair of $(\Delta L_{rp21}, \Delta L_{rp22})$:

$$(12) \begin{cases} \Delta L_{rp1} = \max[\Delta L_{rp11}, \Delta L_{rp12}] \\ \Delta L_{rp2} = \max[\Delta L_{rp21}, \Delta L_{rp22}] \end{cases}$$

In this case, the inequalities are fulfilled

$$(13) \begin{cases} L_1(t) > \Delta L_{rp1}(t); \\ L_2(t) > \Delta L_{rp2}(t), \end{cases}$$

means that the collision avoidance conditions are met both on the lag interval and on the interval to a full stop.

To prevent collisions with an oncoming obstacle $V_{np1} < 0$ the value of the boundary distance is

$$(14) \Delta L_{rp1} = V_m\tau_m + V_{np1}\tau_{np1} + 0,5V_m^2\hat{a}_{Tm}^{-1} + 0,5V_{np1}^2\hat{a}_{np1}^{-1}$$

Analysis of the conditions for collision prevention, presented in the form of the problem of dynamic stabilization of distances, shows that the highest values of boundary distances is characteristic for the oncoming obstacles [7]. Uncertainty of estimates of delays in braking of the driven vehicle and obstacles, along with uncertainty of their decelerations in case of manual control creates difficulties of adequate forecasting of boundary distances.

The solution of the problem of dynamic stabilization of safe distances [8] or deceleration a_{Tm} the driven vehicle is determined from the boundary distance equations provided

$$(15) L_1 = \Delta L_{rp1} \text{ и } L_2 = \Delta L_{rp2}.$$

So, in particular, brake deceleration a_{Tm} , sufficient to prevent collision with a forward fixed, passing or oncoming obstacle is

equal to:

$$(16) a_{Tm} = \begin{cases} \bar{a}_{Tm}, \text{ если } \Delta L_{m1}^* > 0 \text{ и } \bar{a}_{Tm} \leq a_{Tmax}; \\ a_{Tmax}, \text{ если } \Delta L_{m1}^* \geq 0 \text{ или } \bar{a}_{Tm} > a_{Tmax}, \text{ when} \end{cases}$$

$$(17) \bar{a}_{Tm} = 0,5V_m^2(\Delta L_{m1}^*)^{-1};$$

$$(18) \Delta L_{m1}^* = \begin{cases} [L_1 - V_m\tau_m + 0,5V_{np1}^2\hat{a}_{np1}^{-1}], \text{ если } V_{np1} \geq 0; \\ [L_1 - V_m\tau_m + V_{np1}\tau_{np1} - 0,5V_{np1}^2\hat{a}_{np1}^{-1}], \\ \text{ if } V_{np1} < 0; \end{cases}$$

\hat{a}_{np1} – assessment of the developed brake deceleration of the front obstacle;

Braking deceleration a_{T1} , sufficient to prevent a collision with the rear of the associated constraint on the delay interval braking τ_{np2} equally:

$$(19) a_{T1} = \begin{cases} \bar{a}_{T1}, \text{ если } \bar{a}_{T1} \leq a_{Tmax}; \\ a_{Tmax}, \text{ если } \bar{a}_{T1} > a_{Tmax}, \end{cases}$$

when $\bar{a}_{T1} = 2[L_2\tau_{np2}^{-2} + (V_m - V_{np2})\tau_{np2}^{-1}]$.

3.3. Development of algorithm of interaction of CU in the column

After switching to the operating mode, following in the column the leading vehicle, the leading vehicle, on which the Bluetooth access server devices are located, begins the exchange with the driven unmanned vehicles equipped with Bluetooth client modules [9].

Performing the functions of a server (hereinafter server) device with Bluetooth access, transmits to customers (driven by unmanned vehicle) information, on the basis of which the task of managing the course of driven unmanned vehicles is formed.

Messages are exchanged between the server and clients in accordance with the Protocol of exchange that guarantees the delivery of the message.

The exchange session always initializes the server, to verify communication, the server, with the operator specified frequency, sends a command to all clients to send telemetry, the clients, if they have a new regular or emergency telemetry, sends it to the server.

According to the results of telemetry processing, the control program of the column or the operator sends to the selected unmanned vehicle control command to perform certain actions specified in paragraph 3.1.

Driven unmanned vehicles transmit to the server telemetric information necessary for trouble-free movement as part of the column.

In the case of identifying obstacles on the lane column in front of one of the unmanned vehicles, the unmanned vehicle, in the presence of (according to the engineer reconnaissance), the second lane begins the maneuver detour obstacles, with a notification over the communication channel leading unmanned vehicle otherwise the unmanned vehicle is stopped and sends a notification about an emergency stop [10,11].

In the event that one of the unmanned vehicles makes an emergency stop associated with the diagnosed malfunctions, the emergency unmanned vehicle transmits to the driving car a message about the emergency stop.

3. Conclusion

The analysis of results of the carried-out researches in the field of perspective directions of development of systems of functioning of the unmanned vehicle allows to formulate the following conclusions: the principles of construction of multilevel information management systems of the unmanned vehicle and their hierarchy are defined; the review of technical characteristics of available devices and systems of technical vision is carried out; the comparative analysis of opportunities and technical characteristics of systems of navigation and orientation of the unmanned vehicle; modern intelligent communication systems of unmanned vehicles and their technical characteristics are considered..

4. Acknowledgements

This material was prepared based on the results of applied scientific research and experimental developments, which are carried out with the financial support of the Ministry of Education and Science of Russia. The Agreement number is No. 14.625.21.0043. The unique identifier of the project is RFMEFI62517X0043.

5. References

1. Kozlovskiy V.N., Debelov V.V., Deev O.I., Kolbasov A.F., Petrovski S.V., Novikova A.P., Advanced self-diagnosis and management of transport facilities, journal «Gruzovik» №6,2017, p. 21-28
2. Lombacher, J., Hahn, M., Dickmann, J., Wöhler, C. (2017, March). Object classification in radar using ensemble methods. In *Microwaves for Intelligent Mobility (ICMIM), 2017 IEEE MTT-S International Conference on* (pp. 87-90). IEEE
3. Dumitru Erhan, Christian Szegedy, Alexander Toshev, and Dragomir Anguelov. Scalable Object Detection Using Deep Neural Networks. In *Proceedings of the 2014 IEEE Conference on Computer Vision and Pattern Recognition (CVPR 14)*. IEEE Computer Society, Washington, DC, USA, p. 2155-2162.
4. Rabbou M. A., El-Rabbany A. Non-linear filtering for precise point positioning GPS/INS integration //The International Archives of Photogrammetry, Remote Sensing and Spatial Information Sciences. – 2014. – T. 40. – №. 2. – p. 127.
5. Katanaev N.T., Kolbasov A.F., A system of forecasting changes in meteorological factors in order to improve road safety, The “Žurnal AAI” №4, 2016, p. 38-40.
6. S. Patil, G. Kahn, M. Laskey, J. Schulman, K. Goldberg, and P. Abbeel. Scaling up gaussian belief space planning through covariance-free trajectory optimization and automatic differentiation. In *Intl. Workshop on the Algorithmic Foundations of Robotics*, 2014.
7. Saikin A.M., Buznikov S.E., Karpukhin K.E. The Analysis of Technical Vision Problems Typical for Driverless Vehicles, *Research Journal of Pharmaceutical, Biological and Chemical Sciences*. 2016. Vol. 7. № 4. p. 2053-2059.
8. Shadrin S.S., Ivanov A.M., Karpukhin K.E Using Data From Multiplex Networks on Vehicles in Road Tests, in *Intelligent Transportation Systems, and in Self-Driving Cars*,. *Russian Engineering Research*. 2016. Vol. 36. № 10. p. 811-814.
9. Buznikov S.E., Endachev D.V., Karpukhin K.E., Saykin A.M., Terenchenko A.S. Development of Russian driverless electric vehicle, *International Journal of Mechanical Engineering and Technology*. 2017, Vol. 8, Issue 12, p. 955-965.
10. S. Karungaru, H. Nakano, and M. Fukumi. Road Traffic Signs Recognition Using Genetic Algorithms and Neural Networks. *International Journal of Machine Learning and Computing*, Vol. 3, No. 3, 2013, p. 313-317
11. Malhotra N., Charlton, S., Starkey, N. and Masters, R. Driving speed choice: The role of conscious monitoring and control (reinvestment) when driving. *Transportation Research Part F Traffic Psychology and Behaviour*, Available online 24 June 2017, pp. 1-14.

DEPENDENCE OF THE ACTIVE POWER OF THE SERIAL RESONANT BRIDGE CONVERTER FROM THE PHASE DIFFERENCE AND THE DUTY CYCLE

Assist. prof. Dr. Eng. Stefanov G.¹, Prof. Dr. Eng. Karadzinov Lj.², Assos. prof. Dr. Eng. Sarac V.³, Prof. Dr. Eng. Atanasova-Pacemska T.⁴,
 Assist. M.Sc. Kukuseva Paneva M.⁵, Prof. Dr. Eng. Dambov R.⁶
 Faculty of Electrical Engineering- Radovish, University 'Goce Delcev'-Stip, Macedonia^{1,3,4,5}
 FNTS- Stip, University 'Goce Delcev'-Stip, Macedonia⁶
 FELT, University Sv. Kiril and Methodius -Skopje, Macedonia²
 goce.stefanov@ugd.edu.mk, L.Karadzinov@feit.ukim.edu.mk, vasilija.sarac@ugd.edu.mk, tatjana.pacemska@ugd.edu.mk,
 maja.kukuseva@ugd.edu.mk, risto.dambov@ugd.edu.mk

Abstract: Serial resonant bridge converter commonly used in process of induction heating on metal materials. In these applications during the heating process, the converter load equivalent electrical parameters are changed. This contributes to the transferred power from the converter to the induction device to change. In this paper with mathematical analysis are determined the quantities from which depends the active power of the resonant converter. Derived is an equation that gives the dependence of the active power from the phase angle between the voltage and current the converter as and from the duty cycle. This equation can be used in control methods to maintain maximum converter power transfer.

Keywords: ACTIVE POWER, RESONANT CONVERTER, EQUATION

1. Introduction

In power converters of interest is that the power transferred from the converter on the load to be maximal. Often due to the change in the parameters of the output circuit of the converter, this power is not always maximal [1], [2], [3]. To maintain maximum transferred power from the converter to the load is needed knowledge of the parameters that affect the power. Independent of the type of process controlled by the converter, motor drive or induction device, etc., causes leading to a reduction in the transferred power are related to increasing the phase difference between the voltage and the current of the converter as well the deviation of duty cycle of value 0.5. The change in the phase difference is caused by the change of parameters (inductance, resistance, and capacitance) of the output circuit of the converter. To changing the duty cycle on the output voltage of the converter comes as a result of the need to change the effective value of the output voltage, with target to controlling the output power of the converter. The change on the phase difference leads to an increase in reactive power and a reduction in the active power of the converter. Reduction of the duty cycle from 0.5 increases the harmonic distortion of the output voltage and current of the converter. Both reasons reduced the output active power and efficiency of the converter [4], [5], [6] [7].

In this paper with mathematical analysis are determines the quantities from which depends the active power of the resonant converter. Derived is an equation which gives the dependence of the active power from the phase angle between the voltage and current the converter as and from the duty cycle.

2. Impact on Phase Difference and Duty Cycle at Serial Resonant Bridge Converter

Serial the resonant converter is normally used in the devices for induction heating [1], [2]. In Fig. 1 is shown the electrical scheme of this converter with output load: $R = 0.24 \Omega$, $C = 26,6 \mu\text{F}$ and $L = 26,5 \mu\text{H}$ [8]. In Fig. 2 are shown the output voltage and current waveforms in the more usual above-resonance mode of operation. In induction heating/melting and similar applications the heated workpiece equivalent electrical parameters are part of the resonant circuit. As the work-piece temperature increases, its equivalent resistance and inductance change, thus changing the circuit resonant frequency. Consequently, the deviation of the switching frequency from the resonant one is also changed, which results in undesired change of output power.

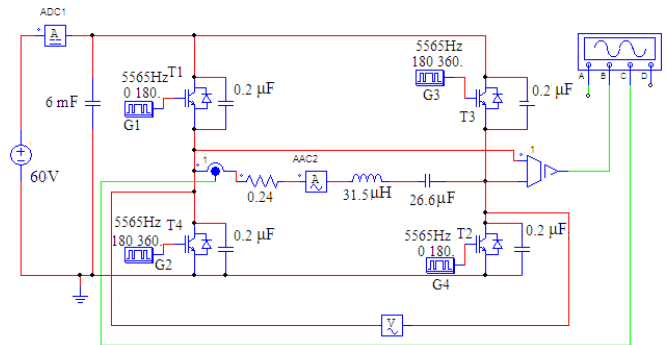


Fig. 1 Serial resonant bridge converter topology in mode of induction device.

The typical R and L change during metal-piece induction melting is in the range of 50%. These real values are used as an example in the following examination giving the values for the resonant frequency $\omega_0 = 37665 \text{ rad/s}$, $f_0 = 5998 \text{ Hz}$ [9], [10].

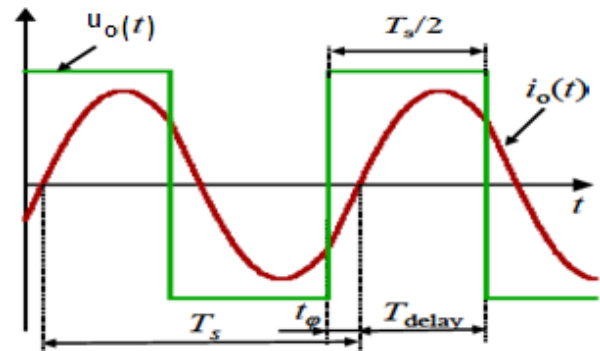


Fig. 2 Output voltage and current waveforms in above-resonance mode.

The mode of induction heating changes the value of the resistance and inductance of the resonant circuit of the converter. This leads to a change in the phase difference between the current and the voltage of the converter and the change of the output power.

In Table I are given the values on the switching frequency f_{sw} , output voltage U_o , output current I_o , output power P_o and phase difference ϕ for change on the resistance and the inductance for 20%, i.e.: change on R from 0.24Ω on 0.29Ω , and change on L from $26.5 \mu\text{H}$ on $31.5 \mu\text{H}$.

To visualize this rather strange dependence, Fig. 3 gives Power-Sim simulation results of steady state for several values of the switching frequency below and above resonance [9].

Table I: Values of the output converter parameters for changes of resistance and inductance for 20%

L [μH]	R [Ω]	φ [$^\circ$]	f_{sw} [kHz]	I_o [A]	U_o [V]	P_o [kVA]
26,5	0,24	5,00	6,27	208	56	10,7
31,5	0,29	31,34	6,27	145	56	6,16

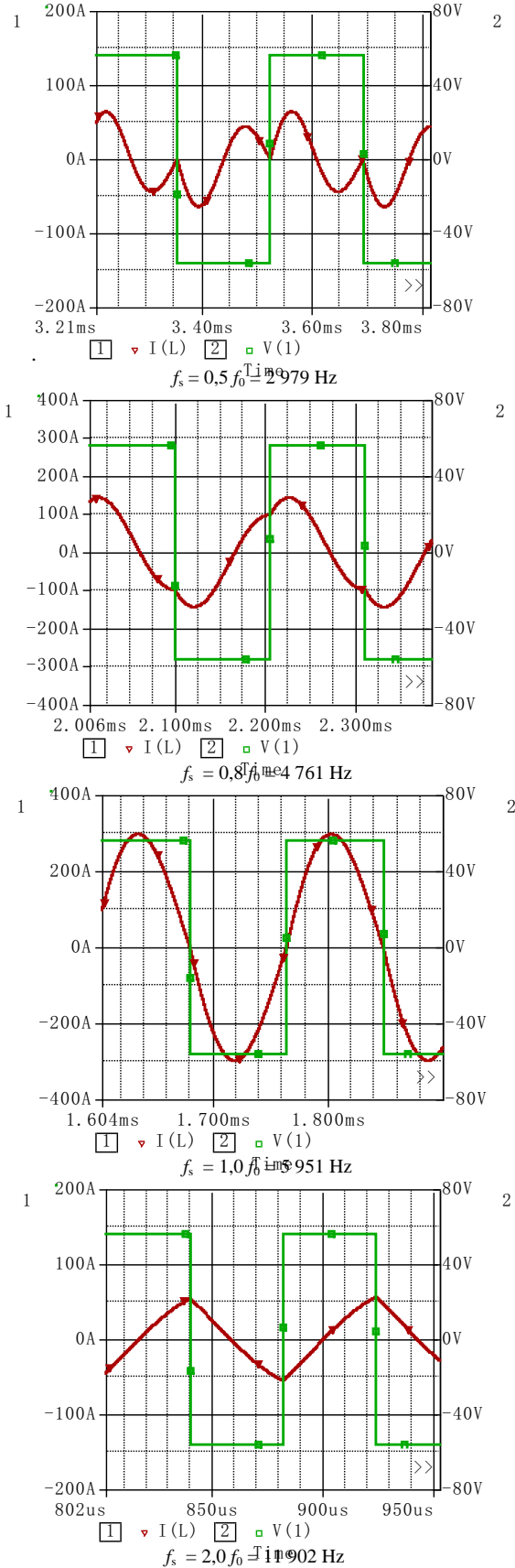


Fig. 3 Steady state voltage and current waveforms below and above resonance ($R = 0.24 \Omega$, $L = 26.6 \mu\text{H}$, $C = 26.6 \mu\text{F}$ and $Q = 4$).

From Table I can be seen that the change in the inductance and the resistance for 20 %, changes the phase angle for 16 % and reduces the output power for 42 %.

The current waveform for $f_s = 0.5 f_0$ shows that is very much distorted deep below resonance, the first harmonic is no longer dominant, which reflects to the amount of active power transferred to the load. This explains why below-resonance mode of power control was less desirable. The first diagram in the Fig. 3 for $f_s = 0.5 f_0$ shows that phase difference gets zero values every time the switching period T_s is multiple of the resonant one T_0 , in this case $T_s = 2 T_0$.

The general conclusion from Fig. 3 is that when switching frequency f_s is different from resonant frequency f_0 the harmonic distortion of the output current are increased.

In Table II are given the values on output voltage U_o , output current I_{out} , output power P_{out} for change on convertor duty cycle.

Table II: Values of the output converter parameters for changes of the duty cycle

L [μH]	R [Ω]	φ [$^\circ$]	f_s [kHz]	D	I_o [A]	U_o [V]	P_o [kVA]
26,5	0,24	5,00	6,27	0,5	208	56	10,7
26,5	0,24	5,00	6,27	0,4	187	56	8,5
26,5	0,24	5,00	6,27	0,3	125	56	3,8
26,5	0,24	5,00	6,27	0,2	43	56	0,45

From Table II can be seen that the change on the duty cycle D significantly reduces the output power P_o . Changing the duty cycle to 0.1 from optimal value 0.5 causes a change on the power for 21 %. Larger changes in the duty cycle D causes significant changes on the power P_o .

Also, the change in the duty cycle causes an increase in the harmonic distortion of the output voltage. In the Fig. 4 is shown harmonic specter for the output voltage of the converter for duty cycle 0.5 and 0.2.

From Fig. 4a can be see that for duty cycle 0.5 the first harmonic (on frequency 6.027 kHz) has the highest value and for duty cycle 0.2, the highest value has third harmonic, Fig. 4b.

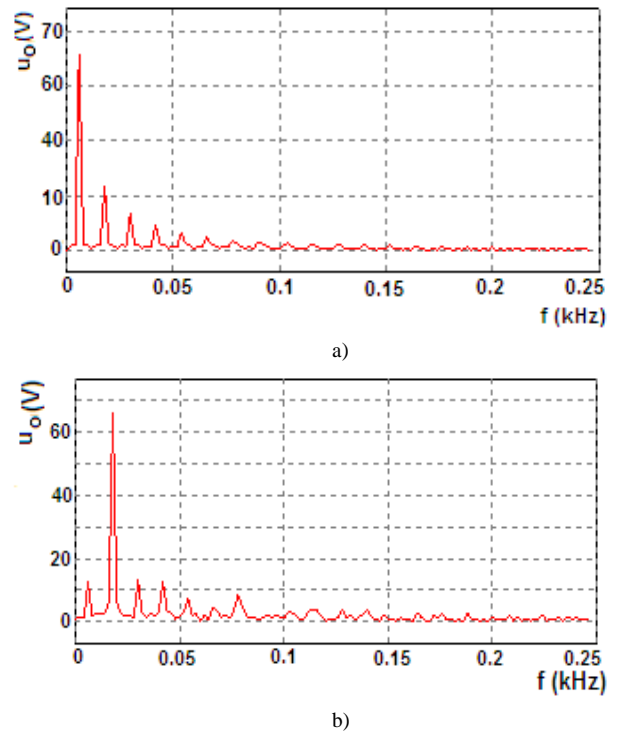


Fig.4 Harmonic specter of the output converter voltage: a) for duty cycle 0.5 and b) for duty cycle 0.2.

The general conclusion from Fig. 4 is that for less duty cycle $D < 0.5$ the harmonic distortion of the output voltage increases.

3. Determination on the active power from phase difference and duty cycle

The output active power of the serial resonant converter is determined as [2], [3]:

$$P_o = U_o I_o PF \quad (1)$$

In (1) U_o is the effective value on the output voltage, I_o is effective value on the output current, and PF is power factor of the converter.

In a converter that generates a voltage with a square waveform at the output, the power factor of the converter is defined as:

$$PF = DF_u \cdot DF_i \cdot DPF \quad (2)$$

In (2) DF_u is a voltage distortion factor and is defined as the ratio of the effective value of the fundamental voltage harmonic U_1 and the effective value of the total voltage U_o , ie:

$$DF_u = \frac{U_1}{U_o} = \frac{1}{\sqrt{1 + THDV^2}} \quad (3)$$

In (3) THDV is a total harmonic distortion of the voltage and is defined as a square root of the ratio of the sum of squares to the effective values of the higher harmonics of the voltage and the square of the effective value of the fundamental harmonic of the voltage U_1 , ie:

$$THDV = \sqrt{\frac{|U_3^2| + |U_5^2| + |U_7^2| + |U_9^2| + |U_{11}^2| + \dots}{|U_1^2|}} \quad (4)$$

The second term in (2), DF_i is a current distortion factor and is defined as the ratio of the effective value of the fundamental current harmonic I_1 and the effective value of the total current I_o , ie:

$$DF_i = \frac{I_1}{I_o} = \frac{1}{\sqrt{1 + THDI^2}} \quad (5)$$

In (5) THDI is a total harmonic distortion of current and is defined as the square root of the ratio of the sum of squares to the effective values of the higher harmonics of current and the square of the effective value of the fundamental current harmonic, ie:

$$THDI = \sqrt{\frac{|I_3^2| + |I_5^2| + |I_7^2| + |I_9^2| + |I_{11}^2| + \dots}{|I_1^2|}} \quad (6)$$

The third term in (2), $DPF = \cos\varphi$ is the displacement factor.

For frequencies close to the resonance, the current is with the sinusoidal waveform, so that the current distortion factor $DF_i = 1$. Based on the above and (1), the power factor in a resonant converter with a square waveform of the output voltage and operating frequencies close to the resonance, is given as:

$$PF = DF_u \cos\varphi = \frac{U_1}{U_o} \cos\varphi \quad (7)$$

In a bridge resonant converter with a square waveform on the output voltage, when the duty cycle is $D = 0.5$, the voltage distortion factor is $DF_u = 0.90$ [2]. With this (7) gets the form:

$$PF = 0.9 \cos\varphi \quad (8)$$

The effective value of the fundamental voltage harmonic U_1 in a bridge resonant converter with a square waveform of the output voltage and the duty cycle factor D is given with [2]:

$$U_1 = \frac{4U_{DC}}{\pi\sqrt{2}} \sin(D\pi) \quad (9)$$

Replacing (9) in (7) for the power factor is obtained:

$$PF = \frac{1}{U_o} \frac{4U_{DC}}{\pi\sqrt{2}} \sin(D\pi) \cos\varphi \quad (10)$$

When the (10) is replaced in (1) the power gets the form:

$$\begin{aligned} P_o &= \frac{I_o U_o}{U_o} \frac{4U_{DC}}{\pi\sqrt{2}} \sin(D\pi) \cos\varphi = \\ &= I_o \frac{4U_{DC}}{\pi\sqrt{2}} \sin(D\pi) \cos\varphi \end{aligned} \quad (11)$$

The equation (11) gives the dependence of the output power of a bridge resonant converter from the output current I_o , the voltage of DC source U_{DC} , the phase difference φ and the duty cycle D .

From (11) can be concluded that the output power of the converter can be controlled with control of the phase difference and with duty cycle D . However, control of the output power with changing the duty cycle D is limited by the increase of the harmonics which comes with a decrease on duty cycle.

When $D < 0.5$ the harmonic distortion increases and the voltage distortion factor $DF_u < 0.90$. For illustration of this, in Fig. 5 is shown the dependence of the voltage distortion factor $DF_u = U_1/U_o$ from duty cycle D .

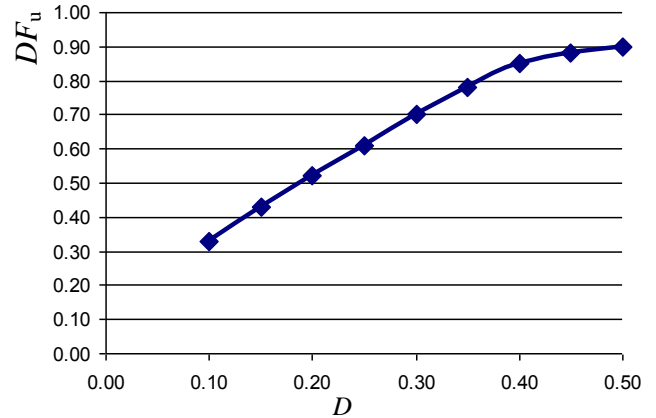


Fig. 5. Dependence of the voltage distortion factor DF_u from duty cycle D .

From Fig. 5 can be noted that to 20 % (value 0.4) decrease of the duty cycle, the voltage distortion factor are decreased to 0.85. With this, the power factor will fall below 0.85, the active power will decrease, and therefore the efficiency will decrease. Therefore, in practice when adjusting the output power of the resonant converter by adjusting the duty cycle, it should go with its change in small range below 0.5.

For greater power deviation from the nominal (due to change in resonant circuit resistance) is more practical to use a DC/DC converter in a DC power source that will supply the inverter. However, even considering that the DC/DC efficiency is about 0.9 and the efficiency of the resonant converter is about 0.9 the total efficiency will fall about 0.8.

In serial resonant converter, the output voltage is with square waveform and in such a case phase differences is [8], [10]:

$$\varphi = \arctg \left(\frac{\sin(\pi \frac{\omega_d}{\omega_s})}{e^{\frac{\pi \omega_0}{2Q \omega_s}} + \cos(\pi \frac{\omega_d}{\omega_s})} \right) \quad (12)$$

where:

$$\omega_d = \sqrt{\omega_0^2 - \left(\frac{R}{2L}\right)^2} \quad (13)$$

is damping frequency and with values for $R = 0.24 \Omega$, $C = 26,6 \mu\text{F}$ и $L = 26,5 \mu\text{H}$ has the value 37392 rad/s . When (12) is replaced in (11), for active power of converter is are obtained:

$$P_o = I_o \frac{4U_{DC}}{\pi\sqrt{2}} \sin(D\pi) \cos \left(\arctg \left(\frac{\sin(\pi \frac{\omega_d}{\omega_s})}{e^{+\frac{\pi \omega_0}{2Q\omega_s}} + \cos(\pi \frac{\omega_d}{\omega_s})} \right) \right) \quad (14)$$

Base on (14) in Table III are given data for the effective value on output current I_o , the voltage on DC supply U_{DC} , ratio on the switching and damping frequency f_s/f_d , the phase difference φ and calculate power P_o . These values are obtain with RLC parameters that are given above.

Table III: Data for f_s/f_d , U_{DC} , I_o , and P_o for $D = 0.5$, $D = 0.4$ and $D = 0.2$

f_s/f_d	U_{DC} [V]	φ [o]	$D= 0.5$		$D= 0.4$		$D= 0.2$	
			I_o [A]	P_o [kW]	I_o [A]	P_o [kW]	I_o [A]	P_o [kW]
0.1	60	-0.02	57	2.88	25	1.26	18	0.91
0.25	60	-0.06	33	1.67	23	1.16	32	1.62
0.3	60	-15.13	62	3.03	52	2.54	34	1.66
0.4	60	20.53	52	2.46	28	1.32	41	1.94
0.5	60	-0.06	42	2.13	41	2.07	41	2.07
0.6	60	-19.72	55	2.62	55	2.62	42	2
0.7	60	-32.56	62	2.64	76	3.24	57	2.43
0.8	60	-37.36	89	3.58	110	4.42	58	2.33
0.9	60	-29.32	157	6.93	155	6.83	47	2.07
1.0	60	0.19	211	10.7	186	9.41	43	2.18
1.1	60	31.10	169	7.32	174	7.54	42	1.82
1.2	60	43.88	129	4.71	128	4.67	33	1.2
1.3	60	47.70	86	2.93	90	3.06	29	0.99
1.4	60	48.17	76	2.57	73	2.46	28	0.95
1.5	60	47.31	62	2.13	62	2.12	26	0.89
1.6	60	45.90	55	1.94	53	1.86	24	0.85
1.7	60	44.29	46	1.67	47	1.70	26	0.94
1.8	60	42.63	41	1.53	44	1.63	23	0.86
1.9	60	40.99	40	1.53	37	1.41	19	0.73
2.0	60	39.42	35	1.37	36	1.40	18	0.7

In the Fig. 6 are shown waveforms of the output power in relation to the normalized circular frequency f_s/f_d obtained with equation (14) for three value of duty cycle: $D = 0.5$ (a), $D = 0.4$ (b) and $D = 0.2$ (c).

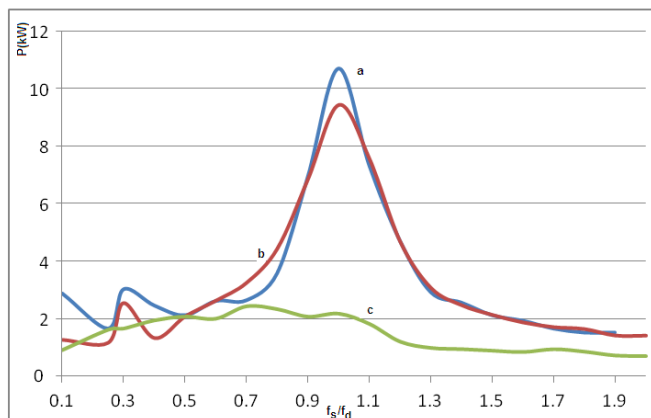


Fig. 6. Waveforms on the output power of the resonant converter for three value on duty cycle: $D = 0.5$, $D = 0.4$ and $D = 0.2$.

Calculating the output power with (14) the effective value on the

output current I_o is obtained with simulation on the circuit from Fig.1 in PowerSim program.

From Table III and Fig. 6 can be seen that: first, the output power is maximal for $f_s = f_d$ and duty cycle $D = 0.5$, second, the output power for $D = 0.4$ and $f_s = f_d$ is reduced for 15 % in ratio on the power for $D = 0.5$.

Also, can be noted that for frequencies larger than $f_s = 1.1 f_d$, the waveforms on the output power for $D = 0.4$ and $D = 0.5$ are almost the same.

The waveform on the output power for $D = 0.2$ shows that in this case is greatly reduced with maximum value for $f_s = 0.7 f_d$.

4. Conclusion

The serial resonant bridge converter have output voltage with square waveform and output current with sinusoidal form when switching frequency is same with the resonant frequency. When this converter operates in mode on induction device RL parameters are changed. This changes cause change on the phase difference between the output voltage and current. This cause change on transferred power from the converter to the output load. On the output power also can be influenced with changes on duty cycle.

To maintain a constant power transfer from the converter to the load, it is necessary to know the dependence of the power on the phase difference and duty cycle. In this paper, an exact equation is derived for the dependence of the output power of the converter from the phase difference and duty cycle. This equation can be used for development of an algorithm for the operation of the converter with constant power.

5. References

- [1] G.E.Totten, Steel Head Treatment, Portland State University, Oregon USA, Second Edition 2006.
- [2] W. B. Williams, Principles and Elements of Power Electronics, University of Strathclyde, Glasgow, 2006.
- [3] W. Shepherd, L. Zhang, *Power Converter Circuits*, Marcel Dekker, 2004, ch.15
- [4] D. Maksimovic, R. Zane, R. Erickson, "Impact of digital control in power electronics", In Proceedings of the IEEE 16th International Symposium on Power Semiconductor Devices and ICs. May: 13–22. 2004.
- [5] K. Harada, Analysis and Design of ZVS-PWM Half-Bridge Converter, IEEE PESC Record, 1995, pp. 280-285.
- [6] J. Shklovski, K. Janson, T. Sakkos, Natural Mode Constant Power Source for Manual Arc Welding, *Elektronika Ir Elektotehnika*, Vol 18, No 9, 2012.
- [7] Y. Kwon, S. Yoo, D. Hyun, "Half-bridge series resonant inverter for induction heating applications with load-adaptive PFM control strategy", Applied Power Electronics Conference and Exposition, pp. 575–581, Dallas, TX, USA, 14–18 Mar 1999.
- [8] G. Stefanov, "Resonant Converter for Induction Heating of Metals with Improved Efficiency", Ph.D. Thesis, Sts. Cyril and Methodius University, Skopje, Macedonia, 2014.
- [9] PowerSim Software, <http://www.powersim.com/>
- [10] Lj. Karadzinov, G. Stefanov, "Direct phase digital control method in power inverters based on dumping frequency analysis", Proceedings of the 16-th IEEE International Conference on Computer as a Tool – IEEE EUROCON 2015, Salamanca, Spain, 8–11 Sep. 2015, pp. 1–6.

PRECISE 3D CARTOGRAPHIC DESIGN USING BING-MAPS RESOURCES, 3D BLENDER AND THE SPECIALIZED BLENDERGIS-ADDON APPLICATION

Tihomir Dovramadjiev PhD.¹

Faculty of Manufacturing Engineering and Technologies, Department Industrial Design – Technical University of Varna, Bulgaria¹

tihomir.dovramadjiev@tu-varna.bg

Abstract: 3D cartographic design is successfully implemented using the modern resources of Bing-Maps, Blender-3D software and the BlenderGIS-addon application. In addition to the quality of the resulting end-models, the performance of these programs and applications is highlighted by its free license and open source. In the present study, a 3D model of a part of a geographical area in Varna, Bulgaria was developed. For the research purposes the geographic area of the Technical University - Varna, comprising a part of the campus is determined. The finished 3D model contains information with the exact positions and names of the selected objects.

Keywords: 3D, GIS, BING, BLENDER, BLENDERGIS-ADDON

1. Introduction

Obtaining quality 3D cartographic models requires the availability of appropriate resources of a different nature. Even if an appropriate methodology, including up-to-date technical and information tools and data, is developed, it is important to keep in mind that keeping up-to-date is of great significance in maintaining a system, including the emergence of new versions of operating systems, especially their interaction. Often, this is accompanied by the passage of a system from a free to paid version or in other cases, the abandonment of the product [1]. In turn, the GIS (Geographic Information System) has its own specific software, hardware, data, training capabilities for creating, manipulating, storing, analyzing, and visualizing spatially-defined data [2 - 5].

2. Materials and Methods

The Bing-Maps [6], Blender-3D [7] and BlenderGIS-addon [8] are methodically supported at this stage (November 2017). For the current study Bing online resources in the Maps section are used within the Blender 3D open source program. This is possible with the support of BlenderGIS-addon. Combining these capabilities into a unified system, the design of 3D cartographic model is fully possible, with the end result being with very good visual qualities. Figure 1 shows the working configuration between the three main components Bing-Maps, Blender-3D and BlenderGIS-addon, emphasizing that work is done in real time without hierarchy.

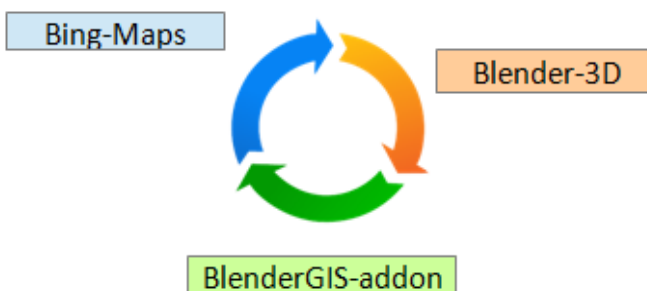


Fig. 1 Interaction between Bing-Maps, Blender-3D and BlenderGIS – addon

Implementation of the 3D cartographic model takes place in a Blender software environment. The program is a powerful free resource that combines a fully-functional and convenient interface with very good capabilities for high-quality finishing images or animations [9-17]. After adding BlenderGIS-addon (the addon is located at: <https://github.com/domlysz/BlenderGIS> and activated in Blender software using File-> User Preferences-> Install add-on from file-> BlenderGis-master.zip) it is necessary to select the Cache folder. The BlenderGIS-addon activates Basemap and Source: Bing; Layer: Map. Directly into the Blender software interface is included Bing-Maps (fig. 2). In order for visualization to be possible, Top View should be positioned in Ortho mode.

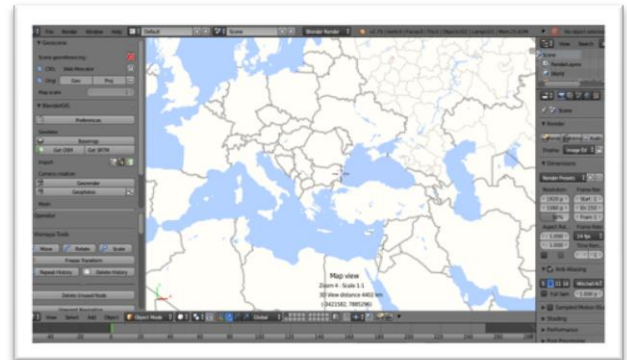


Fig. 2 Online Bing-Maps in Top View / Ortho

The map of the Technical University - Varna, Bulgaria is determined by manual or coordinate positioning of the map (fig. 3).

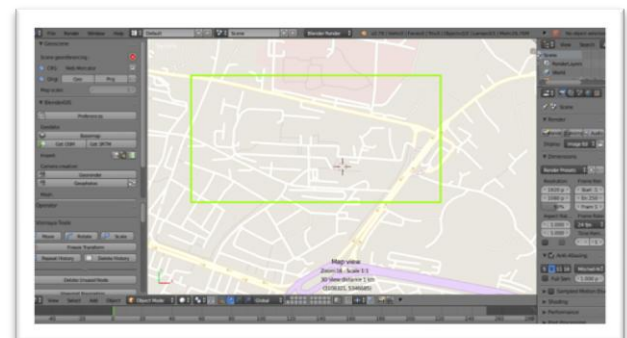


Fig. 3 Selecting the area of the Technical University - Varna, Bulgaria on the map

Once the zone is set, it switches to Satellite Mode (BlenderGIS-addon / Basemap / Layer: Satellite). The satellite visualization in the Blender software of the Technical University - Varna, Bulgaria is shown in figure 4.

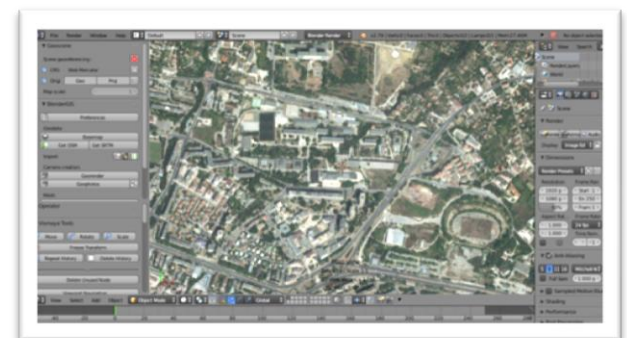


Fig. 4 Satellite Visualization in Blender Software in the region of Technical University - Varna, Bulgaria

The BlenderGIS-addon defines 3D design parameters: Get OSM/Ways/building, highway, natural, Default Height: 20, Level height: 3 and Separate objects. In the workspace of Blender three-dimensional models corresponding to the real objects are designed (figure 5 and figure 6).



Fig. 5 The designed 3D model of the region of the Technical University - Varna, Bulgaria and the surrounding sites

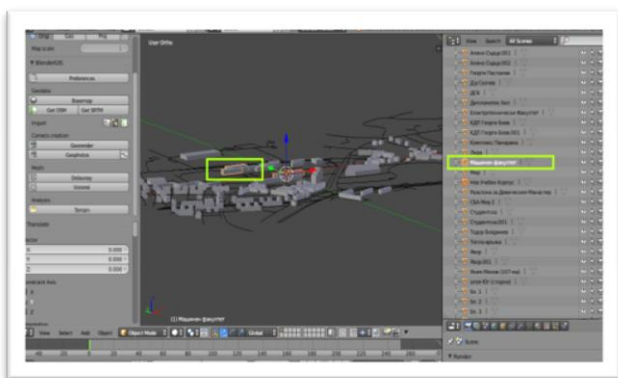


Fig. 6 Exact selection of the Faculty of Mechanical Engineering of the Technical University - Varna, Bulgaria (the selected 3D model and the corresponding name obtained directly online are marked in green)

In figure 7 is shown in isometric view the finished three-dimensional model of a field of Technical University - Varna, Bulgaria and the surrounding objects from the selected zone.

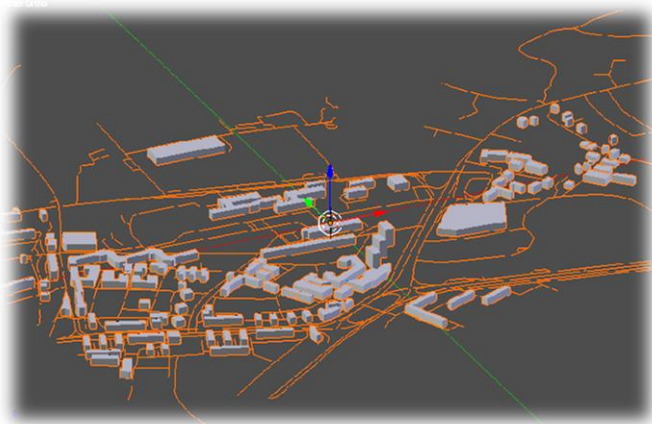


Fig. 7 Isometric view of the finished three-dimensional model of the region of the Technical University - Varna, Bulgaria and the surrounding objects of the selected area

Result: A three-dimensional model of the area including the area of the Technical University - Varna, Bulgaria and surrounding sites is developed through the accessible resources of Bing-Maps, Blender-3D and BlenderGIS-addon.

3. Conclusion

This article details the correct technological pathway for obtaining this model, focusing on the methodological features that contribute to the right design process. The resulting automated design result saves technological time to conventional three-dimensional design according to predefined drawings and parameters. The obtained result is distinguished by the high accuracy of the 3-D model and the detailed accompanying information received in real time..

4. References

- [1] A. Scianna, A. Ammoscato. 3D GIS data model using open source software. ISPRS Archive Vol. XXXVIII, Part 4-8-2-W9, : Core Spatial Databases – Updating Maintenance and Services – from Theory to Practice”, Haifa, Israel, 2010.
- [2] Geographic information system (GIS). https://en.wikipedia.org/wiki/Geographic_information_system
- [3] Kenneth E. Foote and Margaret Lynch. Geographic Information Systems as an Integrating Technology: Context, Concepts, and Definitions. The Geographer's Craft Project, Department of Geography, The University of Colorado at Boulder, 2015. <https://www.colorado.edu/geography/gcraft/notes/intro/intro.html>
- [4] Open Source GIS History – OSGeo Wiki Editors". Retrieved 2009-03-21. http://wiki.osgeo.org/wiki/Open_Source_GIS_History
- [5] Географска информационна система (ГИС). https://bg.wikipedia.org/wiki/Географска_информационна_система
- [6] Bing – Maps. <https://www.bing.com/maps>
- [7] Blender – 3D. <https://www.blender.org/>
- [8] BlenderGIS – addon. <https://github.com/domlysz/BlenderGIS>
- [9] T. Dovramadjiev. “Modern accessible application of the system blender in 3d design practice”. International scientific on-line journal "SCIENCE & TECHNOLOGIES". Publishing House "Union of Scientists - Stara Zagora", 2015. ISSN 1314-4111; p. 10 – 13. http://journal.sustz.com/VolumeV/Number4/Papers/Tiho_mirDovramadjiev1.pdf
- [10] Brian R Kent. 3D Scientific Visualization with Blender. National Radio Astronomy Observatory, Charlottesville, VA, USA. Morgan & Claypool Publishers. 2015.
- [11] John M. Blain. Computer Modeling and Animation. The Complete Guide to Blender Graphics. Taylor & Francis Group, LLC. ISBN:13: 978-1-4665-1704-2. UK, 2012.
- [12] А.А.Прахов, Blender: 3D-моделирование и анимация. СПб.: БХВ, ISBN 978-5-9775-0393-8, Русия, 2009, 272 с: ил.
- [13] Roger D. Wickes, Foundation Blender Compositing, ISBN-13 (pbk): 978-1-4302-1976-7, USA, 2009
- [14] Ami Chopine, 3D Art Essentials The Fundamentals of 3D Modeling, Texturing, and Animation, Elsevier, ISBN: 978-0-240-81471-1, USA, 2011, p. 249 – 252.
- [15] Felician Alecu, Blender Institute – the Institute for Open 3D Projects, Open Source Science Journal Vol. 2, No. 1, Economic Informatics Department, ASE Bucharest, Romania, 2010, 36 – 45.
- [16] James Chronister.: Blender Basics 2.6 (4-rd edition). Cdschools eBook Online, 2011, p. 178.
- [17] James Chronister, Blender 3D Basics 3rd Edition, Creative commons attribution-Non Commercial-share alike 3.0 Unported License, 2009,146 p.

THE DEVELOPMENT OF CALIBRATION FOR THE ROLLING BALLS OF DIAMETER 40 MM IN CONDITIONS OF JSC "SSGPO"

РАЗРАБОТКА КАЛИБРОВКИ ДЛЯ ПРОКАТКИ ШАРОВ ДИАМЕТРОМ 40 ММ В УСЛОВИЯХ АО «ССГПО»

D.t.s., professor Naizabekov A.¹; c.t.s., associate professor Lezhnev S.¹; Stepanov E.¹, PhD Panin E.²

¹ Rudny industrial institute, Rudny, Kazakhstan; ² Karaganda state industrial University, Temirtau, Kazakhstan
e-mail: naizabekov57@mail.ru

Abstract: Paper presents a preliminary calculation of the calibration rolls for rolling balls with a diameter of 40 mm in a rolling mill JSC "SSGPO", which will be rolled from round workpieces with a diameter of 40 mm. The main elements of ball caliber are considered, their design dimensions are determined. It is established that the height of the flange varies linearly and the width of the spherical area increases during rolling.

Keywords: ball, rolling, roll, calibration, calculation.

1. Introduction

For shape rolling mill 320 of JSC "SSGPO" two calibration schemes of round steel rolling were developed [1]:

1) from the billets 150×150 mm are produced round billets with a diameter of 100 mm, which are used as the grinding rods into rod mills factory complex of JSC "SSGPO".

2) from the initial billets 120×120 mm are produced round billets with a diameter of 40 mm, which are used on ball mills in the production of thermally hardened grinding balls diameter 40 mm.

In the analysis of techno-economic indicators was revealed that during the production of round bars with a diameter of 40 mm with the initial billet is 120×120mm, it has the untapped potential of production capacity of the rolling mill. The solution to this problem is the transformation of mill in the production of a round billet with a diameter of 40 mm from the initial billet 150×150 mm (figure 1). Such technological scheme of obtaining of a round billet with a diameter of 40 mm will allow to transfer the workpieces, unsuitable for rolling circle diameter of 100 mm, to the production of a circle with a diameter of 40 mm.

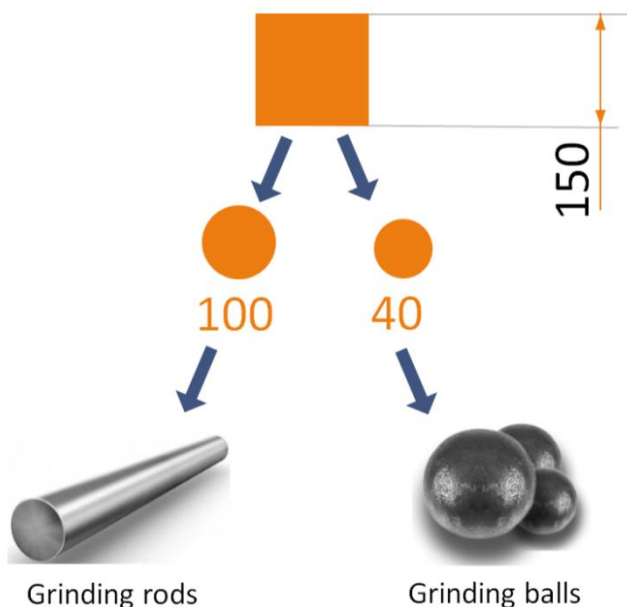


Figure 1 – New scheme of production

In work [2] a calibration of rolls for rolling round steel № 40 from the billet of cross section 150 x 150 mm in a mill 320 was developed. For this goal the total number of passes was increased from 9 to 11, the evaluation of compliance with emerging values of the power parameters of permissible values was considered (for the exception of equipment failure), and also conformity assessment of the shape and size of the final profile plant requirements was performed (to prevent defects of the geometry). In the result, it was

found that new developed calibration for obtaining the round steel with a diameter of 40 mm fully conforms to the technical parameters of shape mill 320. In this work the calculation of the calibration rolls for rolling balls with a diameter of 40 mm under conditions of JSC "SSGPO" from the original round billet with a diameter of 40 mm is presented.

2. Statement of the problem and initial data

Rolling of ball workpieces is performed between the two rolls 1 and 2 rotating in one direction, on their barrels the screw gauges are cut (figure 2). The axis of rolls usually tilted at a small angle to the axis of the rolled workpiece 3, thereby providing axial flow of the metal into the rolls. Rotating workpiece is crimped by flanges of the gauge and takes the form of a ball connected by a bridge with the rest of the workpiece. During the further promotion the ball is calibrated and completely separated from the rod.

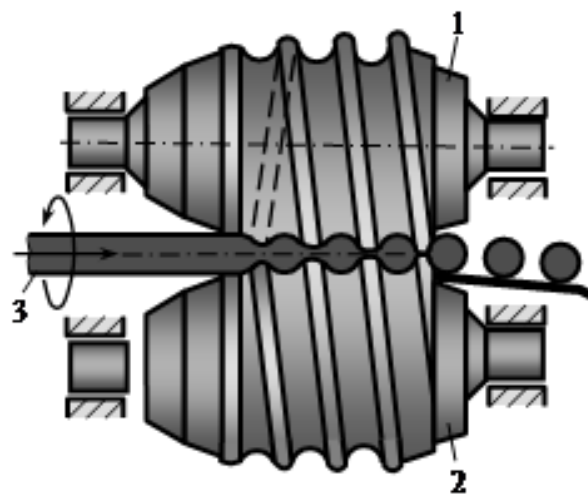


Figure 2 – Scheme of the ball rolling

During balls rolling, the deformation zone has two main sections [3]: forming section, where the workpiece is crimped with a change in the shape and size of the screw flange; and finishing section, where the shape and size of the flange remain constant, but the compression is due to the ovalization of the workpiece. The forming of the ball is performed by the flanges of the rolls, the height of which gradually increases. For ease of calculation, calibration and manufacturing of the rolls it is accepted that the height of the flange of the caliber changes according to the law of a straight line. For normal rolling process the profile and dimensions of the forming section of caliber are calculated so that during the compression of the workpiece there are two basic principles [4]:

1) volume of metal, crimped in the caliber, should remain constant during the forming process;

2) change the profile and size of the caliber flange should match

the stretching of crimping workpiece.

According to the first position, it is necessary that the volume of a certain part of the workpiece captured by the rolls, was unchanged as it passes through the remaining sections of the caliber. In this case, at any time of rolling will not be an excess of metal. When the excess metal the geometric form of sphere is distorted and the formation of voids in the axial zone of the workpiece is possible. The presence of a small excess of metal is permitted only at the beginning of caliber, when the flange is still relatively low and does not interfere with the displacement of the metal from the caliber.

The second condition is that for the normal formation of the ball shape, the stretching of compressed area should match to the changing shape and sizes of flange. The length of compressed bridge must be equal to the width of the straight portion of the flange. If the change of width of the flange is smaller of caliber stretching, the metal will move away from the flange, and the surface of the workpiece to form a reel, which upon further compression of the workpiece is rolled out in defect. If the change of width of the flange is more than the stretching of the workpiece, then in crimped bridge arise axial tensile stresses, which can lead to rupture of the bridge. Thus, to perform both the first and second conditions, the flange on different parts of the caliber must have a certain thickness. In this regard, the forming section of the caliber has a variable cutting step.

When developing the rolls calibration, it was decided to use the calculation algorithm described in detail in works [5-6]. In this work the results of preliminary calculation are presented. The initial data for the calibration are the technical characteristics of the rolling mill, size of the rolls, diameter of the resulting ball.

The calculation of the calibration ball is performed for the left roll, calibration of right roll is similar. The only difference is that after cutting the flange of the right roll it is cut on height by a certain value. The source data for calibration: diameter of the ball $d_B = 40$ mm; diameter of rolls $d = 300$ mm. In the calculation and construction of the sizing rolls it should be guided by the recommendations are given in table 1.

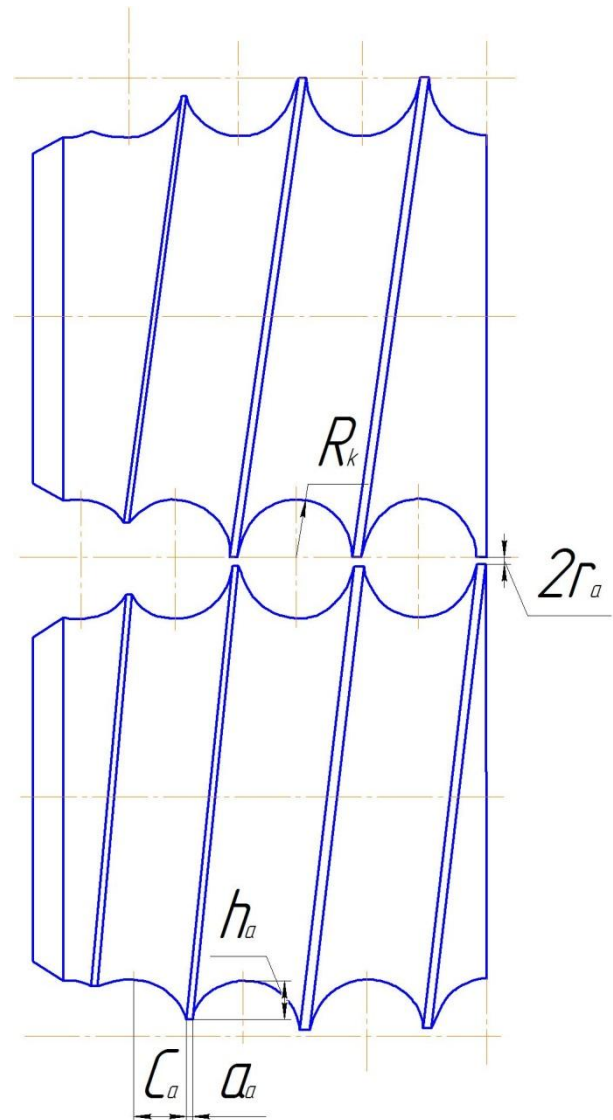


Figure 3 – Basic elements of a calibration for balls rolling:
 h_a and a_a – height and width of flange;
 r_a and R_K – radii of the bridge and caliber;
 C_a and S_a – width of spherical and cylindrical sections of caliber

Table 1 – Initial data for calculation of calibration

d_B , mm	d , mm	Length of the caliber, grad		$2r$, mm	The size of flange, mm		
		α_{FULL}	α_{FIN}		height on the capture	width at the finishing area	width on a area of 270° from the capture
40 - 50	180 - 300	900 - 1080	540 - 720	3,0 - 3,2	2,5 - 3,8	3,7 - 5,4	2,0 - 2,4
60 - 80	280 - 460	1080 - 1350	630 - 810	3,6 - 5,0	4,4 - 4,5	5,8 - 8,4	3,0
100 - 125	550 - 690	1260 - 1350	630 - 810	6,0	5,4	9,0 - 11,0	3,5 - 4,0

According to GOST 7524 - 2015 "Hot-rolled steel balls for ball mills" choose the nominal diameter of the ball for subsequent calibration of the rolls subject to the permissible deviations. Accept that $d_B=40$ mm, allowable deviation of diameter ± 2 mm. Then the diameter of the workpiece is $d_w = d_B / \eta_0 = 40 / 1,03 = 38,8$ mm, where η_0 - coefficient taking into account the radial growth of the ball during rolling (accept that $\eta_0 = 1,03$).

According to the regulations, the balls rolled from a billet of diameter 40 mm. Then the diameter of the ball is equal to:

$$d_B = d_w / \eta_0 = 40 \cdot 1,03 = 41,2 \text{ mm} \quad (1)$$

Basic sizes of rolls for ball-rolling mill are shown in figure 3.

3. Results and discussion

Diameter of caliber

$$d_K = d_B \cdot \eta_t = 41,2 \cdot 1,013 = 41,7 \text{ mm} \quad (2)$$

where $\eta_t = 1,013$ - coefficient taking into account thermal expansion of the metal.

The minimum width of the flange

$$a = 0,04R_K + 1,3 = 0,04 \cdot 20,85 + 1,3 = 2,1 \text{ mm}, \quad (3)$$

where $R_K = d_K / 2$ - radius of the caliber, mm;
The initial height of the flange

$$h_0 = 1,5 + 0,07(R_K - 10) = 1,5 + 0,07(20,85 - 10) = 2,3 \text{ mm}; \quad (4)$$

The minimum radius of the bridge

$$r = 1 + 0,04(R_K - 10) = 1 + 0,04(20,85 - 10) = 1,4 \text{ mm}; \quad (5)$$

The width of the flange before cutting

$$a_{CUT} = 4 + 0,14(R_K - 10) = 4 + 0,14(20,85 - 10) = 5,5 \text{ mm}. \quad (6)$$

The length of the caliber (number of turns) is conventionally measured in degrees of the spiral line. For the beginning of the caliber (0°) the center of the radius of the caliber is adopted, located on a straight line extending along the end face of the roll on the output side of the finished ball. During rolling balls are guided by the recommendations of table 1 and set the total length of caliber as $\alpha_{FULL} = 900^\circ$, the length of the forming area $\alpha_{FORM} = 270^\circ$ and the length of the finishing area $\alpha_{FIN} = \alpha_{FULL} - \alpha_{FORM} = 900 - 270 = 630^\circ$. The length of a caliber is divided in equal portions; for pre-calculation it is sufficient $\Delta\alpha = 90^\circ$.

The radius of the jumper at the end of the forming at $\alpha = \alpha_{FORM} - \Delta\alpha$ is determined from the ratio

$$r_{CUT} = r + \frac{R_K - h_0 - r}{\alpha_{FORM}} \Delta\alpha = 1,4 + \frac{20,85 - 2,3 - 1,4}{270} 90 = 7,1 \text{ mm} \quad (7)$$

Change the height of a flange during turn the roll on 90° :

$$\Delta h = r_{CUT} - r = 7,1 - 1,4 = 5,7 \text{ mm} \quad (8)$$

For each angle of the rolls rotation from α_{FULL} till α_{FORM} after a period of 90° , the height of the flange will be:

$$h_{\alpha-90} = h_\alpha + \Delta h = h_\alpha + 5,7 \quad (9)$$

where h_α - current height of flange, mm.

Then the radius of the bridge is calculated, its size in the finishing area will be $r = 1.4$ mm, and the radius of the bridge on the forming section is defined by the formula

$$r_{\alpha+90} = r_\alpha + \Delta h = r_\alpha + 5,7 \quad (10)$$

The width of the spherical section of the caliber is defined by the expression

$$C_\alpha = \sqrt{R_K^2 - r_\alpha^2} = \sqrt{20,85^2 - r_\alpha^2} \quad (11)$$

So the cut of bridge begins during forming of the ball, then take the width of the spherical area on the angle of rotation of the roll α_{FIN+90} , the previous finishing area of the caliber, i.e. $C_{CUT} = C_{\alpha_{FIN+90}}$. Basic design data of pre-calibration stage are given in table 2.

Table 2 - Basic design data of pre-calibration stage of calibration rolls for rolling ball with a diameter of 40 mm

$\alpha, ^\circ$	$h_{\alpha-90}, \text{ mm}$	$r_{\alpha+90}, \text{ mm}$	$C_\alpha, \text{ mm}$
900	2,3	18,5	9,6
810	8,0	12,8	16,4
720	13,7	7,1	19,6
630	19,4	1,4	20,8
540	19,4	1,4	-
450	19,4	1,4	-
360	19,4	1,4	-
270	19,4	1,4	-

4. Conclusion

Paper presents a preliminary calculation of the calibration rolls for rolling balls with a diameter of 40 mm in a rolling mill JSC "SSGPO", which will be rolled from round workpieces with a diameter of 40 mm. The main elements of ball caliber are considered, their design dimensions are determined. It is established that the height of the flange varies linearly and the width of the spherical area increases during rolling.

5. References

1. Металлопрокатный комплекс РМЗ АО «ССГПО» в г. Рудный. Рабочий проект. Общая пояснительная записка. Том I. КазГипроМаш. 2010. – 147 с.
2. Найзабеков А.Б., Мухаметкалиев Б.С., Лежнев С.Н., Панин Е.А., Андреев Е.В. Разработка калибровки валков для прокатки круглой стали № 40 из заготовки сечением 150 x 150 мм в условиях стана 320 металлопрокатного завода АО «ССГПО». Труды 11-го Международного Конгресса Прокатчиков. Магнитогорск. 9-11 октября 2017. С. 182-188.
3. Афонькин М., Звягин В. Производство заготовок в машиностроении. Политехника, 2007. – 380 с.
4. Целиков А.И., Барбарич М.В., Васильчиков М.В., Грановский С.П., Жукевич-Стоша Е.А. Специальные прокатные станы. М.: Металлургия, 1971. - 336 с.
5. Peretyatko V.N., Klimov A.S., Filippova M.V. Roller grooving in ball-rolling mills. Part 1. Steel in Translation. 2013. T. 43. № 4. С. 168-170.
6. Перетятыко В.Н., Климов А.С., Филиппова М.В. Калибровка валков шаропркатного стана. Сообщение 2. Известия высших учебных заведений. Черная металлургия. 2013. № 6. С. 16-20.

MICROBIAL CLEANING OF MINE WATERS FOLLOWED BY ELECTRICITY GENERATION

Irena Spasova¹, Marina Nicolova¹, Plamen Georgiev¹, Stoyan Groudev¹, Veneta Groudeva²

¹University of Mining and Geology, Sofia 1700, Bulgaria

²Sofia University "St. Kliment Ohridski", Sofia 1000, Bulgaria

spasova@mgu.bg

Abstract: Acid mine drainage waters polluted by iron, several non-ferrous metals (mainly copper, zinc and cobalt) and sulphates as the main pollutants were efficiently treated by a lab-scale passive system consisting of an alkaline limestone drain and a permeable reactive multibarrier connected in a series. The multibarrier was filled by a mixture of solid biodegradable organic substrates (mainly of plant biomass) and was inhabited by different metabolically connected anaerobic microorganisms (mainly different heterotrophs including some iron-reducing and sulphate-reducing bacteria). The effluents from this system were rich in soluble organic compounds and were treated in a microbial fuel cell in which consortium of electrochemically active microorganisms used these compounds as donors of electrons for electricity generation.

Keywords: MINE WATERS, CHEMOLITOTROPHIC MICROORGANISMS, ELECTRICITY GENERATION

1. Introduction

It is well known that the generation of acid drainage waters (both under natural conditions and as a result of the human activity) is a very serious environmental problem. This is due to mainly to the fact that in most cases, apart from the sulphuric acid, such waters contain different toxic elements, mainly heavy metals, radionuclides and arsenic. The prevention of this process is usually more desirable than the subsequent treatment of such waters. However, the intensive development of mining and/or of mineral processing in many countries worldwide is an essential factor for their industrial development and increasing of their living standard. Unfortunately, the efficient prevention of acid generation in the huge dumps consisting of rich-in-sulphides low-grade waste ores or other mineral wastes is usually a difficult and costly process. For that reason, since a long time in several countries such dumps are subjected to leaching of the relevant useful components by means of acidophilic chemolithotrophic bacteria (Groudev, 2015). At present, apart from the extraction of some valuable components from the pregnant leach solutions, the treatment of the residual waste waters by adding some biodegradable organic substrates and different heterotrophic bacteria using sulphates and/or ferric ions as electron acceptors can be used for generation of electricity by means of especially constructed fuel cells (Du et al., 2007; Rabaey and Verstraete, 2005; Spasova et al., 2014, 2016).

2. Materials and Methods

Acid drainage waters generated during the bioleaching of a polymetallic sulphide ore were subjected to treatment by means of lab-scale permeable reactive multibarriers. The multibarriers were plastic cylindrical columns 120 cm high, with an internal diameters of 30 cm. The columns were filled with a mixture of limestone (crushed to a particle size of minus 10 mm) and a biodegradable organic matter consisting of a mixture of spent mushroom compost, fresh leaf compost, animal manure and saw dust. The columns were inoculated by microorganisms of different types: No 1 - by means of mixed populations of sulphate-reducing bacteria; No 2 - by means of mixed population of iron (III)-reducing bacteria; No 3 - by means of mixed populations of sulphate-reducing and iron-reducing bacteria. The pH of the solutions inside the different columns was maintained at different levels - from 5.5 to 9.5.

The solutions from the multibarriers were enriched in soluble organic compounds and were used separately from each other in the experiments for electricity generation by the microbial fuel cells. Each of these cells was a Plexiglas cylindrical column 80 cm high, with an internal diameter of 12 cm. A perforated slab graphite - Mn⁴⁺ anode and a graphite - Fe³⁺ cathode were located in the bottom and in the top sections of the column, respectively. The two sections were separated by a permeable barrier of 5 cm thickness consisting of a 2.5 cm layer of glass wool and a 2.5 cm layer of glass beads. The feed stream, i.e. the effluents from the multibarriers, was supplied to the bottom anodic sections of the column and the effluents passed through the cathodic section and continuously exited at the top. Air was injected during the treatment to the cathodic section.

The quality of the waters treated by means of the permeable reactive multibarriers and by the microbial fuel cells was monitored at the inlet and the outlet of these components of the system for the water cleaning and electricity generation. The parameters measured in situ included: pH, Eh, dissolved oxygen, chemical composition, and temperature. The isolation, identification, and enumeration of microorganisms were carried out by the classical physiological and biochemical tests (Karavaiko et al., 1988) and by the molecular PCR methods (Sanz and Köchling, 2007; Escobar et al., 2008).

3. Results and Discussion

Data about the composition of the polluted waters before and after the treatment by means of sulphate-reducing bacteria as well as by mixed populations of sulphate-reducing and iron-reducing bacteria are shown in Table 1. The sulphate-reducing bacteria used in this study were related to six different genera (*Desulfovibrio*, *Desulfobacteric* and *Desulfococcus* which were able to oxidize the organic substrates to CO₂ as a final product, as well as the genera *Desulfobulbus*, *Desulfomonas* and *Desulfomicrobium* which were able to oxidize the organic substrates only partially to CO₂ and acetate). The bacteria related to the first group as a whole degraded the organic substrates and reduced the sulphates at higher rates than the sulphate-reducing bacteria related to the second group. However, some mixed populations of bacteria from the two groups were also very active. Some iron (III)-reducing bacteria from the genera *Geobacter* and *Schewanella* were able to degrade the

organic sources of energy used in this study at rates close or even higher than these achieved by means of most of the sulphate-reducing bacteria tested in this study. However, the treatment of the polluted waters by means of iron (III) – reducing bacteria acting independently was not efficient. These bacteria were able to transfer electrons from the dissolved organic substrates in the anoxic section of the microbial fuel cells via their own respiratory chains and extracellular matrix directly to the anode located also in this section of the microbial fuel cell. It is well known that some members of the two genera mentioned above differ considerably from each other with respect to their mechanisms of the extracellular electron transport from the relevant organic substrates to the cytochromes of c-type present in their respiratory chains. Furthermore, it is known that the reduction of the Fe (III) – acceptors and the growth of Fe (III)-reducing bacteria depend not only on the type, composition, and concentration of the organic substrates but also on the structure and surface of the iron (III) acceptors.

Table 1. Treatment of polluted waters by means of different anaerobic microorganisms

Parameters	Initial content of the waters	Data about the water treatment by means of:	
		sulphate-reducing bacteria	a mixed population of sulphate-reducing bacteria and iron-reducing bacteria
pH	1.70 – 3.25	6.75 – 7.10	6.90 – 7.21
Eh, mV	(+345) – (+530)	(-190) – (-260)	(-172) – (-280)
Total dissolved solids, mg/l	3250 – 5560	510 – 1320	521 – 1270
Dissolved O ₂ , mg/l	1.0 – 1.9	0.1 – 0.2	0.1 – 0.3
Dissolved org. C, mg/l	1.9 – 3.7	260 – 480	240 – 460
Sulphate, mg/l	640 – 1490	170 - 305	190 – 325
Cu, mg/l	5.0 – 23	<0.1 – 0.40	<0.1 – 0.35
Zn, mg/l	9.5 – 35	<0.1 – 0.35	<0.1 – 0.44
Co, mg/l	2.5 – 12	<0.1 – 0.30	<0.1 – 0.31
Cd, mg/l	0.1 – 0.3	<0.01	<0.01 – 0.3
Mn, mg/l	3.5 – 14	0.21 – 0.28	0.17 – 0.23
Fe, mg/l	560 - 1270	4.4 – 8.2	2.8 – 5.1

Apart from the experiments for treatment of the polluted waters some of the more active sulphate-reducing and iron (III)-reducing bacteria were used in experiments for generating electricity by means of the constructed microbial fuel cells. It was found that the different representatives of these two groups of anoxic microorganisms differed considerably from each other with respect to their ability to generate electricity from biodegradable organic substrates (Table 2).

The sulphate-reducing bacteria as a whole were considerably more efficient in this aspect from the iron(III)-reducing bacteria. However, the high electricity generation during these investigations was achieved by means of a mixed culture consisted of both sulphate-reducing and iron(III)-reducing bacteria.

Table 2. Electricity generation by means of different anaerobic microorganism in the anodic section of the microbial fuel cell

Microorganisms	COD, mg O ₂ /l.h	Cells/ml	Power, mW/m ²
Sulphate-reducing bacteria	400 – 2100	>5.10 ⁸	1700 - 3500
Sulphate-reducing bacteria + Iron(III) reducing bacteria	600 - 2300	>7.10 ⁸	2600 - 4200
Iron(III) reducing bacteria	500 - 1700	>3.10 ⁸	1200 - 2300

Note: Experimental conditions: 37°C, pH 7.1 – 7.5, O₂ dissolved, 7.7 – 8.0 mg/l, COD/SO₄²⁻ ratio 2.1 – 4.1

Acknowledgements: The authors expressed their gratitude to the National Science Found of Bulgaria for the financial support connected with this study (project TO2/2/2014).

References

- Du, Z., Li, H., Gu, T., 2007. A state of the art review on microbial fuel cells: A promising technology for wastewater treatment and bioenergy, *Biotechnology Advances*, 25, 464 – 482.
- Escobar, B., Bustos, K., Morales, G., Salzar, O., 2008. Rapid and specific detection of *Acidithiobacillus ferrooxidans* and *Leptospirillum ferrooxidans* by PCR, *Hydrometallurgy*, 92, 102 – 106.
- Groudev, S.N., 2015. Biohydrometallurgy in Bulgaria – achievements and perspectives, *Acta Microbiologica*, 1, 81 – 92.
- Karavaiko, G.I., Rossi, G., Agate, A.D., Groudev, S.N., Avakyan, Z.A., 1988. *Biogeotechnology of Metals*. Manual, GKNT Center for International Projects, Moscow.
- Sanz, J.I., Köchling, T., 2007. Molecular biology techniques used in wastewater treatment overview, *Process. Bochem.*, 42, 119 – 133.
- Spasova I., Nicolova, M., Georgiev, P., Groudev, S., 2014. Mine waters cleaning connected with electricity generation, *Annual of the University of Mining and Geology, Sofia*, 57(II), 137 – 139.
- Spasova I., Nicolova, M., Georgiev, P., Groudev, S., 2016. Bioleaching of metals from a waste ore in connection with copper recovery, environment protection and electricity generation, *Annual of the University of Mining and Geology, Sofia*, 59(II), 167 - 171.
- Rabaey, K., Verstraete, W. 2005. Microbial fuel cells: novel biotechnology for energy generation, *Trends in Biotechnology*, 23 (6), 291 – 298.

EXTRACTION OF PRECIOUS METALS FROM A PYRITIC CONCENTRATE PRETREATED BY MICROBIAL OXIDATION

Irena Spasova, Marina Nicolova, Plamen Georgiev, Stoyan Groudev
University of Mining and Geology, Sofia 1700, Bulgaria

spasova@mgu.bg

Abstract: A sulphide flotation concentrate containing 15.2 g/t gold and 893 g/t silver finely disseminated in pyrite (4.1 % sulphidic sulphur in the concentrate) was treated by a two-stage process to recover these precious metals. Initially the concentrate was subjected to microbial oxidation by means of different acidophilic chemolithotrophic microorganisms (bacteria at 37 °C and archaea at 59 and 86 °C) to expose the precious metals encapsulated in the pyrite. The precious metals liberated in this way were then subjected to leaching by means of solutions containing different reagents (protein hydrolysate, thiosulphate, cyanide and some chemical oxidizers). The leaching was carried out in agitated reactors and up to 93.6 % of the gold and 80.8 % of the silver were solubilised in this way for 48 hours from a pulp density of 20 % at 57 °C.

Keywords: PRECIOUS METALS, MICROBIAL OXIDATION, EXTRACTION

1. Introduction

Gold-bearing sulphide concentrates, ores and wastes in which the gold is finely disseminated as submicron size particles in the sulphide matrix are refractory to hydrometallurgical treatment for gold extraction since the leachants cannot penetrate into the interior of the minerals to reach the enclosed gold. However, since a relatively long period of time it is known that several acidophilic chemolithotrophic microorganisms (bacteria and archaea) are able to oxidize efficiently the sulphides containing these precious metals and to make them exposed for leaching by means of suitable reagents. Furthermore, it has been found that in most cases such microorganisms are able to attack preferentially just the defect sites of the sulphide minerals in which the precious metals are located (Livesey-Goldblatt et al., 1983; Groudev, 1989; Rawlings and Johnson, 2007; Karavaiko et al., 1985; Van Aswegen et al., 2007). The gold and silver can be extracted from the pretreated sulphidic concentrates by means of cyanides or by other less toxic reagents. The present paper contains some data about laboratory experiments for microbial pretreatment and subsequent leaching of a sulphide concentrate containing gold and silver present mainly as metals finely dispersed in sulphide minerals.

2. Materials and Methods

The concentrate used in this study was produced by flotation of low-grade sulphide ore taken from a dump located near the deposit Zlata in the north-west part of Bulgaria, in a short distance from the small town Trun. The concentrate contained 4.8 % of sulphur (from which 4.1 % was sulphidic, present in pyrite), 8.2 % of iron, 1.49 % copper, 15.2 g/t gold and 893 g/t silver as the valuable components. Data about the phase composition of the precious metals in the concentrate are shown in Table 1.

Table 1: Phase composition of the precious metals in the flotation concentrate.

Phase composition	Distribution, %	
	Au	Ag
Free exposed metals	11.3	-
Metals capsulated in iron oxides	35.2	37.0
Metals finely dispersed in sulphide minerals	50.3	59.4
Metals finely dispersed in silicates	3.2	3.6
Total content, %	100.0	100.0

The preliminary microbial oxidation of the concentrate to expose the precious metals encapsulated in the sulphides was performed by means of different acidophilic chemolithotrophic microorganisms (bacteria at 37 °C, and archaea at 57 and 86 °C). The microbial pretreatment was carried out in the 9K nutrient medium (Silverman and Lundgren, 1959).

The pretreatment was connected with an efficient extraction of the sulphur, copper and iron from the concentrate. The progress of the microbial oxidation was followed by analysis of the leach solutions for ferrous, ferric and total iron species, copper, sulphates, pH, Eh and number of the chemolithotrophic microorganisms. Solvent extraction plus electrowinning were used to recover copper from the pregnant solution after bioleaching. The solvent extraction was carried out by means of the reagent LIX 984N (10 volume percents in a kerosene diluents).

The precious metals exposed in the solid residue as a result of the acidic pretreatment of the concentrate were subjected to leaching by means of different solutions for the comparative testing of their leach efficiency:

Solution type No 1: microbial protein hydrolysate consisting of mixture of protein hydrolysates produced from the biomass of three different microbial species with different amino acids composition and mixed in different correlations with pH from 9 – 11 (by NaOH);

Solution type No 2: microbial protein hydrolysate from the type mentioned above but containing also a chemical oxidizer of the precious metals (KMnO₄, NaNO₂ or H₂O₂) used in concentrations from 5 to 10 g/l, at pH from 9 – 11 (by NaOH);

Solution type No 3: thiosulphate in concentrations from 5 to 20 g/l, at pH from 9 – 11;

Solution type No 4: combinations of the microbial protein hydrolysate and thiosulphate at different ratios and in concentrations from 10 to 20 g/l, at pH from 9 – 11;

Solution type No 5: solutions of NaCN in concentrations from 5 to 10 g/l, at pH from 9 – 11 (by NaOH).

The microbial pretreatment and the subsequent chemical leaching of the pretreated concentrate were formed in agitated reactors with a working volume of 500 ml each and a pulp density from 10 to 20 g/l. The duration of these two operations was within 72 to 168 hours for each of them.

Elemental analysis of the liquid samples was carried out by means of atomic adsorption spectrometry and induced coupled plasma spectrometry. Elemental analysis of the solid samples before and after the leaching were carried out by the above-mentioned methods. Control analyses of the gold and silver in the solid samples before and after the leaching were carried out by cupellation (fire assay).

The isolation, identification and enumeration of microorganisms were carried out by methods described elsewhere (Karavaiko et al., 1988; Hallberg and Johnson, 2001, Rawlings and Johnson, 2007).

3. Results and Discussion

The extraction of precious metals from the initial concentrate not subjected to preliminary oxidation was not efficient due to their significant dispersion and encapsulation in the sulphide minerals, mainly in the pyrite. The addition of chemical oxidizers (KMnO₄, NaNO₂ or H₂O₂) to the protein hydrolysate acting as a complexing agent for the precious metals increased to some extent the level of their extraction but even in these cases the effectiveness of leaching was relatively low (Table 2).

Table 2: Leaching of gold and silver from the flotation concentrate by means of different leach solutions.

Leach solutions	Initial concentrate		Concentrate subjected to preliminary oxidation	
	Metals extraction, %			
	Au	Ag	Au	Ag
Thiosulphate	48.2	37.0	92.3	77.0
NaCN	49.5	39.2	93.6	78.5
Protein hydrolysate	14.0	8.6	20.3	14.5
Protein hydrolysate+ chemical oxidizer:				
- KMnO ₄	43.1	32.0	90.5	74.3
- NaNO ₂	36.1	28.2	85.1	69.1
- H ₂ O ₂	32.0	24.2	84.2	64.0

Portions of the precious metals solubilised during the leaching, especially of silver, precipitated in the cases in which the pH of the leach solution was lower than 9. The maintenance of the pH at levels higher than 9 decreased considerably the precipitation of the dissolved precious metals. The most efficient chemical leaching of these metals was performed within pH of about 9.5 – 10.5.

The optimum concentrations of the chemical oxidizers during the leaching were within the limits of about 5 – 10 g/l. These concentrations were sufficient to maintain the Eh of the leach solutions of values higher than 400 mV for a period of about 55 – 60 hours. The addition of the oxidizers in portions during the leaching was more efficient and decreased to some extent the consumption of these reagents. Regardless of this, the consumption of the reagents were high (within 0.5 – 0.8 g/g concentrate). These high consumptions were due to the fact that the oxidizers reacted not only with the precious metals but also with the sulphides in the concentrate and with the amino acids contained in the protein hydrolysate.

The leaching of the concentrate by means of thiosulphate was much more efficient than this by means of protein hydrolysate alone and even from these achieved by means of the protein hydrolysate in combinations with the chemical oxidizers (Table 2). However, the combination of the protein hydrolysate with the thiosulphate was the most efficient and practically equal to the extraction achieved by means of cyanide.

The microbial oxidative pretreatment of the sulphidic concentrate by means of acidophilic moderately thermophilic chemolithotrophic bacteria at 55 – 60 °C or by means of the extremely thermophilic archaea at 86 – 90 °C gave similar results during the subsequent leaching of the precious metals by means of the leach solutions mentioned above. The extraction of these metals was clearly connected with the level of oxidation of the sulphidic minerals containing the precious metals (Table 3). It must be noted, however, that the subsequent leaching of the pretreated concentrate by means of thiosulphate at temperatures highest than 50 °C was connected with a considerable increase of the consumption of this reagent. The further decrease of the content of sulphidic sulphur in the concentrate (to about 0.7 – 0.8 %) by means of the microbial pretreatment had partially no additional effect on the extraction of silver.

Table 3: Effect of microbial oxidative pretreatment of the sulphidic concentrate by means of moderately thermophilic chemolithotrophic bacteria on the subsequent extraction of the precious metals

Content of sulphide sulphur in the concentrate	Levels of the sulphidic sulphur oxidation, %	Extraction of the precious metals, %	
		Au	Ag
4.1	0	30.7	14.5
3.2	24.4	55.4	41.0
2.6	36.6	73.8	59.0
2.1	51.2	92.3	78.6
1.5	63.4	93.0	80.2
1.0	75.6	93.2	80.8

References

- Groudev, S.N.: Microbiological removal of arsenic from gold-bearing pyrite-arsenopyrite concentrate. Annual of the Higher Institute of Mining and Geology, Sofia, 3(III), pp. 245 – 253, 1989.
- Hallberg, K.B. and Johnson, D.B.: Biodiversity of scidophilic prokaryotes, Adv. Appl Microbiol., 49, pp. 37 – 84, 2001.
- Karavaiko, G.I., Rossi, G., Agate, A.D., Groudev, S.N. and Avakyan, Z.A. (Eds.), 1988. Biogeotechnology of Metals. Manual, Center for International Projects GKNT, Moskow.
- Livesey – Goldblatt, E., Norman, P. and Livesey, D.R.: Gold recovery from arsenopyrite/pyrite ore by bacterial leaching and cyanidation. In G. Rossi and A.E. Torma (eds.), Recent Progress in Biohydrometallurgy, Associazione Mineraria Sarda, pp. 627 – 641, Iglesias, 1983.
- Rawlings, D.E. and Johnson, D.B.: The microbiology of biomining: development and optimization of mineral-oxidizing microbial consortia. Microbiology, 153, pp. 315 – 324, 2007.
- Silverman and Lundgren, D.G., Studies on the chemoautotrophic iron bacterium *Ferrobacillus ferrooxidans*, Journal of Bacteriology, 77, pp. 642 – 647, 1959.
- Vas Aswegen, P.C., Niekerk, J., Van and Oliver, W.: The BIOX® process for the treatment of refractory gold concentrates. In D.E.Rawlings and D.B. Johnson (eds.), Biomining, pp.1 – 5, Springer-Verlag, Heidelberg, 2007.

ВЛИЯНИЕ НА МРЕЖОВОТО ОФОРМЛЕНИЕ И БЯЛОТО ПРОСТРАНСТВО ВЪРХУ КОМПОЗИЦИЯТА НА УЕБ ТИПОГРАФИЯТА

INFLUENCE OF GRID LAYOUT AND WHITE SPACE ON THE COMPOSITION OF WEB TYPOGRAPHY

гл. ас. д-р Илиев, И.

Технически университет – Варна, България

i.iliev@tu-varna.bg

Abstract: The purpose of this report is to study the impact of grid layout and white space on the composition and readability of web typography. For this purpose, the main types of grid systems used in web design have been analysed: column, modular and hierarchical. Reviewed is also the impact of white space on the layout of online texts. Attention is paid to the macro- and micro white space in web design. Based on the research, a conclusion has been drawn on the impact of grid layout and white space on the composition of texts on the Internet.

Keywords: WEB TYPOGRAPHY, GRID SYSTEMS, WHITE SPACE, FONT, WEB DESIGN, COMPOSITION, TEXT DESIGN, READABILITY

1. Увод

Цел на настоящият доклад е да се изследва въздействието на мрежовото оформление и бялото пространство върху композицията и четливостта на уеб типографията. За тази цел са анализирани основните видове мрежови системи използвани в уеб дизайн – колонна, модулна и йерархична. Разгледано е и влиянието на бялото пространство върху оформлението на онлайн текста. Обърнато е внимание на макро и микро бялото пространство в уеб дизайн. На базата на проучването е направен извод за влиянието на мрежовото оформление и бялото пространство върху композицията на текста в интернет.

2. Изложение

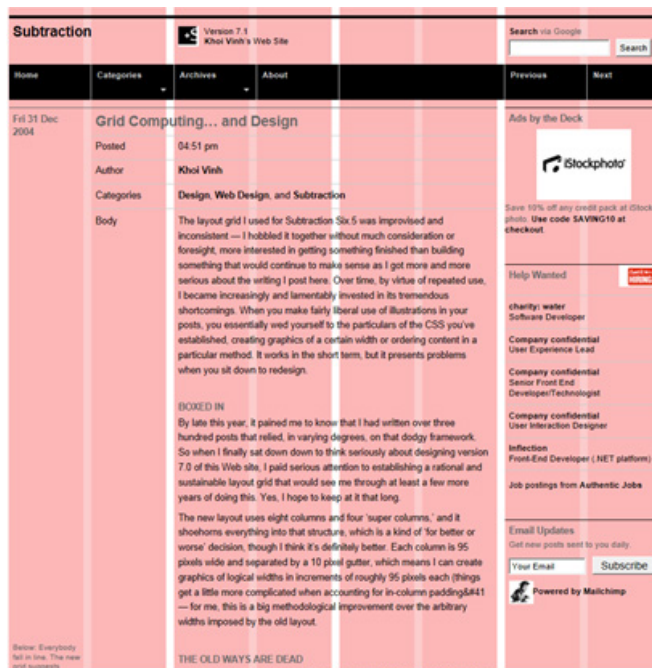
Мрежовото оформление и бялото пространство са едни от важните фактори за четливостта на типографската композиция в уеб страниците. След Втората световна война редица графични дизайнери, като Макс Бил, Емил Рудер и Йозеф Мюлер-Брокман, повлияни от модернистичните идеи на *Новата типография* на Ян Чихолд, започват да поставят под въпрос значимостта на традиционното оформление на печатната страница през този период. Те разработват гъвкава система, която помага на дизайнерите да постигнат съгласуваност в организирането на страницата между отделните елементи – текст и изображения. Резултатът от тяхната работа е модерната типографска мрежа, която се свързва с *Международния типографски стил* (International Typographic Style). Основополагащ труд по този въпрос е книгата *Grid Systems in Graphic Design* (1968) на Йозеф Мюлер-Брокман. Според Брокман основното предимство на мрежовите системи е, че употребата им води до намаляване на броя на използваните визуални елементи и тяхното включване в мрежова система за оформление създава усещане за компактно планиране, разбираемост, яснота и допринася за подреденост на дизайна. Тази системност придава достоверност на информацията и предизвиква доверие [1].

Мрежите в графичния дизайн са инструмент за организация на елементите на дизайна в единна структура. Мрежите са скелетът, върху който е построена цялата композиция на печатните и уеб страниците [2]. Основните характеристики на мрежовото оформление в дизайна са следните:

- Използване на прецизно изчертана мрежа.
- Асиметрично разполагане на оформлението.
- Чисто и организирано подреждане на различните елементи на оформлението.
- Просто и ясно представяне без нищо излишно.
- Разделяне на пространството с хоризонтални и вертикални линии.
- Използване на безсерифни шрифтове.
- Текста по-често е ляво подравнен.

- По-силно присъствие на бялото пространство [3].

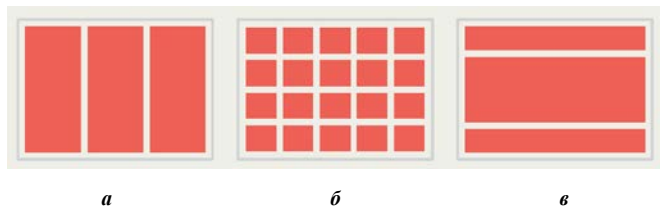
Въпреки, че мрежите се използват основно за дизайн в печатните медии от страна на уеб дизайнерите през последните години се наблюдава засилен интерес към употребата на мрежови структури при оформлението на уеб сайтове. Едни от първите дизайнери, които разглеждат въвеждането на мрежите в уеб дизайнът са Марк Болтън [4] и Хой Вин. При редизайна на своя блог през 2004 г. Вин използва осем колонна мрежа (фиг. 1). В книгата си *Ordering Disorder: Grid Principles for Web Design* [5] Вин разглежда детайлно предимствата при дизайна на сайтове с мрежи и високата организация на съдържанието при този вид проектиране.



Фиг. 1 При дизайна на блога си *Subtraction* през 2004 г. Хой Вин използва осем колонна мрежа – всяка колона е широка 95 px и е разделена с полета от 10 px.

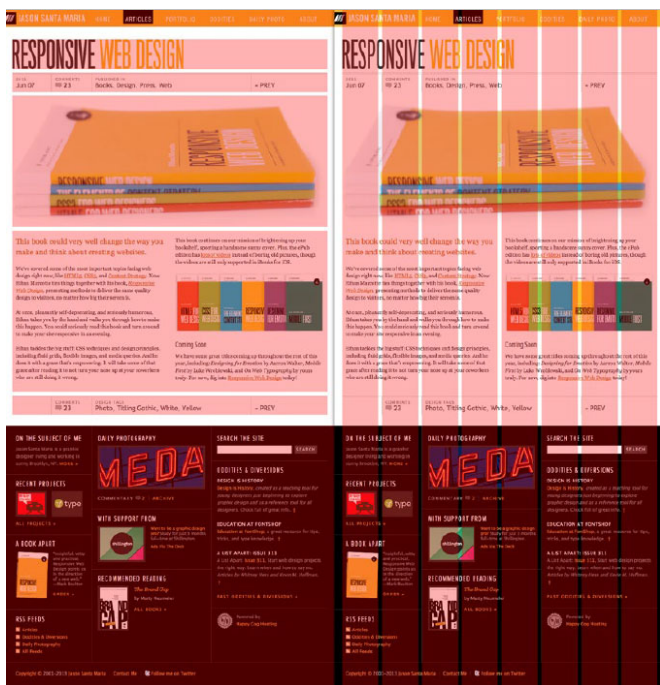
Има няколко основни видове мрежови системи [6] за оформление на уеб страниците, въпреки че най-често се използва колонната мрежа. Повечето мрежови системи в уеб дизайн се състоят от еднакво широки вертикални колони, разпределени равномерно с бели полета. Традиционно онлайн мрежите са съставени от 8, 12 или 16 колони, но в някои сайтове има вариации на броя им. Повечето брой колони дават по-разнообразни възможности за композиция на уеб страниците.

Друг вид мрежи за дизайн са модулните. Модулните мрежи са подобни на колонните мрежи, но имат и хоризонтални линии по които се подравняват отделните елементи на дизайна. Последният вид мрежи са йерархичните мрежи – при тях подравняването става по вертикала. На фиг. 2 са показани отделните видове мрежи за оформление в веб дизайна.



Фиг. 2 Основни видове мрежови системи за дизайн на веб сайтове (а) колонна мрежа, (б) модулна мрежа, (в) йерархична мрежа [6]

Понякога при дизайна на веб сайтове се използва и комбинация от различните мрежи за оформление [6]. Американският дизайнер Джейсън Саната Мария използва за оформление на сайта си йерархична и колонна мрежа за постигане на цялостна композиция (фиг. 3).



Фиг. 3 Джейсън Саната Мария използва за дизайн на сайта си (а) йерархична и (б) колонна мрежа [6]

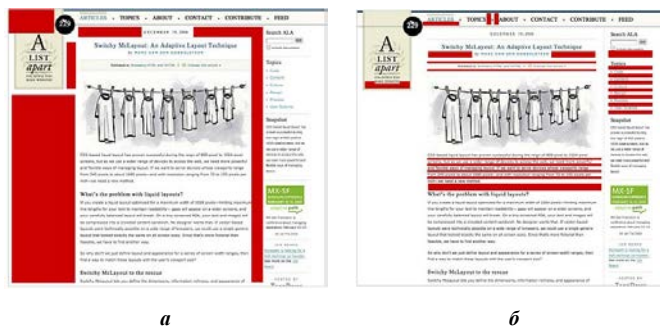
Все повече в съвременния веб дизайн се използват различни CSS фреймворкове за оформление на веб сайтове. Фреймвръкът е част от общ код, който може да се използва многократно, което прави процеса на разработване на веб сайтове по-бърз и по-лесен. Повечето CSS фреймворкове използват решетки за създаване на оформлението на дизайна на веб сайтове. Част от най-популярните CSS фреймворкове са YUI, Blueprint, 960 Grid System, 1KB CSS Grid и др. [7].

Библиотеката на Yahoo User Interface (YUI) се счита за най-стария CSS фреймврък. Основните предимства на YUI е, че има отлично нулиране и типография, а недостатък е странната мрежа, която е трудна за ползване.

За разлика от YUI Blueprint има много добра мрежа, но негативна част на този фреймврък е, че предлага прекалено много дизайнерски решения. 960 Grid System използва много добро оформление на решетките, но има малко дизайнерски предположения. Най-лек фреймврък от разглежданите тук е 1KB CSS Grid – версията е само 640 В, но за сметка на това има много малко функции.

Най-големия проблем при различните фреймворкове е, че използват много излишен код – това води до увеличаване на честотната лента на потребителите и лоша семантика на HTML кода. Затова е добре да се използва само кода от фреймврък, който е нужен за дизайна на сайта.

Бялото пространство в веб типографията е друг важен фактор за четливостта на веб сайтовете. Празното пространство дава възможност на основния текст да „диша“ и помага на читателите да възприемат лесно информацията на веб страницата. Бялото пространство още се нарича „негативно пространство“ и включва пространството между елементите в композицията или части от дизайна, които остават незапълнени, пространството между изображенията и белите полета около текста. Условно бялото пространство може да се раздели на две големи групи – макро бяло пространство, което включва разстоянието между основните елементи на композицията и текстовите колони и микро бяло пространство, в което влиза междуредовото разстояние в текста, разстоянието между думите и буквите (фиг. 4).



Фиг. 4 Макро (а) и микро (б) бяло пространство [8]

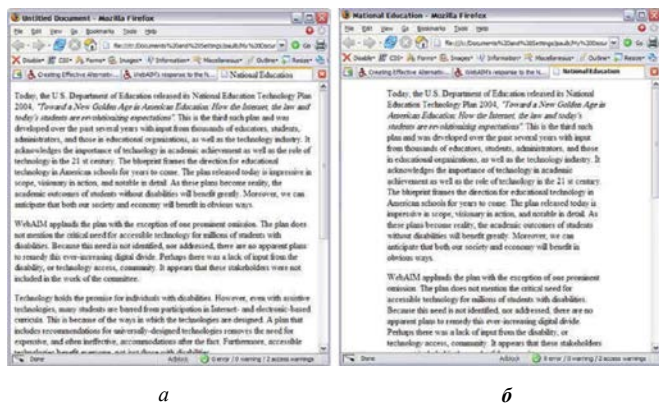
Бялото пространство води погледа на читателя от един елемент към друг, организира композицията на страницата и подпомага информационната структура на веб страницата (фиг.5). С добавянето само на няколко допълнителни пиксели негативно пространство към оформлението на веб страницата може да се подобри цялостната четливост на съдържанието на онлайн текста [8].



Фиг. 5 Madebysofa.com използва бяло пространство, за да създаде чист, минималистичен дизайн. По този начин акцентът се поставя върху категориите и връзките в веб сайта.

Като цяло, документи с повече негативно пространство около текста се четат по-лесно от документи, в които границите на текста са близо до границите на зоната за гледане на компютърния монитор (фиг. 6). Веб страниците с ограничено бяло пространство изглеждат по-претрупани и могат да затруднят четенето на текста. Допълнително пространство около текста осигурява по-чисто оформление и помага на читателите да се съсредоточат по-добре върху текста. Правилното разпределение и големина на белите пространства създават чувство на организираност и спомагат

на потребителите лесно да разделят уеб страницата на различни по значимост и въздействие части.



Фиг. 6 Оформление на текст без бяло пространство (а) и добавяне на 15% бяло пространство (б). Текста с бели полета е по-четлив

В редица изследвания се доказва, че бялото пространство подобрява четливостта на текста и общия дизайн на уеб страницата. Бялото пространство може да направи основния текст по-четлив. В проведено изследване [9] през 2004 г. изследователите стигнали до извода, че използването на добре намереното празно пространство между параграфите и бялото поле заобикалящо текста може да увеличи разбирането на текста с около 20%. Читателите в изследването са заявили, че по-лесно се концентрират върху съдържанието на текста.

Изследователи от Държавния университет на Уичита (САЩ) също изследват въздействието на бялото пространство върху четливостта на текста [10]. Те предлагат на участниците в изследването електронни текстове форматирани по четири различни начина: текст с бели полета с оптимално междуредие, текст с бели полета с малко междуредие, текст без бели полета с оптимално междуредие и текст без бели полета с малко междуредие. Изследователите установили, че хората четат текст без бели полета по-бързо, отколкото текст с бели полета, но разбирането на текста е по-високо, когато хората четат текст с по-големи бели полета. Освен това междуредието не е имало значителен ефект върху времето за четене или разбиране, но участниците предпочитат повече текстове с по-голямо разстояние между редовете, защото това води до намаляване на умората на очите и по-висока удовлетвореност. Като цяло участниците в изследването предпочитат повече текст с бели полета.

В друго изследване на Майкъл Бърнард [11] и неговия скип учените анализират въздействието на три вида текстови оформления с различен обем бяло пространство – ниско, средно и голямо бяло пространство. Участниците в експеримента дали своите предпочитания към средното количество на бялото пространство. От получените резултати, изследователите стигнали до извода, че средните нива на бяло пространство довеждат до по-високи нива на удовлетвореност и разбиране, отколкото липсата или използването на прекалено голямо бяло пространство.

3. Заключение

Оформлението с мрежи и бялото пространство са ключови фактори за цялостна композиция на уеб типографията. В заключение може да се стигне до извода, че използването на мрежи за оформлението на уеб сайтовете води до организация на елементите на дизайна в единна структура. Постига се еднороден системен дизайн на отделните страници, от които се състои уеб сайта. Като резултат от анализа на различни изследвания за влиянието на бялото пространство върху уеб типографията може да се обобщи, че уместната му употреба повишава четливостта на уеб страниците.

4. Литература

1. Müller-Brockmann, Josef. *Grid Systems in Graphic Design/Raster Systeme Fur Die Visuelle Gestaltung*. Basel, Niggli, 1996, p. 13.
2. Радоева, Антоанета. *Графичен дизайн. Основни понятия на визуалния език*. Варна, Славена, 2012, с. 116-121.
3. Райън, Уилям, Коновър, Тиадър. *Графичната комуникация днес, част първа*. София, Дуо Дизайн, 2008, с. 72.
4. Boulton, Mark. *A Practical Guide to Designing for the Web*. Mark Boulton Design Ltd, 2009, pp. 207-214.
5. Vinh, Khoi. *Ordering disorder: grid principles for web design*. Berkeley, Calif, New Riders, 2011.
6. Santa Maria, Jason. *On Web Typography*. New York, A Book Apart, 2014, pp. 113-118.
7. Смит, Нейтън. *Изграждайте по-добри сайтове със CSS фреймуркове*. // .net, №203, 2010, с. 27–32.
8. Boulton, Mark. *Whitespace*. // A List Apart. <<https://alistapart.com/article/whitespace/>> (14.01.2018)
9. Lin, Dyi-Yih Michael. *Evaluating older adults' retention in hypertext perusal: impacts of presentation media as a function of text topology*. // Computers in Human Behavior, Volume 20, Issue 4, July 2004, pp. 491-503.
10. Chaparro, Barbara, Baker, J. Ryan, Shaikh, A. Dawn, Hull, Spring & Brady, Laurie. *Reading Online Text: A Comparison of Four White Space Layouts*. <<http://usabilitynews.org/reading-online-text-a-comparison-of-four-white-space-layouts/>>. (19.01.2018)
11. Bernard, Michael, Chaparro, Barbara & Thomasson R. *Finding Information on the Web: Does the Amount of Whitespace Really Matter?* <<http://usabilitynews.org/finding-information-on-the-web-does-the-amount-of-whitespace-really-matter/>> (22.01.2018)

ADVANCED HYDROGEN STORAGE TECHNOLOGIES

Gjorgji Dosev, Nikola Sokolov, Assoc. Prof. Aleksandar Kostikj, PhD
Faculty of Mechanical Engineering, Ss. Cyril and Methodius University in Skopje, Republic of Macedonia
aleksandar.kostikj@mf.edu.mk

Abstract: The development of ecological and efficient vehicles powered by hydrogen or electricity is one of the priorities of the automotive industry at the moment. These new propulsion systems should come as a replacement for the internal combustion engines, which use gasoline or diesel fuel and therefore produce toxic emissions. One of the problems, that hydrogen powered vehicles face, is hydrogen storage and that is the main topic of our paper. Conventional technologies for hydrogen storage, like high pressure and cryogenic reservoirs, have many drawbacks in terms of compactness, mass (weight), efficiency and safety. In order to get over these problems, there have been many researches throughout the years in effort to develop new, commercially available technologies. The most advanced storage technologies today, are tanks filled with metal hydrides which absorb hydrogen by forming chemical bonds with it, and tanks filled with large contact surface materials that are able to adsorb hydrogen. In this paper we will present the requirements that these solutions have to fulfill, their current level of development and the expectations for future improvement and usage.

Keywords: HYDROGEN STORAGE, TANKS, METAL HYDRIDES, COMPLEX HYDRIDES, CARBON NANOTUBES

1. Introduction

The development of ecological and efficient vehicles powered by hydrogen or electricity is one of the priorities of the automotive industry at the moment. The idea of using hydrogen as a fuel originates from the 20-th century. It was based on the fact that there are no toxic components in the exhaust gases as a result of hydrogen combustion and it doesn't rely on the usage of fossil fuels. If we take into account that hydrogen must be produced, because there is no free hydrogen in nature, we can conclude that hydrogen is not a power source, but a medium for power transfer.

The development of a safe, reliable, compact and energy efficient technology for hydrogen storage is one of the main obstacles for using hydrogen as a propulsion medium in vehicles. In order to be competitive with the other vehicles available on the market, hydrogen storage reservoirs must provide a range of at least 500 km, as small as possible mass and dimensions, high energy efficiency and the most important of all, safety for the passengers.

2. Conventional storage technologies

Nowadays, there are two prevalent and commercially available technologies for hydrogen storage: high pressure reservoirs and cryogenic reservoirs.

2.1. High pressure reservoirs

In high pressure reservoirs (Fig. 1), hydrogen is stored under extremely high pressure of approximately 700 bar. These tanks are widely available on the market today, but have a drawback in terms of their large mass and dimensions. They are also very inefficient, because a lot of energy is wasted on hydrogen compression.

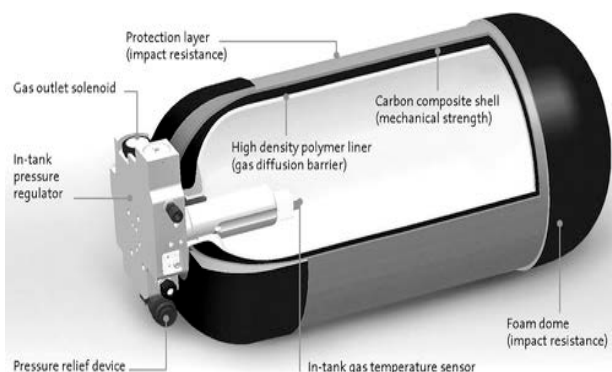


Fig. 1 Section view of a high pressure reservoir

Because of the high pressure they are classified as unsafe. With the increased usage of composite materials, the modern reservoirs have smaller mass and dimensions, but the other problems mentioned remain unsolved.

2.2. Cryogenic reservoirs

Cryogenic reservoirs (Fig. 2) are filled with liquid state hydrogen and are able to store a greater quantity of hydrogen in a smaller volume. However, it requires a lot of energy to bring the hydrogen in a liquified state. Liquid hydrogen has a much greater specific energy than the hydrogen in high pressure reservoirs. The hydrogen must maintain a very low temperature, which means that these reservoirs must have great thermal isolation.

In the last couple of years, hybrid hydrogen reservoirs were made. They allow hydrogen storage under high pressure and at very low temperatures. These reservoirs are more compact, but they also inherit some of the disadvantages of both previously described reservoirs.

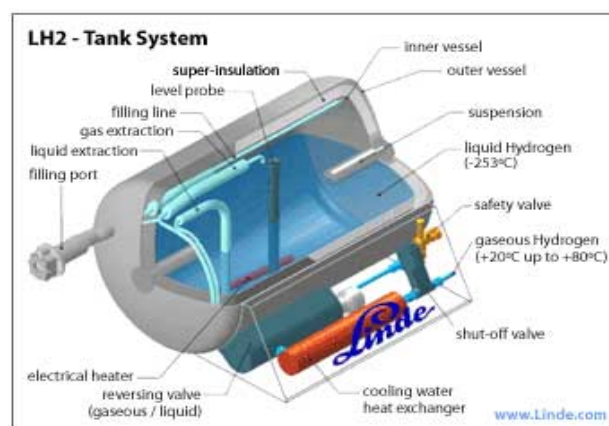


Fig. 2 Section view of a cryogenic reservoir

3. Advanced storage technologies

Because of the major disadvantages of the conventional storage technologies, in the last two decades, there were exhaustive researches, whose goal was development of new, energy efficient and commercially available technologies for hydrogen storage. The most advanced storage technologies today include: storage through absorption in materials (forming chemical bonds between the hydrogen and the material inside the reservoir) and storage through adsorption on the surface of materials (Fig. 3).

3.1. Absorption in materials

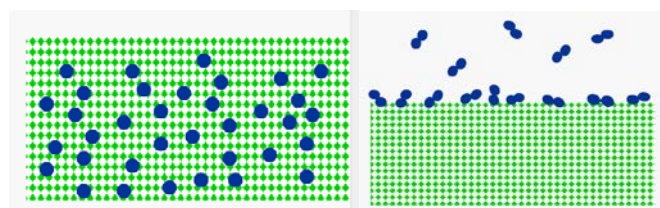


Fig. 3 Mechanism of absorption and adsorption

3.1.1. Metal hydrides

Metal hydrides are compounds formed when a metal element is connected with an atom or molecule of hydrogen. Usually the bond between the elements is covalent, but some hydrides are formed with ionic bonds. Metal hydrides appear in solid state at atmospheric pressure and room temperature. The different types of hydrides, those of biggest interest for hydrogen storage and their structure are mentioned in Table 1.

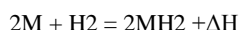
Table 1: Types of metal hydrides and their structure

No.	Typ	Base	Hydrid	Structure
1	AB	TiFe	TiFeH ₂	Cubic
2	AB ₃	CeNi ₃	CeNi ₃ H ₄	Hexagonal
3	AB ₅	LaNi ₅	LaNi ₅ H ₆	Hexagonal
4	AB ₅	TiMn ₂	TiMn ₂ H ₅	Hexagonal or cubic
5	A ₂ B	MgNi	Mg ₂ NiH ₄	Cubic
6	A ₂ B ₇	Y ₂ Ni ₇	Y ₂ Ni ₇ H ₃	Hexagonal

Metal hydrides consist of two different metals. The first one is usually some rare element or alkaline metal, which has the property to bond with the hydrogen and form a stable compound. The other is a so called transitional metal which has the property to form unstable compounds with hydrogen and acts as a catalyst during the phases of hydrogen storage and release.

Metal hydrides which are able to absorb and release hydrogen under conditions such as room temperature and atmospheric pressure, and are able to achieve high values for volumetric and gravimetric density of absorbed hydrogen, can be used as materials in hydrogen storage reservoirs. However, hydrides which are able to absorb hydrogen under atmospheric conditions, are usually composed of transitional metals and have a low gravimetric density. Such an example is LiNi₅H₆, which has a gravimetric density of only 1,15 %wt. An opposite example is TiCr₂H₆, which has a gravimetric density of 2.43 %wt, but needs high temperature to release the stored hydrogen. Recent studies deal with simpler hydrides which are formed from light metals and are easier to produce, such as MgH₂.

The formation of metal hydrides is an exothermic reaction, which means that during the storage phase a certain amount of heat is released. The same amount of heat must be brought back in the system in order for hydrogen to be released. However, if we find a way to absorb the energy released during the formation phase, the same energy can be used later in the release phase. Another way is to use the waste heat from the fuel cell or the ICE.



Where the designations mean the following: M-metal or alloy; MH₂ – metal hydride; ΔH - released heat during the absorption phase. The reaction is reversible and can be used for both hydrogen absorption and release, depending on pressure and temperature.

3.1.2. Complex hydrides

Complex hydrides are inorganic materials that are best described as salts, which are built from complex anions containing hydrogen as terminal ligand, such as the BH₄⁻ (tetrahydroborate or borohydride) or AlH₄⁻ (alanate) anions and counteractions from many different groups in the periodic table. Most of the attention drawn by complex hydrides in the recent past is owed to their large gravimetric hydrogen capacity, i.e. nominal hydrogen-content per weight unit, which makes them competitive candidates for solid state on-board hydrogen storage. This was first suggested in 2001 for LiBH₄. In such materials the hydrogen molecule can be eliminated either by hydrolysis or electrolysis at elevated temperatures.

Although their production was more difficult because of the complicated structure, researchers thought that complex hydrides would be the next phase in the development of hydrogen storage

technologies. However, a problem arose with the slow dynamics of the process of hydrogen release. The process was consisted of a couple of phases for which different conditions were needed. There was a big difference between the theoretical capacity of the reservoirs and the practically achieved capacity. Another problem was the low reliability and the short life span of these reservoirs.

3.2. Adsorption on the surface

Adsorption of hydrogen is based on Van der-Waals interactions between gases and solids (Fig. 4). These interactions are attractive, intermolecular forces which allow hydrogen to bond with solids. Van der-Waals forces originate from charge distribution in atoms and molecules when they get close to each other. Atoms and molecules are attracted by electrostatic forces.

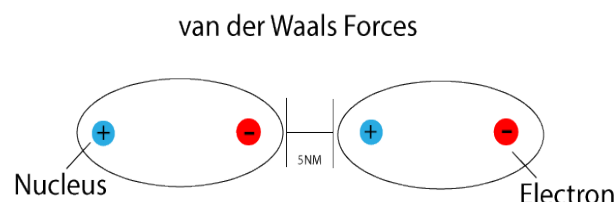


Fig. 4 Van der Waals forces scheme

The balance between attractive and repulsive forces between two molecules causes an energetic minimum of 1-10 kJ/mol and the average energy of adsorbed hydrogen on a carbon surface is 4-5 kJ/mol. This low energy level means a weak bond. That is why hydrogen is released as temperature increases and in high temperature conditions the level of adsorbed hydrogen is very low.

Usually only a single layer of hydrogen is adsorbed on one surface. The maximum amount of adsorbed hydrogen on the surface of a material can be represented as the maximum amount of hydrogen that can be placed in a single layer. In ideal conditions, the minimal surface area needed to adsorb one mol of hydrogen is 85.917 (m²/mol). A single layer of graphite has surface area of 1315 (m²/g) so the maximum amount of hydrogen it can adsorb is 3% wt. Larger quantity of hydrogen can only be adsorbed in low temperature conditions.

3.2.1. Carbon nanotubes as hydrogen storage materials

Porous carbon is considered to be good adsorbent, due to its large contact surface. Adsorption capabilities of normal porous carbon are proportional to its contact surface and pore volume, but it can achieve good gravimetric density (4-6 %wt) only at extremely low temperatures.

Unlike porous carbon, carbon nanotubes have a smaller contact surface and pore volume, but they show remarkably good hydrogen adsorption. At high pressure (10MPa) hydrogen atoms form a dense, compact structure. Using mathematical models, it is shown that at high pressure, a single layer of graphite can adsorb up to 4.1% wt of hydrogen. Single-walled nanotubes (SWNT) can adsorb up to 4% wt of hydrogen (Fig. 5).

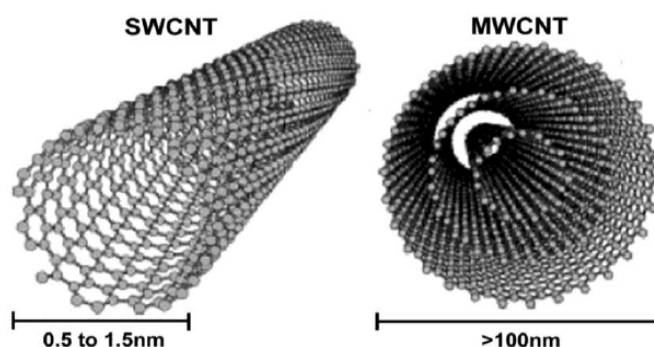


Fig. 5 Single and multi walled carbon nanotubes

Multi-walled nanotubes (MWNT) are nested, concentric, cylindrical layers of graphite with hollow centre and they show great capability for hydrogen adsorption. Catalysts are used to increase the amount of adsorbed hydrogen. Researches show that MWNT activated with KOH (potassium hydroxide) can adsorb up to 4,7% wt hydrogen, whereas ordinary MWNT can adsorb only 0,7% wt.

4. Energy efficiency comparison

In order to obtain a reasonable estimation of the energy required for hydrogen storage with the three different technologies, we must calculate the energy required for compression, cooling and heating. We must also take into account the efficiency of the generator and compressor, and the efficiency of the cooling cycle.

To calculate the energy required to store hydrogen in a high-pressure reservoir one may use the adiabatic compression equation. Compressing hydrogen to 680 bar requires 29 MJ/kg. If we add the efficiency of the compressor and generator, assuming that their combined efficiency is 60%, we obtain that compressing hydrogen to 680 bar requires 47 MJ/kg. These correspond to 30 and 40% of the low heat value (LHV) of hydrogen. Storing hydrogen as a compressed gas is quite energy intensive.

To store hydrogen as a liquid, the energy required to cool hydrogen to the liquid state is critical. Theoretical heat to cool hydrogen from 25 °C to 20 K and condense it to liquid is about 3.4 MJ/kg (2.94 sensible and 0.45 condensation). But the actual required energy is much higher due to the inefficiency of refrigeration at extremely low temperature. The minimum required energy may be calculated using an ideal refrigeration cycle, the reversed Carnot cycle. The efficiency of this cycle depends on the temperatures at which heat is added and rejected, and is equal to $T_1/(T_2-T_1)$, where T_1 =evaporator temperature=20 K, T_2 =condensing temperature=298 K. Therefore the efficiency in our case is $20/(298-20)=7.2\%$. To generate 3.4 MJ to liquefy 1 kg of hydrogen will require 47 MJ ($3.4/0.072=47$). This is 39.2% of the LHV. The actual required energy can be significantly more because the refrigeration cycle will be less than ideal. Heat will also be required to evaporate the liquid and warm up the gas before feeding it to the energy conversion device such as a fuel cell. This may require an additional of 3.4 MJ/kg. This makes the total required energy to store hydrogen as a liquid to be 50.4 MJ/kg. This is 42% of the low heat value of hydrogen. Liquid hydrogen storage is as energy intensive as the compressed hydrogen storage.

Using metal hydride as hydrogen storage requires an absorption step and a desorption step. A typical absorption step requires a supply of 20 bar hydrogen and the removal of about 14.6 MJ/kg heat of absorption. The energy needed to compress hydrogen to 20 bar is about 12 MJ/kg (10% of LHV). The heat of absorption is removed by coolant at temperatures of about 10 °C. The energy required for cooling will be obtained from the adiabatic compression equation and is $14.6/5=3$ MJ/kg. That is $3/120=2.5\%$ of the LHV. Similar amount of heat would be needed to desorb the hydrogen, but this can be provided by the waste heat of the energy conversion device (fuel cell or internal combustion engine) and is practically free. The total energy required to operate a metal hydride storage system is therefore about 15 MJ/kg, or about 12.5% of LHV. This is the lowest operating energy compared to those of compressed hydrogen and liquid hydrogen. Therefore, metal hydride for hydrogen storage has the advantage of low operating energy, moderate pressure and temperature, and high volumetric density.

The analysis performed shows that storing hydrogen in metal-hydride reservoirs improves the energy efficiency 1.45 times in relation to high-pressure reservoirs and 1.5 times in relation to cryogenic reservoirs.

5. Current situation

The properties of modern metal hydrides such as efficiency, volumetric and gravimetric density and the pressure and

temperature at which hydrogen is stored, can be obtained from table 6.1. The newest materials, which are currently tested, are MgH₂, LiNi₅H₆ and LiAlH₄. Metal hydride tanks are commercially available but they are not used in vehicles. The most advanced tanks that are used in commercial vehicles are composite tanks made of carbon fibre, where hydrogen is stored under high pressure.

Researchers in Germany in 2015 have created a 3D model which shows the optimal structure that nanotubes should form. This is a mathematical model and theoretically, a tank with this structure should adsorb 5.5%wt hydrogen at room temperature. Nanotubes are placed parallel to each other and they don't intersect, but they have a large contact surface. This structure allows great storage capabilities. An ideal structure like this is nearly impossible to achieve with the current technology and that is the reason why no carbon nanotube tanks have been made yet.

Table 6.1. Properties of different metal-hydrides

Typ	Base	Temp. (K)	Pressure (bar)	Wt (%)	Density (g/cm ³)	Price (\$/kg)
AB	TiFe	265	4.1	1.86	6.5	4.68
AB2	TiCr2	182	18.2	2.43	6	8.64
AB2	TiMn2	252	8.4	1.86	6.4	5
AB5	MmNi5	217	23	1.46	8.6	7.94
AB5	LaNi5	285	1.8	1.49	8.3	9.87

Table 6.2. Properties of different carbon nanotubes

Material	Wt (%)	Temperature (K)	Pressure (bar)
SWNT (low purity)	3.5-4.5	298	0.4
SWNT (high purity)	5-10	273	0.4
Li-MWNT	20	473	0.1
K-MWNT	14	300	0.1
GNFs	5	300	10.1
Nano-graphite	7.4	300	1

6. Conclusion

The research carried out in this paper presents a series of findings that are connected with the possibilities for more intensive application of hydrogen powered vehicles. Hydrogen storage is one of the basic problems for its commercialisation as a fuel for vehicles. Conventional storage technologies have limited application due to their safety and performance deficiencies. Metal hydrides and carbon nanotubes are imposed as alternative technologies with the ability to overcome these problems.

During the last two decades, a number of research and experiments have been carried out, which have enabled the improvement of the properties of metal hydrides. With further improvement in terms of reliability and cost of production, it is possible to use them commercially in the near future. Carbon nanotubes show even greater potential for hydrogen storage. The research that is ongoing in this direction is still theoretical due to the technological limitations associated with the possibilities of achieving precise nanostructure.

7. References

- [1] Александар Костиќ, „Уреди и опрема кај моторните возила“, Интерна скрипта, Машински факултет, Скопје, Јануари 2017
- [2] Azadeh Maroufmashat, Michael Fowler, „Transition of Future Energy System Infrastructure“ Department of Chemical Engineering, University of Waterloo, 26 July 2017
- [3] Gang Chen, „Hydrogen Storage - ENIC Tutorial“, Department of Energy, MIT, September 2014
- [4] Y.L. Chen, „Mechanics of hydrogen storage in carbon nanotubes“, Journal of the Mechanics and Physics of Solids, 17 July 2008
- [5] Yunjin Yao, „Hydrogen Storage Using Carbon Nanotubes“, HUT, China, March 2010

THE INVESTIGATION OF THE NANORELIEFS OF OPTICAL ELEMENTS OF MEASURING INSTRUMENTS, WHICH MODIFIED BY ELECTRON-BEAM MICROPROCESSING

ДОСЛІДЖЕННЯ МОДИФІКОВАНИХ ЕЛЕКТРОННО-ПРОМЕНЕВОЮ МІКРООБРОБКОЮ НАНОРЕЛЬСФІВ ОПТИЧНИХ ЕЛЕМЕНТІВ ВИМІРЮВАЛЬНИХ ПРИЛАДІВ

Skoryna E.¹, Medyanyk V.¹, PhD. Bondarenko M.¹, PhD Bondarenko I.¹, PhD Bilokin S.², Prof. dr. eng. Antoniuk V.³
Faculty of Electronically Technologies¹, Department of Physics² – Cherkassy State Technological University, Ukraine
Faculty of instrument-making³ – National Technical University of Ukraine “KPI”, Ukraine

Abstract: *The results of microprocessing by the ribbon-shaped electron beam of the elements of optical measuring instruments (the material of such elements - K8 glass) with the initial nanorelief of surfaces 15-22 nm after industrial grinding and polishing are presented. Based on the results of studies using a computerized complex control system based on an atomic force microscope, it was established that after electron-beam microprocessing, the nanorelief of optical elements of measuring instruments decreased to 1.5-2.2 nm, satisfying to the requirements put forward to their surfaces.*

KEYWORDS: *ELECTRON-BEAM MICROPROCESSING, OPTICAL GLASS, COMPLEX CONTROL, COMPUTERIZED SYSTEM, ATOMIC-FORCE MICROSCOPY*

1. Introduction

For the manufacture of optical elements of measuring devices and the formation of their microprofile of the necessary size and shape on them, over the last decades all known materials of amorphous, crystalline, polycrystalline structure have been tested, and for their processing various methods were used, including: industrial deep grinding and polishing methods, grinding and polishing, and the etc.

As research has shown, modern ukrainian optical production is not guaranteed to receive surfaces on an optical glass that would satisfy the requirements imposed on such optical elements. Herewith, the nanorelief in industrially manufactured products exceeds the value of 5 nm, which limits their further use as precision optical elements of optical measuring systems.

At the same time, the impact on the surface of the optical material of abrasive, washing and pickling solutions in the grinding and polishing stages inevitably leads to the formation of chemically heterogeneous defect and fractured layers, the total depth of which can exceed tenths of micrometers. This, in many cases, limits the use of electronic lithography and photolithography technologies.

The problem of compliance with the necessary level of nanorelief of the surface layer of optical materials in the manufacture of elements of a new generation, increasing the productivity of their manufacture is one of the most relevant in the technology and technology of processing optical materials.

One of the ways to overcome this problem is to attract new tools for the energy microprocessing of optical surfaces, including concentrated electron fluxes.

The efficiency of processing optical glass by a ribbon-based electron beam was first shown in the works V.M. Lisochenka [1].

In papers [2, 3], is shown the possibility of flexible

control of the process of electron-beam processing of optical glass and optical ceramics by melting the surface to a depth of up to 200 μm . The authors [4-6] confirmed the efficiency of the use of a ribbon-based electron beam for surface treatment of both optical and technical glass.

At the same time, the question of the qualitative changes in the nanorelief and the defective layer of the optical glass of the silicate group from the action of the low-energy electron beam ($E \leq 6 \text{ keV}$) has not been studied sufficiently and the relationship between these changes and the parameters of electron-beam microprocessing.

The aim of this work is to determine the changes in nanorelief of the surface of elements from optical glass under the influence of a low-energy electron beam and to establish the relationship between the size of the modified nanorelief and the parameters of electron-beam microprocessing.

2. Experimental method

Objects that are treated with an electron beam: plane-parallel round plates (diameter 20 mm, thickness 2, 4, 6 mm) from glass of optical colorless grade K8 (GOST 3514-76) with silver metal coatings applied to their surface. Such objects are widely used in measuring devices as optoelectronic sensors (pressure, capacitance, density of medium, etc.).

The study of processing objects was carried out using a computerized system of complex control, manufactured on the basis of an atomic force microscope (AFM) “NT-206V” (the manufacturer of “Microtestmashines”, GOMEL, Belarus). For visualization of the object of investigation at a magnification of 100 times, used optical chamber “Logitech”, whose viewing field is $1 \times 0,75 \text{ mm}^2$.

The schemes for determining the surface nanorelief

using a computerized integrated control system for non-contact (a) and contact (b) AFM schemes are shown in Fig.1.

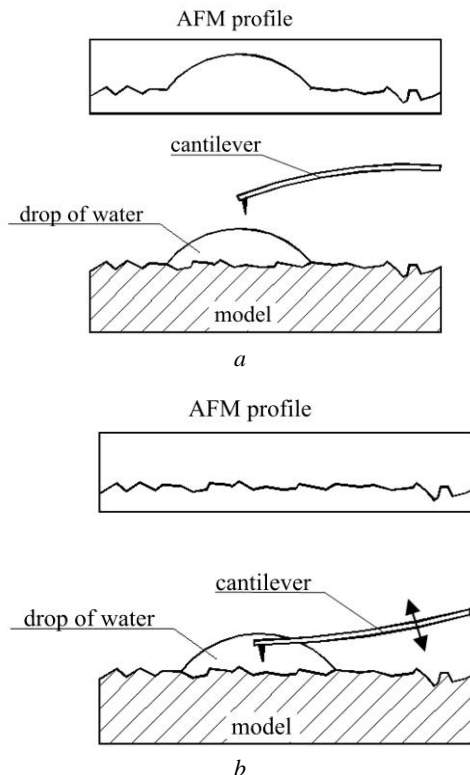


Fig. 1. Obtained surface profiles for noncontact (a) and contact (b) operation schemes of a computerized integrated control system based on the atomic force microscopy method

The sensitive element of the microscope is the cantilever, the deflection of which, when in contact with the surface, is determined by means of a laser beam. The positioning of the surface to be measured under the cantilever is carried out by means of high-precision stepping motors (in the X-Y plane with a pitch of 2.5 μm , along the Z axis with a step of 200 nm).

The profile of the surface to be examined is determined by scanning the cantilever in the X-Y plane in a $13 \times 13 \mu\text{m}$ section using a piezoceramic scanner in steps of up to 1 nm. The displacement of the cantilever along the vertical axis is carried out by a piezotube with a pitch of 0.02 nm in the range 3 μm . The image of the microrelief of the optical surface was obtained by applying the following operating modes of the AFM: static (contact), Fig. 1a, and dynamic (noncontact), Fig. 1 b.

In dynamic mode, the cantilever is superimposed on the vertical axis with a frequency of 10 Hz to 400 kHz. The main advantages of this mode are the significantly increased sensitivity of the measuring system (it is theoretically possible to achieve an atomic resolution of the device) and to ensure the mechanical integrity of the probe and sample.

The positioning of the cantilever above the surface of the optical glass and the further settings of the "laser beam-

cantilever" system occurs in manual mode using the long-focusing camera "Logitech" built into the AFM device with a 150-fold increase in the image on the PC display. As can be seen from Fig. 2, the correct positioning of the cantilever, which provides the most complete and accurate information retrieval by the sensitive AFM system on the topology of the surface, is achieved by focusing the laser of the photo detecting device on the upper edge of the cantilever.

The scanning process is completed automatically, after which the computer monitor received a surface image. For processing and analysis of data from the microrelief, the programm Surface v.6.2 was used, which provides such types of information: three-dimensional visualization of the surface; surface profiling in the required section; distribution of surface heights; angular histogram.

The average time to prepare for work and scan one sample is 10 ... 12 minutes.

The use of the atomic force microscopy method, it was possible to investigate the surface modified by the electron beam and the surface layer of the K8 glass product (Fig. 2).

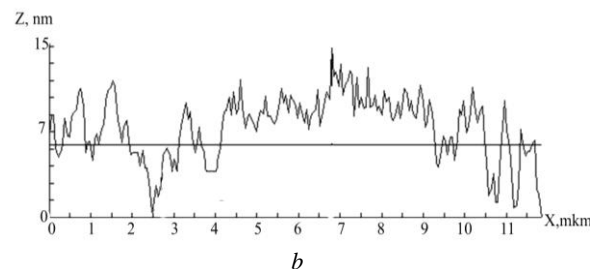
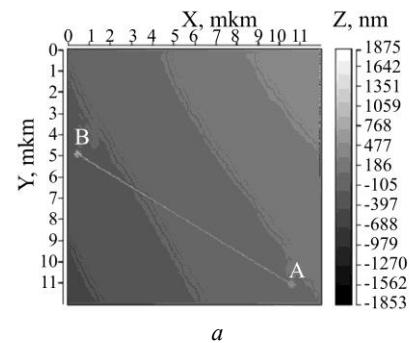


Fig. 2. Appearance (a) and nanorelief along the AB (b) line of the surface area ($12 \times 12 \mu\text{m}$) of the fragment of the plate of the optoelectronic capacitance sensor from K8 glass with a metallic thin silver film fused in its surface by an electron beam (film thickness 350 nm).

3. Results and discussion

The results of the investigation and comparison of the nanorelief of the element surface from the optical glass K8 after machining, laser and electron beam microprocessing with applying a modern computerized complex control system for nanometric studies have shown the promise of this method in metrology, in integral optics at the manufacture and use as elements of measuring devices of micro- and nano-optical elements [7].

According to the profiles shown in Fig. 3, it can be concluded that both after mechanical (deep grinding-polishing) (profile 1, Fig.3.a) and after laser microprocessing (profile 3, Fig.3.b), the surface of the plate from optical glass has a characteristic nanorelief, which is much higher than the allowable value of the arithmetic average of the nanoscale, which is 5 nm.

This indicates the inability to use these methods of surface microprocessing in the manufacture of optical

elements of measuring systems of modern instrumentation.

At the same time, the nanorelief of the surface obtained after electron-beam microprocessing (profile 2, Fig. 3a, b) indicates high accuracy and uniformity of the surface created, and the use of this method allows obtaining high-quality surfaces with guaranteed levels of purity and microroughness, whose value does not exceed 5 nm.

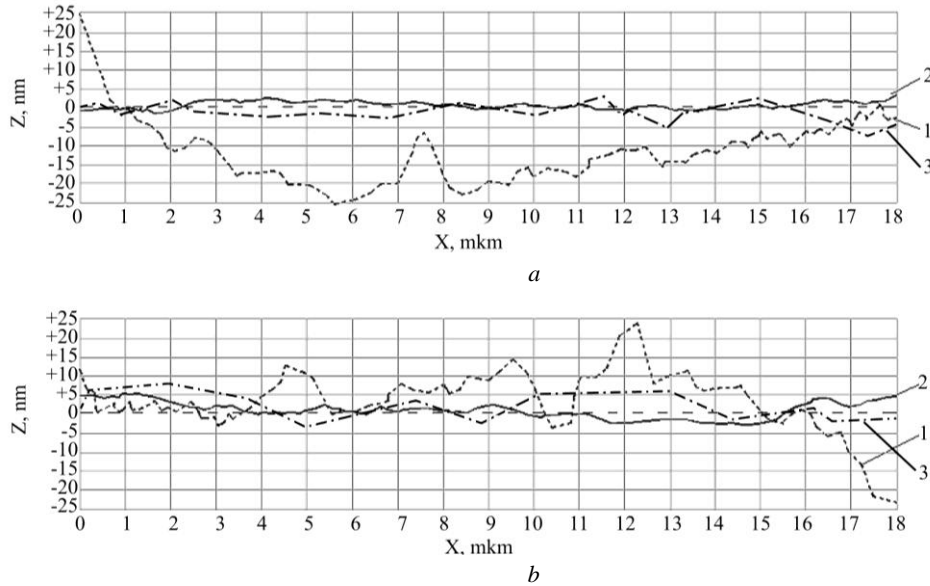


Fig. 3. The characteristic nanorelief of the surface of optical elements from K8 glass after mechanical (1), electron beam (2), and laser (3) processing. NT-206V

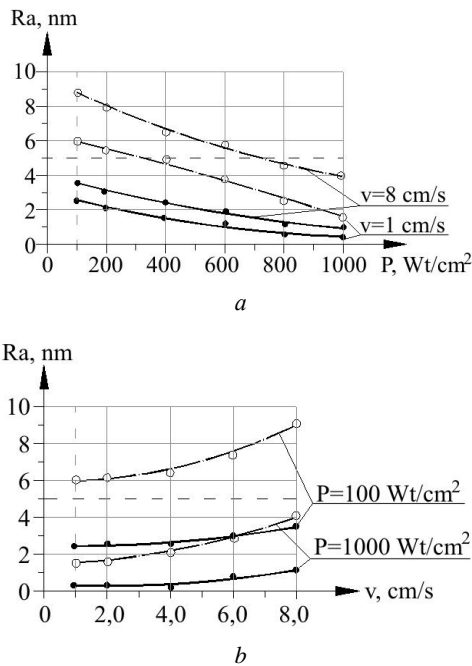


Fig. 4. Dependence of the average arithmetic roughness of the nanorelief Ra on the specific power of the electron beam $P_{\text{ннт}}$ (a) and the speed of electron-beam micromachining $V_{\text{ннт}}$ (b): \circ – by the works [8, 9]; \bullet – by

the advanced technology; - - - the maximum permissible values of the nanorelief on surfaces for optical elements

Further studies of the nanorelief of the surface of elements (on the example of circular plates with a diameter of 20 mm and a thickness of 2 mm, optical glass K8) made it possible to establish the dependence of the arithmetic average roughness Ra on the specific power of the electron beam $P_{\text{ннт}}$ (a) and on the speed of the electron beam $V_{\text{ннт}}$ (b), Fig.4.

As can be seen from the dependences shown in Fig. 4 (a) and (b), according to the technological regimes described in Refs. [8 and 9], an increase in the specific power of the electron beam at 300 W/cm² for electron flow velocities of the order of 1 cm/s sec to 750 W/cm² for electron flow velocities of 8 cm/s leads to a decrease in the arithmetic average of the surface roughness below the permissible value of 5 nm. Herewith, according to the technological regimes obtained for improved technology for electron flow rates of 1-8 cm/s, the average arithmetic nanovelities for the entire range of specific power (100-1000 W/cm²) is 2.2-1.5 nm.

4. Conclusion

In the process of performing scientific research, changes in the nanorelief of the surface of optical elements from glass for measuring system devices from the action of low energy electron flux have been determined, and the relationship between the size of the modified nanorelief and the parameters of electron-beam microprocessing.

It is established that as a result of electron-beam microprocessing the nanorelief of the surfaces of products from optical glass K8 decreases from 4-9 nm to 1.5-2.2 nm. Это достигается путем управлением скоростью и удельной мощностью электронного потока.

The obtained surfaces of optical elements made of K8 glass with a nanorelief of 1.5-2.2 nm satisfy the requirements imposed by modern production of metrological measuring means for such optical elements.

5. Literature

1. Lisochenko V.N. Razrabotka elementov integralno-opticheskikh skhem novymi metodami na osnove elektronno-luchevoi obrabotki (*Development of elements of integrated-optical circuits by new methods based on electron-beam processing*) / V.N.Lisochenko, G.V.Kanashevich, V.A.Vashchenko i dr. – otchet po NIR Cherkasskogo filiala KPI. – Cherkassy. – 1993. – 205 s.
2. Kanashevich G.V. Tekhnologichni mozhlivost elektronno-promenevo obrabki optichnogo skla (*Technological possibilities of electron beam processing of optical glass*) / Visnik CHITI, 1998, No.3. – S. 48-55/
3. Kanashevich G.V., Kotel'nikov D.I., Vashchenko V.A. Special'ni metodi obrabki optichnogo skla (*Special methods of optical glass processing*) / Pid red. Profess. D.I. Kote-l'nikova. – CHernigiv: "Sivers'ka dumka", 2002. – 215 s.
4. Bondarenko M. Peculiarities of metalized surfaces modification of silicon elements of microelectromechanical systems with low-power electronic flow / M.Bondarenko, I.Bondarenko, V.Antoniuk [etc.] // Materials science. Non-equilibrium phase transformations. – 2017. – Year III. – Issue 2. – pp.53-55.
5. Kovalenko Y.I. Study of ordered oxide patterns got on the dielectric surfaces with the combined electronic technology / Y.I.Kovalenko, M.A.Bondarenko, E.V.Vertsanova, I.V.Iatsenko [etc.] // Physics and technology of thin films and nanosystems: XIV Intern. conf.: thesis, May, 20-25, 2013. - Ivano-Frankivsk, 2013. – pp. 92.
6. Antonyuk V.S. Pidvishchennya mikrotverdosti ta znosostijkosti poverhon' elementiv virobiv z optichnogo skla mikroobrobkoyu elektronnim potokom u vakuumi (*Increase of microhardness and wear resistance of elements of products from optical glass by microprocessing by electronic flow in vacuum*) / V.S.Antonyuk, YU.I.Kovalenko, YU.YU.Bondarenko, M.O.Bondarenko // Visnik ZHitomirs'kogo derzhavnogo tekhnologichnogo universitetu. Seriya: Tekhnichni nauki. – ZHitomir: ZHDTU, 2015. – №1 (72) – S. 3-8.
7. Bondarenko M.O. Avtomatizovaniy kompleks dlya nanometrichnih doslidzhen' (*Automated complex for nanometric research*) / M.O.Bondarenko, YU.YU.Bondarenko // Fizika, elektronika, elektrotehnika (FEE-2016): nauk.-tekh. konf., 18-22 kvitnya 2016 r: tezi dop. – Sumi: SumDU, 2016. – S. 200.
8. Yatsenko I. Influence of parameters by electronic ray on properties of superficial layers of optical elements of exact instrument-making / I.Yatsenko, V.Antoniuk, M.Bondarenko, V.Vashchenko // Innovations in ingeneering: Intern. scien.-tech. conf., 9-12 september 2015. – Burgas, Bulgaria. – Vol. 20/183. – 2015. – pp. 64-66.
9. Bondarenko M.O. Optimizaciya parametriv strichkovogo elektronnogo potoku za dopomogoyu zon termichnogo vplivu (*Optimization of the parameters of the tape electronic stream with the help of zones of thermal influence*) / M.O.Bondarenko, V.A.Vashchenko, G.V.Kanashevich // Tezi dopovidej pershoi Mizhnarodnoi NTK "Mashinobuduvannya ta metaloobrobka – 2003". – Kirovograd, 17-19 kvitnya 2003. – S.15-16.

THEORETICAL AND NUMERICAL ASPECTS REGARDING THE THERMOELASTIC BEHAVIOUR OF RUBBERLIKE POLYMERS

M.Sc. Szüle V.¹,

Department of Applied Mechanics – University of Széchenyi István, Győr, Hungary
szule.veronika@sze.hu

Abstract: Vehicle components made of rubber usually exhibit large deformations. Cyclic finite deformations may induce increasing temperature in hyperelastic materials. This case - where changes in deformation and in temperature occur simultaneously - is called coupled thermomechanical problem. Both the mechanical and thermal processes have their own governing equations, that is why special techniques are needed for the computation. A special technique will be presented for solving coupled problems, this is operator split method. The goal of this paper is to show how to solve the coupled thermomechanical problem by the principle of virtual power and the principle of virtual temperature, and how to apply them together.

Keywords: RUBBER, HIGH DEFORMATIONS, THERMODYNAMICS

1. Introduction

Rubber can be classified as a so-called hyperelastic polymer which has a typical geometrical and material nonlinear behavior. It means that the relationship between displacements and internal forces can be described by functions whose order is higher than linear. The geometrical nonlinearity is easy to handle mathematically, however the material nonlinearity is only described approximately [1], [2]. Independently of the experimental investigations which deal with the material behavior of rubber, a number of theoretical works treated rubber as an ideally nonlinear elastic, in particular hyperelastic material. One of the properties of the constitutive equations of hyper-elastic material is that stresses are derived from stored elastic energy function. Hyper-elasticity can be described by particularly convenient constitutive equation given its simplicity and it constitutes the basis for more complex material models such as elastoplasticity, viscoplasticity, and viscoelasticity [1].

Furthermore, the task becomes more complicated because of some features of rubber parts. The temperature of rubber increases significantly. Therefore, the temperature- and displacement fields are coupled, and it means that special solving algorithms are required [7]. So the equations of mechanics and thermodynamics are coupled. As described above, the goals of this paper are the following:

It is necessary to summarize the applied equations and the basic physical laws which are responsible for the theoretical background [8,9]. Clarification of these relationships is essential because the material laws of rubber cannot violate those basic physical laws. It is necessary to extend these relationships like balance of linear momentum and balance of angular momentum, the first and second law of thermodynamics to high deformation of rubber and rubberlike polymers. After this, it will follow the solution of the mechanical and heat conduction problem and the coupled thermomechanical problem by using the operator split method. In this paper, arrows above letters denotes vectors and double underline denotes tensor.

2. Governing equations

2.1 Equilibrium of linear momentum

The differential formulation of the equilibrium of linear momentum in the current configuration is

$$\rho \dot{\underline{\underline{v}}} = \underline{\underline{\sigma}} \cdot \underline{\underline{\nabla}} + \underline{\underline{f}} \quad (1)$$

where ρ is the mass density, $\underline{\underline{v}}$ is the velocity, $\underline{\underline{\sigma}}$ is the Cauchy stress, $\underline{\underline{f}}$ is the volume force.

2.2 Equilibrium of angular momentum

The next equality shows the differential form of the balance of the moments.

$$\underline{\underline{\sigma}} = \underline{\underline{\sigma}}^T \quad (2)$$

2.3 First law of thermodynamics

When deformations repeatedly occur, significant increase in temperature can be observed. The differential form of the first law of thermodynamics is in the current configuration

$$\dot{e} \rho = [-\underline{\underline{\nabla}} \cdot \underline{\underline{q}} + h] + \underline{\underline{\sigma}} \cdot \underline{\underline{l}} \quad (3)$$

where e is the internal energy per unit mass, $\underline{\underline{q}}$ is the heat flux, h is the heat source, $\underline{\underline{l}}$ is the velocity gradient, $\underline{\underline{l}} = \underline{\underline{F}} \cdot \underline{\underline{F}}^{-1}$, $\underline{\underline{l}} = \underline{\underline{v}} \circ \underline{\underline{\nabla}}$.

2.4 Second law of thermodynamics

The behaviour of viscoelastic materials is described by the second law of thermodynamics. The second law of thermodynamics in the current configuration can be written as

$$\eta T \rho \geq -\underline{\underline{\nabla}} \cdot \underline{\underline{q}} + \frac{\underline{\underline{q}} \cdot \underline{\underline{\nabla}} T}{T} + h \quad (4)$$

where η is the entropy per unit mass and T is the absolute temperature. It will be practical to change the variable from entropy per unit mass to temperature by applying the Legendre transformation and by using the Helmholtz-free energy

$$\psi = e - \eta T \quad (5)$$

Substitute the Eqn. (5) into to the Eqn. (3) and subtract Eqn. (3) from Eqn. (4) the following expression will be generated

$$-(\dot{\psi} + \eta \dot{T}) \rho + \underline{\underline{\sigma}} \cdot \underline{\underline{l}} - \frac{\underline{\underline{q}} \cdot \underline{\underline{\nabla}} T}{T} - D \geq 0 \quad (6)$$

which is known as Clausius-Duhem inequality [2].

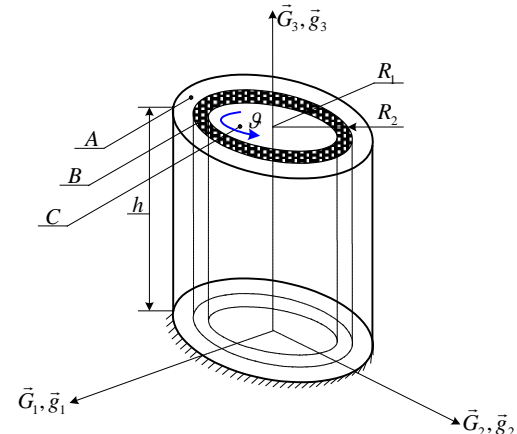


Fig. 1. Mechanical model of a silent block

3. Solution of the coupled thermomechanical problem

3.1 Principle of virtual power

Eq. (1) can be generated in the following form:

$$\underline{\underline{\sigma}} \cdot \nabla + \vec{f} = \vec{0} \quad (7)$$

The solution of Eq. (15) can be generated by finite element method. The basis of the finite element method is an energetical principle, in this case this is the principle of virtual power [4,7].

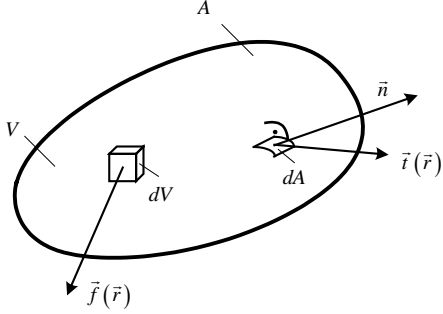


Fig. 2. Types of loads: \vec{t} traction, \vec{f} force per unit volume

Multiplying both sides of Eq. (7) by function \vec{v}^* and integrating the following form will be generated:

$$\int_{(v)} \vec{v}^* \cdot \underline{\underline{\sigma}} \cdot \nabla dv + \int_{(v)} \vec{v}^* \cdot \vec{f} dv = 0 \quad (8)$$

where \vec{v}^* is called virtual velocity field, which is the difference of two different kinematically admissible velocity field and has the following properties: continuous and it can be derivated at least once. The arrow placed above the Cauchy-stress tensor denotes the effect of the Hamiltonian differential operator. Using the $\vec{v}^* \cdot \underline{\underline{\sigma}} \cdot \nabla = \vec{v}^* \cdot \underline{\underline{\sigma}} \cdot \nabla + \vec{v}^* \cdot \underline{\underline{\sigma}} \cdot \nabla$ identity the next expression is generated:

$$\int_{(v)} \vec{v}^* \cdot \underline{\underline{\sigma}} \cdot \nabla dv - \int_{(v)} \vec{v}^* \cdot \underline{\underline{\sigma}} \cdot \nabla dv + \int_{(v)} \vec{v}^* \cdot \vec{f} dv = 0 \quad (9)$$

The first member of Eq. (9) can be converted by Gauss's theorem and the second member can be converted by the application of $\vec{v}^* \cdot \underline{\underline{\sigma}} \cdot \nabla = \underline{\underline{\sigma}} \cdot (\vec{v}^* \circ \nabla)$ identity, where two point means a scalar multiplication between tensors, therefore Eq. (9) results in the following form:

$$\int_{(v)} \vec{v}^* \cdot \underline{\underline{\sigma}} \cdot \vec{n} da - \int_{(v)} \underline{\underline{\sigma}} \cdot (\vec{v}^* \circ \nabla) dv + \int_{(v)} \vec{v}^* \cdot \vec{f} dv = 0$$

The above equation refers to the current configuration so the integration has to be done on the deformed shape of the body. It will be expedient to convert this equation to the reference configuration. Due to this transformation the integrations refer to the undeformable shape of the body.

Let us consider a hyperelastic continuum body in the reference configuration, its volume is indicated by V and its surface is indicated by A . It is known that dv can be expressed by dV

$$dv = JdV \quad (10)$$

and the connection between the surfaces da and dA can be expressed by the Nanson-formula [2]

$$\vec{n} da = J \underline{\underline{F}}^{-T} \cdot \vec{N} dA \quad (11)$$

where $\underline{\underline{F}}^{-T}$ is the inverse of the transpose of the deformation gradient, \vec{N} is the normal vector of surface A , J is the determinant of the deformation gradient. Applying of Eq. (10) and Eq. (11) the Eq. (9) can be obtained, as it can be seen in the next expression:

$$\int_{(A)} \vec{v}^* \cdot \underline{\underline{\sigma}} \cdot \underline{\underline{F}}^{-T} \cdot \vec{N} J dA - \int_{(V)} J \underline{\underline{\sigma}} \cdot (\vec{v}^* \circ \nabla) dV + \int_{(V)} J \vec{v}^* \cdot \vec{f} dV = 0 \quad (12)$$

where $\underline{\underline{P}} = J \underline{\underline{\sigma}} \cdot \underline{\underline{F}}^{-T}$ is the first Piola-Kirchoff stress tensor. The first Piola-Kirchoff stress tensor does not refer to the reference configuration thus it needs to be converted. Multiplying the first member of the left side of Eq. (12) by the $\underline{\underline{I}} = \underline{\underline{F}} \cdot \underline{\underline{F}}^{-1}$ identity tensor and using the $\nabla = \nabla_0 \cdot \underline{\underline{F}}^{-1}$ expression, the following equation will be generated:

$$\int_{(A)} \vec{v}^* \cdot \underline{\underline{F}} \cdot \underline{\underline{F}}^{-1} \cdot \underline{\underline{P}} \cdot \vec{N} dA - \int_{(V)} J \underline{\underline{\sigma}} \cdot (\vec{v}^* \circ \nabla_0) \cdot \underline{\underline{F}}^{-1} dV + \int_{(V)} \vec{v}^* \cdot \vec{f} J dV = 0 \quad (13)$$

where $\underline{\underline{S}}$ is the second Piola-Kirchoff stress tensor which refers to the reference configuration. The surface of the considered body A can be divided into two parts, namely A_u surface where the displacement is defined and A_p where the traction is defined.

The $\underline{\underline{S}} \cdot \vec{N}$ product determines the value of \vec{p}_0 which is the traction vector in the reference configuration. Rearranging the second term of the left side of Eq. (13) the first Piola-Kirchoff stress tensor can be appeared:

$$\int_{(A_p)} \vec{v}^* \cdot \underline{\underline{F}} \cdot \underline{\underline{S}} \cdot \vec{N} dA + \int_{(A_u)} \vec{v}^* \cdot \underline{\underline{F}} \cdot \underline{\underline{S}} \cdot \vec{N} dA - \int_{(V)} J \underline{\underline{\sigma}} \cdot \underline{\underline{F}}^{-T} \cdot (\vec{v}^* \circ \nabla_0) dV + \int_{(V)} \vec{v}^* \cdot \vec{f} J dV = 0 \quad (14)$$

which can be transformed to the second Piola-Kirchoff stress tensor applying the $\underline{\underline{I}} = \underline{\underline{F}} \cdot \underline{\underline{F}}^{-1}$ expression:

$$\int_{(A_p)} \vec{v}^* \cdot \underline{\underline{F}} \cdot \vec{p}_0 dA + \int_{(A_u)} \vec{v}^* \cdot \underline{\underline{F}} \cdot \underline{\underline{S}} \cdot \vec{N} dA - \int_{(V)} \underline{\underline{F}} \cdot \underline{\underline{F}}^{-1} \cdot \underline{\underline{P}} \cdot (\vec{v}^* \circ \nabla_0) dV + \int_{(V)} \vec{v}^* \cdot \vec{f} J dV = 0 \quad (15)$$

The members of this equation can be divided into two groups: virtual power of internal forces (P_{int}) and virtual power of external forces (P_{ext}).

$$P = \int_{(V)} \underline{\underline{S}} \cdot \underline{\underline{F}}^T \cdot (\vec{v}^* \circ \nabla_0) \cdot \underline{\underline{F}} dV - \left(\int_{(A_p)} \vec{v}^* \cdot \underline{\underline{F}} \cdot \vec{p}_0 dA + \int_{(A_u)} \vec{v}^* \cdot \underline{\underline{F}} \cdot \underline{\underline{S}} \cdot \vec{N} dA + \int_{(V)} \vec{v}^* \cdot \vec{f} J dV \right) = 0 \quad (16)$$

Thus the virtual power of internal forces is equivalent the virtual power of external forces [1,2,9].

$$\begin{aligned} & \underbrace{\int_{(V)} \underline{S} \cdot \underline{F}^T \cdot (\underline{v}^* \circ \nabla_0) \cdot \underline{F} dV}_{\underline{r}_{in}} = \\ & \underbrace{\int_{(A_p)} \underline{v}^* \cdot \underline{F} \cdot \underline{p}_0 dA + \int_{(A_n)} \underline{v}^* \cdot \underline{F} \cdot \underline{S} \cdot \underline{N} dA + \int_{(V)} \underline{v}^* \cdot \underline{f}_0 dV}_{\underline{r}_{ex}} \end{aligned} \quad (17)$$

Denoting by P the difference of the two virtual power, P is the function of the position vector \vec{r} , the function \underline{v}^* and the temperature T due to the thermal expansion.

$$P = P(\vec{r}, T, \underline{v}^*) \quad (18)$$

The thermal expansion is denoted by the next differential equation:

$$\frac{\partial J}{\partial T} = 3\alpha_0 J \quad (19)$$

where α_0 is the linear thermal expansion coefficient. Assuming that the temperature variations are not significant ($T - T_0 \ll T_0$, where T_0 is the reference temperature), the linear thermal expansion coefficient can be considered constant and in that case the solution of Eq. (19) can be determined by the next expression [2]:

$$J(T) = e^{3\alpha_0(T-T_0)} \quad (20)$$

Searching the vector field $\vec{r} = \vec{r}(\vec{R})$ (deformed body) which satisfies the nonlinear equation. Assuming that the mechanical processes are quasi-static processes thus the considered system is in a mechanical equilibrium in each time moment. It means that the acceleration of the points of the continuum body can be assumed zero and the other quantities do not depend on time. Since equation $P = 0$ is nonlinear the solution is generated by Newton-Raphson method:

$$P(\vec{r}_k, \underline{v}^*) + DP(\vec{r}_k, \underline{v}^*)[\vec{u}] = 0 \quad (21)$$

where \vec{r}_k ($k=0$) is an arbitrary vector, $DP(\vec{r}_k, \underline{v}^*)$ is the Gateaux-derivative [1] and \vec{u} is the increment of displacement. After k th iteration steps

$$\vec{r}_{k+1} = \vec{r}_k + \vec{u} \quad (22)$$

the iteration will be stopped when the increment of displacement \vec{u} decreases under the certain margin of error:

$$\frac{|\vec{u}|}{|\vec{r}_k - \vec{R}|} < h \quad (23)$$

3.2 Principle of virtual temperature

In order to solve the coupled thermomechanical problem, it is necessary to solve the heat conduction equation, too [7]. Considering an elastic element which has the property that the total mechanical energy is reversible. The free energy of the body is the function of the strain and temperature. Dissipation comes only from heat conduction.

Starting from the first law of thermodynamics Eq. (8) and changing the variable from entropy to temperature by using the following

expressions: $e = \psi + \eta T$, $\dot{e} = \dot{\psi} + \dot{\eta} T + \eta \dot{T}$, $\psi = \psi(T, \underline{E})$, $\eta = -\frac{\partial \psi}{\partial T}$

$\eta = -\frac{\partial^2 \psi}{\partial T^2} \dot{T} - \frac{\partial^2 \psi}{\partial T \partial \underline{E}} \cdot \underline{\dot{E}}$ the equation of heat conduction in the

reference configuration is

$$\rho_0 c \dot{T} = -\nabla_0 \cdot \underline{\bar{q}}_0 + h_0 + \left(\underline{S} - \rho_0 \frac{\partial \psi}{\partial \underline{E}} + \rho_0 T \frac{\partial^2 \psi}{\partial \underline{E} \partial T} \right) \cdot \underline{\dot{E}} \quad (24)$$

where ρ_0 is the mass density in the reference configuration, c is

the heat capacity, $\underline{\bar{q}}_0$ is the heat flux vector in the reference configuration, h_0 is the heat source, where \underline{E} is the Green-Lagrange strain tensor. Correspondingly, the mechanical equation of the heat conduction equation can be solved by finite element method. The solution can be determined by the principle of virtual temperature. Assuming that the considered material is perfectly elastic the non-recoverable part of the mechanical power is:

$$\underline{S} - \rho_0 \frac{\partial \psi}{\partial \underline{E}} = \underline{0} \quad (25)$$

Thus, the equation of heat conduction can be generated in the following form:

$$\rho_0 c \dot{T} = -\nabla_0 \cdot \underline{\bar{q}}_0 + h_0 + \rho_0 T \frac{\partial^2 \psi}{\partial \underline{E} \partial T} \cdot \underline{\dot{E}} \quad (26)$$

Multiplying both sides of Eq. (26) by function $\theta(\vec{r}, t)$ and integrating both sides, the following form will be generated:

$$\int_{(V)} \rho_0 c \dot{T} \theta dV = -\int_{(V)} \nabla_0 \cdot \underline{\bar{q}}_0 \theta dV + \int_{(V)} h_0 \theta dV + \int_{(V)} \rho_0 T \frac{\partial^2 \psi}{\partial \underline{E} \partial T} \cdot \underline{\dot{E}} \theta dV \quad (27)$$

where is $\theta(\vec{r}, t)$ called virtual temperature field, which has the similar properties

such as virtual velocity field, so it is continuous and it can be derivated at least once. Consequence of the second law of thermodynamics is that the heat flux can be expressed by the negative gradient of the temperature field [7]:

$$\underline{\bar{q}}_0 = -\underline{\kappa} \cdot \nabla_0 T \quad (28)$$

where $\underline{\kappa}$ is the heat conduction tensor. Applying Gauss's theorem:

$$\begin{aligned} \int_{(V)} \rho_0 c \dot{T} \theta dV &= -\int_{(A)} \theta \underline{\bar{q}}_0 \cdot \underline{N} dA - \int_{(V)} \theta \nabla_0 \cdot \underline{\kappa} \cdot \nabla_0 T dV + \\ &+ \int_{(V)} h_0 \theta dV + \int_{(V)} \rho_0 T \frac{\partial^2 \psi}{\partial \underline{E} \partial T} \cdot \underline{\dot{E}} \theta dV \end{aligned} \quad (29)$$

Considering that the surface of the body can be divided according to the boundary conditions into two parts, the first member of the right side of Eq. (29) consists of two parts. The first part is the integral on the surface A_T where the temperature is given, the second is the integral on the surface A_q where the heat flux is given, as is presented in Fig. 3.

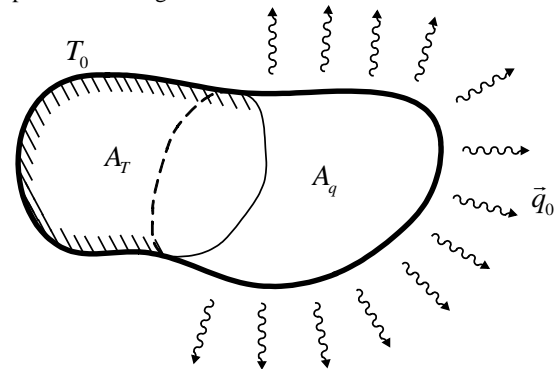


Fig. 3. Boundary conditions: defined temperature, defined heat flux

Furthermore, assuming that the considered material is isotrop in respect of heat conduction, thus $\underline{\kappa} = \kappa \underline{I}$, where \underline{I} denotes the identity tensor, the equation of heat conduction will have the next form:

$$\int_{(V)} \rho_0 c \dot{T} \theta dV = \int_{(A_r)} \kappa \theta (\nabla_0 T) \cdot \bar{N} dA - \int_{(A_s)} \theta \bar{q}_0 \cdot \bar{N} dA - \int_{(V)} \kappa (\theta \nabla_0) \cdot (\nabla_0 T) dV + \int_{(V)} h_0 \theta dV + \int_{(V)} \rho_0 T \frac{\partial^2 \psi}{\partial \underline{E} \partial T} \cdot \underline{E} \theta dV \quad (30)$$

Directing Eq. (30) to zero, the principle of virtual temperature can be determined which can be used for the approximate solution of the differential equation Eq. (26)

$$\Upsilon = \int_{(V)} \rho_0 c \dot{T} \theta dV + \int_{(A)} \theta q_N dA + \int_{(V)} \kappa \theta \nabla_0 \cdot \nabla_0 T dV - \int_{(V)} h_0 \theta dV - \int_{(V)} \rho_0 T \frac{\partial^2 \psi}{\partial \underline{E} \partial T} \cdot \underline{E} \theta dV = 0 \quad (31)$$

where Υ is function of the \bar{r} position vector, the θ function and the T temperature, $\Upsilon = \Upsilon(\bar{r}, T, \theta)$. Searching the temperature field $T(\bar{r}, t)$ which satisfies the equation $\Upsilon = 0$.

3.3 Solution of the coupled thermomechanical problem

For the solution of the coupled problem, a special technique will be presented which is called operator split method. The solution is divided into two parts by the above mentioned method. First of all, the mechanical problem has to be solved with constant temperature:

$$P = P(\bar{r}, T = \text{const.}, \bar{v}^*) = 0 \quad (32)$$

The result of Eq. (32) is the \bar{r} function. It will be followed by the solution of the heat conduction problem with constant \bar{r} function, in the following manner:

$$\Upsilon = \Upsilon(\bar{r} = \text{const.}, T, \theta) = 0 \quad (33)$$

Substituting the resulted temperature field into the mechanical equation, the mechanical equation has to be solved again. These above mentioned two steps have to be repeated till the variation of the \bar{r} function and temperature decrease under these margin of errors:

$$\frac{|\bar{r}_k - \bar{r}_{k-1}|}{|\bar{r}_k - \bar{R}|} < h_1 \quad (34)$$

and

$$\frac{|T_k - T_{k-1}|}{|T_k - T_0|} < h_2 \quad (35)$$

where h_1 and h_2 are margins of errors and T_0 is the reference temperature.

In order to solve the thermomechanical problem, it is necessary to use the weak formulation and to do the linearization of the non-linear formulation of the mechanical problem. The position vector is determined from the weak form of the mechanical problem, the temperature field is determined from the weak form of the heat conduction problem. The flowchart of the numerical solution is presented in Fig. 4.

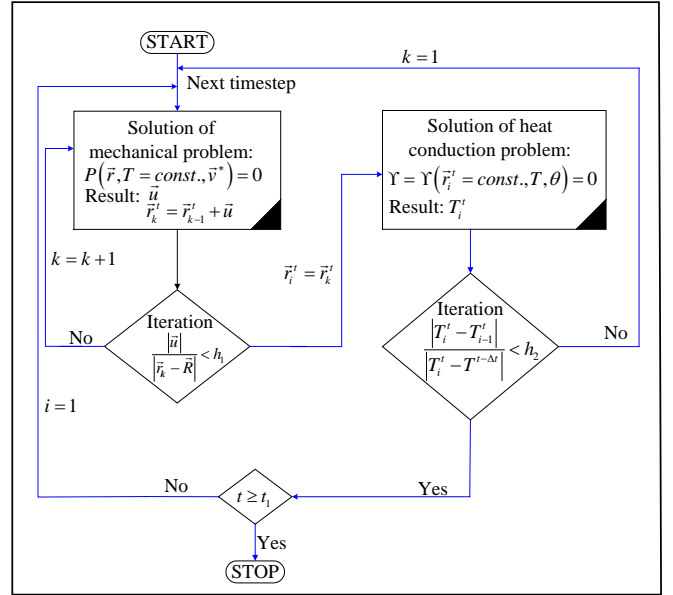


Fig. 4. Flowchart of solution of the coupled thermomechanical problem

4. Summary

We represented an algorithm which allows to calculate strain changes and temperature changes of the rubber part of a vehicle component under certain conditions. In the future we would like to develop a solving computer program in order to apply it as a thermodynamically consistent description.

The present numerical algorithm is the basis of the further fatigue and lifetime-calculations.

References

- [1] Bonet, J., Wood, R. D.: Nonlinear Continuum Mechanics for Finite Element Analysis, Cambridge University Press (1997).
- [2] Holzapfel, G. A.: Nonlinear Solid Mechanics, John Wiley&Sons, Chichester, (2000).
- [3] Ogden, R. W., Large deformation isotropic elasticity: on the correlation of theory and experiment for incompressible rubberlike solids, Proc. Royal Society of London, Series A 326, pp. 565-584. (1972)
- [4] Ogden, R. W., Elastic deformations of rubberlike materials, H.G.Hopkins and M.J. Sewell, eds., Mechanics of Solids, the Rodney Hill 60th Anniversary Volume, (Pergamon Press, Oxford), pp. 499-537, (1982).
- [5] Reese S., Wriggers P.: A material model for rubber-like polymers exhibiting plastic deformation: computational aspects and a comparison with experimental results, Computer methods in applied mechanics and engineering, Vol 148, pp. 279-298, (1997).
- [6] Böl, M., Reese, S.: Finite element modelling of rubber-like polymers based on chain statistics, International Journal of Solids and Structures, Vol 43, pp. 2-26, (2006).
- [7] Pere, B.: Solution of Coupled Thermomechanical Problems Using p-FEM, 8th European Solid Mechanics Conference (ESMC2012), (CD-ROM, 2 pages), Graz, Austria, 9-13 July (2012).
- [8] Holzapfel, G. A., Simo J., C.: Entropy elasticity of isotropic rubber-like solids at finite strains, Computer methods in applied mechanics and engineering, Vol 132, pp. 17-44. (1996).
- [9] Égert J., Pere B.: Finite Element Analysis, Universitas Győr Nonprofit Kft., Hungary, Győr (2011).

OPTIONS OF REAL TIME MONITORING METALWORKING FLUIDS

Ing. Jurina F., Prof. Dr. Ing. Peterka J.

Slovak University of Technology in Bratislava, Faculty of Material Science and Technology in Trnava

xjurina@stuba.sk, peterka@stuba.sk

Abstract: The article is focused to describing the current monitoring systems for cutting liquids used in turning, drilling, milling and grinding operations. Based on the findings, a proprietary monitoring system is designed. The monitoring system consists of the hardware and software parts. The hardware part is a data acquisition device that contains sensors of concentration, conductivity, acidity and temperature. The device is located in the machine tank reservoir with cutting fluids. The Software section - The application displays current real-time information and a historical overview of the measured quantities. The application allows setting of limit values for monitored quantities and, if overtaken, it can alert the operator. The proposed device represents a simple way to control selected fluid properties during their life cycle.

Keywords: REAL TIME MONITORING, CUTTING / METALWORKING FLUIDS

1. Introduction

Cutting area is in process of machining surrounded by cutting ambient which is made of air, fluids, gases and unsaturated steam. For the cutting area, we consider the area near the steam of the chip (1). The physical and chemical properties of the cutting environment significantly affect the mechanism of chip formation, force and friction between the workpiece and the tool, deformation work in the deformation of the workpiece, the formation of an increase, the hardening of the machined surface, the minimum thickness of the material to be taken, the residual stress of the machined surface. The main requirements of the cutting environment include ensuring a cooling, lubricating and cleaning effect at the cutting point(2).

The most commonly used cutting environment for drilling, turning, milling or grinding operations includes cutting liquids. The influence of cutting liquids on the cutting process is determined by their lubricating, cooling, cleaning and cutting action. Depending on the machining operation and the desired properties of the machined surface, greater or lesser emphasis may be placed on some effect of the cutting fluid (5). During operation, they are aged due to oxidation, heat and mechanical stress, pollution and catalytic effects. Aqueous solutions and emulsions, that is, the media whose basic constituents are water, are subject to the most rapid changes. The water has a high degree of evaporation, and due to the temperatures produced by the cutting process, there is increased evaporation which causes the salts of electrolytes to disappear from aqueous solutions and their deposition in the powder coating on the machine and its functional surfaces. At the same time, salt loss results in a decrease in acidity and a risk of corrosion (3). At the same time, dirt and foreign oils (from the sliding surfaces of the machine) enter the solution. In the case of severe contamination, suitable conditions for bacterial growth are created. The physical and chemical parameters are monitored for the condition of cutting liquids. The most important indicators include:(3)

- the value of Ph,
- concentration
- amount of bacteria,
- impurity content,
- the content of foreign oils.

If one or more of the quantities monitored are exceeded, the cutting fluid is degraded. Degraded cutting fluid is not suitable not only for functional but also for health, because working with such an emulsion is a source of serious skin problems. It also has an adverse impact on work and the environment.

Reasons for diagnostics of cutting liquids can be classified into the following aspects: (7)

Functional point - In the case of the use of cooling emulsions, in practice, they are gradually degraded or completely microbiologically decomposed - anaerobic, aerobic or a

combination of both so that after a certain period of time the cutting fluid needs to be replaced, the machine and the system cleaned and put on a new liquid. The uneven consumption of the individual components of the cutting fluid is also undesirable. Due to the higher evaporation of water, the concentration of the emulsion may fluctuate. In order to ensure the stability of the machining process, it is therefore necessary to continuously monitor and maintain the state of the cooling emulsions in the machines in the working range prescribed by the machine manufacturer and the supplier of the cutting fluid.

Ecological point of view - The development and application of cutting fluids is influenced by the ever-increasing demands of legislation. Changes in laws have led to significant changes in the composition of cutting liquids and thus to changes in their technical and application properties. Examples are so-called " alternative process fluids that harm the environment. From an ecological point of view, the application of Minimum quantity liquid machining (MQL) technology is a preferred method of machining with minimal amount of cutting fluid (8).

Health aspects - Employees in engineering companies are in constant contact with cutting fluids. Liquids must therefore be relatively non-toxic, non-volatile, non-combustible so as to maximize the health and safety risks of work (9). The vast majority of cutting liquids are not highly toxic. However, toxicity problems associated with cutting fluids are usually caused by bacterial attack, concentration change, or contamination. Cutting fluids can enter the body through inhalation (evaporation, aerosol inhalation), ingestion or absorption of the skin.

Biodegradation - Biological decomposition of cutting fluid is due to the presence of several species of bacteria and fungi (9). Contamination of the cutting liquid by these microorganisms is the main cause of liquid degradation. All cutting fluids are susceptible to microbial damage that significantly reduces their lifetime.

Diagnostics of cutting fluids

Currently, diagnostics of cutting liquids can be broken down into the following categories based on the method and frequency of the control: (4)

Unchecked - the cutting fluid is used until deficiencies related to workpiece quality, operator health problems, or machine damage have been identified,

Simple operating control without monitoring devices - assessment of appearance, liquid odor and surface appearance washed with cutting fluid. Inspection is often applied, but is not sufficient for the analysis of cutting liquids,

Operational control - laboratory or manual,

Real-time control - monitoring systems without feedback (parameter modification is performed by manual operation), - feedback systems with feedback (parameter modification is performed automatically without human intervention).

Overview of monitoring systems

The overview includes a list of existing feedback systems.

FLUID CONDITION MONITORING AND CONTROLLING SYSTEM FOR A METALWORKING FLUID CENTRAL SYSTEM

System designed for on-line monitoring of water-miscible cutting liquids for central distribution devices. It was patented in 1990 and includes 4 sensors that simultaneously evaluate temperature, pH, conductivity and dissolved oxygen. The measurement is performed every hour and the measured data is stored in the PC. The computer evaluates the measured data and, if necessary, corrections are made either manually or automatically by means of valves, pumps, and under (10).

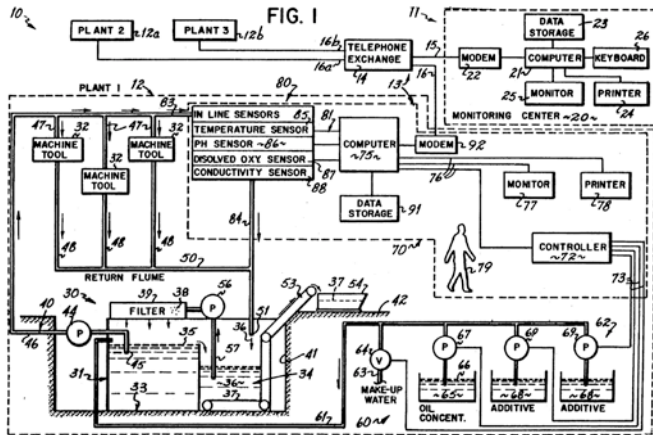


Fig. 1 Schematic of Fluid condition monitoring and controlling system for a metalworking fluid central system(10).

The system is able to monitor properties on multiple devices at the same time. The computers₇₅ of these devices are connected via a modem₉₂ to the central system₁₁ via a telephone network₁₄. The central system₁₁ is connected to the modem₂₂ network. It includes a central computer₂₁, a monitor₂₅, a printer₂₄, a keyboard₂₆ and a data repository₂₃. Four sensors are connected to the computer module₇₅ on the device. They are a temperature sensor₈₅, a pH₈₆ sensor, oxygen solubility sensor₈₇ and a conductivity sensor₈₈. Through these sensors, through the inlet₈₃, the cutting fluid that is being monitored is passed. The cutting fluid simultaneously passes through the machine₃₂ and returns back to the cutting fluid reservoir₃₁. The computer module₇₅ records measured data from sensors, stores them in a data repository₉₁ and into a control mechanism₇₂ which evaluates these values. The control mechanism will, if necessary, take measures to modify the properties of cutting liquids by adding additives₈₆ or by adding a different liquor to the cutting fluid₆₅. The additive and correction cutting fluid is fed into the reservoir₃₁ via a line₆₁. The system can produce graphic outputs (10) based on the measured values.

ORACLE

System designed for cutting and cutting fluids for CNC machine tools. The device consists of temperature, pH, conductivity and concentration sensors. The sensors are connected to the control device which contains the additive container and the concentrate container. The device is located on each machine individually. The system automatically evaluates the condition and amount of cutting fluid and is able to automatically correct the change of quantities by adding the concentrate, water or additives. All measured values and addition records of the concentrate and additives are sent to the server. The user can access and monitor the state of the cutting fluid through the interface (website) to this data. In addition, the tolerance ranges for the variables can be changed (13). The working environment is shown in Fig. 2.

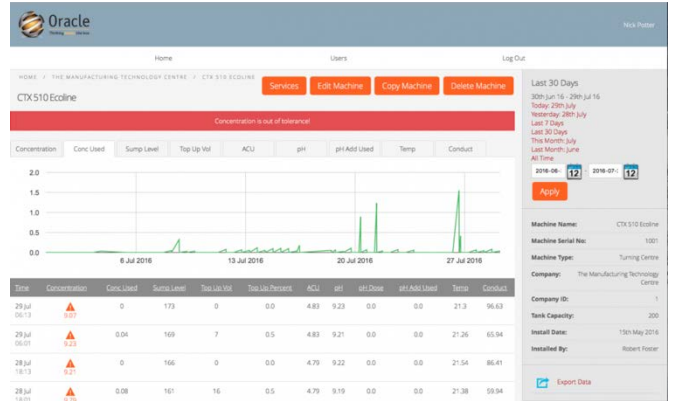


Fig. 2 Oracle work environment (13).

CASTROL SYSTEM RT

System designed for real-time cutting of cutting liquids for metal cutting systems with central cutting fluid distribution. The system automatically monitors quantities such as concentration, pH, conductivity, temperature and biological activity of water-miscible cutting liquids (11) (12). On the basis of the measured values, it is possible to adjust the cutting fluid, which helps to reduce the changes in the concentration. The working environment is shown in Fig. 3. In Fig. 4, the system itself can be seen.

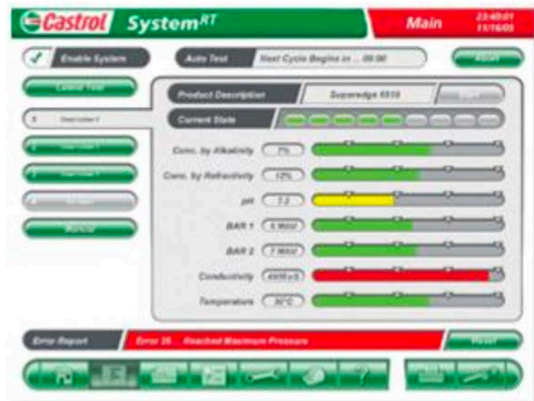


Fig. 3 Castrol work environment (11).



Fig. 4 Castrol system RT.

2. Design of monitoring system

The monitoring system consists of a hardware and a software part. The hardware part consists of a probe placed in the machine's cutting fluid reservoir, which automatically evaluates the selected properties using built-in sensors. The software part is an application that displays the properties and state of the cutting fluid based on the measured values.

Probe

The core of the probe is an electronic circuit consisting of an energy saving communication module ESP 8266. The communication module provides two-way communication between the hardware and the application. The advantage of the used model is that it contains 18 I/O pins for the connection of digital and analog peripherals. The module also has an analogue/digital converter that is replaced by an external 8-channel 10-bit MCP 3008 transducer due to multiple negative facts. Communication between the external transmitter and the communication module takes place via the SPI bus. Analog / digital transducer is connected to pH and concentration sensors. As a pH sensor, an unbreakable pH probe based on ISFET technology is used. Sensing the concentration is provided by a digital refractometer. As a temperature sensor, the DS18B20 digital thermometer is used to communicate with ESP 8266 using a 1-wire interface. The block diagram of the system is shown in Fig. 5. The electronic circuit, together with the sensors, is located in a closed, water-resistant container. The container is placed in a container of cutting liquids.



Fig. 5 Simplified block diagram of the probe.

The capture of variables takes place at intervals that are defined by the user in the application. Intervals can be set within arbitrary limits. Measured values for each dimension are sent using the HTTP GET request. Data is evaluated using the application and stored in the database.

Application

The application is a simple tool for managing measured data. The main window shows individual machines that are equipped with a data collection device. Provides a brief overview of measured data on individual machines (Fig. 6).

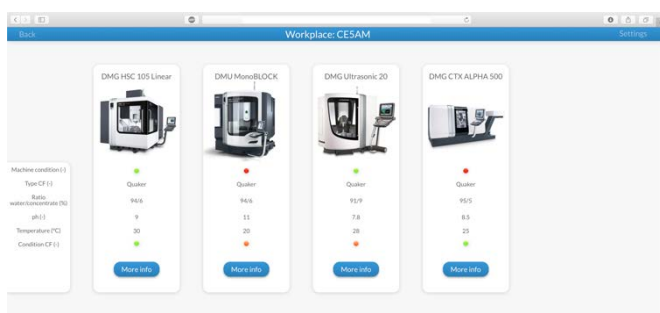


Fig. 6 Main page of monitoring system.

After clicking on the button "more" will call up the details window (Fig 7), which is divided into 4 basic sections. The first part contains information on the cutting fluid used, the date of filling and the recommended replacement date. Also, additional information on the total volume used and the like may be given in this section.

The second part (Actual data) contains information about the actual values of the monitored properties of the cutting liquid.

The third section (History) contains a graphical overview of the monitored values in the past. The entire historical overview can be

clearly divided into smaller time slots such as months, weeks, days, and so on. The selected period can be exported to a spreadsheet or as a photo.

In the fourth section (Settings), it is possible to edit maximum and minimum boundaries for each monitored property. It is also possible to select the method of treating the cutting fluid. When selecting "manual", the system only monitors the individual quantities and alerts the operator when the limits are exceeded (if the Notification box is selected.) When selecting the mode automatically, the system itself is able to take corrective action. If the limit values of one or more of the monitored quantities are exceeded, the system will automatically take the necessary steps to replenish the fluid, to add additives, and the like.

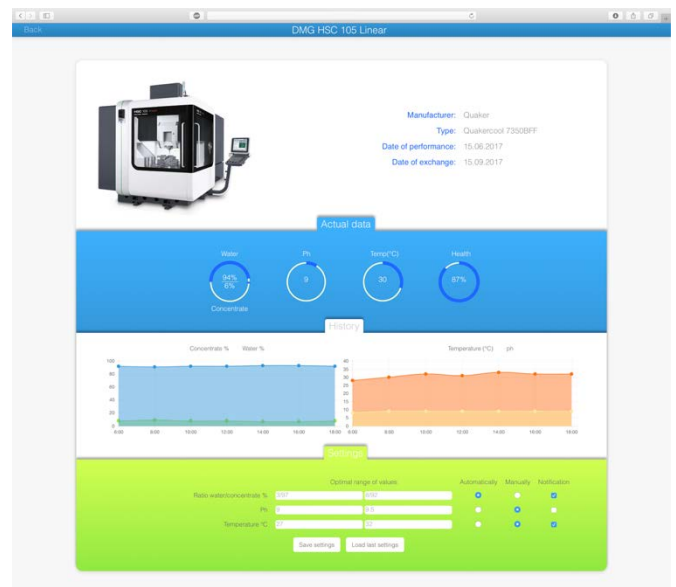


Fig. 7 Page with details of cutting fluid.

3. Conclusion

The article contains a summary of the liquid cutting environment information. It points to the negative phenomena associated with the use of liquids in the machining process in the absence of care for cutting liquids. To prevent premature degradation of the cutting fluid, it must be inspected and maintained at regular intervals. The second part of the article contains a description of the current monitoring systems and their main advantages and disadvantages. The proposed system is an effective tool for cutting liquids. It allows you to get a quick overview of the current state of the cutting fluid and extends its lifetime by corrective measures.

This article was created with support projekt VEGA 1/0097/17 „The research of novel method for cutting edge preparation to increase the tool performance in machining of difficult-to-machine materials”

4. Literature

- 1 Buda J., Békes J. *Teoretické základy obrábání kovov*. Alfa Bratislava 1977
- 2 Čuma M., Zajac J. *The impact analysis of cutting fluids aerosols on working environment and contamination of reservoirs* [online] [quoted on 2018-1-20]. Available on the Internet: <<https://hrcak.srce.hr/file/124864>>

- 3 Gerulová K., Neštický M., Burnáská E., Ružarovský R. *Real time monitoring and automatic regulation system for metalworking fluids* [online] [quoted on 2018-1-21]. Available on the Internet: <https://www.mtf.stuba.sk/buxus/docs/doc/casopis_Vedecke_prace/38/4_Gerulova.pdf>
- 4 Kucháriková E. *Monitoring of cutting fluids* [Dissertation thesis]- Slovak University of Technology in Bratislava. Faculty of Material Science and Technology; Institute of Production Technologies Trnava: MTF STU, 2010. 120 s.
- 5 Zajac J. *Príspevok k riešeniu synergie brúsenia a kvapalín v procesoch brúsenia*. Výrobné inžinierstvo, 2-3(2003) ISSN1335-7972-01 FVTTU Košice so sílom v Prešove.
- 6 Svetský, Š., Balog, K. *Skúšanie rezných kvapalín v technológiách obrábania*. [online] [quoted on 2018-1-10]. Available on the Internet: <<http://www.best.sk/WWW/CasopisyVedecke-2.htm> >
- 7 Číliková, M., Pilc, J., Mádl, J. *Top trendy v obrábaní, VI. časť – procesné médiá*. MEDI A/ST, s.r.o., Žilina, Január 2008, 144 s., ISBN 978-80-969789-3-9
- 8 Suda S., Yokota H., Inasaki I. *A Synthetic Ester as an Optimal Cutting Fluid next term for Minimal Quantity Lubrication Machining*. In CIRP Annals - Manufacturing Technology. [online] [quoted on 2018-1-10]. Available on the Internet: <<http://www.sciencedirect.com>. >
- 9 *Cutting fluid management*. Small Machining operations. Iowa University of northern Iowa, 2003, 62 s. [online] [quoted on 2018-1-10]. Available on the Internet: <<http://www.ec.gc.ca/cppic/en/refView.cfm?refId=1368> >
- 10 Johnson J., T. *Fluid conditional monitoring and controlling system for a metalworking fluid central system* WO/1990/014624 Cincinnati Milacron N 1990.
- 11 Real time fluid monitoring. Castrol industry. [online] [quoted on 2018-1-10]. Available on the Internet: <<http://www.castrol.com/castrol/sectiongenericarticle.do?categoryId=9020676&contentId=7038074> >
- 12 Castrol Introduces Real Time Automated System to Monitor Metalworking Fluids. ThomasNet News. [online] [quoted on 2018-1-10]. Available on the Internet: <<http://news.thomasnet.com/fullstory/Automated-System-monitors-metalworking-fluids-490210>>
- 13 JEMTECH ORACLE *Fluid management* [online] [quoted on 2018-1-11]. Available on the Internet: <<http://www.oraclefms.co.uk/fluid-mmanagement> >
- 14 Peterka J., Jurina F. *Monitoring of cutting fluids*. In COMEC 2016 IX Conferencia Científica Internacional de Ingeniería Mecánica. Del 14 al 17 Noviembre de 2016, Villa Clara, Cuba. 1. vyd : Central University of Las Villas, 2016, [6]s. ISBN 978-959-312-216-0.
- 15 Peterka J., Jurina F. *Monitoring of cutting fluids* In Pro-tech-ma 2017 & Surface engineering 2017 Conference Proceedings. International scientific conferences, Bardejov Spa, 20.-23.6.2017. 1. vyd. Košice : Technical University of Košice, 2017, s. 127-128. ISBN 978-80-553-3181-2.

СЪВРЕМЕННИ МЕТОДИ ЗА ИЗВЛИЧАНЕ НА ЦВЕТНИ И РЕДКИ МЕТАЛИ ОТ ПЪРВИЧНИ И ТЕХНОГЕННИ СУРОВИНИ ИЗТОЧНИЦИ

CONTEMPORARY METHODS FOR OBTAINING NON-FERROUS AND RARE METALS FROM PRIMARY AND TECHNOGENIC RAW MATERIALS

Assoc. Prof. PhD Vania Vassileva¹, Eng. Georgi Savov², Prof. DSc. PhD Katia Vutova¹, Assoc. Prof. PhD Valeriya Kovacheva-Ninova³, Eng. Evgeni Petrov⁴

¹Institute of electronics, Bulgarian Academy of Sciences;
72 Tzarigradsko shosse, 1784 Sofia, Bulgaria
e-mail: vvvania@abv.bg ; katia@van-computers.com

²Premiatec Ltd., Sofia, Bulgaria
e-mail: savov.georgi@gmail.com

³University of Mining and Geology "St. Ivan Rilski", Sofia, Bulgaria
e-mail: valeria.kovacheva@mgu.bg

⁴IPPK Ltd., Sofia, Bulgaria
e-mail: evgpetrov@abv.bg

Abstract: During the last years stable increase of requesting high-purity non-ferrous and rare metals can be seen. They have wide spectrum of applications such as components in many products, for example batteries, catalysts, electronics, special alloys, high-tech and products in electronics, chemical, military industry, energetics, etc.

For the production of non-ferrous metals traditionally in Bulgaria for example is used classical scheme for ores mining and enrichment to produce concentrates which are subject of subsequent processing by pyro- and hydrometallurgical methods. Under this scheme produced metals are suitable for broad industrial use. These metals do not meet the special requirements for high-tech production.

Research on existing primary and technogenic raw materials for obtaining non-ferrous and rare metals (such as copper, cobalt, molybdenum, tungsten) is made and going technologies and contemporary methods for obtaining such metals according the ecological effect of using electron beam method as a final stage in treatment for obtaining high-purity metals, raw material choosing and technological schemes for their processing are presented. Electron beam technologies are a strategic method in the R&D and they are used in more applications in the industry in the industrial-developed countries.

Keywords: PRIMARY AND TECHNOGENIC RAW MATERIALS, NON-FERROUS METALS, RARE METALS, ELECTRON BEAM METHOD

1. Увод

През последните десетилетия се наблюдава устойчив растеж на търсенето на много чисти цветни и редки метали с широк спектър на приложение като компоненти в батерии, катализатори, специални сплави, металокерамики, алтернативни енергийни източници, високотехнологични продукти в електрониката, транспорта, медицината, военната, петролната, химическата, леката промишленост, приборостроене и др.

Оказва се обаче, че световните минерални запаси на редица метали, използвани във високотехнологичните производства (смартфони, инфрачервени оптични уреди, уреди за медицинска образна диагностика и много други) се характеризират с висока скорост на изтощаване [1]. По-голяма част от тях са с висока стойност на *индекса на използване на запасите* (ИИЗ, %). Например, ИИЗ за феросплавните метали волфрам и молибден съответно е 2.88% и 1.51%; за цветните метали мед, олово, цинк и бисмут съответно е 2.69%, 5.48%, 5.41% и 2.76% и за благородните метали злато и сребро съответно е 5.44% и 4.74%. Посочените стойности на ИИЗ говорят за висок риск от изтощаване на световните им минерални ресурси.

Изследване на експерти от Университета Йейл [2] показва, че съществува дисбаланс между предлагането и търсенето, т.н. критерий „критичност“ за 62 от най-използваните метали, като поне 33 от тях се използват за производството на печатни платки. Металите, традиционно използвани в производството, като цинк, мед и алуминий, не са изложени на този риск, но по-новите или по-рядко срещани метали като кобалт, волфрам,

молибден, хром, ниобий, използвани в производството на смартфони, инфрачервени оптични уреди както и в уреди за медицинска образна диагностика, обаче, са сред най-уязвимите. Тези метали се срещат почти изцяло само като странични продукти на други металургични производства. Не може да се организира добив само на такива метали. Те често съществуват в малки количества и се използват за специални цели и за тях няма равностойни заместители.

От 2008г. в Европейската комисия е създадена и действа политика за осигуряване на суровините. Във връзка с това е изготвен списък, включващ 20 критични материала – предимно метали (антимон, берилий, хром, кобалт, коксуващи въглища, флуорит и др.), които се внасят изключително от страни извън съюза. Това създава голям риск от недостиг на тези метали и зависимост от производителите-монополисти, извън Европейския съюз (Китай, Русия). В най-добрия случай, за някои от металите държави от Европа със суровини и производство за тях могат да осигурят до 10% от потребностите, но има и немалко метали, при които тази възможност е под 1%. Важен момент при решаване на проблема е в производството на тези метали да се използват както първичните рудни суровини, така и попълното им извличане при производството на мед, олово, цинк, които са основни продукти и на българската цветна металургия. Огромен потенциал за покриване на голяма част от нужните метали се крие в рециклирането (повторното използване) на електронния и битов скрап [3-6].

Изключителен и уникален потенциал има България в производството на първични суровини на някои феросплавни

метали като молибден, волфрам, манган, които са в ранен стадий на разработка. Например, годишното производство на волфрам в света е приблизително едва 90-95 хиляди тона. Неговото приложение е изключително важно в производството на специални стомани и сплави, за отговорни машини и апаратури, в електронната и електротехническата промишленост. Монополно положение в производството му има отново Китай (85%) [3].

Съществена възможност за българско участие в Инициативата за суровините на ЕС е рециклирането на редки метали от амортизирани електрически и електронни изделия и батерии. В това отношение Европа си поставя много амбициозна цел – до 2020 г. да се достигне 85% събираемост на отработени електронни, електрически и битови съоръжения, което означава, че ще бъдат събрани до 12 млн. t ресурс. В момента, рециклирането на тези ресурси е изключително подценено. Няма строга система за събиране, контрол, еколого-икономически целесъобразно утилизирание. Обикновена практика е, ако нещо е събрано, то или се изнася, или не е ефективно да се преработва.

Добра възможност за успешно реализиране на условията за участие на България в Инициативата за суровините на ЕС, е проучване и анализиране на съществуващите първични и техногенни суровинни източници и действащи съвременни технологии за добив на цветни, редки и високотемпературни метали и сплави, провеждане на изследвания и разработване на ефективни и екологично целесъобразни технологии за тяхното извличане (вкл. и рециклиране), прилагайки електроннолъчев метод като етап от преработката за получаване на свръхчисти метали. Чрез активна инвестиционна политика да се изгради необходимото оборудване за реализирането на тези технологии, което ще е принос за европейската и българската икономика, създаване на работни места и възможности за развиване на промишлени дейности, без да се вреди на околната среда.

2. Методи за получаване на цветни и редки метали

Класическата схема за производство на цветни и редки метали е добив на руди, обогатяване до получаване на концентрати и последваща преработка чрез пиро- и хидрометалургични методи. По тази схема се произвеждат метали за масова промишлена употреба. Тези метали не отговарят на изискванията за висока чистота при използването им в специализираните високотехнологични производства. Обикновено такъв тип метали се получават чрез сложни комбинирани схеми, включващи редица физични и химични технологични методи (ФХТМ) за пречистване на получените по традиционните методи метали.

Поради високата им температура на топене, класическата схема за получаване на металите молибден и волфрам включва редукция на техни оксиди до метален прах, който се превръща в компактен метал чрез спичане по праховометалургичен метод. С появата и развитието на сравнително новите методи на вакуумната електрометалургия, компактен метал се получава и чрез вакуумни електродъгово и електроннолъчево топене.

Използването на електроннолъчевия метод за топене и рафиниране (ЕЛТР) при преработката на суровинните източници на цветни, редки и високотемпературни метали, като краен етап за получаване на високо чисти метали, елиминира редица междинни технологични процеси, някои от които неекологични и вредни за околната среда и хората. Тези технологии са стратегическо направление на научно-техническия прогрес и намират все по-широко приложение в индустрията на напредналите индустриални страни [7-14]. Електроннолъчевата технология за топене и рафиниране на метали и сплави е екологично чиста и безотпадна и би

осигурила обезгазяване и по-висока степен на очистиране (от газове, метали и неметални примеси), както и еднородност на химическия състав и оптимална структура на получените нови материали - хомогенна микроструктура, без дефекти, без голямо разсейване и равномерно разпределени примеси, с подобрени работни характеристики, магнитни и съпротивителни свойства. Методът дава възможност такива метали и сплави да бъдат получавани както от преработка на природна суровина там, където я има, така и чрез рециклиране на отработени вече метали и сплави при липса на природен ресурс. Актуалността на проблема се определя и от възможностите, които електроннолъчевият метод дава за получаване на нови материали, а именно метали, сплави и полуфабрикати с нови или подобрени химичен състав, структура и свойства.

В България съществува дългогодишна традиция в обогатяването на първични и техногенни суровини, за добив на цветни и благородни метали. Съвременен направление е прилагането на хидрометалургични методи (ХММ) за преработка на минерални суровини, съдържащи трудноподобими и цветни метали. ХММ в едни случаи се прилага до получаването на концентрат, който е изходна суровина за следваща преработка, а в други до получаване на краен продукт.

В България е натрупан огромен опит в обогатяването, предимно флотационно, на първични (рудни) суровинни източници на мед, в които съдържанието на мед обикновено варира от 0.2% до 1.4%. При преработката им се получават концентрати със съдържание от 22% до 25%, които след това се подлагат на пирометалургична преработка с получаване на черна и катодна мед с чистота съответно 99.5% и 99.98(9) %. В последните 30 години за преработка на оксидни и вторичносулфидни медни руди се използват и хидрометалургични методи – сяроукисело излужване, течна екстракция и електроутаяване, с което се достига краен продукт катодна мед с чистота не по-висока от 99.99%. Като съпътстващи метали също се получават молибден при преработката на медно-молибденови руди и кобалт при преработката на медно-никелови и никелови руди.

Съдържанието на молибден в медно-молибденовите руди е около 0.04%. Обикновено в кристалната решетка на молибденита (основния молибденов минерал) се съдържа и рений. Чрез флотация се получава концентрат със съдържание 48-50% молибден. От този концентрат се получава технически молибденов оксид (>57% Mo), феромолибденит (60-70% Mo), молибдати, от които след това чрез редукция в присъствието на водород се получава молибден в метална форма.

Комплексната технология за преработка на Mo концентрат с получаване на соли на Mo, Re и Cu, която е създадена през 80-те години на 20 в., е действаща и до днес. Тя е неекологична, тъй като за разлагането на изходната суровина се използват киселини. Като краен продукт се получават Mo разтвори, от които чрез допълнителна селективна преработка се получават MoO₃ (>99.5%), катодна Cu и амониев перренат.

Тази технология е силно токсична и вредна за околната среда и за здравето на хората, а получените крайни продукти са недостатъчни като количество и качество да задоволят съществуващия интерес от външни за България потребители. Съществува натрупано голямо количество молибденсъдържащ отпадък у нас, който остава необработен и неизползван.

Утвърден метод за получаването на технически чист метален молибден и волфрам и при производството на твърди сплави на тяхна основа е праховометалургичният - като първоначално металните прахове се получават чрез редукция на тяхно съединение, обикновено оксид, в атмосфера на водород (Таблица 1) [15].

При получаване на прахообразен волфрам могат да бъдат използвани различни редуктори като водород, въглерод, силиций или металите алуминий, натрий и др. Редукцията протича при сравнително ниски температури (800 – 1200 °C). Най-утвърдени за практиката са редукционните процеси, протичащи по реакциите, представени в Таблица 1.

Поведението и свойствата на компактният метал при следващите етапи на обработка силно зависят от химическия състав и структурата (включваща големина и форма на частиците, разпределението им по размер) на получените метални прахове. Структурата на металните прахове зависи от структурата на изходните съединения и от редукционния режим.

Полученият метален прах се обработва до компактен метал чрез праховометалургичен метод, който включва следните етапи:

- пресоване на металните прахове като брикети, шайби или с форми, близки до вида и размерите на металните изделия след процеса на спичане;
- спичане на заготовките чрез нагряване до определена температура;
- допълнителна обработка (коване, изтегляне, валцоване) на спечената заготовка до крайно изделие.

Тези съвременни технологии за преработка на молибден и волфрам не осигуряват на метала достатъчно добра пластичност и способност да се заварява. Физико-механичните свойства на молибден и волфрам, получени чрез спичане, са твърде анизотропни и зависят от изходното състояние, чистотата и структурата на праховете преди спичане [16]. Металът, получен след редукцията, е с висок процент от метални и газови примеси. Необходимо е той да бъде подложен на допълнително рафиниране. При промишленото производство на чисти волфрам и молибден, както и на техни сплави, в страни като САЩ, Украйна, Русия и други, за допълнително рафиниране са се наложили методи като вакуумно-дъгово топене (ВДТ) и електроннолъчевево топене (ЕЛТ).

При ВДТ изходните материали се топят в електродъгови пещи с изразходващ се електрод във вакуум или в среда от аргон, в меден водоохладен кристализатор или в тигелни пещи с меден или графитов тигел. Особеност при топенето на молибден в електродъгови пещи е, че се налага допълнителна дезоксидация на метала с въглерод, водород или алуминий. При редукция с алуминий, топенето се осъществява в среда от аргон, а във вакуум протича редуцирането на молибден с въглерод или водород.

Най-перспективен метод за топене на молибден и волфрам и негови сплави е електроннолъчевото топене във вакуум, при което се получава метал с най-ниско съдържание на примеси. През последните години страните с развиваща се атомна енергетика и аерокосмическа промишленост (Индия, Китай и др.) проявяват голям интерес към тези технологии и се наблюдава висок ръст в конструирането и успешната експлоатация на оборудване за ЕЛТР. Успешни научни изследвания в тази област се провеждат и у нас [17-19,4,20-21,6].

Кобалтът е скъп метал със свойства, сходни с тези на никела. Той добре се сплавя и заедно с Fe, Cr, W и Mo под формата на ценни износостойчиви сплави се използва в инструменталната промишленост за изработката на режещи и пробивни машини. Като легираща добавка кобалтът увеличава топлинната устойчивост на високотемпературните стомани и ги прави по-устойчиви от хром-никеловите сплави. Постоянни магнити, изработени от кобалт или негови сплави с платина имат най-добри магнитни показатели. Особено важно приложение на кобалта, което повиши многократно търсенето и цената му на международните пазари в последните години, е

при производството на литиево-йонни батерии, които захранват всичко – от електромобили до продукти на Apple. По тази причина пазарът на кобалт се е удвоил за една година – от 4 млрд. на 8 млрд. щатски долара (според Bloomberg), а цената му през 2017г. е нараснала със 120%. Очакванията на Benchmark са, че през 2018 г. цените на кобалта ще продължат да се покачват, макар и с по-бавни темпове.

Метален кобалт се получава чрез редукция на негови оксиди. Като редуктори могат да бъдат използвани въглерод, водород, въглероден оксид и метали (алуминий, цинк, кадмий). В Таблица 1 са представени различни технологични схеми за получаване на метален кобалт.

След редукция с въглерод металният кобалт се отделя от нереагиращия въглерод чрез магнитна сепарация. Оксидът и въглеродът могат да се смесят, брикетират и да се използват като електроди на волтова дъга. При протичането на електрически ток електродите се стаят, а редуцираният метален кобалт се стича в тигел и се събира под шлака от калциеви и силициеви оксиди, за да не се окисли отново.

Таблица 1: Редукционни металургични методи за получаване на чисти метали от техни оксиди.

Редуктор	Me	Реакция	Техн. условия
C	W	$2WO_3 + 3C = 2W + 3CO_2$	800–1200 °C
C	Co	$2Co_3O_4 + 4C = 6Co + 4CO_2$	60min/900 °C 10min/1000 °C
H ₂	W	$WO_3 + 3H_2 = W + 3H_2O$	800 – 1200 °C
H ₂	Co	$Co_3O_4 + 4H_2 = 3Co + 4H_2O$	190 – 250 °C
CO	Co	$Co_3O_4 + 4CO = 3Co + 4CO_2$	300 – 750 °C
Al	Co	$3Co_3O_4 + 8Al = 4Al_2O_3 + 9Co$	2100 °C
алумотермия			

Когато за редуктор вместо въглерод се използва въглероден оксид, реакцията започва още при 300 °C, а при 500 – 750 °C протича интензивно и за няколко минути се редуцират 90% от изходния оксид. Останалите 10% обаче, реагират твърде бавно дори при температура 900 °C.

При редукция с водород реакцията протича на степени като с повишаване на температурата първо се образуват нисши оксиди, които при допълнително загряване се редуцират до метал.

Методът за получаване на кобалт чрез редукция с други метали (цинк и кадмий) е известен като цементация. Металният кобалт се извлича от разтвори на негови соли чрез заместването му в съединенията от цинк или кадмий. Като катализатори за ускоряване на процесите се използват соли на мед и олово. Реакцията протича при ниска температура в слабокисела среда.

Друг начин за получаване на метален кобалт е чрез електролиза на амониеви или нитратни разтвори на кобалтови соли. Изходният материал е кобалтов извлек със съдържание на Co 98.4-98.7%, който се включва като анод, а чистият електролитен кобалт се отлага върху въртящ се катод от неръждаема стомана. Върху повърхността на металния кобалт се образува оксиден слой със съдържание на оксиди 0.28%, който лесно може да бъде отстранен чрез нагряване до червено в поток от водород. Смята се, че този метод е подходящ за получаване на чист кобалт в големи количества.

Поради изключителното търсене и нарастване на нуждите от кобалт с висока чистота непрекъснато се търсят начини за подобряване на технологиите и усъвършенстване на оборудването, които да повишат производството на кобалт, степента на извличането му от природните суровини, понижаване на производствените загуби и пълно оползотворяване на техногенни материали, получени по целия производствен процес. Например, като изходен материал за производство на кобалт може да се използва електролизен

концентрат със съдържание на Co 15-16%, в който да има още 1.3 – 1.6% Ni, 2.5-3.0% Fe и се съдържат още Cu, Mn и други метални примеси. Чрез постепенно намаляване киселинността на средата и регулиране количеството на въздух в системата последователно се окисляват, утаяват и отделят металните примеси Fe като FeO (при pH 3.5-4.5), Cu като CuO (при pH 6.0 – 6.7), Mn като хлориди, сулфиди и сулфати, докато се получи утайка, в която се съдържа 95% от първоначалното количество кобалт под формата на хидроксид.

Голямо количество кобалт се получава при преработката на медно-никелови и никелови руди. Съдържанието на кобалт в никеловите руди е 3-10% от съдържанието на никел. При обработката на сулфидни медно-никелови руди до 95% от кобалта преминава в медно-никеловия щейн и след неговото конвертиране 60-70% Co преминава в конверторната шлака (главно в последните разливи), която е изходна суровина за извличане на кобалт. Установено е, че при разделителното топене на медно-никелов фийншейн 70% от кобалта преминава в никеловия полупродукт (bottom), а 30% от кобалта – в медния полупродукт (top). Така в процеса на преработка на сулфидни медно-никелови руди се получават три полупродукта, които могат да бъдат суровина за производство на кобалт:

- конверторни шлаки – 50% от цялото количество Co;
- шлаки от продуктите на медния полупродукт;
- утайки от очистката на никеловия полупродукт.

От направения анализ за получаване на редки и цветни метали е установено, че:

– от съвременните металургични методи, като достатъчно ефективни за рафинирането на тази група метали са се наложили “праховата металургия”, електролиза на соли, металотермично йодидно рафиниране и някои от методите на специалната електрометалургия като плазменодъгово топене (ПДТ), вакуумно индукционно топене (ВИТ) и електроннолъчево топене (ЕЛТ), които се прилагат успешно в металургичната практика по света. Между изброените методи като беспорен лидер се е доказал ЕЛ метод за топене и рафиниране във вакуум;

– за страни като България, които не произвеждат тези метали поради липса на суровина, особено важно е да бъдат максимално използвани всички налични отпадъци от тях;

– за да бъде конкурентноспособно регенерирането на неголеми количества скъп метал, е необходимо максимално приближаване на състава и качеството на регенериания метал до конкретните нужди на потребители или предлагане на нови материали - нови сплави с достатъчно висок клас чистота.

3. Техногенни материали, съдържащи цветни и редки метали в България

На територията на България съществува наличност от отпадъци, съдържащи цветни, редки и високотемпературни метали и техните сплави, натрупани в резултат от нормална практика за депониране на производствени отпадъци в работещи предприятия и от спрени производства или закрити предприятия. Такива отпадъци се отделят и в резултат на нормалната производствена дейност на функциониращи предприятия.

В резултат от проучване и анализ на наличните в страната метал-съдържащи отпадъци е установено, че те са главно под формата на прахове и късове; отработени катализатори от химическата и хранително-вкусовата промишленост; стружки и малки парчета от молибден, волфрам, волфрамов карбид – отпадък от военно-промишления комплекс; отпадъци под формата на шлаки; скрап от претопяването и рафинирането на метали в спрени производства или закрити металургични предприятия; отпадъци от използвани инструменти, части от зъбни протези и импланти в медицината и стоматологията, които съдържат молибден, волфрам, кобалт, хром, титан; от производството на лекарства; изхабени твърдосплавни

пластини, съдържащи волфрам, молибден, кобалт и цирконий - отпадъци от металообработващата промишленост; морално остарели и дефектирали електронни елементи, съдържащи тантал, кобалт, волфрам и цирконий - отпадъци от електронната промишленост и електротехниката и др. Рециклирането на отработени метал-съдържащи отпадъци чрез претопяване в електродъгови и електроннолъчеви вакуумни инсталации е значително по-екологично, по-икономично и икономически издържано решение (няма да се разпилява наличния ресурс) в сравнение с наложилата се от години практика за депониране на отпадъците в сметища. Очакваният екологичен ефект от рециклирането на отпадъци, съдържащи редки и цветни метали ще бъде изразен главно в:

- освобождаване на площи, заети от отпадъците, за други дейности за рекултивацията им, с последващо използване;
- неутрализация на токсични вещества;
- рециклиране на ценни метали, съответно намаляване на производството им от руда и на съответните съпътстващи замърсители на околната среда.

4. Заключение

Анализирани са действащи технологии и световния опит по съвременни методи за извличане на редки и цветни метали като мед, кобалт, молибден, волфрам и др. от първични и техногенни суровинни източници с оглед на екологичния ефект от прилагането на електроннолъчевия метод. Резултатите дават основание да се определят като подходящи, поради високата им екологичност, методи за рециклиране на разглежданите материали, съдържащи цветни, редки и високотемпературни метали, чрез топене в електродъгови и електроннолъчеви пещи. Предимство на методите са възможностите, които те дават за получаване на нови материали - метали, сплави и полуфабрикати - с нови или подобрени химичен състав, структура и свойства. Електроннолъчевите технологии са стратегическо направление на научно-техническия прогрес и намират все по-широко приложение в индустрията на напредналите индустриални страни. Те са възможно добро решение за повишаване екологичността, производителността и качеството на крайния продукт, ако са приложени като краен етап за получаване на свръхчисти метали, подбора на изходни суровини и технологични схеми за преработката им. Разработването на технологии за получаване на цветни и редки метали и сплави с висока чистота по електроннолъчев метод е ефективно и екологично целесъобразно и изследванията в тази област са актуални за успешното им извличане и по-широкото им приложение.

Благодарности

Работата е реализирана с финансовата подкрепа на Националния Фонд „Научни изследвания” по договор ДН17/9.

Литература

- [1] Ковачева В., В. Велев, Съвременни аспекти за устойчиво развитие на минералните ресурси, Сборник с доклади от Трета национална научно-техническа конференция Минералните ресурси и устойчиво развитие, НТС по Минно дело, геология и металургия, 23 Ноември, 2017, стр.26-34.
- [2] www.economic.bg/bg/news/7/nyakoi-redki-metali-v-smartfonite-sa-na-izchezvane.html
- [3] www.capital.bg/biznes/kompanii/2014/11/24/2425619_bulgariai_moje_da_stane_evropeiski_igrach_na_pazara_na/?sp=1#storystart
- [4] Vutova, K., V.Vassileva, E.Koleva, E.Georgieva, G.Mladenov, D.Mollov and M.Kardjiev, Investigation of electron beam melting and refining of titanium and tantalum scrap, J. Mater. Process. Techn., (210), pp.1089–1094, (2010).
- [5] Roemer, F., Elwert, T., and Goldmann, D., Challenges and a possible solution for the recycling of tantalum from waste electrical and electronic equipment, IMPC 2016: XXVIII International Mineral Processing Congress Proceedings, pp.1-10, ISBN: 978-1-926872-29-2.

- [6] Vutova K., V.Vassileva, E.Koleva, N.Munirathnam, D.Amalnerkar, T.Tanaka, Investigation of Tantalum Recycling by Electron Beam Melting, *Metals*, 6, 287; pp.1-13, doi:10.3390/met6110287, (2016).
- [7] Zhao Y.Q., P. Ge, "Current situation and development of new titanium alloys invented in China", *J. Aeronautical Mater.*, vol. 34, 51e61, (2014).
- [8] Electron Beam Melting – EBM Process, Additive Manufacturing |Arcam AB, <http://www.arcam.com/technology/electron-beam-melting/> (Accessed 5 May 2017).
- [9] Grechanyuk M.I., A.G.Melnyk, I.M.Grechanyuk, V.G.Melnyk, D.V.Kovalchuk, „Modern electron beam technologies and equipment for melting and physical vapor deposition of different materials”, *Electrotechnica and Electronica*, v.49 (5-6), pp.115-125, (2014).
- [10] Wang, Z.; Li, J.; Hua, Y.; Zhang, Z.; Zhang, Y.; Ke, P. Research progress in production technology of titanium. *Chin. J. Rare Met.*, 38, pp.915–927, (2014).
- [11] Sankar, M.; Mirji, K.V.; Prasad, V.V.; Baligidad, R.G.; Gokhale, A.A. Purification of Niobium by Electron Beam Melting. *High Temp. Mater. Process.*, 35, pp.621–627, (2016).
- [12] Tan, Y.; Shi, S. Progress in research and development of electron beam technology in metallurgy refining field. *J. Mater. Eng.*, 8, pp.92–100, (2013).
- [13] You X.G., Y. Tan, Q.F. You, S. Shi, J.Y. Li, F. Ye, X. Wei, "Preparation of Inconel 740 superalloy by electron beam smelting", *J. Alloys and Comp.* vol. 676, pp.202-208, (2016).
- [14] Long, L.; Liu, W.; Ma, Y.; Liu, Y.; Liu, S. Refining tungsten purification by electron beam melting based on the thermal equilibrium calculation and tungsten loss control. *HighTemp. Mater. Process.*, 34, pp.605–610, (2015).
- [15] Morales R., R. E. Aune, O. Grinder, S. Seetharaman, The Powder Metallurgy Processing of Refractory Metals and Alloys, *JOM*, 55 (10), pp.20-23, (2003).
- [16] Мушегян В.О., Электронно-лучевая плавка восстановленного концентрата молибдена, *сп.Современная Электрометаллургия*, 4 (97), стр.26-28, (2009).
- [17] Vassileva V., K.Vutova, G.Mladenov, An Investigation on the Heat Transfer Influence on the Crystallisation Processes during the Electron Beam Melting and Casting of Metals, *Vacuum*, 62, pp.197-202, (2001).
- [18] Vassileva V., G.Mladenov, K.Vutova, T.Nikolov, E.Georgieva, Oxygen removal during electron beam drip melting and refining, *Vacuum*, 77, pp.429-436, (2005).
- [19] Vassileva V., K.Vutova, G.Mladenov, Analysis of the thermodynamic conditions of refining during electron beam melting of refractory metals, *Materials Science and Engineering Technology*, 37 (7), pp.613-618, (2006).
- [20] Vutova K., Donchev V., Vassileva V., Amalnerkar D., Munirathnam N., Prakash T. Application of non-stationary thermal model for simulation and investigation of heat and refining processes of Ti during EBMR, 2013 EPD Congress, TMS2013, Wiley, pp.253-260, (2013).
- [21] Vutova K., V.Donchev, V.Vassileva, G.Mladenov, Thermal processes in electron beam treatment of metals, *Journal Metal Science and Heat Treatment*, v.55, iss.11-12, pp.628-635, (2014).

MODELLING CONCEPTS FOR EFFICIENT PORT LOGISTICS MANAGEMENT

Senior Assistant Prof. PhD Varbanova A.
Faculty of Shipbuilding – Technical University – Varna, Bulgaria

anneta_varbanova@hotmail.com

Abstract: Port logistics is a vital element of international shipping and logistics management. The type and scope of port management influences the overall functioning of the international supply chains. Modern approaches for supply chain management, efficient business processes control and information exchange, based on advanced technology, are to be considered synchronously. The present article analyses the organization of port management processes, its components and the information flows with business stakeholders. The proposed conceptual model aims at improvement of port management performance in terms of logistics management, integration and mainstreaming of business processes.

Keywords: MANAGEMENT PERFORMANCE, KEY PERFORMANCE INDICATORS, PORT LOGISTICS

1. Introduction

Maritime ports are vital part of the international supply chain, logistics systems and serve as main connectors between maritime operations and hinterland systems. To improve ports' competitiveness, port management focuses on customer needs, provides value-added services and aims at decrease of costs to achieve higher levels of efficiency. The relationship between global supply chain management and port logistics management requires profound analysis of port logistics business processes. The port enterprise is facing the increasingly complex international trade patterns, the requirements of global terminal operators and transportation companies and other strategic behaviors, which demand integration of inland transport and port logistics system [5]. Establishing management frameworks for improved port logistics performance increases the port enterprise competitiveness. The proposed modelling concepts are based on the quality management theory. The basic elements of quality management system include various components and processes. Strategic planning and operational control are vital for ensuring of efficient quality management practices via cost reductions and increased production efficiency. The present article analyses the structure of port management processes, its components and the processes within the port enterprise. The proposed conceptual model aims at improvement of port management performance in terms of logistics management, integration and mainstreaming of business processes with stakeholders.

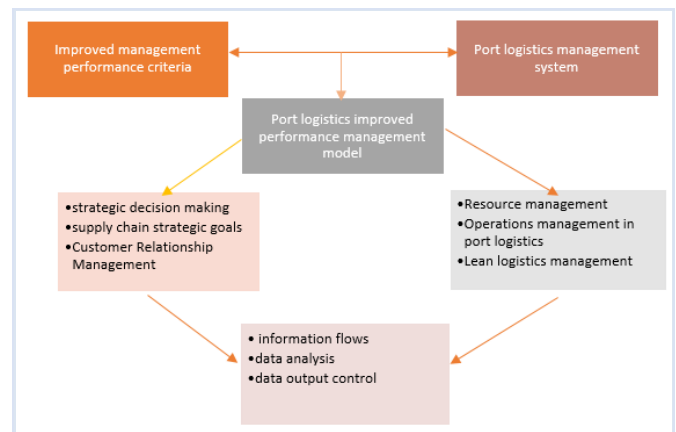
1. Conceptual model for improved port logistics management

Port logistics management is generally focusing on customers and is based on strategies setting efficiency goals both for costs efficiency and time costs reduction. Application of information systems allows for continuous improvement of the system functioning. Effective resource management and the systematic approach to port logistics management require application of certain approaches for optimization of internal processes and production of value-added services. Management of information flows allows for analysis and control at operational level, collecting of data and using data analysis for strategic purposes. Self-assessment procedures, along with the established quality system of the port enterprise, are also factors for improved port logistics management. According to [4] the terminal supply chain integration model is an empirical structural model which includes information and communication systems, value-added services, multimodal systems and operations, supply chain integration practices and other measurement variables [4].

There are several criteria for assessment and development of improved port logistics management model. Strategic decision-making process, linked with supply chain strategic goals are the prerequisite for efficient customer relationship management. On the

other hand, efficient resource management ensures for improved operations management of port logistics processes. Therefore, the core process of resources allocations, management of business processes and achievement of results set the backbone of the port logistics management. Information flows implementation via ICT, data analysis and data output control are the link between the three elements of the core processes. (Figure 1).

Figure 1: Main processes of improved performance model of port logistics management system



Strategic decision system ensures for the establishment of modern port logistics management system. Specific objectives at strategic level and their achievement allow for building of integrated business processes flows as the basis of the decision-making process at management level.

Port enterprises strategic and operational objectives management should be focused on efficient customer relationship management. The latter includes optimization of internal processes according to customer needs, identification of customer values and demand, establishing of certain brand services pertaining to the specific port. Adoption of certain methods for evaluation of customer demand and customer criteria for improved services is part of the overall management system. Port services, standardized by default, should achieve higher level of differentiation to allow for overall efficiency of the customer relationship management processes.

Port logistics system's functioning is based on the available resources – investments, human capital, port infrastructure and superstructure, along with logistics information flows. Strategic goals for resources management in port logistics include establishment of logistics management platform, improvement of the financial control system and corporate investment processes.

Operations management is vital for the logistics systems management. Process management should be based on the total production management concept, forming lean logistics management model basis information technologies for improved model for process management [2].

3. Application of key performance indicators in port logistics management

The established in management theory performance indicators serve as a tool for comparison of performance, provide information of the enterprise functioning and are the basis for establishing relations with the business stakeholders. These indicators are often widely used by publicly owned enterprises to ensure for expenditures transparency. Performance indicators are grouped according to the business processes analyzed. Indicators quantifying output, however, are not very precise in providing information on the businesses processes flows. In the long term, port performance indicators provide a valuable tool for analyzing the factors affecting the port logistics system operations. Furthermore, port management reports to external stakeholders are based on analysis of port performance indicators.

Due to the specialization of port logistics system it is necessary to distinguish between several groups of port products [3]:

- cargo handling and cargo transfer, whereas this type of product is related to handling of ships and providing services to shipping companies;
- logistics product, encompassing warehousing activities, value-added services, cargo inspection, etc. and all activities being focused on logistics companies and forwarding companies;
- port manufacturing product, which includes provision of infrastructure and superstructure for investment in production facilities by international companies.

As ports are the intersection of transportation flows, the cargo handling product is of highest importance. The latter includes operations such as cargo handling, customs procedures, tug services, pilotage, etc. and all activities necessary for the loading and discharging processes to and from vessels and other types of transportation units.

For provision of value-added services many European ports develop logistics centers in close vicinity for optimization of global supply chains cargo flows. As port management strategies include expansion of logistical processes this product allows for higher competitiveness of the port enterprise. As for the port manufacturing product, same refers to specific production activities located within the port premises depending on the types of cargo flows. This product required higher level of external investment and joint ventures with stakeholders thus ensuring for wider variety of added-value services.

The above should be considered interdependently although port users and clients set different requirements for specific port services. The latter is the reason for unbalanced port product portfolio for the medium-sized ports in Europe whereas different ports offer products mainly within a single scope. Table 1 provides a resume of the most important elements of port products.

For the purposes of more detailed analyses of the port logistics performance, specific performance indicators are developed. It should be noted that direct comparison of values of certain port performance indicators of different ports is not precise due to the different market positions of the ports and the scope of port products. Therefore, the internal structure of port performance indicators ensures for provision of a detailed information which is used also for strategic and operational purposes.

Performance indicator	Port performance indicator
Output indicators	* Volume of handled cargo * Added-value services * Investment scope and scale
Improvement indicators	* Market coverage of hinterland areas * Number of liner services * Value of goods handled by the port * Use of EDI
Operational indicators	* Extent of modal shift for hinterland traffic * Customs revenues * Competitiveness of port dues

Table 1. Port performance indicators (adapted from [3])

The volume of cargoes handled in ports is the most widely used port performance indicator. As a rule, the ranking of ports is based on the volumes of cargoes handled with differentiation by cargo type. The values of this type of port performance indicator describe the potential for port development. However, certain limitations apply as concerns volumes of cargoes handled in ports [3]:

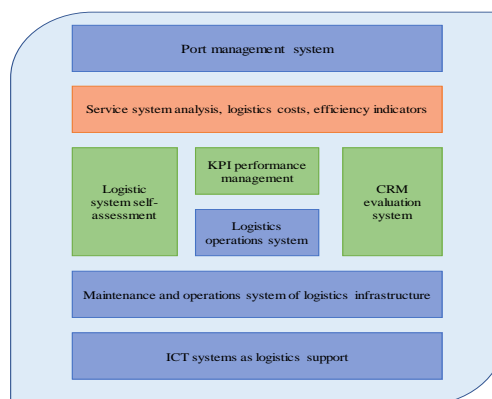
- aggregating the volumes of various cargoes into a single figure distorts the option for comparison of port production;
- volumes of cargo handled do not provide insights on the impact of the port in terms of global supply chains;
- the increase of volumes of handled cargoes is an outcome of global commercial flows and is not entirely based on the performance level of a certain port.

The value-added services port performance indicator quantifies the added value provided by the port activities. The latter indicator is applicable for the evaluation of port economic viability except for the port efficiency.

Market coverage of hinterland areas is achieved mainly via certain marketing strategies through external stakeholders. The attractiveness of the port as considered by major liner operators is based not only on the available infrastructure, allowing for efficient port operations, but on the availability of various added-value services offered. The application of electronic data interchange systems that are compatible with companies' information systems is considered a competitive advantage for the port. The application of port performance indicators is useful for measuring the port development scale and for comparison between ports.

The layout of the improved port logistics management system is presented in Figure 2. The performance management system should be improved based on the new system of port performance indicators. The indicators will allow for profound assessment and quantifying of the logistics system functioning.

Figure 2. Improved port logistics management system



The established logistics center will serve for self-assessment covering all operations. In this way the logistics processes efficiency assessment will be based on evaluation of processes architecture, distribution of responsibility, schedule for reverse response, tracing of bottlenecks and analysis of the results. The communication channels with customers will be improved along with implemented clients' surveys for creating feasible CRM evaluation system for quantifying the efficiency of the port logistics system from customers perspective. As for the cost efficiency, the proposed model structure for improved port logistics management will allow for higher level of analysis that is vital both for operations management and decision-making process at strategic level. Through the analysis of the performance results the pertinent problems can be identified and potential opportunities defined so as to create a well-structured framework for strategic development. The ICT system, as a supportive system for the entire port logistics system, should be further improved and updated.

4. Conclusion

The proposed modelling concepts for improved port logistics management describes a certain set of criteria for enhanced port management system being integrated with contemporary theoretical approaches for quality management. Based on the present article analysis, the improved performance model of the port logistics enterprise will enhance the competitiveness of the port logistics enterprise [1]. The regular internal quality system review ensures for identification of performance failures. The application of the improved port logistics management model will allow for the introduction of the lean logistics concept based on the results at operational level that will allow for analysis and improvement at strategic level. The marketing strategy of the port enterprise will be focused on customer relationship management and will improve the efficiency of the port logistics management. The present article has analyzed and defined the main priorities and concepts for designing of improved port logistics management system. The results show that new approaches are to be applied in port logistics management based on integration of business processes and efficiency of performance.

References

1. H. Chen, Y. Chen, 2016, The performance appraisal of port logistics informationization, International conference on Internet and Distributed Computing Systems, Springer International Publishing., 9, pp. 413-420
2. Jiang, H., W. Xiong, Y. Cao, 2017, Conceptual model of excellent performance mode of port enterprise logistics management, Polish Maritime Research, S3 (95), Vol. 24, pp. 34-40
3. Langen, P., M. Nijdam, M. Horst, 2007, New indicators to measure port performance, Journal of Maritime Research, Vol. IV. No. 1, pp. 23-36
4. P. M. Panayides, D.W. Song, 2008, Evaluating the integration of seaport container terminals in supply chains, International Journal of Physical Distribution & Logistics Management, 38(7): 562-584
5. J.P. Rodrigue, T. Notteboom, 2009, The terminalization of supply chains: reassessing the role of terminals in port/hinterland logistical relationships. Maritime Policy & Management, 36(2), pp. 165-183

3. Container supply chain security measures

Container supply chain security measures can be classified as follows:

- focusing on the monitoring of the container content;
- focusing on the containers integrity;
- aiming at the ensuring of safety of the environment during the transit and handling of containers;
- related to the monitoring of container transportation within the entire supply chain;
- ensuring and usage of supply chain information.

Being a complex structure, each container supply chain element is aiming at optimization of its own processes. According to the well known principle in logistics management, the aggregating of individually optimized relations in some cases results in non-optimal supply chain. Non-harmonized practices, incompatible operations and information management systems, uncoordinated regulations, both on national and international level, can lead to vulnerability of the security system due to lack of coordinated approach.

As concerns the security of physical flows the following should be considered:

- the containerization point is of prime importance as concerns security since it is the last point where the contents of the container can be visually identified and compared with the respective invoice or waybill. Until the moment of decontainerization all information regarding the content of the container will be evident only in the cargo documents (freight manifest, Bill of Lading, etc.)
- containers are most vulnerable when they are standstill which means that security measures are most important in those nodes where containers are being handled or stored;
- crossing of international borders includes extensive customs control that leads to potential delays;
- most of the containers traffic transits through at least one sea port which levels of security and relevant security measures are at a different level.

There are two major types of physical surveillance of containers: X-ray scanning (non-intrusive inspection) and direct physical examination. The latter usually involves at least 8-10 hours per container which can lead to potential delays for the entire delivery.

The Container Security Initiative is structured around the concept of “pushing the border back”, i.e. identifying the security risk at the point of origin and before shipment and serving as protection against pertaining risks during containers transportation. Presently, there are over 50 ports that have been approved for applying the Container Security Initiative (SCI) as shown in Figure 2.

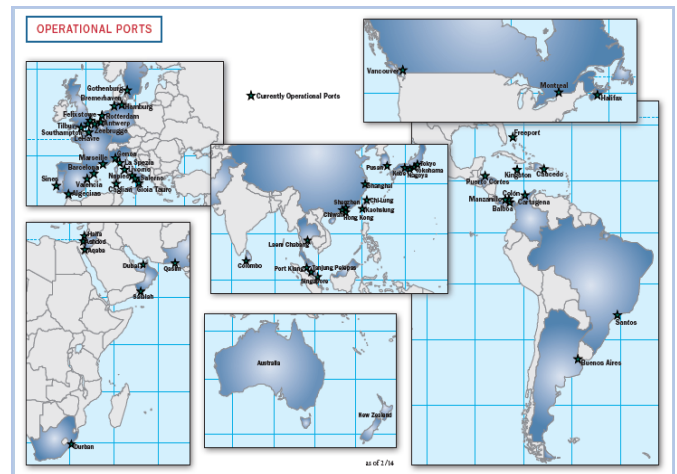
As of April, 2008 the European Union and the USA have signed an agreement for activation and expansion of cooperation in customs procedures and mutual cooperation as concerns containers security. The agreement concerns cooperation for ensuring of containers transportation safety and related issues and is applicable to all containers carried by sea, irrespective of their origin, that are imported, handled or transiting through EU and USA.

The container security initiative (CSI) consists of the following four elements:

- high-risk containers are identified via automated information;
- containers are pre-screened for high-risk identification;
- usage of special equipment for detection and screening of high-risk containers ensuring of inspections without delay;

- usage of smarter containers that are tamper-proofed [6].

Figure 2. Ports, applying the Container Security Initiative [6]



The “24-Hours Rule” is based on automated information for identification of higher risk containers. As of 2002, all carriers are obliged to submit electronic cargo manifest to the US Customs before cargo loading. The mentioned rule is also applicable to transit and empty containers as well as bulk and conventional general cargo shipments. The cargo manifest is the document that legalizes any cargo carried by a seagoing vessel and contains information about the shipper, consignee, notify party, port of origin, port of destination and cargo description. In this way customs authorities are closely monitoring the shipment content along with the time periods needed for the container transportation. The container is being tracked if risk is identified or dangerous goods are carried in the container. The mentioned information, transmitted electronically, is used both for exports and imports. It is the responsibility of the carrier to ensure for information provision which is accurate and complete and is submitted at the required time. Some states do not disclose information contained in cargo declarations for security reasons until the process of cargo manifest filing is completed – the relevant information might be published only after loading is completed and the vessel has left the port.

Screening systems usually use x-rays, gamma-rays machines and GPS. The mentioned technology allows for fast inspection without delay apart from the technological time needed for the screening. This type of equipment can identify specific materials which can potentially pose a risk to the environment.

4. Cost analysis of container supply chain security measures

The costs pertaining to the implementation of security measures can be indirect and direct. The latter are the capital costs, necessary for the design and implementation of the security network:

- purchase of new equipment for physical structure protection;
- adoption and/or implementation of security regulations;
- implementation of security policies and regulations;
- employment of trained security personnel.

Costs that are classified as indirect are the costs related to the system operations: equipment maintenance, application of efficient management strategies, response costs to incidents, costs related to management and operations recovery and reconstruction of infrastructure.

For the ocean carriers the costs include the following elements [1]: costs for setting up a new system for documentary transactions, costs for increased communication, personnel training, increased labor costs (cargo handling and inspection, operations of special equipment), usage of security-related equipment. For example, vessels are equipped with Automatic Identification System (AIS). Carriers also use software for monitoring and tracing of container movements for preventing incidents and illegal actions. As for specific technologies being used - Global Positioning System (GPS), Radio Frequency Identification (RFID) and electronic seals of containers also enhance the tracking of containers. It could be necessary that special security equipment is installed on board the vessels to enhance the global security measures.

The costs of security measures that impact the entire container supply chain are related to:

- time delays due to security inspections, whereas the costs will be higher at the very beginning of the transportation process; delays in the delivery time will eventually lead to penalties to parties and/or damages due to decreased cargo quality;

- costs for providing cargo manifest in advance, whereas this requirement is based on the “24-Hours Rule”; although the information contained in the manifest is not disclosed at an early stage same could be used for illegal purposes and losses related to the latter are borne by several participants in the supply chain;

- the introduction of additional state taxes related to the design and maintenance of the security infrastructure and equipment;

- increased insurance premiums despite the applied new security systems on board ships and in ports.

In addition to the expected higher revenues, the most important benefit from increased security measures is the increase of cargo flows to and from ports applying higher security level system.

Risk analysis and risk management, performed by the various participants of the container supply chain, will enhance the evaluation of potential gains and reduce the cost of investments. Decision makers are to explore the fixed costs for application of the international regulations, increase costs for communication exchange along with increase of operational expenses, inspection and personnel training costs. It should be noted that the economic benefits of increased security measures for container supply chains are more evident in the long run therefore strategic management is to implement such measures.

According to [3] the cost benefit analysis of a new automated cargo manifest estimates direct saving to American importers only at USD 22.2 billion over 20 years and savings of USD 4.4 billion for the American government over the same period.

The CSI requires that all foreign states invest in special equipment (screening, detection) and provides guidance to port management via trained personnel. However, recent evaluations have shown that the overall costs of increased security measures will be borne by the clients and will be calculated as additional costs per container. Depending on the type of port management, the state or the municipality will initially invest in the required special equipment which returns are calculated on the basis of increase of prices for shippers, carriers and port services and, finally, of the final prices of goods.

Given the higher costs of security measures application the less developed countries/ports will bear the largest burden of market share loss. Due to the high competition in the shipping market, both tramp and liner, these companies/ports will inevitably face reduced revenues and loss of market position. According to [5] the CSI program proposed by the US will be difficult to implement by some small developing countries because the cost per port for that program varies between USD 1-5 billion. Table 1 presents an approximate estimation of related costs for the implementation of obligatory and optional security measures.

Measures		Initial costs (approximate, mln USD)	Yearly cost (approximate, mln. USD)
Port facility assessment	Security	27,9	8
Port facility plan	Security	N/A	N/A
Port facility officer	Security	N/A	N/A
Port training	Facility	N/A	N/A
Port facility equipment/staff	Security	N/A	N/A
24-Hour Automated Manifest System	Security	281.7 to 10 000	281.7 to 10 000
Container Security Initiative	Security	N/A	N/A

Table 1. Cost of container supply chain security measures [7]

When implementing only the obligatory requirements as per the IMO conventions (for example, ISPS), apart from the optional requirements (CSI), less developed countries will inevitably face decrease of cargo flows and cargo turnover at ports as supply chain participants would prefer faster and more secure transportation. Even in the medium run the latter will distort the international trade patterns.

5. Conclusion

The present paper analyzes the framework of security measures in container supply chains, outlining the strengths and weaknesses of the mandatory and optional security measures. The existing security measures aim at the protection of international and national interests and ensuring of safe environment.

All the participants of the container supply chain are challenged by the fact that there are no universal standards concerning the container transportation apart from the mandatory regulations of IMO at ports and for sea carriage (ISPS, SOLAS). The other edges of the container supply chain – road and rail transport, as well as inland waterways, are still the vulnerable parts of the system.

The available solutions for security enhancement of container supply chains, however, involve certain delays in cargo flows. All participants should bear the cost and responsibility of the applicable measures. Shippers are responsible for the containers content and provide the relevant info via automatic cargo manifests transfer to the national customs authority as per the “24-Hours rule”. On the other hand, ocean carriers are responsible for vessel’s deviation from the customary route and are obliged as per ISPS code to provide advance ships’ arrival information to port authorities. The strict security procedures of the CSI will lead to delays in the transportation process especially for carriers and shippers. A detailed analysis has been made regarding the cost of the security measures and its effect on the container supply chain. The results show that the benefits from increased security measures are higher for all supply chain participants, allowing for protection from usual hazards during the transportation process.

References

1. Erera, A. et al., 2003, Cost of security for sea cargo transport, White Paper, The Logistics Institute – Asia Pacific, National University of Singapore, Singapore
2. OECD, 2005, Container Transport Security Across Modes, European conference of ministers of transport (ECMT)
3. Organization for Economic Co-operation and Development (OECD), Report in Maritime Transport

Committee 2003, Security in maritime transport: Risk factors and economic impact., OECD publications, Paris

4. Scholliers, J., A. Permala, S. Toivonen, H. Salmela, 2016, Improving the security of containers in port related supply chains, Transportation Research Procedia, 14, pp. 1374 – 1383
5. United Nations Conference on Trade and Development (UNCTAD), 2004, Container Security: Major initiatives and related international developments, Geneva, United Nations
6. US Customs and Border Protection (CBP), 2006, Container Security: Fact sheet, Washington, CBP publication
7. World Maritime University, The Maritime Commons, Digital Repository of the World Maritime University, World Maritime University Dissertations, 2006, Intermodal shipping: an examination of the security framework with emphasis on container security, M. Abdou

ADMINISTRATIVE PROCESS MODELING: BASIC STRUCTURES AND MODELING

M.Sc. Trashlieva V.¹, M.Sc. Radeva T. PhD.¹

Department of Electrical Power Engineering – Technical University of Sofia, Bulgaria
vesselina.trashlieva@gmail.com

Abstract: In this paper a general structure of an administrative process development is proposed. A block diagram showing the logical dependencies in the development is also given and analyzed as well as the basic structures for the variants to implement the core element "task" in an administrative processing. A concept for generalization in some of the administrative process stages is given as well as an approach to the most commonly executed internal procedure that is the approval one.

Keywords: OPTIMIZATION MODELING, ADMINISTRATIVE PROCESSES OPTIMIZATION

1. Introduction

An administrative process can be approached as a sequence of events forming a finite set of discrete elements. In an environment of full information, that is a complete certainty onto activities duration and any other events considered otherwise as uncertainty being ignored or considered fully known a linear programming model can be evaluated. In specifics, a network model of an administrative process brings enough clarity onto the process' development, required steps to fulfill the final result as well as evaluate the overall duration. Unfortunately, as any other real-life process, no matter if it's a business or an administrative one, uncertainty of a different origin exists and it should be properly approached and modeled so the risks and the costs in the final result are evaluated. Here we make a review onto two approaches of dealing with uncertainty in the durations for each operation designating an activity in the process development.

In administrative proceedings, inefficient use (or management) of human resources is often observed as well as delays in the administrative implementation/performance of and management functions and tasks. This requires the search for methods and approaches to solve optimization problems in order to meet deadlines and improve efficiency and quality of management. While an administrative process is considered event-oriented, PERT (Project Evaluation and Review Technique) and CPM (Critical Path Method) methods are key tools for project management [1, 2] and case studies on feasibility and effectiveness are emerging in the research and work process. The demand for PERT structures, reflecting both the uncertainty of the duration and the complexity of the process, is not a novelty [3]. On the other hand, PERT network models, which contain a minimal number of fictitious operations [4], whose presence is noted as the main drawback of PERT, are also sought. The approaches to shortening the process' overall duration and the consequences of its implementation are a key point in the research, especially in conditions of uncertainty [5].

2. Process structure and logical modeling

Administrative process stages

In documents management systems that are designed to deal with the correct structuring and data collection, documents concerning a similar problem (called "subject") are grouped in a file. So a file is the set of documents, there included the first one (initiating document) and all the other documents (intermediary documents) following it no matter of their origin. An intermediary document is also all of the correspondence between an administration and a client or another administration in the administrative process and final result of an administrative service.

The process starts with incoming documents and/or data.

1. The initial processing is called "Registration" and includes the following operations:

- verification if the data for the addressee (correspondent, the client) is available and correct,

- check if there are any other registered documents and procedures initiated with this client

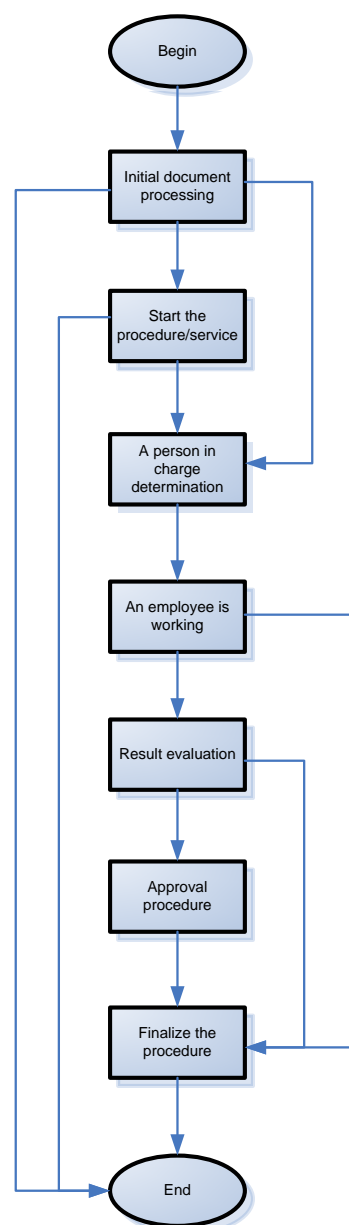


Fig. 1 Administrative process development stages

- check whether the incoming document is somehow connected with any available files with this client,
- check if there is enough data to start the procedure directly - in order to reduce the unnecessary actions it is very common requests of a certain predefined type to be directly transferred to a predefined official. This idea is common for queue management systems where

servers are specialized in the processing of requests of a certain type and there is "a request redirecting/sorting server" before the queue member enters into the processing system.

- check whether the submitted document (i.e. the request) is in the statutory form
- check if the form is filled out correctly
- check the availability and the completeness of a set of attachments to the request legally required to start the process
- Targeting for follow-up action - to allocate, to start a procedure, to place a task for execution

2. Start the administrative service / procedure

3. Direct the data to a relevant official for further action

4. Cascade (successively) redirecting and assignment until the document reaches the actual expert according the procedure's specifics

5. The appropriate and competent expert on the problem described in the document and its attachments (also the other data available in the file) works. This stage ends up with a result that has two components - a report on the implementation of the assigned task and a *material* on its implementation. The material might be a document that will be sent outside of the administration, a report, an internal posture. The task implementation report is a statement that the job is done and it might contain few other

6. The result is redirected for a performance evaluation. In the case of a negative evaluation the result is returned to the employee for improvements until the evaluation is positive. An optimization aims also at a positive evaluation on the first iteration so that no returns for improvement are carried out. A clear and detailed description on the requirements of each task is a prerequisite for a positive evaluation.

7. After a positive evaluation, a conformity and reconciliation procedure might be carried out; this step figuratively is the process of the collection of a set of signatures (named also *approval* signatures) of officials that have to grant their approval and / or any subsequent generalization of the results obtained;

8. The process finishes with signing and registering the *outgoing result* (*internal document* in some cases of administrative procedures) of the administrative processing; the final step includes several options in the work technology, primarily concerning the order of the two sub-activities that is *sign* and *register*.

Logical dependencies between the different development stages

After the stages in the development (Fig. 1) are clearly defined the building of a block diagram of an administrative process follows. The block diagram shows the logical dependencies in the events. Fig. 2 illustrates the conditions that are checked in a general realization of the process described in the previous section with Fig.1. The existence of a certain condition in a process' development may serve as a basis into the *structural* classification of the different types of administrative services/processes for example whether a group of services contains an explicit approval procedure or not. On the other hand, the block diagram on Fig. 2 marks the conditions under which a certain stage in a process development can be curtailed (that is namely - "skipped").

3. Tasks structure types

The main goal in the implementation of a certain managerial administrative function is to assign tasks and functions to a specific, exactly specialized in its competence administrative unit or an official. One side of this effectiveness goal principle is the unambiguous determination of the unit (or official) itself, and the other component is the correct formulation of the task. The two aspects of the principle are difficult to consider separately since the

properly formulated task can determine the structure on the one hand, and on the other the structure affects the formulation of the task, taking into account the particular organizational structure. Because of the fact that a certain task might be posed to a set of officials, whose work might be dependent of each other or not, and also that someone controls the work of the others it should be noted here that a "task" can also represent a set of tasks (named *sub-tasks*) connected in different ways and then this set of sub-tasks is designated as a *composite/complex* task.

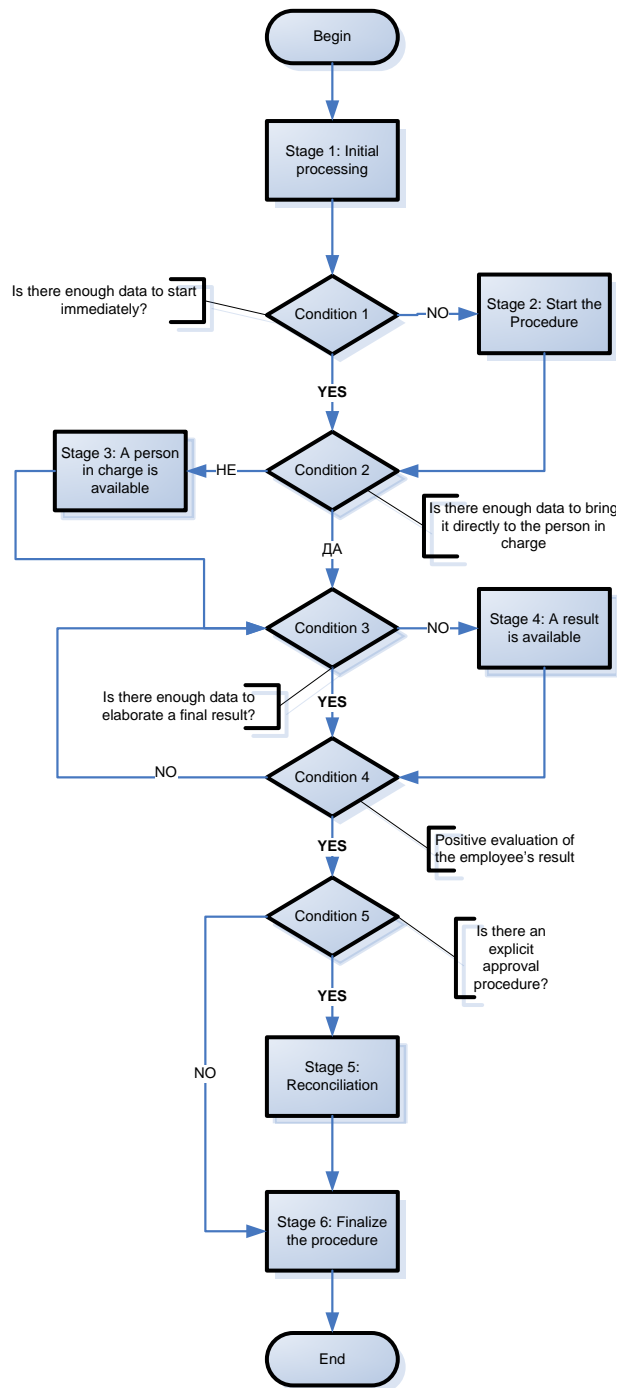


Fig. 2 Administrative process block diagram

Consecutive structure - successive realization

A successive realization of a complex task is the consecutive assignment and execution of different (sub-)tasks, as a positive result from any previous one gives rise to the start of the next one in the chain as shown in Fig. 3. In such configuration, it is the positive evaluation of the *last* sub-task that marks the whole task as done.

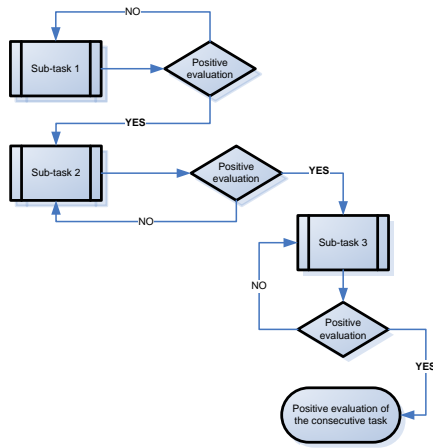


Fig. 3 Consecutive structure of a task

Parallel structure - realization in series

The parallel structure is the realization when the assignment and execution of different and / or similar sub-tasks is done in series. The sub-tasks are placed at the same time and their execution runs regardless of the of work on the other sub-tasks. The whole task is considered done when a positive assessment for each of the sub-tasks in its composition is available. If even one of the sub-tasks is not well-executed, all other sub-tasks are considered not done. This is one of the main problems in the performance reporting on complex tasks. Often in timing controls officials who have in fact received positive ratings (that have done all their work) "receive also" a certain number of tasks not-done because other officials have received negative evaluations.

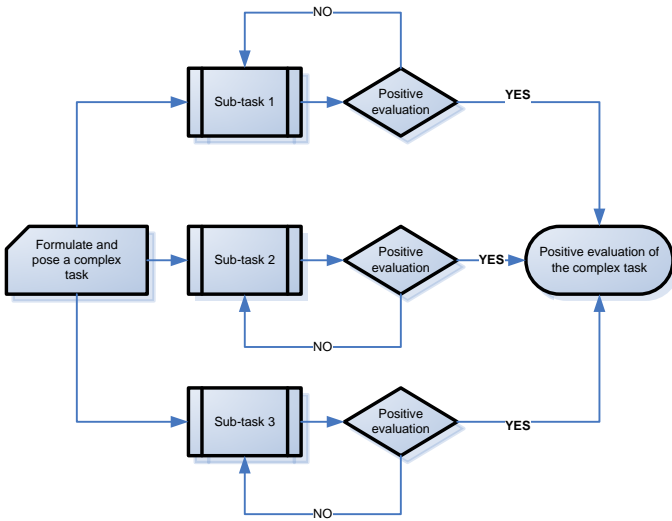


Fig. 4 Parallel structure of a task

Mixed structure - parallel and successive realization

The most common architecture is the mixed one. Usually there are several parallel tasks whose performance is evaluated in a single finalizing task. The finalizing unit has also the performance coordination and monitoring function for the implementation of the preceding parallel processes. It is responsible for the right-moment measures in order to avoid delays. It is also responsible for the overall performance quality and sometimes for summarizing the results from the preceding tasks. In the latter case, a task for the assessment of the summarizing sub-task may also follow but this is very rare in practice.

As a result of an optimization approach a semantically modified version of the mixed structure might be used. At the beginning there are one or more tasks in parallel to one or more officials. The implementation of each one finishes with materials and/or reports

that are directed to the next official. The last official that receives a material must draw up a summary of all other materials received by him and this summary is the result of the composite task. This summary should pass the procedure up to a positive evaluation.

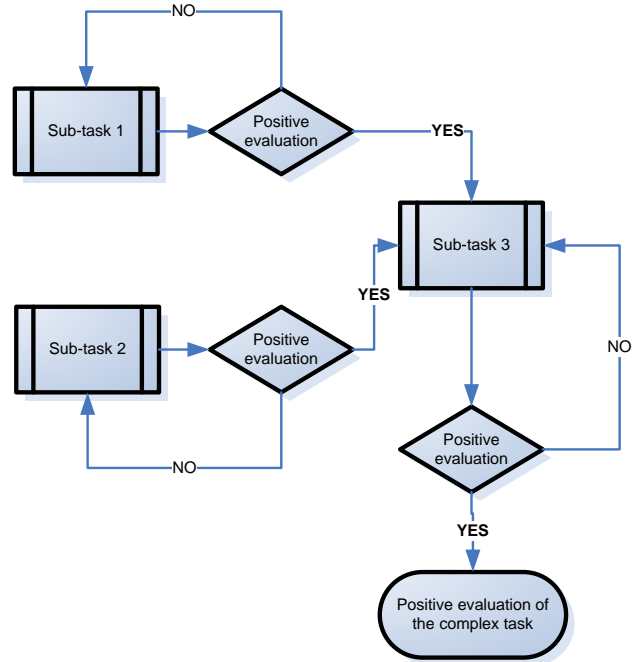


Fig. 5 Mixed structure of a task

Very often in practice, however, the summarizing official is the same one who assesses the precedent materials. This minimizes the time for which the outcome of the process should be directed towards an approval procedure and / or signature.

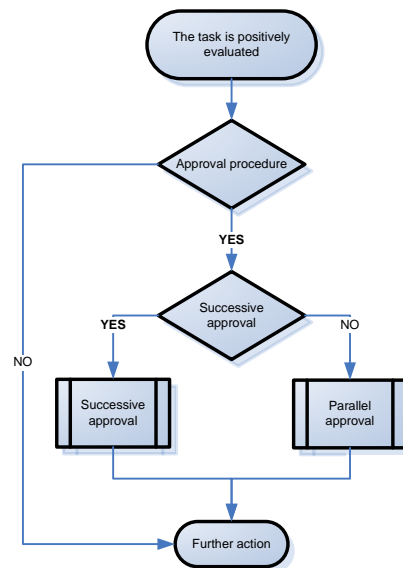


Fig. 6 Block diagram of a general approval procedure (a mixed realization)

4. Approval procedure

The approval procedures are the most common distinct procedures in an administrative processing that appear in almost all services and procedures. This is a sub-process where certain officials approve or not the job done previously by other employees that mainly are their subordinates. As an example, a chief accountant should always approve a contract before it is finally signed, no matter of the fact that an accountant is not responsible for the legal value in the contract. There are also three configurations (successive, parallel and mixed) for the approval procedures as with the "task" according to the number of officials

that have to grant their approval on the final result before it gets official. In many cases, a non-approval in this stage will lead back to the task's implementation and evaluation stage. So in such work technologies an event of a non-approval fires a preceding task status "un-done" and a starting point for the preceding stage.

Successive structure of an approval procedure

In the case of a successive structure, an approval signature shall be applied only in the presence of a preceding approval. If any of the participants is the approval procedure is prevented from explicitly stating this action, the completion of the whole stage is delayed.

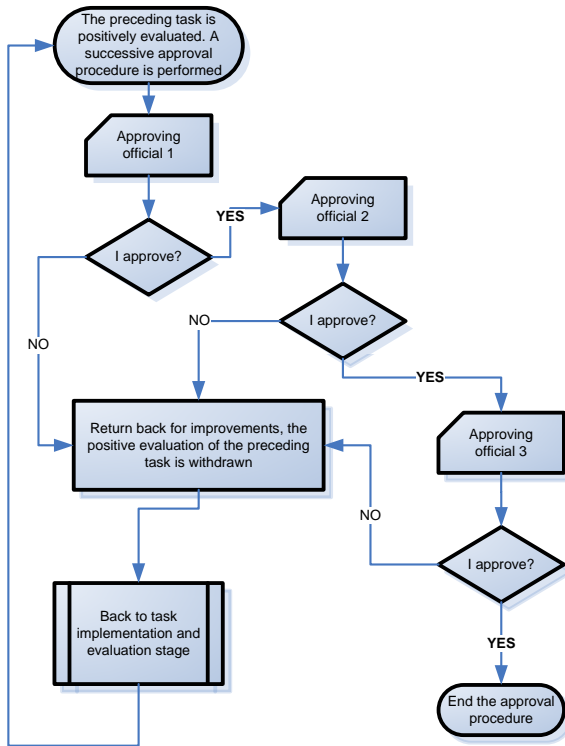


Fig. 7 Successive structure of an approval procedure

Parallel structure of an approval procedure

In this realization all approval signatures are independent one to another (see Fig. 8). The approval procedure will finish only if all approvals are available, meaning that if only one of the officials does not approve the whole stage is revoked while one non-approval leads to the previous task implementation and evaluation stage.

5. Conclusion

Generally in the administrative process modeling approach as an discrete-event process the aim is to achieve a complete determination of the administrative processes. If the correct answers are given to a few simple questions, a network model for each administrative process can be built while the general structure is carried out. The main issues a consultant has to face are:

- What kind of processes take place in an administrative structure? What is the legal basis regulating the progress of each process?
- What are the exact responsibilities of each official and how does its work influence the work of the other officials? That is simply for each employee to obtain full data about the documents and information he/she receives and from who.
- When performing specific tasks, what information is used and generated, where is it processed, stored and updated?

Subsequently, two important nomenclatures are created:

- List of procedures and related document types and / or tasks that trigger their execution;
- Nomenclature of the types of tasks to be performed, for each task of the nomenclature are described in detail the requirements for the final result, the deadlines and its performers.

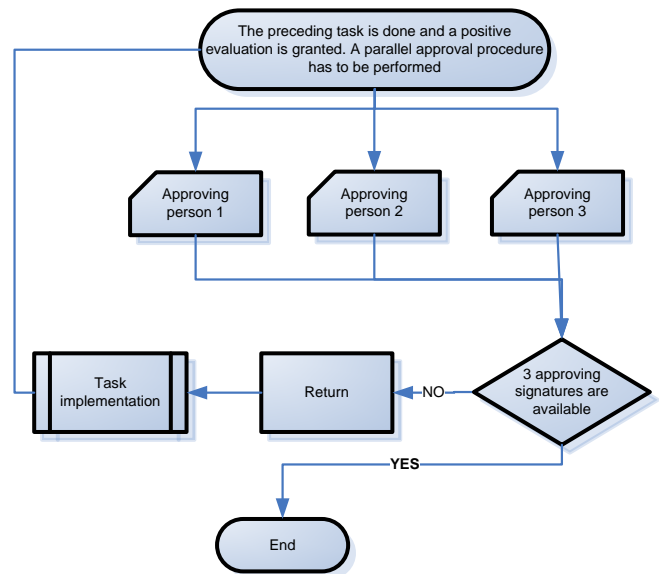


Fig. 8 Parallel structure of an approval procedure

On the basis of the research that lead to the explicit formulation of the structures proposed in this paper and also the accompanying comments a practical methodology for building such models is developed. Subsequently few analysis algorithms can be used for the evaluation of the efficiency of the administrative-management procedures themselves. The description of each process that takes place in an administrative structure has, on the one hand, a disciplinary function and on the other hand it is a prerequisite for an efficient management and relative independence of the processes of staff turnover. In the research, model parameters can always be updated and the effects of these updates on the overall management structure can be assessed. When such a model is available, even the optimization of the staff structure can take place. It should be clear that the basis for building an administrative structure lies primarily with the description of the functions assigned to it and when structural change is planned without taking account of the functions, change is almost always ineffective. Moreover, modeling and analyzes such as those presented in this paper should precede any structural change.

6. Bibliography

- [1] Hillier F. S., Liebermann G. J., Introduction to Operations Research 8th ed., Mc Graw Hill, 2005, ISBN 978-0072527445, 1214 pages.
- [2] Taha H. A., Operations Research: An Introduction" 8th ed., Prentice Hall, 2006, ISBN 978-8120330436, 840 pages.
- [3] Pontrandolfo P., Project Duration in Stochastic Networks by the PERT-path Technique, International Journal of Project Management 18 (2000), pp. 215- 222
- [4] Mouhoub N.E., Benhoucine A., Belouadah H., A New Method for Constructing a Minimal PERT Network, (APM) Applied Mathematical modelling, Elsevier ISSN: 0307904X, Vol. 35, Issue: 9, 4575-4588, March 2011.
- [5] Haga W. A., O'Keefe T., Crashing PERT Networks: A Simulation Approach, 4-th International conference of the Academy of Business and Administrative Sciences, Quebec City, Canada, July 12-14, 2001.

NEW STEELS FOR METAL CONSTRUCTIONS IN THE DESIGN STANDARDS AND REGULATIONS

НОВЫЕ СТАЛИ ДЛЯ МЕТАЛЛИЧЕСКИХ КОНСТРУКЦИЙ В СТАНДАРТАХ И НОРМАХ ПРОЕКТИРОВАНИЯ

Vedyakov I.I. the Doctor of Technical Sciences, Professor, Odessky P.D. the Doctor of Technical Sciences, Professor,
Gurov S.V. engineer, Konina S.M. engineer
The Central Scientific-Research Institute of Building Constructions (TSNIISK) named after V.A.Kucherenko
of JSC Research Centre "Construction", Russia

Abstract: *One of the main ferrous metallurgy products is the rolled pipe of steels with yield strength $\sigma_T=200-700$ N/mm² for metal structures usually welded. The basic concept of development of the considered steels is the grain refinement in combination with increasing the purity of metal harmful impurities and non-metallic inclusions. This problem has been largely solved by the development of new technologies in metallurgy over the past twenty years. Procedures of secondary metallurgy have been widely utilized that allows to significantly reduce the sulphur content in metal as well as to modify the phase of non-metallic inclusions. The new guarantees on impact strength and chemical composition of steels are given in the new building standards for design of buildings and structures.*

KEYWORDS: METAL CONSTRUCTIONS, NORMS, PIPE, ROLLED STOCK, STRENGTH, IMPACT STRENGTH, DESIGN STANDARDS.

Одним из основных видов продукции черной металлургии является производство сталей для строительных металлических конструкций. Здесь ежегодно производятся и потребляются в строительной отрасли миллионы тонн листового и фасонного проката, а также труб с $\sigma_T = 200-700$ Н/мм² с высокими инженерными свойствами, соответствующими современным эксплуатационным, технологическим, сортаментным и экономическим требованиям.

Наименование рассматриваемых сталей, впервые использованное в ГОСТ 27772-88 по аналогии с зарубежными стандартами, основывается на величинах пределов текучести (основная нормативная характеристика при расчетах конструкций). Буква «С» обозначает, что сталь строительная. По прочности стали можно условно разделить на четыре группы, указанные в таблице 1.

Видно, что уровни прочности, а, точнее, потребности строителей в прокате различной прочности, со времени составления ГОСТ 27772-88 в целом не изменились, но произошли значительные изменения в легировании сталей, существенно снизилось содержание углерода, особенно вредных примесей, в первую очередь в случае сталей высокой прочности. Данные изменения связаны с кардинальным улучшением технологии производства и упрочнения, рассматриваемых сталей, произошедшим в металлургии за последние ~20 лет. Хорошо известна основная концепция повышения качества рассматриваемых сталей – это усиление дисперсности структуры прокатки в сочетании с повышением чистоты металла по вредным примесям и газам.

В современной литературе, в том числе [1,2], подробно описаны широко применяемые в металлургии процессы внепечной обработки (ковшовой металлургии) стали с целью очистки от вредных примесей и неметаллических включений. Как следствие освоения этих технологий, гарантированное содержание серы в рассматриваемых сталях массового производства уменьшилось на порядок (таблица 1).

Стандартом ГОСТ 27772-2015 предусмотрена внепечная обработка всех сталей повышенной и высокой прочности. При этом регламентируется массовая доля остаточного кальция, что гарантирует применение технологий, направленных на обогащение (в первую очередь глобулирование) сульфидных и окисульфидных фаз.

Степень дисперсности структуры проката определяется основой легирования стали, но, в первую очередь, финишной обработкой на металлургическом предприятии (состоянием поставки). Два этих фактора взаимосвязаны. На время разработки ГОСТ 27772-88 стали обычной и повышенной прочности поставлялись в горячекатаном состоянии. Термическая обработка с целью измельчения зерна (нормализация, реже термическое улучшение) применялась

лишь для получения проката высокой прочности, производимого в небольших количествах для уникальных инженерных сооружений промышленного и специального назначения.

Для достижения высокой прочности на уровне $\sigma_T \geq 390$ Н/мм² (стали С390 и С440 табл.1) применялись марганцовистые стали, микролегированные нитридами ванадия [3,4], в которых требуемая прочность обеспечивалась измельчением зерна при нормализации (особенно термическом улучшении) и эффектами упрочнения дисперсной фазой карбонитридов ванадия [5].

Однако эти стали обладали недостаточно хорошей свариваемостью, особенно в толщинах свыше 25мм, из-за недостаточно низкого содержания углерода и вредных примесей (таблица 1) как следствие имевшейся в то время технологии. С начала 90-х годов прошлого века эти стали перестали применяться в строительстве.

С середины 90-х годов на комбинате ООО «Уральская сталь» был налажен выпуск стали высокой прочности типа 10ХСНДА с требуемым низким содержанием вредных примесей и углерода (таблица 1). Такие стали повышенной и высокой прочности, называемые сталями второго поколения, до настоящего времени широко используются в мостостроении и строительстве [6] и вошли в новый стандарт ГОСТ 27772-2015 как стали С355-1 и С390-1.

С конца прошлого века в нашей стране широко используются процессы упрочнения проката в потоке станов методами термомеханической прокатки с последующим охлаждением [7,8], прежде всего для обеспечения проката для производства электросварных труб большого диаметра до 1420 мм для магистральных газопроводов. Были введены в действие станы «5000», такой прокат повышенной и высокой прочности и трубы из него стали широко использоваться в строительстве, например, стадионов [8].

Эти стали с высоко дисперсной структурой и высокой чистотой по вредным примесям относим к сталям третьего поколения, они также включены в стандарт ГОСТ 27772-2015 и характеризуются низким содержанием углерода, вредных примесей, а также микролегированием ниобием (для измельчения аустенитного зерна) и ванадием (для обеспечения эффектов дисперсионного твердения) (стали С355, С390 и С440 в таблице 1).

Таблица 1. Стали для металлических конструкций по ГОСТ 27772

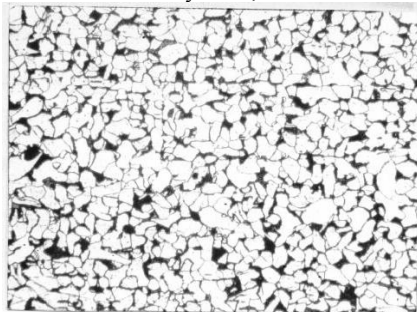
некристаллизованных зёрен аустенита (рис.1,в) формируется дисперсная многослойная структура из сочетания большеугловых и малоугловых границ с характерным размером зерна $d=1\text{мкм}$ (рис. 1,г,д).

Уровень прочности	Предел текучести σ_t , Н/мм ² ,	Характеристика химического состава, марка стали	
		ГОСТ 27772-88	ГОСТ 27772-2015
Обычный	<290	Малоуглеродистые стали типа Ст3, например С255	
		C≤0,22%; Mn≤0,65%; S≤0,050%; P≤0,040%	C≤0,17%; Mn≤1,0%; S≤0,025%; P≤0,035%
Повышенный	290≤ σ_t <390	Малоуглеродистые низколегированные стали с C≤0,15%, с содержанием легирующих ~2,5% типа 09Г2С, например:	
		С345: S≤0,040%; P≤0,035%; C≤0,15%	С355, допускается микролегирование V и Nb: S≤0,015%; P≤0,017%; C≤0,14%
Высокий	390≤ σ_t <540	Стали, микролегированные нитридами ванадия марок 14Г2АФ (С390) и 16Г2АФ (С440) (S≤0,040%; P≤0,035%; C≤0,18% и ≤0,20% соответственно)	1) Микролегированная сталь 09Г2ФБ (С390 и С440)
			2) Cr-Si-Ni-Cu-сталь типа 10ХСНДА (С390-1). В случаях 1) и 2) C≤0,12%; S≤0,010%; P≤0,017%
Высокий	$\sigma_t \geq 540$	Термически улучшенная сложнолегированная сталь с молибденом марки 12ГН2МФАЮ (С590); C≤0,14%; S≤0,035%; P≤0,035%	Сталь с молибденом типа 08Г2МФБ, упрочненная ТМО с ускоренным охлаждением (С590) C≤0,10%; S≤0,004%; P≤0,015%

На рисунке 1 представлены характерные структуры основных сталей, поставляемых по ГОСТ 27772.

Малоуглеродистые стали обычной прочности имели феррито-перлитную структуру с диаметром зерна $d=50-25\text{мкм}$ (зерно №5-7 по ГОСТ 5639; у низколегированных сталей повышенной прочности диаметр $d=35-15\text{мкм}$ (зерно №7-9 (рис. 1,а); у нормализованных сталей высокой прочности $d=15-10\text{мкм}$ (зерно №9-11).

Рисунок 1, а



Термически улучшенные стали имеют дисперсную сложную структуру (рис. 1,б), формирующуюся при высокотемпературном отпуске при развитии процессов полигонизации и ранних стадий рекристаллизации ферритной матрицы; характерный размер субзерна $d=4\text{мкм}$. Наконец, после термомеханической прокатки с последующим ускоренным охлаждением в прокате при $\gamma \rightarrow \alpha$ из

Рисунок 1, б



Рисунок 1, в

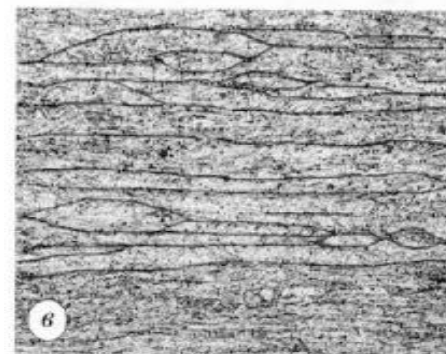
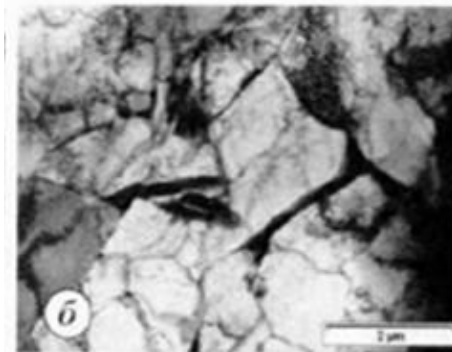


Рисунок 1, г



Видно, что размер зерна в строительных сталях может изменяться буквально на два порядка, так же может уменьшаться и загрязненность стали (с 4-5 до 0,5-1 балла по шкале в ГОСТ 1778).

Рисунок 1, д

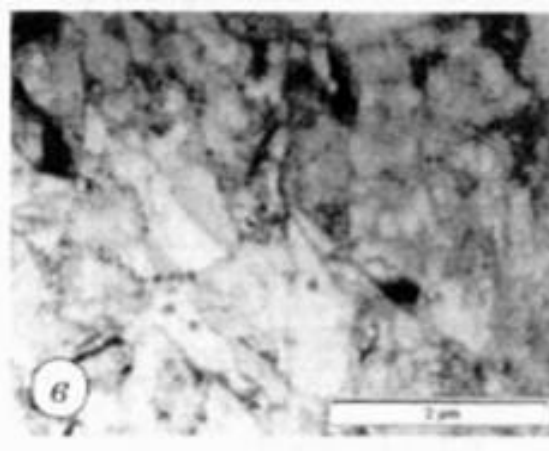
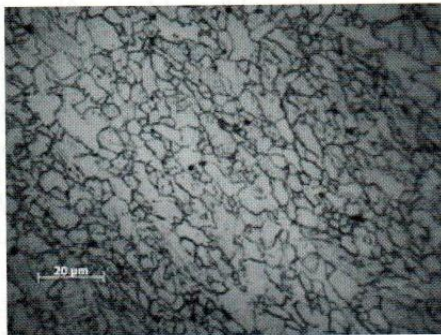


Рисунок 1, е



В вступающем в силу стандарте на электросварные трубы для строительных металлических конструкций химический состав и механические свойства металла, в том числе в сварном соединении, полностью соответствуют требованиям ГОСТ 27772-2015. При производстве двутавров с параллельными гранями полок достаточно больших размеров на отечественных комбинатах отсутствуют технологии по специальному охлаждению (в отличии, например, от производства двутавровых профилей на заводе «Arcelor Mittal» в Люксембурге). Вместе с тем в новом стандарте впервые в нашей стране предусмотрен и производится выпуск такого проката с прочностью С355, С390 и С440 достаточно больших толщин полок до 40 мм. Здесь получение требуемой прочности обеспечивается микролегированием нитридами ванадия (практически $V \leq 0,10\%$; $N \approx 0,015\%$; $Ti \leq 0,035\%$; $Al \ 0,02-0,06\%$) при $C \leq 0,17\%$ и $Mn \approx 1,5\%$ и обеспечением при горячей прокатке достаточно мелкого зерна, не крупнее №9-10 ($d_{\text{зерна}} \leq 15 \text{ мкм}$); требуемая высокая хладостойкость обеспечивается технологиями рафинирования металла и модифицирования фазы неметаллических включений ($S \leq 0,010\%$; $P \leq 0,017\%$; $Ca \leq 0,006\%$). Данные профили, как и трубы, в настоящее время успешно применяются в практике строительства.

Важнейшей стандартной характеристикой по оценке сопротивления проката разрушению является ударная вязкость, определяемая на образцах размером –брутто 10x10x55мм с надрезом различной формы при испытаниях на ударный изгиб по ГОСТ 9454-78*. Для определения ударной вязкости в ГОСТ 27772-88 и других подобных стандартах, традиционно применялся образец типа 1 по ГОСТ 9454 с U-образным надрезом.

В новых стандартах, например ГОСТ 27772-2015, в этой части произошли кардинальные изменения: здесь регламентировано определение ударной вязкости на образцах с острым V-образным надрезом (тип 11 по ГОСТ 9454). Рассмотрим причины сделанного изменения, а также перспективные требования к рассматриваемой характеристике.

Исследователи работы материалов с надрезом обращали внимание на необходимость учитывать соответствие остроты надреза и микроструктуры для эффективных оценок прочности [9-11] и др.

Известно, что при нагружении образца с надрезом в условиях перехода из вязкого состояния в хрупкое размер сильно деформируемой области соизмерим с радиусом надреза. Я.Б.Фридман [10] считал, что для хорошей чувствительности испытаний к структуре радиус у дна надреза должен быть на порядок больше, чем размер зерна. У горячекатаных сталей, долго применявшихся в нашей стране, в том числе регламентированных ГОСТ 27772-88, размер зерна имел порядок 10^{-1} мм и испытания на ударный изгиб образцов типа 1 по ГОСТ 9454 с радиусом у дна надреза $r=1\text{мм}$ хорошо описывали возможность вязко-хрупкого перехода в интервале климатических температур.

Однако, когда после нормализации или термического улучшения диаметр зерна уменьшался на порядок (а число зерен под надрезом увеличивается в 10^3) величина КСУ теряет структурную чувствительность, воспринимая металл под надрезом как бесструктурное твердое тело. При испытании на ударный изгиб мелкозернистых сталей эффективными оказались образцы с острым V-образным надрезом типа 11 по ГОСТ 9454.

В настоящее время металлургические предприятия достаточно широко оснащены технологиями, направленными на измельчение зерна (в ГОСТ 27772-2015 закреплено применение нормализации, улучшения, контролируемой прокатки и т.п.).

Именно поэтому при разработке новых стандартов в качестве основного образца для испытаний на ударный изгиб был принят образец с V-образным надрезом (тип 11 по ГОСТ 9454) для оценки величины КСВ, что также позволило гармонизировать отечественные нормы с европейскими (EN 10025).

Принятые гарантии по ударной вязкости полностью соответствуют требованиям современных действующих строительных норм (таблица 2). Узаконенный в новых стандартах переход на образец с V-образным надрезом фактически закрепил возможность существенного повышения сопротивления разрушению современных сталей по отношению к сталям, регламентированным ГОСТ 27772-88 и ГОСТ 19281. Переход от КСУ к КСВ при одинаковом критерии 34 Дж/см^2 указывает на повышение хладостойкости на $\sim 40^\circ\text{C}$.

Расчетная температура, °C	Группа конструкций	Предел текучести проката, Н/мм ²							
		$R_{\text{вн}} < 290$		$290 \leq R_{\text{вн}} < 390$		$390 \leq R_{\text{вн}} < 490$		$R_{\text{вн}} \geq 490$	
		Показатели ударной вязкости, Дж/см ²							
		КСВ		КСВ		КСВ		КСВ	
		При температуре испытаний на ударный изгиб, °C							
		+20	0	-20	-20	-40	-40	-60	-60
$t \geq -45$	1,2,3	34	-	-	34	-	34	-	40
$-45 > t \geq -55$	1	-	-	34	-	34	34	-	40
	2,3	-	34	-	34	-	34	-	40
$t < -55$	1,2,3	-	-	34	-	34	-	34	40

Таблица 2. Нормируемые показатели ударной вязкости проката по СП 16.13330.2017

Примечания:

- КСВ – ударная вязкость образцов с V-образным надрезом (тип 11 по ГОСТ 9454)
- В толстолистовом прокате испытываются поперечные образцы, в фасонном и сортовом – продольные
- Группы конструкций:

1. Сварные конструкции, работающие в особо тяжелых условиях, в том числе при максимально стесняющих развитие пластических деформаций, а также при воздействии динамических или переменных нагрузок, (подкрановые балки и т.п.)

2. Сварные конструкции, работающие при статической нагрузке, преимущественно растягивающей (фермы, балки и т.п.).

3. Сварные конструкции, работающие при статической нагрузке, преимущественно на сжатие (колонны и т.п.).

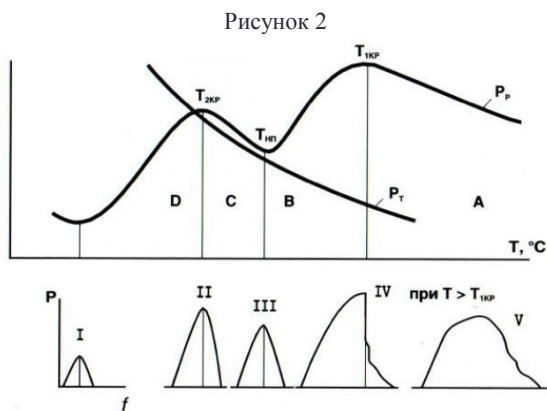
При отсутствии сварных соединений группа конструкций понижается на единицу.

Правильность сделанного перехода подтверждается установленным соответствием результатов испытаний на ударный изгиб с испытаниями образцов натурных толщин, более полно имитирующих работу стали в конструкциях.

На рис. 2 представлена картина перехода элементов конструкций из вязкого состояния в хрупкое.

Верхняя критическая температура $T_{\text{кр}}$ разделяет область вязкого разрушения А и область В, где разрушение происходит в условиях определенного стеснения пластических деформаций, но после деформационного упрочнения. Эксплуатационная надежность конструкций с большим

запасом упругой энергии (например, газопроводы) обеспечивается при работе в области А, строительных металлических конструкций, также и в области В.



Эксплуатация последних должна быть выше температуры пластичности $T_{нп}$. При $T_{нп}$ разрушение происходит при $\sigma_n^p \approx \sigma_t$, т.е. при незначительных пластических деформациях, при этом диаграмма разрушения приобретает макрочрупкую треугольную форму. Излом имеет полностью кристаллическое строение.

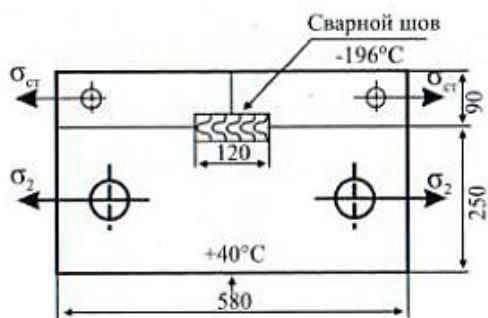
Требуемую информацию для оценки $T_{нп}$ получают при испытаниях в интервале температур образцов натурных толщин с наплавкой и V-образным надрезом на статический трёхточечный изгиб. Основная оцениваемая характеристика – деформационная: сужение разрушенного образца у дна надреза (Ψ , %). При этом для оценки $T_{нп}$ критерием служит $\Psi=1\%$, т.е. за $T_{нп}$ принимается самая низкая температура испытаний, при которой $\Psi \geq 1\%$ ($T_{\Psi=1}$).

Из испытаний, позволяющих оценить способность материала останавливать трещину, т.е. фактически оценивать температуру $T_{1кр}$, выше которой трещины не распространяются самопроизвольно, наиболее эффективным считают метод Робертсона и его модификации.

Метод заключается в следующем. Крупную пластину помещают в градиентное температурное поле и нагружают растяжением в диапазоне определенного уровня номинальных напряжений ($\sigma_n < \sigma_t$).

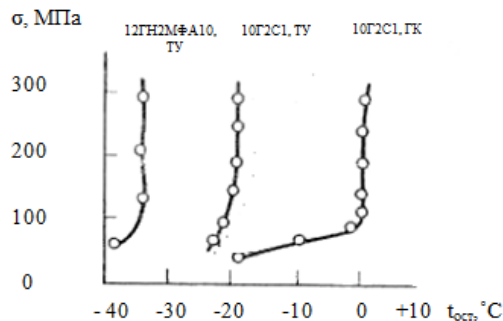
Затем на торце пластины, охлаждаемой азотом, инициируется хрупкая трещина при статическом напряжении $\sigma_{ст}$ (рис. 3). Возникшая трещина увязает при определенной температуре $t_{ост}$, называемой температурой Робертсона t_p .

Рисунок 3



В результате испытаний строится зависимость $t_{ост}$ от уровня напряжений σ_n и определяется область напряжений и температур, при которых возникшая хрупкая трещина не будет распространяться в стали (рис. 4).

Рисунок 4



В таблице 3 по результатам наших многолетних исследований представлены данные о соответствии испытаний натурных образцов с результатами испытаний на ударный изгиб образцов типа 1 и 11 по ГОСТ 9454.

Из результатов испытаний видно, что при температуре нулевой пластичности $T_{нп}$ соответствуют критические температуры T_{11}^R (в некоторых случаях последние лежит немного выше); еще точнее $T_{нп}$ совпадает температура t_{11} по деформационному критерию $\Psi_v = 4\%$; Соответствующие температуры, полученные при испытаниях на образцах с U-образным надрезом лежат на $\sim 40^\circ\text{C}$ ниже.

Представленные результаты являются доказательством эффективности применения в новых стандартах образцов с V-образным надрезом при испытаниях на ударный изгиб. Температура Робертсона t_p в целом соответствует $T_{1кр}$. В случае термически упрочненных сталей высокой прочности эта температура несколько выше, чем $T_{1кр}$ из-за снижения в случае сталей обычной чистоты вязкоёмкости вязкого разрушения.

Специально следует отметить несовпадение температур $T_{1кр}$ и $t_{ост}$ в случае полуспокойной термически улучшенной стали высокой прочности 17Г2МАФс (№9 таблицы 3); где данное явление проявилось достаточно сильно, что лишнее раз показывает несовершенство оценок сопротивления распространению трещины при визуальных исследованиях соотношения вязкой и хрупкой составляющей в изломе.

В заключение остановимся на некоторых вопросах, необходимых для развития стандартов как в части оценок склонности к хрупким разрушениям, так и применения материалов новых уровней прочности и сортамента.

В случае стандартных сталей высокой чистоты после термомеханической прокатки с ускоренным охлаждением (таблица 1) в прокате, как отмечено выше (рис. 1,е,ж) формируется высокодисперсная многослойная структура с зубчатым строением границ ферритных зерен (рис. 1,е). Оказалось, что в этом случае образец с V-образным надрезом типа 11 по ГОСТ 9454 также перестает отвечать принципу структурного соответствия, как образец с U-образным надрезом не соответствовал сталям высокой прочности по ГОСТ 27772-88.

В диапазоне климатических температур у таких сталей даже $KCV^{60} > 250$ Дж/мм², стали плохо ранжируются. Даже в нижнем диапазоне этих температур прокат имеет как высокое сопротивление зарождению трещин (высокая чистоты металла), так и распространению (высокодисперсная структура), что хорошо видно при осциллографической записи диаграмм разрушения «нагрузка ($P_{дин}$) – прогиб (f)» при испытаниях на ударный изгиб.

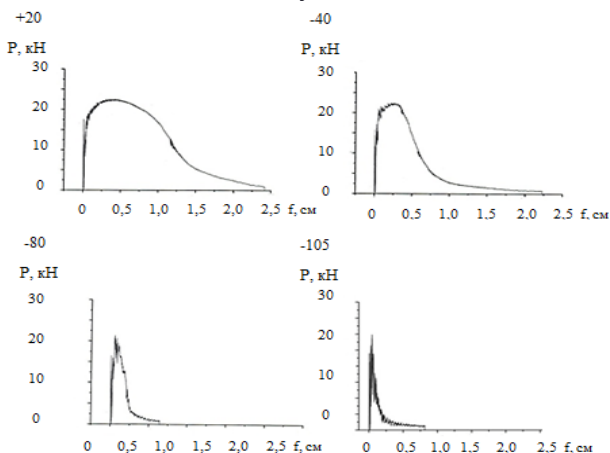
Чувствительность к изменению температуры в климатическом диапазоне, а также и структуры естественно возрастает при переходе к образцам с более острым надрезом (образец с усталостной трещиной типа 15 по ГОСТ 9454), (рис.5).

Также следует заметить, что у этих материалов сопротивление зарождению трещине с понижением температуры исчерпывается быстрее, чем сопротивление распространению трещины; последнее достаточно велико и при криогенных температурах, чем эти стали отличаются от горячекатаных, нормализованных и даже улучшенных.

№ № П.п.	Марка стали	Состояние поставки	σ_T , Н/мм ²	Критическая температура вязко-хрупкого перехода, °С					
				$T_{нп}$	T_1^k	T_{11}^R	t_{11}^4	$T_{1кр}$	t_p
1	ВСт3сп	ГК	285	0	-40	0	0	+20	+20
2	14Г2	ГК	330	+10	-40	0	0	+20	0
3	10Г2С1	ГК	356	-20	-40	-10	-	0	0
4	09Г21С	Н	325	-20	-70	-20	20	0	-10
5	14Г2	ТУ	453	-30	-70	-20	-	0	0
6	10Г2С1	ТУ	428	-40	-90	-40	20	-20	-20
7	14Г2АФ	Н	406	-40	-70	-40	-	-20	-20
8	14Г2АФ	ТУ	435	-60	-	-60	30	-40	-30
9	17Г2МАФпс	ТУ	657	-20	100	-20	-	-70	-10
10	14ГСМФР	ТУ	631	-40	-40	-30	40	-20	-20
11	12ГН2МФАЮ	ТУ	610	-60	-40	-60	-	-40	-35
12	10ХСНДА	ТУ	420	-70	-	-60	40	-50	-50
					100		-		
					-		60		
					100		0		
					-		40		
					-		-		
					-		60		
					-		-		
					-		70		

Поэтому стоит задача введения этих образцов в стандарты (рис. 5).

Рисунок 5



У данного проката вторая критическая температура $T_{2кр}$ (рис. 2) лежит в области криогенных температур, такой прокат можно отнести к материалам, у которых $T_{нп}$ совпадает с $T_{2кр}$; в этом случае эксплуатационная надежность элементов конструкций из данного материала обеспечена при прочих равных условиях во всем диапазоне климатических температур.

Наконец следует заметить, что в настоящее время при возведении крупных общественных зданий начинают применяться стали более высокой прочности ($\sigma_T \geq 690 \text{ Н/мм}^2$) и больших толщин (более 50 мм, вплоть до 200 мм), как правило зарубежного производства. По-видимому, в отечественной промышленности имеются возможности производства таких материалов, желательна их реализация.

Таблица 3. Критические температуры вязко-хрупкого перехода проката толщиной 20 мм из сталей для металлических конструкций

Выводы.

1. Новый стандарт на прокат «Прокат для строительных металлических конструкций. Общие технические условия» ГОСТ 27772-2015, а также стандарты на трубы и двутавровые балки с параллельными гранями полков учитывают новейшие достижения металлургии в части производства металла с высокодисперсной структурой и высокой чистотой по вредным примесям и неметаллическим включениям. По отношению к

действующему стандарту ГОСТ 27772-88 новый документ регламентирует производство сталей второго и третьего поколений, применение которых обеспечивает высокую эксплуатационную надежность металлических конструкций.

2. Показано, что применяя стандартные оценки ударной вязкости как характеристики сопротивления разрушению металла, наиболее чувствительной к микроструктуре, можно управлять изменениями последней в направлении улучшения эксплуатационных свойств проката и изделий из него. Переход в новом стандарте ГОСТ 27772-2015 на образцы с V-образным надрезом (KCV) вместо образцов с U-образным надрезом (КСУ в ГОСТ 27772-88) оказался необходимым из-за возросшего в последнее время сопротивления разрушению металла и изделиям из него благодаря освоению в металлургии соответствующих новых технологий, обеспечивающих высокую дисперсность структуры в сочетании с высокой чистотой металла. Кроме того, применение образцов с острым надрезом обеспечивает гармонизацию с зарубежными нормами.

3. Показано, что при эффективном использовании результатов испытаний на ударный изгиб напряженное состояние в устье концентратора напряжений должно находиться в определенном соответствии со степенью дисперсности структуры. Оценку ударной вязкости металла высокой чистоты, тем более упрочненного термомеханической прокаткой с последующим ускоренным охлаждением, следует проводить на образцах с усталостной трещиной типа 15 по ГОСТ 9454, а в ряде случаев (на сталях $\sigma_T \geq 540 \text{ Н/мм}^2$) – с дополнительными острыми боковыми канавками. В ближайшей перспективе первые следует ввести в ГОСТ 27772-2015, а вторые – в ГОСТ 9454 с последующим включением в ГОСТ 27772.

Список литературы

1. Одесский П.Д., Кулик Д.В. Сталь нового поколения в уникальных сооружениях. – М.: Интермет, 2005-176с.
2. Гладштейн Л.И., Одесский П.Д., Ведяков И.И. Слоистое разрушение сталей. М.: Интермет Инжиниринг, 2009 – 256с.
3. Гладштейн Л.И., Литвиненко Д.А. Высокопрочная строительная сталь. – М.: Металлургия, 1972-240с.
4. Скороходов В.Н., Одесский П.Д., Рудченко А.В. Строительная сталь. – М.: Металлургиздат, 2002 – 624с.
5. Гольдштейн М.И., Литвинов В.С. Металлофизика высокопрочных сплавов – М.: Металлургия, 1986-312с.
6. Шабалов И.П., Шафигин З.К., Муратов А.Н. Ресурсосберегающие технологии производства толстолистового проката с повышенными потребительскими свойствами. – Металлургиздат. 2007-352с.
7. Матросов Ю.И., Литвиненко Д.А., Голованенко С.А. Сталь для магистральных газопроводов – М.: Металлургия. 1989-288с.
8. Эфрон Л.И. Металловедение в большой металлургии. Трубные стали – М.: Металлургиздат, 2012-696с.
9. Нейбер Г. Концентрация напряжений. – М.: ОГИЗ, 1947.204с.
10. Фридман Я.Б. Механические свойства металла. Часть вторая. Механические испытания. – М.: Машиностроение. 1974-368с.
11. Злочевский А.Б. Экспериментальные методы в строительной механике – М.: Стройиздат, 1983-191с.

ION PLAZMA NITRIDING OF MECHANICAL PARTS

Ass. Jashari N. MSc¹, Prof. Dr Cvetkovski. S. PhD.², Nacevski G. PhD.².

State University, Tetova, Republic of Macedonia²
Faculty of Technology and Metallurgy – Ss. Cyril and Methodius University, Skopje Republic of Macedonia¹
sveto@tmf.ukim.edu.mk

Abstract:

This practical research work is devoted to the adaptation of technology for ion plasma nitriding of mechanical parts (pins and gears). Formerly these parts were inductive hardened, and requirement of the purchaser was to replace inductive hardening technology with the chemical-heat treatment i.e. ion plasma nitriding.

Procedure for ion plasma nitriding of pin hammers and gears made of 4M2CrMo4 steel was described. Starting from the heat treatment of the parts, their cleaning and charging of the parts in the chamber. Description of the chamber and complete installation for nitride in is described. Experimental nitriding parameters are given too. Finally, accuracy of obtained results was checked using hardness measured of nitrided parts. Hardness values were in accordance with purchaser requirement,

Keywords: HARDNESS, ION PLAZMA NITRIDING, NITROGEN, PINS HAMER, GEAR

1. Introduction

Implementation of ion plasma nitriding started in the second decade of the former century as an alternative of conventional gas nitriding after the world war second this process was widely implemented in many industrial countries [1-4].

Implementation of plasma nitriding as a process of surface hardening of steels gives very good and applicable results. Phenomena of plasma is very well known natural phenomena which is deeply elaborated in the current years [5-7].

Advantages of ion plasma nitriding are the following: lower distortion compared with other processes of surface engineering, wear characteristic of parts can be controlled and even improved [8,9].

Nitriding in pulse glowing discharge (plasma nitriding) is an efficient method for increasing the hardness and wear-resistance of metals and alloys. Basic technological advantage of this method, is the low temperature at which the process is directed (450-520°C) resulting in partly volume deformations and piece distortion. Plasma nitriding of materials is characterized by the active participation of these materials in glow discharge, since they serve as cathode [10-12].

As results of these the tool life is increased from some to ten and more times. Characteristics of the ordinary steels can be significantly improved [13-14].

Achieved hardening of the surface couldn't be reach wig any other process of surface engineering. Good combination of the properties on the surface and in the core of the part [15]. Could be used in the treatment of the massive parts too. Scaling and decarburization are minimal [16].

Plasma ionized gas is the fourth state of matter. It is very reactive media which contain ions and neutral atoms occurred as results of the molecules dissociation of molecules in the electric field. Glow discharge which surround the working parts consists of these positive ions. Plasma nitriding is performed using direct current [17].

Typical process parameters are the following: Temperature (400-600°C), pressure (0.5 – 7 mbars), gas composition (ammonia, methane, hydrogen and argon), time (4-30 hours depending of the layer thickness). Additional process parameters are: voltage current intensity, pulse frequency and pulse duration.

During the plasma nitriding process, the job part and the cathode inside the furnace will be emitting a purple glow. This is because voltages had dropped sharply at these regions. This provided a large amount of discharged energy, which causes the cathode and job part to glow treatment [18].

During the plasma nitriding process, the job part and the cathode inside the furnace will be emitting a purple glow. This is because voltages had dropped sharply at these regions. This provided a large

amount of discharged energy, which causes the cathode and job part to glow [19, 20].

Knowing the basic characteristics and parameters of the ion plasma nitriding, the main task in this work was to optimize process parameters and to obtain surface layers of the treated parts with necessary parameters which enable their practical usage.

2. Material and investigations

Ion plasma nitride parts (pins hammer and conical gears) are made of low alloyed steel 42CrMo4. Chemical composition of parts is given in the table 1. The view of the parts before nitriding is given in the figure 1.

Table 1 Chemical composition of the ion nitrided parts

element	%	
	pin	gear
C	0.41	0.45
Si	0.2	0.26
Mn	0.75	0.8
Cr	1.05	1.11
Mo	0.23	0.25
rest	-	-



Figure 1 Parts for nitriding

Preparing of the parts for nitriding

Before to start with plasma nitriding, heat treatment (quenching and tempering) of the parts was done.

Parameters of the heat treatment are the following:

- Quenching T=820 – 860 °C (oil)
- Tempering T=550 °C, t=20 h

After heat treatment machining of the parts to final dimension was done. Finally grinding of the parts was made too.

Nitriding parts have to be clean from corrosion products and impurities like grease oil or similar. Organic solvents are used for removing of organic impurities while oxides are removed by grinding or by chemical solutions mainly H₃PO₄.

Charging of the chamber

After cleaning of the part from grease oil and similar impurities the parts were charged in the working area of the chamber. Treated parts are put on the working surface which is supported by three auxiliary insulators. Positive part is connected with the body of the working chamber

Dimension of the chamber, figure 2

- Useful diameter – 1000 mm;
- Useful highness – 1300 mm;
- Useful volume – 0.8 m³ ;
- Capacity for the electric and heat insulation – 1000kg;
- Operating force for the electric support and cathodic insulation - max. 1500V;
- Working temperature 300 – 600 °C;
- Working pressure 0 – 10 bar;
- Cooling – with cold water.

Technical characteristics of the chamber

- Outer characteristics of the vacuum chamber, 1360x1800 mm;
- Inner working dimensions of the chamber: 1000x1400 mm;
- Maximal weight of the treated parts: 1000 kg;
- Working gasses: nitrogen, hydrogen propane (natural gas), argon
- The process is fully automated and computerized.
- After process finishing, the parts are leaved in the chamber and cooled in vacuum. When the temperature falls to 100 °C the lin can be opened and process of ion plasma nitriding is completely finished.



Figure 2 Chamber of ion plazma nitriding instalation

Electric current supply

Electric current, installation for supply is covered with metallic coverage with the following dimensions 2000x600x1800

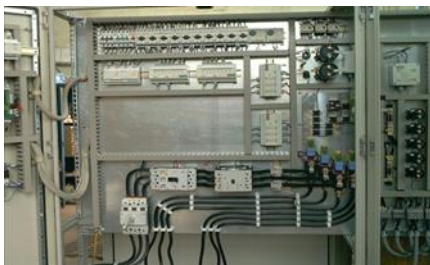


Figure 3 Electric current supplies

Input voltage	3/380V + 10% - 10%; 50Hz
Max outer power	100 kW
Outer voltage	0 – 800 V
Average current	0 – 100 A
Inputs current	0 – 120 A
Frequency	5 – 10 kHz
Impulse/pause	adjustable

Plasma nitriding parameters

The parts were nitrided under the following parameters of the chamber:

- Constant temperature of the chamber 500 °C;
- Gas composition: 99,9%;
- Pressure of the chamber (partial) 3,0 mbar;
- Cathode voltage (600V).

Technical description of nitriding installation

Working chamber is in the form of bell. It consists of bottom and lid. There are two windows on the lid from the upper and lateral side. Both parts have double walls. Between the walls circulated cold water. In order to lower heat exchange between the treated parts and working part, inner part of the chamber is covered with layers of stainless steel.

Vacuum system works permanently during technological cycle. It is controlled by the system controller according technologic program.

System for gas supply

System for gas supply contains manual valves, plastic tubes, adjusting equipment, and controllers for monitoring electric valves. Installation use the following gases: nitrogen, hydrogen, propane (natural gas) air under pressure

Nitrogen is used as active gas for technological process of plasma nitriding (Nitrogen purity, N₂: 99,999%)

Hydrogen is used as active gas in technological process of plasma nitriding (Purity of hydrogen H₂ : 99,999%).

Necessary inner pressure 3,5 до 5,0 bar.

Argon (nitrogen is used for cooling of parts of ion plasma nitriding

Monitoring control system, figure 4

Monitoring system control all mechanisms and phases of the nitriding process i.e.

- Three systems guidance;
- IGBT transistor;
- Vacuum pumps;
- Water cooling system;
- Large number of controllers;
- Electromagnetic pumps.

It controls condition in the chamber and record history of the process. The process is led according material type and shape.

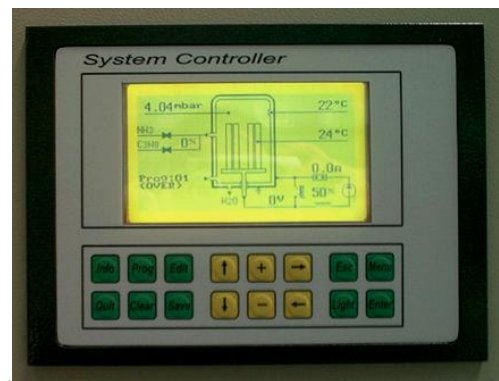


Figure 4 Monitoring control system

3. Results of the investigation

After finishing the ion plasma nitriding process the parts gears (figure 5) and pins were subdued to surface hardness measurement.

For measuring of the part was used mobile hardness tester, figure 6. And for prepared specimens from the same steel and nitreded under the same conditions was used hardness and micro hardness tester, figure 7.

Results of hardness measurements are given in the tables 2 and 3.



Figure 5 Pins hammer after ionization



Figure 6 Mobile hardness tester

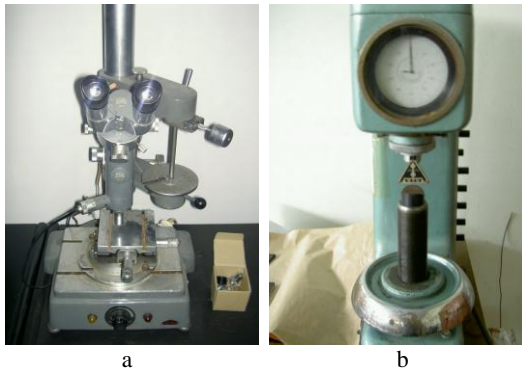


Figure 7 Hardness and micro hardness tester
a. Micro hardness tester
b. Hardness tester

Obtained results for hardness values, for both types of parts, are given in the table 2 and 3. Hardness values are measured before and after plasma nitriding using Rockvel (HRc) and Vickers (HV1) units. In both cases measured values fulfill requirement of the purchaser i.e. surface hardness after nitriding is between 50-55 HRc.

Table 2 Hardness values of nitride pins hammer

	<i>Before nitriding</i>		<i>After nitriding</i>	
	HRc 150kg load	HV1	HRc 150 kg load	HV 1
1	30	278	55	649
2	30	278	52	549
3	32	303	52	549
4	29	277	53	587
5	28	271	54	589
Σ	29,8	286	53,2	592

Table 2 Hardness values of nitrided conical gear

	<i>Before nitriding</i>		<i>After nitriding</i>	
	HRc 150 kg load	HV1	HRc 150kg load	HV1
1	28	271	52	549
2	30	285	51	538
3	30	285	52	549
4	31	285	50	505
5	32	303	51	531
Σ	30	303	51	549

4. Discussion

In the experimental work of this paper was described procedure for ion plasma nitriding of the pin hammers and gears made of 42CrMo4 steel. The base task of this practical research work was to give technology for ion plasma nitriding.

Formerly induction hardening of these parts was used for obtain increased surface hardness. But this process was in many cases impractical because bending of parts, particularly pins appear. Because of that it was decided to replace process of the heat treatment. New implemented process ion plasma nitriding has to show at least the same surface hardness like induction hardening.

In such way increased wear resistance and corrosion resistance could be reached too. Requirement of the purchaser to obtain hardness values 50-55 HRc was reach without any problem.

5. Conclusion

The basic idea in this practical research work was to increase surface hardness of two different parts i.e. pins hammer and conical gear. Instead of formerly used induction hardening, ion plasma nitriding was performed in this case. The requirement was to obtain hardness between 50-55 HRc, to perform this task; the parts were ion plasma nitrided. Plasma nitrided parts were produced from 42CrMo4 steel. Besides other advantages ion plasma nitriding enable deformation of parts, wear resistance and corrosion protection. All nitriding parameters were taken according personal experience. Measuring of hardness shows that obtained values are 53 HRc for the hammer pin and 51 HRc for conical gear which completely fulfill requirements of the purchaser.

Literature

1. Pye, D., Industrial Heating Magazine.
2. A.H. Герасимов, Плазменная технология, 1980
3. Center for Plasma technologies, catalog
4. Pye, D., private communication with J.U. Dillon, Bayside Motion Group.
5. Fry, A., U.S. Patent 1,487,554.
6. SSI personal communication.
7. Hawkins, D.T., The source book on nitriding, ASM international.
8. Pye, D., Practical nitriding and ferritic nitrocarburizing, ASM international.
9. Clayton, D.B. and sachs, W., Heat-treatment 1976.
10. Pye, D., Practical nitriding and ferritic nitrocarburizing.
11. Pye metallurgical consulting, nitriding notes.
12. Totten, G.E. and Howes, M.A.H., nitriding techniques and methods, the steel heat treatment handbook.
13. ICI Cassell, manuel of heat treatment and case hardening.
14. Reynoldson, R.W., principles of heat treatment in fluidized beds, ASM international.
15. Krauss, G., principles of heat treatment of steel.
16. Totten, G.E. and howes G.A.H., the steel heat treatment handbook.
17. Anon., Source book on nitriding, ASM international.
18. Pye metallurgical consulting and PlaTeg, personal correspondence.
19. Thomas auf dem Brinke, Jürgen Crummenauer, Rainer Hans, Werner Oppel, Nitriding, nitrocarburizing and oxidation of steel, cast iron and sintered materials
20. Paul K.Chu end Xiubo Tian, Plasma Basied Surface Modification

SOFTWARE DEVELOPMENT FOR NUMERICAL SIMULATION OF FORMATTING THE PERIODIC NANOSTRUCTURES AFTER LASER IRRADIATION

B.Sc. Phys. Zaimis U.¹, Prof. Dr. Sc. Comp. Jansone A.¹
Faculty of Science and Engineering – Liepajas University, Latvia ^{1,2}
Institute of Fundamental Science And Innovative Technologies, Liepajas University, Latvia ^{1,2}

¹uldis.zaimis@liepu.lv, ²anita.jansone@liepu.lv

Abstract: Nano-level surface processing is becoming increasingly important in the development of modern materials. Laser technology allows to change the processing parameters in a wide range and achieve the desired surface properties - hydrophilic and hydrophobic for various fluids. In such circumstances, the benefit of any researcher would be to provide software that can quickly and visibly see and measure the shape, size and configuration of nano and microstructures to be obtained. It is especially important that the obtained results in the form of 3D graphs allow us to see the evolutionary trends of surface nanostructures and help to decide on changes in the processing parameters. The researcher would be given the opportunity to input a wide variety of parameters - laser wavelength, pulse power, polarization angle, pulse frequency, pulse duration, processing time or number of impulses per coordinate - and the result obtained in a short time would serve to better understand common trends and help to make an informed decision for the actual processing parameters to be used in the experiment.

KEYWORDS: LASER IRRADIATION, NANOSTRUCTURES, MATHEMATICAL MODELLING

1. Introduction

1.1. The prevalence and role of nanostructures in nature

If you look carefully, you will see that there are practically no absolutely smooth surfaces in natural formations. Whether it's a leaf of a plant, an insect's wings, an animal's skin or a fish's scales, we are faced with a characteristic structure that fulfils its intended purpose - in one case it repels water, it is attracted in another, it helps in another, it even adheres to objects whose presence is an integral part of the residential area. An example here is the skin of the foot of the gecko (see Figure 1). It's easy to keep in mind that structures are periodic, i.e., repeat with a certain period.

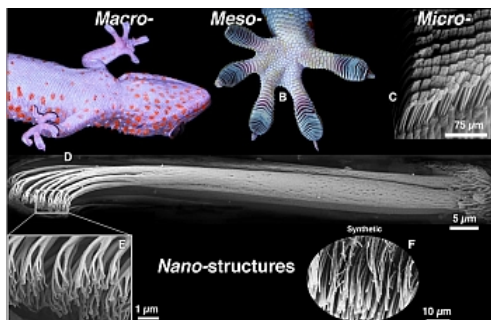


Figure 1. Micro- and nanostructures of the gecko's legs. [1].

Widespread in nature is the micro- and nano-structures that are tasked with attracting, or, conversely, rejecting water, that is, to provide hydrophilic or hydrophobic properties. An example of classic hydrophobic properties is shark skin (see Figure 2), which helps to repel water, thus reducing viscous friction and giving a speed advantage in water compared to other water users. The author has investigated that similar structures are on predators such as perch, characteristic of Latvia, but not on peaceful fish - carp, scallops.

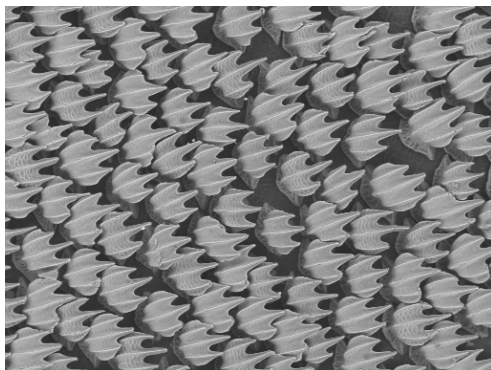


Figure 2. Structured formations of shark skin. [2]

The structures of the wings and bodies of birds, insects and other living creatures play a distinctive role - periodically arranged ribs help to prevent bacterial access to the skin, thereby improving the survival of the population.

1.2. The use of nanostructures in medicine and technology

Inspired by nature, micro- and nanostructures are increasingly appearing in engineering structures where they perform certain functions. As in the example of the shark skin, structured shapes help improve the mobility of underwater pilots and unmanned aerial vehicles (drones) to achieve higher speeds or save energy.

A special field of application is medicine. Nanorobotics have been developed and tested, with a characteristic feature of negligible dimensions and, hence, energy supplies, for the transport of medicine in blood vessels and for other applications. A nano-structured surface would help reduce energy consumption to overcome viscous friction.

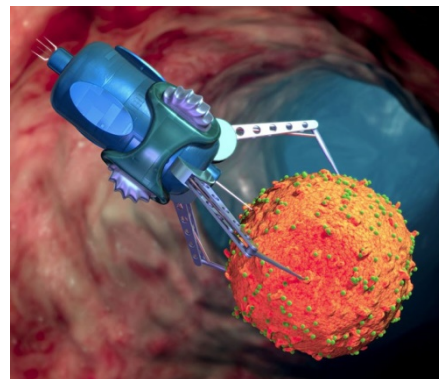


Figure 3. Nanoparticles transport medicine in the blood vessel. [3]

Another example of the use of structured surfaces in medicine is the development of implants. If, for example, the median required life of a hip implant was 5-15 a few years ago, today, due to unhealthy food and sedentary lifestyles, the a service period of 30-50 years is often required [4] (here it should be noted that for hip joints, the probability of a successful replacement of the implant is not more than 2%). In the past, the surface of the joint head was a mirrored surface. As a result, body fluids are squeezed out of contact surfaces, and the result of dry friction is, first, the wear of the material, and secondly, the human body is contaminated with wear products. The solution, as evidenced by studies at the University of Liepaja Nanomaterial Laboratory, could also be the treatment of the titanium implant head - the only metal suitable for contact with the human body - to create a controlled structured that

attracts body fluids that act as a lubricant and greatly increases the friction surface's service life time [12] (see Figure 4).

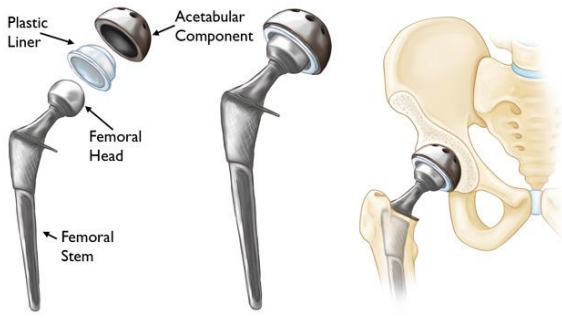


Figure 4. Hip implant. [4]

The technique for reducing friction is very important. Lubrication problems in slide bearings, such as vacuum or high temperature conditions, have still not been solved. In addition, the lubricant can be either synthetic or mineral oils, or emulsions whose hydrophobic or hydrophilic properties are basically determined by the base material. In these cases, the situation can also save the surface of the treated contact surface to retain the lubricant.

1.3. Nanostructures extraction techniques

It is possible to artificially obtain nanostructured surfaces in several ways - by mechanical, chemical treatment, electrolysis, and by laser irradiation (radiation).

The first method for obtaining micro / nano structures is mechanical processing, with tools and special materials (grinding). This method makes it relatively difficult to process surfaces different from the plane, as well as to create precise, structured shapes.

The second method for obtaining the surface of a structured material is to use chemical treatment [5]. This involves the use of acids /alkalis. The third method, which can also be used for micro nano roughness, is electrolysis. The main drawbacks are: high consumption of time and materials, poor repeatability of results, impossibility of obtaining specific surface parameters, and high costs.

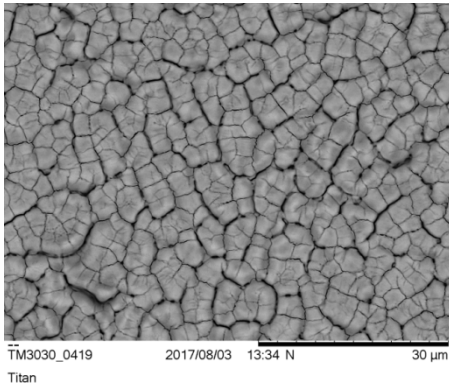


Figure 5. SEM image of laser-irradiated nanostructures on the surface of titanium (Ti).

And the last, most appropriate, presently known method for obtaining nanostructures on the top layer of materials is the laser irradiation method. This method is based on thermal effects or warming. Due to the parameters of the laser beam (wavelength, polarization direction, pulse energy, pulse duration, pulse repetition range), it is possible to achieve control of the surface of the material by controlled laser irradiation, phase change (dislocation) and the formation of uplifts under the influence of thermophilic forces, thus forming a surface relief (see Figure 5). Of great importance is the shape of the cross section and the distribution of energy in it, as well as the number of hits in the given coordinate and the distribution of the coatings [6] - [9].

2. Numerical modelling advantages in formation of nanostructures design

Understandably, due to the lack of suitable mathematical models and software products based on them, the surface treatment of materials has so far been carried out with a tray and error method - the sample was processed, then examined in an electron microscope, tested for the required properties, assumptions made about the desired changes, followed by the next sample processing with changed parameters, etc. The process was generally long lasting, time-consuming and material-intensive.

It should be noted that the materials are often not cheap because the work of laboratories involves processing materials such as chemically pure copper (Cu) and titanium (Ti), medical titanium alloys Grade1÷Grade54, platinum (Pt). An important factor is the depreciation costs of scientific hardware, which can reach significant amounts - for example, in the acquisition of surface nanostructures, the minimum necessary short pulses, the best femtosecond laser, precision machine for moving the sample through 2 coordinates (x-y stage), or a laser beam precision device, an electron microscope for analysis of the samples obtained.

In such circumstances, the benefit of any researcher would be to provide software that can quickly and visibly see and measure the shape, size and configuration of the nano and microstructures to be obtained [10]. It is especially important that the obtained results in the form of 3D graphs allow us to see the evolutionary trends of surface nanostructures and help to decide on changes in the processing parameters. The researcher would be given the opportunity to enter a wide range of parameters - laser wavelength, pulse energy, polarization angle, pulse repetition range, pulse duration, processing time or number of impulses per coordinate - and the result obtained in seconds or minutes would serve to better understand common trends and help make a reasoned decision about the actual processing parameters to be used in the experiment.

3. The mathematical model of formation of nanostructures

The formation of nanostructures is described by the following 1D mathematical model [10]:

$$\frac{\partial \rho^e}{\partial t} = \theta \cdot \frac{\partial^2 \rho^e}{\partial x^2} + \mu \cdot E \cdot \frac{\partial \rho^e}{\partial x} + \frac{\mu}{\varepsilon \cdot \varepsilon_0} \cdot \rho^e \cdot [\rho]^{e,h} + \left(g^{m.i.} + V^{c.i.} \right) \cdot \frac{\rho^{n.a.}}{\rho^{n.a.} + \rho^h} - g^{e.r.} - F^{ph.e.}; \quad (1)$$

- Poisson's equation:

$$\frac{\partial \vec{E}}{\partial x} = - \frac{|e|}{\varepsilon \cdot \varepsilon_0} \cdot [\rho]^{e,h}; \quad (2)$$

- the following is a formula for calculating the intensity of femtosecond laser radiation onto a target Gaussian time profile:

$$I(t) = \sqrt{\frac{\ln 2}{\pi}} \cdot (1 - \Phi(t)) \cdot \frac{2 \cdot f}{t_l} \cdot e^{-4 \cdot \ln 2 \left(\frac{t}{t_l} \right)^2}; \quad (3)$$

- the radiation intensity equation inside the dielectric depending on the time and distance of the target depth considering the multi-photon absorption and absorption by free electrons:

$$\frac{\partial I(x,t)}{\partial x} + a(x,t) \cdot I(x,t) = -g^{m.i.} \cdot \frac{\rho^{n.a.} \cdot m \cdot \hbar \cdot \mu}{\rho^{n.a.} + \rho^h}; \quad (4)$$

- the following formula calculates the absorption coefficient of a free electron:

$$a(x, t) = \frac{4 \cdot \pi \cdot k(x, t)}{\lambda}; \quad (5)$$

- Fresnel's formula for the estimation of the reflection coefficient:

$$\Phi(t) = \frac{\left(\sqrt{\frac{\operatorname{Re}(\varepsilon) + \sqrt{(\operatorname{Re}(\varepsilon))^2 + (\operatorname{Im}(\varepsilon))^2}}{2}} - 1 \right) + k^2}{\left(\sqrt{\frac{\operatorname{Re}(\varepsilon) + \sqrt{(\operatorname{Re}(\varepsilon))^2 + (\operatorname{Im}(\varepsilon))^2}}{2}} + 1 \right) + k^2}; \quad (6)$$

- Einstein's formula for the diffusion coefficient:

$$\theta = \frac{k \cdot T^e \cdot \mu}{|e|}; \quad (7)$$

- formula estimation for the photoemission:

$$F^{ph.e.} = \frac{(g^{m.i.})^n \cdot I^n + g^{c.i.} \cdot \rho^e \cdot I \cdot \frac{\rho^{n.a.} \cdot e^{-\frac{x}{\xi}}}{\rho^{n.a.} + \rho^h}}{2}; \quad (8)$$

In equations (20)-(27) have the following designated variables (refer to those who met earlier, below are not listed):

$V^{m.i.} = g^{m.i.} \cdot I \cdot \rho^e$ the acceleration/development of cumulative ionization;

$g^{e.r.} = \frac{\rho^e}{\tau_r}$ the recombination velocity electron capture of the coupled state;

$\rho^{n.a.}$ the density of neutral atoms;

$\xi \approx 1 \text{ nm}$ the characteristic depth of the target, which photoemission depth (maximum photoemission takes place on the surface of the dielectric material) decreases exponentially.

4. Justification of the choice of the implicit differential scheme

Two types of methods, the explicit and implicit differential equation scheme [11], [12], can be used to create the difference scheme. The explicit differential scheme is simpler, easier to program, but it has a significant drawback - the condition of stability (convergence) of the scheme must be clarified and strictly followed, otherwise the scheme will diverge and it does not give a result. It is important that this condition depends on the time step, so changing the coordinates or the time step requires the conversion of the stability condition. The implicit difference scheme is more complicated, more difficult to program - in each step of the calculation step, 4 dynamic variables must be implemented and temporarily maintained, but the unconditional stability and thus the guarantee of a solution are a major advantage.

This work uses an implicit differential scheme as it is unconditionally stable and does not require compliance with the convergence conditions.

5. Development of the implicit differential scheme

Let's start by looking at the method of solving differential equations - the reduction method, or the Thomas algorithm. Let's look at the border problem:

$$\begin{cases} A_i y_{i-1} - C_i y_i + B_i y_{i+1} = -f_i, & A_i \neq 0, B_i \neq 0, i = 1, 2, \dots, N-1 \\ y_0 = \chi_1 y_1 + \mu_1, \\ y_N = \chi_2 y_{N-1} + \mu_2, \end{cases} \quad (9)$$

which is to be conveyed by $(N+1) \times (N+1)$ size three diagonal matrix:

$$A = \begin{bmatrix} 1 & -\chi_1 & 0 & \dots & 0 & 0 & 0 & 0 & 0 & 0 \\ A_1 - C_1 & B_1 & \dots & 0 & 0 & 0 & 0 & 0 & 0 & 0 \\ \dots & \dots \\ 0 & 0 & 0 & \dots & A_i - C_i & B_i & \dots & 0 & 0 & 0 \\ \dots & \dots \\ 0 & 0 & 0 & \dots & 0 & 0 & 0 & \dots & A_{N-1} - C_{N-1} & B_{N-1} \\ 0 & 0 & 0 & \dots & 0 & 0 & 0 & \dots & 0 & -\chi_2 & 1 \end{bmatrix}. \quad (10)$$

In the Dirichlet, or in the first kind of boundary problem, the size of the corresponding matrix will be $(N-1) \times (N-1)$.

To solve the boundary problem, we will look for a solution in the following form:

$$y_i = \alpha_{i+1} y_{i+1} + \beta_{i+1}, \quad (11)$$

which is a linear equation with variable coefficients α_{i+1} and β_{i+1} ; by analogy $y_{i-1} = \alpha_i y_i + \beta_i$ we put in the initial expression:

$$(A_i \alpha_i - C_i) y_i + B_i y_{i+1} = -(f_i + A_i \beta_i); \quad (12)$$

comparing this equation with the original, we find:

$$\begin{aligned} \alpha_{i+1} &= \frac{B_i}{C_i - A_i \alpha_i}, & i = 1, 2, \dots, N-1, \\ \beta_{i+1} &= \frac{A_i \beta_i + f_i}{C_i - A_i \alpha_i}, & i = 1, 2, \dots, N-1. \end{aligned} \quad (13)$$

To find the coefficients α_1, β_1 at $i=0$, we can use initial conditions. At $i=0$ we get $\alpha_1 = \chi_1, \beta_1 = \mu_1$.

Knowing α_i and β_i and switching from i to $i+1$, we determine α_i and β_i for all $i=2, 3, \dots, N$. The part of this calculation is carried increasing the order of the indexes.

For the search function y , the calculation is then carried out in the opposite direction, with the indices falling from $i+1$ to i (i.e., knowing the next one, we find the preceding index number); You need to know the start of calculations y_N . We find it from the starting condition $y_N = \chi_2 y_{N-1} + \mu_2$ and expressions at $i = N-1$:

$$y_{N-1} = \alpha_N y_N + \beta_N. \quad (14)$$

From this, we get:

$$y_N = \frac{\mu_2 + \chi_2 \beta_N}{1 - \alpha_N \chi_2}. \quad (15)$$

And so, all the methods of reduction formulas together:

$$\begin{aligned} \alpha_{i+1} &\stackrel{(\rightarrow)}{=} \frac{B_i}{C_i - A_i \alpha_i}, & i = 1, 2, \dots, N-1, & \alpha_i = \chi_i; \\ \beta_{i+1} &\stackrel{(\rightarrow)}{=} \frac{A_i \beta_i + f_i}{C_i - A_i \alpha_i}, & i = 1, 2, \dots, N-1, & \beta_i = \mu_i; \\ y_N &= \frac{\mu_2 + \chi_2 \beta_N}{1 - \alpha_N \chi_2}, \\ y_i &\stackrel{(\leftarrow)}{=} \alpha_{i+1} y_{i+1} + \beta_{i+1}, & i = N-1, N-2, \dots, 2, 1, 0. \end{aligned} \quad (16)$$

The arrows show the direction of the solution: (\rightarrow) from i to $i+1$, in turn (\leftarrow) from $i+1$ to i . To find the solution to this differential equation, such a Thomas algorithm must be applied at each given time step.

Consider the given differential equation:

$$\begin{aligned} \frac{\partial \rho^e}{\partial t} &= \theta \cdot \frac{\partial^2 \rho^e}{\partial x^2} + \mu \cdot E \cdot \frac{\partial \rho^e}{\partial x} + \frac{\mu}{\varepsilon \cdot \varepsilon_0} \cdot \rho^e \cdot [\rho]^{e,h} + \\ &+ (g^{m.i.} + V^{c.i.}) \cdot \frac{\rho^{n.a.}}{\rho^{n.a.} + \rho^h} - g^{e.r.} - F^{ph.e.} \end{aligned} \quad (17)$$

We first perform a DV discretization :

$$\frac{\partial \rho_i^j}{\partial t} = \theta \cdot \frac{\partial^2 \rho_i^j}{\partial x^2} + \mu \cdot E \cdot \frac{\partial \rho_i^j}{\partial x} + \frac{\mu}{\varepsilon \cdot \varepsilon_0} \cdot \rho_i^j \cdot (\rho_i^j - \rho^h) + \left(g^{m.i.} + V^{c.i.} \right) \cdot \frac{\rho^{n.a.}}{\rho^{n.a.} + \rho^h} - g^{e.r.} - F^{ph.e.} \quad (18)$$

We define differential operators with differences:

$$\frac{\partial \rho}{\partial x} \approx \frac{\rho_{i+1} - \rho_i}{h_x}; \quad \frac{\partial \rho}{\partial t} \approx \frac{\rho_i^{j+1} - \rho_i^j}{h_t}; \quad \frac{\partial^2 \rho}{\partial x^2} \approx \frac{\rho_i^{j+1} - 2\rho_i^j + \rho_i^{j-1}}{h_x^2}; \quad (19)$$

where h_x , h_t - steps along the corresponding variable axes. We obtain the coefficients A, B, C, f for the reduction (Thomas) algorithm [11], [12]:

$$A_i = \frac{\theta}{h_x^2} + \frac{\mu E}{h_x}, \quad C_i = \frac{1}{h_t} + \frac{2\theta}{h_x^2} + \frac{\mu E}{h_x}, \quad B_i = \frac{\theta}{h_x^2}, \quad (20)$$

$$f_i = F_i^j - \left(\frac{1}{h_t} + \frac{\mu \cdot e}{\varepsilon \cdot \varepsilon_0} \right) \cdot (R_i^j - \rho h_i^j) - \frac{1}{\tau} \cdot R_i^j - g^{m.i.} \cdot (1 + I_{luc} R_i^j) \cdot \frac{\rho n a_i^j}{\rho n a_i^j + \rho h_i^j}. \quad (21)$$

Using the found coefficients A, B, C, source function f, initial and border conditions and the Thomas algorithm described above, a computer program is written in the MatLab environment.

6. Algorithm development

The algorithm follows the following requirements:

- functions that describe laser radiation and exposure to materials are preserved for short-term exposure, namely, at each time step, it is checked that the moment coincides with the time given by the laser beam;
- Considering that the solution contains multiple integrals that are summed, the algorithm does not accumulate to be unnecessarily massive, but uses dynamic variables or other solutions to avoid unnecessary loading of computer resources;
- Since no user interface is created (the number of parameters to enter is not high, and the program is intended for internal use by one employee - the program developer), then tags are made in the code, which helps to enter the constants and parameters in their places;
- The laser parameter described uses the main parameters of the pulsed laser contained in the Laboratory of Nanomaterials of Liepajas University, Latvia.

7. Using of developed software

7.1. Periodic nanostructures on the SiO₂ surface - 1

Using the following substance, SiO₂ (silicon dioxide),

parameters:

$$\mu = 1, \quad \varepsilon = 3.9, \quad k = 0.4, \quad T^e = 400, \quad \lambda = 532, \quad n = 5, \quad \tau = 2 \cdot 10^{-4},$$

$$g^{m.i.} = 2 \cdot 10^4, \quad g^{c.i.} = 3 \cdot 10^6,$$

and applying a real laser operating at a frequency of 10 Hz for 6 seconds yielded the following dynamics of nanostructures (see Figure 8):

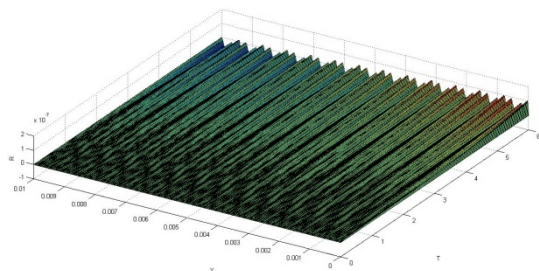


Figure 8. Dynamics of Nanostructures on the surface of silicon dioxide - 1.

We see that periodic structures are formed across the time axis, and, due to the relatively high relaxation time, their growth is flattened.

7.2. Periodic nanostructures on the SiO₂ surface - 2

Similar simulation with modified multiphoton recombination rates and periodic dielectric permeability index is shown in Figure 9:

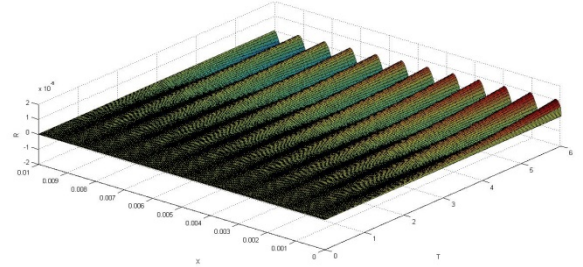


Figure 9. Dynamics of Nanostructures on the surface of silicon dioxide SiO₂.

The obtained graph perfectly correlates with the results of a real experiment, whose SEM image is shown in Figure 10.

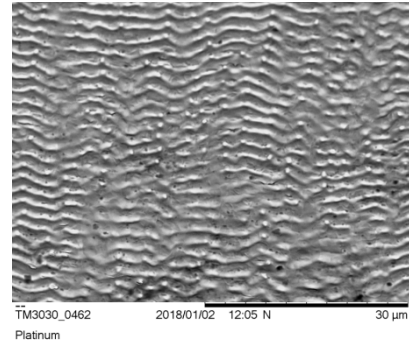


Figure 10. SEM image of periodic wave structures on the surface of the material. Magnification 3000x.

7.3. Periodic nanostructures on SiO₂ surface - 3

Another example is that the density of the substance decreases, thus forming an elevation in the 1D cross-section; observed periodic wave structures:

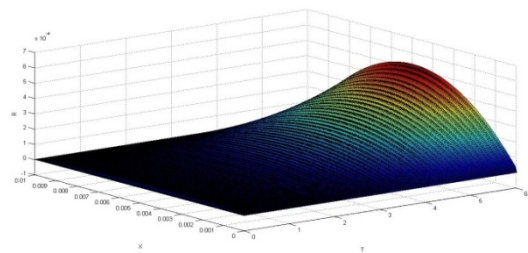


Figure 11. Dynamics of Nanostructures on the surface of silicon dioxide - 3.

7.4. The time needed for a numerical solution

Calculating all of the examples in this section on a computer with an Intel CORE i7 processor and a NVIDIA GT 635M graphics card, the time consumed was: 1) at the nodes $[0:40] \times [0:40]$ approximately 4-5 seconds, 2) at the nodes $[0:280] \times [0:280]$ approximately 8-10 seconds, 3) at the nodes $[0:2000] \times [0:2000]$ approximately 140-150 seconds.

8. Acknowledgements

The first author of the work thank professor dr. sc. math. Sh. E. Guseynov for the experience and cooperation provided in developing the theoretical part of the topic.

9. References

- [1] Lee J., R.S. Fearing, The pitter patter of little feet. Climbing strait up a wall. 01/2008, Journal of the Royal Society Interface, UC Berkeley
- [2] Harris J. Biometric Shark Skin Design Fabrication And Hydrodynamic, blog: daneshetabiat.com
- [3] Ames B., Burill G. S., Grey A., Haseltine W., Perry D. New work on nanorobotics design, simulation and control for nanomedicine, UCLA conference, Los Angeles, 2008
- [4] <https://orthoinfo.aaos.org>
- [5] Kim George E. Nanostructured Materials: Processing, Properties, and Applications [Book] ed. Carl Koch C. – USA, Norwich: William Andrew Publishing, 2007 – Second Edition: pp. 113-115
- [6] Климков Ю.М., В.С. Майоров, М.В. Хорошев Взаимодействие лазерного излучения с веществом: учебное пособие. — М.: МИИГАиК, 2014.— 108 с.
- [7] Либенсон М.Н., Яковлев Е.Б., Шандыбина Г.Д. Взаимодействие лазерного излучения с веществом (силовая оптика) Конспект лекций под редакцией Вейко В.П. Часть I Механизмы поглощения и диссипации энергии в веществе. Санкт–Петербург, 2005
- [8] Тимченко Е.В. Взаимодействие лазерного излучения с веществом, Самара 2012.
- [9] Либенсон М.Н., Яковлев Е.Б., Шандыбина Г.Д. Взаимодействие лазерного излучения с веществом (силовая оптика). Часть II. Лазерный нагрев и разрушение материалов. Учебное пособие. Под общей редакцией В.П. Вейко – СПб: НИУ ИТМО, 2014. –181с.
- [10] Guseynov Sh.E., Žaimis U. *On A Physico-Mathematical Model For Controlled Formation Of Periodic Nanostructures At Solid Surfaces Irradiated By Femtosecond Laser Pulses*, Journal "Machines. Technologies. Materials.", Issue 7/2016, ISSN 1313-0226
- [11] Самарский А.А. Теория разностных схем. – Москва: Наука, 1983
- [12] Samarskii A.A. The Theory of Difference Schemes. – CRC Press, 2001

STUDY OF STRUCTURE FORMATION AND HARDENING IN CARBON STEELS DURING HPT AT TEMPERATURES BELOW RECRYSTALLIZATION

ИССЛЕДОВАНИЕ ОСОБЕННОСТЕЙ СТРУКТУРООБРАЗОВАНИЯ И УПРОЧНЕНИЯ В УГЛЕРОДИСТЫХ СТАЛЯХ ПРИ ИПДК В ОБЛАСТИ ДОРЕКРИСТАЛЛИЗАЦИОННЫХ ТЕМПЕРАТУР

Dr.Sci. Raab G.¹, Dr.Sci. Aleshin G.¹, Kodirov I.¹, Raab A.¹

¹Ufa State Aviation Technical University, Institute of Physics of Advanced Materials, Ufa, Russia

E-mail: giraab@mail.ru, galioshin@mail.ru, ilyas-kodirov@mail.ru, agraab@mail.ru

Abstract: The impact of the parameters of thermomechanical treatment on the structural changes and micro-hardness of low- and medium carbon steels under a high hydrostatic pressure at high pressure torsion (HPT) is investigated. It is established that for HPT the deformation temperature has a decisive impact on the efficiency of refinement and hardening. This is caused by the effect of dynamic strain ageing (DSA) at 250 and 400°C during HPT. At the same time the level of accumulated strain in the sample intensifies the refinement under the effect of dynamic strain ageing (DSA). It should be noted that an increase of the carbon content to 0.2 % and 0.45% in steel leads to an increase in the temperature of dynamic strain ageing (DSA) to 400°C. It is stated that HPT under the effect of dynamic strain ageing (DSA) results in the formation of a gradient structure in the samples after five rotations of the anvil ($e_{\max}=6.26$) at a hydrostatic pressure of 6 GPa.

Keywords: MICROSTRUCTURE, DSA, CARBON STEEL, HPT, SPD, MICROHARDNESS

1. Introduction

High pressure torsion is widely used to increase the properties of metal materials [1-4]. Generally, this is cold treatment with the high level of accumulated strain. However, the strength of materials increases 2-3 times due to the formation of a grain structure of the ultrafine and/or nanostructured range [4-8]. During the cold treatment by HPT the hardening of the samples subjected to 5 rotations of the anvil $e_{\max} = 3.45$ as a rule levels, this is especially typical of pure metals [2, 4]. HPT processing of the alloys with the solution supersaturated with alloying elements (thermal-hardened) generally leads to the formation of new stable phases as nanoparticles located both in the bodies and boundaries of ultrafine and nano grains. Consequently, this contributes to more effective hardening of the samples after deformation [7, 8].

Recently the attention of researchers has been focused on the effect of dynamic strain ageing (DSA), its full occurrence depends on the temperature of deformation. The temperature range of occurrence of this effect is usually 200-400°C, and it is located in the range below the recrystallization temperatures. The effect of DSA also impacts the intensity of dispersion of the structure and the degree of its defects (hardening) [8, 9]. Of particular interest in that connection is the study of the features of structure formation and hardening of commercial steels depending on the temperature and the carbon content under the critical conditions relevant to HPT, i.e. a high hydrostatic pressure of 6 GPa and ultrahigh accumulated strain of $e_{\max}=6.26$. Besides, the DSA effect is observed in steels during traditional plastic deformation [9–12].

2. Material and procedures of experiments

This paper investigates the impact of the carbon content in steels on the formation of a gradient structure under severe plastic deformation of steels 10, 20 and 45 with standard chemical composition [13].

The initial samples for the investigation are discs with a diameter of 10 and 20 mm, thickness of 0.5 mm. The steel samples are subjected to HPT under 6 GPa at temperatures of 20, 250 and 400°C. Figure 1 shows the scheme of the HPT process [8, 9].

The strain degree is determined by the equation [2, 3]

$$\varepsilon = \ln(\vartheta \cdot r/h), \quad (1)$$

where ϑ – the angle of torsion (radian), r and h – the radius and thickness of disc, correspondingly.

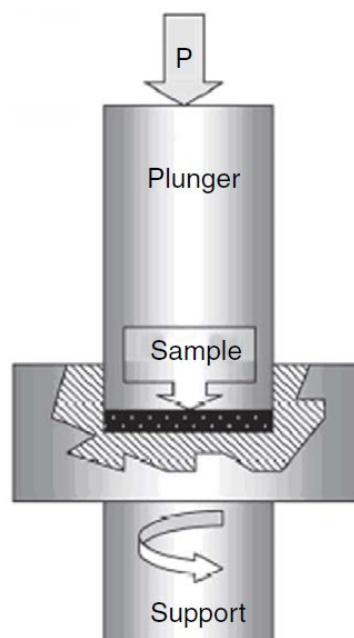
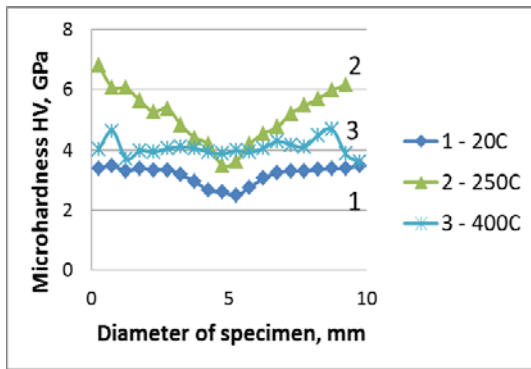


Fig. 1 Scheme of the deformation node for high pressure torsion

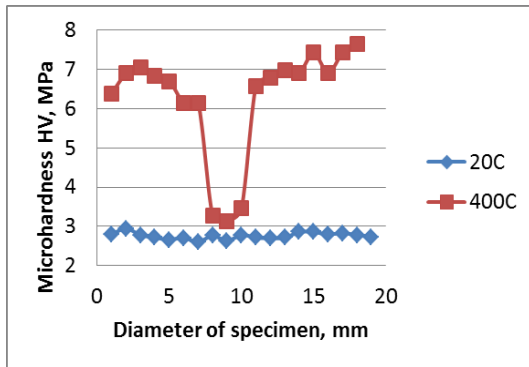
After the deformation the microhardness of these samples is determined by their diameter, and the structure of the central and peripheral parts is investigated by light and scanning electron microscopes.

3. Results of experiments and their discussion

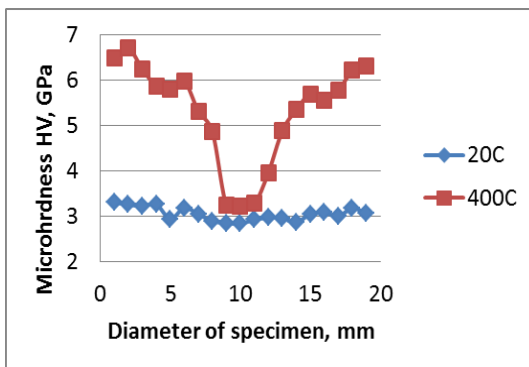
Figure 2 shows the results of the investigations of microhardness of the steels after HPT at the chosen temperatures for the three chosen steel grades. Figure 3 demonstrates the microstructure of steel 10 after HPT at a temperature of 20°C.



a)



b)

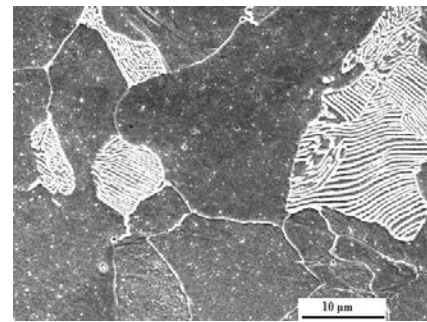


c)

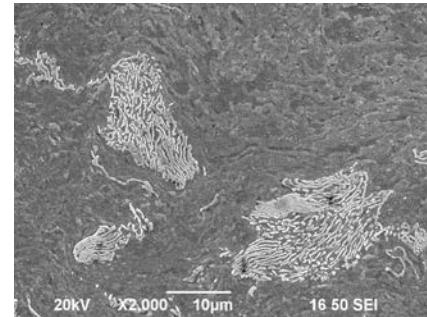
Fig.2 Plots of microhardness distribution in the samples where a) Steel 10 after deformation at 20°C(1), 250°C(2), 400°C(3); b) Steel 20 after deformation at 20°C(1) and 400°C(2); c) Steel 45 after deformation at 20°C(1) and 400°C(2).

The analysis of the microhardness distribution along the diameter section of the samples shows that the minimum values of the hardness are obtained after cold treatment of the steels (20°C). However, the lower values HV in comparison with the periphery are observed in the center of the steel 10 samples, but the microhardness values are roughly the same along the whole diameter of the samples of steel 20 and steel 45.

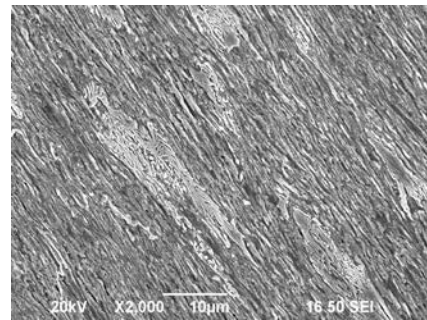
The microstructural studies are conducted to determine the causes of the observed features of the microhardness change of the sample after HPT. Figure 3 shows the images of the microstructure of steel 10 in the initial state and after HPT. The plates of cementite in the grains of perlite in the initial state are located mainly parallel with each other. After HPT the plates of cementite are divided into pieces which are randomly located towards each other in the most grains of perlite. This demonstrates the development of dislocation sliding and occurrence of rotary modes of deformation in the grains of perlite. Such action of rotary modes of deformation were also observed in [8], which described equal channel angular pressing of steel 10.



a)



b)



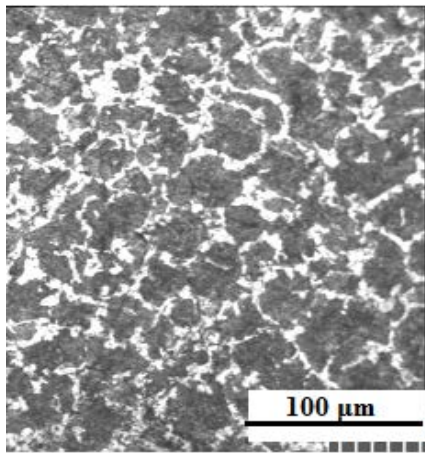
c)

Fig. 3 Microstructure of steel 10: a – initial state, b, c – 5 HPT rotations at 20°C, b – centre of samples, c – periphery. Scanning electron microscope

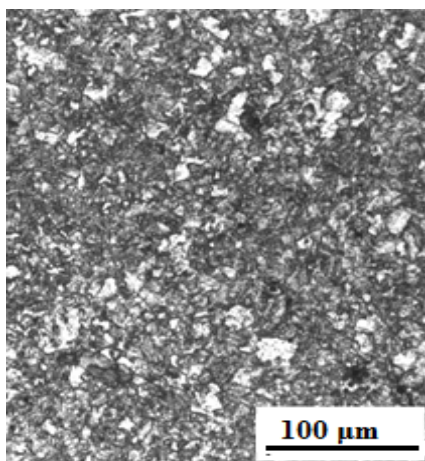
In the periphery of the samples, where the strongest structure refinement occurs, perlite and ferrite grains are highly elongated along slip bands (Figure 3c). A substructure with relatively equiaxed cells forms in these ferrite and perlite grains during HPT, which corresponds to the previously obtained data on other materials [3].

A decrease in the microhardness values in the steel 10 samples deformed at 400°C in comparison with the HV values obtained after HPT at 250°C indicates that the effect of DSA becomes weaker at a temperature of 400°C for low carbon steel 10 due to activation of diffusion processes. An increase of the carbon content in the steel to 0.2% and 0.45% leads to an increase in the temperature the DSA effect to 400°C (Figure 2).

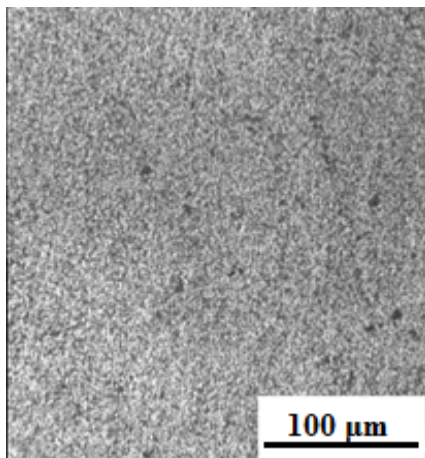
Figure 4 shows the microstructure of steel 45 after 5 rotations ($\epsilon \approx 3.45$) of HPT. The structure refinement is $\sim 300\text{--}400$ nm in the center, and in the periphery of samples it is $\sim 100\text{--}200$ nm especially at increased temperatures (Figure 4). Consequently, the microhardness values in the periphery of the samples after HPT at 400°C exceed more than two times (to 6.5 GPa) the values of HV in the centre of the samples (~ 3 GPa). The similar change in the microstructure and microhardness is observed in steel 20 under HPT.



a)



b)



c)

Fig. 4 Microstructure of the samples of steel 45: a – initial state; b, c – after 5 HPT rotations ($\epsilon \approx 3.45$) at 400°C; b – center of the sample, c – periphery of the sample. Light electron microscope

Consequently, the cell size reduction from the center to the periphery of the samples and a considerable increase in the microhardness demonstrate the formation of the gradient structure and properties of the steel samples subjected to HPT under DSA. Similar behavior under HPT are observed in [14, 15].

Nowadays the study of regularities of formation of gradient structures is an urgent trend in modern material science [16-20], and this investigation contributes to it.

4. Conclusions

1. The features of formation of the gradient structure at high pressure torsion of steel 10, steel 20 and steel 45 have been investigated, when the effect of dynamic strain aging occurs. The deformation mechanisms in different parts of the samples of the steels during HPT have been analyzed.

2. The temperature range of 250 – 400°C of the DSA effect exhibition during high pressure torsion of the studied steels has been determined. The relation between activation of the DSA effect and the structure state has been demonstrated.

3. The structural changes of the steels under HPT and, consequently, the formation of the gradient structure in the steels have been investigated in the temperature range of the DSA effect. It is shown that under HPT the most effective refinement of the structure (cell sizes d_{cell} decrease to 0.1-0.2 μm) is in the periphery of the samples in comparison with the center ($d_{\text{cell}} > 0.3 \mu\text{m}$) that is characterized as a gradient structure.

4. As a result of the DSA effect, in the process of severe plastic deformation, additional refinement of the structure of the alloys and, consequently, a more significant increase in the yield stress and microhardness takes place in comparison with the samples deformed at room temperature. The increase in the lattice friction stress due to the interaction of atoms atmospheres of impurities with mobile dislocations leads to the additional increase in the density of dislocations in ferrite and perlite grains.

Acknowledgments. The authors acknowledge gratefully the financial support by the Russian Foundation for Basic Research through project № 17-08-00720.

5. References

1. A. G. Raab, M. V. Chukin, G. N. Aleshin and G. I. Raab / Investigation of a new shear deformation method for the production of nanostructures in low-carbon steel // 2014 IOP Conf. Ser.: Mater. Sci. Eng. 63 012008 [doi:10.1088/1757-899X/63/1/012008](https://doi.org/10.1088/1757-899X/63/1/012008)
2. Valiev, R.Z. Bulk nanostructured materials from severe plastic deformation. / R.Z. Valiev, R. K. Islamgaliev, I.V. Alexandrov. // Prog. Mater. Sci. 45 (2000) 103–189
3. R.Z. Valiev, A. P. Zhilyaev and T. G. Langdon, Bulk Nanostructured Materials: Fundamentals and Applications, Wiley STM, USA 2014, p. 440.
4. A.V. Ganeev, E.A. Korneeva, R.Z. Valiev/ Study on the nanostructured state of steel 10 subjected to high pressure torsion. // Nauchnye vedomosti: Matematika. Fizika. 2012. №23(142). Iss. 29. Pp. 110-116.
5. G. I. Raab, D. V. Gunderov, L. N. Shafigullin, Yu. M. Podrezov, M. I. Danylenko, N. K. Tsenev, R. N. Bakhtizin, G. N. Aleshin, A. G. Raab / Structural variations in low-carbon steel under severe plastic deformation by drawing, free torsion, and drawing with shear // Materials Physics and Mechanics, 2015, No 3, Vol. 24, 242-252
6. S.O. Firstov, T.H. Rogul, O.A. Shut / Transition from microstructures to nanostructures and ultimate hardening // Functional Materials. 2009. 16 №4. P. 364-373.
7. O. Firstov, T. H. Rohul, V. I. Svechnikov, S. M. Dub. / Concept of "useful" impurities and mechanical properties of nanostructured chromium and molybdenum films. // Materials Science. 42 (1) (2006) 121-126.
8. G. N. Aleshin, G. I. Raab, I. S. Kodirov. / Features of Dynamic Strain Aging of Low-Carbon Steels during Severe Plastic Deformation Processing // Key Engineering Materials. 2017, Vol. 743, pp 191-196.
9. E.D. Shcherbakov, V.P. Lapin, O.R. Essenson / Impact of strain ageing on the properties of different items from steel // Casting and metallurgy, 2010, 3 (57). pp. 216-221
10. V. K. Babich, Yu. P. Gul, I. E. Dolzhenkov, Strain aging of steel, Metallurgiya, Moscow, 1972

11. K. V. Popov, Dynamic strain aging and brittleness of hydrogen type, 1979. 98 c.
12. A. H. Cottrell, B. A. Bilby, Dislocation theory of yielding and strain ageing of iron, Proc. Phys. Soc. A. 62 (1949) 49–53.
13. Grade reference of steels and alloys / V.G. Sororkin, A.V. Volosnikova, S.A. Vyatkin, et al: M.: Mashinostroenie. 1989. 640 p.
14. E.V. Kozlov, V.E. Gromov, V.V. Kovalenko, et al. gradient structures in perlite steel /Novokuznetsk: SibSIU. -2004. – 224p.
15. Ivanov Y.F., Kovalenko V.V., Kozlov E.V., et al. gradient structure and phase states in steels. Novosibirsk: Nauka. - 2006. – 280p.
16. K. Lu. Making strong nanomaterials ductile with gradients. Science 19 Sep 2014: Vol. 345, Issue 6203, pp. 1455-1456.
17. T. H. Fang*, W. L. Li*, N. R. Tao*, K. Lu† Revealing Extraordinary Intrinsic Tensile Plasticity in Gradient Nano-Grained Copper. Science 25 Mar 2011: Vol. 331, Issue 6024, pp. 1587-1590.
18. G.I. Raab, L.A. Simonova, G.N. Aleshin / Tailoring the gradient ultrafine-grained structure in low-carbon steel during drawing with shear // Metalurgija 55 (2016) 2, 177-180
19. Ivanov Y.F., Kovalenko V.V., Kozlov E.V., et al. gradient structure and phase states in steels. Novosibirsk: Nauka. - 2006. – 280p.
20. G. I. Raab, Y. M. Podrezov, G. N. Aleshin, "Structure Evolution during Plastic Deformation of Low-Carbon Steel", Materials Science Forum, Vol. 870, pp. 253-258, 2016

THE LABORATORY TESTING OF STEEL 20MnCr5

Opačak I., mag.ing.mech. ¹, Marić A., dipl.ing. ², Hon.D.Sc. Dašić P. ³, Prof. dr. sc. Marušić V. ¹
Faculty of Mechanical Engineering, University of Osijek, Trg Ivane Brlić-Mažuranić 2, Slavonski Brod, Croatia ¹
HEP-Toplinarstvo d.o.o., Pogon Osijek, Ulica cara Hadrijana 7, Osijek, Croatia ²
SaTCIP Publisher LTD., Tržni centar Pijaca 106a, Vrnjačka Banja, Serbia ³
iopacak@sfsb.hr, alen.marić@hep.hr, dasicp58@gmail.com, vmarusic@sfsb.hr

Abstract: In this paper the laboratory tests on the selected steel for cementation 20MnCr5 was performed. The influence of the contact load resistance to the adhesion wear of high-temperature carbonitrided MnCr steels was analyzed. As a representative example was selected a tribosystem drive/driven gear of reducers in which are expressed high contact loads. For the purposes of these tests, the samples were first high-temperature carbonitrided, and then they are carried to the appropriate chemical and metallographic analysis, control of the surface hardnesses and the resistance to the adhesion wear. The aim of this paper was to observe the representative tribosystem as much possible to define its working parameters in order to determine the optimum conditions for testing the influence of the contact load on resistance to the adhesion wear. The analysis results show that high-temperature carbonitrided steel where the atmosphere of furnace at the beginning of carburizing was enriched with nitrogen, and finally with carbon showed significantly greater resistance to the adhesion wear compared to steel that at the beginning of carburizing had atmosphere of furnace rich in carbon, and finally with nitrogen.

Keywords: STEEL 20MnCr5, MICROSTRUCTURES, HARDNESSES, ADHESION WEAR

1. Introduction

Tribology is the scientific-expert discipline that deals with the phenomena and processes on surfaces which are in mutual interaction, direct or indirect contact and relative motion [1]. The study of friction and wear problems as well as the role of lubrication, tribology approaches as parts of a one whole in which the phenomena and processes are mutually connected and have a significant influence on the economy of technical resources that are produced and used. Tribological problems are present in all branches of the industry. The termination of a functional work of parts may occur due to breakage, due to wear and due to corrosion effects [2]. One of the more common types of wear that occurs in practice is the case of adhesion wear. This wear is reflected in the transition of material from one friction surface to the other in conditions of immediate contact of the metal surfaces body in relative motion. Any wear caused by adhesion can be described in three phases: I - formation of the adhesion compound, II - breaking of the adhesion compound, III - rupture and eventual breaking of particles [3]. The aim of this paper was by chemical and metallographic analysis and flow of surface hardnesses and resistance tests to the adhesion wear on the selected high-temperature carbonitrided samples to investigate the dependence of the measured wear intensity on the applied contact loads. In selecting of the material samples and materials of the counter body, should take care of their compliance modeled on observed representative tribocouple gear. Expected tests and analysis should provide insight into the properties of steel achieved by the processes of high-temperature carbonitriding and their resistance to the adhesion wear conditions at different load levels.

2. The properties of steel 20MnCr5

Steel 20MnCr5 belongs to a group of steel for cementation. These steels represent a structural steels which after machining by particle separation are carburizing on the edge of the layer. After carburizing of the edge layer, by hardening is achieved high resistance to wear of the edge layers and the increased toughness of the non-carburized core [4]. Steels for cementation mainly contain from 0,1 to 0,2 % carbon before carburizing, and may be a non-alloyed or low-alloyed. The edge layer after process of carburizing contain from 0,8 to 0,9 % carbon, and with hardening is achieved hardness from 61 to 64 HRC. After the process of cementation carburized core remains a ferrite-perlite structure, if the material is not hardenability. In the case of hardenability the low-carbon martensite is formed. Both of these microstructures are characterized by high toughness with high wear resistance.

After the process of cementation the surface layers contain high-carbon martensite. The most common application of steel 20MnCr5 is in the production of gears, shafts and axles of machines, camshafts etc. [5]. Declared mechanical properties of steel 20MnCr5 are shown in Table 1 [6].

Table 1: Mechanical properties of steel 20MnCr5.

Steel mark	Properties			
	Hardness, HB	$R_{p0.2}$, MPa	R_m , MPa	A_5 , %
20MnCr5	152 ÷ 201	685	980 ÷ 1280	7

3. Experimental tests

In the experimental part of this paper, as an representative example of the tribosystem was selected gear assembly of the reducers, Figure 1.



Fig. 1 The representation of tribosystem drive/driven gear.

In this assembly drive/driven gear are expressed to a high contact loads. The drive gear (sample UZ) is made from steel for cementation 20MnCr5, while the driven gear (counter body KT) is made from steel for improvement 42CrMo4, Figure 2.



Fig. 2 Samples for laboratory testing.

By this selection of materials and test conditions, it was attempted to imitate the real machine elements in the process, both in terms of the material from which they were made and in view of their working conditions.

3.1. The experiment plan

Plan of the experimental tests performed on samples of steel 20MnCr5, marked with 421 and 422 was showed in Table 2.

Table 2: Plan of the experimental tests.

Sample mark	Tests performed on steel 20MnCr5					
	VTKN	KA	MG	HV1	Testing of wear resistance	Traces of wear
421	+	+	+	+	+	+
422	+	+	+	+	+	+

* VTKN - high-temperature carbonitriding; KA - chemical analysis; MG - metallographic tests.

3.2. The heat-chemical treatment

Tables 3 ÷ 5 are showing parameters of high-temperature carbonitriding steel 20MnCr5. High-temperature carbonitrided samples are marked with 421 and 422 and they are provided for resistance testing to the adhesion wear. Before high-temperature carbonitriding soft annealing was performed, the parameters are shown in Table 3. The parameters of high-temperature carbonitriding are shown in Table 4. After completion of the ten-hour carburizing, directly hardening and subsequent low-temperature loosening are performed, Table 5.

Table 3: The selection of parameters of the previous heat treatment of steel 20MnCr5.

Name	Parameters	
Previous heat treatment	Duration	40'
	Temperature	660 °C
Soft annealing	Cooling	In furnace

Table 4: The selection of parameters of the heat-chemical treatment of steel 20MnCr5.

Name	Parameters	Process 1	Process 2
High-temperature carbonitriding	Duration of carburizing	300'	300'
	Temperature of carburizing	920 °C	920 °C
	C _{pot}	0,5 % C	1,0 % C
	NH ₃	10 %	5 %

Table 5: The selection of parameters of the subsequent heat treatment of steel 20MnCr5.

Name	Parameters	
Subsequent heat treatment	Austenitization temperature	820 °C
	Duration	45'
Hardening	Cooling	Oil
Subsequent heat treatment	Loosening temperature	180 °C
	Duration	40'
Loosening	Cooling	In furnace

The high-temperature carbonitriding of samples was performed using the variable potential of the carbon (C) and nitrogen (N), or with a combination of parameters of the process 1 and process 2. Carburizing was conducted in the furnace with natural gas as a carrier of carbon and ammonia as a carrier of nitrogen at a temperature of 920 °C.

On the sample 421 are first applied parameters of process 1 and then parameters of process 2, while on the sample 422 are first applied parameters of process 2 and then parameters of process 1. The duration of each process was amounted by 300'. The only difference is in the order of their application.

3.3. Testing of the chemical composition

Testing of the chemical composition was performed on steel 20MnCr5. Chemical analysis was used to determine the composition of steel used for high-temperature carbonitriding. To determine the chemical composition a spectrometric method was used, and the test was performed with the device „Belec“, Figure 3.



Fig. 3 Device for chemical analysis.

Results of the chemical composition testing of steel 20MnCr5, as well as the values prescribed by standard are shown in Table 6.

Table 6: The chemical composition of steel 20MnCr5.

	Chemical composition, %					
	C	Si	Mn	P	S	Cr
Declared [7]	0,17 ÷ 0,2	max. 0,4	1,1 ÷ 1,4	max. 0,025	max. 0,035	1 ÷ 1,3
Tested	0,18	0,35	1,23	0,021	0,028	1,26

3.4. Metallographic tests

Metallographic tests and recordings of the microstructures were carried out on the cross-section of high-temperature carbonitriding steel 20MnCr5 on samples 421 and 422. Microstructures of the edge of high-temperature carbonitriding steel 20MnCr5 are shown in Figure 4. In Figure 4.a, on the edge of cross section of sample 421 rough martensitic structure can be seen, while in Figure 4.b, on the edge of cross section of sample 422 finely distributed nitride can be detected.

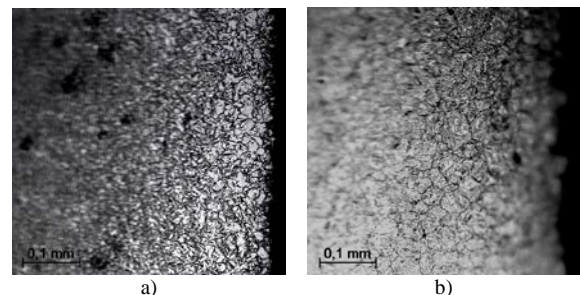


Fig. 4 The microscopic appearance of the edge of steel 20MnCr5.
a) sample 421, etched 3 % nital;
b) sample 422, etched 3 % nital

Microstructures of the core of high-temperature carbonitriding steel 20MnCr5 are shown in Figure 5. In Figure 5.a is shown the fine grained structure of the core of sample 421, in contrast to coarse grain structure of the core of sample 422, shown in Figure 5.b.

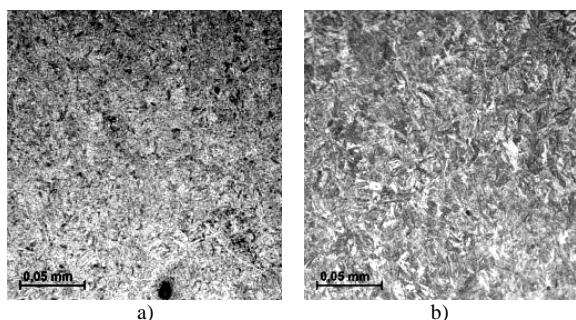


Fig. 5 The microscopic appearance of the core of steel 20MnCr5.
a) sample 421, etched 3 % nital;
b) sample 422, etched 3 % nital

3.5. Hardness tests

To image the mechanical properties was complete, after metallographic tests were measured values of surface hardnesses by device „TH 720“, Figure 6.



Fig. 6 Device for hardness testing „TH 720“.

The hardness flow of high-temperature carbonitriding steel 20MnCr5 was measured with Vickers method HV1 on the cross-section of the samples 421 and 422, and the direction of measurement was from the surface edge to the core. The results are shown in Table 7.

Table 7: The measurement results of the surface hardnesses of steel 20MnCr5.

Distance from the edge, mm	HV1	
	Sample 421	Sample 422
0,10	646	707
0,20	645	671
0,30	650	669
0,40	655	668
0,50	664	665
0,60	693	651
0,70	704	637
0,80	641	617
0,90	642	603
1,00	623	605
1,10	578	571
1,20	553	559
1,30	533	520
1,40	496	513
1,50	489	505
2,00	452	459
2,50	447	456
5,00	441	452

3.6. Resistance testing to the adhesion wear

Resistance testing to the adhesion wear was carried out on the device „SMT-1 2070“ by method disc/disc, Figure 7.



Fig. 7 Device for testing of the adhesion wear „SMT-1 2070“.

Method disc/disc is a laboratory test method. Test samples used for testing by this method are shown in Figure 8. During testing the lower sample (UZ) and the upper counter body (KT) rotate independently of each other. Their mutual contact is realized on the peripheral surface. There is a possibility of selecting the appropriate rotational speed of the sample UZ and counter body KT from the available range 75 ÷ 1500 r/min and selecting the appropriate load from the available range 0 ÷ 5000 N.

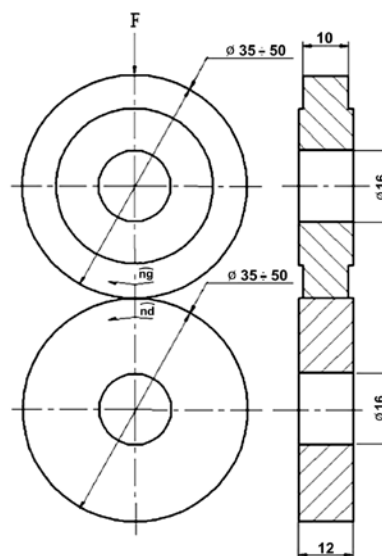


Fig. 8 Test samples for resistance testing to the adhesion wear by method disc/disc.

Test parameters of the adhesion wear resistance of steel 20MnCr5 are shown in Table 8. Marks A, B and C represent parameters of resistance test to the adhesion wear with method disc/disc. Samples of steel 20MnCr5 marked with 421 and 422 during the resistance test to the adhesion wear are loaded with different forces to the constant speed of rotation.

Table 8: Test parameters of the adhesion wear resistance.

Mark	A	B	C
F [N]	400	1200	2000
v [o/min]	600	600	600

In Figure 9 by histogram are presented mass loss of steel 20MnCr5 for samples 421 and 422 at selected conditions of the resistance test to the adhesion wear.

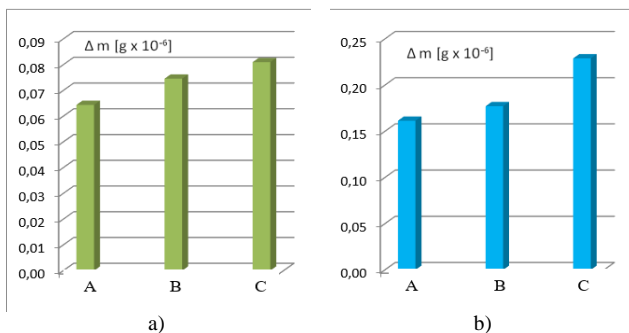


Fig. 9 The histogram representation of the mass loss of steel 20MnCr5.
a) sample 421;
b) sample 422

After performed resistance tests to the adhesion wear of steel 20MnCr5, the traces of sample 421 and sample 422 were recorded, Figure 10.

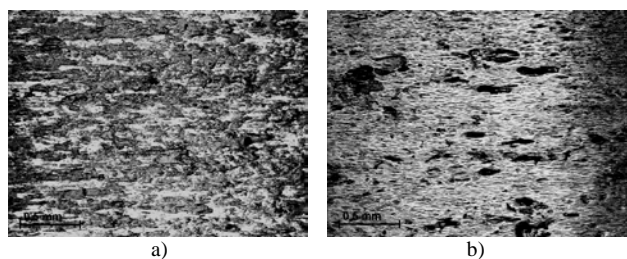


Fig. 10 The representation of the traces wear of steel 20MnCr5.
a) sample 421;
b) sample 422

4. Analysis of the results

Selection of representative gear's tribocouple are defined frameworks for analyzing of high-temperature carbonitriding MnCr steel, with a focus on the resistance to the adhesion wear. Analysis of the results obtained by testing the chemical composition of steel intended for high-temperature carbonitriding, followed by resistance testing to the adhesion wear, it was established that it is a steel 20MnCr5, Table 6. In Figure 4.a, on the edge of cross section of sample 421, etched with 3 % nital, with an increase 200:1, rough martensitic structure can be seen, while in Figure 4.b, on the edge of sample 422, also etched with 3 % nital and with the same increase, finely distributed nitride can be detected. In Figure 5.a, etched with 3 % nital and with an increase of 500:1 is shown the fine grained structure of the core of sample 421, in contrast to coarse grain structure of the core of sample 422, shown in Figure 5.b. Values of the measured hardnesses of the edge of sample 421 and sample 422 are higher than 700 HV1, while the values of the measured hardnesses of the core range about 450 HV1, Table 7. From the histogram in Figure 9 can be seen that to increase the force to the constant speed of rotation, an increase in mass loss of high-temperature carbonitriding steel 20MnCr5. After completion of resistance testing to the adhesion wear, the traces of wear of sample 421 and sample 422 are recorded, Figure 10. There is an appearance of typical adhesion wear on sample 421 and sample 422, with note that the sample 422 has more pronounced presence of surface „craters“ which are probably the consequence of the presence of fragile chemical compound Fe₂N.

5. Conclusion

High-temperature carbonitriding was performed on the steel 20MnCr5, by varying the potential of carbon and nitrogen in the atmosphere of furnace during carburizing. Considering to a relatively unexplored area of the higher contact loads, the emphasis on these tests is placed on the researchs of resistance to the adhesion wear in the conditions of contact load up to 2000 N to the constant speed of rotation. The range of selected loads are provided the opportunity to establishing relation with the available literature data, and make conclusions on a wide area of the influence of high contact loads on resistance to the adhesion wear. At both of the tested samples, with the increase in load during testing of resistance to the adhesion wear by method disc/disc it came to mass loss. Despite the somewhat lower of the surface hardness values it was noticed that a high-temperature carbonitrided steel where the atmosphere of furnace at the beginning of carburizing was enriched with nitrogen, and finally with carbon showed significantly greater resistance to the adhesion wear. His mass loss was up to three times lower compared to the mass loss of steel that at the beginning of carburizing had atmosphere of furnaces rich in carbon, and finally with nitrogen. This behavior can be related with the claim that the variable potential of the high-temperature carbonitriding has a significant influence on the diffusion of carbon than nitrogen diffusion, as well as the fact that in both steel for high-temperature carbonitriding are created the higher share of retained austenite.

6. References

- [1] Grilec, K.; Jakovljević, S.; Marić, G.: *Tribologija u strojarstvu*, Fakultet strojarstva i brodogradnje, Zagreb, 2015.
- [2] Czichos, H.: *Tribology: a systems approach to the science and technology of friction, lubrication and wear*, Federal Institute for Testing Materials, Berlin, 2009.
- [3] Arias-Cuevas, O.; Li, Z.; Lewis, R.: *A laboratory investigation on the influence of the particle size and slip during sanding on the adhesion and wear in the wheel-rail contact*, Wear 271 (2011) 1-2, 14-24.
- [4] Brnic, J.; Brcic, M.: *Comparison of Mechanical Properties and Resistance to Creep of 20MnCr5 Steel and X10CrAlSi25 Steel*, Procedia Engineering 100 (2015), 84-89.
- [5] Belahssen, O.; Benramache, S.: *Improving Tribological Properties of 20MnCr5 Steel by Plasma Nitriding*, Journal of Chemistry and Materials Research 4 (2015) 2, 45-48.
- [6] Brnic, J.; Turkalj, G.; Lanc, D.; Canadija, M.; Brcic, M.; Vukelic, G.: *Comparison of material properties: Steel 20MnCr5 and similar steels*, Journal of Constructional Steel Research 95 (2014), 81-89.
- [7] EN 10084: 2008. *Case hardening steels - Technical delivery conditions*.

EFFECTS OF MECHANOCHEMICAL TREATMENT OF ThO₂ WITH UO₃ AND CeO₂

ЕФЕКТИ ОТ МЕХАНОХИМИЧНО ТРЕТИРАНЕ НА ThO₂ С UO₃ И CeO₂

Assoc. Prof. P. Kovacheva PhD¹⁾, Prof. D. Todorovsky DSc¹⁾, M. Sc. N. Mirchev²⁾

¹⁾University of Sofia "St. Kliment Ohridski", Faculty of Chemistry and Pharmacy, Sofia, Bulgaria

²⁾Bulgarian Academy of Sciences, Institute for Physical Chemistry "Rostislav Kaishev", Sofia, Bulgaria

kovacheva.petya@gmail.com

Abstract: The paper presents the effects of the mechanochemical activation of ThO₂-UO₃ and ThO₂-CeO₂ mixtures in air and (for ThO₂-UO₃) in suspension in H₂O or CHCl₃. Planetary ball mill (Pulverisette 5, Fritch) with stainless steel triboreactors and milling balls from the same materials are used. Milling for 5 h of the ThO₂-UO₃ mixture does not affect significantly the crystal structure of the ThO₂ but leads to amorphization of UO₃, sharp decrease of its crystallites size and increase of the ionic character of the U-O bond. Storage of the activated product (2 months at room temperature) or heating (3 h, 165 °C) leads to partial relaxation of the UO₃ crystal structure. The X-ray diffraction data does not give proves for formation of ThO₂-UO₃ solid solution.

Formation of solid solution Ce_{0.6}Th_{0.4}O₂ accompanied with some amount of amorphized ThO₂, is established as a result of co-milling at the same conditions of the mixture ThO₂ - CeO₂ with a mole ratio 1. XRD-determined lattice parameter (5.4804(9) Å) and crystallites size (14 nm) of the obtained solid solution are in satisfactory agreement with literature data for the same product obtained via wet chemistry route.

Keywords: THORIUM DIOXIDE, URANIUM TRIOXIDE, CERIUM DIOXIDE, MECHANOCHEMISTRY, SOLID OXIDE SOLUTIONS, XRD, IR-SPECTROSCOPY

1. Introduction

At least two factors determine the research interest for mixed actinide dioxides of the type ThO₂-UO₂ and ThO₂-PuO₂: (i) they are considered as a promising fuel for some types of nuclear reactors. The application of solid solutions is preferred because they insure uniform mixing of the individual oxides; (ii) thorium-based dioxides are expected to have good performances in long-term storage of radioactive waste because of the low solubility and very low dissolution rates. In the same time it is known that cerium/CeO₂ is suitable surrogate for Pu/PuO₂ due to the closeness of the cation radii and the identity of the oxides crystal structure. So solid solutions of the type ThO₂-CeO₂ are of significant interest as model systems [1-3], strengthened by the fact that Ce/CeO₂ is one of the major fission products produced in the nuclear fuel.

The mentioned solid solutions are usually prepared through dry chemistry routes but wet chemistry methods were also proposed recently. A short review of the methods proposed for U-Th mixed oxides is presented in [4]. Practically, all of the used methods require transformation of U(VI) to U(IV) oxidation state, realized electrochemically or by heating in reducing atmosphere or in presence of reducing agent. Later on, the photochemically-induced preparation of nano-powders of crystalline UO₂-ThO₂ solid solution has been investigated [5-7]. Preparation of Ce_xTh_{1-x}O₂ solid solutions through thermally induced transformation of oxalate precursors [1, 2] or by citric sol-gel combustion technique followed by a thermal annealing (1000 °C for 24 h) [3] is proposed.

The literature data on the effects of the mechanoactivation on the 5f-elements compounds are rather limited. The mechanochemical behavior of uranium oxides is reported in [8-11]. It was shown that they are comparatively stable upon mechanical treatment. The main effect of the mechanoactivation on the U₃O₈ and UO₃ in air or in suspension with organic solvents is the reduction of U(VI) with the formation of UO₂, U₃O₇ and U₂O₅; the degree of reduction and the leaching of ²³⁸U and the decay product ²³⁴Th (the later - as a result of mechanoactivation in suspension with organic solvents) is found to depend on the mechanical treatment conditions and of the complexing agent nature. Mechanochemically assisted preparation of U-Th [4], U-La and U-Ce [12] oxide solid solutions was proposed: the polyphase product of external gelation process with the participation of U- and Th nitrates (analogous to the one described by Kumar et al. [13] for synthesis of U-Ce mixed oxides) is undergone to mechanical treatment, the later leading to

phase homogeneous product. Solid (U,Pu)O₂ solution is obtained by co-milling of UO₂ and PuO₂ [14]. Nanocrystalline UO_{2+x} powders have been prepared by high-energy ball milling and subsequently consolidated into dense fuel pellets under high pressure [15].

In the present work the potential is studied of the solely mechanochemical treatment for synthesis of Th-U and Ce-Th oxide solid solutions via co-milling of the individual oxides ThO₂-UO₃ and ThO₂-CeO₂, respectively.

2. Materials and Methods

Pure ThO₂ (5 g, Carlo Erba Reagents, Italy) and its mixture with UO₃•0.8H₂O (Chemapol) (3 g ThO₂ and 2g UO₃) were mechanically activated in air or as suspension in 8 ml CHCl₃ or in 6 ml distilled H₂O as shown on Fig. 1. After activation in suspension the solid phase was separated by filtering through fine-porous filter, rinsed few times with a total volume of 50 ml CHCl₃ or H₂O (when suspensions are used) and dried at room temperature. Part of the mixture milled in CHCl₃ was heated for 3 h at 165 °C.

Another set of experiments was performed with a mixture of ThO₂ and CeO₂ (total mass about 5.2 g mole ratio Th:Ce = 1), mechanically activated in air.

Planetary ball mill (Pulverisette 5, Fritch) with stainless steel vessels of 80 cm³ volume and balls from the same material (7-15 mm in diameter) were used. The activation was performed for 5 h at mechanical load of 12g.

The X-ray diffractograms of the samples before and after the mechanochemical processing were taken by a powder diffractometer Siemens D500 using CuK_α radiation filtered by a secondary monochromator (40 kV, 30 mA, 0.05° 2θ/2 s). The relative content and mean crystallite size of the oxides were determined from XRD pattern using the program POWDER CELL [16]. The crystal cell parameter, size of crystallites and density (for the ThO₂-CeO₂ system) were determined by the BRASS program [17].

The IR spectra in the range 4000-400 cm⁻¹ were recorded by a Bruker spectrometer in capillary layer.

Optical microscope B-130 (Optika, Italy) equipped with Celestron digital microscope Imager with 2 mega-pixel sensor and IR cut-off filter was used for observation of the mixture of ThO₂ and CeO₂ before and after the mechanical processing.

3. Results and Discussion

3.1. Mechanochemical effects on ThO_2 in air and in suspension

The mechanical treatment of ThO_2 neither in air [4], nor in CHCl_3 -suspension (at above described experimental conditions) leads to any changes in its X-ray diffractogram (Fig. 1) which completely correspond to the one of the referent ThO_2 (JCPDS 78-0685, 2001).

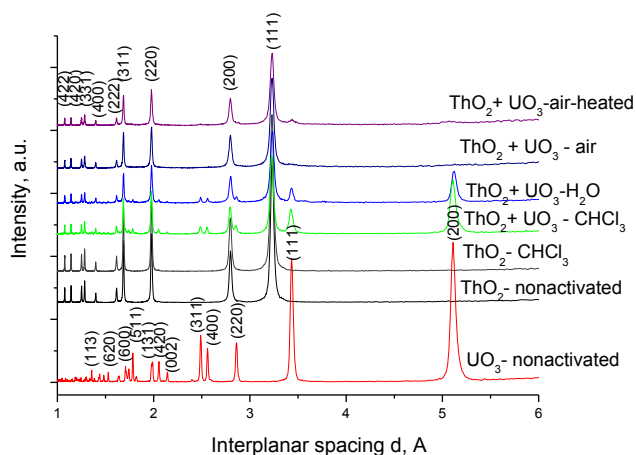


Fig. 1 X-ray diffractograms of the initial UO_3 and ThO_2 ; mechanoactivated products; ThO_2 - UO_3 mixture post activation heated. Miller indices for UO_3 and ThO_2 are shown.

3.2. Mechanochemical effects on mixture of ThO_2 and UO_3

Milling in air of the ThO_2 - UO_3 mixture practically does not change the X-ray diffraction behavior of the ThO_2 (compared with the initial oxide) but drastically decreases the crystallites size of UO_3 (Table 1). Amorphization of the UO_3 as a result of mechanoactivation is reported in [10], also. The intensity of the UO_3 -peaks vigorously decrease (the diffractogram of the milled mixture becomes rather close to that of the initial thorium, Fig. 1). Due to that the relative content of UO_3 , calculated from the diffraction data is much lower (Table 1) than that in the initial mixture (60 %). The activation of the mixture in CHCl_3 - or H_2O -suspension leads to similar, but less (especially in CHCl_3 medium) pronounced effect of UO_3 amorphization (Fig. 1). The X-ray diffraction data does not give proves for formation of ThO_2 - UO_3 solid solution.

Table 1: Relative content (RC, %) and crystallites size (CS, nm) of ThO_2 and UO_3 in studied samples before and after mechanical treatment in air

Sample	Mechano-activation	Post-activation heating	ThO_2		UO_3	
			RC	CS	RC	CS
ThO_2	No	-	100	32	-	-
UO_3			-	-	100	56
ThO_2 - UO_3 mixture	Yes	No	95	29	5	5
		160 °C, 3 h	85	28	15	17
		25 °C, 2 months	64	25	36	47

An interesting effect of relaxation of the UO_3 crystal structure is observed with time at ambient temperature which is promoted by heating for 3 h at 165 °C (Fig. 1, Table 1). Relaxation of the crystal structure of mechanoactivated UO_3 promoted by heating (at 300 °C) is also reported in [9].

The mechanochemically-induced amorphization is the probable reason for the changes in the general pattern of the samples IR-spectra (Fig. 2). Besides that, some changes in the region 950-850 cm^{-1} (connected with uranyl-type U-O-bond vibration) are observed. While the band around 937 cm^{-1} (asymmetric stretching

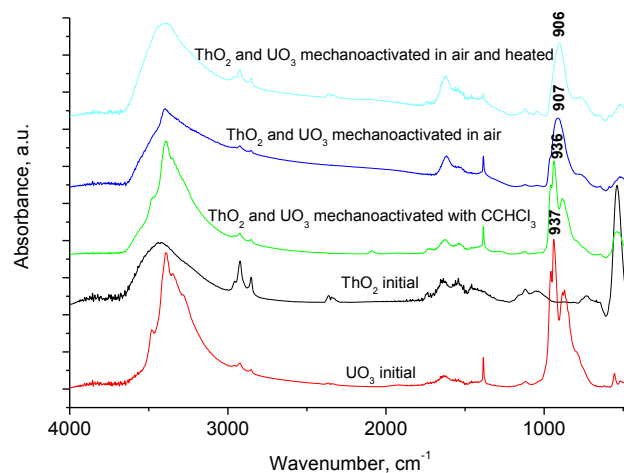


Fig. 2 IR-spectra (4000 – 400 cm^{-1}) of the initial UO_3 and ThO_2 ; mechanoactivated products and of activated ThO_2 - UO_3 mixture heated for 3 h at 165 °C.

vibration $\nu_{\text{as}}(\text{U-O})$ [9]), existing in the initial UO_3 , is slightly affected by the activation in CHCl_3 -suspension, it is significantly shifted to lower wave-lengths (to 907 cm^{-1}) when activation in air is performed. The shift reveals an increase of the ionic character of the U-O bond and, respectively, its weakening. The subsequent heating of the activated sample (3 h, 165 °C) does not lead to restoration of the bond character, i.e. it seems that the heating leads to relaxation of the crystal, but not the molecular structure.

3.3. Mechanochemical effects on mixture of ThO_2 and CeO_2

The X-ray diffractograms of the initial ThO_2 and the product obtained after mechanoactivation of a mixture ThO_2 - CeO_2 are shown on Fig. 3. Table 2 contains the data for the interplanar distances and the diffraction peaks relative intensity of ThO_2 , CeO_2 and the product of activation of their mixture.

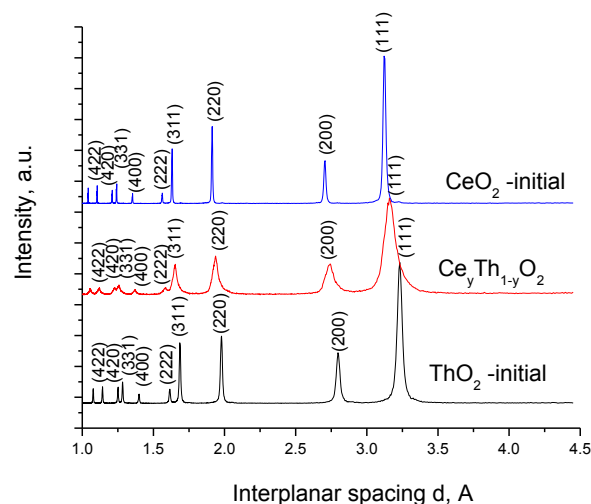


Fig. 3 X-ray diffractograms of the initial ThO_2 and CeO_2 and the product obtained after mechanoactivation of the ThO_2 - CeO_2 mixture.

Data for the lattice constant, the density and the size of crystallites of the components of the studied system are shown in Table 3. The sharp decrease of the size of the crystals as a result of milling, seen on the optical microscopy images (Fig. 4), is accompanied with more than two times decrease of crystallites size of the obtained mixed oxide compared with that of the initial ThO_2 and more than four times, compared to the initial CeO_2 .

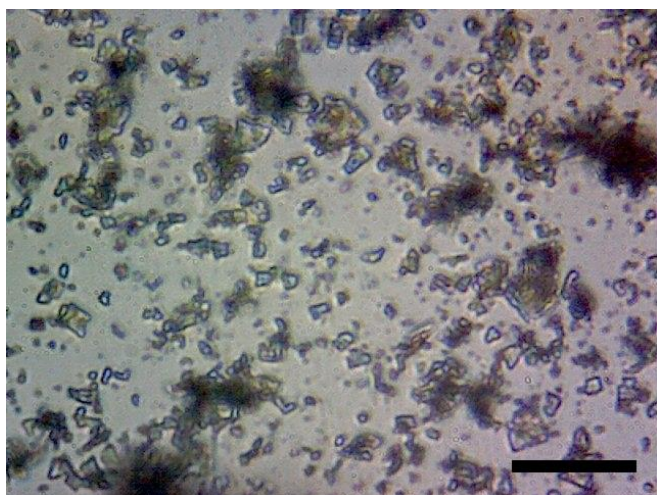
The density and the lattice parameter of the activated product (Table 3) takes an intermediate values between the constants of the

Table 2: Interplanar distances and relative intensity of ThO_2 , CeO_2 and the product of their mixture activation

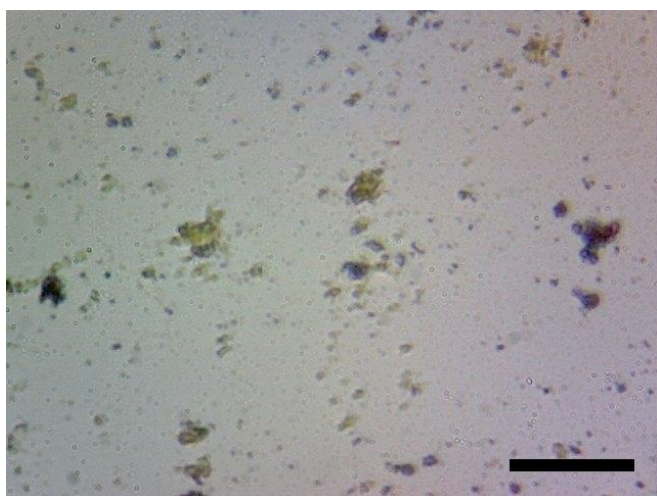
ThO_2 JCPDS 42-1462		CeO_2 JCPDS 43-1002		$\text{Ce}_y\text{Th}_{1-y}\text{O}_2$ Present work	
d, Å	I, %	d, Å	I, %	d, Å	I, %
3.232	100	3.1240	100	3.166	100
2.799	41	2.7060	27	2.739	33
1.9787	45	1.9132	46	1.937	39
1.6877	46	1.6316	34	1.654	32
1.6159	11	1.5621	6	1.588	8
1.3993	7	1.3528	6	1.366	6
1.2841	18			1.264	10
1.2516	14	1.2414	12	1.223	8
1.1426	13	1.2100	7	1.119	7

Table 3: Some physical parameters of the initial oxides and the mechanoactivated product

Parameter	ThO_2	CeO_2	$\text{Ce}_y\text{Th}_{1-y}\text{O}_2$
Lattice constant, Å	5.5915	5.4037	5.4804(9)
Density, g/cm^3	10.0223	7.2261	8.7986
Crystallites size, nm	32	65	14



a



b

Fig. 4 Microscopic images of the mechanical mixture of ThO_2 and CeO_2 before (a) and after (b) mechanochemical treatment; magnification 40x, size bar 20 μm .

initial oxides (without any distortion in unit cell) suggesting formation of a solid solution. The same FCC fluorite-type structures

of both initial oxides and closeness of the ionic radii (96 pm for Ce^{4+} and 105 pm for Th^{4+} [2]) are good grounds for a solid solution formation.

The stoichiometry of the product of mechanoactivation was determined using the Vegard's law (linear dependence exists between the lattice parameter and the molar part of the elements in the solid solution). The dependence of the lattice parameter a and Th-content c_{Th} in the activated product is shown on Fig. 5 using literature values for the lattice constants of the initial oxides (Table 3). From the derived straight line equation

$$a [\text{Å}] = 5.4037 + 0.00188c_{\text{Th}} [\text{mol \%}],$$

accounting for the found (from the X-ray data) value of the solid solution constant (Table 3) follows that $c_{\text{Th}} = 40 \text{ mol\%}$, i.e. the solid oxide solution has to be written as $\text{Ce}_{0.6}\text{Th}_{0.4}\text{O}_2$. The so found composition is different from the composition of the initial oxide mixture in which the mole ratio $\text{Ce}/\text{Th} = 1$. This fact leads to two important deductions: (i) it has to be supposed that in this system ThO_2 is much more inclined to amorphization than in the ThO_2 - UO_3 system and some amount of strongly amorphized ThO_2 is present in the mechanically treated system; (ii) despite the availability of ThO_2 in the milled system, solid solution, richer to ThO_2 , is not produced. Other synthetic methods permit preparation of such mixed oxides, up to $\text{Ce}_{0.1}\text{Th}_{0.9}\text{O}_2$ [3].

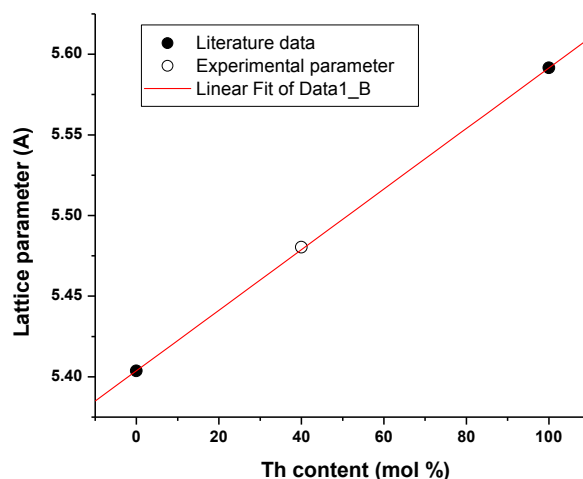


Fig. 5 Dependence of the lattice parameter on the relative content of ThO_2 in the mechanochemically formed solid solution

Table 4: Lattice parameter (a) in dependence of the mole part (y) of Ce in the $\text{Ce}_y\text{Th}_{1-y}\text{O}_2$

y	a, Å	Reference
0.4	5.43	3, JC-PDF 78-0704
0.5	5.5044(1)	2
0.6	5.4942(1)	2
0.6	5.4804(9)	Present work

A satisfactory agreement is found between literature data for the lattice constants of the mixed oxides of the type $\text{Ce}_y\text{Th}_{1-y}\text{O}_2$ and the value determined in the present paper (Table 4).

The size of the particles of the newly synthesized product is two times smaller than that of the initial ThO_2 suggesting that radical changes take part in the course of the mechanochemical treatment.

An interesting comparison can be made between the crystallites size of the mechanochemically obtained $\text{Ce}_{0.6}\text{Th}_{0.4}\text{O}_2$ and that of the analogous mixed oxide prepared through thermally induced transformation of oxalate precursors [2]. The size of crystallites of the later product increases with the increase of the heating temperature and is found to be 5 nm after heating at 400 °C, 15 nm at 900 °C and 50-60 nm at 1200 °C [2]. As it is shown in Table 3, 14 nm were determined in the present work. So, one can speculate that the mechanical treatment (at the conditions described in the

Materials and Methods part of the paper) is equal to heating of roughly 800-900 °C. Such an approximation is supported by the general pattern of the X-ray diffractograms of the compared products. Shapely, but relatively broad XRD lines are seen on Fig. 3, similar to the ones obtained in the diffractogram of the solid solution produced via wet chemistry route after heating at about 800 °C [2].

4. Conclusions

The present study shows that the ThO₂ is rather stable upon mechanical treatment in air or as CHCl₃-suspension. The mechanoactivation of a mixture of ThO₂ and UO₃ in air and in suspension in H₂O or CHCl₃ affects the UO₃ only, leading to its amorphization and destroying of its crystal structure; this effect is strongly revealed at air-milling and is lowest in CHCl₃-suspension. No X-ray proves for mechanochemical formation of solid solution ThO₂-UO₃ is found.

The response of the ThO₂ to the mechanochemical treatment in mixture with CeO₂ is rather different. The main effect is formation of solid solution Ce_yTh_{1-y}O₂ where, it seems that at the conditions applied in this work, $y \leq 0.6$. Most probably, the excess of Th in the activated system remains in amorphous state. The lattice constant and crystallites size of the obtained solid solution are in satisfactory agreement with literature data for the same product obtained via wet chemistry route.

Acknowledgment

The work is performed with the financial support of the Bulgarian National Science Fund under Contract X-1409/2004. The authors are grateful to Dr. Georgi Avdeev (Bulgarian Academy of Sciences) for the quantitative analysis of the XRD data and to Dr. Georgi Yordanov (Sofia University) for the microscopic images.

References

1. Claparede, L., N. Clavier, N. Dacheux, A. Mesbah, J. Martinez, S. Szenknect, Ph. Moisy. Multiparametric dissolution of thorium-cerium dioxide solid solutions. - *Inorg. Chem.*, 50, 2011, 11702-11714.
2. Claparede, L., F. Tocino, S. Szenknect, A. Mesbah, N. Clavier, Ph. Moisy, N. Dacheux. Dissolution of Th_{1-x}U_xO₂: Effects of chemical composition and microstructure. - *J. Nucl. Mat.*, 457, 2015, 304-316.
3. Naik, Y. P., G. A. Ramarao, A. Banthiya, D. Chaudhary, Ch. Arora. Synthesis and characterization of nano-structured Th_{1-x}Ce_xO₂ mixed oxide. - *J. Therm. Anal. Calorim.*, 107, 2012, 105-110.
4. Kovacheva, P., G. Avdeev, D. Todorovsky. Mechanochemically induced synthesis of UO_{2+x} and uranium-thorium mixed oxides from sol-gel produced precursors. - *J. Radioanalyt. Nuclear Chem.*, 287, 2011, 519-524.
5. Pavelková, T., V. Čuba, F. Sebesta. Photo-induced low temperature synthesis of nanocrystalline UO₂, ThO₂ and mixed UO₂-ThO₂ oxides. - *J. Nucl. Mater.*, 442, 2013, 29-32.
6. Pavelková, T., V. Čuba, E. de Visser-Týnová, Ch. Ekberg, I. Persson. Preparation of UO₂, ThO₂ and (Th,U)O₂ pellets from photochemically-prepared nano-powders. - *J. Nucl. Mater.*, 469, 2016, 57-62.
7. Pavelková, T., V. Vaněček, I. Jakubec, V. Čuba. E-beam and UV induced fabrication of CeO₂, Eu₂O₃ and their mixed oxides with UO₂. - *Radiat. Phys. Chem.*, 124, 2015, 252-257.
8. Kovacheva, P., D. Todorovsky, D. Radev, V. Mavrudiev, R. Petrov, D. Kovacheva. Mechanochemical effects in U₃O₈. - *J. Radioanalyt. Nuclear Chem.*, 262, 2004, 573-578.
9. Kovacheva, P., D. Todorovsky, D. Radev, N. Minkova. Mechanochemistry of the 5f-elements compounds. 4. Mechanochemistry of uranium (IV and VI) oxides. - *J. Radioanalyt. Nuclear Chem.*, 274, 2007, 481-490.
10. Kovacheva, P., D. Todorovsky, D. Radev. Mechanochemistry of the 5f-elements compounds. 5. Influence of the reaction medium on the mechanochemically induced reduction of U₃O₈. - *J. Radioanalyt. Nuclear Chem.*, 287, 2011, 193-197.
11. Kovacheva P. G., D. S. Todorovsky. Mechanochemically induced phase transformation and leaching of decay products from U(IV, VI) oxide. - *Internat. J. Materials science. Nonequilibrium phase transformations*, 4, 2016, 6-9.
12. Kovacheva, P., G. Avdeev. Application of mechanochemical activation for synthesis of uranium-lanthanoid mixed oxides. - *J. Radioanalyt. Nuclear Chem.*, 288, 2011, 221-227.
13. Kumar Suresh, K., H. P. Nawada, N. P. Bhat. Comparative study of thermal decomposition of the sol-gel products of U and Ce by external and internal gelation processes. - *J. Nucl. Mater.*, 321, 2003, 263-268.
14. Kleykamp, H. Post-irradiation studies on LWR-MOX fuel fabricated by the optimized co-milling process. - *J. Nucl. Mater.*, 324, 2004, 198-202.
15. Yao, T., M. S. Spencer, G. Xin, B. Gong, J. Lian. Dense nanocrystalline UO_{2+x} fuel pellets synthesized by high pressure spark plasma sintering. - *J. Amer. Ceramic Soc.*, 101, 2018, 1105-1115.
16. Kraus, W., G. Nolze. PowderCell – a program for the representation and manipulation of crystal structures and calculation of the resulting X-powder patterns. - *Acta Appl. Cryst.*, 29, 1996, 301-303.
17. Birkenstock, J., R.X. Fischer, T. Messner. BRASS 1.0 beta. The Bremen Rietveld Analysis and Structure Suite. Zentrallabor für Kristallographie und Angewandte Materialwissenschaften, Fachbereich Geowissenschaften, Univ. of Bremen, 2003.

APPLICATION OF NONLINEAR CONTROLLED COOLING REGIMES FOR STRUCTURE FORMATION MANAGEMENT IN EUTECTOID STEEL

ПРИМЕНЕНИЕ РЕЖИМОВ НЕЛИНЕЙНОГО КОНТРОЛИРУЕМОГО ОХЛАЖДЕНИЯ ДЛЯ УПРАВЛЕНИЯ СТРУКТУРООБРАЗОВАНИЕМ В ЭВТЕКТОИДНОЙ СТАЛИ

Ph.D. Kaverinsky V., Prof., Dr.Sc. Trotsan A., eng. Sukhenko Z., Prof., Dr.Sc. Bagliuk G.
Institute for Problems in Material Science, Ukraine

Abstract: Using computer modelling with originally developed semi empirical physical grounded models study of structure formation when austenite transformation during cooling by certain regime in eutectoid steel was carried out. The model allowed us to predict final structure. Cooling curves leading to fine pearlite (almost without bainite) and lower bainite (with a small part of fine pearlite) structures were found out. The results obtained could be useful for high carbon ordinary instrumental and constructional steels with higher manganese production and processing (rails, cord and rope wire, springs, low stressed instruments). Realization of the fine pearlite obtaining regime needs equipment that could provide cooling rates from 0.04 deg./sec. to 6.6 deg./sec. with average value of 1.1 deg./sec.. For bainitic structure obtaining the range of cooling rates provided should be from 0.14 deg./sec. to 14.0 deg./sec. with average value of 2.2 deg./sec. The cooling intensity must have an ability to arbitrary and controlled changing during process.

KEYWORDS: STEEL, STRUCTURE FORMATION, AUSTENITE TRANSFORMATION, HEAT PROCESSING

1. Introduction

The objective of the research is to define cooling two regimes one of which leads to formation of a fine pearlite structure without or almost without bainite and martensite, and another that provides a lower bainite structure with less content of pearlite (only fine one) and higher bainite, martensite also is not wished.

Ordinary high carbon eutectoid steels have quite wide area of usage. They have their application in cases where high hardness or resiliency or wear resistant is needed. They do not have so much hardness and ability to rapid cutting (which needs from material ability to save hardness at higher temperatures) as some high alloyed instrumental steels. But they are rather useful for hand tools, or wood and plastic machining cutting tools. As a constructional material they are known as steel for springs, steel for cord and metal rope wire, and very important area of their application is material for rails [1, 2].

Normal equilibrium structure of this type of steels is pearlite – eutectoid which consists of ferrite and carbide (cementite) plates. The smaller thickness of this plates the finer pearlite is the higher its mechanical properties. Finer pearlite is forming at lower temperatures. Along with pearlite in some conditions at lower temperatures bainitic structures also could be obtained in these steels. Bainite could be present in this steels mixed with pearlite or the structure could be almost fully bainitic. High carbon steels have also good ability to quenching during which martensite is forming [1].

There is no one certain opinion whether lower bainite or fine pearlite is better. The most wide spread and useful now are steels with pearlitic structure. Bainitic structure for construction materials was studied [3, 4], but the properties obtained in steel with bainite were not much better, sometimes even worse than in the same steel but with fine pearlitic structure [4]. But in work [3] it was shown that changing chemical composition of the steel it is possible to obtain much better complex of properties (especially wear resistance) in bainitic steels. These steels have much less content of carbon, more Mn and some amount of Mo and Cr [3]. But bainitic structure sometimes is helpful in instrumental steels instead of martensite. It is because lower bainite is less brittle and more elastic than martensite.

Detailed description of the mathematic model of austenite transformation is given in our works [5, 6] and detailed model examples with experimental verifications are presented in [5, 7]. It allows calculation of nucleation and grows of different phases that could occur in steels. Thermodynamics of phase transformation is also calculated by the model. But the main objective of it is calculation of kinetics. One of the most important essences of the model is that it allows to predict the material structure which could

form in the certain conditions of temperature regime during transformation process.

2.1. Studied material

Chemical composition of the studied steel in this work is given in table 1.

Table 1

Chemical composition of the studied steel							
Fe	C	Mn	Si	Cr	Ni	Mo	Cu
base	0.75	0.95	0.35	0.03	0.05	0.02	0.06

It's seen that the steel is near to eutectoid and has higher amount of Mn and normal concentration of Si. Content of other elements is small, but they were also taken into account in simulation. It is a typical rail or spring steel.

According to thermodynamic calculations equilibrium critical points of this steel are $A_1 = 729$ °C and $A_3 = 733$ °C.

2.2. Calculation and its results

Different shapes of cooling curves were used in the simulations. It was predicted that the structure which almost totally consists of fine pearlite could be formed when the cooling regime is responding to one that is shown on figure 1.

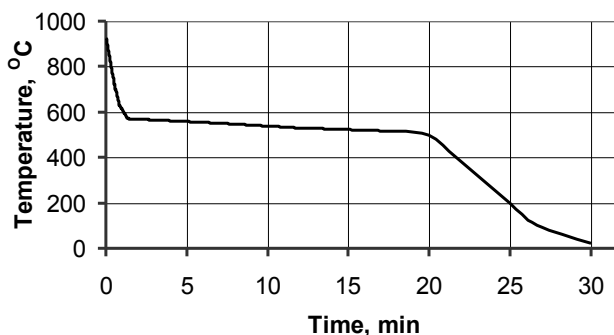


Figure 1 – Cooling regime for fine pearlite bainiteless structure obtaining in the eutectoid steel

Results of austenite transformation simulation (kinetic curve) in the investigated steel when temperature changes according to the cooling curve from figure 1 is shown on figure 2. From this illustration we can see that the transformations are almost completely end at about 514 °C. This moment comes after 1094 s

from the beginning of the process and after 1063 s after the pearlite transformation starts (about 18 min) according to computer simulation. The pearlite transformation starts below 727 °C, but goes very slowly at the beginning. Because we don't need rough pearlite the cooling rate in this period should be competently fast: from 5.0 to 6.6 deg./sec.

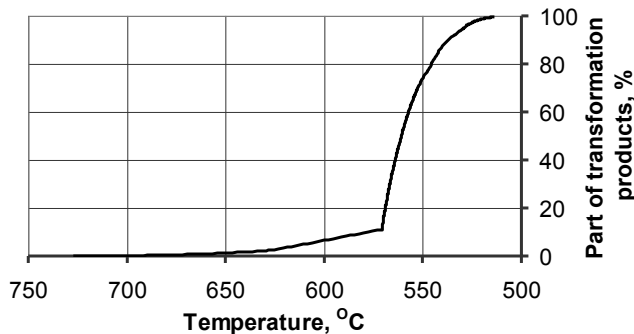


Figure 2 – Kinetic curve of austenite transformation in the regime of fine pearlite structure obtaining

Especially fast cooling rate is necessary lower 650 °C when the transformation process becomes quite swift. In this research it was considered that the fine pearlite structure should be obtained without quenching or cooling in liquid metal melts but by fast air cooling. This process has its limits, so that we obtain about 10 % of pearlite formed higher 575 °C. But fortunately amount of the pearlite formed higher 630 °C is very small. The bent of the kinetic curve near 570 °C is caused by slowing of the cooling rate (see figure 1). This deliberately decrease of the cooling rate to 0.4...0.7 deg./sec is needed to make pearlite transformation completely performed in a limited temperature range. This range is from 570 to 515 °C and its duration is about 19 minutes. This is enough to make pearlite transformation completely finished. Lower 515 °C according to calculations there is a possibility of higher bainite formation which is not wished in this case.

Another regime is aimed to a bainite structure obtaining. Its cooling curve is shown on Figure 3.

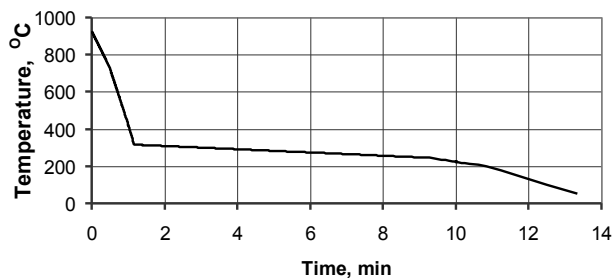


Figure 3 – Cooling regime for lower bainite structure obtaining in the eutectoid steel

This technique needs faster cooling rate at the beginning of the process. During first 80 seconds it should be 7...14 deg./sec. After this time metal should have temperature 325 °C. According to simulation it is the temperature when lower bainite becomes forming, but significantly higher than temperature of martensite transformation start which is 228 °C. Thus for lower bainite structure obtaining it is necessary to decrease the cooling rate to value 0.14...0.15 deg./sec. After about 7 minutes the bainite transformation is complete. The temperature at the end of the transformation is about 250 °C which is higher than temperature of martensite transformation start. Thus there is no martensite in the structure. A kinetic curve of the process is given on figure 4.

From the curve a certain separation of pearlite and bainite transformation is seen. Some pearlite which seems to be a fine one appear between 630 and 455 °C. Its amount in the structure is astimated to be 25.3 % from which 22.8 is a fine disperse pearlite

and 2.3 is ordinary pearlite. The fastest cooling rate should be set in the temperature range from 450 °C to 325 °C. Austenite is less stable in this period and is able to transform to brittle higher bainite, which is not a wished structure. Thus the cooling rate should be raised up to 14 deg./sec. Lower 325 °C austenite transforms to lower bainite. In the final structure by our computer model presence of 74.1 % of lower bainite was estimated.

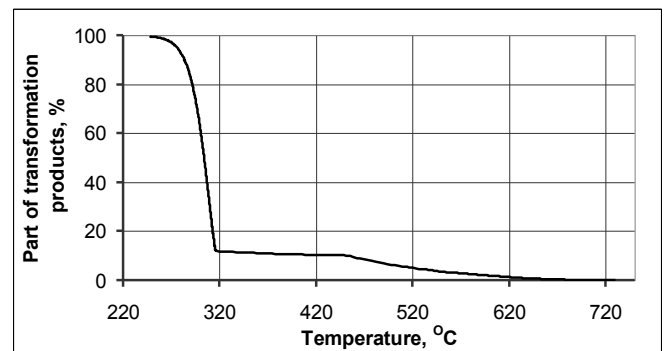


Figure 4 – Kinetic curve of austenite transformation in the regime of bainite structure obtaining

3. Conclusions

Using self developed computer model regimes for fine pearlite and bainite structure in eutectoid steel with higher manganese obtaining were developed. The regimes provide turning of higher cooling rate to slower ones at certain temperatures. Pearlite forming needs cooling rate 5.0...6.6 deg./sec. before 575 °C and than slowing it to 0.04...0.7 deg./sec. for 19 minutes. Regime for bainite structure obtaining is some faster. It needs cooling with rate 7...14 deg./sec. higher 325 °C (especially intensive at 450... 325 °C) and than slowing it to 0.14...0.15 deg./sec. for 7...8 minutes.

The obtained results present in the paper are useful for high carbon ordinary instrumental and constructional steels with higher manganese thermal processing regimes developing.

3. References

1. Houdremont E. Special steels / E. Houdremont - M: "Metallurgy", V.1 - 1966. - 736 p., V.2 - 1966. - 538 p. (Rus.)
2. Perfection of an assortment and the production technology of railway rails / [D. V.Stalinsky, A. S. Ruduk, I. V.Ganoshenko, etc.]/ Metallurgical and mining industry. - №6. - 2010. - P. 66 - 68. (Rus.)
3. Bhadeshia H.K.D.H. Bainite in steels / H.K.D.H. Bhadeshia // The Institute of Materials: London, UK. - 1992. - 468 p.
4. Clayton P. wear Behavior of bainitic steels / P. Clayton, K. J. Sawlay, P. J. Bolton, G. M. Pell // wear - 1987. - vol. 120. - is. 2. - p. 199 - 200.
5. V. V. Kaverinsky, A. I. Trotsan, Z. P. Sukhenko, V. S. Synuk XV Vseukrains'ka naukovo-praktichna konferencija «Special'na metalurgija: vchora, s'ogodni, zavtra - 2017» (XV National Scientific Conference "Special Metals: Yesterday, Today and Tomorrow - 2017") (Kiev: "KPI": 2017), p. 1158. (in Russian).
6. A. I. Trotsan, V. V. Kaverinsky, I. L. Brodetskiy, Z. P. Sukhenko, Sbornik materialov konferentsii "Stroitel'stvo, materialovedenie, mashinostroenie: Starodubovskie chteniya - 2016" (The collection of materials of the conference "Construction, materials science, mechanical engineering: Starodubov reading - 2016") (Dnepropetrovsk: PGSA: 2016), vol. 89, p. 177. (in Russian).
7. Kaverinsky V. V. About computer simulation of austenite transformation in bulk [Text] / V. V. Kaverinsky // Journal of materials science and applications. - 2017. - Vol. 3. - P. 46 - 52.

A INVERSE PROBLEM IN ULTRASONIC TESTING AND MECHANICAL PROPERTIES OF POLYCRYSTALLINE MATERIALS

ОБРАТНАЯ ЗАДАЧА В УЛЬТРАЗВУКОВОМ ТЕСТИРОВАНИИ И МЕХАНИЧЕСКИЕ СВОЙСТВА ПОЛИКРИСТАЛЛИЧЕСКИХ МАТЕРИАЛОВ

Assoc. Prof, PhD. Alexander Popov¹ · MSc Eng. Georgy Dobrev²,
¹Institute of Mechanics - BAS, Sofia, Bulgaria, ²Institute of Metal Science - BAS, Sofia, Bulgaria,
 E-mail: alpopov@abv.bg ; dobrevbg@mail.bg

KEYWORDS: INVERSE PROBLEM, ULTRASONIC TESTING, MECHANICAL PROPERTIES, POLYCRYSTALLINE MATERIALS

Abstract: The direct problem in ultrasonic testing (UT) is: "Evaluation of attenuation coefficient by means velocity of ultrasonic wave propagation, frequency and grain size in polycrystalline materials". The inverse problem in UT is formulate as "Non-destructive evaluation of grain size by measurement of acoustical characteristics". The values of acoustical characteristics $(V_L; V_T; \alpha_L; f)$ are measured, according ASTM E 494:2015. In this article a equation for grain size (\bar{D}) is derived.

Key words:, ultrasonic testing, acoustical characteristics, grain size, yield stress, ultimate tensile stress, fatigue limit.

1. Introduction

In UT investigation of polycrystalline materials the relationship $\alpha_L = \alpha_L(V_L; V_T; f; \bar{D})$ is obtain. This is Lifshic-Parhomenko-Merkulov's formula [1]

$$(1) \quad \alpha_L = \frac{8\pi^3}{375} \cdot \frac{\mu}{\rho^2} \left[\frac{4\pi}{3} \left(\frac{\bar{D}}{2} \right)^3 \right] \cdot f^4 \cdot W(V)$$

where ρ - density; (\bar{D}) - grain size; f - frequency; $(V_L; V_T; \alpha_L; f)$ - velocity of longitudinal $-V_L$ and transversal V_T - ultrasonic waves, α_L - attenuation in ultrasonic wave propagation, $\mu = \rho \cdot (V_T)^2$,

$$W(V) = \left(\frac{1}{V_L^3} \right) \left(\frac{2}{V_L^5} + \frac{3}{V_T^5} \right).$$

This is direct problem in ultrasonic testing (UT).

2. Inverse problem in ultrasonic testing

The inverse problem in UT is formulate as "Non -destructive evaluation (NDE) of grain size (\bar{D}) by measurement of acoustical characteristics $(V_L; V_T; \alpha_L; f)$ of the material".

After reversing the direct problem (1), a cubic equation (with a single real root) to determine the grain size is obtained [2]

$$(2) \quad \left[\frac{4\pi^4}{1125} \left(\frac{V_T^4}{V_L^3} \right) \left(\frac{2}{V_L^5} + \frac{3}{V_T^5} \right) f^4 \right] \cdot (\bar{D})^3 - \alpha_L = 0$$

This is equation for evaluation of the grain size (\bar{D}) by means measured acoustical characteristics $(V_L; V_T; \alpha_L; f)$, according ASTM E 494:2015.

3. Mechanical properties

3.1. Yield stress - σ_S

This value is evaluated by means Hall-Petch's relationship [3]

$$(3) \quad \sigma_S = \sigma_0 + K_y (\bar{D})^{-1/2}$$

It is accepted that the constant is called "Pierre-Nabarro's tension" [3]. It takes into account the frictional tension - which compensates for the forces overcome by the dislocations when they move into the grain, [3]:

$$(4) \quad \tau_{PN} = \frac{2G}{1-\nu} \exp \left[- \frac{2\pi}{(1-\nu)} \left(\frac{c}{a} \right) \right]$$

where ν - Poisson coefficient, G - sliding module, a and c - crystalline grid parameters in a plane {100}. For $c \sim 0.2\%$ i.e. low - carbon steels. The approximation of parameter σ_0 is

$$(5) \quad \sigma_0 \approx \frac{2}{3} \cdot \frac{G}{1-\nu}$$

where $[\sigma_0] = MPa$; $[G] = GPa$.

The constant K_y is called Petch's coefficient. It takes into account the passage of dislocations from one grain to another [4]:

$$(6) \quad \frac{K_y}{G} = \frac{2}{\cos \vartheta} \left\{ \frac{|b|}{25\pi(1-\nu)} \right\}^{1/2}$$

where ϑ - angle of maximum deviation of the slip directions, $|b|$ - module of the Burger,s vector [3].

After regrouping the values in (6), for the Petch's coefficient K_y is obtain

$$(7) \quad K_y \approx \frac{1}{4} \cdot \frac{G}{\sqrt{1-\nu}}$$

where $[K_y] = MPa / mm^{1/2}$, $[G] = GPa$. As

$$(8) \quad G = \rho \cdot (V_T)^2; \quad \nu = \frac{0.5 - (V_T/V_L)^2}{1 - (V_T/V_L)^2},$$

then from relationships (5) and (7) are obtain

$$(9) \quad \sigma_0 \approx \frac{2}{3} \cdot \frac{G(V_L; V_T)}{1 - \nu(V_L; V_T)};$$

$$(10) \quad K_y \approx \frac{1}{4} \cdot \frac{G(V_L; V_T)}{\sqrt{1 - \nu(V_L; V_T)}}.$$

This is the obvious look of coefficients $(\sigma_0; K_y)$ in Hall-Petch's relationship (3).

NDE of yield stress - σ_S is by (9), (10) and the solution $\bar{D} = \bar{D}(V_L; V_T; \alpha_L; f)$ of equation (2).

3.2. Ultimate tensile stress - σ_B

Is being considered the Busibesq's solution [6,7]

$$(11) \quad \sigma_S = \varphi(\nu) \cdot HB$$

where HB - Brinel's hardness, ν - Poisson ratio,

$$\varphi(\nu) = \left\{ \frac{1}{2}(1 - 2\nu) + \frac{2}{9}(1 + \nu) \cdot [2 \cdot (1 + \nu)]^{1/2} \right\};$$

$$\nu = \frac{0.5 - (V_T/V_L)^2}{1 - (V_T/V_L)^2}.$$

Putting (11) in Hall-Petch's relationship (3) we have

$$(12) \quad \sigma_S = \sigma_0 + K_y (\bar{D})^{-1/2} = \varphi(\nu) \cdot HB$$

This is Stroh's relationship [5] in type

$$(13) \quad HB = \sigma_0^{(HB)} + K_y^{(HB)} (\bar{D})^{-1/2}$$

where

$$(14) \quad \sigma_0^{(HB)} = \frac{\sigma_0}{\varphi(\nu)};$$

$$(15) \quad K_y^{(HB)} = \frac{K_y}{\varphi(\nu)}.$$

If $\varphi(\nu) \equiv \varphi(V_L; V_T)$, then according (5), (7), and (8), the relationships (14) and (15) are recorded in the form

$$(16) \quad \sigma_0^{(HB)} = \frac{2}{3} \cdot \frac{G(V_L; V_T)}{1 - \nu(V_L; V_T)} \cdot \frac{1}{\varphi(V_L; V_T)};$$

$$(17) \quad K_y^{(HB)} = \frac{1}{4} \cdot \frac{G(V_L; V_T)}{\sqrt{1 - \nu(V_L; V_T)}} \cdot \frac{1}{\varphi(V_L; V_T)}$$

The value of σ_B , by Markovic's relationship, $\sigma_B \approx 0.34HB^{0.989}$ [7], is obtain.

NDE of ultimate tensile stress - σ_B is by (16), (17), the solution $\bar{D} = \bar{D}(V_L; V_T; \alpha_L; f)$ of equation (2) and Markovic's relationship.

3.3. Fatigue limit - σ_{-1}

This value is evaluated by Terentiev's relationship [9]

$$(18) \quad \sigma_{-1} = \sigma_0^{(-1)} + K_y^{(-1)} \left\{ \bar{D} \right\}^{-1/2}$$

To derivate the coefficients $(\sigma_0^{(-1)}; K_y^{(-1)})$ in (18) is being considered the ratio [8]

$$\frac{\sigma_{-1}}{\sigma_S} = \frac{0.165HB}{\varphi(\nu)HB} = 0.165\varphi^{-1}(\nu)$$

We have the recording

$$(19) \quad \frac{\sigma_{-1}}{0.165\varphi^{-1}(\nu)} = \sigma_0 + K_y (\bar{D})^{-1/2}.$$

Therefore

$$(20) \quad \sigma_0^{(-1)} = \frac{0.165}{\varphi(\nu)} \sigma_0;$$

$$(21) \quad K_y^{(-1)} = \frac{0.165}{\varphi(\nu)} K_y.$$

According (5) and (7) for the coefficients (20) and (21) are obtain

$$(22) \quad \sigma_0^{(-1)} \approx \frac{1}{10} \cdot \frac{G}{\varphi(\nu)(1 - \nu)};$$

$$(23) \quad K_y^{(-1)} \approx \frac{2}{5} \cdot \frac{G}{\varphi(\nu)\sqrt{1 - \nu}}.$$

According (8) the coefficients $(\sigma_0^{(-1)}; K_y^{(-1)})$ are

$$(24) \quad \sigma_0^{(-1)} \approx \frac{1}{10} \cdot \frac{G(V_L; V_T)}{(1 - \nu(V_L; V_T))} \cdot \frac{1}{\varphi(V_L; V_T)};$$

$$(25) \quad K_y^{(-1)} \approx \frac{2}{5} \cdot \frac{G(V_L; V_T)}{\sqrt{1 - \nu(V_L; V_T)}} \cdot \frac{1}{\varphi(V_L; V_T)}.$$

This is the obvious look of coefficients $(\sigma_0^{(-1)}; K_y^{(-1)})$ in Terentiev's relationship (18).

NDE of Fatigue limit - σ_{-1} is by (24), (25) and the solution $\bar{D} = \bar{D}(V_L; V_T; \alpha_L; f)$ of equation (2).

4. Conclusion

It's resolved the inverse problem: Non destructive evaluation of (\bar{D}) by means measure of acoustical characteristics of the material i.e.

$$(26) \quad \bar{D} = \bar{D}(V_L; V_T; \alpha_L; f).$$

The values measurement of $(V_L; V_T; \alpha_L)$ are according ASTM E 494:2015.

For the non-destructive evaluation of mechanical properties:

σ_S , σ_B and σ_{-1} by means

$$(27) \quad \sigma_S = \sigma_S(V_L, V_T; \alpha_L; f);$$

$$(28) \quad \sigma_B = \sigma_B(V_L, V_T; \alpha_L; f);$$

$$(29) \quad \sigma_{-1} = \sigma_{-1}(V_L; V_T; \alpha_L; f).$$

are could be used.

5. Reference

1. E.Papadakis, Ultrasonic attenuation and scattering in polycrystalline materials, Physical Acoustics, Vol.IV, B, edited by U.Mezon, Fizmatlit, Moscow, 1963.
2. Popov Al., Mesomechanics of ferrous alloys, Series "Applied Mathematics and Mechanics", Vol. 8, Institute of mechanics - BAS, Sofia, 2017, (ISSN: 1314-3034).
3. Zolotarevskii V.S., Mechanical properties of metals, Misis, Moscow, 1998.
4. Meshkov Ju.Ia., The physical basis for the destruction of steel structures, Naukova dumka, Kiev, 1981.
5. Petch N., Metallographic Aspirations of Destruction, in Fracture Vol.1, edd.by H.Liebowitz, Mir, Moscow, 1973.
6. Timoshenko S.P., J.Gudier, Elasticity theory, Nauka, Moscow, 1979.
7. Markovic M.P., Un samples methods for determining the mechanical properties of metals, MEI, Moscow, 1983.
8. Kuzmov D., &, Calculation and testing of fatigue in mashinbuilding, Technika, Sofia, 1979.
9. Terentiev V.F., Fatigue of metal materials, Nauka, Moscow, 2003.

MICROSTRUCTURAL EVOLUTION AND MECHANICAL PROPERTIES OF ALUMINUM IN THE PROCESS "PRESSING-DRAWING"

ЭВОЛЮЦИЯ МИКРОСТРУКТУРЫ И МЕХАНИЧЕСКИХ СВОЙСТВ АЛЮМИНИЯ В ПРОЦЕССЕ «ПРЕССОВАНИЕ-ВОЛОЧЕНИЕ»

Prof. dr. Nayzabekov A.¹, Ass.prof. Lezhnev S.¹, Ph.D. Volokitina I.², Volokitin A.³

¹Rudny industrial institute, Rudny, Kazakhstan

²Karaganda State Industrial University, Temirtau, Kazakhstan

³Kazakh National Technical University after K.I. Satpayev, Almaty, Kazakhstan

Abstract: The aim of this work is to study the influence of the combined process of "pressing-drawing" on the microstructure and mechanical properties of aluminium wire. Analysis of the results of the research has shown that the proposed combined method of deformation "pressing-drawing" has a significant advantage over the existing technology of production of aluminium wire. This method of deformation due to combination of two ways: by severe plastic deformation in equal channel step die and the process of drawing through a drawing die, allows obtaining aluminium wire with ultrafine-grained structure and a high level of mechanical properties, required size and shape of the cross section at a small number of cycles of deformation. Also would like to mention that this method of deformation in implementing it in production does not require significant economic investments, and substantial refitting of existing drawing mills.

KEYWORDS: PRESSING-DRAWING; COMBINED PROCESS; ALUMINIUM WIRE; MICROSTRUCTURE.

1. Introduction

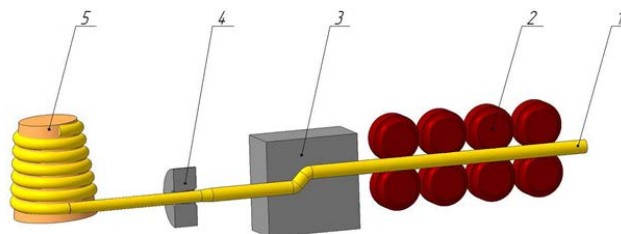
The contemporary level of electronic technology development has led to the appearance of devices that often have moving parts and / or work in difficult conditions. Therefore, interest in the problems of forming physical and mechanical properties of functional conductor materials has recently grown abroad in connection with the need to stabilize the properties of current conductors and increase their reliability, including in heavily loaded cable systems, motor and generators windings and low-current computer networks [1-2]. The increased interest of researchers in such materials has greatly increased in recent decades in connection with the use of severe plastic deformation (SPD) methods to obtain bulk materials with fine grains characterized by high physical and mechanical properties [3-4].

Nowadays, the mechanical properties of bulk nanostructured materials generate particular interest. It is known that they are characterized by an increase in the yield point by 2-5 times compared with the corresponding values on SPD at coarse-crystalline state [5-6]. The paradox of SPD, consisting in the simultaneous growth of strength and plasticity as the degree of SPD increases, low-temperature and highspeed superplasticity, deviations from the Hall-Petch law to the higher values of the yield point [7-9].

The SPD method is free from disadvantages of other methods of obtaining such materials, such as the method of compacting powders obtained previously by various methods, and the method of depositing gas atoms on a substrate or electric deposition of atoms from an electrolyte solution. When the materials are compacted or deposited, impurities and pores flow into the boundaries of their grains, influencing the properties of the obtained materials. Among the SPD methods, the ECAP method is especially noteworthy [10-12].

A polycrystalline sample of a macroscopic volume subjected to ECAP retains its shape after multiple extrusions through a curved channel. As a rule, ultrafine-grained or nanocrystalline materials, obtained at the output, have nonequilibrium grain boundaries and a considerable density of lattice defects [13]. These features of the microstructure formed in the SPD process underlie the mechanical properties of the materials. However, the ECAP has a disadvantage – the impossibility of processing products of relatively large length due to loss of stability by a pressing punch. On the basis of a comprehensive analysis of the existing schemes of plastic structure formation and also taking into account the promising directions of their development [14-15], a new combined "pressing-drawing" process using an equal-channel step matrix (Figure 1) was proposed. It enables to obtain a wire with an ultrafine-grained

structure and increased level of mechanical properties, required dimensions and shape of the cross section at insignificant number of deformation cycles.



1 – wire; 2 – pushing device; 3 - equal channel step matrix; 4 – calibrating drawing tool; 5 - winding drum

Fig. 1. Scheme of the combined process of "pressing-drawing"

The gist of the proposed deformation method consists in the following. Preliminary sharpened end of the wire is set to equal-channel step die and then subsequently in the finishing die. At its core, process setting metal does not differ from the setting of the wire in a drawing die at a standard process of drawing. After the end of the workpiece exits the die it is fixed by means of gripping tongs and is wound on a drum drawing machine. In this case, the process of drawing the workpiece through an equal channel step die and a caliber die is realized by the application to the end of the workpiece stretching force. The external load is applied to the drawing metal and on the surface of the contact metal - tool contact stresses arise. Unlike other methods of material forming, the implementation of which cannot be carried out without the presence of the contact friction forces at drawing on metal-tool, directed against metal movement, are negative phenomena of the process, which undoubtedly involves the use of technology lubricants that reduce friction.

To determine the effects of a new combined method of deformation "pressing-drawing" on the changes in the microstructure and mechanical properties of aluminum wire laboratory experiment was carried out at an industrial drawing machine - I/550 M. For the first cycle of deformation before the draw plate with working diameter of 7 mm equal channel step die with channel diameter is 7 mm and the angle of the junction of channels equal to 135° was fixed. The die was placed in a container for lubrication.

The initial diameter of the wire was 7.0 mm. After the process of pressing-drawing wire diameter has been 6.0 mm. All compression was carried out only in the drawing die, after exiting the workpiece from the equal channel step die wire diameter stayed

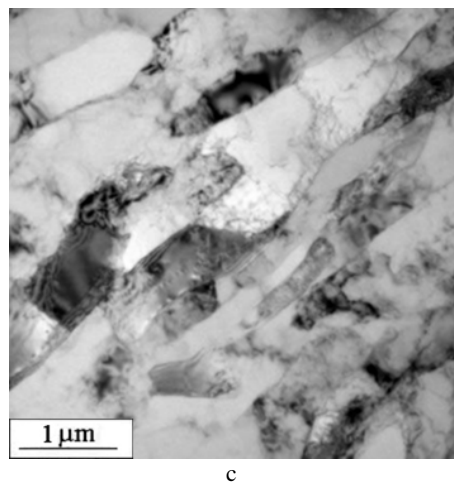
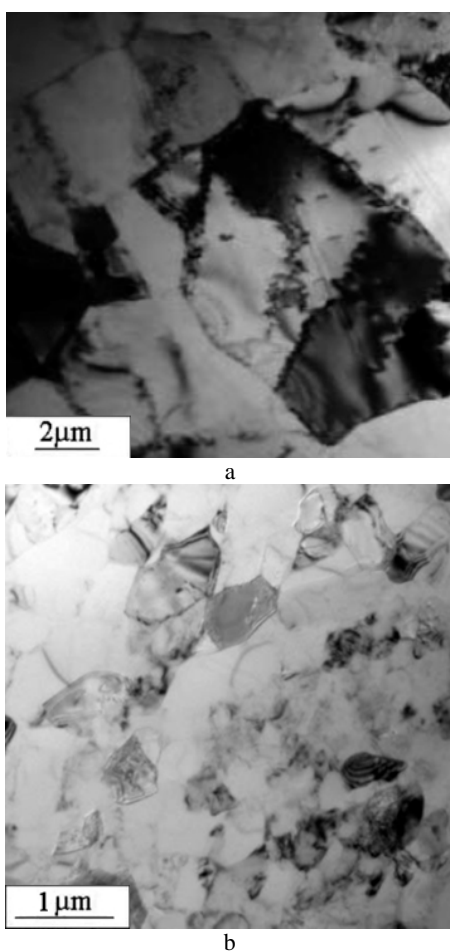
unchanged at 7.0 mm. The experiment was duplicated four times. In this case after each experiment wire diameter was measured and cut templates for production of microsections in the transverse and longitudinal direction.

In order to identify the advantages of the proposed technology in comparison with the current technology of drawing three passes annealed wire of aluminum for each technology were carried out. I.e. clean drawing wire rod was carried out diameter of 7.0 mm in the drawing die on diameter 6.0 mm, equal channel angular drawing and combined process of "pressing-drawing". In this case also, after each experiment wire diameter was measured and cut templates for production of microsections in the transverse and longitudinal direction. As a lubricant chips of soap were used.

2. Results and discussion

Preparation microsections for metallographic investigations carried out by the standard method, for the study a scanning electron microscope JEOL JSM 5910 was used.

The results of the study of the microstructure of aluminum before and after the third cycle of deformation are shown in Fig. 2.



a – the initial structure, b – by the proposed ECAP-D technology, transverse direction, c - at existing technology of drawing, transverse direction

Fig. 2. Structure of wire of aluminum

Having conducted metallographic analysis of the deformed samples it can be concluded that the cold deformation when drawing at the current technology with a moderate and high total compression leads to the formation of a distinct textured structure. However, even as a result of substantial compressions produced wire in drawing process, not all grains are crushed and are deployed in the direction of the axis of deformation. As shown by metallographic analysis of the samples, resulting in uneven allocation the deformation over the cross section in the central part of the longitudinal sectional of the wire area of large grains is retained, resulting in an inadequate level of the plastic properties of the finished wire, in particular elongation. Thus from figure 3c it is shown that in this case deformation leads to insignificant of grain refinement in the transverse direction, in the longitudinal direction grains are elongated and somewhat refined with the formation a visible axial texture. Also it should be noted that in the longitudinal direction of the deformed samples the texture is pronounced and has striated character. The appearance of texture of drawing leads to anisotropy of the material properties in the longitudinal and transverse directions, which may adversely affect the operation parameters of the finished product. To reduce the appearance of axial deformation texture it is necessary to carry out recrystallization annealing of obtained wire with correctly chosen heat treatment parameters.

When using the proposed technology of deformation, i.e. combined process of "pressing-drawing", as shown in Figure 3b, already in three passes change of the initial microstructure was a significant, at the same time significantly in the less degree texture expressed and anisotropy, respectively. The proposed combined technology "pressing-drawing" eliminates the disadvantages of drawing process. In the first stage of drawing to a 30-40% breakdown cellular structure is formed. The local increase in internal stress field causes the formation of stable microcracks. Intensive disclosure of stable microdefect leads to stress relaxation that during subsequent deformation opens previously blocked the Frank-Read sources. Simultaneously cellular structure being improved fibrous structure is arisen and texture is formed. To achieve ultra-fine grain structure only by the uniform flow of dislocations is impossible: the accumulation of plastic deformation and dislocation density growth there is disproportionately rapid increase detents and obstacles hindering their progress through the crystal. Dislocation flow gradually depletes the level of internal stress increases. This continues until cracks begin to appear, brittle fracture of the sample occurs. To avoid this, and the energy delivered to the sample is not accumulated in the material mainly in the form of elastic distortions, and continue to dissipate, equal channel step die will be applicable, where the shear deformation

are and large-borders will be formed as a result of conditions for continuation of the plastic deformation at large strains creates.

Results of mechanical studies are presented in Tab. 1. The strength characteristics of aluminum represented by the values of tensile yield σ_T and yield strength σ_b ; plastic characteristics represented by values of percentage reduction and elongation of samples before destruction.

Table 1 - Results of mechanical testing of wire samples

Designation processing technology	Yield strength σ_b , MPa	Tensile yield σ_T , MPa	Percentage of elongation δ_s , %	Percentage reduction ψ_s , %
Annealing	115	120	18,0	60,0
Classic drawing	203	198	15,5	44,0
ECAP-D Technology	316	312	16,0	49,0

The greatest change in the yield strength and tensile strength values (as changes in the microhardness) during the pressing-drawing occurs after the first pass. At subsequent passes, this increase occurs more uniformly. The values of tensile strength and yield increase for three passes from 115 to 316 MPa (absolute increase is 201 MPa) and from 120 to 312 MPa (absolute increase is 192 MPa), respectively.

As is known, the characteristic that most fully reflects the ability of the material to plastic deformation is a percentage reduction in the area of neck. Percentage reduction in the aluminum is changed from 60 to 49%.

From the analysis of carried out mechanical tests of samples by different technologies, we can conclude that the best mechanical characteristics there has a treated wire by the combined technology of "pressing-drawing". An increase in the yield strength and tensile strength values are observed and also index of the hardness, with the preservation of plasticity.

3. Conclusion

Based on this research we can conclude that the proposed combined method of deformation "pressing-drawing" has a significant advantage compared to previously known methods of producing a metal with subultrafine structure, because this method of deformation due to the combining two ways: severe plastic deformation in the equal channel step die and drawing process through a drawing die, allows to obtain the workpieces (aluminum wire) of required dimensions and shape cross section, having subultrafine structure at insignificant number of cycles and also removes restrictions on the length of the initial workpiece, and hence allows to obtain finished products length of up to several tens of meters.

Also would like to note that this method of deformation when introducing it into production does not require significant economic investment and can be implemented in industrial enterprises of the country for the production of wire so that it does not require retrofitting of existing drawing mills. Because for implementation of this combined process only the addition requires in construction equipment, equal channel step die, intended for drawing through it the material.

4. Literature

- [1] Ma Z.Y., Liu F.C., Mishra R.S. Superplastic deformation mechanism of an ultrafine-grained aluminum alloy produced by friction stir processing, *Acta Materialia*, 2010, 58, p. 4693-4704.
- [2] Degtyarev M.V., Chashchukhina T.I., Voronova L.M., Patselov A.M., Pilyugin V.P. Influence of the relaxation processes on the structure formation in pure metals and alloys under high-pressure torsion, *Acta Mater*, 2007, 55, p. 6039–6050.
- [3] Kurapov G., Orlova E., Volokitina I., Turdaliev A. Plasticity as a physical-chemical process of deformation of crystalline solids, *Journal of Chemical Technology and Metallurgy*, 2016, 51, p. 451-457.
- [4] Lezhnev S., Volokitina I., Koinov T. Research of influence equal channel angular pressing on the microstructure of copper, *Journal of Chemical Technology and Metallurgy*, 2014, 49, p. 621-630.
- [5] M. Kawasakia, Z. Horitab, T. G. Langdona, Microstructural Evolution in High Purity Aluminum Processed by ECAP, *Materials Science and Engineering A*, 2009, p 143-150.
- [6] G. Raab, R. Valiev, T. Lowe, Y. Zhu, Continuous processing of ultrafine grained Al by ECAP-Conform, *Materials Science and Engineering*, 2004, 382, p 30-34.
- [7] Astafurova E.G., Zakharova G. G., Naydenkin E.V. Effect of equal channel angular pressing on the structure and mechanical properties of low carbon steel 10Г2ФТ, *FMM*, 2010, 3, p. 275-284. (In Russian).
- [8] Naizabekov A., Lezhnev S., Knapinski M., Kurapov G., Volokitina I.E. Research of influence equal channel angular pressing combined with a heat treatment on the microstructure of the steel 45. 24-th International Conference on metallurgy and materials METAL, Brno, Czech Republic. 2015, P. 125.
- [9] Naizabekov A.B., Lezhnev S.N., Volokitina I.E. Change in copper microstructure and mechanical properties with deformation in an equal channel stepped die, *Metal Science and Heat Treatment*, 2015, 57, p. 5-6.
- [10] Gleiter, H. Nanostructured materials: basic concepts and microstructure, *Acta Mater*. 2000, 48, p. 1-29.
- [11] Fakhretdinova E.I., Raab G.I., Ganiev M.M. Development of force parameters model for a new severe plastic deformation technique – Multi-ECAP-Conform, *Applied Mechanics and Materials*, 2015, 698, p. 386-390.
- [12] Raab G., Lapovok R. Modelling of Stress-Strain Distribution in ECAE by analytical-experimental method, *Ultrafine Grained Materials IV TMS Meeting*, 2006, 1, p. 189-194.
- [13] Kawasakia M., Horitab Z., Langdona T. G. Microstructural Evolution in High Purity Aluminum Processed by ECAP, *Materials Science and Engineering A*, 2009, 524, p. 143-150.
- [14] Chukin, M.V., Emaleeva, D.G.,. The influence of heat treatment on the evolution of the structure and properties of steel wire in the process of ECAP broaching. *Bulletin of the MSTU. G.I. Nosova* 2, 2008, p. 70-71
- [15] Lezhnev S., Naizabekov A., Panin E., Volokitina I. Influence of combined process "rolling-pressing" on microstructure and mechanical properties of copper, *Procedia Engineering*, 2014, 81, p. 1499-1505.

ROBUST BI-CRITERIA APPROACH TO OPTIMIZE THE COMPOSITION AND PROPERTIES OF MAGNESIUM ALLOY

Yordan Kalev Hai Hao¹ Nikolay Tontchev²

¹Dalian University of Technology (DUT): 大连理工大学

²Todor Kableshtov» Higher School of Transport, Sofia, Bulgaria

Abstract. The paper presents standard statistical robust bi-criteria procedure for determining expert assessments for the influence of magnesium alloy components on the controlled mechanical properties: tensile strength and relative elongation. There are obtained regression models describing mechanical characteristics from the amount of aluminum, manganese, nickel and silicon directly related to the exploitation properties of the product. The applied bi-criteria approach makes it possible to determine of compositions ensuring relatively optimal values of the explored quality indicators.

KEY WORDS. SIMULATION, MAGNESIUM ALLOYS, MODELING, OPTIMIZATION, METALLURGICAL DESIGN.

I. Introduction

Modern industry has to improve the parameters of creating products taking into account environmental and economic constraints. In this aspect competing magnesium companies need to have software tools and approaches to assist their activity in finding rational decisions related to the impact of composition and processing parameters on the final properties of the manufactured products. The possession of such tools helps to monitor and control production and technology change with reaching various technological properties of the final product. The creation of mathematical models to analyze the objects of metallurgical and casting process under examination is an important stage in achieving this goal. These models contribute to improve the set of properties and the final product quality. It is confirmed that it is possible to meet the requirements of the current market by implementation of such models. The wide range of problems, which Taguchi method has been applied to, is shown in [1].

The core of Taguchi approach consists of the method for reducing the influence of factors called noise (disturbing) that impair the quality parameters of the product/process. It is where the radical difference from the traditional technique of quality, which provides identification of existing sources and conduction of measurements that are often costly due to their control. The parametric design of Taguchi ensures non-sensitivity to noise along the way to the proper selection of certain parameters called controllable factors. The centerpiece of this approach is the method of reducing the impact of factors called noise that reduce the product/process quality parameters. It is where the radical difference from the traditional technique of quality, which provides identification of existing sources and conducting measurements often costly due to their control, lies. Taguchi parametric design ensures non-sensitivity to noise through a proper selection of certain parameters called controllable factors.

The aim of this paper is to present a robust approach for determining the influence of alloying elements on the properties of magnesium-based casing alloys that ensures better results than the input ones used to obtain a mathematical model.

The proposed approach facilitates the optimization of the magnesium alloy chemical composition improving the properties of the final product. These requirements generally are followed according to the standards but also may be associated with certain additional requirements claimed by users. All these pre-imposed conditions lead to a set of constraints that must be satisfied by acceptable solutions. Some restrictions can be defined as relations with true quantitative nature. This is especially important to restrictions on mechanical properties of the final product. Their proper formula is based on good mathematical models describing the effect of alloy composition and processing parameters on the

final properties of casting magnesium alloy. The statistical analysis of industrial data is an important and supporting alternative in such cases. That is why we have limited the field of study only to the influence of the chemical composition of the heat-treated alloys on the set of properties. In the context of the analysis of metallurgical processes, different methods to study the data described in the references can be found [2],[3] and [4].

The statistical analysis presented in this paper is based on of data collected during the real production process described in [5] and [6].

The ranges of change of the used alloying elements of ferrous alloys are listed in Table 1.

Table 1. Minimum and maximum values of alloying components

Input parameter	Chemical symbol	min [%]	max [%]
x ₁	Al	0.0	10.0
x ₂	Mn	0.0	1.5
x ₃	Zn	0.0	6.5
x ₄	Cu	0.0	2.7
x ₅	Ni	0.0	0.3
x ₆	Si	0.0	1.0

Regardless of that, the proposed optimization approach for modeling the final mechanical properties of alloys can be applied to any production process with steel manufacturing.

II. General description of the approach

The analysis presented in this paper is related to the analysis of mechanical properties of magnesium specimens described by the following parameters: tensile strength - R_m [MPa] and relative elongation - A [%]. The limitations connected with these parameters are due to magnesium grade characteristics and customer's specifications. However, the main problem is that these parameters cannot be under direct observation during the manufacturing process, so any limitations associated with them can not be clearly defined in the optimization model. That means that we must develop models linking the final mechanical properties of the specimen/sample of the steel chemical composition as all as the parameters of the production process.

The regression analysis allows describing the relation between the variables of input and output, without going into the phenomenon nature during the process.

The regression models presented below have been created based on the data collected during the industrial production process.

The statistical analysis described in this section is based on a data set of 53 records extracted from the whole database.

The Least Squares method, LS is used to estimate the regression parameters. The estimated models of parameters *Rm* and *A* obtained in the examinations are given below.

In respect to the problem under examination, nonlinear regression dependencies have been identified for each of the mechanical properties of magnesium alloys. The regression dependencies are of the following kind:

$$f_i(x) = b_0^i + \sum_{j=1}^6 b_j^i x_j + \sum_{j=1}^6 \sum_{l=j+1}^6 b_{jl}^i x_j x_l + \sum_{j=1}^6 b_{jj}^i x_j^2 \quad (1)$$

Here b_{ij} are the regression model parameters. The coefficients in equations are defined in Table 2. The models can be used for prediction if the check-up $F > F(0.5, v_1, v_2)$ described in details has been made.

Relation $(S/N) = \frac{\text{signal}}{\text{noise}}$ The effects of the factors are determined for each row, using the formula to minimize performance characteristics:

$$\frac{S}{N} = -10 \log \left(\frac{1}{n} \sum_{j=1}^n y_{ij}^2 \right) \quad (2),$$

for maximize

$$\frac{S}{N} = -10 \log \left(\frac{1}{n} \sum_{j=1}^n \frac{1}{y_{ij}^2} \right) \quad (3)$$

Table 2. Coefficients of regression models of the examined target parameters.

No	Coefficient	Rm [MPa]	A [MPa]
1	Free member	114.255	16.33366
2	X ₁	25.97015	0.6716988
3	X ₂	9.704941	-18.22966
4	X ₃	74.42215	-3.222518
5	X ₄	66.06575	12.28882
6	X ₅	3114.254	101.5687
7	X ₆	140.6771	12.65238
8	X ₁ X ₂	-0.4041829	-0.1963183
9	X ₁ X ₃	-1.084408	-0.006829805
10	X ₁ X ₄	-72.2078	-0.6545856
11	X ₁ X ₅	237.9817	9.555618
12	X ₁ X ₆	-0.7780583	0.1666764
13	X ₂ X ₃	-44.53689	2.326275
14	X ₂ X ₄	101.9566	-15.04205
15	X ₂ X ₅	1768.658	336.508
16	X ₂ X ₆	-36.39456	21.76996
17	X ₃ X ₄	0.7895336	0.1440411
18	X ₃ X ₅	-414.173	18.49442
19	X ₃ X ₆	-99.81348	0.05190802
20	X ₄ X ₅	2369.462	150.6452
21	X ₄ X ₆	138.7343	-61.84769
22	X ₅ X ₆	-2435.761	-121.6928
23	X ₁ ²	-1.798813	-0.1700993
24	X ₂ ²	53.00094	7.873145
25	X ₃ ²	-5.917203	0.3912327
26	X ₄ ²	-43.78463	-2.977206
27	X ₅ ²	-74966.48	-4711.342
28	X ₆ ²	-105.1666	-24.45902
	R	0.888	0.914
	F	3.449	4.684

The composition optimization is applied only in respect to yield strength *Rm* and respective elongation *A*.

Table 3. Orthogonal matrix I (27,13) developed by Taguchi with factors at three levels

Run	X1	X2	X3	X4	X5	X6	X7	X8	X9	X10	X11	X12	X13
1	1	1	1	1	1	1	1	1	1	1	1	1	1
2	1	1	1	1	2	2	2	2	2	2	2	2	2
3	1	1	1	1	3	3	3	3	3	3	3	3	3
4	1	2	2	2	1	1	1	2	2	2	3	3	3
5	1	2	2	2	2	2	2	3	3	3	1	1	1
6	1	2	2	2	3	3	3	1	1	1	2	2	2
7	1	3	3	3	1	1	1	3	3	3	2	2	2
8	1	3	3	3	2	2	2	1	1	1	3	3	3
9	1	3	3	3	3	3	3	2	2	2	1	1	1

10	2	1	2	3	1	2	3	1	2	3	1	2	3
11	2	1	2	3	2	3	1	2	3	1	2	3	1
12	2	1	2	3	3	1	2	3	1	2	3	1	2
13	2	2	3	1	1	2	3	2	3	1	3	1	2
14	2	2	3	1	2	3	1	3	1	2	1	2	3
15	2	2	3	1	3	1	2	1	2	3	2	3	1
16	2	3	1	2	1	2	3	3	1	2	2	3	1
17	2	3	1	2	2	3	1	1	2	3	3	1	2
18	2	3	1	2	3	1	2	2	3	1	1	2	3
19	3	1	3	2	1	3	2	1	3	2	1	3	2
20	3	1	3	2	2	1	3	2	1	3	2	1	3
21	3	1	3	2	3	2	1	3	2	1	3	2	1
22	3	2	1	3	1	3	2	2	1	3	3	2	1
23	3	2	1	3	2	1	3	3	2	1	1	3	2
24	3	2	1	3	3	2	1	1	3	2	2	1	3
25	3	3	2	1	1	3	2	3	2	1	2	1	3
26	3	3	2	1	2	1	3	1	3	2	3	2	1
27	3	3	2	1	3	2	1	2	1	3	1	3	2

By Taguchi methodology (Khosrow Dehnad, 1989) an experiment modeled on orthogonal matrices developed by him is carried out. The experiment can be accomplished in two ways by:

- a real experiment leading to obtaining results for processing;
- a numerical experiment with the presence of adequate regression models.

The availability of the described model coefficients, which can be used to predict, give a possibility to make a numerical experiment involving Taguchi method. The noise matrix is selected from orthogonal matrix I (27,13) with 27 rows and 13 columns developed by Taguchi. The matrix is worked out with factors at three levels – Table 3.

The methodology proposed is implemented for tensile strength Rm and relative elongation A. To take out the models of these two target functions, 53 experiments that form the data matrix A (53, 6 +1) have been used. Here the added column "1" is for the output target function Rm or A stored compactly in the matrix.

To optimize the computing process, the scheme, which having been processed for the particular case takes the following kind, is selected.

In numerical experiments that use models based on the chemical composition the noise can be expressed only in the change of the respective components. It is assumed to express noise Δ in the following way

$$\Delta_i = \frac{\bar{x}_i}{k} \text{ where further calculations are made for } k \text{ equal to } 100 \text{ and } 70.$$

Here \bar{x}_i is the mean value of relevant variable "i".

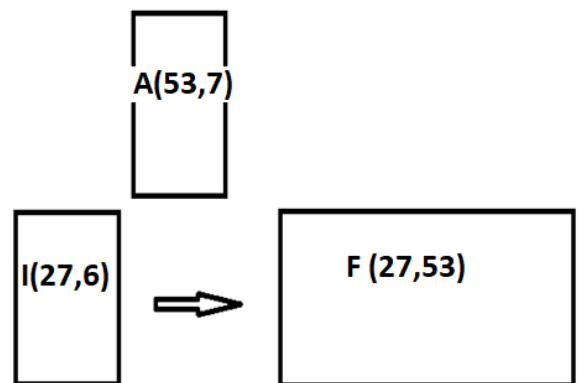


Fig.1. Organizing experiments with parametric planning with matrices I, A and F

For level "1" of I (27,6) noise is subtracted from relevant x_i taking the value of $x_i - \Delta_i$. With level "2" no correction is applied, the value of x_i is preserved. With level "3" noise is added to relevant x_i taking the value of $x_i + \Delta_i$. In numerical experiments where models based on chemical composition are used, noise can be expressed only in the change of the respective components. Noise Δ is

$\Delta_i = \frac{\bar{x}_i}{k}$, where the further calculations are made for k equal to 100

and 70. Here \bar{x}_i is the average value of the respective variable "i". In level "1" noise is subtracted from respective x_i taking the value of $x_i - \Delta_i$. In level "2" no correction is applied, the value of x_i is preserved. In level "3" noise is added to respective x_i taking the value of $x_i + \Delta_i$.

Thus, noise is expressed in the change of chemical composition. The calculation process is organized as follows:

A row of matrix I (27,6) is taken (for example, row 1 - I (1,6)). In this row level "1" is assigned for each x_i , i.e. noise will be taken out from each value x_i .

Thus F (1,1) of the matrix F (27,53) is obtained from the first row of A (53,7). The same rule is applied to the rest of the series F (53,6) and it forms F (27,53).

It is continued with the next row of matrix I (27,6) performing the following sequence. Each row of matrix I (27,6) forms a relevant row of matrix F (27,53).

Calculations are performed according to the following algorithm.

If we take the first column of matrix I (27,6) relevant to X_1 , it is evident that the first nine rows correspond to level "1" of noise, the second nine lines correspond to level "2" and the third nine rows correspond to level "3" of noise. This makes possible to use the values of the first nine rows of matrix F (27,53) to calculate level "1", to use the second nine rows to calculate level of "2" and the third nine rows for calculation at level "3" for X_1 . For other columns from 2 to 8 it is necessary to sort in ascending order X_i from I(27,6). After sorting the column obtains the kind of the first column.

After sorting of the respective variable, calculations for different levels can be made. It is continued with the next matrix row I (27,6) performing the following sequence. Each row of matrix I (27,6) forms a corresponding row of matrix F (27,53). If we take the first column of matrix I (27,6) corresponding to the X_1 , one can see that the first nine rows correspond to noise level "1" of noise, the second nine rows correspond to level "2" and the third nine rows correspond to noise level "3". That allows using the values of the first nine rows of matrix F (27,90) to calculate level "1", the second nine rows to calculate level "2" and the third nine rows to calculate level "3" for X_1 . For the rest columns from 2 to 6 it is necessary to sort by ascending order of X_i of I(27,6). After sorting the column takes the kind of the first column. With sorting, if shifts are made, they are reflected in matrix F (27,53). After sorting the corresponding variable it is possible to make calculations for different levels.

In the numerical experiment noise was first determined with K=70. The analysis of the graphics shows low sensitivity for both Rm and A. In these calculations, as shown in the Table 4.

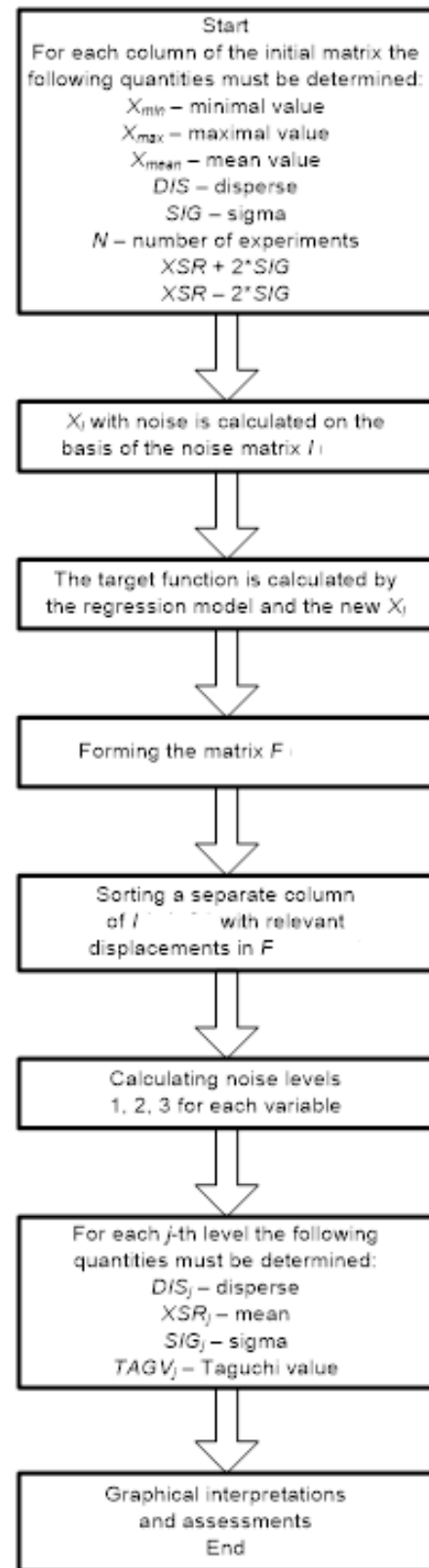


Fig. 2. Computational algorithm

The conclusion that can be made for the tensile strength – Rm is that all the factors have a significant effect on aluminum, manganese, zinc and nickel and it is expected they to change in the direction of decreasing values, and copper and silicon to increasing values. About the results for the relative elongation – A, from all six variables two of the variables - nickel and silicon – should not be changed, and the rest of the variables – aluminum, manganese, zinc and copper – need to change in the direction of increasing their

value. As the experiment is numerical, it is possible to perform numerical optimization with the mathematical models obtained as the values of X_i are remained to change within the limits defined by the output data (Table 1). That some of the variables remain unchanged, i.e. keep their initial values it imposes the necessity to separately carry out optimization for the chemical composition of each alloy. As a method of optimization, the method of Hook and Jives was chosen. This method is characterized as one of the best to solve problems with different parameters of the goal functions. Specifically, the tensile strength R_m is changed from X_1 , X_2 , X_3 , X_4 , X_5 and X_6 , and the relative elongation is varied from X_1 , X_2 , X_3 and X_4 .

Table 4. Levels of noise factors for the research parameters

Variable	Element of composition	Noise level	
		Rm	A
X_1	Al	1	3
X_2	Mn	1	3
X_3	Zn	1	3
X_4	Cu	3	3
X_5	Ni	1	2
X_6	Si	3	2

The fact that one of the variables does not change, i.e. they preserve their initial values requires optimization to be performed separately with chemical composition for each alloy. The ones mentioned, X_5 and X_6 , are maintained at their level, but are held by changing the rest. In this way, 53 optimizations are performed, with each case obtaining a separate value of the extremum. Then all maxima are sorted in ascending order and the largest is selected. With the values of the variables of the relative elongation, the value of the tensile strength R_m is calculated. Thus, the two-criteria approach is implemented. The optimal composition is shown in the table.

Al	Mn	Zn	Cu	Ni	Si
10.0%	1.5%	6.5%	2.7%	0.3%	1%

Such an approach is justified because the task, if viewed from the point of view of technology, is that individual optimization is the refinement of a separate actual alloy.

Optimization in this way coincides with the approach of searching for a global extremum from a set of starting points.

This outcome indicates that the task is feasible and the approach applied can result in improvement of the alloy composition.

III. Conclusion

The numerical experiment has proved the ability to improve the quality of magnesium alloy of a certain class. Mathematical models suitable for forecasting and optimization have been derived. The approach of Taguchi applied has led to a desired result, to separate variables X_i for the examined parameters that do not influence significantly on the final result. With this limit, the numerical optimization for maximum search has been conducted with each chemical composition. That allows improving it. Relative elongation A turned to be less variable index and tensile strength R_e requires caution with extreme selecting. The decision of bi-criteria problem set has been defined thus proving that the Taguchi approach is applicable to a similar class of problems.

References.

1. Tontchev N., Y. Kalev, (2013): Determining Influence of Alloying Elements on Properties of Alloys by Robust Experiment, MEST Journal, July, pp. 31 – 39.
2. Talar J., Data mining methods – application in metallurgy, Archives of Metallurgy and Materials 2, 52, 239-250 (2007).
3. Moravka J., K. Michalek, B. Chmiel, Statistical analysis of heats with targeted overheating realized in the EAF at Trinec Steelworks, Archives of Metallurgy and Materials 2, 53, 1-8 (2008).
4. Xie H.B., Z.Y. Jiang, X.H. Liu, G.D. Wang, A.K. Tieu, Prediction of coiling temperature on run-out table of hot strip mill using data mining, Journal of Materials Processing Technology 177, 121-125 (2006).
5. Kainer K.U. (Ed.) Magnesium Alloys and Technologies Wiley-VCH, 2003. 285.
6. Monteiro W.A. (Ed.) New Features on Magnesium Alloys, InTech, 2012. 174 p.
Czerwinski F. (Ed.) Magnesium Alloys: InTAe, 2014, 176 p

THE IMPACT OF ELECTRIC FIELD DISTRIBUTION DURING Ti – Al – C SYSTEM BLEND PREPARATION ON PHYSICAL-MECHANICAL PROPERTIES OF CONSOLIDATED MATERIALS

ВЛИЯНИЕ РАСПРЕДЕЛЕНИЯ ЭЛЕКТРИЧЕСКОГО ПОЛЯ ПРИ ПОДГОТОВКЕ ШИХТЫ СИСТЕМЫ Ti – Al – C НА ФИЗИКО-МЕХАНИЧЕСКИЕ СВОЙСТВА КОНСОЛИДИРОВАННЫХ МАТЕРИАЛОВ

Prof., Dr. of Science Sizonenko O, PhD Zaichenko A., Lypian Ye., PhD Prystash M, Torpakov A., PhD Trehub V.
Institute of Pulse Processes and Technologies of NAS of Ukraine – Mykolaiv, Ukraine, E-mail: sizonenko43@rambler.ru

Abstract: The possibility of control of efficiency of different factors of high voltage electric discharge (HVED) impact on Ti – Al – C powders system for aimed synthesis of dispersion-hardening components is shown. Nanolaminate-composite Ti_3AlC_2 – TiC with hardness of $HV5 = 7$ GPa, obtained by consolidation of blend of 85 % Ti + 15 % Al initial composition after HVED with the use of multi-point electrode system has needle structure of Ti_3AlC_2 ($a = 0.3068$ nm, $c = 1.844$ nm) with size up to 10 μ m, and TiC dispersion-hardening phase ($a = c = 4.4331$ nm) with particle size no more than 1 μ m is situated between grains of Ti_3AlC_2 . Dynamic strength of specimens depending on electrode system used during HVED treatment of blend varied in range from 160 to 620 MPa, Young modulus – from 13 to 22 GPa at deformation rate from 600 to 900 s^{-1} . Material has high levels of heat resistance, relative change of mass is no more, than 0.001.

KEYWORDS: ELECTROMAGNETIC FIELD, METAL-MATRIX COMPOSITE, POWDER MATERIAL, DISPERSE FILLER, HIGH VOLTAGE ELECTRIC DISCHARGE, POWDER METALLURGY, BLEND PREPARATION, ALUMINUM MATRIX COMPOSITES, PHASE COMPOSITION, SYNTHESIS, DISPERSION, MAX-PHASE

1. Introduction

Efficiency of the usage of high voltage electric discharge (HVED) for preparation of homogeneous highly disperse blend for production of metal-matrix composites (MMC) of different compositions was shown earlier in papers [1, 2]. The possibility of control of efficiency of different HVED impact factors for aimed synthesis of dispersion-hardening fillers was shown in work [2]. HVED treatment combines even distribution of interparticle discharges plasma and hydrodynamic impact, which intensifies processes of structure and phase formation.

It is shown in paper [3], that control of volumetric distribution of interparticle discharges plasma in powder is possible by control of electromagnetic field (EMF) by variation of electrode system construction, which can impact processes of structure and phase formation in treated blend.

The goal of present work is to study the impact of electrode system configuration on the distribution of plasma formations in “kerosene – powder” disperse system and on the properties of obtained blend and consolidated materials.

2. Preconditions and means for resolving the problem

Mixture of metal powders of PA-4 GOST 6058-73 (ПА-4 ГОСТ 6058-73) Aluminum powder (mean diameter 23 μ m) and TU U14-10-026-98 (ТУ У 14-10-026-98) Titanium powder (mean diameter 63 μ m) of 15 % Al : 85 % Ti mass relation was used as initial material.

HVED treatment was performed at experimental stand, which is described in detail in work [2]. Powder mixture was loaded into discharge chamber, then TS-1, GOST 11128-65 (ТС-1, ГОСТ 11128-65) kerosene was added (relation of disperse and continuous phases was 1:10 [4]). Specific treatment energy was 25 MJ/kg, which allowed synthesis of necessary for dispersion-hardening components synthesis quantity of nanocarbon as a result of hydrocarbon destruction under the impact of discharge channel plasma [4].

Consolidation of powder materials was performed at spark-plasma sintering (SPS) device [5] in vacuum by passage of superposition of direct and pulsating currents with 10 kHz

frequency at working voltage of 2 V. Powder was poured into MPG-6 (МПГ 6) graphite matrixes with inner diameter of 10 mm, pressure of blend pre-pressing was ~ 30 MPa and sintering pressure was ~ 60 MPa in all considered experiments. Measurement of specimens temperature during sintering was performed by standard K-type thermal couple. Al – Ti – C system specimens isothermal holding temperature was 1100 °C according to MAX-phases formation zones [6]. Specimens heating rate during consolidation was selected according to works [7, 8] and was 10 °C/s. According to work [9], it was determined that isothermal holding time has to be no more, than 3 min, in order to preserve ultrafine nanostructured phases during consolidation.

BIOLAM-I (БИОЛАМ-И) optical microscope with maximal magnification of $\times 1350$ and REMMA-102 (РЕММА-102) raster electron microscope with magnifications range from $\times 10$ to $\times 250000$ were used for analysis of powder particles morphology.

Studies of phase composition and crystal structure were performed by X-ray diffraction analysis using Rigaku Ultima IV X-ray diffraction meter ($Cu_{K\alpha}$ radiation). Vickers hardness was determined using IT 5010 (ИТ 5010) hardness meter.

Dynamic compression strength of specimens was studied using their compression diagrams, obtained by using experimental device for dynamic tests by Hopkinson-Kolsky method [10].

3. Results and discussion

Three types of electrode system (ES) construction were used during powders HVED treatment: “point – plane” (P – P), No. 1 (See Fig. 1, a) and two variants of “multipoint anode – plane” ES (MP – P), No. 2 and No. 3 ((See Fig. 1, b and c correspondingly).

It is worth noting, that cyclic formation gas-vapor cavity only in near-electrode zone while using ES No. 1 (see Fig. 1, a) leads to ejection of powder from chamber central part and leads to amplification of hydrodynamic impact. Yet, amplification of hydrodynamic impact leads to weakening of erosion (ablation) of particles due to decrease of solid phase concentration in chamber central part.

The picture of plasma formations distribution caused by No. 2 ES construction (see Fig. 1, b) is not qualitatively different from distribution, caused by No. 3 ES construction (see Fig. 1, c) – in both cases interparticle discharges plasma is almost evenly distributed in powder volume.

Due to cone shape of No. 3 ES, which follows the shape of chamber bottom, volumetric distribution of plasma formations is more even if compared to No. 2 ES.

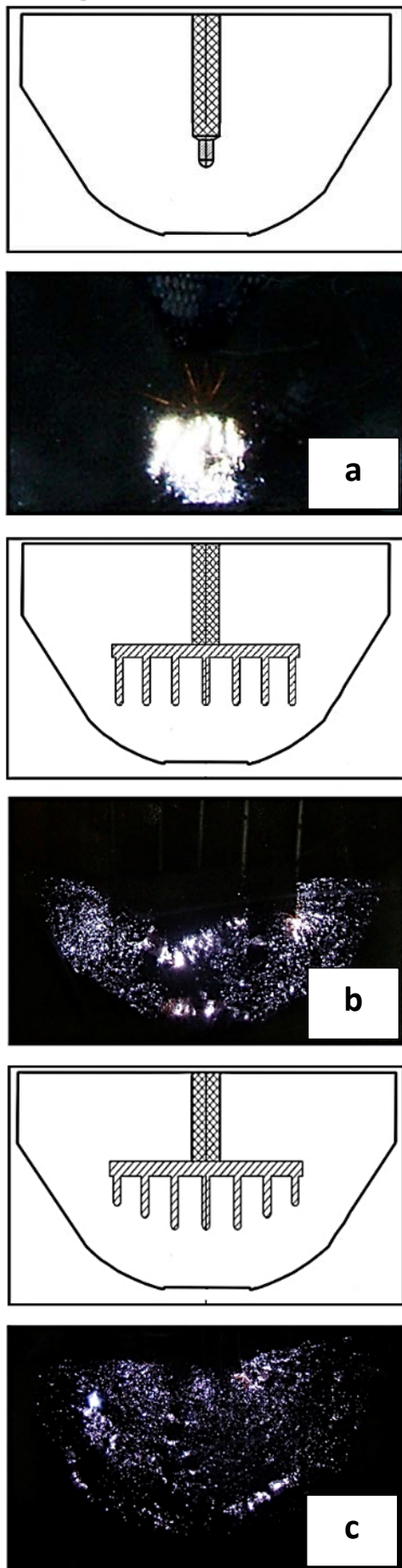


Fig. 1. Construction of electrode systems and plasma formations distribution

a – ES No. 1; *b* – ES No. 2; *c* – ES No. 3

The possibility of control of efficiency of different HVED factors impact on Ti–Al system for aimed synthesis of dispersion-hardening components (TiC titanium carbide, AlTi₃, AlTi, Al₂Ti, Al₃Ti, Ti₃AlC intermetallic compounds, Ti₃AlC₂ and Ti₂AlC MAX-phases and Lonsdaleite) by changing electric field configuration by using different types of ES was shown earlier in works [11, 12]. It was experimentally found out, that HVED treatment of Ti–Al powder systems (75 % Ti + 25 % Al, 50 % Ti + 50 % Al and 25 % Ti + 75 % Al) in kerosene leads to their dispersion, main peak of their size distribution moves to point of ~ 3 μm, and no less than 20 % of particles have size less than 1 μm.

As a result of HVED treatment of powder mixture of 85 % Ti + 15 % Al composition, considered in present work, particles mean diameter decreased ~ 4.5 times in case of ES No. 1 usage, and while using ES No. 2 and No. 3 dispersion efficiency decreases ~ 3 times. Change of phase composition also occurs TiC dispersion-hardening component is synthesized ($a = c = 4.329 \pm 0.003$ nm), intensity of its synthesis increases when using ES No. 2 and No. 3.

From practical point of view, it is important to study the impact of powder blend characteristics change due to the use of different ES types on consolidated materials properties.

SPS consolidation of blend, obtained while using ES No. 1, led to phase transformations in consolidated material – formation of TiC ($a = c = 0.86413 \pm 0.0015$ nm) and Al₃Ti ($a = 0.38512 \pm 0.0019$ nm, $c = 0.8607 \pm 0.0004$ nm) with the release of free Carbon (see Fig. 2). Large quantity of Carbon impacted the structure and hardness of obtained material. Carbon is uniformly distributed by specimen volume (see Fig. 2), creating dark zones with microhardness of 0.7 GPa and light zones with microhardness of 1.3 GPa. Vickers hardness of specimens was 0.9 GPa.

As a result of HVED treatment with the use of ES No. 2 and subsequent consolidation, formation of Ti₃AlC₂ ($a = c = 0.390 \pm 0.003$ nm) and Al₄C₃ ($a = 0.33357 \pm 0.00006$ nm, $c = 2.5288 \pm 0.0004$ nm) occurs, as well as absorption of Aluminum (see Fig. 3). This leads to formation of light zones with microhardness up to 11 GPa and gray zones of hardened Titanium with microhardness up to 8 GPa (see Fig. 3). Vickers hardness of obtained material was 5.28 GPa.

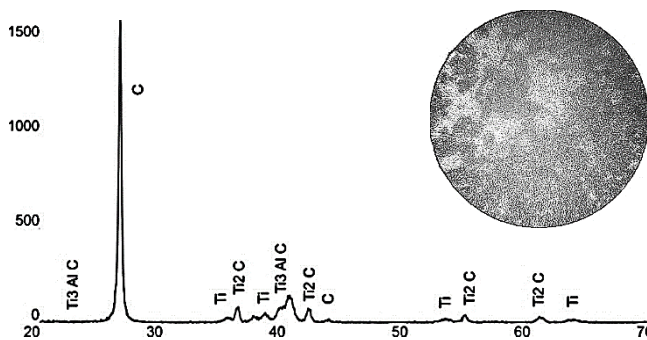


Fig. 2. Phase composition and structure (magnification ×250) of MMC, obtained from powder of 85 % Ti + 15 % Al initial composition after HVED treatment with the use of ES No. 1

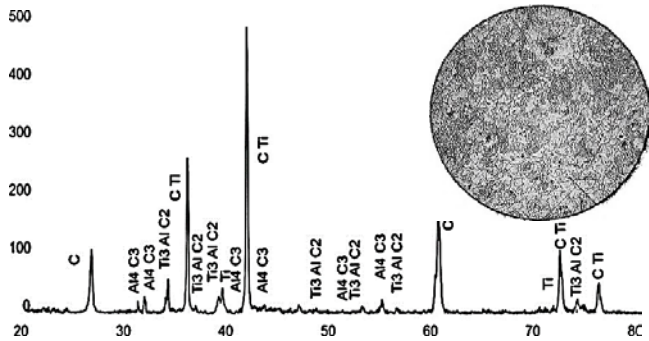


Fig. 3. Phase composition and structure (magnification $\times 250$) of MMC, obtained from powder of 85 % Ti + 15 % Al initial composition after HVED treatment with the use of ES No. 2

Metal-matrix composite, obtained from blend, prepared by HVED with the use of ES No. 3 consists of Ti_3AlC_2 ($a = c = 0.4131 \pm 0.0007$ nm) and Al_4C_3 ($a = 0.3344 \pm 0.0004$ nm, $c = 2.509 \pm 0.003$ nm) phases (see Fig. 4). Light zones with microhardness up to 13.8 GPa and gray zones of hardened Titanium with microhardness up to 7 GPa are formed in specimen structure (see Fig. 4). Vickers hardness of obtained nanolaminate-composite $Ti_3AlC_2 - TiC$ with homogeneous fine grain structure is 7 GPa.

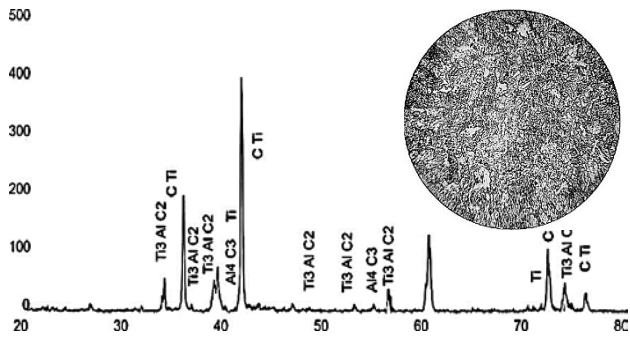


Fig. 4. Phase composition and structure (magnification $\times 250$) of MMC, obtained from powder of 85 % Ti + 15 % Al initial composition after HVED treatment with the use of ES No. 3

Materials, obtained from powder of 85 % Ti + 15 % Al initial composition after HVED treatment with the use of ES No. 3 have the highest hardness ($HV_5 = 7$ GPa) among considered specimens (see Fig. 5).

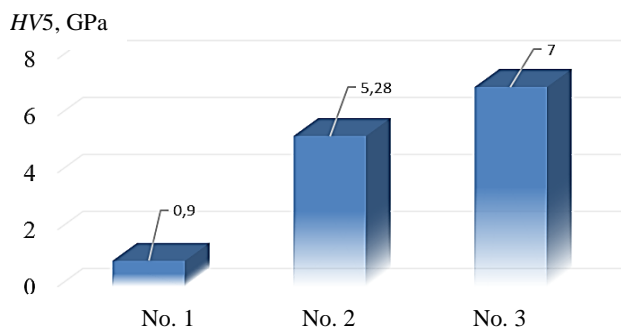


Fig. 5. Vickers hardness of MMC specimens, obtained by consolidation of blend of 85 % Ti + 15 % Al initial composition after HVED treatment with different ES types

Dynamic strength of specimens, obtained from blend after HVED treatment, depending on used ES type, varied in range from 280 MPa to 600 MPa (see Fig. 6), and Young modulus varied in range from 13 GPa to 22 GPa at deformation rate from 600 s^{-1} to 900 s^{-1} (see Fig. 7).

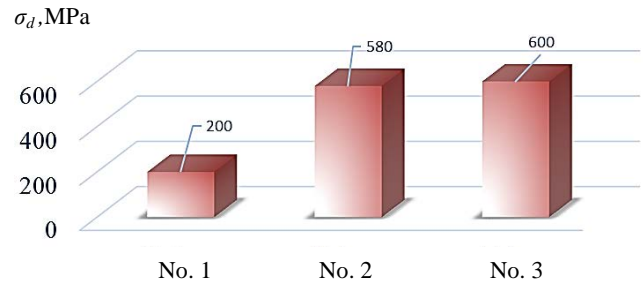


Fig. 6. Dynamic strength of MMC specimens, obtained by consolidation of blend of 85 % Ti + 15 % Al initial composition after HVED treatment with different ES types

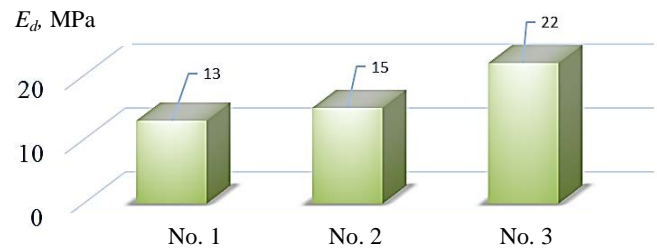


Fig. 7. Young modulus of MMC specimens, obtained by consolidation of blend of 85 % Ti + 15 % Al initial composition after HVED treatment with different ES types

Results of heat resistance studies show, that unbound Carbon has negative impact on heat resistance of composite, consolidated from blend after HVED treatment with ES No. 1. Relative mass change for such specimens was 0.09. Nanolaminate-composite $Ti_3AlC_2 - TiC$, obtained by consolidation of blend of 85 % Ti + 15 % Al initial composition after HVED treatment with ES No. 2 and No. 3, contrary to case of ES No. 1, have high values of heat resistance (see Fig. 8)

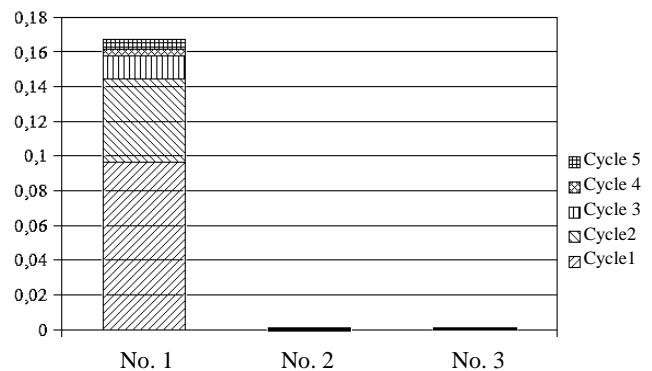


Fig. 8. Relative mass change of MMC specimens, obtained by consolidation of blend of 85 % Ti + 15 % Al initial composition after HVED treatment with different ES types

4. Conclusions

1. It is found out, that control of efficiency of different HVED impact factors for aimed synthesis of dispersion-hardening components is possible by changing EMF configuration due to use of different ES types.

2. Nanolaminate-composite $Ti_3AlC_2 - TiC$ with hardness of $HV5 = 7$ GPa) obtained by consolidation of blend of 85 % Ti + 15 % Al initial composition after HVED treatment with ES No. 3, has needle structure of Ti_3AlC_2 ($a = 0.3068$ nm, $c = 1.844$ nm) with size up to 10 μm , and TiC dispersion-hardening phase ($a = c = 4.4331$ nm) with particle size no more than 1 μm is situated between grains of Ti_3AlC_2 .

3. Dynamic strength of specimens, obtained from blend after HVED treatment, depending on used ES type, varied in range from 280 MPa to 600 MPa, and Young modulus varied in range from 13 GPa to 22 GPa at deformation rated from 600 s^{-1} to 900 s^{-1} .

4. Nanolaminate-composite $Ti_3AlC_2 - TiC$, obtained by consolidation of blend of 85 % Ti + 15 % Al initial composition after HVED treatment with ES No. 2 and No. 3, contrary to case of ES No. 1, have high values of heat resistance due to formation of fine grain hardened $Ti_3AlC_2 - TiC$ structure – relative mass change is 0.001.

5. Literature

1. Sizonenko O. N., G. A. Baglyuk, A. I. Raichenko, G. P. Bogatyreva, N. A. Oleinik, E. I. Taftai, E. V. Lipyanyan, A. S. Torpakov. Effect of high-voltage discharge on the particle size of hard alloy powders. – Powder Metallurgy and Metal Ceramics, Vol. 49, No. 11/12, 2011, P. 630–636.
2. Sizonenko O. N., G. A. Baglyuk, A. I. Raichenko, E. I. Taftai, E. V. Lipyanyan, A. D. Zaichenko, A. S. Torpakov, E. V. Guseva. Variation in the particle size of Fe–Ti– B_4C powders induced by high-voltage electrical discharge. – Powder Metallurgy and Metal Ceramics, Vol. 51, No. 3/4, 2012, P. 129–136.
3. Sizonenko O. N., V. A. Tregub, E. I. Taftay. Modelirovanie i analiz elektrorazryadnykh protsessov v sloe poroshka Ti v kerosine (Modeling and analysis of electric discharge processes in a layer of Ti powder in kerosene). – Visnyk Ukrainського Materialoznavchoho Tovarystva (Ukrainian Materials Research Society Bulletin), Iss. 7, 2014, P. 55–61. (In Russian).
4. Sizonenko O. N., A. Zaichenko, A. Torpakov, Ye. Lypian, S. Prokhorenko. Pulsed-discharged technology of metal-matrix composite materials obtainment. – Materials Science. Non-equilibrium phase transformations, Vol. 1, No. 1, P. 15–18.
5. Syzonenko O., A. Zaichenko, M. Prystash, A. Torpakov. The influence of the heating rate in the process of spark-plasma sintering on the kinetics of compaction, structure formation and properties of the materials of Fe–Ti–C–B system. – Materials Science. Non-equilibrium phase transformations, Vol. 2, Iss. 4, 2016, P. 3–5.
6. Zhang M. X., Y. A. Chang. Phase diagrams of Ti–Al–C, Ti–Y–O, Nb–Y–O, and Nb–Al–O at 1100 °C. – Journal of Phase Equilibria, Vol. 15, No. 5, 1994, P. 470–472.
7. Nordahl C. S., G. L. Messing. Transformation and densification of nanocrystalline θ -alumina during sinter forging. – Journal of the American Ceramic Society, Vol. 79, No. 12, 1996, P. 3149–3154.
8. Pristash N. S., O. N. Sizonenko, A. A. Kovalenko. Vliyanie skorosti nagreva v protsesse iskro-plazmennogo spekaniya na kinetiku uplotneniya i strukturoobrazovanie poroshka zheleza

(Influence of the heating rate in the process of spark-plasma sintering on the kinetics of compaction and the structure formation of iron powder). – Naukovi Notatky (Scientific Notes), Iss. 53, 2016, P. 126–129. (In Russian).

9. Ragulya A. V., V. V. Skorokhod. Konsolidirovannyye nanostrukturnyye materialy (Consolidated nanostructured materials), Kiev, Naukova dumka publ., 2007, 376 p. (In Russian).
10. Kolsky H. An investigation of mechanical properties of materials at very high rates of loading. – Proceedings of the Physics Society of London. Section B, Vol. 62, No 11. 1949, P. 676–700.
11. Torpakov, A. S., O. N. Sizonenko, E. V. Lipyanyan, E. V. Solodkiy. Vliyanie vysokovol'tnoy obrabotki poroshkovykh smesey systemy Al–Ti na izmenenie ikh morfologii i fazovogo sostava, in: Materialy dlya roboty v ekstremal'nykh umovakh–6 (Materials for use in extreme conditions-6), proc. of int. sci. conf., Kiev, 1–2 Dec 2016, P. 78–81. (In Russian).
12. Syzonenko O., E. Sheregii, S. Prokhorenko, A. Torpakov, Ye. V. Lypian. Method of preparation of blend for aluminium matrix composites by high voltage electric discharge. – Machines, Technologies, Materials, Vol. 11, Iss. 4, 2017, P. 171–173.

SOLIDIFICATION ON SURFACE

Ass. Prof. Eng. St. Bushev PhD.¹, Ass. Prof. Eng. I. Georgiev PhD.²
Bulgarian academy of sciences

¹ Institute of Metal Science, Equipment and Technologies With Hydro- and Aerodynamics Center „Acad. A. Balevski“

Sofia 1574, 67 „Shipchenski prohod“ blvd. Bulgaria

² Institute of Information and Communication Technologies
„Acad. G. Bonchev“ str. bl. 2 Sofia 1113 Bulgaria
and

² Institute of Mathematics and Information Technologies
„Acad. G. Bonchev“ str. bl. 8 Sofia 1113 Bulgaria
stbushev@abv.bg, ivan.georgiev@parallel.bas.bg

Abstract: This article uses mathematical models of tasks by Stefan and Stefan-Schwarz describing the technologies of IMSCHA "Acad. A. Balevski ". Described are processes for solidifying a drop (droplet) over a surface of a metal substrate. Processes of solidifying of metal melts in the form of spheres having a radius of 50 nm are described. The temperature fields of the open thermodynamic system drop / substrate system are presented. The influence of the change of specific parameters from the hardening process is represented by the type of the temperature field of the OTS.

Keywords: Stefan and Stefan-Schwarz problem, drop (droplet) on the surface of substrate, temperatures curves

1. Introduction – основен процес

In Fig. 1 is shown the solidification on surface process:

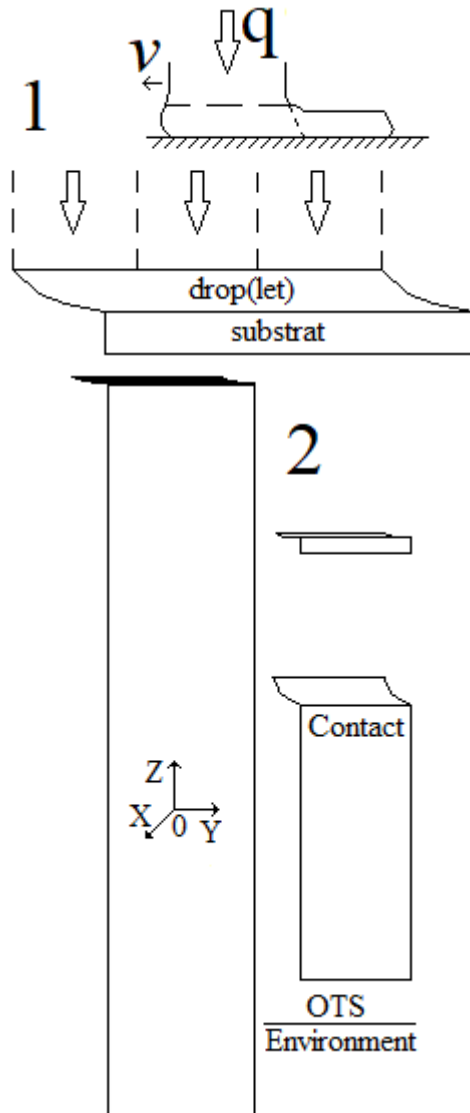
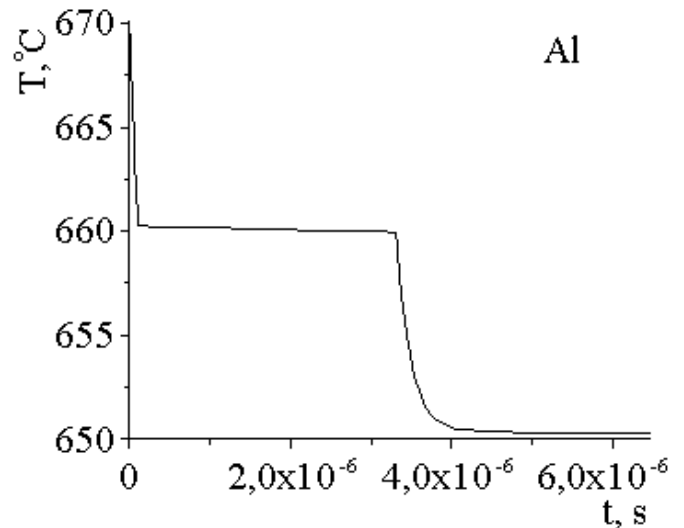
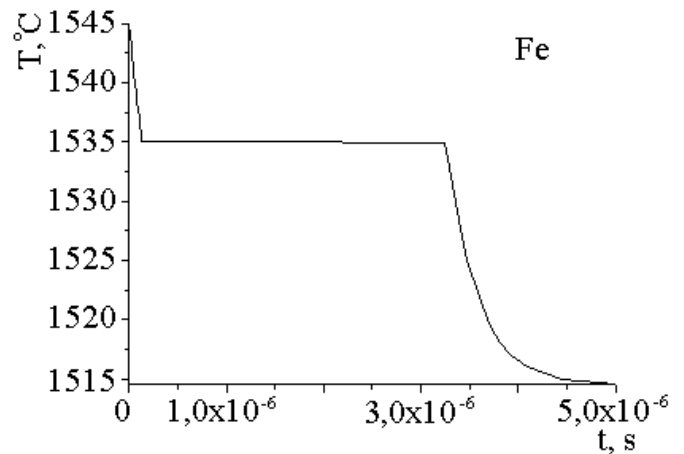


Fig. 1 Geometric idea by cross section of the open thermodynamic system (OTS) – drop (let) solidification on surface of the substrate: 1 – Physics: drop and flow of melt, v and q are velocity and stream; 2 – different size of system.

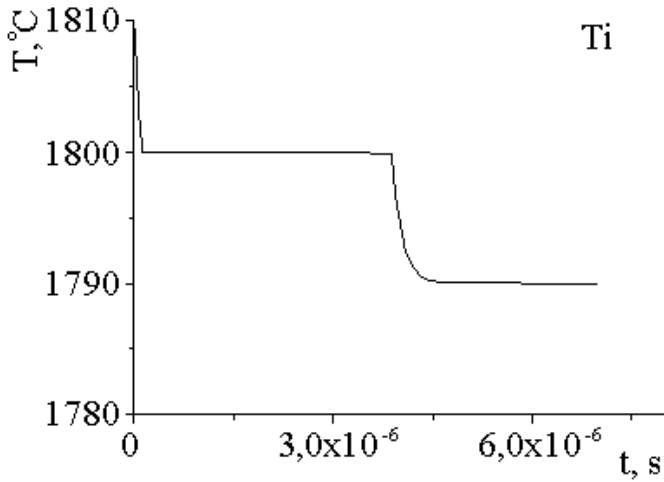
Figure 2 presents our results [20], supplemented by new ones. These are time-temperature curves of solidification of spheres of different materials with a radius $R = 50$ nm:



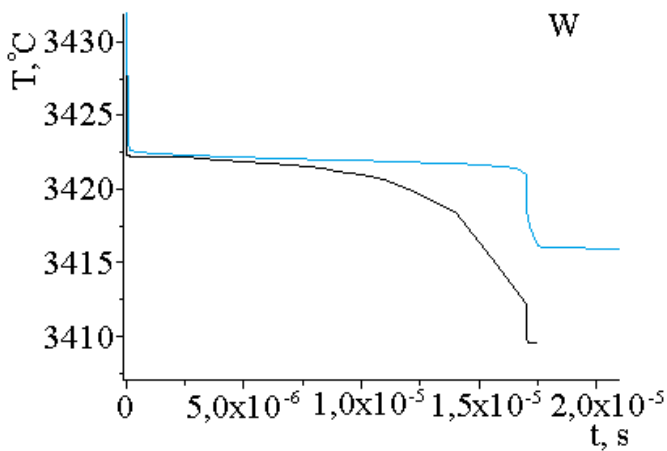
Pure Al: $T_m = 660, 1^\circ \text{C}$, latent heat of fusion at T_m is $Q_m = 401,819 \text{ kJ/m}^3$, heat conductivity $\lambda_S = 209 \text{ w/(m}^3 \cdot \text{K)}$ $\lambda_L = 104,675 \text{ w/(m}^3 \cdot \text{K)}$, heat capacity $c_S = 2540 \text{ kJ/(kg} \cdot \text{K)}$ $c_L = 2380 \text{ kJ/(kg} \cdot \text{K)}$, density $\rho_S = 2540 \text{ kg/m}^3$, $\rho_L = 2380 \text{ kg/m}^3$, index S – solid, index L – liquid;



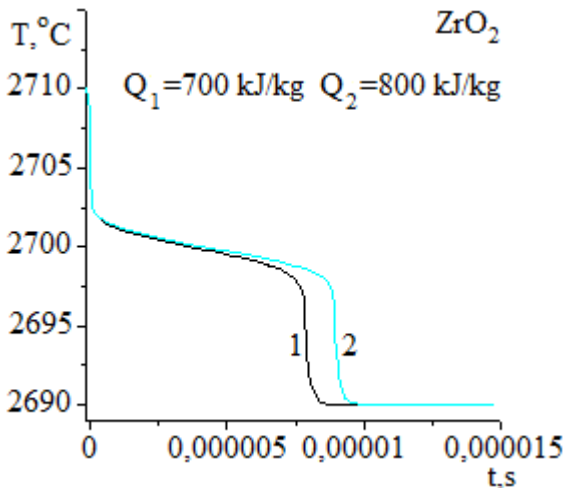
Pure Fe: $T_m = 1535^\circ \text{C}$, $Q_m = 272 \text{ kJ/m}^3$, $\lambda_S = 33 \text{ w/(m}^3 \cdot \text{K)}$ $\lambda_L = 29 \text{ w/(m}^3 \cdot \text{K)}$, $c_S = 447 \text{ kJ/(kg} \cdot \text{K)}$ $c_L = 800 \text{ kJ/(kg} \cdot \text{K)}$, $\rho_S = 7400 \text{ kg/m}^3$, $\rho_L = 7145 \text{ kg/m}^3$;



Pure Ti: $T_m = 1800^\circ\text{C}$, $Q_m = 376,810\text{ kJ/m}^3$, heat conductivity $\lambda_S = 22.5\text{ w/(m}^3\cdot\text{K)}$ $\lambda_L = 18\text{ w/(m}^3\cdot\text{K)}$, heat capacity $c_S = 523\text{ kJ/(kg}\cdot\text{K)}$ $c_L = 628\text{ kJ/(kg}\cdot\text{K)}$, density $\rho_S = 4540,6\text{ kg/m}^3$, $\rho_L = 4500\text{ kg/m}^3$, index S – solid, index L – liquid;



Pure W: $T_m = 3422^\circ\text{C}$, $Q_m = 255,390\text{ kJ/m}^3$, $\lambda_S = 196\text{ w/(m}^3\cdot\text{K)}$ $\lambda_L = 76,2\text{ w/(m}^3\cdot\text{K)}$, $c_S = 150,7\text{ kJ/(kg}\cdot\text{K)}$ $c_L = 152,8\text{ kJ/(kg}\cdot\text{K)}$, $\rho_S = 19300\text{ kg/m}^3$, $\rho_L = 19200\text{ kg/m}^3$. Important: the difference between the two curves is due to the precision of defining the parameters of the mathematical model of the heat source in Stephen's task [].



Material ZrO: $T_m = 2700^\circ\text{C}$, $Q_m = 700 \div 800\text{ kJ/m}^3$, $\lambda_S = 1.95\text{ w/(m}^3\cdot\text{K)}$ $\lambda_L = 2.44\text{ w/(m}^3\cdot\text{K)}$, $c_S = 730\text{ kJ/(kg}\cdot\text{K)}$ $c_L = 730\text{ kJ/(kg}\cdot\text{K)}$, $\rho_S = 3300\text{ kg/m}^3$, $\rho_L = 3200\text{ kg/m}^3$; curve 1 - $Q_m = 700\text{ kJ/m}^3$; 2 - $Q_m = 800\text{ kJ/m}^3$ [14].

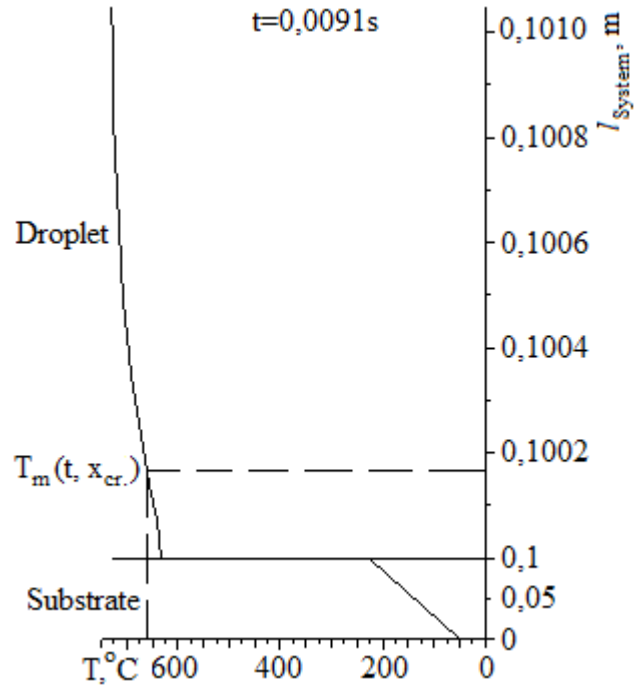
Fig. 2 Solidification of different materials – spheres of different materials with a radius $R = 50\text{ nm}$.

Mathematical models are based on the tasks of Stefan and Stefan-Schwarz, created and realized through non-commercial software products at IMSETCHA "Acad. A. Balevski "BAS [2, 3, 4,

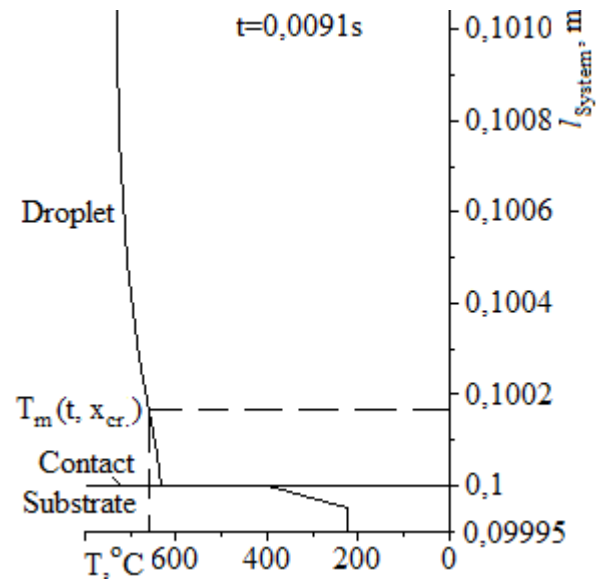
5 and 6]. The process of solidification (phase transition of first order) is fundamental in material science for obtaining structures bearing different working properties of the respective materials [1, 6]. The aim of this work is the calculation process of solidification a drop on different sizes on the surface of a metal substrate.

2. Numerical solutions - Stefan-Schwarz tasks

In Fig. 3 are introduced solidification temperature field by Finite elements method (FEM) of this task (see Fig.1):



Stefan-Schwarz temperature field: The geometry space of FEM is 3D but the temperature task in the direction of axis OZ is 1D;



Important: ccontact heat exchange with the temperature difference at the surface of the drop-substrate contact;

Fig. 3 Stefan-Schwarz temperature great OTS with size (substrate $x_{max}=0,02$, $y_{max}=0,02$, $z_{max}=0,1$) [m] and (drop $x_{max}=0,02$, $y_{max}=0,02$, $z_{max}=0,00105$) [m].

The results of Fig. 3 present the possibilities of computational mathematics and physics of non-stationary field of solidification (phase transition of first order) on a macro-scale. The technological parameters of the phase transition of first order i.e. the process of formation of the polycrystalline structure on a macro-scale.

The technological parameters of the hardening process are known for a long time or for the phase transition of the first

generation. We choose the parameter: the initial temperature field of the corresponding OTS $T(x, y, z, t = 0)$ and the coefficient of heat transfer at the contact surface α_c (see Fig. 1 and Fig. 2). In Fig. 4 we present the influence of these two parameters on the temperature field of the drop only:

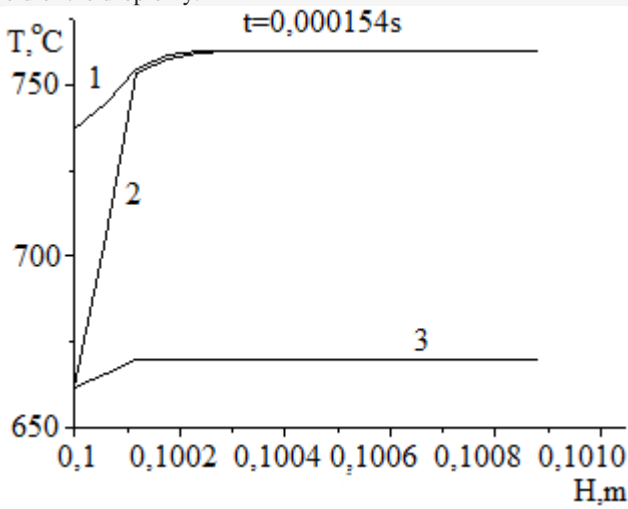


Fig. 4 Comparative analysis by the type of temperature field only at the drop by changing the initial melt temperature and by changing the coefficient of contact heat transfer: 1 $T_{drop}(x, y, z, 0) = 760, 1^\circ C, \alpha_c = 56000 \text{ w/m}^2 \text{ s}^\circ C$; 2 $T(x, y, z, 0) = 760, 1^\circ C, \alpha_c = 560000 \text{ w/m}^2 \text{ s}^\circ C$; 3 $T(x, y, z, t=0) = 670, 1^\circ C, \alpha_c = 56000 \text{ w/m}^2 \text{ s}^\circ C$.

From Fig. 4 clearly shows the influence on the type of the temperature field at time $t = 0.0091s$.

The thermophysical properties of the substrate have a definite effect on the phase transition of first order. For this reason, the following figures shows the influence of the temperature field in the droplet and the substrate in a small OTC with dimensions ($x_{max} = 0,00002 \text{ m}, y_{max} = 0,00002 \text{ m}, z_{substrate \ max} = 0,1$ and $z_{droplet} = 0,00105 \text{ m}$):

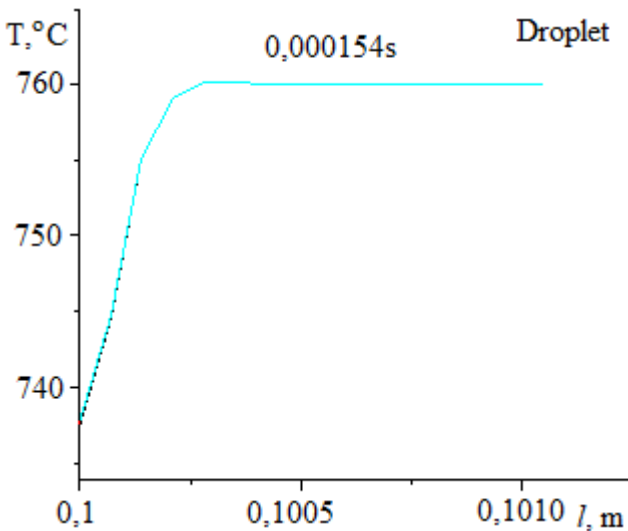


Fig. 5 Temperature fields of the droplet at time $t = 0,000154s$ steel (black line) and aluminum (blue line) substrates. Initial conditions are: $T_{drop}(x, y, z, 0) = 760, 1^\circ C, \alpha_c = 56000 \text{ w/m}^2 \text{ s}^\circ C$; 2 $T(x, y, z, 0) = 760, 1^\circ C$. The minimal effect is very clearly seen even at start time $t = 0,000154s$.

Here, we note that the thermophysical parameters of the substrate are part of the macro-level influence parameters.

Important: Your own substrate is related to modern technology called 3DPrinter.

On the following figure 6 presents a comparative analysis of the temperature fields of the OTC in substrates with different heat-physical properties (aluminum and steel substrates):

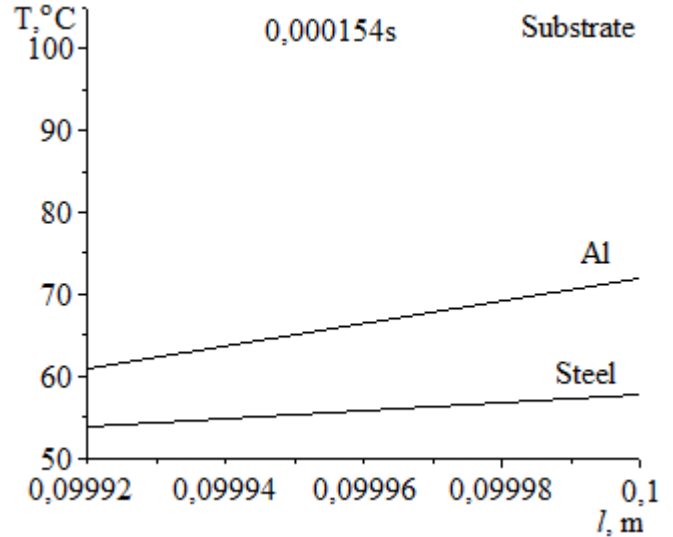


Fig. 6 Comparative analysis of temperature fields in substrates with different thermophysical properties in the case of Al and Steel. Initial conditions are: $T_{drop}(x, y, z, 0) = 760, 1^\circ C, \alpha_c = 56000 \text{ w/m}^2 \text{ s}^\circ C$; 2 $T(x, y, z, 0) = 760, 1^\circ C$. The minimal effect is very clearly seen even at start time $t = 0,000154s$.

From Fig. 6 shows the significant difference with the direct relationship to the contact heat exchange, namely the influence of the surface temperature of the contact substrate/droplet.

The results obtained relate to different technological processes. Stefan Schwarz's main task allows him to develop as a connecting task with mathematical and mathematical physics tasks. The latter are related to lower levels. These ideas have been developed in various studies by many authors.

Stephen-Schwartz's task is the natural aggregate mathematical approach to describe technological processes in phase transitions of first and secondary order. Material science has evolved as an interdisciplinary field of study [7, 8, 9 and 10]. The next figure presents the multi-scale linking possibility of heat conduction theory and mathematical modeling [2, 3, 4, 5, 6, 11, 12 and 13]:

LEVELS OF DESCRIPTION OF PHASE TRANSITION OF FIRST AND SECONDARY ORDERS

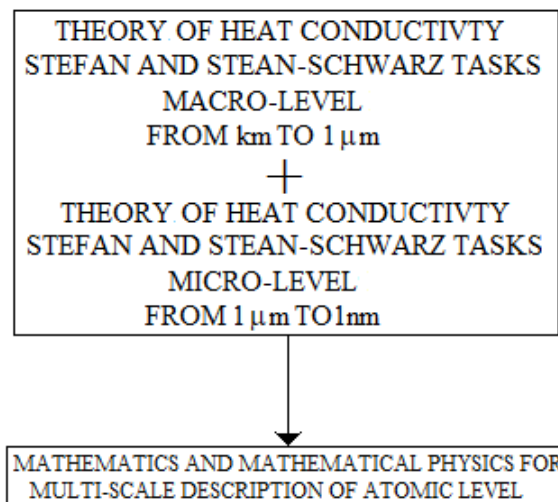


Fig. 7 Multi-scales description of phase transition of first and secondary orders by Stefan-Schwartz tasks + Mathematics and mathematical physics.

According to the principles of material science [7, 8, 9 and 10] and mathematical modeling [2, 3, 4, 5, 6, 11, 12 and 13], a methodology for Basic Knowledge is proposed: Methodology for Basic Knowledge is proposed: 1. General evaluation of the structure (on the meso-level) and the properties of the material; 2. Select a section of mathematics and mathematical physics for multi-scale

description; 3. A specific mathematical model of the structure, with the working properties, the technological process, the work and the life of the material. A very important point is the use of this methodological frame work for the additive capabilities of the 3Dprinter [15, 16 and 17] technology i.e. *3Dprinter interaction with die casting and heat treatment*. 3Dprinter + die casting + heat treatment are an essential task of Industry 4.0 [1]. Mathematical modeling in Industry4.0, in our view, is close to pure mathematics [6]. Such an assumption can be accepted on the basis of works [2, 3, 4, 5, 6, 11, 12, 13, 18 and 19]. The 3Dprinter technology has a great application (from food, medicine and weapons) and is an incentive for its mathematical modeling [17 and 18].

Additive manufacturing AM [15] is a concept that covers: casting, separation of metal turning, milling, plastic deformation, welding, forging and electroerosion processing heat treatment. But at the end of the 20th century new technologies for depositing materials such as micro-casting [21] and spraying were developed at Stanford University and Carnegie Mellon University [22]. 3DPrinter modifies the AM concept by expanding its idea of sequentially adding and linking material sequentially, following a three-dimensional profile of the blank, with automated control [15].

Significant results have been achieved with 3D printer technologies [23, 24 and 25]. The reason for the powerful entry of a 3D printer is the good price that falls great convenience to work with full control of the technology. This makes the 3D printer actually leading the Industry 4.0 revolution [1].

3. Conclusions

The obtained results represent the broad application of Stefanov type tasks in macro and nano-scale areas.

4. References

1. K. Schwab, The fourth industrial revolution, Hermes, Plovdiv, 2016. ISBN 978-954-26-1630-6
2. S. Bushev, M. Dimitrov, N. Miloshev, S. Stefanov, N. Stoichev, V. Todorov. Generalized Description of Microphenomena and Processes for Use in Various Technological Systems, Proceedings of Mini-symposium "MICRO-FLOWS" 10th Jubilee National Congress on Theoretical Applied Mechanics, 13 – 16 September, 2005, Bulgaria, 408-413.
3. S. Bushev, N. Stoichev, M. Dimitrov, N. Miloshev, Stefan's problem in modeling the metals rapid solidification, Proc. of Fifth International Congress Mechanical Engineering Technologies'06, September 20-23.2006, Varna, Bulgaria, 8-11.
4. S. Bushev, Computational physics – casting and heat treatment, Proceedings of "Fifth National Conference with International Participation Materials Science, Hydro- and Aerodynamics and National Security'2015", 22-23, October, 2015, Sofia, 170-177, ISSN 1313-8308.
5. S. Bushev, N. Stoichev, N. Miloshev, M. Dimitrov, V. Todorov, Temperature Field and Crystallization During Solidification of Liquids, Journal of Materials Science and Technology, v. 18, 2010, No 4, 228-239.
6. S. Bushev, Industrial mathematics –phase transitions, scattering, structures, Innovations, year V, ISSUE 2/2017, Sofia, 57-63. ISSN PRINT 1314-8907
7. W.D. Callister, Jr., Fundamentals of Materials Science and Engineering, 2001, John Wiley & Sons, Inc., Fifth Edition, CD-ROM. ISBN 0-471-39551-X
8. Materials science -Wikipedia,
https://en.wikipedia.org/wiki/Materials_science
9. Material science,
<https://bg.wikipedia.org/wiki/Материалознание> (In Bulgarian)
10. The Ten Principles of Material Handling–Material Handling Institute (MHI)
www.mhi.org/downloads/learning/cicmhe/.../10_principles.pdf
11. Mathematical Modeling Handbook II: The Assessments, The Consortium for Mathematics and Its Applications Bedford, MA 01730, 2013, USA,
www.comap.com/product/samples/MHBII-DRAFT.pdf
12. S. Heinz, Mathematical modeling, Springer-Verlag Berlin Heidelberg, 2011.
13. K. Velten, Mathematical Modeling and Simulation: Introduction for Scientists and Engineers, WILEY-VCH Verlag GmbH & Co. KGaA, Weinheim, 2009. ISBN: 978-3-527-40758-8
14. <https://www.azom.com/properties.aspx?ArticleID=133>
15. 3DPrinter www.etiket.bg/bg/news-view/40.html
16. 3D printers for direct printing in metal (In Bulgarian)
www.spacecad.bg/printeri-za-metal
17. Second National Forum "3D Printing - the Precursor of the 4th Industrial Revolution", March 16, 2017, Sofia, Bulgaria, (In Bulgarian),
www.computerworld.bg/50916_aditivnoto_proizvodstvo_i_3d_pech_atat...
18. I. Akinola, Modelling the Stereo-lithography Process, Electrical Engineering, Stanford University, iakinola@stanford.edu
19. A. Anastasiou et al., 3D Printing: Basic concepts Mathematics and Technologies... - Semantic Scholar,
<https://pdfs.semanticscholar.org/.../7486320e82081935ac20bc...>
20. S. Bushev, Material science theory in Industry 4.0 for phase transition technologies, 12th Annual Meeting of the Bulgarian Section of SIAM "BGSIAM'17", December 20.-22, 2017, Sofia, 20-21.
21. C. H. Amon, et al. Shape Deposition Manufacturing With Microcasting: Processing, Thermal and Mechanical Issues. // Journal of Manufacturing Science and Engineering 120 (3). 1998.
<https://pdfs.semanticscholar.org/7a7a/6961f6dac7861db7de51e7680e9990a09e85.pdf>
22. Beck, J.E. и др. Manufacturing Mechatronics Using Thermal Spray Shape Deposition. // Proceedings of the 1992 Solid Freeform Fabrication Symposium. 1992.
<https://pdfs.semanticscholar.org/c27c/50c0061aac1b842636cf5d0ad711195f5fb6.pdf>
23. Military aircraft "Tornado" with metal parts, printed in 3D, made a successful test flight, www.bnr.bg/.../voenen-samole-tornado-s-metalni-chasti-otpechatani-s-3d-printer-e-napravit-
24. General Electric: <https://bg.id-forex.com/general-electric-aircraft-engine-on-3d-printer>
25. [www.geomedia.bg/.../5251-...airbuse"-with-first-in-the-world-airplkane-printed-of-3d-pr...](http://www.geomedia.bg/.../5251-...airbuse)